DOC.20040301.0004

OCRWM	MODEL COVER SHEET	1. QA: QA Page 1 of 264

2. Type of Mathematical Model:

☒ Process Model ☒ Abstraction Model ☐ System Model

Describe Intended Use of Model:

This model provides thermohydrologic information and data for other reports supporting License Application.

3. Title:

Multiscale Thermohydrologic Model

4. DI (including Rev. No. and Change No., if applicable):

ANL-EBS-MD-000049 Rev 01

5. Total Attachments:	6. Attachment Numbers - No. of Pages in Each:
Nine (9)	I-16; II-6; III-4; IV-24; V-20; VI-4; VII-6; VIII-6; IX-14

	Printed Name	Signature	Date
7. Originator:	Thomas A. Buscheck	SIGNATURE ON FILE	2/25/04
8. CSO:	Bruce E. Kirstein	SIGNATURE ON FILE	2/24/04
9. Checker:	James T. Kam	SIGNATURE ON FILE	2/25/04
10. QER:	Darrell K. Svalstad	SIGNATURE ON FILE	2/26/04
11. Responsible Manager/Lead:	Ernest L. Hardin	SIGNATURE ON FILE	2/26/04
12. Responsible Manager:	Robert W. Andrews (Acting)	SIGNATURE ON FILE	2/26/04

13. Remarks:

2. Title:

Multiscale Thermohydrologic Model

3. DI (including Rev. No. and Change No., if applicable):

ANL-EBS-MD-000049 Rev 01

4. Revision / Change Number:	5. Description of Revision/Change:
00	Original issue. Supported TSPA-SR, Rev 00 for the Backfill Case. Used 1.54 kW/m line load.
00 ICN 01	This ICN was developed to include the No Backfill Case supporting TSPA-SR Rev 00 ICN 01. The DTN:SN9908T0872799.004 references were removed. The data and inputs were referenced to updated DTNs and references, or entered as assumptions. Revised invert thermal conductivity values and an adjusted heat load of 1.45 kW/m were used for the no-backfill case.
00 ICN 02	This ICN was developed to address the NRC KTI Agreement TEF 2.9 and show the influence of drift-scale fracture heterogeneity on TH behavior for the No Backfill Case. This was accomplished with the use of the 3-D heterogeneous Line-averaged-heat-source Drift-scale TH (LDTH) model, which was developed for this ICN, and which is completely described in Section 6.14. The 3-D heterogeneous LDTH model is based on the 2-D homogeneous LDTH model. The data and inputs were referenced to updated DTNs and references, or entered as assumptions. Section 7 has also been updated to include the conclusions developed from the 3-D heterogeneous LDTH model. A postprocessor, XLDTH, was developed and used to address the influence of drift-scale heterogeneity of fracture properties as described above. This postprocessor is qualified in accordance with the currently approved version of AP-SI.1Q, Software Management. Deficiency Report LVMO-00-D-039, Inaccurate Documentation and Validation of Software Routines and/or Macros, identified software issues that are addressed in MOL.20010910.0181 (Schreiner, R.L. 2001; Stand Alone DR-39 package for ANL-EBS-MD-000049, Rev. 00, ICN01, Multiscale Thermohydrologic Model). Attachment I contains a cross-walk between attachments in the Stand Alone Package and the attachments formerly included in this AMR. The Stand Alone package provides additional software documentation, e.g., source code listings, validation text files, input/output files and other corrections for routines formerly documented in Attachments I through XVII and XIX through XX of ICN 01 of this AMR. Attachment II in this ICN 02 lists files supporting each version of this document, including the file lists previously documented in Attachment XVIII of ICN 01. ICN 02 also addresses in Section 2 the issues and concerns identified in Deficiency Report BSC-01-D-100, pertaining to control of electronic information. ICN 02 also addresses NRC KTI agreements pertinent to this AMR, in Section 1. The following sections have been affected by this ICN: Section 1, Section 2, Section 3, Section 4, Section 5, Section 6, Section 7, Section 8, Attachment I and Attachment II
01	Complete revision to support TSPA-LA.

EXECUTIVE SUMMARY

For the Yucca Mountain geologic repository for high-level nuclear waste, the planned method of disposal involves the emplacement of cylindrical packages containing the waste inside horizontal tunnels, called emplacement drifts, bored several hundred meters below the ground surface. The emplacement drifts reside in highly fractured, partially saturated volcanic tuff. An important phenomenological consideration for the licensing of the repository is the generation of decay heat by the emplaced waste and the consequences of this decay heat. Changes in temperature will affect the hydrologic and chemical environment at Yucca Mountain. A thermohydrologic-modeling tool is necessary to support the performance assessment of the engineered barrier system of the repository. This modeling tool must simultaneously account for processes occurring at a scale of a few tens of centimeters around individual waste packages, for processes occurring around the emplacement drifts themselves, and for processes occurring at the multikilometer scale of the mountain. Additionally, many other features must be considered including nonisothermal, multiphase-flow in fractured porous rock of variable liquid-phase saturation and thermal radiation and convection in open cavities.

The Multiscale Thermohydrologic Model (MSTHM) calculates the following thermohydrologic variables: temperature, relative humidity, liquid-phase saturation, evaporation rate, air-mass fraction, gas-phase pressure, capillary pressure, and liquid- and gas-phase fluxes. The thermohydrologic variables are determined as a function of position along each of the emplacement drifts in the repository and as a function of waste package type. These variables are determined at various generic locations within the emplacement drifts, including the waste package and drip-shield surfaces and in the invert; they are also determined at various generic locations in the adjoining host rock; these variables are determined every 20 m for each emplacement drift in the repository. The MSTHM accounts for three-dimensional drift-scale and mountain-scale heat flow and captures the influence of the key engineering-design variables and natural system factors effecting thermohydrologic conditions in the emplacement drifts and adjoining host rock:

- Repository–scale variability of percolation flux
- Temporal variability of percolation flux (as influenced by climate change)
- Uncertainty in percolation flux (as addressed by the low-, mean, and high-percolation flux cases)
- Repository–scale variability in thermal properties (notably thermal conductivity)
- Repository–scale variability in hydrologic properties (with an emphasis on those that influence matrix imbibition and capillary wicking in fractures)
- Repository–scale variability in overburden thickness
- Edge–cooling effect (which increases with proximity to the edge of the repository)

- Dimensions and properties of the engineered barrier system components (waste packages, drip shield, and invert)
- Variability in heat-generation rate of waste packages
- Time- and distance-dependent heat-removal efficiency of preclosure drift ventilation.

There are several ways in which multiscale thermohydrologic problems might be addressed. The most straightforward method would be to create a monolithic thermohydrologic model that accounts for the entire repository system at all scales including representation of all emplacement drifts. Such a model, however, would bear overwhelming computational costs. The modeling approach presented herein is the MSTHM. The MSTHM is more than an efficient equivalent of a monolithic model. The advantage of the MSTHM approach is that it breaks the problem into smaller tractable pieces. Taking advantage of the linear nature of thermal conduction, the results of three-dimensional mountain-scale and three-dimensional drift-scale thermal models can be superimposed onto those of two-dimensional drift-scale thermohydrologic models. By dividing the problem, detailed three-dimensional heat-flow at the mountain and drift scales are modeled independently of more complicated thermal and hydrologic interactions modeled in two dimensions at the drift scale. Additionally the MSTHM is consistent with the unsaturated-zone hydrology model for Yucca Mountain.

This report describes MSTHM calculations conducted to support the Total System Performance Assessment for the License Application (TSPA-LA) base case. Throughout this report the term "TSPA-LA base case" is used to refer to the preliminary feed to the planned TSPA-LA base case. The MSTHM provides input to process models and abstractions addressing the following:

- General corrosion of the waste package
- Localized corrosion of the waste package
- Waste-form degradation
- Radionuclide solubility
- In-drift seepage evolution and thermal seepage
- Dust-leachate evolution
- Radionuclide transport in the Engineered Barrier System

This report addresses the impact of parameter uncertainty of key input variables. To address the impact of percolation flux uncertainty, MSTHM simulations are conducted for three (lower-bound, mean, and upper-bound) infiltration flux cases; additional cases are run to address the possibility of flow focusing of percolation flux. The impact of parameter uncertainty of thermal properties is also addressed with an emphasis on thermal conductivity in the repository host-rock units. For the purpose of model-confidence building, results from the MSTHM are compared against those from a mountain-scale thermohydrologic model, which is an alternative conceptual model. The validation of the MSTHM is systematically addressed in multiple stages, including those utilizing results from field-scale thermal tests.

CONTENTS

Page

CONTENTS (Continued)

Page

CONTENTS (Continued)

Page

INTENTIONALLY LEFT BLANK

FIGURES

Page

FIGURES (Continued)

Page

FIGURES (Continued)

Page

FIGURES (Continued)

Page

FIGURES (Continued)

Page

FIGURES (Continued)

Page

FIGURES (Continued)

Page

FIGURES (Continued)

Page

FIGURES (Continued)

Page

FIGURES (Continued)

Page

FIGURES (Continued)

Page

FIGURES (Continued)

Page

FIGURES (Continued)

Page

FIGURES (Continued)

Page

TABLES

Page

TABLES (Continued)

Page

TABLES (Continued)

Page

TABLES (Continued)

Page

TABLES (Continued)

Page

INTENTIONALLY LEFT BLANK

ACRONYMS

AC	acceptance criteria
AP	absorber plate
AML	areal mass loading (mass of spent nuclear fuel and high-level waste per unit area of heated repository footprint MTU/acre)
BWR	boiling water reactor (in reference to a waste package type)
CR	control rod
CSNF	commercial spent nuclear fuel (in reference to a waste package type)
DDT	Discrete-heat-source, Drift-scale, Thermal-conduction submodel of the MSTHM (a three-dimensional NUFT model)
DHLW	DOE-owned high-level radioactive waste
DKM	Dual Permeability Model
DMTH	Discrete-heat-source, Mountain-scale, Thermohydrologic model (result of the MSTHM)
DOE	U.S. Department of Energy
D/LMTH	Discrete/Line-averaged-heat-source, Mountain-scale, Thermohydrologic model (a monolithic three-dimensional NUFT model, using a nested mesh)
DST	Drift Scale Test
DTN	Data Tracking Number
FEP	feature, event, or process
HLW	high-level radioactive waste (in reference to a waste package type)
LANL	Los Alamos National Laboratory
LBNL	Lawrence Berkeley National Laboratory
LBT	Large Block (Thermal) Test
LDTH	Line-averaged-heat-source, Drift-scale, Thermohydrologic submodel of the MSTHM; this submodel is a two-dimensional NUFT submodel
LMTH	Line-averaged-heat-source, Mountain-scale, Thermohydrologic model (an intermediate result of the MSTHM)
LPD	Linear Power Density (kW/m)
MSTHAC	Multiscale Thermohydrologic Abstraction Code
MSTHM	Multiscale Thermohydrologic Model
MTU	metric tons of uranium (measure of mass of radioactive waste, which is also a measure of the thermal power loading (1 MTU = 1.323 kW))
NRC	U.S. Nuclear Regulatory Commission
PWR	pressurized water reactor (in reference to a waste package type)
RH	Relative Humidity

QA	Quality Assurance
RTD	Resistance Temperature Device (used in the field thermal tests, including the Large Block Test and Drift Scale Test)
SDT	Smeared-heat-source, Drift-scale, Thermal-conduction submodel (a one-dimensional NUFT model)
SMT	Smeared-heat-source, Mountain-scale, Thermal-conduction submodel (this submodel is a three-dimensional NUFT model)
SNF	spent nuclear fuel
SNL	Sandia National Laboratory
TSPA	Total System Performance Assessment
TSPA-LA	Total System Performance Assessment for the License Application
TSPA-SR	Total System Performance Assessment for the Site Recommendation
TSPA-VA	Total System Performance Assessment for the Viability Assessment
UZ	Unsaturated Zone
WAPDEG	Waste Package Degradation (Model)

1. PURPOSE

The purpose of the Multiscale Thermohydrologic Model (MSTHM) is to predict the evolution of thermohydrologic conditions in the repository emplacement drifts, also called the engineered barrier system, and in the adjoining host rock for the repository at Yucca Mountain. The MSTHM calculates the following thermohydrologic variables: temperature, relative humidity, liquid-phase saturation, evaporation rate, air-mass fraction, gas-phase pressure, capillary pressure, and liquid- and gas-phase fluxes (Table 1-1). These thermohydrologic variables are required to support the Total System Performance Assessment for the License Application (TSPA-LA) base case. Throughout this report the term "TSPA-LA base case" is used to refer to the preliminary feed to the planned TSPA-LA base case. The thermohydrologic variables are determined as a function of position along each of the emplacement drifts in the repository and as a function of waste package type. These variables are determined at various generic locations within the emplacement drifts, including the waste package and drip-shield surfaces and in the invert. The variables are also determined at various generic locations in the adjoining host rock; these variables are determined every 20 m for each emplacement drift in the repository. The primary objectives of the MSTHM simulations are to provide the downstream process models and model abstractions with the thermohydrologic variables (as a function of time) that influence the evolution of in-drift coupled flow and transport processes. The MSTHM provides input to process models and abstractions addressing the following:

- General corrosion of the waste package
- Localized corrosion of the waste package
- Waste-form degradation
- Radionuclide solubility
- In-drift seepage evolution and thermal seepage
- Dust-leachate evolution
- Radionuclide transport in the Engineered Barrier System.

The primary limitation of the MSTHM is that it does not predict drift seepage during the postboiling period as influenced by drift-scale heterogeneity. A related limitation is that the MSTHM-predicted evaporation rate on the drip shield pertains to the case with no dripping on the drip shield. For cases with dripping onto the drip shield, evaporation rate on the drip shield must be determined from a different means (i.e., determined on the basis of the local evaporative capacity limited either by the local heat flux or the local liquid-phase flux). Another primary limitation of the MSTHM is that it does not address the potential impact of fine-scale heterogeneity on thermohydrologic conditions in the emplacement drifts and adjoining host rock.

The MSTHM accounts for three-dimensional drift-scale and mountain-scale heat flow and captures the influence of the key engineering-design variables and natural system factors effecting thermohydrologic conditions in the emplacement drifts and adjoining host rock. The natural system factors include:

- Repository-scale spatial variability of percolation flux
- Temporal variability of percolation flux (as influenced by climate change)

- Uncertainty in percolation flux (as addressed by the low-, mean, and high-percolation flux cases)
- Repository-scale variability of thermal conductivity (notably in repository host rock)
- Repository-scale variability of bulk rock density and specific heat (notably in host rock)
- Repository-scale variability of hydrologic properties of the rock matrix (notably those effecting matrix imbibition)
- Repository-scale variability of hydrologic properties of fractures (notably those effecting capillary wicking)
- Repository-scale variability in overburden thickness.

The engineering-design variables include:

- Overall areal heat-generation density of the waste inventory, which is quantified by the Areal Mass Loading (AML, expressed in MTU/acre)
- Line-averaged thermal load along emplacement drifts, which is quantified by the Lineal Power Density (LPD, expressed in kW/m)
- Distance between emplacement drifts (also called drift spacing)
- Age of spent-nuclear fuel at time of emplacement
- Location of the repository with respect to the stratigraphy
- Repository footprint shape, which influences the evolution of the edge-cooling effect that increases with proximity to the repository edges
- Dimensions of the in-drift design, including those of the waste packages, drip shield, and invert
- Properties of the in-drift engineered barrier system components
- Waste package spacing along the drift (line-load versus point-load spacing)
- Waste package sequencing (particularly with respect to the heat output from the respective waste packages)
- Time- and distance-dependent heat-removal efficiency of preclosure drift ventilation
- Duration and heat-removal efficiency of preclosure drift ventilation.

The MSTHM (Figure 1-1, Tables 1-2 and 1-3) couples the Smeared-heat-source Drift-scale Thermal-conduction (SDT), Line-average-heat-source Drift-scale Thermohydrologic (LDTH),

Discrete-heat-source Drift-scale Thermal-conduction (DDT), and Smeared-heat-source Mountain-scale Thermal-conduction (SMT) submodels such that the flow of water, water vapor, air, and heat through partially saturated fractured porous rock is adequately addressed. The relationships between the various submodel and model types are diagramed in Figure 1-1. The submodel and model types are defined in Table 1-2. The MSTHM accounts for three-dimensional drift-scale and mountain-scale heat flow, repository-scale variability of stratigraphy and percolation flux, and variability in heat output of waste packages. All submodels use the nonisothermal unsaturated-saturated flow and transport (NUFT) simulation code (Nitao 1998).

This model report provides a detailed description of the MSTHM concept and approach detailing the software and the routines used in the MSTHM. It describes the inputs to the software and details the specific parameters of that data. It provides a brief but complete discussion of the criteria. It discusses the specific assumptions made in this modeling system and provides the rationale for each assumption. The report includes a full description of the MSTHM and the specific submodel components, input-data-preparation and model-building steps, and the MSTHM calculation sequence. Finally, the report includes a discussion of the MSTHM validation in accordance with *Technical Work Plan for: Engineered Barrier System Department Modeling and Testing FY03 Work Activities* (BSC 2003a).

Table 1-1. List of Thermohydrologic Variables Predicted with the MSTHM

Thermohydrologic Variable	Drift-Scale Location
Temperature	Near-field environment host rock (5 m above crown of drift)
	Near-field environment host rock (mid-pillar at repository horizon)
	Maximum lateral extent of boiling
	Drift wall (perimeter average)
	Drip shield (perimeter average)
	Drip shield (upper surface)
	Waste package (surface average)
	Invert (average)
Relative humidity	Drift wall (perimeter average)
	Drip shield (perimeter average)
	Waste package
	Invert (average)
Liquid-phase saturation (matrix)	Drift wall (perimeter average)
	Drip shield (perimeter average)
	Invert (average)
Liquid-phase flux	Near-field environment host rock (5 m above crown of drift)
	Near-field environment host rock (3 m above crown of drift)
	Drift wall (upper surface)
	Drift wall (lower surface below invert)
	Drip shield (crown)
	Drip shield (upper surface average)
	Drip shield (lower side at the base)
	Invert (average)
Gas-phase air-mass fraction	Drip shield (perimeter average)
Gas-phase pressure	Drip shield (perimeter average)
Capillary pressure	Drip shield (perimeter average)
	Invert (average)
	Drift wall (crown, in matrix)
	Drift wall (crown, in fractures)
Gas-phase (water vapor) flux	Drift wall (perimeter average)
Gas-phase (air) flux	Drift wall (perimeter average)
Evaporation rate	Drip shield (crown)
	Drip shield (perimeter total)
	Drift wall (upper surface)
	Drift wall (lower surface below invert)
	Invert (total)

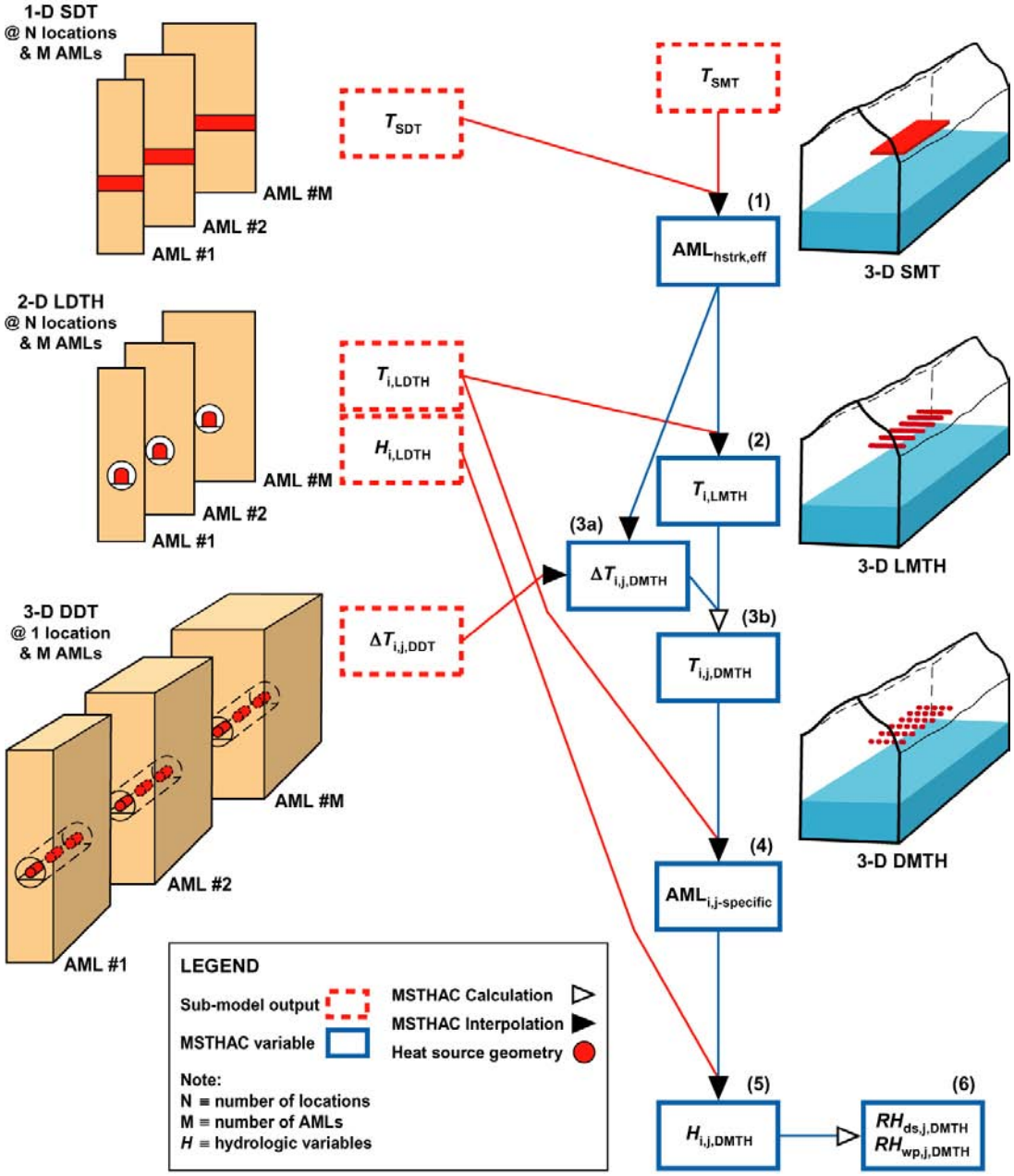

Figure 1-1. Six stage flow chart diagram of the MSTHM. SDT, LDTH and DDT submodels are run at different AMLs (left side); SMT, LMTH and DMTH are the series of 3-D mountain scale models of increasing complexity (right side). The six stages illustrate the process of constructing intermediate variables ($AML_{hstrk,eff}$, $\Delta T_{i,j,DMTH}$, $T_{i,LMTH}$ and $AML_{i,j\text{-specific}}$) and final MSTHM variables ($T_{i,j,DMTH}$, $RH_{i,j,DMTH}$ and $H_{i,j,DMTH}$) from NUFT submodel output (T_{SDT}, T_{SMT}, $T_{i,LDTH}$, $H_{i,LDTH}$ and $\Delta T_{i,j,DDT}$). The submodel and model types are defined in Table 1-2. The variables are defined in Table 1-3. Note that the four submodels of the MSTHM are the SDT, LDTH, DDT, and SMT submodels. The LMTH model is an intermediate result of the MSTHM and the DMTH model is the final result of the MSTHM.

Table 1-2. The submodel and model types used in the MSTHM are described. Note that the four submodels of the MSTHM are the SDT, LDTH, DDT, and SMT submodels. The LMTH model is an intermediate result of the MSTHM and the DMTH model is the final result of the MSTHM.

Submodel / Model Type	Description
MSTHM	Multiscale Thermohydrologic Model
SMT	Smeared-heat-source, mountain-scale, thermal-conduction: three-dimensional NUFT submodel
SDT	Smeared-heat-source, drift-scale, thermal-conduction: one-dimensional NUFT submodel
LDTH	Line-averaged-heat-source, drift-scale, thermohydrologic: two-dimensional NUFT submodel
DDT	Discrete-heat-source, drift-scale, thermal-conduction: three-dimensional NUFT submodel
LMTH	Line-averaged-heat-source, mountain-scale, thermohydrologic model: three-dimensional MSTHM intermediate result
DMTH	Discrete-heat-source, mountain-scale, thermohydrologic model: three-dimensional MSTHM final result
D/LMTH	Discrete / line-averaged-heat-source, mountain-scale, thermohydrologic model: the nested monolithic three-dimensional NUFT model used in the MSTHM validation (Section 7.3)

Table 1-3. The variables used in the MSTHM methodology are listed. Subscript i refers to a generic location in the drift; i = dw refers to drift wall, i = ds refers to drip shield, i = in refers to invert, and i = wp refers to waste package. Subscript j refers to the waste package type, such asj = DHLW, 21-PWR CSNF, or 44-BWR CSNF. The MSTHM methodology is described in detail in Section 6.2.4.

Variable Name	Description	Stage (see Figure 1-1)
T_{SDT}	Host-rock temperature output from the one-dimensional SDT submodel.	Stage 1 (NUFT output)
T_{SMT}	Host-rock temperature output from the three-dimensional mountain-scale SMT submodel.	Stage 1 (NUFT output)
$\Delta T_{i,j,DDT}$	Temperature deviation of individual waste package from averaged drift-wall temperature for generic-drift-location i and waste package j.	Stage 3a (NUFT output)
$\Delta T_{i,,j,DMTH}$	Temperature deviation of individual waste package from averaged drift-wall temperature for generic-drift-location i and waste package j, adjusting for three-dimensional mountain-scale heat loss.	Stages 3a, 3b
$T_{i,LDTH}$	Temperature output from two-dimensional LDTH drift-scale submodel.	Stages 2, 4 (NUFT output)
$T_{i,LMTH}$	Temperature for generic-drift-location i adjusted for the three-dimensional mountain scale heat loss.	Stages 2, 3b
$T_{i,j,DMTH}$	Temperature for generic-drift-location i and waste package j adjusted for the three-dimensional mountain-scale heat loss and for waste package variation.	Stages 3b, 4
$H_{i,LDTH}$	Set of hydrologic variables for generic-drift-location i. This set includes $RH_{i,LDTH}$ and $S_{i,LDTH}$.	Stage 5 (NUFT output)
$H_{i,j,DMTH}$	Set of hydrologic variables for generic-drift-location i and waste package j adjusted for three-dimensional mountain-scale heat loss and for waste package variation. This set includes $RH_{i,j,DMTH}$ and $S_{i,j,DMTH}$.	Stages 5, 6
$RH_{i,j,DMTH}$	Relative humidity of the generic-drift-location i and waste package j for the DMTH model.	Stage 5, 6
$S_{i,j,DMTH}$	Liquid-phase saturation of the generic-drift-location i and waste package j for the DMTH model.	Stage 5, 6
$T_{dw,cav}$ $RH_{dw,cav}$	Perimeter averages of surfaces adjoining the open cavity outside of the drip shield only for the DMTH.	Stage 6
$AML_{hstrk,eff}$	A time-varying variable that incorporates the influence of three-dimensional mountain-scale heat-loss (determined by the combined use of the SMT and SDT submodels) onto the LDTH-submodel results.	Stages 1, 2, 3a
$AML_{i,j\text{-}specific}$	A time-varying variable that combines the influences of waste-package-to-waste-package variation (determined by the DDT submodels) and three-dimensional mountain-scale heat loss (represented by the LMTH-modeled temperatures), resulting in DMTH-model results for generic-drift-location i and waste package j.	Stages 4, 5
P_{sat}	Saturated vapor pressure, which is a function of temperature.	Stage 6

INTENTIONALLY LEFT BLANK

2. QUALITY ASSURANCE

The Quality Assurance program applies to the development of this document (BSC 2003a, Section 8). This document was prepared in accordance with *Technical Work Plan for: Engineered Barrier System Department Modeling and Testing FY03 Work Activities* (BSC 2003a), which directs the work identified in work package AEBM01. The technical work plan was prepared in accordance with AP-2.27Q, *Planning for Science Activities*. There were no variances from the planned activities. The methods used to control the electronic management of data are identified in the technical work plan (BSC 2003a, Section 8). As directed in the technical work plan, this document was prepared in accordance with AP-SIII.10Q, *Models*; AP-SI.1Q, *Software Management*; AP-3.15Q, *Managing Technical Product Inputs*; and reviewed in accordance with AP-2.14Q, *Document Review*.

The work scope described in this report has been determined to be subject to *Quality Assurance Requirements and Description* (DOE 2003). The work scope of this report involves conducting investigations or analyses of engineered barrier system components contained in *Q-List* (BSC 2003b). Safety Categories for the components are provided in Table 2-1.

Table 2-1. The engineered barrier system components addressed in this report are listed along with the corresponding Safety Category (SC) level that has been assigned to each component.

Engineered Barrier System Component	Safety Category
Drip Shield	SC
Invert	SC
Waste Emplacement Pallet	Non SC
Emplacement Drift	Non SC
DOE and Commercial Waste Packages	SC
DOE Spent Nuclear Fuel Disposable Canister	SC
Naval Spent Nuclear Fuel Waste Package	SC

Source: BSC 2003b

Furthermore, this report provides analysis of data indirectly supporting performance assessment activities for the Total Systems Performance Assessment for License Application.

This report documents the determination of in-drift thermohydrologic conditions that are required by TSPA-LA. It provides in-drift thermohydrologic parameters that are important to the performance of the engineered barriers that are classified in *Q-List* (BSC 2003b) as "Safety Category" because they are important to waste isolation as defined in AP-2.22Q, *Classification Analyses and Maintenance of the Q-List*. The results of this report are important to the demonstration of compliance with the postclosure performance objectives prescribed in 10 CFR 63.113.

INTENTIONALLY LEFT BLANK

3. USE OF SOFTWARE

A complete list of the software and the associated software tracking number is listed in Table 3-1.

Table 3-1. Software Used

Code	Software Tracking Number	Software Qualification Status	Computers Used to Run Software (DOE Property Number)	Sections Where the Software Output is Used
NUFT v3.0s	10088-3.0s-02	Qualified	6549273, 6549266, 6700902, 6290847, 6426406, 6290830, 6877864, 6481320, 6290823, 6813251, 6877857, 6524867, 6878182, 6575968, 6274861, 6813244, 6877840, 6549297	6.2, 6.3, 6.4, 7.1, 7.3, 8.3
NUFT v3.0.1s	10130-3.0.1s-01	Qualified	6700902, 6426406, 6290830	7.2, 7.3
RADPRO v4.0	10204-4.0-00	Qualified	6877840, 6878182	6.2, 6.3, 7.2, 7.3, 8.3
XTOOL v10.1	10208-10.1-00	Qualified	6496843	6.2, 6.3, 6.4, 7.1, 7.2, 7.3
MSTHAC v7.0	10419-7.0-00	Qualified	6813251, 6290830, 6878182	6.2, 6.3, 7.3, 8.3
readsUnits v1.0	10602-1.0-00	Qualified	6371317	6.2, 6.3, 7.2, 7.3, 8.3
YMESH v1.54	10172-1.54-00	Qualified	6813251, 6813244, 6877864, 6878182	6.2, 6.3, 7.2, 7.3, 8.3
boundary_conditions v1.0	11042-1.0-00	Qualified	6877840	6.3, 7.2, 8.3
heatgen_ventTable_emplace v1.0	11039-1.0-00	Qualified	6813251	6.3, 8.3
rme6 v1.2	10617-1.2-00	Qualified	6813251	6.3, 8.3
xw v1.0	11035-1.0-00	Qualified	6813251	6.3, 8.3
colCen v1.0	11043-1.0-00	Qualified	6877840	6.3, 8.3
repository_percolation_calculator v1.0	11041-1.0-00	Qualified	6813251	6.3, 8.3
extractBlocks_EXT v1.0	11040-1.0-00	Qualified	6877857	6.3, 8.3
chimney_interpolate v1.0	11038-1.0-00	Qualified	6813251, 6290830	6.3, 8.3
reformat_EXT_to_TSPA v1.0	11061-1.0-00	Qualified	6813251, 6290830, 6878182	6.3, 8.3

* These are the sections that directly or indirectly utilize the output from the listed software.

3.1 QUALIFIED SOFTWARE

The software described in this section is used in the following data-flow diagrams (Figures 6-1 and 6-2) of Section 6. The computer software used was run on computers located in Lawrence Livermore National Laboratory.

3.1.1 NUFT v3.0s

NUFT v3.0s (NUFT, V3.0s, 10088-3.0s-02) is classified as qualified software per AP-SI.1Q, *Software Management*, and is used to conduct all of the submodel calculations required by the MSTHM. NUFT v3.0s was obtained from software configuration management and was run on Sun workstations with the Sun, SUN O.S. 5.8 operating system. NUFT v3.0s is appropriate for this task.

3.1.2 NUFT v3.0.1s

NUFT v3.0.1s (NUFT, V3.0.1s, 10130-3.0.1s-01) is classified as qualified software per AP-SI.1Q, and is used to conduct all of the nested-mesh model calculations in the model-validation exercises for the MSTHM. NUFT v3.0.1s was obtained from software configuration management and was run on Sun workstations with Sun OS 5.8 operating systems. NUFT v3.0.1s is appropriate for this task.

3.1.3 RADPRO v4.0

RADPRO v4.0 (RADPRO, V4.0, 10204-4.0-00) is classified as qualified software per AP-SI.1Q, and was obtained from software configuration management and was run on a Sun workstation with a SunOS 5.8 (Solaris 8) operating system. RADPRO v4.0 is used to calculate the radiative heat-transfer coefficients in the emplacement drift. RADPRO v4.0 is appropriate software for this task.

3.1.4 XTOOL v10.1

XTOOL v10.1 (XTOOL V10.1, V10.1, 10208-10.1-00) is classified as a qualified software routine per AP-SI.1Q, and was obtained from software configuration management and was run on a Sun workstation with a SunOS 5.6.1 operating system. XTOOL v10.1 is used to generate graphical representations of the results given in the NUFT and MSTHAC v7.0 time-history files (which are files with the suffix: *.ext). XTOOL v10.1 is appropriate software for this task.

3.1.5 MSTHAC v7.0

MSTHAC (MSTHAC, V7.0, 10419-7.0-00) is classified as qualified software per AP-SI.1Q, and was obtained from software configuration management and was run on a Sun workstation with a SunOS 5.8 (Solaris 8) operating system. MSTHAC v7.0 integrates the results of NUFT submodel calculations to predict the multiscale thermohydrologic conditions in the emplacement drifts and adjoining host rock throughout the repository area. MSTHAC v7.0 is appropriate software for this task.

3.1.6 readsUnits v1.0

Software code readsUnits (readsUnits, V1.0, 10602-1.0-00) is classified as qualified software per AP-SI.1Q, and was obtained from software configuration management and was run on a Sun workstation with a SunOS 5.5.1 operating system. This code reads YMESH-generated data describing a stratigraphic column and generates comment lines for NUFT input files that

summarize the thicknesses of each of the hydrostratigraphic units (also called UZ Model Layers) in that column. readsUnits v1.0 is appropriate software for this task.

3.1.7 YMESH v1.54

YMESH v1.54 (YMESH, v1.54, 10172-1.54-00) is classified as qualified software per AP-SI.1Q, and was obtained from software configuration management and was run on a Sun workstation with a SunOS 5.8 (Solaris 8) operating system. YMESH v1.54 is used to generate the thicknesses of the hydrostratigraphic units (also called the UZ Model Layers) in the various MSTHM submodels on the basis of *Development of Numerical Grids for UZ Flow and Transport Modeling* (BSC 2003c). YMESH v1.54 is appropriate software for this task.

3.1.8 boundary_conditions v1.0

boundary_conditions (boundary_conditions, V 1.0, 11042-1.0-00) is classified as qualified software per AP-SI.1Q, and was obtained from software configuration management and was run on a Sun workstation with a SunOS 5.8 (Solaris 8) operating system. The purpose of this routine is to generate upper and lower boundary conditions for the LDTH, SMT, and SDT submodels of the MSTHM (Section 6.2), as well as for other models such as the three-dimensional thermohydrologic model for the Drift Scale Test (DST) (Section 7.2). The code boundary_conditions v1.0 is appropriate software for this task.

3.1.9 heatgen_ventTable_emplace v1.0

heatgen_ventTable_emplace (heatgen_ventTable_emplace, V1.0, 11039-1.0-00) is classified as qualified software per AP-SI.1Q, and was obtained from software configuration management and was run on a Sun workstation with a SunOS 5.8 (Solaris 8) operating system. heatgen_ventTable_emplace v1.0 modifies a heat-generation-rate-versus-time table in two ways. First, it can "age" the heat-generation table by adding a specified number of years to the time entries. Second, it can account for the heat-removal efficiency of ventilation by multiplying the heat-generation-rate values by a specified fraction during the specified ventilation period. heatgen_ventTable_emplace v1.0 also can incorporate the dependence of the heat-removal efficiency table on distance (along the emplacement drift) from the ventilation inlet. heatgen_ventTable_emplace v1.0 is appropriate software for this task.

3.1.10 rme6 v1.2

rme6 (rme6, v1.2, 10617-1.2-00) is classified as qualified software per AP-SI.1Q, and was obtained from software configuration management and was run on a Sun workstation with a SunOS 5.8 (Solaris 8) operating system. This code converts the grid from *Development of Numerical Grids for UZ Flow and Transport Modeling* (BSC 2003c) to a format that is readable by YMESH v1.54. The code rme6 v1.2 is appropriate software for this task.

3.1.11 xw v1.0

xw (xw, V1.0, 11035-1.0-00) is classified as qualified software per AP-SI.1Q, and was obtained from software configuration management and was run on a Sun workstation with a SunOS 5.8 (Solaris 8) operating system. xw v1.0 extends the grid from the three-dimensional UZ Flow

Model in the horizontal direction for the purpose of building mountain-scale submodels that extend laterally beyond the grid of the three-dimensional UZ Flow Model. xw v1.0 is appropriate software for this task.

3.1.12 colCen v1.0

colCen (colCen, V1.0, 11043-1.0-00) is classified as qualified software per AP-SI.1Q, and was obtained from software configuration management and was run on a Sun workstation with a SunOS 5.8 (Solaris 8) operating system. The purpose of colCen v1.0 grid is to determine the gridblock column in the three-dimensional UZ Flow Model that a given gridblock column in a MSTHM submodel resides in. colCen v1.0 is appropriate software for this task.

3.1.13 repository_percolation_calculator v1.0

repository_percolation_calculator (repository_percolation_calculator, V1.0, 11041-1.0-00) is classified as qualified software per AP-SI.1Q, and was obtained from software configuration management and was run on a Sun workstation with a SunOS 5.8 (Solaris 8) operating system. The purpose of repository_percolation_calculator is to determine the value of percolation flux for each of the LDTH submodels on the basis of the percolation flux map from the three-dimensional UZ Flow Model. repository_percolation_calculator v1.0 is appropriate software for this task.

3.1.14 extractBlocks_EXT v1.0

extractBlocks_EXT (extractBlocks_EXT, V1.0, 11040-1.0-00) is classified as qualified software per AP-SI.1Q, and was obtained from software configuration management and was run on a Sun workstation with a SunOS 5.8 (Solaris 8) operating system. The purpose of extractBlocks_EXT is to determine the effective thermal conductivity for the gridblocks in the drift cavity of an LDTH submodel based on a correlation accounting for the influence of natural convection (Francis et al. 2003, Table 6). extractBlocks_EXT v1.0 is appropriate software for this task.

3.1.15 chimney_interpolate v1.0

chimney_interpolate (chimney_interpolate, V1.0, 11038-1.0-00) is classified as qualified software per AP-SI.1Q, and was obtained from software configuration management and was run on a Sun workstation with a SunOS 5.8 (Solaris 8) operating system. The purpose of chimney_interpolate is to create a set of virtual SDT and LDTH chimney models from the representative chimney models. The virtual chimney models are an input to the MSTHAC v7.0 micro-abstraction process. chimney_interpolate v1.0 is appropriate software for this task.

3.1.16 reformat_EXT_to_TSPA v1.0

reformat_EXT_to_TSPA (reformat_EXT_to_TSPA, V1.0, 11061-1.0-00) is classified as qualified software per AP-SI.1Q, and was obtained from software configuration management and was run on a Sun workstation with a SunOS 5.8 (Solaris 8) operating system. The purpose of reformat_EXT_to_TSPA v1.0 is to postprocess the micro-abstraction data produced by MSTHAC V7.0. The processing includes finding the typical waste package and location from a

set of locations forming a bin and writing an output file in a format specified by the TSPA-LA organization. reformat_EXT_to_TSPA v1.0 is appropriate software for this task.

3.2 EXEMPT SOFTWARE

Exempt software was used in the creation of tables and figures shown in this document as well as some data processing.

The figures can be divided into the following types: line plots showing time histories, contour plots showing the variation in some property at a particular point in time for a cross sectional area of interest, plots showing material properties for the repository plan view, and schematic drawings showing repository design parameters.

Plots showing material properties for the repository plan view were created using Matlab v6.1.0.450 release 12.1. Example: Figure 6.3-1.

Schematic drawings showing repository design information were created using Adobe Illustrator v8.0. Example: Figure 6.2-2.

All Tables were created using Microsoft Word 2000 9.0.4402 SR-1.

Microsoft Excel 2000 9.0.4402 SR-1 was used to process data for the development of chimney percolation data as detailed in Attachment I.

INTENTIONALLY LEFT BLANK

4. INPUTS

4.1 DIRECT INPUTS

Data, parameters, design information, and other model/analyses inputs are compiled and presented in Table 4-1. There are seven major sections of the table: (1) geometry of the engineered system, (2) geometry of the natural system, (3) properties of the engineered system inside the emplacement drift, (4) properties of the natural system, (5) boundary conditions of the natural system, (6) distribution of percolation flux just below the base of the PTn unit and (7) waste package heat-generation data and ventilation heat-removal efficiency. The seven sections are further delineated to distinguish separate data, design information, and parameters. The majority of the information compiled in Table 4-1, which is direct input, falls into the parameter and design information categories.

4.1.1 Data

Data compiled in Table 4-1 is limited to the invert thermal and hydrologic properties, specifically invert bulk density, specific heat, thermal conductivity, and emissivity.

4.1.2 Parameters and Parameter Uncertainty

The parameters required as input for the development of parameter values used in the models/analyses documented in this report are summarized in Table 4-1. The following sections of the table include information about parameters: geometry of natural system, invert thermal and hydrologic properties, hydrologic properties of all hydrostratigraphic units (also called UZ Model Layers), bulk thermal properties of the UZ Model Layers, and percolation flux below the base of the PTn unit.

Section 6.3.2 provides an analysis of the impact of uncertainty of key natural system parameters.

4.1.3 Design Information

Other inputs required as input for the development of parameter values used in the models/analyses documented in this report take the form of design information. The following sections of Table 4-1 include design information: geometry of the engineered system, waste package thermal properties, drip shield thermal properties, drift-wall emissivity and waste package heat generation and ventilation heat-removal efficiency.

Table 4-1. Summary of Input Data and Information Required by the MSTHM

Model Input	Value	Source
Geometry of the Engineered System: Design Information		
Repository emplacement-drift layout (elevations and end-point coordinates for each emplacement drift)	See IED	BSC 2003d
Drift spacing	81 m	BSC 2004a
Waste package spacing	0.1 m	BSC 2004a

Table 4-1. Summary of Input Data and Information Required by the MSTHM (Continued)

Model Input	Value	Source
Drift diameter	5.5 m	BSC 2004a
Location of 21-PWR AP WP centerline above invert	1.018 m	BSC 2004a
Invert height from bottom of drift	0.806 m	BSC 2003e
21-PWR AP WP length	5.165 m	see Assumption, Section 5.4.1
21-PWR AP WP diameter	1.644 m	see Assumption, Section 5.4.2
21-PWR CR WP diameter	1.644 m	see Assumption, Section 5.4.2
21-PWR AP WP inner-shell thickness	0.05 m	BSC 2004b
Geometry of the Engineered System: Design Information		
21-PWR AP WP outer-barrier thickness	0.02 m	BSC 2004b
Nominal quantity of 21-PWR AP waste packages in LA-design inventory	4299	BSC 2004b
Nominal quantity of 21-PWR CR waste packages in LA-design inventory	95	BSC 2004b
44-BWR WP length	5.165 m	see Assumption, Section 5.4.1
44-BWR WP diameter	1.674 m	see Assumption, Section 5.4.2
44-BWR WP inner-shell thickness	0.050 m	BSC 2004b
44-BWR WP outer-barrier thickness	0.020 m	BSC 2004b
Nominal quantity of 44-BWR AP waste packages in LA-design inventory	2831	BSC 2004b
5 DHLW/DOE SNF-LONG WP length	5.217 m	see Assumption, Section 5.4.1
5 DHLW/DOE SNF-LONG WP diameter	2.110 m	see Assumption, Section 5.4.2
5 DHLW/DOE SNF-LONG WP inner-shell thickness	0.050 m	BSC 2004b
5 DHLW/DOE SNF-LONG WP outer-barrier thickness	0.025 m	BSC 2004b
5 DHLW/DOE SNF-SHORT WP length	3.590 m	see Assumption, Section 5.4.1
5 DHLW/DOE SNF-SHORT WP diameter	2.110 m	see Assumption, Section 5.4.2
5 DHLW/DOE SNF-SHORT WP inner-shell thickness	0.050 m	BSC 2004b
5 DHLW/DOE SNF-SHORT WP outer-barrier thickness	0.025 m	BSC 2004b
Drip-shield length	6.105 m	see Assumption, Section 5.4.5
Drip-shield width	2.512 m	see Assumption, Section 5.4.6
Drip-shield thickness	0.015 m	BSC 2004c
Intersection of drip-shield plate-1 with drip-shield plate-2 from base/top of invert	1875 mm	see Assumption, Section 5.4.7
Total nominal quantity of waste package in LA-design inventory	11,184	BSC 2004b
Geometry of Natural System: Parameters		
Grid of three-dimensional Unsaturated-Zone Flow and Transport Model		DTN: LB03023DKMGRID.001
Properties of the Engineered System		
Invert Thermal and Hydrologic Properties: Parameters		
Intragranular permeability (tsw35 matrix continuum for mean infiltration flux property set)	4.48×10^{-18} m^2	DTN: LB0208UZDSCPMI.002
Porosity of crushed-tuff grains (tsw35 matrix continuum for mean infiltration flux property set)	0.131	DTN: LB0208UZDSCPMI.002

Table 4-1. Summary of Input Data and Information Required by the MSTHM (Continued)

Model Input	Value	Source
Intragranular van Genuchten α (tsw35 matrix continuum for mean infiltration flux property set)	1.08×10^{-5} 1/Pa	DTN: LB0208UZDSCPMI.002
Intragranular van Genuchten m (tsw35 matrix continuum for mean infiltration flux property set)	0.216	DTN: LB0208UZDSCPMI.002
Intragranular residual saturation (tsw35 matrix continuum for mean infiltration flux property set)	0.12	DTN: LB0208UZDSCPMI.002
Intergranular permeability (fracture continuum) (3-mm particle size)	1.51×10^{-8} m^2	DTN: MO0307SPAVGSUM.000
Intergranular permeability (fracture continuum) (0.317-mm particle size)	1.68×10^{-10} m^2	DTN: MO0307SPAVGSUM.000
Intergranular saturated volumetric moisture content (fracture continuum)	0.45	DTN: MO0307SPAVGSUM.000
Intergranular porosity (fracture continuum)	0.45	DTN: MO0307SPAVGSUM.000
Intergranular van Genuchten α (fracture continuum) (3-mm particle size)	624 bar^{-1}	DTN: MO0307SPAVGSUM.000
Intergranular van Genuchten m (fracture continuum) (3-mm particle size)	0.875	DTN: MO0307SPAVGSUM.000
Intergranular residual volumetric moisture content (fracture continuum) (3-mm particle size)	0.05	DTN: MO0307SPAVGSUM.000
Invert Thermal and Hydrologic Properties: Data		
Bulk Density of 4-10 crushed tuff	Table IV-8 in Attachment IV	DTN: GS020183351030.001
Specific heat of 4-10 crushed tuff	Table IV-9 in Attachment IV	DTN: GS000483351030.003
Thermal conductivity of 4-10 crushed tuff	Table IV-9 in Attachment IV	DTN: GS000483351030.003
Emissivity (upper invert surface)	0.88 to 0.95	Incropera and DeWitt 1996, Table A.11 for Rocks
Waste Package Thermal Properties: Design Information		
Weight of 21-PWR AP WP	43,000 kg	see Assumption, Section 5.4.3
Weight of 44-BWR WP	43,000 kg	see Assumption, Section 5.4.3
Weight of 5 DHLW/DOE SNF-SHORT WP	39,000 kg	see Assumption, Section 5.4.3
Weight of 5 DHLW/DOE SNF-LONG	57,000 kg	see Assumption, Section 5.4.3
Emissivity of Alloy 22, which is the outer shell of the following WPs: 21-PWR AP, 44-BWR, 5 DHLW/DOE SNF-SHORT, 5 DHLW/DOE SNF-LONG	0.87	DTN: MO0003RIB00071.000 (see Table 5-10 of BSC 2001a for reference only)
Mass density of Alloy 22, which is the outer shell of the following WPs: 21-PWR AP, 44-BWR, 5 DHLW/DOE SNF-SHORT, 5 DHLW/DOE SNF-LONG	8690 kg/m^3	DTN: MO0003RIB00071.000 (see Table 5-10 of BSC 2001a for reference only)
Mass density of Stainless Steel Type 316, which is the inner shell of the following WPs: 21-PWR AP, 44-BWR, 5 DHLW/DOE SNF-SHORT, 5 DHLW/DOE SNF-LONG	7.98 g/cm^3	Table XI of ASTM G 1-90 (see Table 5-12 of BSC 2001a for reference only)
Mass density of the internal cylinder of the	3495 kg/m^3	BSC 2004d, Table 20

Table 4-1. Summary of Input Data and Information Required by the MSTHM (Continued)

Model Input	Value	Source
21-PWR AP WP		(see Table 5-6 of BSC 2001a for reference only)
Mass density of the internal cylinder of the 44-BWR WP	3342 kg/m^3	BSC 2004d, Table 20 (see Table 5-6 of BSC 2001a for reference only)
Mass density of the internal cylinder of the 5 DHLW/DOE SNF-SHORT WP	2175 kg/m^3	BSC 2004d, Table 20 (see Table 5-6 of BSC 2001a for reference only)
Mass density of the internal cylinder of the 5 DHLW/DOE SNF-LONG WP	2302 kg/m^3	BSC 2004d, Table 20 (see Table 5-6 of BSC 2001a for reference only)
Thermal conductivity of Alloy 22 (at T = 100°C), which is the outer shell of the following WPs: 21-PWR AP, 44-BWR, 5 DHLW/DOE SNF-SHORT, 5 DHLW/DOE SNF-LONG	11.1 W/m·K	DTN: MO0003RIB00071.000 (see Table 5-11 of BSC 2001a for reference only)
Thermal conductivity of Stainless Steel Type 316, which is the inner shell of the following WPs: 21-PWR AP, 44-BWR, 5 DHLW/DOE SNF-SHORT, 5 DHLW/DOE SNF-LONG	8.4 BTU/hr-ft-°F at 200°F 8.7 BTU/hr-ft-°F at 250°F	ASME 1995, Section II-D, Table TCD, p. 606
Thermal diffusivity of Stainless Steel Type 316, which is the inner shell of the following WPs: 21-PWR AP, 44-BWR, 5 DHLW/DOE SNF-SHORT, 5 DHLW/DOE SNF-LONG	0.141 ft^2/hr at 200°F 0.143 ft^2/hr at 250°F	ASME 1995, Section II-D, Table TCD, p. 606
Thermal conductivity of the internal cylinder of the following WPs: 21-PWR AP, 44-BWR, 5 DHLW/DOE SNF-SHORT, 5 DHLW/DOE SNF-LONG	1.5 W/m·K	BSC 2004d, Table 20 (see Table 5-6 of BSC 2001a for reference only)
Specific heat of Alloy 22 (at T = 100°C), which is the outer shell of the following WPs: 21-PWR AP, 44-BWR, 5 DHLW/DOE SNF-SHORT, 5 DHLW/DOE SNF-LONG	423.0 J/kg·K	DTN: MO0003RIB00071.000 (see Table 5-11 of BSC 2001a for reference only)
Specific heat of the internal cylinder of the 21-PWR AP WP	378.0 J/kg·K	BSC 2004d, Table 20 (see Table 5-6 of BSC 2001a for reference only)
Specific heat of the internal cylinder of the 44-BWR WP	395.0 J/kg·K	BSC 2004d, Table 20 (see Table 5-6 of BSC 2001a for reference only)
Specific heat of the internal cylinder of the 5 DHLW/DOE SNF-SHORT WP	718.0J/kg·K	BSC 2004d, Table 20 (see Table 5-6 of BSC 2001a for reference only)
Specific heat of the internal cylinder of the 5 DHLW/DOE SNF-LONG WP	731.0 J/kg·K	BSC 2004d, Table 20 (see Table 5-6 of BSC 2001a for reference only)
Drip-Shield Thermal Properties: Design Information		
Weight of drip shield (for a nominal length of 5.805 m)	5000 kg	BSC 2004c, Table 1
Mass density of titanium	0.163 lb/in^3	ASME 1995, Section II-D, Table NF-2 (see Table 5-14 of BSC 2001a for reference only)

Table 4-1. Summary of Input Data and Information Required by the MSTHM (Continued)

Model Input	Value	Source
Thermal conductivity of titanium	12.00 BTU/hr-ft-°F at 200°F; 11.85 BTU/hr-ft-°F at 250°F	ASME 1995, Section II-D, Table TCD, p. 611 (see Table 5-15 of BSC 2001a for reference only)
Thermal diffusivity of titanium	0.331 ft^2/hr at 200°F 0.322 ft^2/hr at 250°F	ASME 1995, Section II-D, Table TCD, p. 611
Emissivity of titanium	0.63	Lide 1995, p. 10-298 (see Table 5-14 of BSC 2001a for reference only)
Drift-Wall Emissivity: Design Information		
Emissivity of rock	0.88 to 0.95	Incropera and DeWitt 1996, Table A.11 for Rocks
Properties of the Natural System		
Hydrologic Properties of all Unsaturated-Zone Model Layers: Parameters		
Matrix and fracture properties of UZ Model Layers for mean infiltration flux property set	Table IV-4 in Attachment IV	DTN: LB0208UZDSCPMI.002
Matrix and fracture properties of UZ Model Layers for upper-bound infiltration flux property set	Table IV-6 in Attachment IV	DTN: LB0302UZDSCPUI.002
Matrix and fracture properties of UZ Model Layers for lower- infiltration flux property set	Table IV-5 in Attachment IV	DTN: LB0208UZDSCPLI.002
Fracture frequency and fracture-matrix interfacial area of UZ Model Layers for lower-bound, mean, and upper-bound infiltration flux property sets	Table IV-7 in Attachment IV	DTN: LB0205REVUZPRP.001
Fracture-contact-length factor	0.0	BSC 2003c, Section 6.7, Equation 4
Tortuosity of a range of porous media	0.1 (for clays) to 0.7 (for sands)	de Marsily 1986, p. 233;
Tortuosity of fractures	0.7	DTN: LB991091233129.006
Maximum (satiated) liquid-phase saturation of matrix continuum for lower-bound, mean, and upper-bound infiltration flux property sets	1.0	Liu et al. 1998, Equations 2 and 4
Maximum (satiated) liquid-phase saturation of fracture continuum for lower-bound, mean, and upper-bound infiltration flux property sets	1.0	Liu et al. 1998, Equations 2 and 4
Residual gas-phase saturation of fracture continuum for lower-bound, mean, and upper-bound infiltration flux property sets	0.0	Liu et al. 1998, Equations 2 and 4
Bulk Thermal Properties of the Unsaturated-Zone Model Layers: Parameters		
Bulk thermal conductivity and bulk mass density of the GFM2000 Layers of the nonrepository layers	Tables IV-3a and IV-3b in Attachment IV	DTN: SN0303T0503102.008
Bulk thermal conductivity and bulk mass density of the repository horizon GFM2000 Layers	Tables IV-3a and IV-3b in Attachment IV	DTN: SN0208T0503102.007 Table 7-10 of BSC 2002a
Specific heat capacity of the Mineralogic Model Layers	Tables IV-3a and IV-3b in Attachment IV	DTN: SN0307T0510902.003

Table 4-1. Summary of Input Data and Information Required by the MSTHM (Continued)

Model Input	Value	Source
Boundary Conditions of the Natural System: Parameters		
Temperatures at upper boundary (ground surface) of the three-dimensional Site-Scale UZ Flow Model	File: INCON_thm_s32.dat	DTN: LB991201233129.001 [a]
Gas-phase pressures at upper boundary (ground surface) of the three-dimensional Site-Scale UZ Flow Model	File: INCON_thm_s32.dat	DTN: LB991201233129.001 [a]
Temperatures at lower boundary (water table) of the three-dimensional Site-Scale UZ Flow Model	File: INCON_thm_s32.dat	DTN: LB991201233129.001 [a] (data pertains to an elevation of 730 m)
Grid of the three-dimensional mountain-scale coupled processes (thermohydrologic) model; this grid is related to the file: INCON_thm_s32.dat, which is used to obtain temperatures and gas-phase pressures at the boundary for the three-dimensional Site-Scale UZ Flow Model (above)	File: MESH_rep.VF	DTN: LB991201233129.001 [a]
Percolation Flux Below PTn Unit: Parameters		
Percolation Flux from PTn to TSw unit for mean infiltration flux case (two-dimensional map of PTn-to-TSw percolation flux)	Entire DTN	DTN: LB0302PTNTSW9I.001
Percolation Flux from PTn to TSw unit for upper-bound infiltration flux case (two-dimensional map of PTn-to-TSw percolation flux)	Entire DTN	DTN: LB0302PTNTSW9I.001
Percolation Flux from PTn to TSw unit for lower-bound infiltration flux case (two-dimensional map of PTn-to-TSw percolation flux)	Entire DTN	DTN: LB0302PTNTSW9I.001
Waste Package Heat-Generation and Ventilation Heat-Removal Efficiency: Design Information		
Heat-generation rate history for entire repository (70,000 MTU)	See IED	BSC 2004e
Average initial heat-generation rate per meter	1.45 kW/m	BSC 2004a
Ventilation-period duration	50 years after final emplacement	BSC 2004a
Duration of waste package emplacement	23 years	BSC 2004a
Heat-generation rates for each of the waste package types	See IED	BSC 2004f
Ventilation heat-removal efficiency as a function of time and distance from the inlet of the emplacement drift	Entire DTN	DTN: MO0306MWDASLCV.001

NOTE: [a] These DTNs provide common properties that support both the MSTHM model and the validating model.

4.2 CRITERIA

Technical Work Plan for: Engineered Barrier System Department Modeling and Testing FY03 Work Activities (BSC 2003a) identifies the following acceptance criteria (AC) for this model report based on the requirements mentioned in *Project Requirements Document* (Canori and Leitner 2003) and *Yucca Mountain Review Plan, Final Report* (NRC 2003).

AC1: System Description and Model Integration are Adequate
AC2: Data are Sufficient for Model Justification
AC3: Data Uncertainty is Characterized and Propagated Through the Model Abstraction
AC4: Model Uncertainty is Characterized and Propagated Through the Model Abstraction
AC5: Model Abstraction Output is Supported by Objective Comparisons

AC1 is addressed in Sections 1, 6.1, and 6.2 which respectively describe the role of the MSTHM in the TSPA-LA, the Yucca Mountain thermohydrology, and the Multiscale Thermohydrologic modeling approach. AC2 is addressed in Sections 4 and 7, which present the input data and parameters used in the development and validation of the model. AC3 is addressed in Section 6.3, which presents the results of the MSTHM for ranges of uncertainty in key input parameters. AC4 is addressed in Section 6.2, which describes the MTSH modeling approach. AC5 is addressed in Section 6.4, which compares the results of the MSTHM with an alternative conceptual model.

4.3 CODES AND STANDARDS

This report was prepared to comply with 10 CFR Part 63, the NRC rule on high-level radioactive waste. Subparts of this rule that are applicable to data include Subpart E, Section 114 (Requirements for Performance Assessment). The subpart applicable to models is also outlined in Subpart E Section 114. The subparts applicable to features, events, and processes (FEPs) are 10 CFR 63.114(d), (e), and (f). *Standard Practice for Preparing, Cleaning, and Evaluating Corrosion Test Specimens* (ASTM G 1-90) was also used in preparing this report, as was Section II of *1995 ASME Boiler and Pressure Vessel Code* (ASME 1995).

4.4 DATA FROM FIELD MEASUREMENTS IN THE LARGE BLOCK TEST AND DRIFT SCALE TEST

The source DTNs for the field measurements in the Large Block Test (LBT) are listed in Table 4-2; these DTNs are used for model validation purposes only and are not direct input to the MSTHM. The source DTNs for the field measurements in the Drift Scale Test (DST) are listed in Table 4-3. Except for the boundary conditions DTN, these DTNs are used for model validation purposes only and are not direct input to the MSTHM.

Table 4-2. Source DTNs are listed for field measurements made in the Large Block Test (LBT). Also listed is one of the data sets used in the thermohydrologic model calculations of the LBT. Note that these DTNs are used for validation purposes only.

Model Input	Value	Source
Heater power history	Heater power input for each of 5 heater boreholes; power history read from 7 tables; table name and time range as follows: • S98461_018 2/27/1997-4/30/1997 • S98461_019 5/1/1997-7/31/1997 • S98461_020 8/1/1997-10/31/1997 • S98461_021 11/1/1997-1/20/1998 • S98461_011 1/20/1998-3/31/1998 • S98461_012 4/1/1998-6/30/1998 • S98461_013 7/1/1998-9/16/1998	DTN: LL980918904244.074
Top surface boundary temperature controlled by heat exchanger	Temperature averaged from 4 RTDs, TNE-1, TNW-1,TSE1-1, and TSW-1; table name and time range as follows: • S98461_022 2/27/1997-4/30/1997 • S98461_023 5/1/1997-7/31/1997 • S98461_024 8/1/1997-10/24/1997 • S98461_025 10/25/1997-12/31/1997 • S98461_026 1/1/1998-3/31/1998 • S98461_027 4/1/1998-6/30/1998 • S98461_028 7/1/1998-9/16/1998	DTN: LL980918904244.074
Snapshots of rock temperature profile along Borehole TT1	Temperature profile along Borehole TT1 at five different times.Given below are table (or file) name, elapsed time in hours (h), and the range of row numbers that contain the data for each time. S98461_033 719.8 h 1 – 41136 S98461_034 2399.6 h 1 – 159235 S98461_ 035 4800.13 h 1 – 149893 S98461_029 7200.03 h 1 – 90950 S98461_031 9600.22 h 1 – 98329	DTN: LL980918904244.074
Initial volumetric water content from neutron measurements	Initial water content obtained from average of values measured along Borehole TN3 prior to heating; data from file at row numbers 1 -- 159	DTN: LL980919304244.075
Volumetric water content from neutron measurements	Rock water content profile along Borehole TN3 at 103 d, 361 d, and 501 d; data from file at row numbers 2200 – 2254 for 103 d, 2365 – 2419 for 361 d, and 2585 – 2639 for 501 d	DTN: LL980919304244.075
Air temperature: 1/1/1997 – 12/31/1997	Bureau of Land Management Site 8 temperature data used in boundary conditions. Data under table name S04010_001, and parameter name Temperature. Data in Microsoft Access folder MET1997t.MDB, in table S008_97t. The Julian day number is in Column 3 (1-365), time of day in Column 4 (hr, min) and temperature in Column 8 (^{o}C).	DTN: MO0312SEPQ1997.001
Air temperature: 1/1/1998 – 3/31/1998	Bureau of Land Management Site 8 temperature data used in boundary conditions. Data file: 1q98b_sr.txt. The site number is in Column 1 (used only Site 8 data), Julian day number in Column 3 (1-365), time of day in Column 4 (hr) and temperature in Column 7 (K).	DTN: MO98METDATA114.000
Air temperature: 4/1/1998 – 6/30/1998	Bureau of Land Management Site 8 temperature data used in boundary conditions. Data file: 2q98a_sr.txt. The site number is in Column 1 (used only Site 8 data), Julian day number in Column 3 (1-365), time of day in Column 4 (hr) and temperature in Column 7 (K).	DTN: MO98METDATA117.000
Air temperature: 7/1/1998 – 9/30/1998	Bureau of Land Management Site 8 temperature data used in boundary conditions. Data file: 3q98_sr.txt. The site number is in Column 1 (used only Site 8 data), Julian day number in Column 3 (1-365), time of day in Column 4 (hr) and temperature in Column 7 (K).	DTN: MO98METDATA120.000
Drift-scale calibrated one-dimensional property set, FY99: Basecase infiltration	Entire DTN.	DTN: LB990861233129.001

Table 4-3. Source DTNs are listed for field measurements made in the Drift Scale Test (DST). Note that these DTNs are used for validation purposes only.

Model Input	Value	Source
As-built locations of boreholes, sensors, and heaters	Location of temperature sensors in Table S00085_001; locations of temperature and neutron boreholes and heaters in Table S00085_002	DTN: MO0002ABBLSLDS.000
Heater power and sensor temperatures: November 7, 1997 – May 31, 1998	Floor heater and wing heater power in Table S98349_001; Table names and time intervals for temperatures are as follows: • S98349_004 11/7/1997 – 11/30/1997 • S98349_005 12/1/1997 – 12/31/1997 • S98349_006 1/1/1998 – 1/31/1998 • S98349_007 2/1/1998 – 2/28/1998 • S98349_008 3/1/1998 – 3/31/1998 • S98349_009 4/1/1998 – 4/30/1998 • S98349_010 5/1/1998 – 5/31/1998	DTN: MO9807DSTSET01.000
Heater power and sensor temperatures: June 1, 1998 – August 31, 1998	Floor heater and wing heater power in Table S99012_001; Table names and time intervals for temperatures are as follows: • S99012_004 6/1/1998 – 6/30/1998 • S99012_005 7/1/1998 – 7/31/1998 • S99012_006 8/1/1998 – 8/31/1998	DTN: MO9810DSTSET02.000
Heater power and sensor temperatures: September 1, 1998 – May 31, 1999	Floor heater and wing heater power in Table S99304_010; Table names and time intervals for temperatures are as follows: • S99304_001 9/1/1998 – 9/30/1998 • S99304_002 10/1/1998 – 10/31/1998 • S99304_003 11/1/1998 – 11/30/1998 • S99304_004 12/1/1998 – 12/30/1998 • S99304_005 1/1/1999 – 1/31/1999 • S99304_006 2/1/1999 – 2/28/1999 • S99304_007 3/1/1999 – 3/30/1999 • S99304_008 4/1/1999 – 4/29/1999 • S99304_009 5/1/1999 – 5/31/1999	DTN: MO9906DSTSET03.000
Heater power and sensor temperatures: June 1, 1999 – October 31, 1999	Floor heater and wing heater power in Table S00044_001; Table names and time intervals for temperatures are as follows: • S00044_004 6-/1/1999 – 6/30/1999 • S00044_005 7/1/1999 – 7/31/1999 • S00044_006 8/1/1999 – 8/31/1999 • S00044_007 9/1/1999 – 9/30/1999 • S00044_008 10/1/1999 – 10/31/1999	DTN: MO0001SEPDSTPC.000
Heater power and sensor temperatures: November 1, 1999 – May 31, 2000	Floor heater and wing heater power in Table S00327_009; Table names and time intervals for temperatures are as follows: • S00327_002 1/1/2000 – 1/31/2000 • S00327_003 2/1/2000 – 2/29/2000 • S00327_004 3/1/2000 – 3/31/2000 • S00327_005 4/1/2000 – 4/30/2000 • S00327_006 5/1/2000 – 5/31/2000 • S00327_007 11/1/1999 – 11/30/1999 • S00327_008 12/1/1999 – 12/31/1999	DTN: MO0007SEPDSTPC.001
Sensor temperatures: January 15, 2002 – June 30, 2002	Data obtained from text files: TDIF_009_0201_2.txt, TDIF_009_0202.txt, TDIF_009_0203.txt, TDIF_009_0204.txt, TDIF_009_0205.txt, and TDIF_009_0206.txt	DTN: MO0208SEPDSTTD.001

Table 4-3. Source DTNs are listed for field measurements made in the Drift Scale Test (DST). Note that these DTNs are used for validation purposes only. (Continued)

Model Input	Value	Source
Heater power and sensor temperatures: June 1, 2000 – November 30, 2000	Floor heater and wing heater power in Table S00468_002; Table names and time intervals for temperatures are as follows: • S00468_003 10/1/2000 – 10/31/2000 • S00468_004 6/1/2000 – 6/30/2000 • S00468_005 9/1/2000 – 9/30/2000 • S00468_006 8/1/2000 – 8/31/2000 • S00468_007 7/1/2000 – 7/31/2000 • S00468_008 11/1/2000 – 11/30/2000	DTN: MO0012SEPDSTPC.002
Heater power and sensor temperatures: December 1, 2000 – May 31, 2001	Floor heater and wing heater power in Table S01100_002; Table names and time intervals for temperatures are as follows: • S01100_004 12/1/2000 – 12/31/2000 • S01100_005 1/1/2001 – 1/31/2001 • S01100_006 2/1/2001 – 2/28/2001 • S01100_007 3/1/2001 – 3/31/2001 • S01100_008 4/1/2001 – 4/30/2001 • S01100_009 5/1/2001 – 5/31/2001	DTN: MO0107SEPDSTPC.003
Heater power and sensor temperatures: June 1, 2001 – January 14, 2002	Floor heater and wing heater power in Table S02060_010; Table names and time intervals for temperatures are as follows: • S02060_001 6/1/2001 – 6/30/2001 • S02060_002 7/1/2001 – 7/31/2001 • S02060_003 8/1/2001 – 8/31/2001 • S02060_004 9/1/2001 – 9/30/2001 • S02060_005 10/1/2001 – 10/31/2001 • S02060_006 11/1/2001 – 11/30/2001 • S02060_007 12/1/2001 – 12/31/2001 • S02060_008 1/1/2002 – 1/14/2002	DTN: MO0202SEPDSTTV.001
Sensor temperatures: July 1, 2002 – December 31, 2002	Data obtained from text files: TDIF_010_0207.txt, TDIF_010_0208.txt, TDIF_010_0209.txt, TDIF_010_0210.txt, TDIF_010_0211.txt, and TDIF_010_0212.txt	DTN: MO0303SEPDSTTM.000
Sensor temperatures: January 1, 2003 – June 30, 2003	Data obtained from text files: TDIF_011_0306.txt, TDIF_011_0302.txt, TDIF_011_0303.txt, TDIF_011_0304.txt, TDIF_011_0305.txt, and TDIF_011_0301.txt	DTN: MO0307SEPDST31.000
Water content in rock from neutron measurements: August 1997 – May 2002	Following are the neutron boreholes and files that supply the water content data: • Borehole 68 File N10HV.XLS • Borehole 79 File N11HV.XLS • Borehole 80 File N12HV.XLS	DTN: LL020710223142.024
Water content in rock from neutron measurements: January 2003 – May 2003	Following are the neutron boreholes and files that supply the water content data: • Borehole 68 File TD100307.xls • Borehole 79 File TD110307.xls • Borehole 80 File TD120307.xls	DTN: LL030709023122.032
Temperatures and gas-phase pressures at upper boundary (ground surface) and lower boundary (water table) of the three-dimensional Site-Scale UZ Flow Model (Table 4-1)	Files: INCON_thm_s32.dat and MESH_rep.VF	DTN: LB991201233129.001

5. ASSUMPTIONS

5.1 BOUNDARY CONDITIONS

5.1.1 Ground-Surface Relative Humidity

Assumption: The relative humidity at the ground surface above the repository is assumed to be 100 percent.

Rationale: The liquid-phase flux distribution applied at the upper boundary of the LDTH submodels of the MSTHM is the percolation flux distribution (from the base of the PTn unit into the top of the TSw sequence of units) calculated by *UZ Flow Models and Submodels* (BSC 2003h). Note that the three-dimensional UZ Flow Model accounts for the influence of evapotranspiration in the soil zone on net infiltration flux at Yucca Mountain by virtue of the fact that it is addressed in the net-infiltration flux distribution applied at the top of the three-dimensional UZ Flow Model. A relative humidity of 100 percent is applied at the atmosphere boundary at the top of the MSTHM to ensure that the PTn-to-TSw percolation flux is neither significantly diminished nor increased by virtue of gas-phase moisture flux at the top of the MSTHM. To verify that the PTn-to-TSw percolation flux is neither significantly diminished nor increased, the ambient present-day percolation flux above the repository horizon was compared to the PTn-to-TSw percolation flux, which is imposed at the upper boundary in the LDTH submodels (Section 6.2.6). It was found that the differences between the imposed PTn-to-TSw percolation flux at the upper boundary and the percolation flux above the repository horizon never exceeds 3.61×10^{-4} mm/yr for the mean infiltration flux case. For example, the percolation flux above the repository is 3.11×10^{-5} mm/yr greater than the imposed PTn-to-TSw percolation flux for the LDTH-submodel location with the lowest present-day PTn-to-TSw percolation flux; because this difference is only 0.01 percent of the PTn-to-TSw percolation flux, which is 0.23 mm/yr, it is negligible. The percolation flux above the repository is 3.61×10^{-4} mm/yr greater than the imposed PTn-to-TSw percolation flux for the LDTH-submodel location with the highest present-day PTn-to-TSw percolation flux; because this difference is only 0.003 percent of the PTn-to-TSw percolation flux, which is 13.8 mm/yr, it is negligible. Note that these small differences are positive; that is to say that imposing a relative humidity of 100 percent at the ground surface slightly increases the moisture flux above the repository horizon (by the very small quantities given above) compared to the imposed liquid-phase flux at the top of the LDTH submodel.

Confirmation Status: Because this assumption is justified, it does not require confirmation.

Use in the Model: This assumption effects all LDTH submodels, and is used in Sections 6.2, 6.3, 7.2, and 7.3.

5.1.2 Ambient Percolation Flux above Repository Horizon

Assumption: The ambient percolation flux distribution above the repository horizon is assumed to be unaffected by mountain-scale repository-heat-driven thermohydrologic effects until it reaches the boiling condensation zones surrounding the emplacement drifts. Moreover, between

the base of the PTn UZ Model Layers and the repository horizon, ambient percolation flux is assumed to be one-dimensional vertically downward with no lateral diversion caused by layering or heterogeneity in the hydrologic-property distributions. Therefore, the repository-scale percolation flux distribution is taken to be the percolation flux distribution from the PTn to the upper TSw UZ Model Layer Unit that is predicted by *UZ Flow Models and Submodels* (BSC 2003h).

Rationale: The influence of subboiling evaporation has a negligible influence on the magnitude or direction of liquid-phase flux. Moreover, the LDTH submodels already account for the influence of subboiling evaporation within the confines of the two-dimensional chimney geometry. Fracturing within the sequence of UZ Model Layer Units between the PTn and the repository horizon is extremely dense and ubiquitous (BSC 2003i), which is not conducive to laterally diverting gravity-driven ambient percolation; thus, percolation within this interval is vertically downward. The denseness of the fracture spacing is evident in the data on fracture frequency (DTN: LB0205REVUZPRP.001). As is discussed in Section 6.1 of *Calibrated Properties Model* (BSC 2003i), heterogeneity of hydrologic properties (including fracture spacing) is treated as a function of geologic layering; thus, any one geologic layer has homogeneous properties throughout the grid from *UZ Flow Models and Submodels* (BSC 2003h), as well as throughout the MSTHM.

Confirmation Status: Because this assumption is justified, it does not require confirmation.

Use in the Model: Section 6.2.6.6 describes the use of percolation flux in the MSTHM LDTH submodels. This assumption is used in Sections 6.2, 6.3, and 7.3.

5.1.3 Barometric Pressure Fluctuations at the Ground Surface

Assumption: Barometric (i.e., gas-phase) pressure fluctuations at the ground surface above the repository are assumed to be negligible. Consequently, the gas-phase pressure at the ground surface is held constant (i.e., does not fluctuate with time) in all thermohydrologic models.

Rationale: The magnitude of gas-phase pressure fluctuations resulting from barometric pumping is small compared to the gas-phase pressure gradients resulting from (1) forced convective cooling of emplacement drifts during the preclosure ventilation period and (2) repository-heat-driven boiling during the postclosure period. Moreover, barometric pumping is not a significant contributor to the removal of water vapor from emplacement drifts and the adjoining host rock, compared to the effect of drift ventilation during the preclosure period and the effect of boiling during the postclosure period.

Confirmation Status: Because this assumption is justified, it does not require confirmation.

Use in the Model: This assumption is used in Sections 6.3, 7.2, and 7.3.

5.2 HEAT FLOW PROCESSES

5.2.1 Mountain-Scale Heat Flow

Assumption: The following assumption only applies to the SMT submodels (Section 6.2.5). For the SMT submodels, differences in temperature that arise as a result of proximity to the repository edges are assumed to be governed by thermal conduction in the rock. This assumption is equivalent to saying that convective heat transfer mechanisms (notably, buoyant gas-phase convection and the heat pipe effect) have a negligible influence on lateral mountain-scale heat flow at Yucca Mountain. This assumption tends to preserve temperature differences that arise as a result of differences in proximity to the repository edges. This assumption allows mountain-scale heat flow to be represented using thermal-conduction models. This assumption is applied to the SMT submodels.

Rationale: The bulk permeability k_b of much of the unsaturated zone is much less than the threshold k_b value at which buoyant gas-phase convection begins to significantly influence heat flow (Buscheck and Nitao 1994); therefore, heat flow is dominated by heat conduction. Moreover, the primary role of the SMT submodel in the MSTHM methodology is to predict the rate at which the edge-cooling effect propagates inward from the repository edges to the repository center. Mountain-scale buoyant gas-phase convection has a negligible effect on controlling the rate at which the edge-cooling effect propagates in toward the center of the repository. This assumption is also justified because it tends to preserve temperature differences that arise as a result of differences in proximity to the repository edges.

Confirmation Status: Because this assumption is justified, it does not require confirmation.

Use in the Model: This assumption is used in the MSTHM calculations in Sections 6.3, 6.4, and 7.3.

5.2.2 Drift-Scale Heat Flow

Assumption: The following assumption only applies to the DDT submodels. For the DDT submodels, the influence of repository-scale thermal-conductivity variability and drift-scale buoyant gas-phase convection within the host rock are assumed to have a negligible influence on waste-package-to-waste-package temperature deviations along the emplacement drifts. This assumption allows the MSTHM methodology to rely upon only one set of DDT-submodel calculations conducted at a single LDTH-SDT-submodel location. This assumption is only applied to the DDT submodels.

Rationale: During the preclosure period, thermal radiation between the waste package and drift wall controls the longitudinal temperature deviations along the emplacement drift in the DDT submodels. During the postclosure period, thermal radiation between the waste package and drip shield and between the drip shield and drift wall control the temperature deviations along the emplacement drift. Heat flow in the longitudinal direction in the host rock (both by conduction and convection) plays a much smaller role on attenuating waste-package-to-waste-package temperature variations along the drift wall than does thermal radiation in the drift (Hardin 1998, Section 3.7.5.4).

The DDT submodel is only used for two purposes: (1) calculating the temperature difference between the waste package and drip shield and (2) calculating the longitudinal temperature variations along the drift axis. Neither of these quantities is significantly influenced by the thermal conductivity in the host rock (or in any of the other UZ Model Layers). Therefore, it is not necessary to run the DDT submodels at multiple locations because the only potential benefit of running at multiple locations would be to capture the influence of the local thermal conductivity values, which is relatively unimportant with regards to the two quantities that the DDT submodel is required to predict. Convective heat transfer driven by thermohydrologic behavior in the host rock has little effect on longitudinal temperature variation in the drift. In other words, thermohydrologic processes in the host rock do not contribute significantly to equalization of axial temperature variations in the drift. Therefore, the conduction-only DDT submodel adequately represents longitudinal temperature deviations in the drifts or adjoining host rock (relative to line-average-heat-source conditions). This assumption is also justified because it tends to preserve temperature variability along the drifts.

Drift-scale latent heat and convective heat transport by seeping water are included in the MSTHM methodology because these effects are fully addressed by the LDTH submodels. Section 6.2.1 outlines the MSTHM approach and the thermohydrologic processes accounted for by the model.

Confirmation Status: Because this assumption is justified, it does not require confirmation.

Use in the Model: This assumption is used in the MSTHM calculations in Sections 6.2.8, 6.3, 6.4, and 7.3.

5.2.3 Waste Package Emplacement

Assumption: The assumption is made that the entire waste package inventory of the repository is emplaced at the same time.

Rationale: The heat-generation-rate-versus-time tables (BSC 2004e) for the entire waste package inventory, as well as for the individual waste package types (BSC 2004f), were effectively developed for a single time of emplacement and therefore, do not represent how the heat-generation-rate tables may vary for the inventory and respective waste package types during the 23-year emplacement period. Therefore this assumption is consistent with the heat-generation-rate-versus-time tables. The 50-year ventilation duration is the minimum time that any waste package location in the repository will experience ventilation. For a sequential emplacement repository analysis with all waste packages assumed to be the same years out of reactor at the time of emplacement, packages emplaced at the beginning of the 23-year period would experience higher peak temperatures relative to those emplaced at the end of the emplacement period. The assumption that all waste packages are emplaced simultaneously at 50 years results in an analysis that maximizes peak temperatures compared to other emplacement assumptions.

Confirmation Status: Because this assumption is justified, it does not require confirmation.

Use in the Model: This assumption is applied to the SMT submodels (Section 6.2.5), and is used in the MSTHM calculations in Sections 6.3 and 7.3.

5.3 MATERIAL PROPERTIES

5.3.1 Hydrologic Properties

5.3.1.1 Permeability of the Drip Shield and Waste Package for the MSTHM

Assumption: The drip shield and waste packages are assumed to be impermeable for the entire duration of the MSTHM simulation.

Rationale: These components will take a long time to fail, and it is beyond the scope of this document to model their failure.

Confirmation Status: Because this assumption is justified, it does not require confirmation.

Use in the Model: This assumption is used in Sections 6.3, 7.1, 7.2, and 7.3.

5.3.1.2 Hydrologic Properties of the Intragranular Porosity in the Invert Materials

Assumption: The hydrologic properties of the intragranular porosity of the invert materials are assumed to be the same as that of the matrix of the host rock. Because the Tptpll (tsw35) unit is the host-rock unit for 75.1 percent of the repository area as modeled in the MSTHM (Table 6.3-2), it is assumed that matrix properties of the tsw35 unit are applicable to the crushed-tuff invert for the entire repository area. The ratio of the surface area of the crushed tuff grains divided by the connection length into the grains is assumed to be 1×10^5 for the intragranular porosity. These assumptions are used in all LDTH submodels (Sections 6.2.6 and 6.3).

Rationale: The invert is comprised of crushed-tuff gravel, which is derived from the host rock. The dual-permeability model (DKM) is applied to represent flow in crushed-tuff gravel, with flow within the tuff grains (called the intragranular porosity) corresponding to flow in the matrix continuum of the DKM and flow around the tuff grains (called the intergranular porosity) corresponding to flow in the fracture continuum of the DKM. Therefore, it is reasonable to assume that the hydrologic properties of the intragranular porosity are the same as those for the matrix of the predominant host-rock unit. Applying the *intact* host-rock matrix properties to the intragranular porosity of the invert implies that there is no reduction in the rewetting rate of the invert by virtue of limited rock-to-grain or grain-to-grain contact area. The limited contact area will not prevent the crushed-tuff grains from eventually attaining capillary-pressure equilibrium with the adjoining host rock. When the drift wall has rewet to ambient liquid-phase saturation, relative humidity at the drift wall will be very high (> 99 percent). The crushed-tuff grains in the invert cannot remain dry when exposed to a high-relative humidity environment. However, the limited rock-to-grain (and grain-to-grain) contact area may impede the rate at which rewetting allows the invert to attain capillary-pressure equilibrium with the adjoining host rock. Thus, there is some uncertainty about the time required for the invert to rewet to ambient liquid-phase saturation conditions. The fact that the crushed-tuff invert could be derived from material from the other three host-rock units (Tptpll, Tptpmn, and Tptpln) is also a source of uncertainty with regards to the time required for the invert to rewet to ambient liquid-phase saturation conditions.

The assumption that the ratio of the surface area of the crushed-tuff grains divided by the connection length into the grains is equal to 1×10^5 affects the disequilibrium between the

intergranular porosity and the intergranular porosity. For 3-mm-diameter grains and 45 percent intergranular porosity that apply to the invert (Table 4-1), this ratio is 7.33×10^5. A smaller ratio (than 7.33×10^5) is appropriate because it is unlikely that all of the grain surfaces will be wetted as water drains through the intergranular porosity.

Confirmation Status: Because these assumptions are considered to be adequate, they do not require confirmation.

Use in the Model: This assumption is used in Sections 6.3, 7.1, 7.2, and 7.3.

5.3.1.3 Hydrologic Properties for the Concrete Invert in the Drift Scale Test

Assumption: The hydrologic properties for the Tptpmn (tsw34) host rock in the Drift Scale Test (DST) are assumed to be applicable to concrete invert in the Heated Drift of the DST.

Rationale: Hydrologic properties for the concrete invert were not measured and are not readily available from the literature. Because the invert comprises such a small volume relative to the thermally perturbed volume of the host rock in the DST, this assumption is justified.

Confirmation Status: Because this assumption is justified, it does not require confirmation.

Use in the Model: This assumption is used in Section 7.2.

5.3.1.4 Fracture Permeability of the Host Rock in the Wing-Heater Array of the Drift Scale Test

Assumption: The boreholes that contain the wing heaters in the Drift Scale Test (DST) are not explicitly represented in the DST thermohydrologic models. The boreholes, which intersect the Heated Drift are not sealed and provide preferential conduits for gas flow. It is assumed that increasing the fracture permeability by a factor of 1,000, in the lateral (horizontal) direction, for the wing-heater array (Figures 7.2-2 and 7.2-16) adequately represents the influence of the wing-heater boreholes as preferential conduits to gas flow. Note that the lateral direction is parallel to the axis of the wing-heater boreholes. Note also that for the interval between the wing heaters and the Heated Drift the fracture permeability is also increased by a factor of 1,000 in the lateral (horizontal) direction.

Rationale: The wing-heater arrays consist of 50 open boreholes (with 25 boreholes located on each side of the Heated Drift) that function as preferential conduits (in the lateral direction) to gas flow within the boiling and dryout zones of the DST. The effect on thermohydrological behavior is to provide a means of relieving gas-phase pressure buildup in the center of the boiling zone and to allow some of the water vapor generated in that zone to enter the Heated Drift and to exit the Heated Drift through the leaky bulkhead. A thousand-fold increase in lateral fracture permeability effectively eliminates resistance to gas flow from the wing-heater array into the Heated Drift. In Section 7.2 it is found that modeled temperatures and liquid-phase saturations are weakly dependent on whether water vapor leaves the DST through the bulkhead. It should be noted that much of this water vapor entered in the Heated Drift from the wing-heater array. Therefore, the assumption for fracture permeability in the wing-heater array is justified in light of its small impact on modeled thermohydrologic behavior in the DST.

Confirmation Status: Because this assumption is justified, it does not require confirmation.

Use in the Model: This assumption is used in Section 7.2.

5.3.1.5 Permeability of the Bulkhead in the Drift Scale Test

Assumption: The bulkhead in the Drift Scale Test (DST) is assumed to be extremely permeable, with a permeability that is one-tenth that of the open drift. This assumption is made because the bulkhead is not sealed at the perimeter of the drift and because it contains several openings between the hot and cold side of the bulkhead.

Rationale: Section 7.3.4 of *Drift-Scale Coupled Processes (DST and TH Seepage) Models* (BSC 2003j) discusses how the bulkhead functions as an open boundary for gas-phase flow. In Section 7.2, it is found that modeled temperatures and liquid-phase saturations are weakly dependent on whether water vapor leaves the DST through the bulkhead. Therefore, the assumption for the permeability of the bulkhead is justified in light of its small impact on modeled thermohydrologic behavior in the DST; thus, this assumption is justified.

Confirmation Status: Because this assumption is justified, it does not require confirmation.

Use in the Model: This assumption is used in Section 7.2.

5.3.1.6 Permeability of the Bulkhead in the Three-Dimensional Monolithic D/LMTH Model Used in the MSTHM Validation Test Case

Assumption: The nested three-dimensional monolithic thermohydrologic model, called the D/LMTH model and which is used in the MSTHM validation test case (Section 7.3), has a leaky bulkhead located just beyond the location of last waste package at the edge of the drift. It is assumed that this bulkhead is leaky, with the same bulk permeability as that of the adjoining fractured rock mass.

Rationale: The influence of an extremely leaky bulkhead on the DST thermohydrologic model results is investigated in Section 7.2, where it is found that modeled temperatures and liquid-phase saturations are weakly dependent on whether water vapor leaves the DST through the bulkhead. Therefore, the permeability of the bulkhead in the DST has a small impact on modeled thermohydrologic behavior in the DST. Because the thermally perturbed (boiling) zone of the DST is in closer proximity to the bulkhead than it will be for most of the interval of most emplacement drifts in the repository, the impact of the bulkhead on predicted thermohydrologic conditions along emplacement drifts will be no greater than that demonstrated for the DST in Section 7.2. Therefore, the assumed permeability of the bulkhead in the three-dimensional monolithic D/LMTH model does not play a significant role in thermohydrologic behavior predicted in that model; thus, this assumption is justified.

Confirmation Status: Because this assumption is justified, it does not require confirmation.

Use in the Model: This assumption is used in Section 7.3.

5.3.1.7 Permeability of the Gas-Filled Cavities Inside the Emplacement Drifts in the LDTH Submodels

Assumption: The gas-filled cavity between the drip shield and drift wall is represented as a porous media with 100 percent porosity and a very large permeability of 1.0×10^{-8} m^2.

Rationale: The value for permeability (1.0×10^{-8} m^2) for the gas-filled cavity in the emplacement drifts is much larger than the bulk permeability (which is nearly the same as the fracture permeability in Table IV-4) of the four host-rock units (7.8×10^{-13}, 3.3×10^{-13}, 9.1×10^{-13}, and 1.3×10^{-12} m^2 for the tsw33, tsw34, tsw35, and tsw36, respectively). The effective permeability is large enough so that it does not impede gas-phase flow within the emplacement drifts.

Confirmation Status: Because this assumption is considered to be adequate, it does not require confirmation.

Use in the Model: This assumption is used in Sections 6.3, 7.1, 7.2, and 7.3.

5.3.1.8 Permeability of the Intergranular Porosity of the Invert Materials

Assumption: The permeability of the intergranular porosity of the crushed-tuff invert is 1.0×10^{-9} m^2, which is between the permeability values for the 0.317-mm particle size (1.681×10^{-10} m^2) and for the 3-mm particle size (1.511×10^{-8} m^2) from DTN: MO0307SPAVGSUM.000. It should be noted that there is some uncertainty about the actual particle sizes of the emplaced crushed-tuff invert.

Rationale: The potential range of values for the permeability of the intergranular porosity of the crushed-tuff invert (DTN: MO0307SPAVGSUM.000) has little effect on thermohydrologic conditions in the invert for the following two reasons. The first reason relates to liquid-phase flow. An inspection of the LDTH-submodel output related to the MSTHM basecase calculations for the TSPA-LA shows that the intergranular porosity remains dry for all but the initial one-to-two years of the postclosure period. During the first year or two following the end of the ventilation period, boiling and condensation within the invert results in a very small amount of condensate drainage at the base of the invert. After this condensate has drained and the invert has become dry as a result of boiling, the intergranular porosity is completely dry (i.e, 100 percent gas-filled). Therefore, liquid-phase flow in the intergranular porosity does not occur after the brief period of condensate drainage. The second reason relates to gas-phase flow. The value for permeability (of 1.0×10^{-9} m^2) for the intergranular porosity of the crushed-tuff invert is much larger than the bulk permeability (which is nearly the same as the fracture permeability in Table IV-4) of the four host-rock units (7.8×10^{-13}, 3.3×10^{-13}, 9.1×10^{-13}, and 1.3×10^{-12} m^2 for the tsw33, tsw34, tsw35, and tsw36, respectively). The effective permeability is large enough so that it does not impede gas-phase flow within the emplacement drifts. Thus, any development of buoyant gas-phase convection cells (also called natural convection) in the emplacement drift and adjoining host rock will not be impeded by the permeability of the intergranular porosity in the invert.

Confirmation Status: Because this assumption is considered to be adequate, it does not require confirmation.

Use in the Model: This assumption is used in Sections 6.3, 7.1, 7.2, and 7.3.

5.3.1.9 Tortuosity Factor for Binary Gas-Phase Diffusion

Assumption: Appropriate values for the tortuosity factor are selected for the matrix and fracture continuum on the basis of the parameter range given by de Marsily (1986, p. 233), which ranges from a value of 0.1 for clays to 0.7 for sands. A value of 0.2 is assumed for the matrix continuum because the pore sizes for the matrix are closer to that of clays than to that of sands. A value of 0.7 is assumed for the fracture continuum because the effective pore sizes for fractures are similar to those of sands.

Rationale: The tortuosity factor is used for determining the binary gas-phase diffusion of air and water vapor. Binary gas-phase diffusion is of negligible importance to the MSTHM results because its influence is primarily confined to being a negligible impact on heat flow, compared to the impact of conductive and convective heat flow (Buscheck and Nitao 1994, pp. 2464 and 2465). Therefore, exact quantification of the tortuosity factor is not required; instead appropriate values are taken from the literature, as discussed above. A value of tortuosity factor of 0.2 is selected for the rock matrix because the pore sizes of the matrix are similar to those of clay, which has a value for tortuosity factor of 0.1. The tortuosity factor is set to 0.7 for the fractures, which corresponds to the highest value reported by de Marsily (1986), which corresponds to the value for sand. Binary gas-phase diffusion is further modified for the fracture-to-fracture connections by multiplication of the tortuosity factor by the fracture porosity of the bulk rock (Buscheck and Nitao 1994, Equation 8). This operation yields the appropriate value for fracture-to-fracture interconnection area. Similarly, binary gas-phase diffusion is modified for the matrix-to-matrix connections by multiplication of the tortuosity factor by the matrix porosity of the bulk rock. This operation yields the appropriate value for matrix-to-matrix interconnection area.

Confirmation Status: Because this assumption is considered to be adequate, it requires no further confirmation.

Use in the Model: This assumption is used in Sections 6.3, 7.1, 7.2, and 7.3.

5.3.2 Thermal Properties

5.3.2.1 Thermal Conductivity in SDT, DDT, and SMT Submodels

Assumption: The thermal conductivity data is provided for both dry and wet conditions. The conduction-only submodels (SDT, DDT, and SMT submodels in Section 6.2) cannot explicitly represent the influence of liquid-phase saturation on thermal conductivity. Since the rock is generally much closer to being fully saturated than being completely dry, the wet value of thermal conductivity are applied to all conduction-only submodels. This assumption has no effect on the results of the MSTHM.

Rationale: This assumption must be judged in light of how the MSTHM combines the results of four families of submodels: SDT, DDT, SMT, and LDTH. The MSTHM methodology (see Figure 1-1, Table 1-1, Table 1-2, Table 1-3, Section 6.2.4, and Attachment IX) accounts for the influence of thermohydrologic processes (including liquid-phase saturation changes) on the temperature distribution around and inside the emplacement drifts. Thus the MSTHM fully accounts for the significant liquid-saturation dependence of thermal conductivity as it is affected by rock dryout and condensation buildup (if any). The LDTH submodels also represent the influence of the ambient liquid-phase saturation distribution, which is consistent with that of the three-dimensional UZ Flow Model, on drift-scale heat flow. It is also important to note that the zone for which the dry thermal conductivity is applicable is confined to a narrow cylindrically shaped dryout zone with a radius generally no greater than 10 m for the mean infiltration flux case (Figure 6.3-4b). The primary influence of the narrow zone of decreased thermal conductivity is on the temperature buildup in the immediate vicinity of the emplacement drifts; this influence is fully captured in the finely gridded LDTH submodels of the MSTHM, which account for the liquid-phase saturation dependence of thermal conductivity. While significantly affecting the drift-scale temperature gradients around the drifts, this narrow region of reduced thermal conductivity has a no influence on mountain-scale heat flow. Because the volume of reduced thermal conductivity around the drifts is so small, compared to the scale at which mountain-scale heat flow occurs, it has a negligible influence on mountain-scale heat flow. For the purposes of the SDT, SMT, and DDT submodels, the approximation is made that ambient liquid-phase saturation is 100 percent. The difference in thermal conductivity between a liquid-phase saturation of 90 percent (which is prevalent in the host-rock units) and 100 percent is small in comparison to parametric uncertainty of thermal conductivity (Section 6.3.2.2). Moreover, the LDTH submodel utilizes the ambient liquid-phase saturation values in determining thermal conductivity; thus, for drift-scale heat flow the MSTHM fully accounts for the ambient liquid-phase saturation conditions.

As for the validity of this assumption in the DDT submodel, it should be noted that the DDT submodel is only used for two purposes: (1) calculating the temperature difference between the waste package and drip shield and (2) calculating the longitudinal temperature variations along the drift axis. Neither of these quantities is influenced by whether wet or dry thermal conductivity is applied in the host rock.

Section 7.3 describes the comparison between the MSTHM and a corresponding three-dimensional monolithic thermohydrologic model of the same three-drift system. The good agreement between the MSTHM and the corresponding monolithic thermohydrologic model attests to the validity of this approach, as well as justifying the appropriateness of the assumption of the thermal conductivity used in the SDT, SMT, and DDT submodels.

Confirmation Status: Because this assumption is justified, it does not require confirmation.

Use in the Model: This assumption is used in the MSTHM calculations in Sections 6.3 and 7.3.

5.3.2.2 SMT-Submodel Saturated-Zone Thermal Properties

Assumption: The SMT submodel (Section 6.2.5) is the only submodel that explicitly represents the saturated zone. An assumption is made that the saturated zone is comprised of a material

with average thermal properties, including thermal conductivity, mass density, and specific heat capacity. The averaging is accomplished by determining area-weighting factors for each of the UZ Model Layers that occur at the water table, which is the base of the grid from *UZ Flow Models and Submodels* (BSC 2003h).

Rationale: The range in thermal properties of the units occurring at the water table is relatively narrow, and because the saturated zone is far enough away from the repository horizon (on the order of 200 m or greater), the results of the MSTHM are insensitive to the averaging scheme selected for the thermal properties of the saturated zone.

Confirmation Status: Because the output of the MSTHM is not sensitive to this assumption, this assumption is justified and does not need confirmation.

Use in the Model: This assumption is used in the MSTHM calculations in Sections 6.3 and 7.3.

5.3.2.3 Thermal Conductivity and Mass Density for the Dual-Permeability Model

Assumption: The dual-permeability model (DKM) is comprised of a fracture and matrix continuum. It is necessary to apportion the bulk thermal property values to the fracture and matrix continuum. The values of thermal conductivity K_{th} and mass density ρ are apportioned to the fracture and matrix from the values for the bulk rock mass on the basis of the fracture porosity ϕ_{frac} by the following relationship:

$$K_{th,frac} = K_{th,bulk} \times (\phi_{frac})$$

$$K_{th,mat} = K_{th,bulk} \times (1 - \phi_{frac})$$

$$\rho_{frac} = \rho_{bulk} \times (\phi_{frac})$$

$$\rho_{mat} = \rho_{bulk} \times (1 - \phi_{frac})$$

The apportioning of fracture and matrix values of K_{th} and ρ is shown in Table IV-3b in Attachment IV. This assumption is used in the MSTHM calculations in Sections 6.3 and 7.3.

Rationale: This approach conserves the total value of thermal conductivity and the total value of mass density. Therefore, the total conductive heat flow is the same as a single continuum with the same total value of thermal conductivity. Similarly, during the transient (heat-up) period, the correct mass density of the rock mass is honored. This method is only used in the LDTH submodels. This assumption has no impact on the results of the MSTHM; thus, this assumption is justified.

Confirmation Status: Because this assumption is justified, it does not require confirmation.

Use in the Model: This assumption is used in Sections 6.3 and 7.3.

5.3.2.4 Thermal Properties of the Lumped Drip-Shield/Waste Package Heat Source in the LDTH Submodels

Assumption: The drip shield and waste package are represented as a lumped monolithic heat source in the LDTH submodels with thermal property values that are an average of the respective values for the waste package and drip shield. The mass density, specific heat, and thermal conductivity of the lumped monolithic heat source are a mass-weighted-average of the respective waste package and drip-shield values.

Rationale: The purpose of the LDTH submodel within the context of the MSTHM (Section 6.2.4) does not require that the LDTH submodel provide a description of the temperature or hydrological effects inside the drip shield; thus, this assumption is justified.

Confirmation Status: Because this assumption is justified, it does not require confirmation.

Use in the Model: This assumption is used in the MSTHM calculations in Sections 6.2, 6.3 and 7.3.

5.3.2.5 Thermal Properties for the Concrete Invert in the Drift Scale Test

Assumption: The thermal properties for the Tptpmn (tsw34) host rock in the Drift Scale Test (DST) are assumed to be applicable to concrete invert in the Heated Drift of the DST. It is worth noting that the TSPA-LA design does not include a concrete liner.

Rationale: Thermal properties for the concrete invert were not measured and are not readily available from the literature. Because the invert comprises such a small volume relative to the thermally perturbed volume of the host rock in the DST (Figures 7.2-2 and 7.2-16) this assumption has a negligible effect on thermohydrologic behavior in the DST; therefore, this assumption is justified.

Confirmation Status: Because this assumption is justified, it does not require confirmation.

Use in the Model: This assumption is used in Section 7.2.

5.3.2.6 Thermal Conductivity of the Bulkhead in the Drift Scale Test

Assumption: The bulkhead in the Drift Scale Test is assumed to have a very large value of thermal conductivity (5.5 W/m°C).

Rationale: As described in *Drift-Scale Test As-Built Report* (CRWMS M&O 1998a), the bulkhead in the Drift Scale Test (DST) consists of a complex mix of steel, glass, and fiberglass. The thermal conductivity of the bulkhead is assumed to be very large because portions of the bulkhead (such as the glass window) are not insulated and because the bulkhead is penetrated by a large array of metal conduit containing instrument cables and power lines. Moreover, during the DST, the fiberglass insulation became extremely wet as a result of the condensation of water vapor that was passing through the bulkhead. The total effect of these conditions results in a large value of thermal conductivity for the bulkhead that is very difficult to quantify. In Section 7.2, it is found that modeled temperatures and liquid-phase saturations are weakly dependent on

whether water vapor leaves the DST through the bulkhead. In Section 7.2, it is also found that the heat loss through the bulkhead resulting from the convection of water vapor is much larger than the heat loss resulting from thermal conduction. Therefore, the assumption for the thermal conductivity of the bulkhead is justified in light of its small impact on modeled thermohydrologic behavior in the DST.

Confirmation Status: Because this assumption is justified, it does not require confirmation.

Use in the Model: This assumption is used in Section 7.2.

5.4 WASTE PACKAGE AND DRIP SHIELD DESIGN INFORMATION

During the preparation of this report, some of the design information was updated as several IEDs were superseded. These revisions resulted in small changes to the dimensions of the waste packages and drip shield as summarized in Table 5-1. These small changes to the dimensions necessitate the assumption that they negligibly affect the results of the MSTHM described in this report; this assumption requires confirmation. The details of this assumption are itemized in Sections 5.4.1 through 5.4.7.

Table 5-1. Changes to the Waste Package and Drip Shield Design Information

Model Input	Superseded IED		Current IED		Relative Change in Value
	Value	Source	Value	Source	
21-PWR AP WP length	5.165 m	BSC 2003f	5.024 m	BSC 2004b	-2.7%
21-PWR AP WP diameter	1.644 m	BSC 2003f	1.718 m	BSC 2004b	+4.5%
21-PWR CR WP diameter	1.644 m	BSC 2003f	1.718 m	BSC 2004b	+4.5%
Weight of 21-PWR AP WP	43,000 kg	BSC 2003f	41,100 kg	BSC 2004b	-4.4%
44-BWR WP length	5.165 m	BSC 2003f	5.024 m	BSC 2004b	-2.7%
44-BWR WP diameter	1.674 m	BSC 2003f	1.756 m	BSC 2004b	+4.9%
Weight of 44-BWR WP	43,000 kg	BSC 2003f	41,700 kg	BSC 2004b	-3.0%
5 DHLW/DOE SNF-LONG WP length	5.217 m	BSC 2003f	5.059 m	BSC 2004b	-3.0%
5 DHLW/DOE SNF-LONG WP diameter	2.110 m	BSC 2003f	2.126 m	BSC 2004b	+0.8%
Weight of 5 DHLW/DOE SNF-LONG	57,000 kg	BSC 2003f	53,100 kg	BSC 2004b	-6.8%
5 DHLW/DOE SNF-SHORT WP length	3.590 m	BSC 2003f	3.453 m	BSC 2004b	-3.8%
5 DHLW/DOE SNF-SHORT WP diameter	2.110 m	BSC 2003f	2.126 m	BSC 2004b	+0.8%
Weight of 5 DHLW/DOE SNF-SHORT WP	39,000 kg	BSC 2003f	36,100 kg	BSC 2004b	-7.4%
Drip-shield length	6.105 m	BSC 2003g	5.805 m	BSC 2004c	-4.9%
Drip-shield width	2.512 m	BSC 2003g	2.533 m	BSC 2004c	+0.8%
Intersection of drip-shield plate-1 with drip-shield plate-2 from base/top of invert	1875 mm	BSC 2003i	1891 mm	BSC 2003o	+0.9%

5.4.1 Waste Package Lengths

Assumption: The small differences in waste-package lengths between those used in this report, which are obtained from the superseded IED (BSC 2003f), and those given in the current IED (BSC 2004b) have a negligible effect on in-drift and near-field thermohydrologic conditions.

Therefore, it is assumed that the results from the MSTHM described in this report adequately address the waste-package lengths given in the current IED (BSC 2004b).

Rationale: As summarized in Table 5-1, the differences in waste-package lengths between those used in this report, which are obtained from the superseded IED (BSC 2003f), and those listed in the current IED (BSC 2004b) are small, ranging from –2.7 to –3.8 percent.

Confirmation Status: This assumption requires confirmation.

Use in the Model: This assumption is used in Section 6.3.

5.4.2 Waste Package Diameters

Assumption: The small differences in waste-package diameters between those used in this report, which are obtained from the superseded IED (BSC 2003f), and those given in the current IED (BSC 2004b) have a negligible effect on in-drift and near-field thermohydrologic conditions. Therefore, it is assumed that the results from the MSTHM described in this report adequately address the waste-package diameters given in the current IED (BSC 2004b).

Rationale: As summarized in Table 5-1, the differences in waste-package diameters between those used in this report, which are obtained from the superseded IED (BSC 2003f), and those listed in the current IED (BSC 2004b) are small, ranging from +0.8 to +4.9 percent.

Confirmation Status: This assumption requires confirmation.

Use in the Model: This assumption is used in Section 6.3.

5.4.3 Waste Package Weights

Assumption: The small differences in waste-package weights between those used in this report, which are obtained from the superseded IED (BSC 2003f), and those given in the current IED (BSC 2004b) have a negligible effect on in-drift and near-field thermohydrologic conditions. Therefore, it is assumed that the results from the MSTHM described in this report adequately address the waste-package weights given in the current IED (BSC 2004b).

Rationale: As summarized in Table 5-1, the differences in waste-package weights between those used in this report, which are obtained from the superseded IED (BSC 2003f), and those listed in the current IED (BSC 2004b) are small, ranging from –3.0 to –7.4 percent.

Confirmation Status: This assumption requires confirmation.

Use in the Model: This assumption is used in Section 6.3.

5.4.4 Average Waste Package Diameter

Assumption: The waste package outer diameter is 1.644 meters, which is the diameter of the 21-PWR AP waste package (Table 4-1 and Table 5-1). This value is taken as the average

diameter for the waste packages emplaced over the entire repository. This information is used only in the DDT submodels (Section 6.2.8).

Rationale: This assumption only influences two aspects of the MSTHM: (1) the temperature difference between the waste package and drip shield and (2) the waste-package-to-waste-package variation of this temperature difference. Note that this temperature difference depends on the waste package heat output. The 21-PWR AP waste packages, 21-PWR CR waste packages, and 44-BWR AP waste packages, comprising the majority of waste packages with an appreciable heat output, have diameters of 1.644, 1.644, and 1.674 meters, respectively (Table 4-1) which are very close to the value of 1.644 meters in the DDT submodels. Table 11 of *D&E /PA/C IED Typical Waste Package Components Assembly (2)* (BSC 2004b) gives the nominal quantities of the various waste package types for the TSPA-LA design, including 4,299 21-PWR AP waste packages, 95 21-PWR CR waste packages, 2,831 44-BWR AP waste packages, and 11,184 total waste packages; thus, these waste packages comprise a large portion (64.6 percent) of the waste package inventory in the TSPA-LA design. Waste packages that deviate more from a value of 1.644 meters, such as the 24-BWR 1.318-m-diameter AP waste packages and the 5-DHLW/DOE-SNF 2.110-m-diameter co-disposal waste packages (Table 4-1), generate much less heat and also comprise a relatively small portion of the overall waste package inventory (BSC 2003c, Table 3). Therefore, 1.644 meters is very close to the actual diameter for the majority of waste packages in the overall inventory and is also very close to the diameter of the waste packages generating an appreciable temperature difference between the waste package and drip shield.

Confirmation Status: This assumption requires confirmation.

Use in the Model: This assumption is used in Sections 6.3 and 7.3.

5.4.5 Drip Shield Length

Assumption: The small difference in drip-shield length between that used in this report, which are obtained from the superseded IED (BSC 2003g), and that given in the current IED (BSC 2004c) has a negligible effect on in-drift and near-field thermohydrologic conditions. Therefore, it is assumed that the results from the MSTHM described in this report adequately address the drip-shield length given in the current IED (BSC 2004c).

Rationale: As summarized in Table 5-1, the difference in drip-shield length between that used in this report, which is obtained from the superseded IED (BSC 2003g), and that listed in the current IED (BSC 2004c) is small (–4.9 percent).

Confirmation Status: This assumption requires confirmation.

Use in the Model: This assumption is used in Section 6.3.

5.4.6 Drip Shield Width

Assumption: The very small difference in drip-shield width between that used in this report, which are obtained from the superseded IED (BSC 2003g), and that given in the current IED (BSC 2004c) has a negligible effect on in-drift and near-field thermohydrologic conditions.

Therefore, it is assumed that the results from the MSTHM described in this report adequately address the drip-shield width given in the current IED (BSC 2004c).

Rationale: As summarized in Table 5-1, the difference in drip-shield width between that used in this report, which is obtained from the superseded IED (BSC 2003g), and that listed in the current IED (BSC 2004c) is extremely small (+0.8 percent).

Confirmation Status: This assumption requires confirmation.

Use in the Model: This assumption is used in Section 6.3.

5.4.7 Intersection of Drip-Shield Plate-1 with Drip-Shield Plate-2 from Base/Top of Invert

Assumption: The very small difference in the intersection of drip-shield plate-1 with drip-shield plate-2 between that used in this report, which are obtained from the superseded IED (BSC 2003i), and that given in the current IED (BSC 2003o) has a negligible effect on in-drift and near-field thermohydrologic conditions. Therefore, it is assumed that the results from the MSTHM described in this report adequately address the intersection of drip-shield plate-1 with drip-shield plate-2 given in the current IED (BSC 2003o).

Rationale: As summarized in Table 5-1, the difference in the intersection of drip-shield plate-1 with drip-shield plate-2 between that used in this report, which is obtained from the superseded IED (BSC 2003i), and that listed in the current IED (BSC 2003o) is extremely small (+0.9 percent).

Confirmation Status: This assumption requires confirmation.

Use in the Model: This assumption is used in Section 6.3.

5.5 RELATIVE HUMIDITY IN EMPLACEMENT DRIFTS

Assumption: For the purposes of calculating relative humidity (*RH*) on the drip shield and on the waste package the assumption is made that the partial pressure of water vapor P_v in the drift is uniform and the same as that on the drift-wall surface at a given location. This is the same as saying that the absolute humidity in the drift is the same as that on the drift wall.

Rationale: This assumption recognizes that the gas in the drift (which consists of air and water vapor) is well mixed as a result of buoyant gas-phase convection and binary vapor diffusion of air and water. This mixing causes the absolute humidity to be uniform inside the emplacement drift at a given location along the drift. This assumption is validated in Sections 7.3.2.2 and 7.3.2.6 by virtue of the good agreement between the MSTHM predictions of relative humidity in the drift and those of the corresponding three-dimensional monolithic thermohydrologic model, which does not make this assumption about relative humidity in emplacement drifts.

Confirmation Status: Because this assumption is justified, it does not require confirmation.

Use in the Model: This assumption is used in Sections 6.3 and 7.3.

5.6 CONDENSATE DRAINAGE AROUND EMPLACEMENT DRIFTS

Assumption: Condensate that drains around the boiling zone surrounding an individual drift is assumed not to cross the vertical midplanes, which lie between that drift and the adjoining emplacement drifts (note that these vertical midplanes are 40.5 m away from the centerline of each drift). This assumption is implied with the use of the two-dimensional LDTH submodels (Section 6.2.6), which have adiabatic, no-fluid-flow boundaries on either side of the LDTH submodels.

Rationale: The boiling zones surrounding each emplacement drift are relatively narrow. As discussed in Section 6.3.1.1, the maximum lateral extent of boiling relative to the centerline of the emplacement drift is always much smaller than the half-drift spacing for the TSPA-LA design. Therefore, the majority of the host rock between emplacement drifts always remains below the boiling point, thereby enabling condensate and percolation flux to continuously drain between emplacement drifts. Fracturing within the sequence of UZ Model Layer Units at the repository horizon is extremely dense and ubiquitous (BSC 2003i), which is not conducive to laterally diverting condensate drainage; thus, condensate drainage is extremely unlikely to cross the vertical midplane separating emplacement drifts.

Confirmation Status: Because this assumption is justified, it does not require confirmation.

Use in the Model: This assumption is used in Sections 6.3 and 7.3.

5.7 GAS- AND LIQUID-PHASE FLOW IN THE LONGITUDINAL DIRECTION ALONG EMPLACEMENT DRIFTS (THE COLD-TRAP EFFECT)

Assumption: Gas- and liquid-phase flow in the longitudinal direction along drifts is assumed to have a negligible effect on all MSTHM predictions. This is equivalent to saying that the cold-trap effect does not play a significant role in the evolution of the temperature, relative humidity, and liquid-phase saturation histories within the emplacement drifts, as well as in the adjoining host rock. At the repository scale, the cold-trap effect involves the flow of water vapor from the hotter intervals of emplacement drifts (typically closer to the center of the repository) to cooler intervals (typically located closer to the edges of the repository) where this water vapor condenses. In principal, the cold-trap effect results in the transport of heat and moisture from hotter to cooler intervals of the emplacement drift. For all MSTHM predictions, it is assumed that heat and moisture transport in the longitudinal direction along emplacement drifts do not significantly affect thermohydrologic conditions along (and adjacent to) emplacement drifts. Thus, it is assumed that heat flow along the drifts is dominated by thermal radiation and that within the invert there is no capillary wicking of moisture in the longitudinal direction.

Rationale: This assumption is tested in Section 7.3, where the MSTHM is compared against a corresponding three-dimensional monolithic thermohydrologic model in which gas- and liquid-phase flow (i.e., the cold-trap effect) is allowed to occur along the emplacement drift. For the waste packages at the center of the repository, the MSTHM calculations are found to agree closely with those of the three-dimensional monolithic D/LMTH model, with the differences between the two models being much smaller than the range of thermohydrologic conditions

arising from parametric uncertainty. For the waste packages at the outer edge of the repository, the differences between the MSTHM predictions and those of the corresponding three-dimensional monolithic thermohydrologic model are larger than at the center of the repository. These differences, however, are still smaller than the range of thermohydrologic conditions arising from parametric uncertainty. The results of the validation study in Section 7.3 demonstrate that the MSTHM methodology (which includes the assumption of negligible gas- and liquid-phase flow in the longitudinal direction along drifts) is validated for its intended purpose of predicting thermohydrologic conditions in emplacement drifts and in the adjoining host rock. Thus, this assumption is also justified.

Confirmation Status: Because this assumption is justified, it does not require confirmation.

Use in the Model: This assumption is used in Section 6.3 and tested in Section 7.3.

6. MODEL DISCUSSION

This section of the model report describes the Multiscale Thermohydrologic Model (MSTHM), including a discussion about its conceptual framework and how the MSTHM methodology implements that framework. The MSTHM is implemented in several input-data-processing and submodel-building steps (Figures 6-1 and 6-2). The four major steps are (1) submodel input-file preparation, (2) execution of the four submodel families with the use of the NUFT v3.0s code (Section 3.1.1), (3) execution of MSTHAC v7.0 (Section 3.1.5), and (4) binning and postprocessing (i.e., graphics preparation) of the output from MSTHAC v7.0. The overall organization of Section 6 is as follows:

- Section 6.1 presents the scientific framework for Yucca Mountain thermohydrology, beginning with an overview of the ambient hydrological system. This is followed by a discussion of radioactive-decay-heat-driven thermohydrologic behavior within the repository emplacement drifts and in the adjoining repository host rock.

- Section 6.2 describes the MSTHM approach. Before discussing the details of the MSTHM approach, this section presents the governing equations that are solved by the NUFT code to represent the coupled flow of water, water vapor, air, and heat at the drift scale and to represent heat flow at the mountain scale. This is followed by a detailed description of the four families of MSTHM submodels, which are run with the NUFT code, and how the Multiscale Thermohydrologic Model Abstraction Code (MSTHAC v7.0) integrates the results from those four families of submodels.

- Section 6.3 presents the results of the MSTHM for three (lower-bound, mean, and upper-bound) infiltration flux cases. This section also covers the sensitivity analysis of parameter uncertainty.

- Section 6.4 describes a study that compares the results of the MSTHM against those of a corresponding alternative conceptual model.

Before continuing, it is important to distinguish between the MSTHM and the Multiscale Thermohydrologic Abstraction Code (MSTHAC v7.0). The MSTHM is the process-level model itself, which consists of four families of submodel types (Section 6.2.4) that are run using the thermohydrologic-simulation code NUFT v3.0s (Section 3.1.1) and the software that integrates the results of those submodel families. The integrating software used in this report is MSTHAC v7.0 (Section 3.1.5). Supporting and corroborating data or product outputs are identified in Section 4.4.

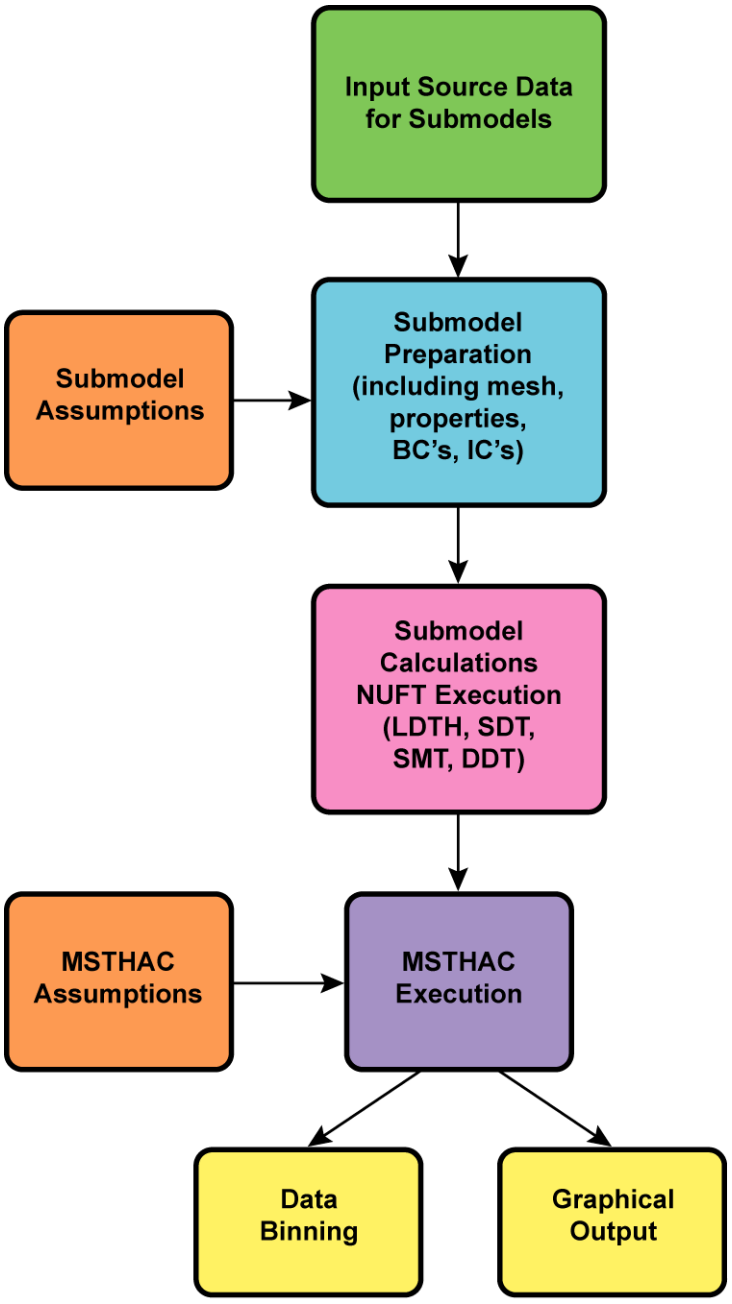

TB_AMR_fig1-2_MSTHM_flow

NOTES: BC = boundary conditions; IC = intitial conditions

Figure 6-1. Overall Data Flow Diagram for the MSTHM

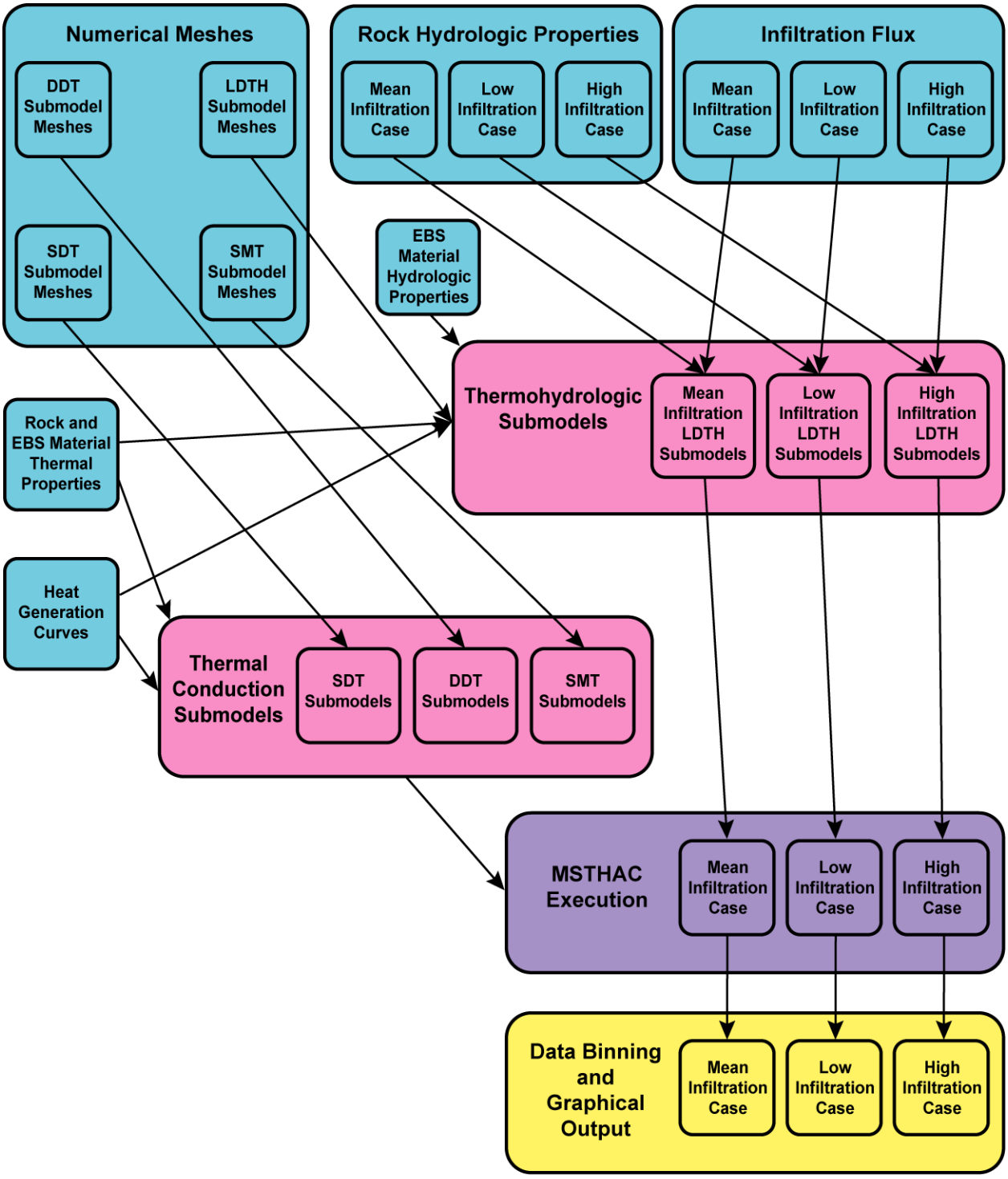

TB_AMR_fig1-3_MSTHM_flow2

Figure 6-2. Relationship Between Input Data and Submodels for Three Infiltration Flux Cases

6.1 YUCCA MOUNTAIN THERMOHYDROLOGY CONCEPTUAL MODEL

The role of the movement of water and heat within the repository is treated by the study of thermohydrology, which combines the more traditional fields of hydrology and heat transfer.

The physical domain that this model report is concerned with is the unsaturated zone of Yucca Mountain which lies above the groundwater table (i.e., the immediate and near-field location where the emplacement drifts will be constructed and the waste will be disposed). The geology of Yucca Mountain consists of several sequences of fractured volcanic rock depositions, while the main ambient hydrologic concern is that of vertical water infiltration associated with rainfall and snowmelt (Section 6.1.1). The thermal component of this model is concerned primarily with the radioactive decay heat-source associated with waste emplacement into the repository (Section 6.1.2). When examining thermohydrologic phenomena, there are two distinct regions of concern: (1) the phenomena associated with the host rock, and (2) the phenomena occurring within the repository emplacement drifts. The thermohydrologic phenomena associated with the host rock is primarily dealing with zones of boiling and re-wetting near, but outside of, the emplacement drifts (Section 6.1.3), while the thermohydrologic phenomena within the emplacement drift is associated with boiling, evaporation and condensation of water on the waste packages, drip shield, and drift wall (Section 6.1.4). There are several factors that can influence thermohydrologic phenomena either through the design of the repository (e.g., changing the average areal-heat-density of the waste inventory (Section 6.1.5)) or through the parameterization of the natural system (e.g., percolation flux and thermal conductivity (Section 6.1.5)).

6.1.1 Ambient Hydrology and Geology

Yucca Mountain is composed of a sequence of volcanic tuffs deposited as ash flow sheets about 13 million years ago. Some units are completely devitrified and welded, while others are vitric or partially vitric with various degrees of welding. Some are also zeolitized to varying degrees. In general, the more welded units are more densely fractured. Hydrostratigraphic units, which are called UZ Model Layers in the grid from *UZ Flow Models and Submodels* (BSC 2003h), have been defined primarily based on the degree of welding (Montazer and Wilson 1984). From the ground surface to the water table, these units are generally referred to as Tiva Canyon welded (TCw), Paintbrush nonwelded (PTn), Topopah Spring welded (TSw), Calico Hills nonwelded (CHn) and Crater Flat, which is broken down into Prow Pass (pp) and Bullfrog (bf).

Most of the total fluid storage capacity of the welded units at Yucca Mountain is contained in the matrix pores of this rock. The permeability in the rock matrix in these units, however, is very low, and therefore, fractures are the primary conduits for large-scale flow of water, air, and water vapor in these units. In some of the nonwelded units, fracturing is much less extensive, and the rock matrix is more permeable than in the welded units, causing gas and liquid-phase fluid flow to occur predominantly through the rock matrix.

The climate at Yucca Mountain is arid to semiarid, with infiltration from rainfall and snowmelt. Field data to date suggest that water that infiltrates at the ground surface percolates more-or-less vertically downward to the water table 700 m beneath the surface, with some degree of lateral diversion and the occasional occurrence of perched or semiperched aquifers (Flint et al. 2001). Note that under ambient conditions, the relative humidity (*RH*) in the unsaturated zone at the elevation of the repository is very high with relative humidity generally being above 99 percent (Buscheck et al. 2002).

6.1.2 Incorporating Radioactive Decay Heat

The repository is located in the unsaturated zone in the TSw hydrostratigraphic unit along a very gently dipping plane, approximately midway between the ground surface and the water table. The repository will accommodate the emplacement of spent nuclear fuel from commercial nuclear power plants and solidified high-level waste. Heat output declines exponentially with time, continuing for tens of thousands of years because of the very long half-life of many of the radionuclides (Figure 6.1-1).

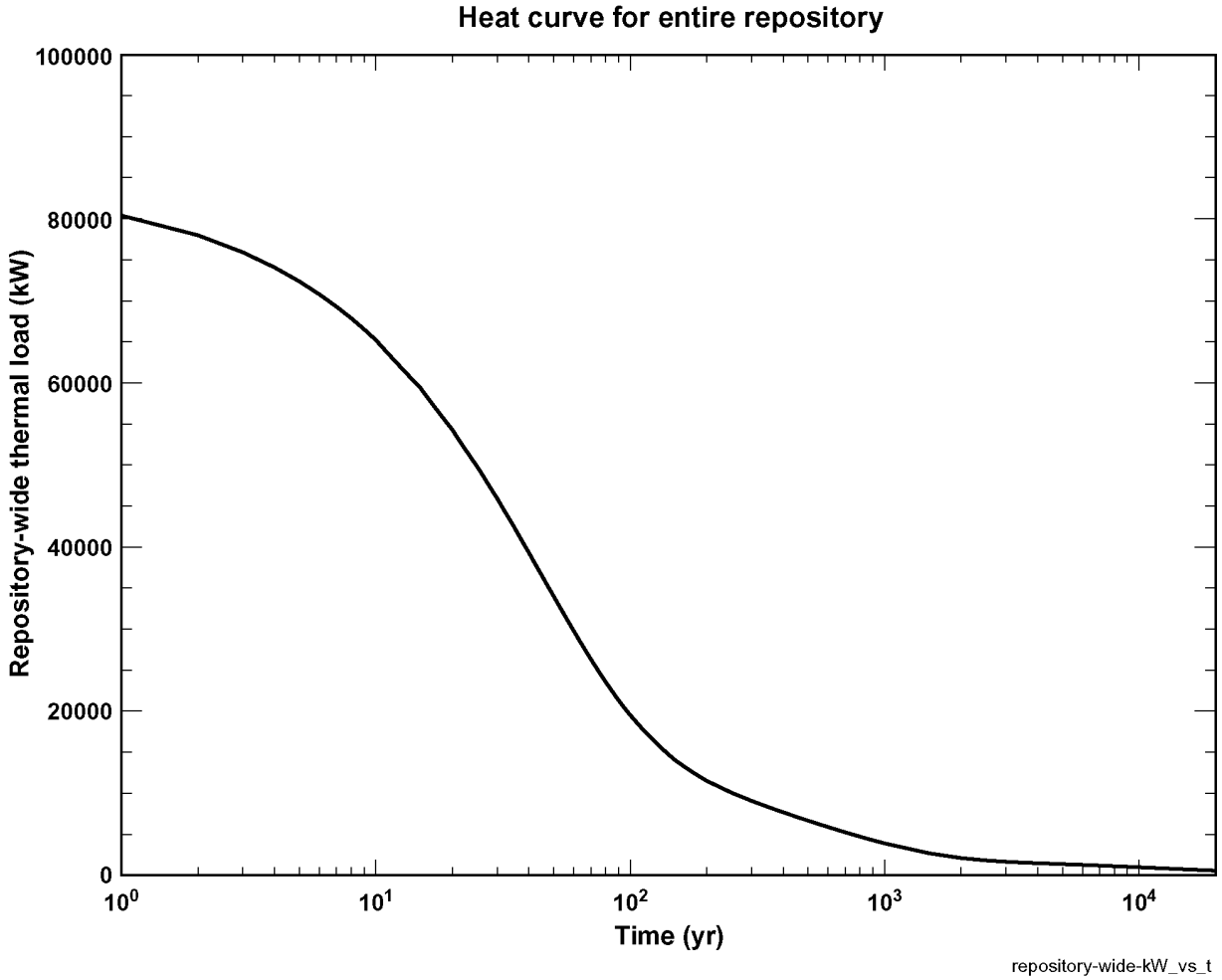

Figure 6.1-1. Repository heat output is plotted as a function of time for the TSPA-LA design. Note that the total repository heat load divided by the total length of emplacement drift in the repository (57.48 km) is equal to the line-averaged heat load. At the time of emplacement the total repository heat load is 77,000 kW, resulting in an initial line-averaged heat load of 1.45 kW/m. This is the total thermal load represented in the SMT submodel (Section 6.2.5) using the information from BSC 2004e.

After the emplacement of heat-generating nuclear waste, the thermally driven flow of water vapor away from the heat source causes a redistribution of the pore fluids within a potentially large volume of rock. Depending on the thermal design of the repository, this volume can extend from the ground surface to some distance below the water table and over an area larger than the repository footprint. Water in the matrix pores evaporates, creating zones of rock dryout (with

liquid-phase saturation less than ambient values) around the emplacement drifts. This water vapor is driven (primarily in fractures) away from the heat source in the emplacement drifts to where cooler temperatures cause it to condense, forming condensation zones outside of the dryout zones. The reduction in liquid-phase saturation causes a reduction in relative humidity in both the near-field host rock as well as in the emplacement drifts. Heat pipes can result from the countercurrent flow of water vapor and liquid water between the dryout and condensation zones. The magnitude of the liquid flux in this heat pipe can greatly exceed the magnitude of ambient liquid-phase fluxes. As the heat pulse decays, the system gradually rewets, returning to ambient (humid) preheating conditions.

6.1.3 Thermohydrology in the Repository Host Rock

In the host rock, local thermohydrologic behavior is dominated by whether a location is inside or outside of the zone of boiling temperatures, 96°C at the elevation of the repository horizon at Yucca Mountain approximately 1,100 m above mean sea level. Although evaporation, vapor flow (away from the heat source), and condensation occur at below-boiling temperatures, the thermally driven vaporization rates and vapor fluxes in the repository horizon are generally not great enough to result in significant dryout (and relative humidity reduction) in the rock unless temperatures are well above the boiling point.

The boiling zone evolves with time. Because the majority of the decay heat is removed with the ventilation air during the preclosure period, boiling does not occur during this period. After drift ventilation ceases (which occurs at the onset of the postclosure period), a small zone of boiling-to-above-boiling temperatures forms in the volume immediately encircling each individual emplacement drift. For a “globally boiling” design, these boiling zones grow and coalesce, forming one large boiling zone. As thermal output wanes, the boiling zones shrink, and the boiling zone in the host rock eventually dissipates completely. In “locally boiling” designs, these zones never coalesce; the boiling zones around each drift always remain distinct and separate. A “subboiling” design is one in which the thermal loading conditions are insufficient to produce boiling conditions in the host rock or in the drifts.

Whether or not the boiling zones around individual drifts coalesce is important because globally boiling conditions promote the development of a thick condensate zone above the repository. Note that this condensate zone will also include the percolation of ambient water that is unable to drain through or around the repository (because it is blocked by the coalesced boiling zone) and on down to the water table. The thickness of this condensate zone may reach tens of meters or more. A thick condensate zone may result in unstable and/or focused condensate drainage into relatively cooler regions of the repository, possibly resulting in seepage into emplacement drifts. A thick condensate zone will also result in somewhat greater liquid flux above the repository horizon during the postboiling rewetting period and, more generally, increases uncertainty with respect to infiltration flow paths above the repository. If the thermal design does not result in coalescence of boiling zones, condensate will be able to drain continuously between the drifts. As discussed in Section 6.3.1.1, the maximum lateral extent of boiling relative to the centerline of the emplacement drift is always much smaller than the half-drift spacing for the TSPA-LA design. Therefore, the majority of the host rock between emplacement drifts always remains below the boiling point, thereby enabling condensate and percolation flux to continuously drain between emplacement drifts. Because of this continuous drainage of condensate around a

relatively narrow cylindrically shaped boiling zone, the condensate cap above the emplacement drifts is of very limited spatial extent. Therefore, it is extremely unlikely that the condensate cap could augment liquid-phase saturation during postboiling rewetting period. Variation in the spatial extent and duration of the boiling zone along the drift axis is also important. Nonuniformity in boiling conditions along the drift axis (resulting from waste-package-to-waste-package variability in heat output) causes longitudinal variability in the radial extent and duration of boiling; it may also make it more likely for seepage and/or condensate to be focused onto cooler waste packages. The end-to-end waste package spacing (with a 10 cm gap separating waste packages) (Table 4-1), used in the TSPA-LA repository design minimizes this longitudinal variability.

6.1.4 Thermohydrology in Repository Emplacement Drifts

The TSPA-LA repository design includes 1.644- to 2.11-m-diameter (on average) waste packages constructed of corrosion-resistant materials, which are overlain by upside down, U-shaped, corrosion-resistant metallic barriers called drip shields. Both the waste packages and drip shields are supported on an invert made of granular material on the floor of the drift. All of these engineering components are important to address in analyzing thermohydrologic behavior within the emplacement drifts.

Two important factors influence the thermohydrologic conditions within the emplacement drifts. The first is whether or not temperatures at the drift wall are above the boiling point, which affects whether the relative humidity in the near-field host rock is reduced relative to ambient (humid) conditions as well as the likelihood of water seeping into the drift. The second is the temperature difference between the waste package and drift wall, which strongly affects how much lower relative humidity is on the waste package than on the drift wall (Figure 6.1-2). Note that the ratio of relative humidity on the waste package to relative humidity on the drift wall for a given temperature difference between these two surfaces decreases as the absolute temperature on the waste package increases. Because of the edge-cooling effect, waste packages located closer to the repository edges cool down more quickly than those located closer to the repository center. Consequently, relative humidity reduction for waste packages located closer to the repository edges can be greater than for those located closer to the repository center.

6.1.5 Design Factors Influencing Thermohydrology

There are many thermal design variables that affect thermohydrologic behavior in an underground nuclear waste repository (Table 6.1-1). These design variables include the average areal-heat-generation density of the waste inventory over the heated repository footprint and the average lineal-heat-generation density along the drifts (called the line-averaged thermal load). For a given waste inventory, these two variables constrain both the distance between drifts and the size of the required repository footprint. One way to reduce the heat-generation density is to age the waste in surface storage, because older spent nuclear fuel has a lower thermal power output. Forced (or natural) ventilation of the emplacement drifts also reduces the effective heat output of the emplaced waste.

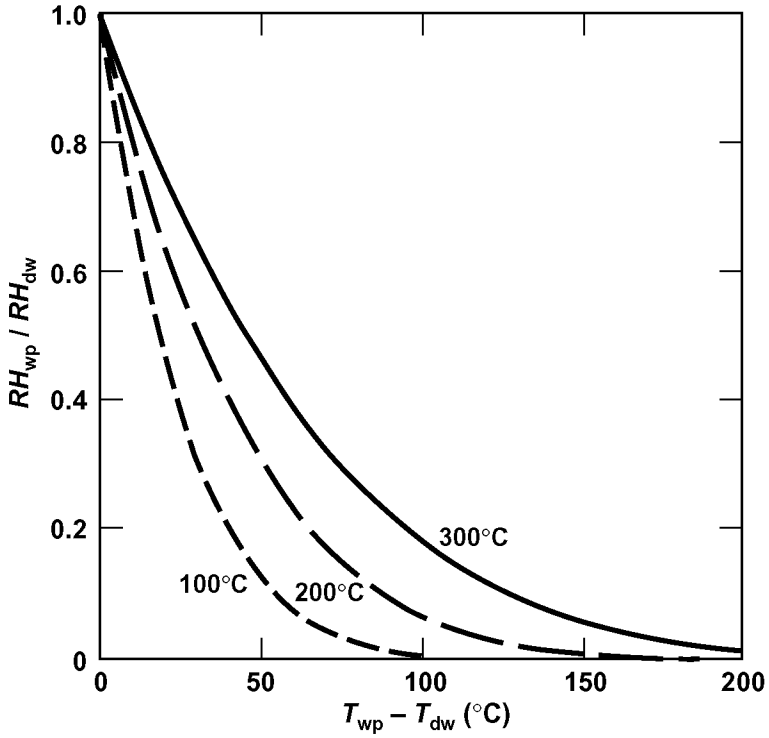

Source: Buscheck et al. 2002, Figure 2

Figure 6.1-2. The ratio of relative humidity (RH) on the waste package surface to relative humidity on the drift-wall surface versus the temperature difference between these surfaces is plotted for three different temperatures (taken to be the average of the drift wall and waste package temperatures).

Table 6.1-1. Key thermal design variables and natural system factors influencing thermohydrologic conditions in the emplacement drifts and near-field host rock.

Engineering Design Variables	Natural System Factors
• Overall areal-heat-generation density of waste inventory • Line-averaged thermal load along drifts • Distance between emplacement drifts • Age of spent nuclear fuel at time of emplacement • Location of repository horizon with respect to stratigraphy • Repository footprint • Waste package spacing (line load versus point load) • Waste package sequencing • Duration and heat-removal efficiency of drift ventilation • In-drift design and materials	• Percolation flux above the repository horizon • Thermal conductivity (particularly for host-rock units) • Bulk rock density and specific heat • Matrix imbibition • Capillary wicking in fractures • Overburden thickness (depth of repository below ground surface)

Other engineering variables include the placement of the repository horizon relative to the ground surface and the local hydrostratigraphy. The depth of the repository below the ground surface (called overburden thickness) translates to the thickness of insulating rock between the repository and the ground surface, which is a constant-temperature boundary that acts like a heat

sink. In-drift configuration, including most notably the presence or absence of backfill in the emplacement drifts, and the properties of any in-drift materials are also important to thermohydrology.

Waste package spacing affects the degree of nonuniformity of heating conditions along the axis of the drift. Individual waste packages are cylindrical in shape and 3.59 to 5.217 m long (Table 4-1). If waste packages are spaced far apart from each other along the drift ("point-load" waste package spacing), heating conditions along the drift will be less uniform. For waste packages spaced nearly end-to-end ("line-load" waste package spacing), which is being considered in the TSPA-LA repository design, the line of waste packages will share their heat output more effectively and will therefore act like a uniform line source of heat. Line-load waste package spacing results in more intense, localized, uniform, and persistent rock dryout around the drifts and more efficient condensate shedding between drifts than does point-load waste package spacing with the same overall areal-heat-generation density. Point-load waste package spacing results in less intense and less uniform rock dryout around the drifts and less uniform thermohydrologic conditions along the drifts (Buscheck et al. 1999). Fuel blending (i.e., the mixing and matching of spent-fuel assemblies of different thermal power in a given waste package, as well as the mixing and matching of waste packages of different thermal power along emplacement drifts), can be utilized to help reduce the nonuniformity of thermohydrologic conditions along drifts.

6.1.6 Natural System Factors Influencing Thermohydrology

Important natural system factors that affect the thermohydrologic environment include thermohydrologic properties of the repository host rock, overburden thickness above the repository, and the magnitude and spatial and temporal distribution of the percolation flux above the repository horizon (Table 6.1-1). Of these factors, the host-rock thermal conductivity and percolation flux above the repository horizon are the most important. Unlike the engineering design variables, there is nothing that can be done to change the natural system. However, it is possible to minimize the impact of this uncertainty by learning as much as possible about the natural system and engineering the repository with natural system variability and uncertainty in mind.

6.2 THE MULTISCALE THERMOHYDROLOGIC MODELING APPROACH

6.2.1 Overview of the MSTHM

The motivation behind the multiscale modeling approach is the need for a modeling tool that simultaneously accounts for processes occurring at a scale of a few tens of centimeters around individual waste packages and emplacement drifts and also at the scale of the mountain. Currently, a single numerical model cannot do this because it requires too large a computational cost to be a viable simulation tool for performance assessment and engineering design. Note that performance assessment and design analysis both require the ability to conduct a relatively large number of realizations. This multiscale modeling approach was used to model more than 20 different realizations for *Total System Performance Assessment-Viability Assessment (TSPA-VA) Analyses Technical Basis Document* (CRWMS M&O 1998b). This approach has also been used to model more than 20 alternative repository designs during the license application design

selection process (Buscheck 1999) and in six different realizations for *Total System Performance Assessment for the Site Recommendation* (CRWMS M&O 2000a) and six different realizations for *FY 01 Supplemental Science and Performance Analyses, Volume 1: Scientific Bases and Analyses* (BSC 2001b). The following description is a brief overview; a detailed description of the MSTHM is found in Section 6.2.4.

Conceptually, the approach is simple. Thermohydrologic behavior is directly simulated for an "average" waste package using a two-dimensional drift-scale cross section for a variety of areal-heat-generation densities at numerous locations throughout the repository footprint. In these simulations, the flow of liquid and gas (water vapor and air) through variably saturated fractured porous media is represented with a dual-permeability description of permeability. This model also accounts for two-phase behavior (i.e., evaporation, boiling, and condensation). Open drifts are modeled as porous media with very high permeability and porosity. The model represents thermal conduction and convection in rock, and thermal conduction, convection, and radiation in the open cavities in the emplacement drifts.

These two-dimensional thermohydrologic model results are then modified with three-dimensional thermal-model results that rely on the assumption (Section 5.2.1) that three-dimensional convection and mass transfer in the rock and drift is not significant. The three-dimensional thermal model accounts for three-dimensional heat flow at the mountain scale and for three-dimensional heat flow at the drift scale, which account for waste-package-to-waste-package variability in heat output (some waste packages will generate much less heat than other waste packages). This multiscale model approach assumes (Sections 5.2.2 and 5.6) that any mountain-scale movement of water and water vapor along the drift axes or between drifts can be neglected (i.e., all fluid flow and convection are confined to a two-dimensional vertical cross section orthogonal to the drift axis, with no fluid flow across the vertical midplane in the rock pillar between the drifts). The multiscale model also neglects any changes in rock properties due to any coupled thermohydrologic-chemical-mechanical processes and the effect of dissolved solutes on the thermohydrologic properties of water.

The multiscale modeling approach considers the influence of the following variables as a function of geographic location in the repository: local stratigraphy, overburden thickness (i.e., distance between the repository and ground surface, which varies by approximately 150 m across the repository), thermal boundary conditions, and infiltration flux. It also considers the influence of the proximity to the edge of the repository, which is important because a waste package close to the repository edge will cool more quickly than one at the repository center. As discussed in Section 5.2.1, it is assumed that the differences in temperature that arise as a result of proximity to the repository edges are governed by thermal conduction in the rock. This assumption is equivalent to saying that convective heat transfer mechanisms have a negligible influence on lateral mountain-scale heat flow at Yucca Mountain. These mechanisms (notably, buoyant gas-phase convection and the heat pipe effect) are included in the two-dimensional thermohydrologic (drift-scale) submodels of the MSTHM. The assumption of conduction dominance at mountain scale tends to preserve temperature differences that arise as a result of differences in proximity to the repository edges, which preserves the "tails" of the distribution of boiling-period duration across the entire repository.

The MSTHM represents all possible waste packages emplaced in the repository by four major types: CSNF from pressurized-water reactors (PWRs), CSNF from boiling-water reactors (BWRs), high-level radioactive waste (HLW), and DOE-owned spent nuclear fuel. The relevant point here is that the heat-generation-rate-versus-time relationships for these four waste package types are different. It is effectively assumed that waste packages will be sequenced in such a way to minimize the heating variability along the drift (i.e., placing hot waste packages next to cold waste packages). The model effectively considers a narrow range of possible waste package sequencing (Figure 6.2-2) that results in eight distinct local heating conditions for waste packages. For example, the model distinguishes between a BWR placed between a PWR and a HLW and a BWR placed between two PWRs. As discussed in Section 5.2.2, it is assumed that the differences in temperature between relatively hotter and cooler waste package locations are governed by thermal conduction in the host rock and emplacement drift and thermal radiation in the open cavities in the drift. This assumption is equivalent to saying that convective heat transfer mechanisms (notably, buoyant gas-phase convection) do not significantly contribute to the attenuation of temperature variations along the axis of the drift. However, note that the influence of buoyant gas-phase convection is represented in the vertical plane perpendicular to the drift axis. This assumption tends to preserve temperature variability along the drifts.

To implement this multiscale approach, a modeling system (BSC 2001c) has been developed that is called the MSTHM, which is described in detail in Section 6.2.4. The following discussion begins with the unsaturated zone hydrology model on which the natural system aspects of the MSTHM are based, followed by a detailed discussion of the governing equations that are used in all the MSTHM simulations.

6.2.2 Incorporating the Unsaturated-Zone Hydrology Model in the MSTHM

The basis of the MSTHM modeling approach is *UZ Flow Models and Submodels* (BSC 2003h), which was developed at Lawrence Berkeley National Laboratory (LBNL). From *Development of Numerical Grids for UZ Flow and Transport Modeling* (BSC 2003c), a three-dimensional definition of hydrostratigraphic units (called UZ Model Layers) is incorporated in the MSTHM, including position of the water table and surface topography; thermohydrologic properties for these units; and model boundary conditions. The model includes 36 UZ Model Layers, each of which is considered to be homogeneous with respect to thermal and hydrologic properties. These hydrologic properties are determined through an inverse modeling approach constrained by site hydrologic data; the assumption is made that heterogeneity is captured by the detailed stratification (Bandurraga and Bodvarsson 1999). The thermal properties are determined on the basis of laboratory measurements (BSC 2002a).

The MSTHM also incorporates the conceptualization for flow through unsaturated fractured porous rock at Yucca Mountain from the LBNL unsaturated-zone hydrology model. The current conceptual model is based on a dual-permeability representation of overlapping fracture and matrix continua, modified from the traditional approach such that only a portion of connected fractures actively conduct liquid water (Liu et al. 1998), a portion which depends on liquid-phase saturation in the fractures.

The next step in building the MSTHM involves the addition of the repository emplacement drifts and the engineered components inside those drifts to the unsaturated zone hydrology model

discussed above. The geometric configuration of the engineered components inside the drifts the MSTHM calculations in support of the TSPA-LA base case is shown in Figures 6.2-1 and 6.2-2.

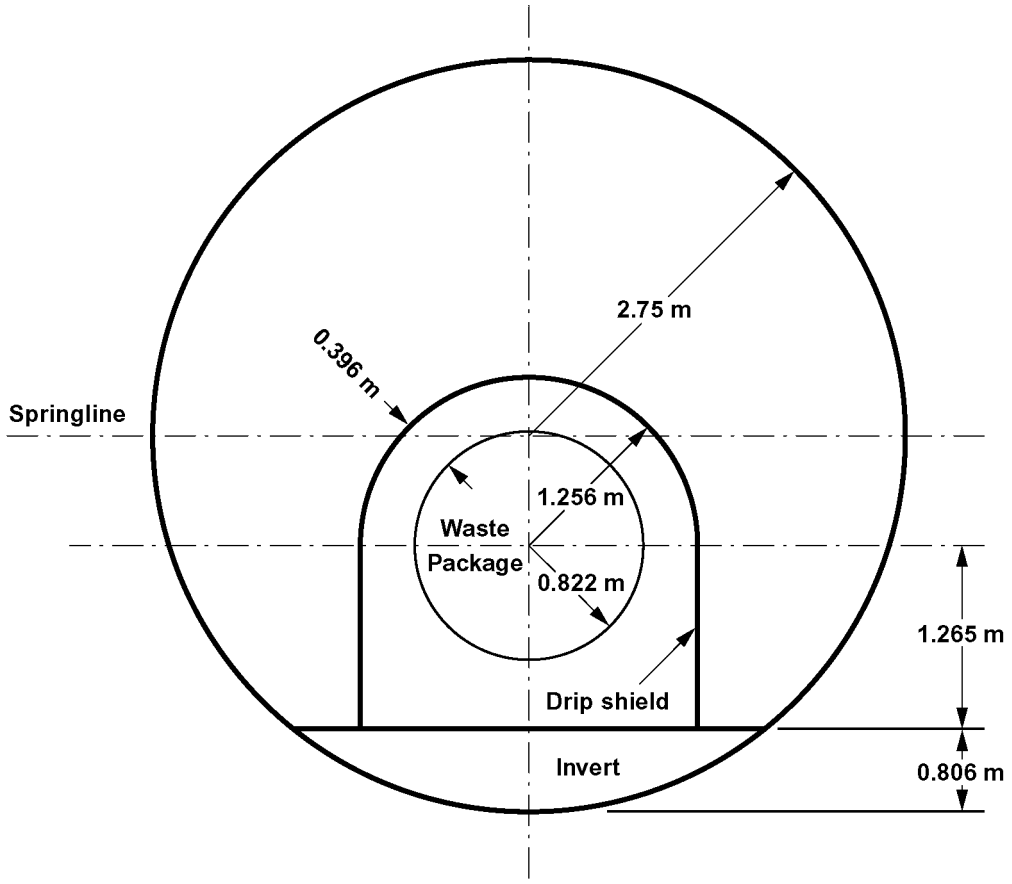

Source: BSC 2003f; BSC; BSC 2004e

Figure 6.2-1. Geometric Configuration of the Engineered Components is Shown for an Average Cross-Section Inside the Emplacement Drifts

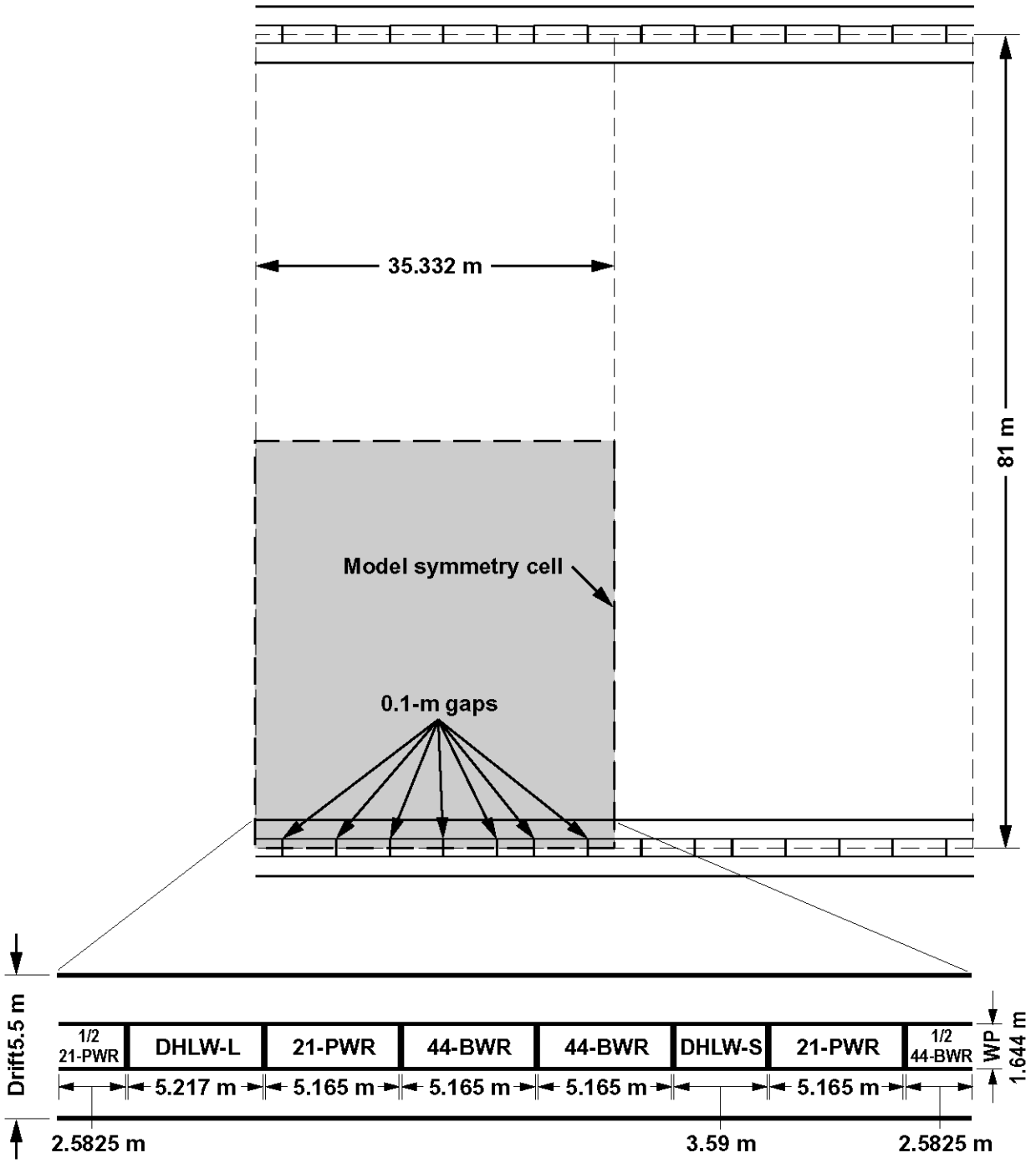

Source: BSC 2003f; BSC 2004c; BSC 2004e

Figure 6.2-2. Diagram showing assumed drift spacing, waste package lengths, and waste package spacing considered in the MSTHM calculations for the TSPA-LA base case. The names of the respective waste packages (21-PWR, 44-BWR, etc.) used in the DDT submodel are shown above for each waste package

6.2.3 Governing Equations for Unsaturated-Zone Thermohydrology

6.2.3.1 Mass-Balance Equation for Thermohydrologic Models

All thermohydrologic models in this report solve the mass-balance equation for air, water, and energy components for liquid- and gas-fluid phases and a nondeformable solid. The mass-balance equation for the air and water components is:

$$\frac{\partial}{\partial t}\sum_{\varsigma}\phi\rho_{\varsigma}S_{\varsigma}\omega_{\varsigma}^{\beta} = -\sum_{\varsigma}\nabla\cdot\phi\rho_{\varsigma}S_{\varsigma}\left(\omega_{\varsigma}^{\beta}\mathbf{V}_{\varsigma}+\mathbf{J}_{\varsigma}^{\beta}\right) \quad \text{(Eq. 1)}$$

where t is time, the superscript β denotes a component (e.g., air and water), the subscript ς denotes fluid phases (e.g., liquid and gas), ϕ is porosity, ρ_{ς} is density of phase ς, S_{ζ} is saturation of a ς phase, $\omega_{\varsigma}^{\beta}$ denotes mass fraction of β component in phase ς, $\mathbf{v}_{\varsigma}$ is velocity vector for ς phase advection, and $\mathbf{J}_{\varsigma}^{\beta}$ is combined diffusive and dispersive flux tensor, which can be further given by Fick's law (Nitao 2000):

$$\mathbf{J}_{\varsigma}^{\beta} = -D_{\varsigma}^{\beta}\nabla\omega_{\varsigma}^{\beta} \quad \text{(Eq. 2)}$$

D_{ς}^{β} is combined diffusion and dispersion coefficient for β component in ς phase. Darcy's law gives the advective flux vector (Nitao 2000):

$$S_{\varsigma}\phi\,\mathbf{V}_{\varsigma} = -\frac{k_{\varsigma}\left(S_{\varsigma}\right)}{\mu_{\varsigma}}\left(\nabla p_{\varsigma}+\rho_{\varsigma}g\nabla z\right) \quad \text{(Eq. 3)}$$

where k_{ς} is the permeability function, μ_{ς} is phase viscosity, p_{ς} is phase pressure, g is gravitational acceleration, and z denotes distance in the vertical direction. The capillary pressure relationship is given by:

$$p_{\alpha} = p_{g} - p_{c} \quad \text{(Eq. 4)}$$

and p_c is the retention pressure function. In addition to the mass balance equation, there are the constraints:

$$\sum_{\beta}\omega_{\varsigma}^{\beta} = 1 \quad \text{(Eq. 5)}$$

$$\sum_{\varsigma}S_{\varsigma} = 1 \quad \text{(Eq. 6)}$$

Local thermodynamic equilibrium is assumed between all phases. Partitioning of components between phases is expressed in terms of partitioning coefficients:

$$n_{\varsigma}^{\beta} = K_{\varsigma,\xi}^{\beta}n_{\xi}^{\beta} \quad \text{(Eq. 7)}$$

where n_ς^β is the mole fraction and $K_{\varsigma,\xi}^\beta$ is the partitioning coefficient between phase ς and phase ξ. For predicting the partitioning of water between the aqueous phases the model includes the "vapor pressure lowering" effect based on the Kelvin law.

6.2.3.2 Energy Balance Equation for Thermohydrologic Models

For all thermohydrologic models in this report, the balance equation for energy is:

$$\frac{\partial}{\partial t}\left[\sum_\varsigma \phi\rho_\varsigma u_\varsigma S_\varsigma + (1-\phi)\rho_s C_p (T - T_{\text{ref}})\right] = \sum_\beta \sum_\varsigma \left[\nabla\cdot\phi h_\varsigma^\beta \rho_\varsigma S_\varsigma \left(\omega_\varsigma^\beta \mathbf{V}_\varsigma + \mathbf{J}_\alpha^\gamma\right)\right] + \nabla\cdot K_H \nabla T \qquad \text{(Eq. 8)}$$

where T denotes temperature, T_{ref} is reference temperature, u_ς is specific internal energy, ρ_S is solid density, C_p is specific heat of solid, h_ς^β is partial specific enthalpy, and K_H is thermal conductivity. Note that thermal-conductivity is a function of liquid-phase saturation *S*, varying linearly from a "dry" value of K_H ($S = 0.0$) to a "wet" value of K_H ($S = 1.0$).

It is worth noting that it is possible to use either a specific internal energy accumulation term or a specific enthalpy accumulation term for the fluid phases of Equation 8. *Transport Phenomena* (Bird et al. 1960) discusses the validity of either approach. The justification for the use of specific internal energy in the accumulation term of the fluid phases in the NUFT code is discussed in detail in Section 6.2.3.6.

The balance equations (1) and (8) are discretized in space using the integrated finite difference method and discretized in time using the fully implicit backward Euler method. The resulting nonlinear system of equations is solved at each time step using the Newton-Raphson method.

6.2.3.3 Radiative Heat Transfer

Where relevant, model simulations include radiative heat transfer in the energy balance model for the open cavities within the repository drifts in which waste packages are emplaced. In this case, the surfaces of the drift wall and waste package are subdivided into surface elements, each of which is mapped to a computational volume element. Radiative heat flux is calculated for connections between each pair of surface elements using temperatures from the corresponding volume element. The net radiative heat transferred between two model nodes is calculated from the Stefan-Boltzmann law:

$$Q = c(T_1^4 - T_2^4) \qquad \text{(Eq. 9)}$$

where T_1 is the absolute temperature of the radiator, T_2 is the absolute temperature of the receiver, and *c* is a coefficient defined by:

$$c = AF\varepsilon\sigma \qquad \text{(Eq. 10)}$$

where *A* is the area of the radiating surface element, *F* is the radiative view factor (Holman 1990), ε is emissivity, and σ is the Stefan-Boltzmann constant.

6.2.3.4 Energy Balance Equations for Thermal-Conduction-Only Models

For all thermal-conduction models in this report, the energy balance is written:

$$(1-\phi)\rho_s C_p \frac{\partial T}{\partial t} = \nabla \cdot K_H \nabla T \qquad \text{(Eq. 11)}$$

where ϕ is porosity, ρ_S is solid density, C_p is specific heat of solid, and K_H is thermal conductivity. For thermal-conduction-only models, thermal conductivity is not a function of liquid-phase saturation.

6.2.3.5 Dual-Permeability and Active-Fracture Models

All thermohydrologic models in this report utilize a dual-permeability approach in which the fracture and matrix systems are treated as two separate continua with a complete set of balance equations and computational grid for each continuum. Each continuum has coupling terms for mass and energy fluxes between the two continua. These terms have the general form:

$$q_{\text{exchange}} = a\kappa\Delta u / L\,, \qquad \text{(Eq. 12)}$$

where q_{exchange} is flux of mass or energy per unit bulk volume, Δu is the difference in pressure or temperature between the continua, and K is a transfer coefficient. The coefficient κ for advective flux is of the form $K k_r / \mu$, where K is saturated permeability, and k_r is relative permeability. For diffusive mass flux of a phase, κ is equal to the apparent diffusion coefficient $D_{app} = \phi S \tau D$, where τ is tortuosity factor, and D is the free diffusion coefficient. For energy flux, κ is the bulk thermal conductivity K_H. In the conventional dual-permeability approach, a is the surface area of the fracture walls per unit bulk volume, and L is the average distance between centers of the matrix elements, which is proportional to the fracture spacing. Also used is an active-fracture model modification to the traditional dual-permeability approach in which a and L are modified to account for inactive fractures (or portions of fractures) as suggested by Liu et al. (1998).

Specifically, a is multiplied by S_e, and L is multiplied by $S_e^{-\gamma}$, where:

$$S_e = \frac{S_f - S_r}{S_{\max} - S_r}\,, \qquad \text{(Eq. 13)}$$

and S_r and $S_{\max}$ are residual and maximum liquid-phase fracture saturations, respectively, while S_f is the fracture saturation.

The relationships between permeability, saturation, and capillary pressure described in Equations 14 and 15 are described by the formulations of van Genuchten (1980) and Mualem (1976), modified to account for the active fracture model by the parameter γ which has a value between 0 and 1 (0 if all fractures are active).

The relative permeability for the liquid phase is given by:

$$k_{rl} = S_e^{(1+\gamma)/2}\left[1.0-\left(1.0-S_e^{(1-\gamma)/m}\right)^m\right]^2 \quad \text{(Eq. 14)}$$

It is assumed that $k_{rl}+k_{rg}=1$; the subscripts "*l*" and "*g*" refer to the liquid and gas phases, respectively. The capillary pressure is given by:

$$p_c = \frac{1}{\alpha}\left(S_e^{\frac{\gamma-1}{m}}-1\right)^{\frac{1}{n}} \quad \text{(Eq. 15)}$$

where α is a curve-fitting parameter (units of inverse pressure), n is a dimensionless curve-fitting parameter, and $m = 1\text{-}1/n$.

The parameters used in this model are functions of pressure p, temperature T, mass fraction ω, and/or saturation S as follows: $\rho_\alpha(p,T,\omega)$, $D_\alpha^\gamma(p,T)$, $\mu_\alpha(p,T,\omega)$, $K_{\alpha\beta}^\gamma(p,T,S)$, $u_\alpha(p,T,\omega)$, $h_\alpha^\gamma(p,T)$, $k_\alpha(S)$, $\tau_\alpha(S)$, and $p_c(S,T)$.

6.2.3.6 Formulation of Energy Balance Equation for Thermohydrologic Models

It is possible to formulate the energy balance equation (Equation 8) using either specific internal energy (u) or specific enthalpy (h) in the fluid-phase accumulation terms inside the time derivative. Numerical models for subsurface flow and transport have formulated the equation of energy for multicomponent systems both using enthalpy (e.g., Manteufel et al. 1993; Pollock 1986) and using specific internal energy (e.g., Lichtner and Walton 1994; Nitao 1998). Bird et al. (1960, Table 18.3-1, p. 562) demonstrate that both formulations are valid, as follows:

$$\rho\frac{D}{Dt}h = -(\nabla\cdot\mathbf{q}) + \frac{Dp}{Dt} - (\boldsymbol{\tau}:\nabla\mathbf{v}) + \sum_{i=1}^{n}(\mathbf{j}_i\cdot\mathbf{g}_i) \quad \text{(Eq. 16)}$$

$$\rho\frac{D}{Dt}u = -(\nabla\cdot\mathbf{q}) - (\boldsymbol{\pi}:\nabla\mathbf{v}) + \sum_{i=1}^{n}(\mathbf{j}_i\cdot\mathbf{g}_i) \quad \text{(Eq. 17)}$$

One may note the fact that specific enthalpy of evaporation (h_{evap}) is greater than the specific internal energy of evaporation (u_{evap}) because the specific enthalpy includes a compressible work term. For example, at standard atmospheric pressure (101.3 kPa), h_{evap} = 2,257 kJ/kg while u_{evap} = 2088 kJ/kg, a difference of approximately 8 percent (Keenan et al. 1969). Such a difference is crucial when considering a simplified batch system (i.e., zero-dimensional reactor). In such simplified cases, one must consider different approaches to the system (i.e., approaching the problem as a closed system versus approaching the problem as an open system). The partial differential equation formulation as represented by Bird et al. (1960) in Equations 16 and 17 incorporates multidimensional transient processes, however. With the appropriate application of boundary conditions, both the enthalpy formulation (Equation 16) and the internal energy formulation (Equation 17) results in equivalent solutions.

The energy-balance equation in NUFT is based on the derivation of Equation 17, which is the internal energy formulation of the energy equation for *n* species. Expanding the total derivative on the left-hand side of Equation 17 and incorporating the continuity equation, Equation 17 can be rewritten as:

$$\frac{\partial}{\partial t}(\rho u) + \nabla \cdot (\rho u \mathbf{v}) = -(\nabla \cdot \mathbf{q}) - (\boldsymbol{\pi} : \nabla \mathbf{v}) + \sum_{i=1}^{n} (\mathbf{j}_i \cdot \mathbf{g}_i) \qquad \text{(Eq. 18)}$$

The thermal energy flux *q* is composed of three terms (Bird et al. 1960, Equation 18.4-2, p. 566):

$$\mathbf{q} = -k\nabla T - \sum_{i=1}^{n} h_i \rho D_i \nabla \omega_i + \mathbf{q}^{(x)} \qquad \text{(Eq. 19)}$$

representing, respectively, thermal conduction, species diffusion enthalpy transport, and the Dufour energy flux. Note that according to Bird et al. (1960), the Dufour energy flux is of minor importance and is therefore, typically neglected. Incorporating Equation 19 (less the Dufour energy flux) into Equation 18 and noting that gravitational work (the last term in Equation 18) is zero (Nitao 2000), results in the simplified equation:

$$\frac{\partial}{\partial t}(\rho u) + \nabla \cdot (\rho u \mathbf{v}) = \left(\nabla \cdot \left[k\nabla T + \sum_{i=1}^{n} h_i \rho D_i \nabla \omega_i \right] \right) - (\boldsymbol{\pi} : \nabla \mathbf{v}) \qquad \text{(Eq. 20)}$$

The stress tensor π is related to the viscous shear tensor and pressure as follows:

$$\pi = \tau + p\boldsymbol{I} \qquad \text{(Eq. 21)}$$

Incorporating Equation 21 into the last term of Equation 20 and noting that $p\nabla \cdot \boldsymbol{v} = \nabla \cdot (p\boldsymbol{v}) - \boldsymbol{v} \cdot \nabla p$, Equation 20 can be rewritten as:

$$\frac{\partial}{\partial t}(\rho u) + \nabla \cdot (\rho u \mathbf{v}) = \left(\nabla \cdot \left[k\nabla T + \sum_{i=1}^{n} h_i \rho D_i \nabla \omega_i \right] \right) - (\tau : \nabla \mathbf{v}) - \nabla \cdot (p\mathbf{v}) + \mathbf{v} \cdot \nabla p \qquad \text{(Eq. 22)}$$

As discussed by Nitao (2000), both the viscous dissipation term $(\tau : \nabla \boldsymbol{v})$ and the pressure gradient term $(\boldsymbol{v} \cdot \nabla p)$ are typically neglected in Equation 22 because these terms are small compared to other terms. Estimates of the approximate potential error incurred by neglecting these two terms are discussed below. The third term on the right-hand side of Equation 22 can be incorporated into the second term on the left-hand side resulting in a convective enthalpy term. This results in the energy equation as it is employed in the NUFT code for the Yucca Mountain Project:

$$\frac{\partial}{\partial t}(\rho u) + \nabla \cdot (\rho h \mathbf{v}) = \left(\nabla \cdot \left[k\nabla T + \sum_{i=1}^{n} h_i \rho D_i \nabla \omega_i \right] \right) \qquad \text{(Eq. 23)}$$

For a more rigorous mathematical development of Equation 23 from Equation 17, see *Documentation of the Thermal Energy Balance Equation Used in the USNT Module of the NUFT Flow and Transport Code* (Nitao 2000). Note that the above equations apply only at the "pore level" and not at the porous medium, or macroscopic, level. Nitao (2000) also discusses the method used to derive the porous medium energy balance equation by volume averaging the pore level equations.

It is possible to estimate the error incurred by neglecting the viscous dissipation term $(\tau : \nabla \boldsymbol{v})$ in Equation 22 by considering the maximum error that could occur during a Yucca Mountain thermohydrologic-model calculation using the NUFT code. Nitao (2000) estimates that the maximum error caused by neglecting this term would occur during infiltration through the rock fractures. The maximum possible error in temperature at the repository for a high infiltration of 100 mm/yr would be $\Delta T \sim 0.3$°C.

The largest potential source of error lies in neglecting the pressure gradient term in Equation 22. Note that this assumption does not mean that a constant pressure is assumed—only that this particular term in the energy equation is neglected. In fact, pressure is a variable in all of the remaining terms in Equation 22 where it appears. It is possible to estimate the maximum potential error incurred by neglecting the heat gradient term $(\boldsymbol{v} \cdot \nabla p)$ by comparing it to the convective enthalpy term $(\nabla \cdot (\rho h \mathbf{v}))$. The greatest pressure would occur in the host rock immediately adjacent to the drift wall during a boiling event. As an extreme example, consider a maximum drift-wall temperature of 140°C as estimated for the higher-temperature operating mode conditions analyzed in *FY 01 Supplemental Science and Performance Analyses, Volume 1: Scientific Bases and Analyses* (BSC 2001b, Figure 5.4.1-2). Such a temperature would result in a P_{sat} of 361 kPa. The results of the supplemental analyses indicate that such a drift-wall temperature incurs a relative humidity of 30 percent, thus the pressure can be estimated as approximately 120 kPa. The extreme downstream temperature and pressure at the repository level would be about 96°C and 84.5 kPa. If the ratio of $(\boldsymbol{v} \cdot \nabla p) / \nabla (\rho h \boldsymbol{v})$ is approximated as $\Delta p / \Delta (\rho_{sat} h_{sat})$ then the maximum difference is (120 kPa–84.5 kPa)/(1.12 kg/m^3 × 2,706 kJ/kg - 0.353 kg/m^3 × 2,652 kJ/kg) or about 2 percent. Note that this is a conservative error estimate for this particular problem; the estimate neglects thermal conduction as an energy transport mechanism and thus greatly exaggerates the potential error of this scenario where heat flow is dominated by thermal conduction. Hence, it can be readily concluded that neglecting the pressure gradient in Equation 22 would result in a maximum error of less than 2 percent for a short time over only the small area of host rock immediately adjacent to drift wall. Neglecting the influence of viscous dissipation and the pressure gradient in the energy equation is therefore, acceptable for the Yucca Mountain Project.

6.2.4 MSTHM Calculation Sequence

The MSTHM consists of four submodel types (Figure 1-1, Tables 1-2 and 1-3), all of which are run using the NUFT computer code (Nitao 1998). For this report, the LDTH and SDT submodels are run at 108 geographic locations distributed uniformly over the repository area (Figure 6.2-3); these submodels use the stratigraphy, overburden thickness, thermohydrologic boundary conditions, and infiltration fluxes appropriate for each location. At each of those 108 geographic locations, the LDTH- and SDT-submodel calculations are conducted at different

values of thermal loading, which can be quantified by the Areal Mass Loading (AML). Note AML is expressed in terms of metric tons of uranium per acre. For the current repository design, the initial Lineal Power Density (LPD) is 1.45 kW/m (BSC 2004a), which for a drift spacing of 81 m corresponds to an areal power density of 17.9 W/m^2. The current repository design has 57,480.2 m of emplacement drift (Table 6.2-1), which corresponds to a heated repository footprint of 4,655,896 m^2. From Table 6.2-1 it can be seen that the SMT submodel represents the repository as having 57,480 m of emplacement drift. For a 63,000 MTU inventory of commercial spent nuclear fuel (CSNF) waste packages, this corresponds to an AML of 54.76 MTU/acre. Therefore, 1 MTU/acre is equivalent to 0.327 W/m^2 at the time of emplacement for the TSPA-LA design. The modeled AML is obtained by virtue of the selected drift spacing in the model.

Section 7.3 describes a MSTHM validation test case, also reported by Buscheck, Glascoe et al. (2003), in which the MSTHM and a corresponding monolithic thermohydrologic model are used to predict the thermohydrologic behavior of a three-drift repository. The following description of the MSTHM calculation sequence also pertains specifically to that test case, which utilizes six modeled AMLs: 66, 55, 37, 27, 14, and 7 MTU/acre. Because of the very small heated footprint of the three-drift repository in that test case, the influence of the edge-cooling effect occurs more abruptly and in a more pronounced manner, which requires that the LDTH-SDT-submodel pairs be run at six different AMLs, rather than at just four (as is typically done for a full-scale repository example). An AML of 55 MTU/acre corresponds to 81-m drift spacing, while 27 MTU/acre corresponds to 162-m drift spacing. The emplaced AML for the repository is 55 MTU/acre for a total repository-wide heat load of 70,000 MTU (YMP 2001). The modeled AMLs that are less than the emplaced AML account for the evolving influence of the edge-cooling effect (i.e., waste package locations close to the repository edges cool faster than those at the center). The modeled AML that is higher than the emplaced AML accounts for hotter-than-average waste package thermal-loading conditions. The LDTH-submodel domain is a two-dimensional drift-scale cross-section extending down from the ground surface to the water table. The LDTH submodels are the only submodels to include coupled thermohydrologic processes; these submodels assume a heat-generation history that is effectively that of the entire waste package inventory line-averaged over the total length of emplacement drifts in the repository.

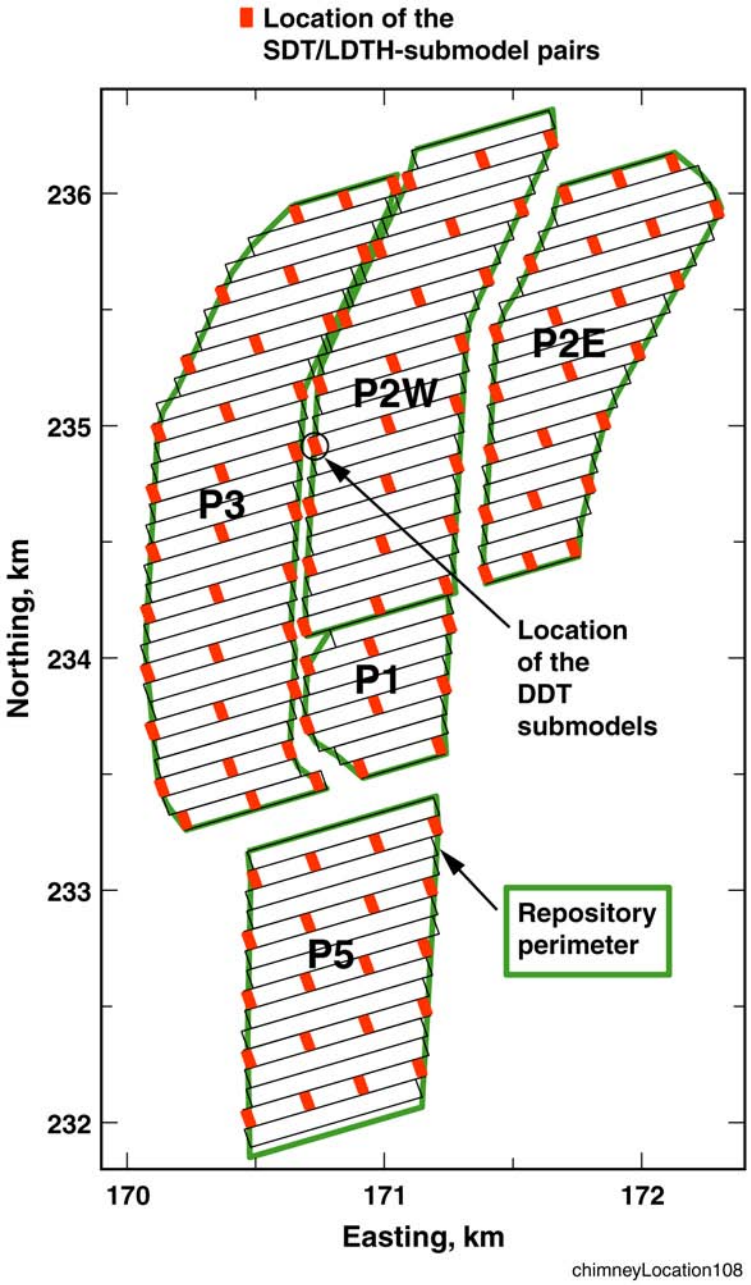

Figure 6.2-3. The repository layout considered in the MSTHM calculations for the TSPA-LA base case includes four of the five emplacement panels. Note that Panel 2 consists of a western portion (P2W) and an eastern portion (P2E). Nevada State Northing and Easting coordinates are given in kilometers. Panel 4 is not shown because it is not included in the TSPA-LA base case. The subhorizontal lines depict the rows of gridblocks in the SMT submodel that represent each of the emplacement drifts. The rectangles correspond to the locations of LDTH-SDT submodel pairs. Note that the northernmost 20 LDTH-SDT-submodel locations are used in Panel 5 for the TSPA-LA base case. A total of 108 LDTH-SDT-submodel locations are used in the TSPA-LA base case.

The three-dimensional SMT submodel, which solves for thermal conduction of a heat source smeared over the repository area, represents the heated footprint of the repository and allows for consideration of edge-cooling effects and the influence of the varying overburden thickness above the repository. For this example, originally by Buscheck, Glascoe et al. (2003), the linear power density is 1.35 kW/m of emplacement drift. Note that this linear power density is different from that being analyzed for the TSPA-LA (Section 6.3). The SMT submodel assumes a heat-generation history that is areally averaged for the entire waste package inventory over the entire heated footprint of the repository. The one-dimensional SDT submodels are run at the same 108 geographic locations as the two-dimensional LDTH submodels such that every LDTH submodel is paired to a corresponding SDT submodel. The SDT submodels utilize the same heat-generation history as the LDTH submodels except that for the SDT heat is smeared over the repository plane.

The fundamental concept in the MSTHM is that the results from the two-dimensional LDTH submodels can be modified to account for the influence of three-dimensional mountain-scale heat flow as well as for local deviations arising from waste-package-to-waste-package variability in heat output. Output from the SMT submodel, together with the LDTH-SDT submodel pairs, is integrated to create the LMTH model (Figure 1-1). The DDT submodel is then used to further modify the LMTH model to account for waste-package-specific deviations from average waste package behavior. For past MSTHM calculations (BSC 2001c; Buscheck, Rosenberg et al. 2003) the DDT submodels represent 10 different waste packages, which fall in two major categories: commercial spent nuclear fuel (CSNF) waste packages, which include pressurized water reactor (PWR) and boiling water reactor (BWR) waste packages; and defense high-level waste (DHLW) waste packages. Four different waste package types are used in the model-validation study: PWR1, PWR2, DHLW and BWR (Table 7.3-2). DDT-submodel temperature variations are superimposed on LMTH-model temperatures to generate the temperatures of the final discrete-heat-source mountain-scale thermohydrologic (DMTH) model (Figure 1-1, Tables 1-2 and 1-3).

For the MSTHM analysis of the repository, after all of the submodels have been run using the NUFT code, LDTH and SDT submodel results are spatially interpolated from the geographic locations (a total of 108 for the TSPA-LA MSTHM) to all of the repository subdomains in the SMT submodel (2,874 for the TSPA-LA MSTHM). This is equivalent to having run the LDTH-SDT-submodel pairs at all repository subdomains in the SMT submodel.

The MSTHM calculation sequence to obtain temperature, relative humidity, and liquid-phase saturation is shown in Figure 6.2-4 and Figure 6.2-5 and can be divided into the six stages of Figure 1-1. While this analysis pertains to the three-drift repository model-validation test case (Section 7.3), it also illustrates the MSTHM calculation sequence for each of the repository subdomains. The six calculation stages conceptually illustrated in Figure 1-1 are discussed in detail below.

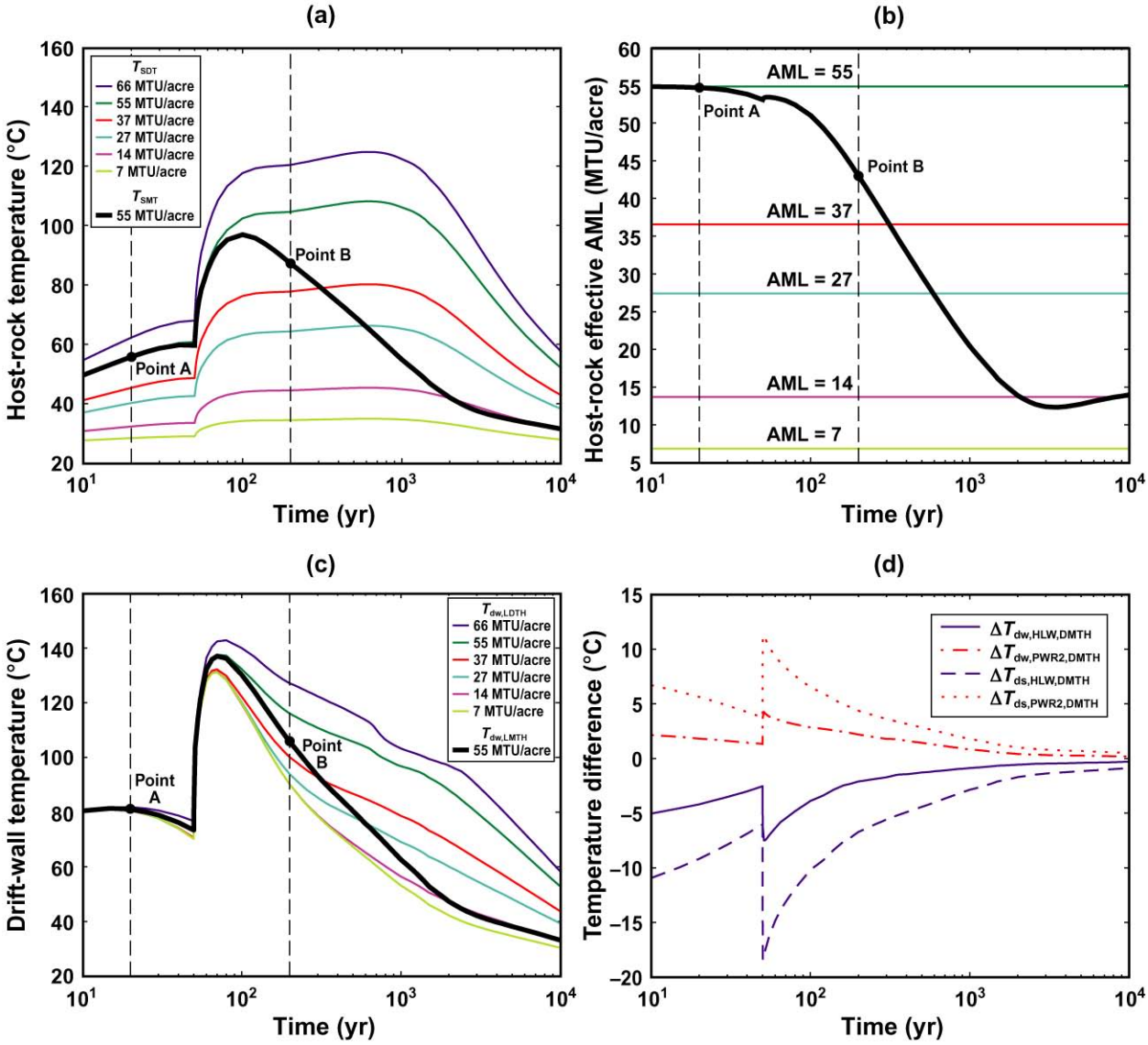

Figure 6.2-4. The MSTHM calculation sequence is shown for a three-drift 55-MTU/acre-repository example. (a) Host-rock temperature T_{SDT} vs. time calculated for the six listed AMLs; also plotted is T_{SMT} vs. time calculated at the repository center. Because the SDT and SMT submodels use smeared heat sources, the SDT and SMT host-rock temperatures are averaged temperatures for the repository horizon (from pillar mid-point to pillar mid-point) at a given drift location. (b) $AML_{hstrk,eff}$ vs. time calculated at the repository center. (c) Drift-wall temperature $T_{dw,LDTH}$ vs. time calculated for the six listed AMLs; also plotted is $T_{dw,LMTH}$ vs. time determined at the repository center. (d) Temperature deviation $\Delta T_{dw,j,DMTH}$ between the local and the axially averaged $T_{dw,LMTH}$ calculated using the six DDT submodels and interpolated on the basis of $AML_{hstrk,eff}$ vs. time (Figure 6.2-4b) for the HLW and PWR2 waste packages; also plotted are the corresponding temperature deviations $\Delta T_{ds,j,DMTH}$ between the local drip-shield temperature and the axially averaged $T_{ds,LMTH}$.

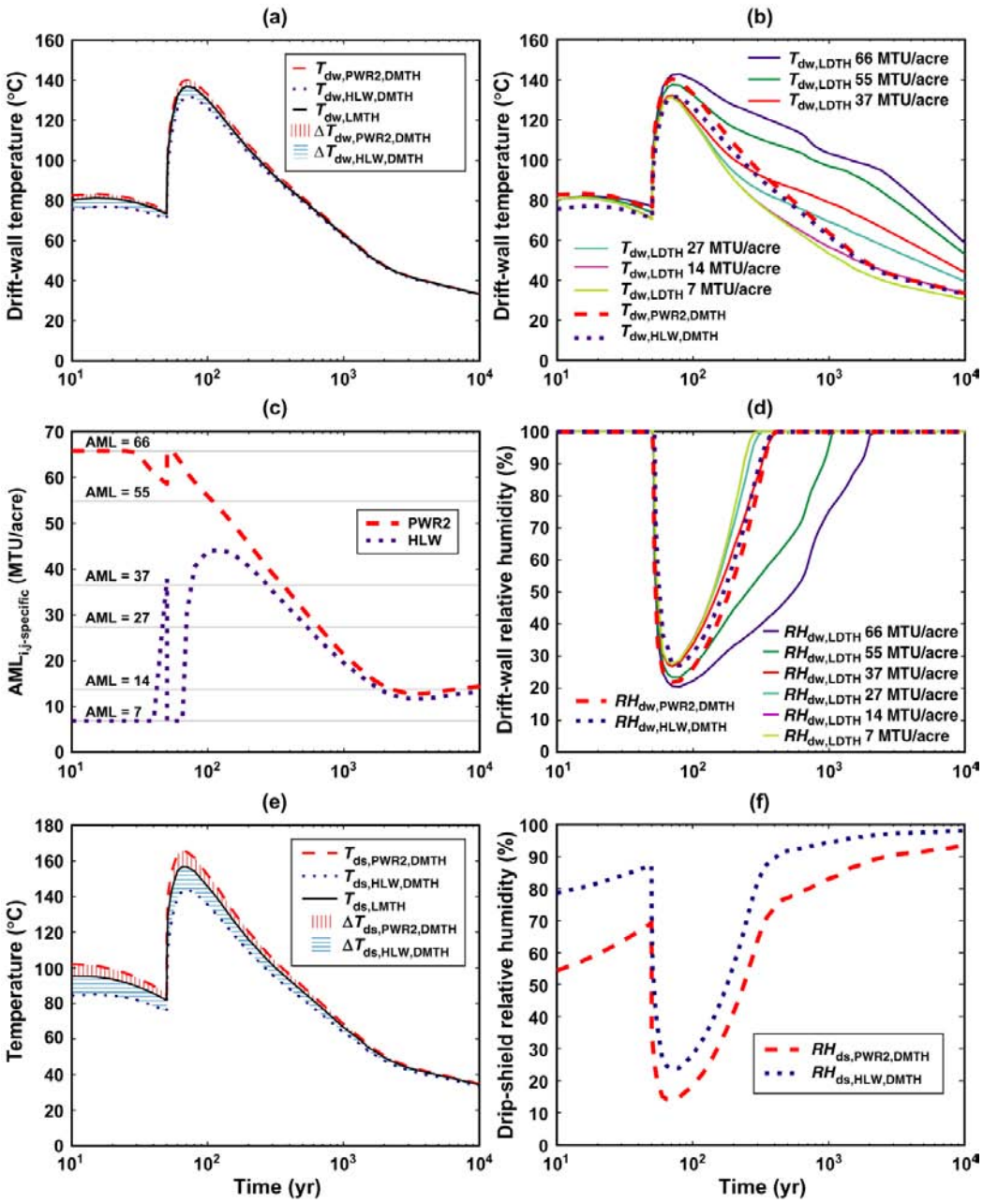

Figure 6.2-5. MSTHM-calculation sequence is shown (continued). (a) $T_{dw,j,DMTH}$ vs. time for the HLW and PWR2 waste packages at the repository center; also plotted is $T_{dw,LMTH}$ vs. time at the repository center (Figure 6.2-4c). (b) $T_{dw,LDTH}$ vs. time calculated for the six listed AMLs; also plotted is $T_{dw,j,DMTH}$ vs. time for the HLW and PWR2 waste packages at the repository center. (c) $AML_{i,j\text{-specific}}$ at the drift wall for the HLW and PWR2 waste packages at the repository center. (d) Drift-wall relative humidity $RH_{dw,LDTH}$ vs. time calculated for the six listed AMLs; also plotted is $RH_{dw,j,DMTH}$ vs. time for the HLW and PWR2 waste packages at the repository center, which is determined on the basis of $AML_{i,j\text{-specific}}$ vs. time for the respective waste packages. (e) $T_{ds,j,DMTH}$ vs. time for the HLW and PWR2 waste packages at the repository center; also plotted is $T_{ds,LMTH}$ vs. time at the repository center. (f) $RH_{ds,j,DMTH}$ vs. time for the HLW and PWR2 waste packages.

STAGE 1–The first calculation stage generates the host-rock effective AML, referred to as $AML_{hstrk,eff}$. The $AML_{hstrk,eff}$ is generated at each repository subdomain in the following manner:

1. First, the repository subdomain's host-rock temperature history simulated by the three-dimensional SMT submodel is compared with temperature histories simulated by the by the one-dimensional SDT submodels for a range of heat loading conditions (e.g., for 55 MTU/acre, for 46 MTU/acre). Note that because the SDT and SMT submodels use smeared heat sources, the SDT and SMT host-rock temperatures are averaged temperatures for the repository horizon (from pillar centerline to pillar centerline) at a given location.

2. Second, the value of $AML_{hstrk,eff}$ at any given time is the AML that a one-dimensional SDT submodel would have to be in order to match the three-dimensional SMT modeled temperature at that location. By using the $AML_{hstrk,eff}$, the influence of three-dimensional mountain-scale heat flow is imposed on the two-dimensional LDTH submodels discussed in Stage 2. As an example, Figure 6.2-4a-c illustrates how the concept of the $AML_{hstrk,eff}$ is used to account for three-dimensional mountain-scale heat flow. The host-rock temperature T_{SMT} calculated by the three-dimensional SMT submodel is compared with temperatures T_{SDT} calculated by the family of AML-dependent SDT submodels (Figure 6.2-4a). For each timestep, $AML_{hstrk,eff}$ (Figure 6.2-4b) is obtained by interpolating for T_{SMT} among the family of AML-dependent T_{SDT} curves. For example, Point A, which is at 20 years, finds the T_{SMT} to be virtually the same as T_{SDT} for 55 MTU/acre, thus yielding an $AML_{hstrk,eff}$ of 55 MTU/acre at 20 years. Point B, which is at 200 years, finds T_{SMT} lying between T_{SDT} for 55 and 37 MTU/acre; linear interpolation between T_{SMT} and the two T_{SDT} curves straddling Point B results in an $AML_{hstrk,eff}$ of 43 MTU/acre at 200 years.

Initially, T_{SMT} at the center of this three-drift repository corresponds exactly to T_{SDT} calculated by the 55-MTU/acre SDT submodel because there has been no thermal communication between the center and edge of the repository. Thus, $AML_{hstrk,eff}$ is the emplaced AML of 55 MTU/acre for early time (Figure 6.2-4b). Because of the relatively small size of the repository in this example (which corresponds to the MSTHM validation test problem described in Section 7.3), it takes only 50 years to establish thermal communication between the center and edge of the repository. Thus, the edge-cooling effect begins to influence the repository center at about 50 years, causing T_{SMT} to begin a steady decline relative to the family of AML-dependent T_{SDT} curves. This relative decline in T_{SMT} (Figure 6.2-4a) results in a corresponding steady decline in $AML_{hstrk,eff}$ (Figure 6.2-4b).

STAGE 2–This stage generates the three-dimensional LMTH-model (Table 1-2) temperatures at each of the repository subdomains; it does not address the influence of waste-package-to-waste-package variability in heat output. The LMTH-model drift-wall temperature $T_{dw,LMTH}$ is determined by linearly interpolating, to the variable $AML_{hstrk,eff}$ among the family of six AML-dependent LDTH-submodel drift-wall temperature $T_{dw,LDTH}$ curves. Returning to the example discussed in Stage 1 and examining Figure 6.2-4c, the $AML_{hstrk,eff}$ is 55 MTU/acre at Point A (t = 20 years) and thus, $T_{dw,LMTH}$ is equal to $T_{dw,LDTH}$ for 55 MTU/acre, which is about 81°C. At Point B (t = 200 years), the $AML_{hstrk,eff}$ is 43 MTU/acre and thus, an interpolated value of $T_{dw,LMTH}$ of 105°C is determined, which is between $T_{dw,LDTH}$ for

55 MTU/acre (115°C) and $T_{dw,LDTH}$ for 37 MTU/acre (100°C). The process of using $AML_{hstrk,eff}$ to generate LMTH-model temperatures is repeated for invert temperatures $T_{in,LMTH}$, for drip-shield temperatures Tds, LMTH, and for temperatures at various generic locations in the host rock. LMTH-model temperatures are determined for each of the repository subdomains. It is important to note that the LDTH and DDT submodels include the mechanism of thermal-radiative heat transfer between the waste package, drip-shield, invert, and drift-wall surfaces. Because thermal-radiative heat transfer is proportional to the temperature difference between two surfaces raised to the fourth power (i.e., ΔT^4), it is dependent on temperature differences within the drifts, as well as on the absolute temperature (history) in the drifts. Consequently, a DDT submodel, which is run at only one AML, cannot address the manner in which thermal-radiative heat transfer is dependent on absolute temperature (history). To address this issue, DDT submodels are run at a variety of AMLs so that thermal-radiative heat transfer incorporates the influence of the temperature differences, as well as the influence of the absolute temperature in the drift, all as a function of time. Because the DDT submodels are run for (at least) four different AMLs that cover a wide range of temperature histories, interpolations between the respective DDT submodels are performed over small enough temperature-history ranges that piecewise linear interpolation adequately characterizes the underlying nonlinear process of thermal-radiative heat transfer.

STAGE 3–LMTH-model temperatures have been determined at all generic locations (except for on the waste package) and for all repository subdomains, the next stage in the MSTHM process is to build the DMTH-model (Table 1-2) by incorporating the influence of waste-package-to-waste-package variability in heat output obtained from the family of DDT submodels. For each DDT submodel, the local deviation from an axially averaged temperature (i.e., averaged along the axis of the drift) is determined for each of the four waste package types (PWR1, PWR2, BWR, and HLW) for a variety of generic locations (e.g., drift wall, drip shield, invert, etc.). This local deviation is the difference between the local temperature of interest (e.g., the drift-wall temperature) and the corresponding axially averaged temperature. For example, local temperature deviations are computed for the drift wall ($\Delta T_{dw,j,DDT}$) and for the drip shield ($\Delta T_{ds,j,DDT}$). These temperature deviations are then interpolated as a function of the $AML_{hstrk,eff}$ in the same manner as $T_{i,LDTH}$ is interpolated to determine $T_{i,LMTH}$, as discussed in Stage 2. This is done to determine a temperature deviation accounting for the evolving influence of the edge-cooling effect at that repository subdomain. Computed temperature deviations for the drift wall and drip shield ($\Delta T_{dw,j,DMTH}$ and $\Delta T_{ds,j,DMTH}$) are illustrated in Figure 6.2-4d. The DMTH-model values of drift wall temperature ($T_{dw,j,DMTH}$, Figure 6.2-5a) are determined by adding $\Delta T_{dw,j,DMTH}$ (Figure 6.2-4d) to $T_{dw,LMTH}$ (Figure 6.2-4c). Note, the DMTH-model values of drip-shield temperature $T_{ds,j,DMTH}$ are similarly determined by adding $\Delta T_{ds,j,DMTH}$ to $T_{ds,LMTH}$ (Figure 6.2-5e).

STAGE 4–The $AML_{i,j\text{-}specific}$ accounts for axial variations due to waste package sequencing and waste-package-to-waste-package variability in heat output and is necessary for the calculation of all hydrologic variables in the DMTH-model. The $AML_{i,j\text{-}specific}$ is generated in much the same manner as the $AML_{hstrk,eff}$ in Stage 1. A number of values of $AML_{i,j\text{-}specific}$ are generated at each of the repository subdomains. For example, at the drift wall $AML_{dw,j\text{-}specific}$ is calculated in the following manner: (1) the local drift-wall temperature for a specific waste package $T_{dw,j,DMTH}$ is compared to the family of AML-dependent $T_{dw,LDTH}$ curves (Figure 6.2-5b); (2) the value of

$AML_{dw,j\text{-specific}}$ at any given time is the AML that an LDTH submodel would have to be to match the three-dimensional DMTH-model result. Figure 6.2-5c illustrates the $AML_{dw,PWR2\text{-specific}}$ and $AML_{dw,HLW\text{-specific}}$ curves.

STAGE 5–Once $AML_{i,j\text{-specific}}$ is determined from the temperature at a particular repository subdomain and a generic/waste-package-specific location, it is possible to determine the corresponding hydrologic variables, using output from the family of AML-dependent LDTH submodels. Note that the hydrologic variables from the LDTH submodels are collectively referred to as $H_{i,j,LMTH}$ in Figure 1-1 and Table 1-3. For example, $RH_{dw,j,DMTH}$ is obtained by linear interpolation for each timestep, using the $AML_{dw,j\text{-specific}}$ and the family of AML-dependent $RH_{dw,LDTH}$ curves (Figure 6.2-5d). The value of $RH_{dw,j,DMTH}$ accounts for both the generic/waste-package-specific deviations in local temperature and for the influence of three-dimensional mountain-scale heat flow at that particular repository subdomain. With the exception of drip-shield relative humidity $RH_{ds,j,DMTH}$ and waste package relative humidity $RH_{wp,j,DMTH}$, all other hydrologic variables are calculated in a similar manner to $RH_{dw,j,DMTH}$.

STAGE 6–The determination of relative humidity on the drip shield and waste package ($RH_{ds,j,DMTH}$ and $RH_{wp,j,DMTH}$) is determined by a relation of thermohydrologic variables that were determined by the DMTH model. The drip-shield relative humidity, $RH_{ds,j,DMTH}$ is obtained by the following relation:

$$RH_{ds,j,DMTH} = RH_{dw,cav} \frac{P_{sat}\left(T_{dw,cav}\right)}{P_{sat}\left(T_{ds,j,DMTH}\right)} \qquad \text{(Eq. 24)}$$

Here $RH_{ds,j,DMTH}$ and $T_{ds,j,DMTH}$ are the perimeter-averaged relative humidity and temperature on the drip shield, $RH_{dw,cav}$ and $T_{dw,cav}$ are the perimeter-averaged relative humidity and temperature on the drift wall and invert surfaces that adjoin the open drift cavity outside of the drip shield, and P_{sat} is the saturated vapor pressure. The waste package relative humidity $RH_{wp,j,DMTH}$ is calculated in an analogous manner. From a heat-transfer perspective, the drip shield functions like a thermal-radiation shield (between the waste package and the drift wall) that causes the waste package to be hotter than it would have been without the presence of the drip shield. Figure 6.2-5f illustrates $RH_{ds,j,DMTH}$ at two waste package locations at the center of the repository. Note that Equation 24 depends on the assumption discussed in Section 5.5 and that it holds in the absence of water dripping onto the drip shield. Depending on the magnitude of this dripping flux, relative humidity reduction on the drip shield will be diminished (BSC 2001c, Section 6.14).

6.2.5 SMT Submodels

The three-dimensional SMT submodel is used to determine the repository-scale variations in host-rock temperature (T) resulting from the heat output from the entire inventory of 70,000 MTU of waste, including 63,000 MTU of civilian spent nuclear fuel (CSNF) and 7,000 MTU of DHLW. The SMT submodel includes the influence of mountain-scale thermal-property distribution, the edge-cooling effect, which results from lateral heat loss at the repository edges, and the overburden-thickness distribution. Overburden thickness is defined to be the depth of the repository horizon below the ground surface. The SMT submodel domain extends from the ground surface to 1,000 m below the present-day water table and the lateral (adiabatic)

boundaries are far enough away from the repository so that they do not affect repository temperatures. The temperature 1,000 m below the water table is found by extrapolation using bound_conditions v1.0.

6.2.5.1 SMT-Submodel Mesh

The actual and modeled repository footprints (Figure 6.2-3) cover nearly identical areas of approximately 4.656 km^2, which is based on the emplacement-drift end-point coordinates given in *Repository Design, Repository/PA IED Subsurface Facilities* (BSC 2003d). The repository footprint corresponds to the area that is heated by the smeared-heat-source representation of heat generation from waste packages. The areal distribution of gridblocks in the repository area of the SMT submodel is shown in Figure 6.2-3. The SMT submodel discretely represents each emplacement panel (Panels 1, 2E, 2W, 3, and 5) as well as each emplacement drift by using rows of heated gridblocks that are 20 m in the longitudinal, 81 m perpendicular to the drift axis, and 6-m thick in the vertical direction. The 6-m-thickness of the smeared heat source in the SMT submodel is consistent with that of the SDT submodel discussed in Section 6.2.7. There are 2,874 20-m intervals along the 95 emplacement drifts in the SMT submodel. The actual total heated length of emplacement drift in the repository is 57,480.2 m; the modeled length of emplacement drifts is 57,480.0 m. Table 6.2-1 lists the actual and modeled lengths of heated emplacement drifts in each of the panels. The heated length of each emplacement drift is obtained from the end-point coordinates given in *Repository Design, Repository/PA IED Subsurface Facilities* (BSC 2003d).

Table 6.2-1. Summary of Emplacement Panels and Drifts Represented in the SMT Submodel

Panel	Total heated drift length (m)	Number of emplacement drifts	Number of heated gridblocks	Total modeled length of drifts (m)
1	4,100.4	8	206	4,120.0
2E	10,882.0	19	545	10,900.0
2W	13,845.1	23	689	13,780.0
3	17,493.6	30	877	17,540.0
5	11,159.1	15*	557	11,140.0
Total	57,480.2	95	2874	57,480.0

Source: BSC 2003d

NOTES: Note that each of the heated gridblocks represents a 20-m interval along the emplacement drift.
*Panel 5 has a total of 27 drifts; the 15 northernmost drifts are emplacement in the TSPA-LA base case.

The SMT-submodel mesh is constructed so that boundary effects have a negligible effect on the predicted temperatures near the repository. This is accomplished by extending the lateral boundaries at least 1,000 m beyond the repository edges and by extending the lower boundary 1,000 m below the water table.

YMESH v1.54 is used to generate the SMT-submodel mesh file so that it is consistent with the three-dimensional distribution of UZ Model Layers in the Site-Scale UZ Flow and Transport Model (DTN: LB03023DKMGRID.001) as described in Table 11 of *Development of Numerical Grids for UZ Flow and Transport Modeling* (BSC 2003c). The process of building the

SMT-submodel mesh is described in Attachment I. Note that the lower boundary (corresponding to the water table) of the three-dimensional Site-Scale UZ Flow Model is a gently sloping surface. It is also worth noting that the previous version of the Site-Scale UZ Flow Model (DTN: LB990701233129.001) had a horizontal lower boundary at an elevation of 730 m, which was based on an assumption that the water table was horizontal.

The 2,874 gridblocks in the SMT submodel are the 2,874 locations for which the MSTHM provides thermohydrologic output. Because each of these 2,874 locations is represented by a gridblock that is 20-m-long in the axial direction along the drift, they can each contain approximately four waste packages. The MSTHM uses the DDT submodel (Section 6.2.8) to discretely represent the thermohydrologic conditions for a wide range of waste packages, ranging from those that have low heat-generation rates (e.g., DHLW waste packages) to those that have high heat-generation rates (e.g., 21-PWR CSNF waste packages). The DDT submodel discretely represents eight waste packages, including three 21-PWR CSNF waste packages, three 44-BWR CSNF waste packages, and two DHLW waste packages. The MSTHM is constructed to provide thermohydrologic-parameter histories (e.g., temperature and relative humidity) for each one of those eight waste packages at all 2,874 locations in the repository, which results in a total of 22,992 sets of thermohydrologic-parameter histories. The 22,992 thermohydrologic-parameter sets are greater than the number of waste packages that could be emplaced in 57,480 m of emplacement drifts. The additional thermohydrologic-parameter sets are provided to address uncertainty concerning the actual emplaced sequencing of waste packages. In other words, it cannot be known *a priori* what the actual emplaced waste package sequencing will be. The 22,992 thermohydrologic-parameter sets are provided for multiple scenarios, such as lower-bound, mean, and upper-bound infiltration flux cases to allow downstream process models to sample from a broad set of thermohydrologic conditions that encompasses the influence of various sources of uncertainty.

6.2.5.2 SMT-Submodel Boundary Conditions

The SMT submodel domain extends from the ground surface to 1,000 m below the present-day water table. The lateral boundaries, which are adiabatic boundaries, are at least 1,000 m from the repository edges, which is far enough away from the repository so that they do not affect thermal behavior in the repository. The temperature at the ground surface is based on ground-surface temperatures from the three-dimensional UZ Flow Model (DTN: LB991201233129.001), which is based on a correlation of temperature versus elevation.

The temperature at the lower boundary of the model domain is extrapolated vertically from the temperature gradient at the (sloping) water table of the current Site-Scale UZ Flow Model. The temperature at the sloping water is interpolated, based on the temperature at an elevation of 730 m, which was the water table in the previous three-dimensional UZ Flow Model, and the ground-surface temperature. Both the ground-surface temperature distribution and the (730-m-elevation) water-table temperature distribution are found in DTN: LB991201233129.001. Attachment II describes the process of generating boundary temperatures for the SMT submodels, as well as for the other submodels.

6.2.5.3 SMT-Submodel Heat-Generation Rates

The heat-generation rate for the SMT submodel is in the form of a heat-generation-rate-versus-time table located in NUFT input-file "include" files. For the TSPA-LA base case there is an assumption that all waste packages are simultaneously emplaced (Section 5.2.3). Thus, heating starts at the same time for the entire repository represented in the SMT submodel. The heat-removal efficiency of drift ventilation is represented by the reduction of the net heat-generation rate during the preclosure period. It is important to note that the heat-removal efficiency depends on the distance from the ventilation inlet and it also varies with time. Thus, the effective heat-generation rate along an emplacement drift depends on the distance from the edge of that drift during the preclosure period. The heat-removal effect of drift ventilation is incorporated into the heat-generation-rate-versus-time tables for the heated repository blocks, using heatgen_vent_emplace v1.0. For the postclosure period, the same heat-generation-rate-versus-time table is applied to the entire repository because drift ventilation has ceased and the effective heat-generation rate is the full nominal rate. Attachment III describes the process of generating heat-generation-rate-versus-time tables for the SMT submodel, as well as for the other submodels.

6.2.5.4 SMT-Submodel Material Properties

Because the SMT submodel is a thermal-conduction model, it only requires thermal properties. Material properties are read into the SMT-submodel NUFT-input files as "include" files for the natural system thermal properties.

The SMT submodel uses thermal-conduction properties for the UZ Model Layers (BSC 2003h), consistent with the SDT submodel (Section 6.2.7). These properties are based on Table 4-1 and the assumption of using the wet thermal conductivity as is discussed in Section 5.3.2.1.

Where saturated zone thermal properties are required the thermal properties are a weighted average of UZ Model Layers as discussed in Section 5.3.2.2. The averaging is accomplished by determining area-weighting factors for each of the UZ Model Layers that occur at the water table, which is the lower boundary of the three-dimensional Site-Scale UZ Flow Model. The process of building the SMT-submodel material property files is described in Attachment IV.

6.2.5.5 SMT-Submodel Simulations

The initialization of the SMT submodel is accomplished by running the SMT submodel with no repository thermal load until a steady-state temperature distribution is achieved. Only one SMT-submodel simulation is required to represent the preclosure and postclosure period. This simulation is run for 20,000 years after closure of the repository. The process of building the SMT-submodel input files is described in Attachment V.

6.2.6 LDTH Submodels

The two-dimensional LDTH submodels use the dual-permeability method, modified with the active-fracture concept, to represent two-phase heat and fluid flow in the fractured porous rock. The LDTH submodels are run at the 108 drift-scale-submodel locations (Figure 6.2-3) and for 4 different values of modeled AML (14, 27, 55, and 66 MTU/acre). Representing the influence of

edge-cooling effects requires that most of the LDTH-submodel runs use a modeled AML that is less than the actual AML of the repository.

These submodels are required to obtain functional relationships between "line-averaged" temperatures predicted by the LDTH submodel and the "smeared" host-rock temperatures predicted by the SDT submodel.

The NUFT code is used to model flow through a fractured porous media in the LDTH submodels. The key NUFT options that are required for LDTH simulations include the dual-permeability and the active-fracture concept. These NUFT options are required to be consistent with the hydrologic property set (DTN: LB0208UZDSCPMI.002) used in the MSTHM calculations supporting the TSPA-LA.

The DKM conceptualizes the fractured rock as having two interacting materials, one representing the matrix and one representing the fractures. The interaction between the fractures and the matrix is explicitly calculated from the local temperature and pressure differences, thus allowing transient behavior to be predicted.

The active fracture concept accounts for the contact area between the fracture and the matrix, as well as the frequency of fractures. The active fracture concept is that fracture flow only occurs through some of the fractures. This is more conservative than assuming the influx flows evenly through all fractures. The flux through a fracture is greater when it has higher saturation and, therefore, focusing flow through a portion of the fractures (i.e., to active fractures) maximizes flux and results in fast pathways for flux through the mountain.

The natural system hydrologic properties in the calibrated drift-scale hydrologic property set (DTN: LB0208UZDSCPMI.002) were calibrated in *Calibrated Properties Model* (BSC 2003i), using an inverse modeling technique that assumes the use of the DKM and the active-fracture concept. Therefore, the DKM and active-fracture concept are required NUFT options.

6.2.6.1 LDTH-Submodel Locations

The LDTH submodel locations are shown in Figure 6.2-3, and represent repository-scale variability of thermal properties, hydrologic properties, percolation flux, and overburden thickness.

6.2.6.2 LDTH-Submodel Mesh

The cross-sectional dimensions of the drift for the postclosure period is shown in Figure 6.2-1; these dimensions were used to build the numerical meshes of the LDTH submodels (Figure 6.2-6). The same mesh is used for the initialization submodel runs, which establish steady-state conditions for the time of emplacement and the submodel runs for the preclosure and postclosure periods. The process of building the LDTH-submodel input files is described in Attachment V.

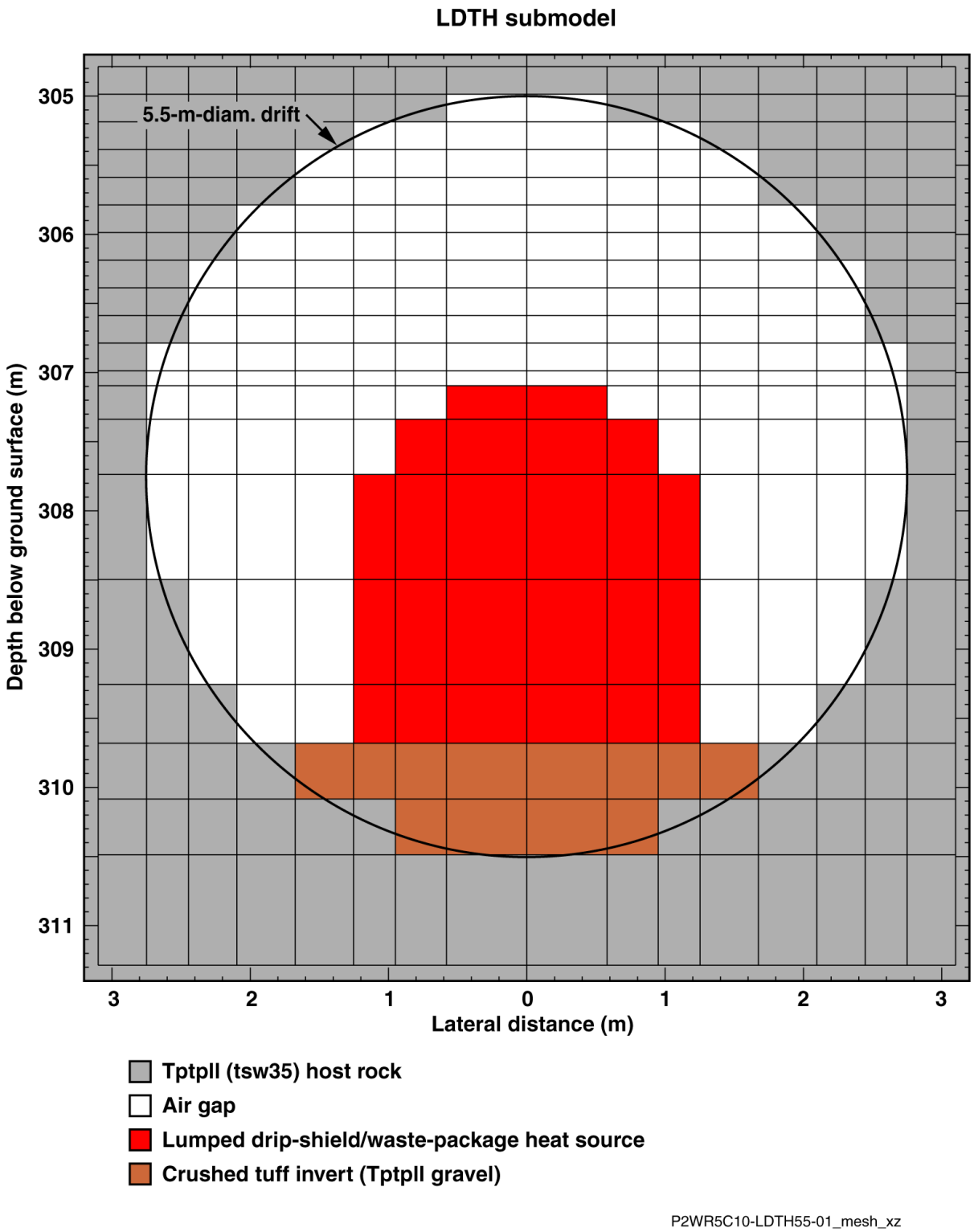

Figure 6.2-6. Cross-sectional view of the numerical mesh used in the vicinity of the drift for all LDTH submodels, including both the initialization runs and the preclosure and postclosure runs.

The numerical mesh for the LDTH submodel (Figure 6.2-6) assumes that the drip shield and waste package are lumped as a monolithic heat source. This lumped approximation of the drip

shield and waste package allows for the representation of thermohydrologic behavior down to the surface of the drip shield. This lumped heat source is 1 m in the longitudinal direction along the drift axis (as it is in the smeared heat source in the SDT submodel, discussed in Section 6.2.7). This lumped representation for the waste package and drip shield is applied during both the preclosure period and the postclosure period. For the preclosure period, this lumped approximation of the drip shield and waste package is corrected by the manner in which the preclosure DDT submodel (Figure 6.2-7), which rigorously accounts for the actual dimensions of the waste package (without the presence of the drip shield), is applied in the MSTHAC methodology (Section 6.2.4). The postclosure DDT submodel (Figure 6.2-8), which rigorously accounts for the actual waste package and drip-shield dimensions (including the correct dimensions of the gap between the waste package and drip shield), is applied in the MSTHAC methodology (Section 6.2.4) to represent thermohydrologic behavior between the drip shield and waste package.

6.2.6.3 LDTH-Submodel Boundary Conditions

Because the LDTH submodels are for a symmetry cell between the vertical plane down the center of the drift and the vertical midplane between drifts, the lateral boundaries are adiabatic and no-mass-flow boundaries. The LDTH submodels require temperature, pressure, and gas-phase air-mass fraction at the upper boundary, which represents the ground surface and the lower boundary, which represents the water table. The upper boundary also requires the enthalpy associated with the infiltration flux at the top of the model. Note that the correct enthalpy is determined from the temperature of the upper boundary.

Both the upper and lower boundaries have constant conditions with time. Note that the process of calculating air-mass fraction at the ground surface utilizes the assumption that the atmosphere is at 100 percent relative humidity (Section 5.1.1). The process of adding the boundary conditions to the LDTH submodels is described in Attachment II.

6.2.6.4 LDTH-Submodel Heat-Generation Rates

The heat-generation rates for the LDTH submodels are in the form of heat-generation-rate-versus-time tables located in NUFT include files. Because any given LDTH submodel covers the same model domain (including the same area in plan view) as the corresponding SDT submodel, the LDTH and corresponding SDT submodel use the same heat-generation-rate-versus-time tables. The drip shield and waste package are lumped as a monolithic heat source that is 1 m in the longitudinal direction along the drift axis (as it is in the smeared heat source in the SDT submodel, discussed in Section 6.2.7). The heat-removal efficiency of drift ventilation is represented by the reduction of the net heat-generation rate during the preclosure period. It is important to note that the heat-removal efficiency depends on the distance from the ventilation inlet and it also varies with time. Thus, the effective heat-generation rate along an emplacement drift depends on the distance from the edge of that drift during the preclosure period. The heat-removal effect of drift ventilation is incorporated into the heat-generation-rate-versus-time tables for a given LDTH-SDT-submodel location, using heatgen_ventTable_emplace v1.0. For the postclosure period, the same heat-generation-rate-versus-time table is applied to all LDTH-SDT-submodel locations because drift ventilation has ceased and the effective heat-generation rate is the full nominal rate at all

locations. The input files for the LDTH submodels involve assumptions described in Sections 5.1.1, 5.1.2, 5.3.1.1, 5.3.1.2, 5.3.2.3, and 5.3.2.4. Attachment III describes the process of generating heat-generation-rate-versus-time tables for the LDTH submodels.

6.2.6.5 LDTH-Submodel Material Properties

Material properties are read into the LDTH-submodel NUFT-input files as "include" files for the natural system properties and for the engineered barrier system properties inside the emplacement drifts.

One hydrologic property set, called the modified-mean infiltration flux hydrologic-property set (dkm-afc-1Dds-mc-mi-04), is used to conduct the LDTH-submodel calculations for lower-bound, mean, and upper-bound infiltration flux cases. The modified-mean infiltration flux property set is the same as the mean infiltration flux property set (DTN: LB0208UZDSCPMI.002) with the one modification being that the van Genuchten fracture alpha in the Tptpul (tsw33) is set to be the same (1.02×10^{-4} Pa^{-1}) as that in the Tptpll (tsw35) unit (Section 6.3.1). The file dkm-afc-EBS-mi-03 gives the thermal and hydrologic properties of the materials inside the emplacement drift. The thermal properties inside the emplacement drifts, such as the drip shield and invert, are given in Table 4-1. The thermal properties inside the drifts also include the emissivity values of the surfaces within the drifts. The engineered barrier system thermal properties also include the use of an effective thermal conductivity for the gas-filled drift cavity that is based on a correlation (Francis et al. 2003, Table 6) accounting for the influence of natural convection, which is described in Attachment I. The gas-filled cavity between the drip shield and drift wall is represented as a porous media with 100 percent porosity and a very large permeability of 11×10^{-8} m^2 (Section 5.3.1.7). Note that because the dual-permeability method is used to represent fracture-matrix flow, it is necessary to partition the gas-filled cavity into the matrix and fracture continuum. This portioning, which is taken to be 50 percent matrix continuum and 50 percent fracture continuum, has no effect on flow because of conditions in these respective continuum are in equilibrium within the gas-filled drift. The input files require the assumptions described in Sections 5.1.1, 5.1.2, 5.2.3, 5.3.1.1, 5.3.1.2, 5.3.1.7, 5.3.1.8, 5.3.2.3, and 5.3.2.4. The process of generating the LDTH-submodel material properties files is described in Attachment IV. The input files require the assumptions described in Sections 5.1.1, 5.1.2, 5.2.3, 5.3.1.1, 5.3.1.2, 5.3.1.7, 5.3.1.8, 5.3.2.3, and 5.3.2.4. The process of generating the LDTH-submodel material properties files is described in Attachment IV.

6.2.6.6 LDTH-Submodel Percolation Flux

The liquid-phase flux must be specified at the upper boundary of the LDTH submodels. For the TSPA-LA base case the upper-bound boundary liquid-phase flux corresponds to the distribution of percolation flux just below the base of the PTn unit; this data is generated by the three-dimensional UZ Flow Model for the three climate states: present-day, monsoonal, and glacial-transition. Thus, the MSTHM accounts for the influence of lateral diversion in the PTn as represented in the three-dimensional UZ Flow Model.

Percolation flux is provided for the present-day, monsoonal, and glacial-transition climates for lower-bound, mean, and upper-bound infiltration flux cases (DTN: LB0302PTNTSW9I.001),

resulting in nine files. repository_percolation_calculator v1.0 is used to determine the percolation flux at each of the 108 LDTH-SDT-submodel locations (Figure 6.2-3) in Panels 1, 2E, 2W, 3, and 5. The process of generating LDTH-submodel percolation flux is described in Attachment I.

6.2.6.7 LDTH-Submodel Simulations

The LDTH submodel is the only submodel type that has to be run for each of the three infiltration flux cases (low, mean, and high). The simulations for the other three submodel types are applicable to all infiltration flux cases.

Each LDTH-submodel set for a given infiltration flux case consists of 432 simulations, which comes from 108 drift-scale-submodel locations (Section 6.3.1) and 4 AML values run at each location ($108 \times 4 = 432$). The process of building the LDTH-submodel input files is described in Attachment I.

6.2.7 SDT Submodels

The one-dimensional smeared-heat-source drift-scale thermal-conduction (SDT) submodels are run in parallel with the LDTH submodels at the same 108 locations and for the same AMLs (14, 27, 55, and 66 MTU/acre). These submodels are required to obtain functional relationships between "line-averaged" temperatures predicted by the LDTH submodel and the "smeared" host-rock temperatures predicted by the SDT submodel.

6.2.7.1 SDT-Submodel Locations

The SDT submodels are run at the same 108 drift-scale-submodel locations (Figure 6.2-3) as the LDTH submodel (Section 6.2.6.1)

6.2.7.2 SDT-Submodel Mesh

The SDT submodels use the same vertical discretization of gridblocks as is used in the SMT submodels (Section 6.2.5). The manner in which the LDTH-SDT temperature relationships are developed and used to modify SMT-predicted host-rock temperatures (Section 6.2.4) requires consistency between how vertical heat flow is modeled in the respective SDT and SMT submodels, including consistency in the vertical gridblock discretization in the respective submodels.

6.2.7.3 SDT-Submodel Boundary Conditions

The SDT-submodel boundary temperature conditions are the same as the corresponding LDTH submodel (Section 6.2.6.3). Consistent upper and lower boundary temperatures ensure self-consistency with respect to how the LDTH and SDT submodels are used to generate LDTH-temperature versus SDT-temperature relationships and how these relationships are used in the MSTHAC v7.0 methodology to correct SMT-predicted temperatures to LMTH conditions (Section 6.2.4).

Because the SDT submodels are for a symmetry cell between the vertical plane down the center of the drift and the vertical midplane between drifts, the lateral boundaries are adiabatic and no-mass-flow boundaries. The SDT submodels require temperature at the upper boundary, which represents the ground surface, and the lower boundary, which represents the water table. Both boundaries have constant temperature conditions with time. The process for generating SDT-submodel boundary conditions is described in Attachment II.

6.2.7.4 SDT-Submodel Heat-Generation Rates

Because any given SDT submodel covers the same model domain (including the same area in plan view) as the corresponding LDTH submodel, the SDT and corresponding LDTH submodel use the same heat-generation rate-versus-time table (Section 6.2.6.4). Attachment III describes the process of generating heat-generation-rate-versus-time tables for the SDT submodels. The heat generation is smeared over a gridblock that is 6-m thick in the vertical direction (as it is in the SMT submodel, discussed in Section 6.2.5), 1 m in the longitudinal direction along the drift axis (as it is in the LDTH submodels, discussed in Section 6.2.6), and which extends from the drift centerline to the midpillar location between drifts.

6.2.7.5 SDT-Submodel Material Properties

Because the SDT submodel is a conduction-only model, the material properties only involve thermal properties. Material properties are read into the SDT-submodel NUFT-input files as "include" files for the natural system thermal properties. The SDT submodel uses the same thermal properties (for the UZ Model Layers) that are used in the SMT submodel (Section 6.2.5.4). The material properties of the SDT submodels utilize assumptions described in Section 5.3.2.1. The process of building the SDT-submodel material-property file is described in Attachment IV.

6.2.7.6 SDT-Submodel Simulations

Each SDT-submodel set consists of 432 simulations that come from 108 LDTH-SDT-submodel locations (Figure 6.2-3) and 4 AML values run at each location ($108 \times 4 = 432$). The process of building the SDT-submodel input files is described in Attachment V.

6.2.8 DDT Submodels

The three-dimensional DDT submodel is used to account for waste-package-specific heat output and for thermal radiation between all waste package and drift surfaces to determine waste-package-specific deviations (relative to line-averaged-heat-source conditions) in temperatures in the drift and adjoining host rock. For the preclosure and for the postclosure periods, thermal radiation between the waste package and drift surfaces controls the longitudinal temperature deviations along the drift. The values of thermal conductivity or convective heat-flow processes in the host rock play a minor role on the magnitude of longitudinal temperature deviations along the drift (Hardin 1998, Section 3.7.5.4). This allows a MSTHM calculation to only require a set of DDT-submodel calculations conducted at a single location in the repository. The P2WR5C10 LDTH-SDT-submodel location is located in Panel 2W, which is located in the appoximate center of the repository (Figures 6.2-3 and 6.3-1). This location was

selected because the repository horizon at that location is in the middle of the Tptpll (tsw35 UZ Model Layer), which is the predominant host-rock type in the repository and because the overburden thickness at that location is close to the average for the repository. The DDT submodels utilize assumptions described in Sections 5.2.2, 5.2.3, 5.3.2.1, and 5.4.

6.2.8.1 DDT-Submodel Locations

The P2WR5C10 LDTH-SDT-submodel location, which is in the center of Panel 2W (Figures 6.2-3 and 6.3-1), is used for all DDT-submodel calculations.

6.2.8.2 DDT-Submodel Mesh

The cross-sectional and longitudinal dimensions of the drift for the preclosure and postclosure periods are shown in Figures 6.2-1 and 6.2-2, respectively. Note that the drip shield (Figure 6.2-1) is not present during the preclosure ventilation period. These dimensions were used to build the numerical meshes of the DDT submodels. The cross-section view of the mesh is shown in Figures 6.2-7 and 6.2-8 for the preclosure and postclosure periods, respectively. The longitudinal view of the mesh is shown in Figures 6.2-9 and 6.2-10 for the preclosure and postclosure periods, respectively. The DDT submodel utilizes symmetry in all four directions: (1) about the vertical midplane down the center of the drift, (2) the vertical midplane down the center of the rock pillar between drifts, (3) the vertical plane that is orthogonal to and intersects the "one-half" 21-PWR waste package, and (4) the vertical plane that is orthogonal to and intersects the "one-half" 44-BWR waste package (Figure 6.2-2). Thermal radiation is represented between all surfaces in the drift. From a heat-transfer perspective, the drip shield functions like a thermal-radiation shield (between the waste package and the drift wall) that causes the waste package to be hotter than it would have been without the presence of the drip shield. The increased temperature difference between the waste package and the drift wall reduces the relative humidity on the waste package in a fashion that is analogous to that given in Equation 24 (Section 6.2.4) for the drip shield itself.

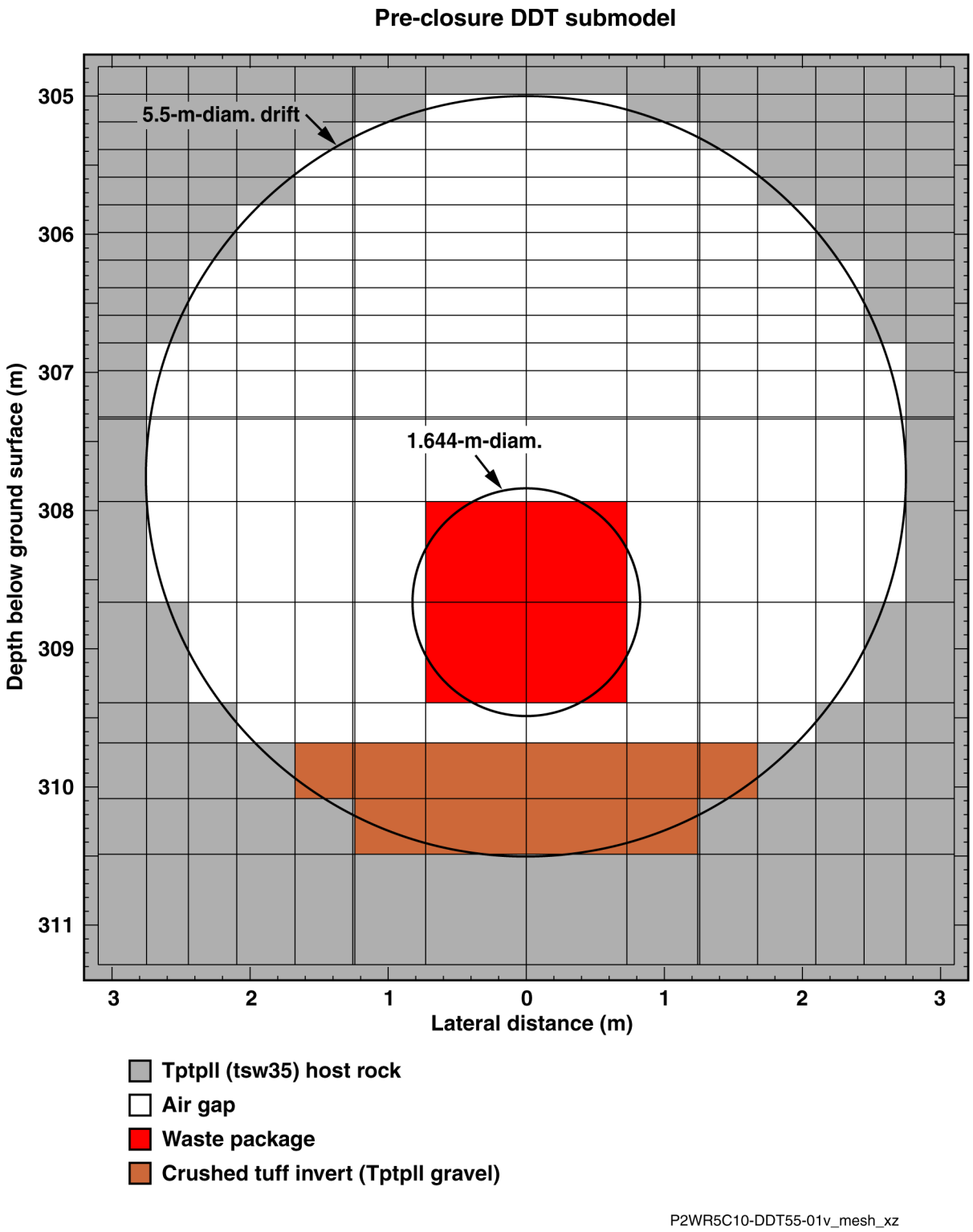

Figure 6.2-7. Cross-Sectional View of the Mesh Used in the Preclosure DDT Submodels

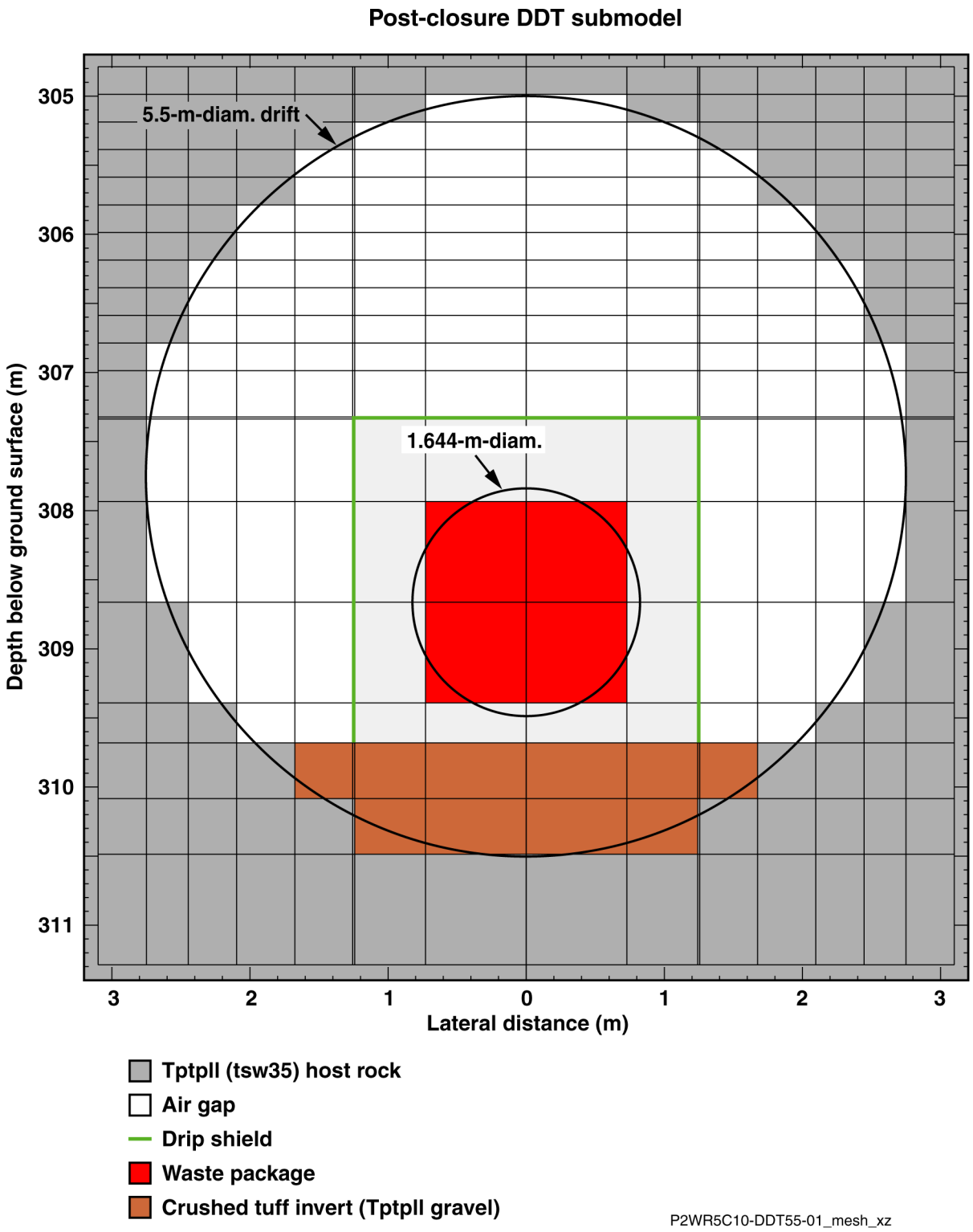

Figure 6.2-8. Cross-Sectional View of the Mesh Used in the Postclosure DDT Submodels

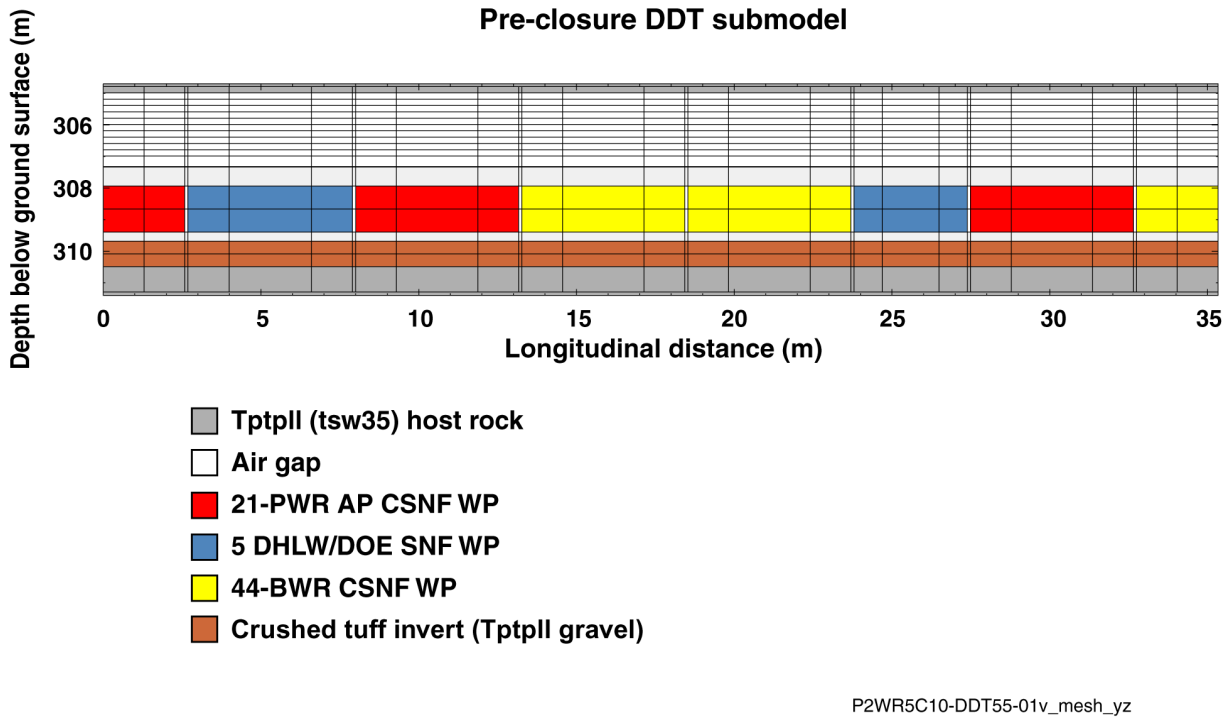

NOTE: WP = waste package

Figure 6.2-9. Cross-Sectional View of the Mesh Used in the Preclosure DDT Submodels

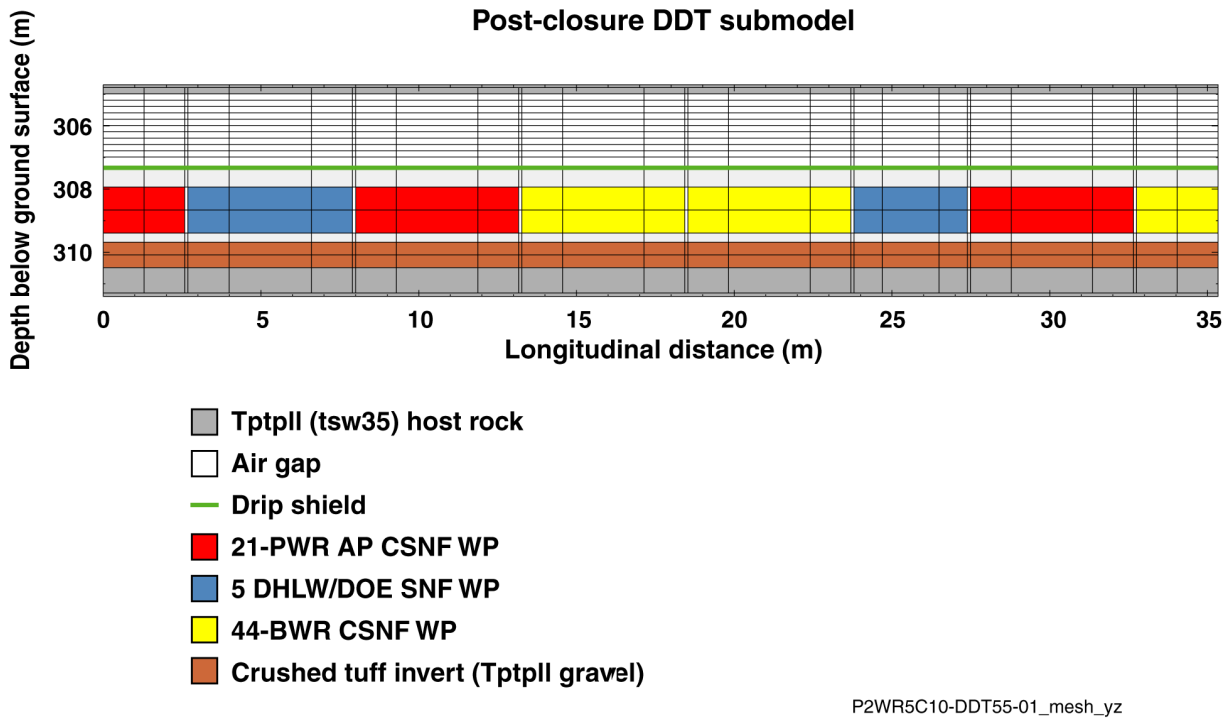

NOTE: WP = waste package

Figure 6.2-10. Cross-Sectional View of the Mesh used in the Postclosure DDT Submodels

6.2.8.3 DDT-Submodel Boundary Conditions

The temperature boundary conditions for the DDT submodels are the same as those for the SDT submodel at the P2WR5C10 LDTH-SDT-submodel location (Figures 6.2-3 and 6.3-1), which is in the center of Panel 2W. The DDT-submodel temperature boundary conditions are the same as the corresponding LDTH submodel.

Because the DDT submodels are for a symmetry cell between the vertical plane down the center of the drift and the vertical midplane between drifts, the lateral boundaries are adiabatic and no-mass-flow boundaries. The DDT submodels require temperature at the upper boundary, which represents the ground surface and the lower boundary, which represents the water table. Both boundaries have constant temperature conditions with time. The process for generating DDT-submodel boundary conditions is described in Attachment II.

6.2.8.4 DDT-Submodel Heat-Generation Rates

Heat-generation-rate-versus-time tables are required for the 8 different waste packages represented in the DDT submodels (Figure 6.2-2), which are read into the DDT-submodel NUFT-input files as "include" files. The heat-generation-rate-versus-time tables utilize the assumption described in Section 5.2.3. During the preclosure period, the DDT submodel has the same heat-removal-efficiency-versus-time table that is applicable to the P2WR5C10 LDTH-SDT-submodel location (Figures 6.2-3 and 6.3-1). Note that the heat-removal-efficiency-versus-time tables are derived from DTN: MO0306MWDASLCV.001. Attachment III describes the process of generating heat-generation-rate-versus-time tables for the DDT submodel, as well as for the other submodels.

6.2.8.5 DDT-Submodel Material Properties

Because the DDT submodel is a conduction/radiation-only model, the material properties only involve thermal properties. Material properties are read into the SDT-submodel NUFT-input files as "include" files for the natural system thermal properties. The DDT submodel uses the same thermal properties (for the UZ Model Layers) that are used in the SMT and SDT submodels (Sections 6.2.5.4 and 6.2.7.5). The DDT submodels also use thermal properties of the engineered barrier system components, such as the drip shield, invert, and respective waste packages (Table 4-1). The thermal properties of the engineered barrier system components include the emissivity values of the surfaces within the emplacement drifts. The engineered barrier system thermal properties also include the use of an effective thermal conductivity for the air in the drift cavity that is based on a correlation (Francis et al. 2003, Table 6) accounting for the influence of natural convection, which is described in Attachment IV. The material properties of the DDT submodels utilize assumptions described in Section 5.3.2.1. The process of building the DDT-submodel material-property file is described in Attachment IV.

6.2.8.6 DDT-Submodel Simulations

A single set of DDT-submodel simulations (for modeled AMLs of 14, 27, 55, and 66 MTU/acre) was conducted for this report at the P2WR5C10 LDTH-SDT-submodel location (Figures 6.2-3 and 6.3-1). This set of DDT-submodel simulations is used in all three (low, mean, and high)

infiltration flux cases. The process of building the DDT-submodel NUFT-input files is described in Attachment V.

6.3 MSTHM RESULTS

6.3.1 TSPA-LA Base Case

This section discusses the MSTHM calculations that were conducted for the TSPA-LA base case. As was done for the Total System Performance Assessment for the Site Recommendation (called the TSPA-SR), the base case consists of three infiltration flux cases: lower-bound, mean, and upper-bound infiltration flux cases for three climate states: present-day, monsoonal, and glacial-transition. Past MSTHM calculations directly used the infiltration maps for these three cases with the underlying assumption being that there is no lateral attenuation of infiltration in the PTn unit (or in any other unit above the repository); thus, percolation above the repository occurs strictly as one-dimensional vertical downward flow. For the TSPA-LA base case, the upper-boundary liquid-phase flux in the MSTHM corresponds to the distribution of percolation flux just below the base of the PTn unit; this data (Table 4-1) is generated by *UZ Flow Models and Submodels* (BSC 2003h) for the three climate states: present-day, monsoonal, and glacial-transition. Thus, the TSPA-LA-base-case MSTHM accounts for the influence of lateral diversion in the PTn as represented in the three-dimensional UZ Flow Model.

Previous MSTHM calculations (such as those in support of the TSPA-SR) used different hydrologic property sets for each of the infiltration flux cases; thus, lower-bound, mean, and upper-bound one-dimensional drift-scale hydrologic property sets were applied to their respective infiltration flux cases. For this study it was found that only one hydrologic property set (called the modified-mean infiltration flux property set) is needed for conducting MSTHM calculations for the three infiltration flux cases. In Section 6.6.3 of *Abstraction of Drift Seepage* (BSC 2003k), which addresses the van Genuchten fracture alpha and permeability distributions for the Tptpul (tsw33) and Tptpln (tsw36) units, it is noted that the Tptpul (tsw33) unit is hydrogeologically similar to the Tptpll (tsw35) unit; furthermore, it is stated that the two units with lithophysal cavities in the rock (the Tptpul and Tptpll units) should have similar hydrogeological characteristics. The modified-mean infiltration flux property set is the same as the mean infiltration flux property set (DTN: LB0208UZDSCPMI.002) with the one modification being that the van Genuchten fracture alpha in the Tptpul (tsw33) is set to be the same (1.021×10^{-4} Pa^{-1}) as that in the Tptpll (tsw35) unit.

For this study, it was found that the application of the modified-mean infiltration flux property set to lower-bound, mean, and upper-bound infiltration flux cases produces uniform calculated host-rock liquid-phase saturation for the three infiltration flux cases. It was also found that host-rock liquid-phase saturation consistently increases (slightly) with increasing percolation flux. The purpose for conducting lower-bound, mean, and upper-bound infiltration flux cases with the MSTHM is to address the influence of percolation flux uncertainty on thermohydrologic conditions within emplacement drifts and in the adjoining host rock. In conducting a sensitivity study to a particular parameter (in this case, percolation flux), it is preferred to vary only one parameter at a time. Table 6.3-1a lists the initial (ambient) liquid-phase saturation in the host rock (immediately above the crown of the emplacement drift) for lower-bound, mean, and upper-bound infiltration flux cases when the modified-mean drift-scale hydrologic property set is

applied to the MSTHM. Table 6.3-1a shows that the use of the modified-mean infiltration flux property set results in similar initial liquid-phase saturation at a given location for lower-bound, mean, and upper-bound infiltration flux cases.

Table 6.3-1b lists the initial (ambient) capillary pressure in the fracture and matrix continuum of the host rock for the same locations given in Table 6.3-1a. Notice that the mean infiltration flux property set produces very small values of capillary pressures in the fracture continuum for locations where the host rock is the Tptpul (tsw33) unit; these small values of fracture capillary pressure are much smaller than it is for regions of the repository where the host rock is not the Tptpul (tsw33) unit (i.e., where the local host-rock unit is either Tptpmn (tsw34), Tptpll (tsw35), or Tptpln (tsw36)). Moreover, the mean infiltration flux property set produces a large (order of magnitude) contrast in capillary pressure between the matrix and fracture continuum in the Tptpul (tsw33) unit, whereas the contrast in capillary pressure is much smaller for the other three host-rock units: Tptpmn (tsw34), Tptpll (tsw35), and Tptpln (tsw36). The modified-mean infiltration flux property set produces fracture capillary pressures in the Tptpul (tsw33) unit that are consistent with those in the rest of the repository (i.e., in regions where the host rock is either Tptpmn (tsw34), Tptpll (tsw35), or Tptpln (tsw36)). Moreover, for all four host-rock units, the modified-mean infiltration flux property set produces a consistent contrast in capillary pressure between the matrix and fracture continuum, which is generally on the order of a factor of two throughout most of the repository area, with the only exception being in the Tptpln (tsw36) unit where the contrast is larger (about a factor of six).

Table 6.3-1a. The initial (ambient) liquid-phase saturation in the host rock (prior to waste emplacement) obtained by applying the modified-mean infiltration flux property set to the MSTHM, is listed at several locations in the repository for lower-bound, mean, and upper-bound infiltration flux cases.

LDTH-SDT-submodel location	Host-Rock unit	Nevada State Coordinates		Initial Liquid-Phase Saturation in the Host Rock (%)		
		Easting (m)	Northing (m)	Lower-Bound Infiltration Flux Case	Mean Infiltration Flux Case	Upper-Bound Infiltration Flux Case
P2ER4C4	Tptpul (tsw33)	172138.9	235625.9	96.4	96.4	96.9
P2ER5C5	Tptpul (tsw33)	171985.7	235320.6	95.5	95.6	95.8
P2ER6C6	Tptpul (tsw33)	171623.3	234947.4	95.4	95.5	95.7
P2ER8C7	Tptpul (tsw33)	171393.1	234361.5	94.0	97.2	97.3
P2ER8C6	Tptpul (tsw33)	171564.3	234417.2	90.5	95.6	95.7
P2ER8C5	Tptpul (tsw33)	171735.5	234472.8	93.6	97.4	97.3*
P2ER7C6	Tptpul (tsw33)	171584.3	234679.2	93.0	96.5	96.3*
P2ER7C5	Tptpul (tsw33)	171793.5	234747.2	95.1	95.2	95.3
P2ER6C5	Tptpul (tsw33)	171851.6	235021.5	93.6	95.5	95.6
P2ER3C4	Tptpmn (tsw34)	172292.1	235931.1	97.5	97.8	98.0
P2ER2C5	Tptpll (tsw35)	172121.9	236131.4	92.0	92.0	92.1
P2WR1C8	Tptpll (tsw35)	171647.4	236232.7	94.0	94.0	94.1
P3R1C11	Tptpll (tsw35)	171038.7	236034.9	94.6	94.6	94.7
P3R8C13	Tptpln (tsw36)	170080.6	233935.1	98.6	98.7	98.7

NOTE: *The value of percolation flux for the upper-bound infiltration flux case is less than that for the mean infiltration flux case.

Table 6.3-1b. The initial (ambient) capillary pressure for the fracture and matrix continuum in the host rock (prior to waste emplacement) obtained by applying the mean and the modified-mean infiltration flux property set to the MSTHM, are listed for the same locations given in Table 6.3-1a.

LDTH-SDT-submodel location	Host-Rock Unit	Fracture capillary pressure (Pa)		Matrix capillary pressure (Pa)	
		Mean Infiltration Flux Property Set	Modified-Mean Infiltration Flux Property Set	Mean Infiltration Flux Property Set	Modified-Mean Infiltration Flux Property set
P2ER4C4	Tptpul (tsw33)	1.46×10^3	2.28×10^4	3.23×10^4	4.27×10^4
P2ER5C5	Tptpul (tsw33)	1.46×10^3	2.28×10^4	4.51×10^4	5.06×10^4
P2ER6C6	Tptpul (tsw33)	1.46×10^3	2.27×10^4	4.38×10^4	5.18×10^4
P2ER8C7	Tptpul (tsw33)	1.45×10^3	2.27×10^4	2.03×10^4	3.50×10^4
P2ER8C6	Tptpul (tsw33)	1.45×10^3	2.26×10^4	4.51×10^4	5.09×10^4
P2ER8C5	Tptpul (tsw33)	1.47×10^3	2.29×10^4	3.14×10^4	3.34×10^4
P2ER7C6	Tptpul (tsw33)	1.43×10^3	2.22×10^4	3.46×10^4	4.25×10^4
P2ER7C5	Tptpul (tsw33)	1.46×10^3	2.28×10^4	5.34×10^4	5.43×10^4
P2ER6C5	Tptpul (tsw33)	1.47×10^3	2.30×10^4	4.55×10^4	5.13×10^4
P2ER3C4	Tptpmn (tsw34)	2.22×10^4	2.22×10^4	2.32×10^4	2.32×10^4
P2ER2C5	Tptpll (tsw35)	2.40×10^4	2.40×10^4	5.78×10^4	5.78×10^4
P2WR1C8	Tptpll (tsw35)	2.44×10^4	2.44×10^4	4.37×10^4	4.37×10^4
P3R1C11	Tptpll (tsw35)	2.44×10^4	2.44×10^4	3.95×10^4	3.95×10^4
P3R8C13	Tptpln (tsw36)	3.32×10^3	3.32×10^3	1.94×10^4	1.94×10^4

Table 6.3-2 and Figure 6.3-1 show the distribution of host-rock units over the repository area. The majority of the repository area (81.1 percent) is in the two units (Tptpll and Tptpul) with lithophysal cavities. Most of the remainder of the repository area is in the nonlithophysal units (Tptpmn and Tptpln) with a small percentage (1.2 percent) being in fault zones. These areas are based on *Development of Numerical Grids for UZ Flow and Transport Modeling* (BSC 2003c).

Table 6.3-2. The distribution of the host-rock units is summarized for the emplaced repository area (Figure 6.3-1). The values of emplacement-drift length and area are as they are represented in the SMT submodel (Section 6.2.5). In the SMT submodel, the represented lengths of the emplacement drifts are based on information from BSC 2003d; the distribution of host-rock units (with respect to the UZ model layers) is consistent with the grid in BSC 2003h, which is given in DTN: LB03023DKMGRID.001.

GFM2000 Lithostratigraphic Unit	UZ Model Layer Unit	Length of Emplacement Drift (m)	Area (km^2)	Percentage of Repository Area
Tptpul	tsw33	3,460	0.2803	6.0%
Tptpmn	tsw34	9,260	0.7501	16.1%
Tptpll	tsw35	43,160	3.4960	75.1%
Tptpln	tsw36	940	0.0761	1.6%
Fault zone	tswfl	660	0.0535	1.2%
Total	N/A	57,480	6.6560	100%

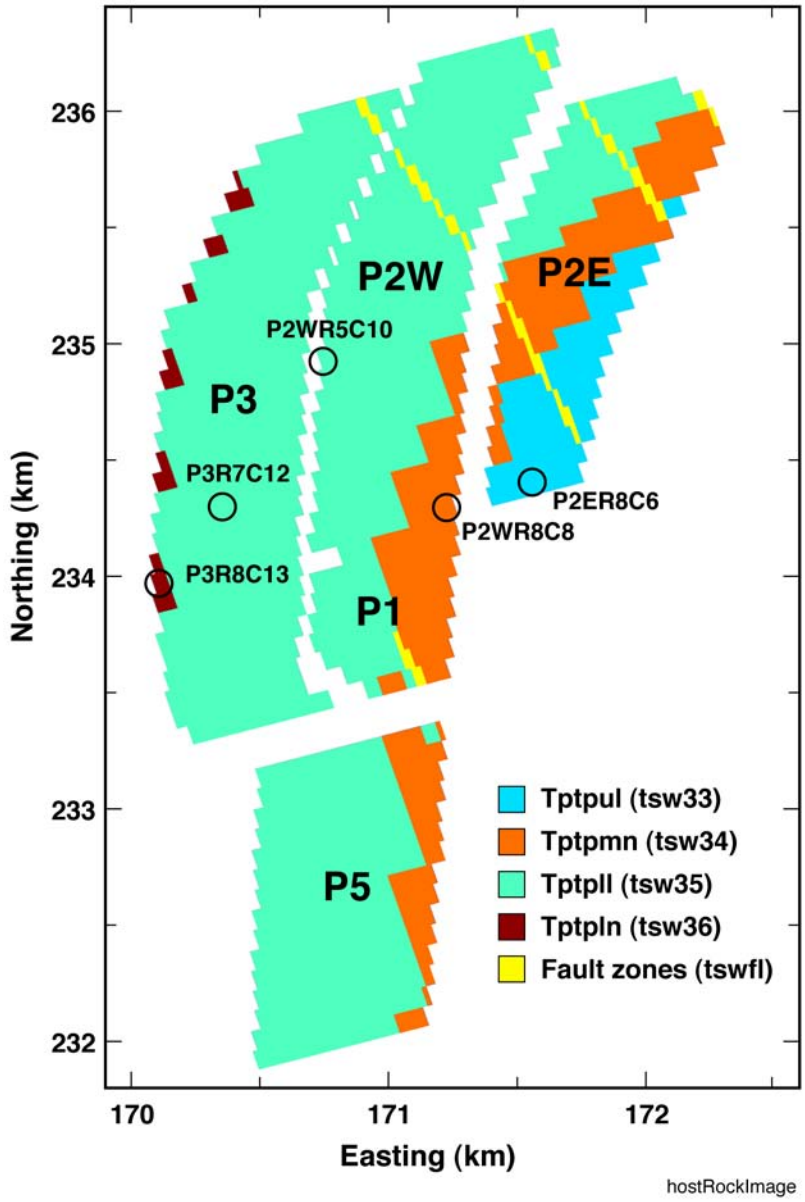

Figure 6.3-1. The distribution of the four primary host-rock units is shown for the repository layout considered in the MSTHM calculations for the TSPA-LA base case. Note that tswfl stands for fault zone. Also shown are the five representative locations that were selected to examine thermohydrologic conditions in the four primary host-rock units.

6.3.1.1 Lower-Bound, Mean, and Upper-Bound Infiltration Flux Cases

The repository-wide-averaged percolation flux for the three (present-day, monsoonal, and glacial-transition) climate states is summarized in Table 6.3-3 for the Mcases. Figure 6.3-2 gives the complementary cumulative distribution function for the peak temperature on the drift wall and on waste packages; these complementary cumulative distribution functions are for all waste packages over the entire repository area. Table 6.3-4 gives the coolest, median, and hottest peak drift-wall and waste package temperatures for the three infiltration flux cases. The spatial extent (and duration) of dryout of the host rock increases with decreasing percolation flux. Because the

thermal conductivity of dry rock is less than that of wet rock, peak temperatures increase with decreasing percolation flux. The sensitivity of peak temperature to percolation flux is strongest at either end of the complementary cumulative distribution function distributions. The differences between the mean and lower-bound infiltration flux cases are greatest for the hottest waste package locations. The differences between the mean and upper-bound infiltration flux cases are greatest for the coolest waste package locations. In general, the sensitivity of peak temperature to percolation flux is stronger for the hottest waste package locations.

Table 6.3-3. The repository-wide-averaged percolation flux is summarized for lower-bound, mean, and upper-bound infiltration flux cases. These averages are based on averaging the percolation data from DTN: LB0302PTNTSW9I.001 over the heated repository footprint represented in the SMT submodel, as described in Attachment I.

Infiltration Flux Case	Repository-Wide Averaged Percolation Flux (mm/yr)		
	Present-Day (0 years < *t* < 600 years)	**Monsoonal (600 years < *t* < 2,000 years)**	**Glacial-Transition (2,000 years < *t*)**
Lower	0.41	4.23	1.95
Mean	3.77	11.15	17.29
Upper	10.84	19.48	34.35

Table 6.3-4. Peak Drift-Wall and Waste Package Temperatures for Lower-Bound, Mean, and Upper-Bound Infiltration Flux Cases (based on Figure 6.3-2).

Infiltration-Flux Case	Peak Drift-Wall Temperature (°C)			Peak Waste Package Temperature (°C)		
	Coolest	**Median**	**Hottest**	**Coolest**	**Median**	**Hottest**
Lower	105.7	135.4	154.8	116.3	156.0	182.9
Mean	105.0	133.0	144.2	115.6	153.3	172.0
Upper	98.6	131.6	142.5	108.6	152.1	170.8

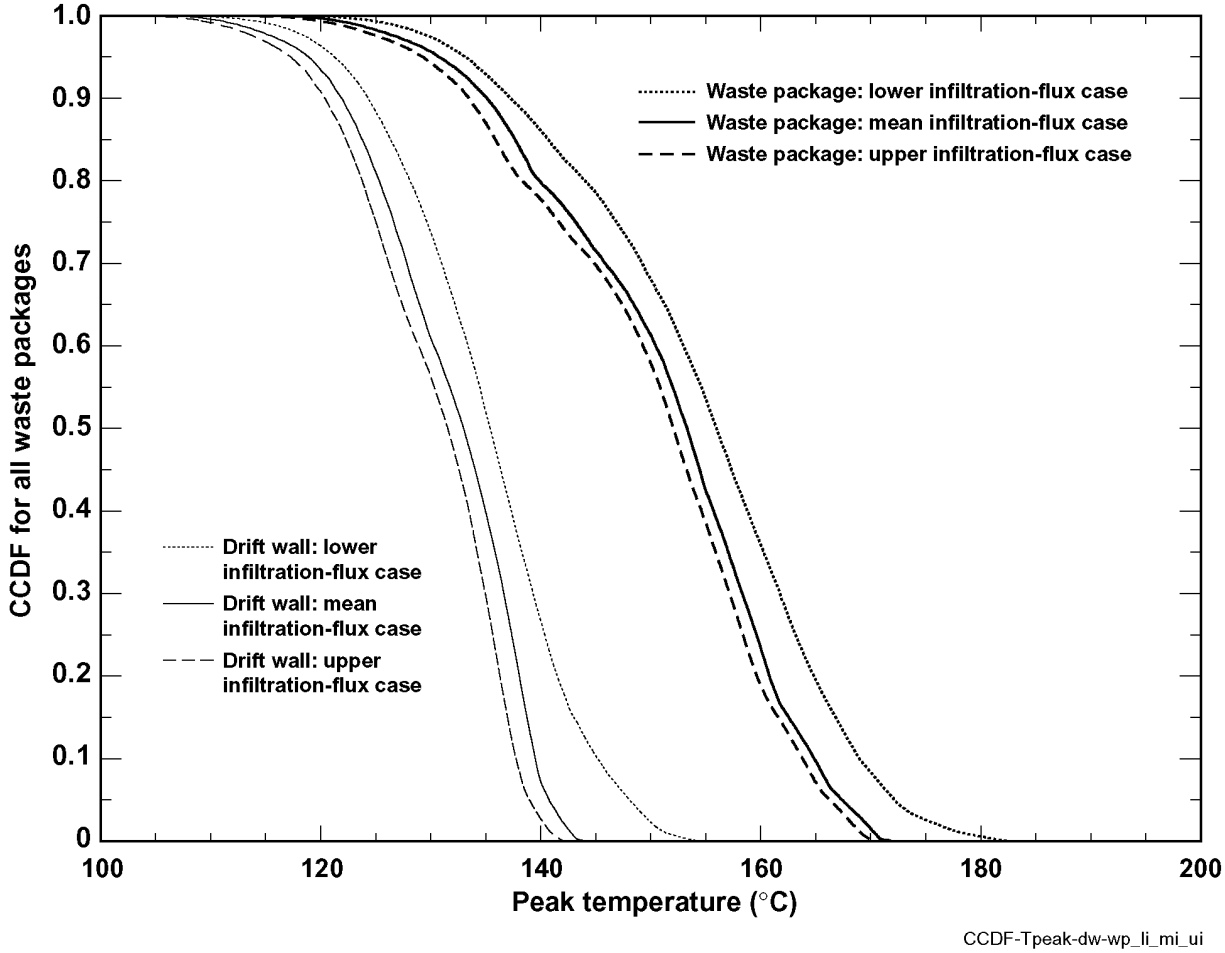

Figure 6.3-2. The complementary cumulative distribution function (CCDF) for peak temperature on the drift wall and on the waste packages is plotted for lower-bound, mean, and upper-bound infiltration flux cases.

Figure 6.3-3, which is the contour map of peak waste package temperature for a PWR waste package, illustrates how peak temperatures increase with distance from the repository edges. There are two reasons for this relationship. First, the edge-cooling effect, which results from lateral heat loss at the repository edges, is strongest for locations close to the edge of the repository. Consequently, both the host rock and waste packages experience greater cooling for locations closer to the repository edges. Second, the direction of the ventilation-air flow is from the ventilation inlets located at the repository edges in towards the ventilation outlets, which are generally located close to the center of the repository. Heat-removal efficiency (resulting from ventilation of the emplacement drift) decreases with distance from the ventilation inlet. Thus locations closer to the repository edge receive more of the ventilation cooling effect than locations closer to the repository center. One slight variation of this trend is in Panel 5 where the ventilation inlet is on the eastern edge and the ventilation outlet is on the western edge. Figure 6.3-3 shows that peak temperatures on the eastern side of Panel 5 (where the heat-removal efficiency is greatest) are lower than on the western side (where the heat-removal efficiency is least).

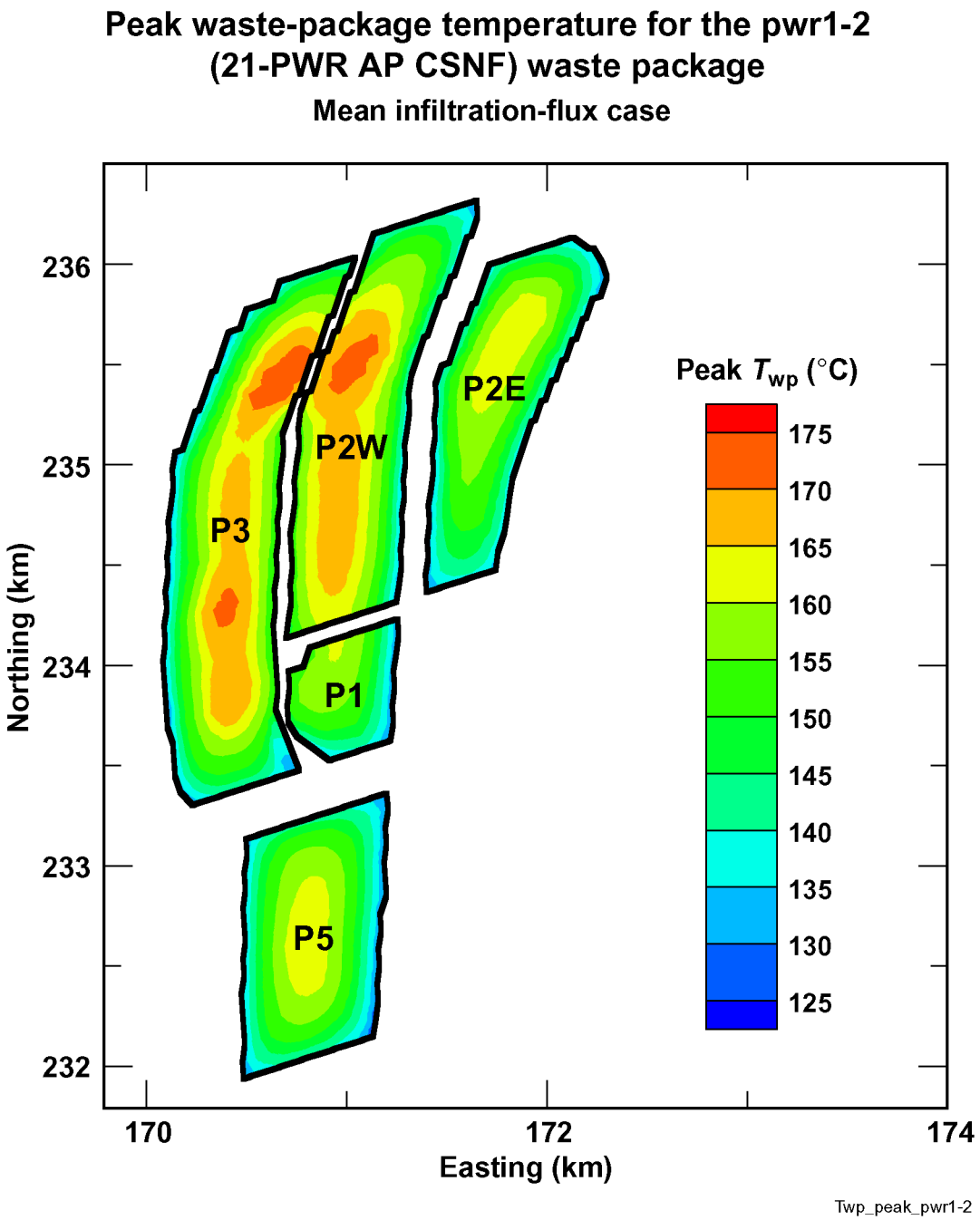

Figure 6.3-3. The contour map of peak waste package temperature for the pwr1-2 waste package is plotted over the repository area for the mean infiltration flux case. The pwr1-2 (21-PWR AP CSNF) waste package is the hottest waste package in the sequence (Figure 6.2-2).

Figure 6.3-4a and Table 6.3-5 give the complementary cumulative distribution function for the time when boiling at the drift wall ceases for lower-bound, mean, and upper-bound infiltration flux cases; these complementary cumulative distribution functions are for all waste package locations throughout the repository area. As was the case for peak temperatures, the boiling-period duration increases with decreasing percolation flux. Figure 6.3-5, which is the contour map of the time when boiling at the drift wall ceases for a PWR CSNF waste package

for the mean infiltration flux case, clearly shows that the boiling-period duration increases strongly with distance from the repository edges. The sensitivity of boiling-period duration to percolation flux is greatest for those locations with the longest boiling-period duration, which correspond to locations furthest away from the repository edges where differences in the spatial (and temporal) extent of rock dryout (resulting from differences in percolation flux) have more time to develop. There is a strong relationship between boiling-period duration and the spatial (and temporal) extent of rock dryout. Areas with low percolation flux will have a greater spatial extent of dryout, increasing the volume of rock in which the dry (low) value of thermal conductivity pertains, which enhances the temperature rise around the drifts. The enhanced temperature rise around the drift has the effect of extending the duration of boiling. Areas with high percolation flux will have a smaller spatial (and temporal) extent of rock dryout, decreasing the volume of rock in which the dry (low) value of thermal conductivity pertains, which reduces the temperature rise around the drifts. This reduced temperature rise around the drifts has the effect of shortening the duration of boiling. Rock dryout is much more sensitive to percolation flux during the boiling period than it is during the postboiling period. Thus, areas of the repository with the overall longest boiling-period duration (by virtue of being more distant from the repository edges) tend to have a larger contrast in boiling-period duration between areas of high and low percolation flux.

Table 6.3-5. The time when boiling ceases at the drift wall is summarized for lower-bound, mean, and upper-bound infiltration flux cases (based on Figure 6.3-4a).

Infiltration flux case	Time when boiling at the drift wall ceases (years)						
	Shortest	10th Percentile	30th Percentile	Median	70th Percentile	90th Percentile	Longest
Lower	130.2	349.9	630.9	859.6	1,122.5	1,453.3	1,734.6
Mean	127.2	297.5	535.8	721.0	870.6	1,006.5	1,356.0
Upper	97.7	267.7	471.6	643.7	768.6	887.2	1,162.9

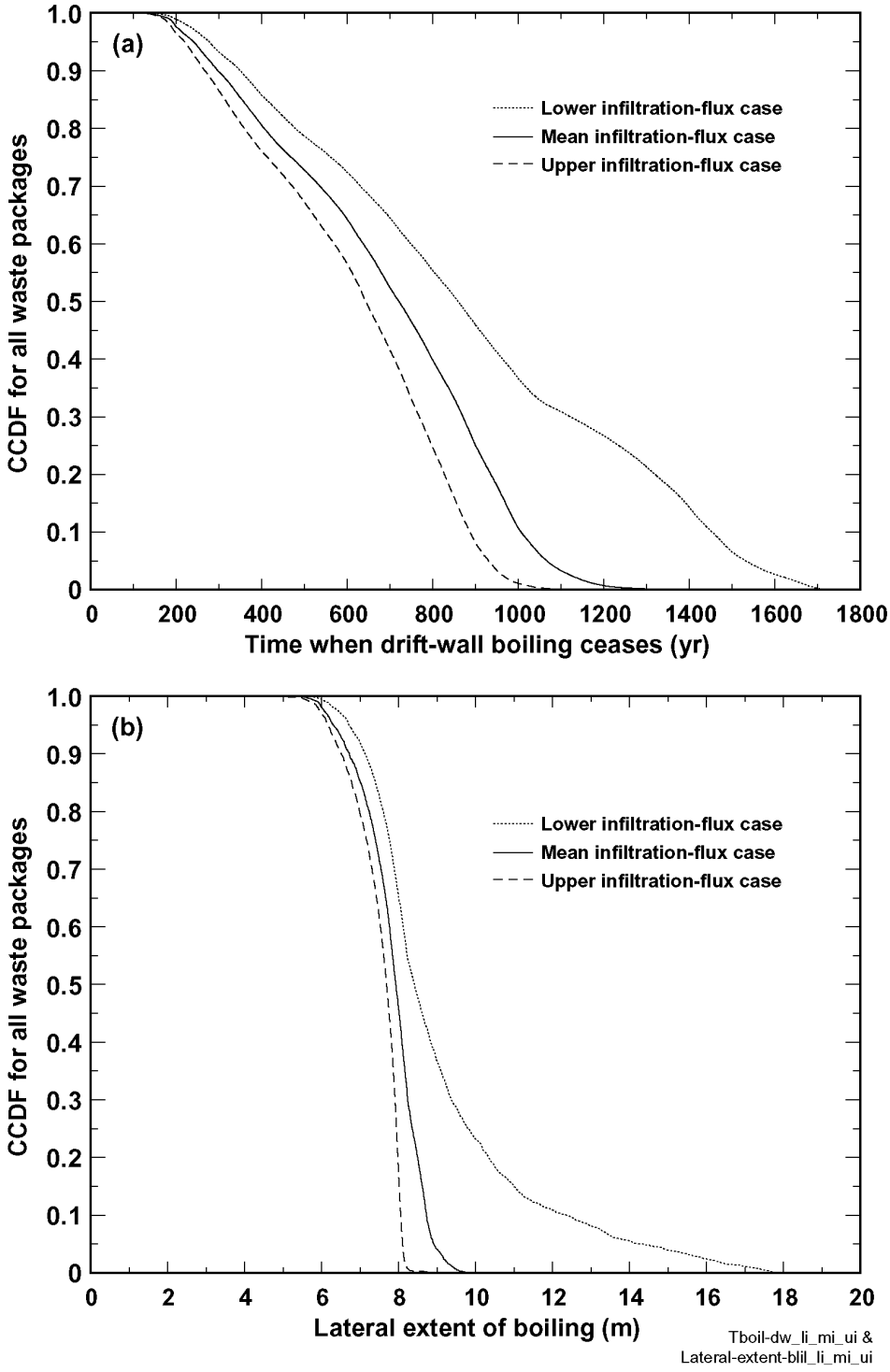

Figure 6.3-4. The complementary cumulative distribution functions (CCDF) for (a) the time when boiling at the drift wall ceases and (b) the maximum lateral extent of the boiling-point isotherm (96°C) are plotted for the lower-bound, mean, and upper-bound infiltration flux cases. The lateral extent of the boiling-point isotherm is measured from the center of the emplacement drift.

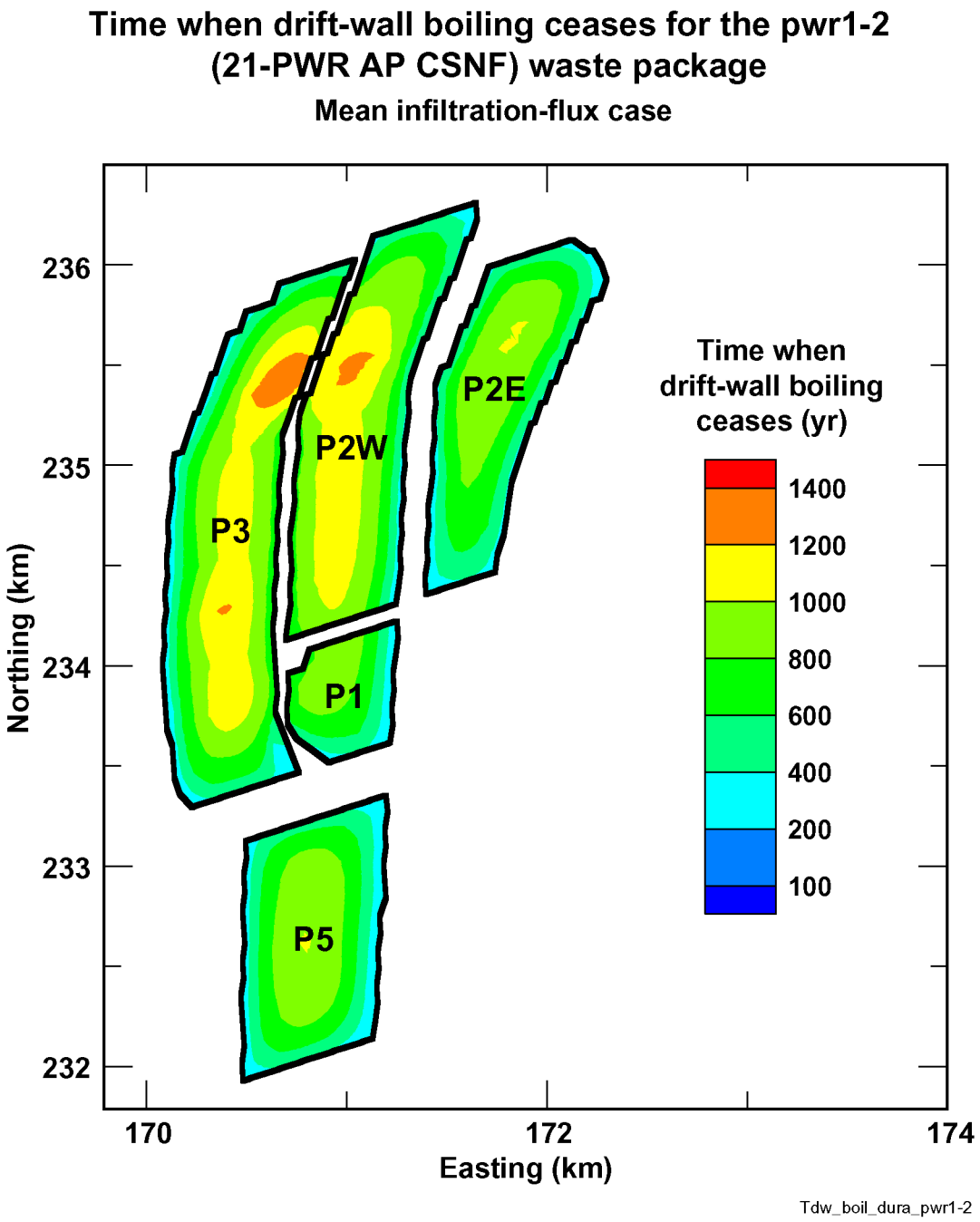

Figure 6.3-5. The contour map of the time when boiling at the drift wall ceases for the pwr1-2 waste package is plotted over the repository area for the mean infiltration flux case. The pwr1-2 (21-PWR AP CSNF) waste package is the hottest waste package in the sequence (Figure 6.2-2).

Figure 6.3-4b and Table 6.3-6 give the complementary cumulative distribution function for the maximum lateral extent of the boiling-point isotherm for lower-bound, mean, and upper-bound infiltration flux cases. As was the case for the peak temperatures and boiling-period duration, the maximum lateral extent of boiling increases with decreasing percolation flux. Figure 6.3-6 is the contour map of the maximum lateral extent of boiling for a PWR CSNF waste package. It is

apparent that the maximum lateral extent of boiling increases with distance from the repository edges. As is the case for boiling-period duration, the sensitivity of the maximum extent of boiling to percolation flux is greatest for those waste package locations furthest away from the repository edges where differences in the spatial (and temporal) extent of rock dryout (resulting from differences in percolation flux) have more time to develop. Areas with low percolation flux will have a greater spatial extent of dryout, increasing the volume of rock in which the dry (low) value of thermal conductivity pertains, which enhances the temperature rise around the drifts. This enhanced temperature rise has the effect of increasing the volume of rock dryout around the drifts. Areas with high percolation flux will have a smaller spatial (and temporal) extent of rock dryout, decreasing the volume of rock in which the dry (low) value of thermal conductivity pertains, which reduces the temperature rise around the drifts. This reduced temperature rise around the drifts has the effect of limiting the volume of rock dryout around the drifts. Rock dryout is much more sensitive to percolation flux during the boiling period than it is during the postboiling period. Thus, for areas of the repository with the overall longest boiling-period duration (by virtue of being more distant from the repository edges), the maximum lateral extent of boiling is more sensitive to percolation flux.

It is important to note that the lateral extent of boiling is always much smaller than the half spacing between emplacement drifts. Therefore, the majority of the host rock between emplacement drifts always remains below the boiling point, thereby enabling condensate and percolation flux to continuously drain between emplacement drifts. Because of this continuous drainage of condensate around a relatively narrow cylindrically shaped boiling zone, the condensate cap above the emplacement drifts is of very limited spatial extent.

Table 6.3-6. The maximum lateral extent of the boiling-point isotherm (96°C) is summarized for lower-bound, mean, and upper-bound infiltration flux cases (based on Figure 6.3-4b). The lateral extent of the boiling-point isotherm is measured from the center of the emplacement drift.

Infiltration flux case	Maximum Lateral Extent of Boiling (T > 96°C) (m)						
	Least	10th Percentile	30th Percentile	Median	70th Percentile	90th Percentile	Greatest
Lower	5.6	7.1	7.9	8.4	9.4	12.3	17.8
Mean	5.3	6.7	7.5	7.9	8.2	8.7	9.9
Upper	5.1	6.5	7.3	7.7	7.9	8.1	9.0

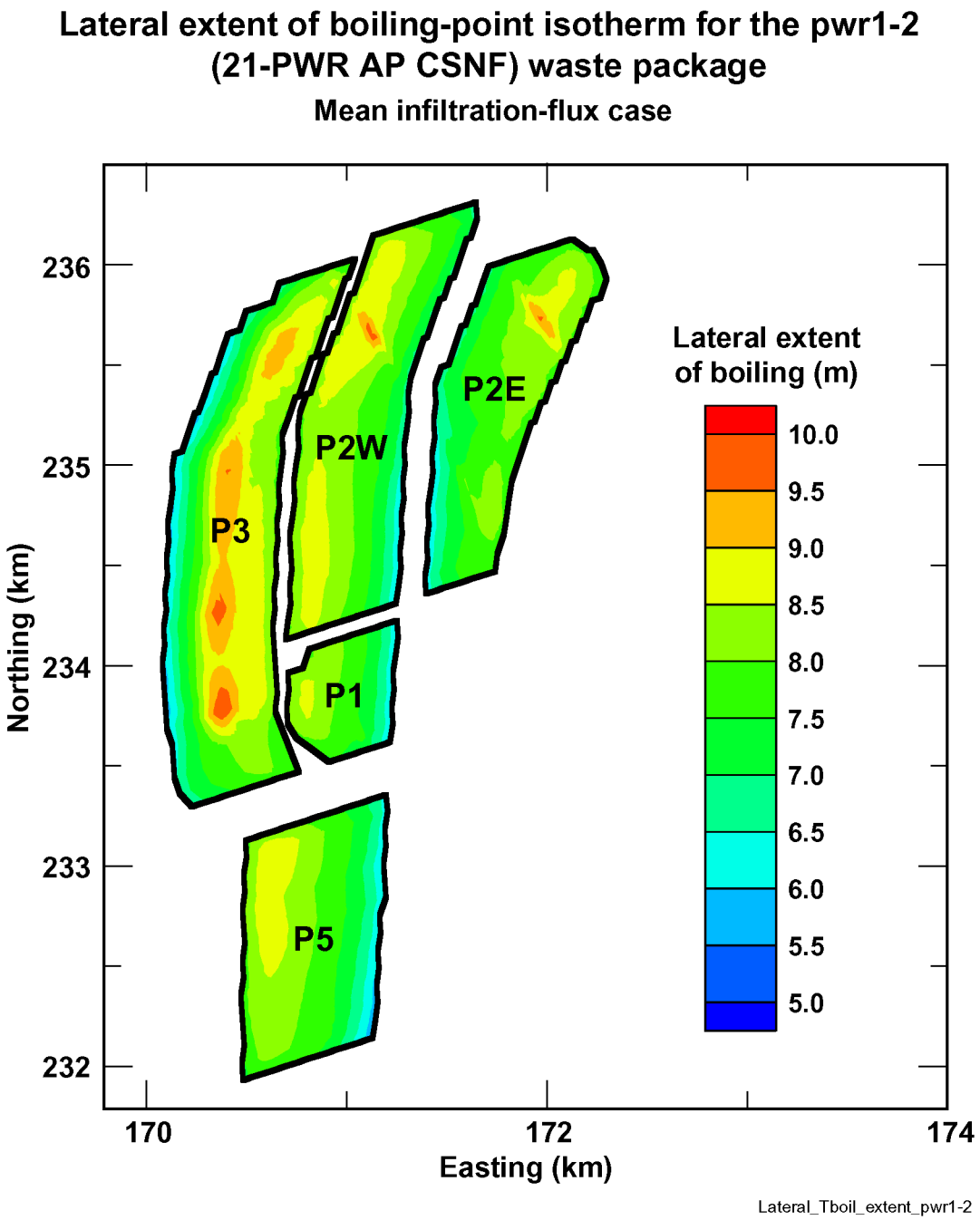

Figure 6.3-6. The contour map of the maximum lateral extent of the boiling-point isotherm (96°C) from the drift centerline for the pwr1-2 waste package is plotted over the repository area for the mean infiltration flux case. The pwr1-2 (21-PWR AP CSNF) waste package is the hottest waste package in the sequence (Figure 6.2-2).

For the purpose of examining the details of thermohydrologic behavior in emplacement drifts, five locations were chosen that cover all four of the host-rock units (Tables 6.3-7a, 6.3-7b and Figure 6.3-1). Four of these locations (P2ER8C6, P2WR8C8, P2WR5C10, and P3R8C13) were chosen because their respective values of percolation flux are relatively close to the repository-wide averages (Table 6.3-3). The fifth location (P3R7C12) was chosen because it has

close to the longest boiling-period duration over the entire repository area; note that this location is in a region of low percolation flux, which is a major contributing factor to its very long boiling-period duration. Time histories of drift-wall temperature and liquid-phase saturation, waste package temperature and relative humidity, and invert liquid-phase saturation are plotted (Figures 6.3-7 through 6.3-11) for these five locations (Figure 6.3-1). Tables 6.3-7a and 6.3-7b summarize the relationship between percolation flux and infiltration flux case for the five locations and three climate states. Using Tables 6.3-7a and 6.3-7b as a guide, the influence of percolation flux on peak temperatures is summarized in Table 6.3-8 for the five locations. The influence of percolation flux on the duration of boiling is summarized in Table 6.3-9, which gives the time when boiling at the drift wall ceases.

Table 6.3-7a. The percolation flux for lower-bound, mean, and upper-bound infiltration flux cases is summarized for five locations in the repository used to examine thermohydrologic conditions in the repository (Figure 6.3-1 for locations). The percolation flux is obtained from DTN: LB0302PTNTSW9I.001, as discussed in Attachment I.

LDTH-SDT-submodel location	Host-rock unit	Nevada State Coordinates		Percolation flux for the mean infiltration flux case (mm/yr)		
		Easting (m)	Northing (m)	Present-day	Monsoonal	Glacial-transition
P2ER8C6	Tptpul (tsw33)	171564.3	234417.3	5.41	11.70	23.03
P2WR8C8	Tptpmn (tsw34)	171240.9	234312.1	4.47	10.45	15.65
P2WR5C10	Tptpll (tsw35)	170730.3	234912.7	4.71	14.60	22.07
P3R7C12	Tptpll (tsw35)	170347.9	234277.5	0.86	3.43	6.32
P3R8C13	Tptpln (tsw36)	170080.6	233935.1	7.07	21.95	31.66

Table 6.3-7b. The percolation flux for the lower, mean, and upper infiltration flux cases is summarized for five locations in the repository used to examine thermohydrologic conditions in the repository (Figure 6.3-1 for locations). The percolation flux is obtained from DTN: LB0302PTNTSW9I.001, as discussed in Attachment I.

LDTH-SDT-submodel location	Percolation Flux for the Lower-Bound Infiltration Flux Case (mm/yr)			Percolation Flux for the Upper-Bound Infiltration Flux Case (mm/yr)		
	Present-day	Monsoonal	Glacial-transition	Present-day	Monsoonal	Glacial-transition
P2ER8C6	6.331×10^{-2}	3.57	1.79	7.22	14.11	34.53
P2WR8C8	2.621×10^{-3}	3.44	1.31	7.31	12.51	22.14
P2WR5C10	2.261×10^{-3}	5.58	2.02	15.22	26.12	43.60
P3R7C12	1.081×10^{-4}	0.91	0.12	6.76	12.82	24.28
P3R8C13	0.36	6.66	3.69	16.57	33.64	54.99

Table 6.3-8. The range of peak temperatures over the three infiltration flux cases for the pwr1-2 waste package is summarized for five locations in the repository (Figure 6.3-1 for locations).

LDTH-SDT-submodel location	Host-rock unit	Peak Drift-Wall Temperature (°C)				Peak Waste Package Temperature (°C)			
		Lower	Mean	Upper	Range	Lower	Mean	Upper	Range
P2ER8C6	Tptpul (tsw33)	138.2	135.5	135.2	3.0	165.8	163.2	163.5	2.3
P2WR8C8	Tptpmn (tsw34)	127.4	123.0	122.3	5.1	154.8	150.6	150.8	4.0
P2WR5C10	Tptpll (tsw35)	149.3	141.5	139.6	9.7	177.8	169.4	168.2	9.6
P3R7C12	Tptpll (tsw35)	148.9	140.0	138.7	10.2	176.6	167.3	166.5	10.1
P3R8C13	Tptpln (tsw36)	121.4	120.5	118.8	2.6	149.2	148.2	147.4	1.8

Table 6.3-9. The range of time when boiling at the drift wall ceases over the three infiltration flux cases for the pwr1-2 waste package is summarized for five locations in the repository (Figure 6.3-1 for locations).

LDTH-SDT-submodel location	Host-rock unit	Time When Boiling at the Drift Wall Ceases for Three Infiltration flux cases (years)				
		Lower	Mean	Upper	Range	Range*
P2ER8C6	Tptpul (tsw33)	425.3	365.6	359.8	65.5	16.7%
P2WR8C8	Tptpmn (tsw34)	298.8	221.0	213.1	85.7	33.5%
P2WR5C10	Tptpll (tsw35)	1,230.7	686.1	540.4	690.3	78.0%
P3R7C12	Tptpll (tsw35)	1,592.3	1,200.1	1,030.9	561.4	42.8%
P3R8C13	Tptpln (tsw36)	242.3	218.8	199.2	43.1	19.5%

NOTE: * The range (%) is the range (years) divided by the average time when drift-wall boiling ceases [(shortest + longest)/2].

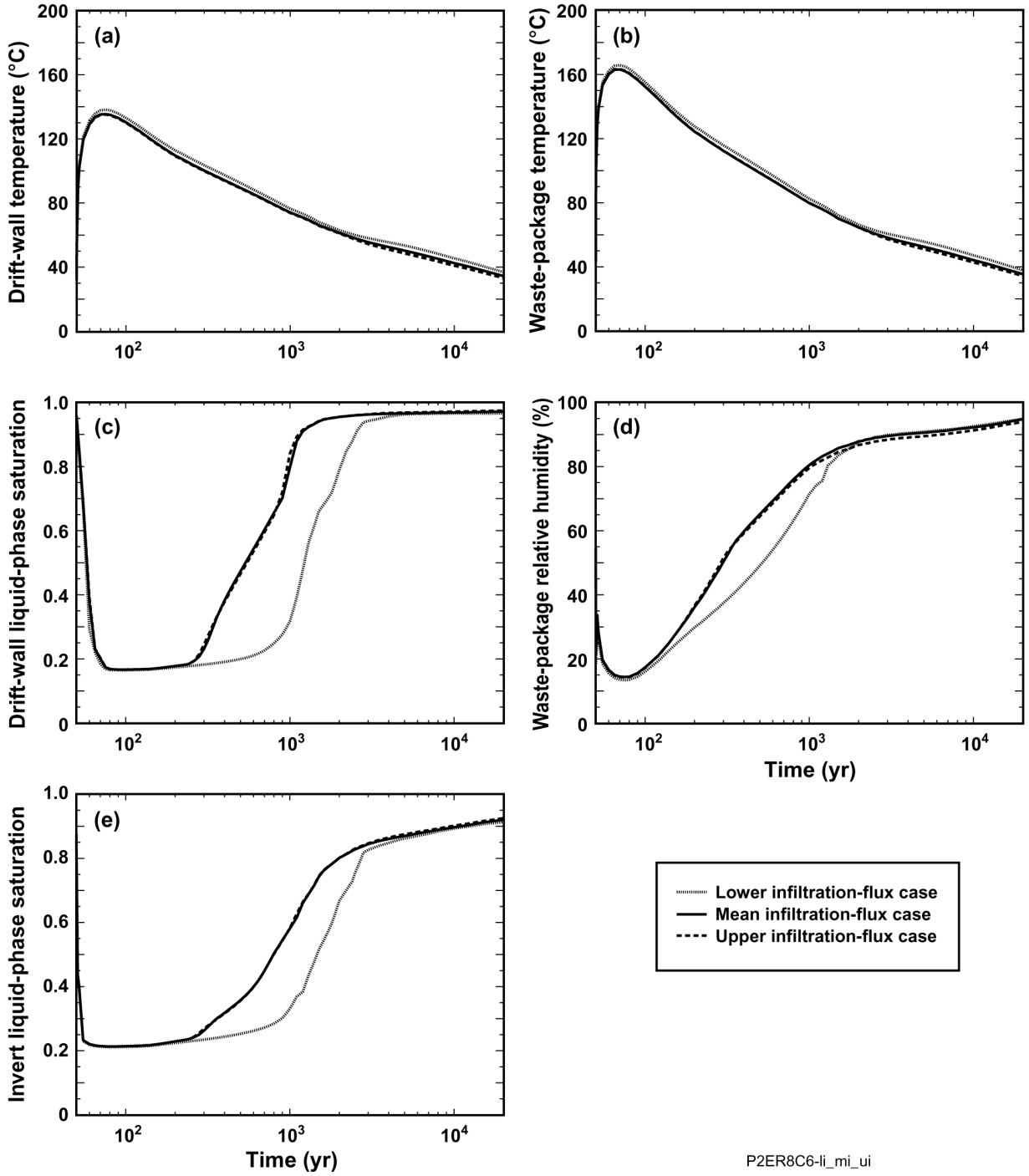

Figure 6.3-7. Thermohydrologic conditions for the pwr1-2 waste package are plotted for lower-bound, mean, and upper-bound infiltration flux cases at the P2ER8C6 location, which is in the Tptpul (tsw33) unit (Figure 6.3-1 for location). The plotted thermohydrologic variables are (a) drift-wall temperature, (b) waste package temperature, (c) drift-wall liquid-phase saturation, (d) waste package relative humidity, and (e) invert liquid-phase saturation. The pwr1-2 (21-PWR AP CSNF) waste package is the hottest waste package in the sequence (Figure 6.2-2).

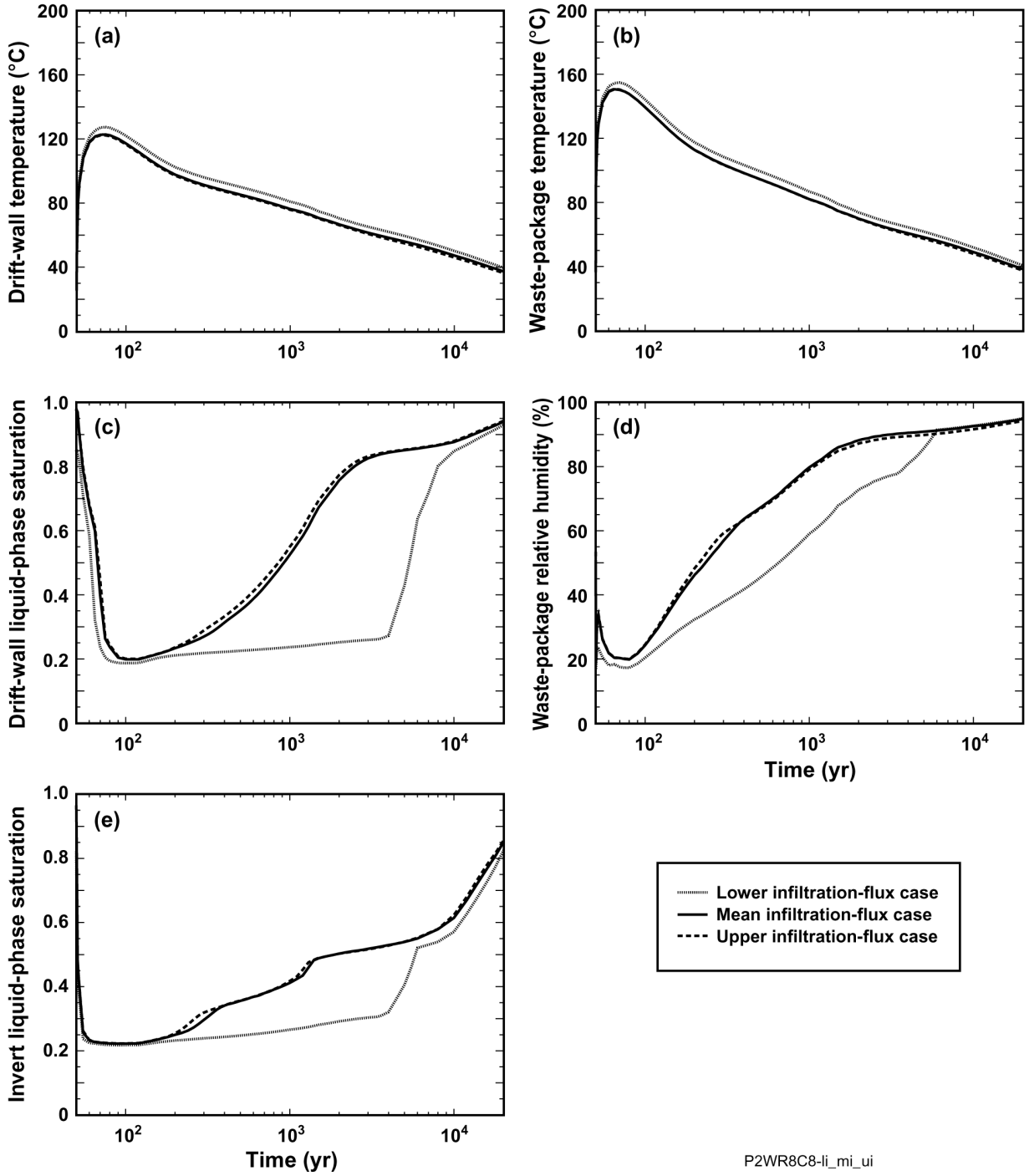

Figure 6.3-8. Thermohydrologic conditions for the pwr1-2 waste package are plotted for lower-bound, mean, and upper-bound infiltration flux cases at the P2WR8C8 location, which is in the Tptpmn (tsw34) unit (Figure 6.3-1 for location). The plotted thermohydrologic variables are (a) drift-wall temperature, (b) waste package temperature, (c) drift-wall liquid-phase saturation, (d) waste package relative humidity, and (e) invert liquid-phase saturation. The pwr1-2 (21-PWR AP CSNF) waste package is the hottest waste package in the sequence (Figure 6.2-2).

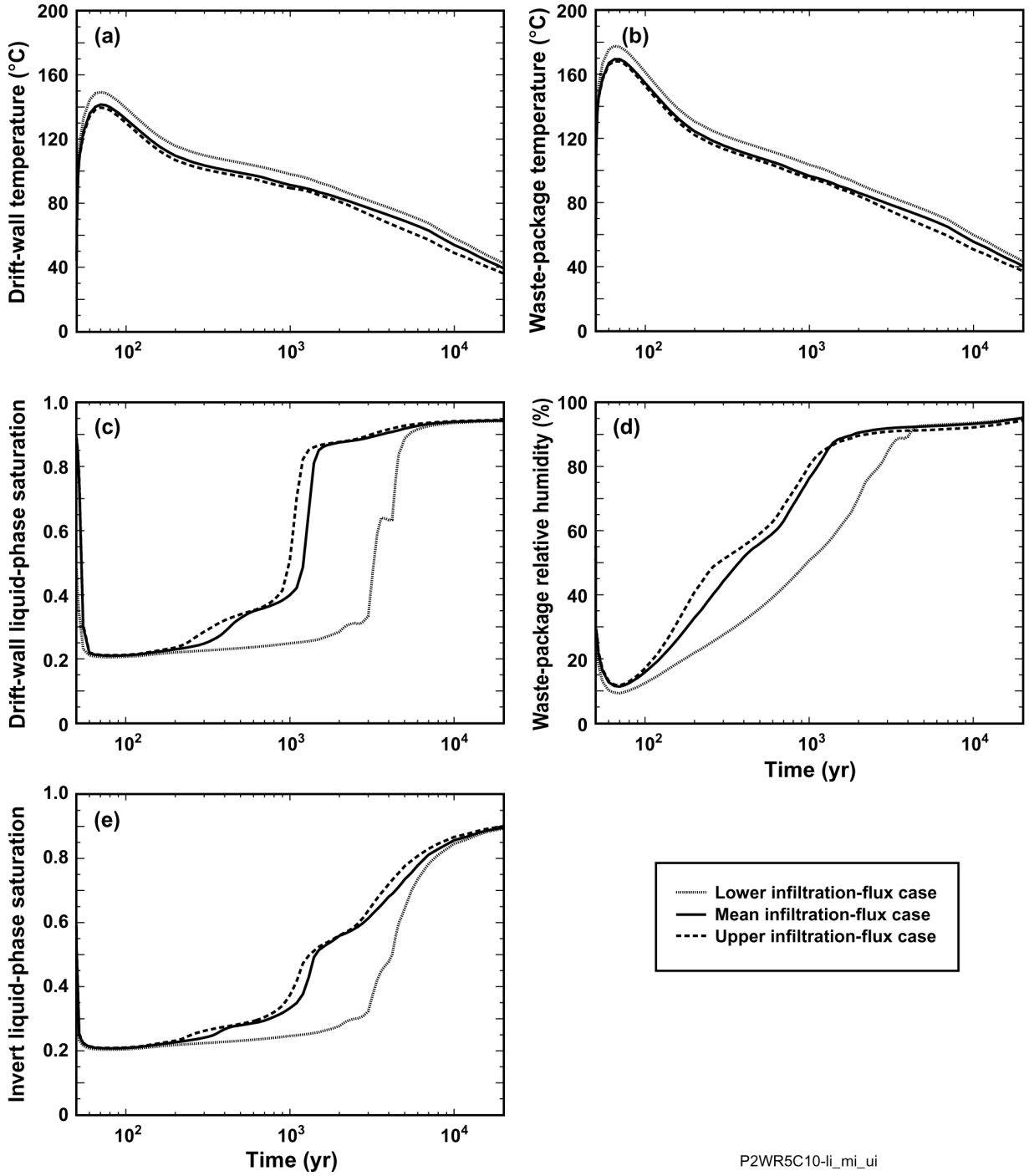

Figure 6.3-9. Thermohydrologic conditions for the pwr1-2 waste package are plotted for lower-bound, mean, and upper-bound infiltration flux cases at the P2WR5C10 location, which is in the Tptpll (tsw35) unit (Figure 6.3-1 for location). The plotted thermohydrologic variables are (a) drift-wall temperature, (b) waste package temperature, (c) drift-wall liquid-phase saturation, (d) waste package relative humidity, and (e) invert liquid-phase saturation. The pwr1-2 (21-PWR AP CSNF) waste package is the hottest waste package in the sequence (Figure 6.2-2).

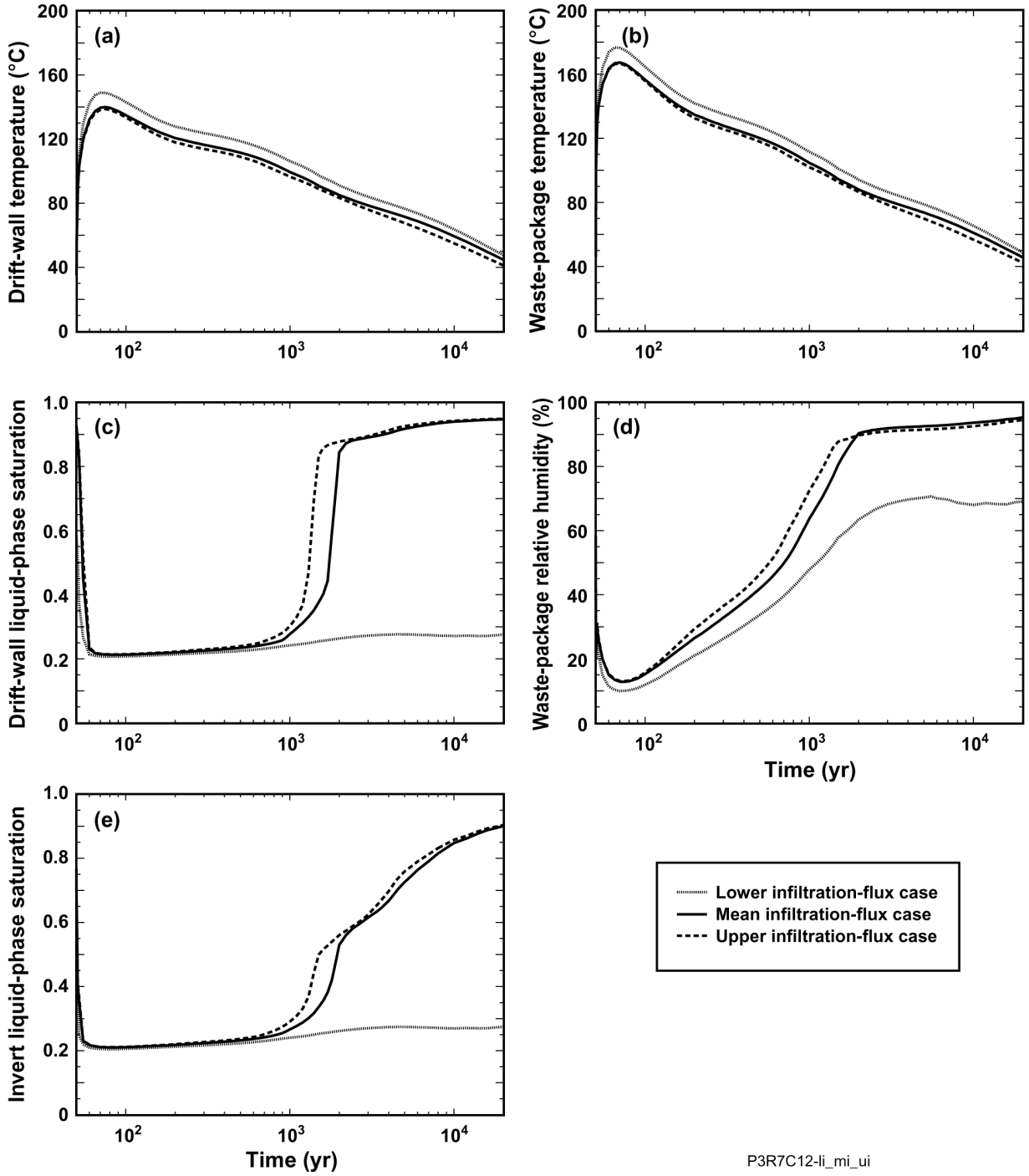

Figure 6.3-10. Thermohydrologic conditions for the pwr1-2 waste package are plotted for lower-bound, mean, and upper-bound infiltration flux cases at the P3R7C12 location, which is in the Tptpll (tsw35) unit (Figure 6.3-1 for location). The plotted thermohydrologic variables are (a) drift-wall temperature, (b) waste package temperature, (c) drift-wall liquid-phase saturation, (d) waste package relative humidity, and (e) invert liquid-phase saturation. The pwr1-2 (21-PWR AP CSNF) waste package is the hottest waste package in the sequence (Figure 6.2-2).

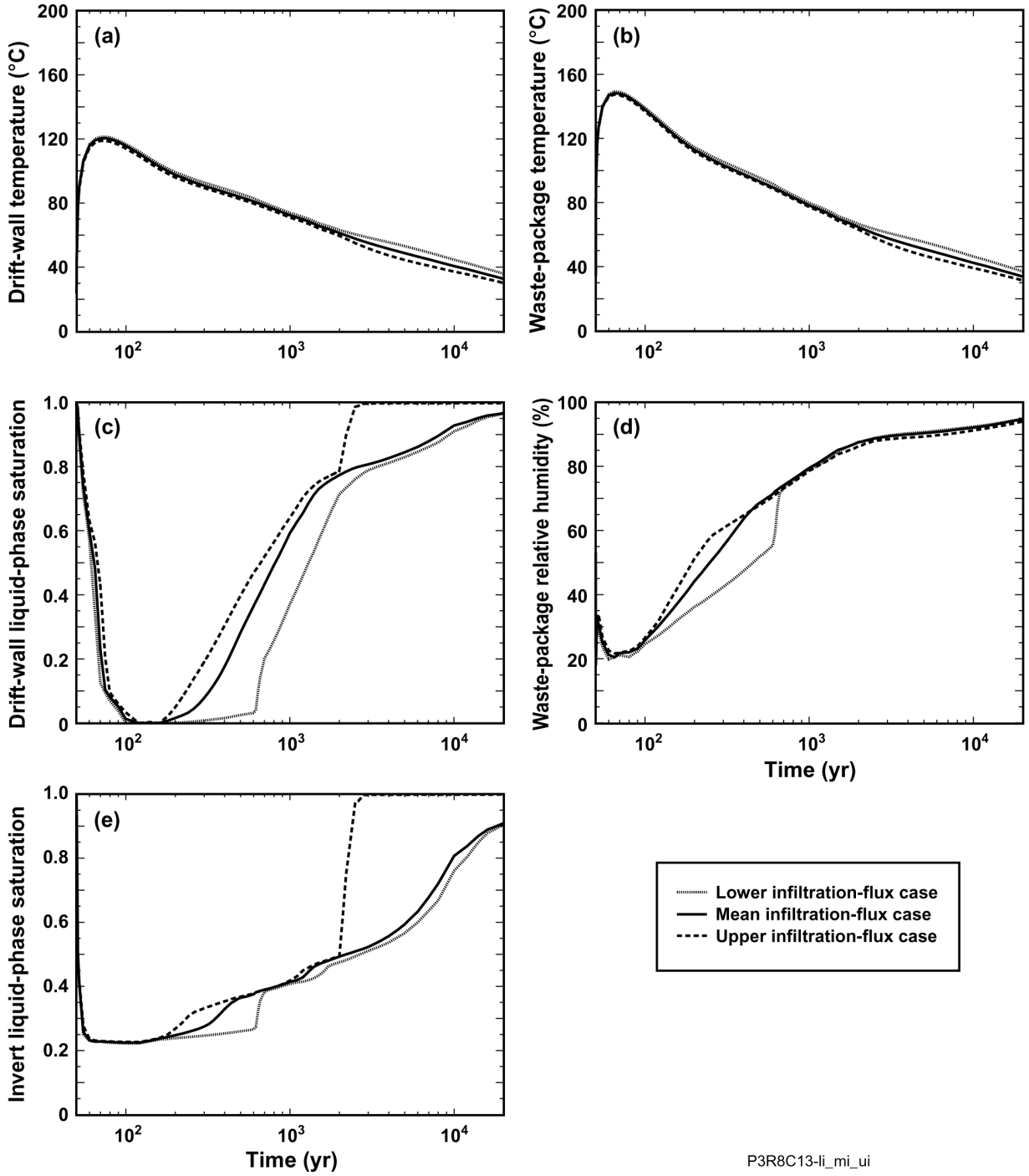

Figure 6.3-11. Thermohydrologic conditions for the pwr1-2 waste package are plotted for lower-bound, mean, and upper-bound infiltration flux cases at the P3R8C13 location, which is in the Tptpln (tsw36) unit (Figure 6.3-1 for location). The plotted thermohydrologic variables are (a) drift-wall temperature, (b) waste package temperature, (c) drift-wall liquid-phase saturation, (d) waste package relative humidity, and (e) invert liquid-phase saturation. The pwr1-2 (21-PWR AP CSNF) waste package is the hottest waste package in the sequence (Figure 6.2-2).

The influence of percolation flux on peak temperature is about the same for the waste package as it is for the drift wall (Table 6.3-8). The range of peak temperatures (from lower-bound to upper-bound infiltration flux case) is slightly less for the waste package than it is for the drift wall. The reason for this relationship is that the effectiveness of thermal radiation increases slightly with temperature; consequently, the difference in peak temperature between the waste package and drift wall decreases slightly with increasing peak drift-wall temperature. Because the thermal conductivity of the rock is less for the lithophysal units (Tptpul and Tptpll) than it is for the nonlithophysal units (Tptpmn and Tptpln), peak temperatures are greater in the lithophysal units than in the nonlithophysal units.

The influence of percolation flux on the duration of boiling at the drift wall is greater for the locations (P2WR5C10 and P3R7C12) further from the repository edges than for those closer to the repository edges (P2ER8C6, P2WR8C8, and P3R8C13). Because location P2WR8C8 (located on the eastern edge of Panel 2W) receives some heat from the southern portion of Panel 2E, its boiling duration is somewhat greater than it is for the other two "edge" locations (P2ER8C6 and P3R8C13). Locations away from the repository edges have longer boiling durations that allow more time for the differences in rock dryout between lower and higher percolation fluxes to develop. There is a strong relationship between boiling-period duration and the spatial (and temporal) extent of rock dryout. Areas with low percolation flux will have a greater spatial extent of dryout, increasing the volume of rock in which the dry (low) value of thermal conductivity pertains, which enhances the temperature rise around the drifts. The enhanced temperature rise around the drift has the effect of extending the duration of boiling. Areas with high percolation flux will have a smaller spatial (and temporal) extent of rock dryout, decreasing the volume of rock in which the dry (low) value of thermal conductivity pertains, which reduces the temperature rise around the drifts. This reduced temperature rise around the drifts has the effect of shortening the duration of boiling. Rock dryout is much more sensitive to percolation flux during the boiling period than it is during the postboiling period. Thus, areas of the repository with the overall longest boiling-period duration (by virtue of being more distant from the repository edges) tend to have a larger contrast in boiling-period duration between areas of high and low percolation flux.

The influence of percolation flux on dryout/rewetting is illustrated by the drift-wall and invert liquid-phase saturation histories (Figures 6.3-7c, 6.3-7e, 6.3-8c, 6.3-8e, 6.3-9c, 6.3-9e, 6.3-10c, 6.3-10e, 6.3-11c, and 6.3-11e). Locations P2ER8C6 and P2WR8C8 have small differences in dryout/rewetting between the upper-bound and mean infiltration flux cases (Figures 6.3-7c, 6.3-7e, 6.3-8c, and 6.3-8e), while having larger differences between the lower-bound and mean infiltration flux cases. Location P2WR5C10 has moderate differences in dryout/rewetting between the upper-bound and mean infiltration flux cases (Figures 6.3-9c and 6.3-9e), while having larger differences between the lower-bound and mean infiltration flux cases. Tables 6.3-7a and 6.3-7b show that location P2WR5C10 has larger differences in percolation flux between the lower-bound, mean, and upper-bound infiltration cases than do locations P2ER8C6 and P2WR8C8; consequently, location P2WR5C10 shows a greater sensitivity to infiltration flux case. Tables 6.3-7a and 6.3-7b show that location P3R7C12 has larger differences in percolation flux between the lower-bound, mean, and upper-bound infiltration flux cases than does location P2WR5C10; thus, location P3R7C12 (Figures 6.3-10c and 6.3-10e) has larger differences in dryout/rewetting between the upper-bound and mean infiltration flux cases than does location P2WR5C10 (Figures 6.3-9c and 6.3-9e). Location P3R7C12 has substantial differences in

dryout/rewetting between the lower-bound and mean infiltration flux cases, with the lower-bound infiltration flux case remaining at low liquid-phase saturation beyond 20,000 years (Figures 6.3-10c and 6.3-10e). Location P3R8C13 has large differences in dryout/rewetting between the upper-bound and mean infiltration flux cases (Figures 6.3-11c and 6.3-11e) and between the lower-bound and mean infiltration flux cases.

The influence of percolation flux on waste package relative humidity histories is similar to its influence on dryout/rewetting (Figures 6.3-7d, 6.3-8d, 6.3-9d, 6.3-10d, and 6.3-11d). Locations P2ER8C6 and P2WR8C8 have very small differences in waste package relative humidity history between the upper-bound and mean infiltration flux cases (Figures 6.3-7d and 6.3-8d), while having larger differences between the lower-bound and mean infiltration flux cases. Location P2WR5C10 has moderate differences in waste package relative humidity history between the upper-bound and mean infiltration flux cases (Figure 6.3-9d), while having larger differences between the lower-bound and mean infiltration flux cases. Location P3R7C12 has moderate differences in waste package relative humidity history between the upper-bound and mean infiltration flux cases (Figure 6.3-10d), while having substantial differences between the lower-bound and mean infiltration flux cases. Location P3R8C13 has small differences in waste package relative humidity history between the upper-bound and mean infiltration flux case (Figure 6.3-11d); moderate differences between the lower-bound and mean infiltration flux cases persist for about 700 years. With the exception of location P3R7C12, differences in waste package relative humidity history among the infiltration flux cases generally diminish within one to several thousand years.

6.3.1.2 Influence of Waste-Package-to-Waste-Package Heat-Generation Variability

This section investigates the influence of waste-package-to-waste-package heat-generation variability on thermohydrologic conditions in the emplacement drifts. The eight different waste packages considered in all of the MSTHM calculations (Figure 6.2-2) are summarized in Table 6.3-10. Time histories of drift-wall temperature and liquid-phase saturation, waste package temperature and relative humidity, and invert liquid-phase saturation are plotted (Figures 6.3-12 through 6.3-16) for three of these waste packages (dhlw-l1, bwr1-1, and pwr1-2) for the five locations discussed in the previous section (see Figure 6.3-1 for locations). Note that these three waste packages include the coolest and hottest in the waste package sequence considered. The influence of waste-package-to-waste-package heat-generation variability on peak temperatures is summarized in Table 6.3-11 for the five locations. The influence of waste-package-to-waste-package heat-generation variability on the duration of boiling is summarized in Table 6.3-12, which gives the time when boiling at the drift wall ceases.

Table 6.3-10. Summary of waste packages included in the MSTHM calculations (Figure 6.2-2). Waste packages included in Figures 6.3-12 through 6.3-16 are shown in bold.

Waste Package Name in MSTHM	Waste Package type	Length in Model (m)	Initial Heat-Generation Rate (kW)	Notes (based on MSTHM output temperatures and heat output)
pwr1-1	21-PWR AP CSNF	2.5825	5.764*	Half waste package in model; coolest PWR waste package in sequence, but "average" PWR waste package with respect to heat output
dhlw-l1	5 DHLW/DOE SNF-LONG	5.217	0.990	Coolest waste package in sequence with the lowest heat output
pwr2-1	21-PWR AP CSNF	5.165	11.800	"Average" PWR waste package in sequence with respect to temperatures, but highest heat output in sequence
bwr1-1	44-BWR CSNF	5.165	7.377	Hottest BWR waste package in sequence, but "average" BWR waste package with respect to heat output
bwr2-1	44-BWR CSNF	5.165	7.100	"Oldest" BWR waste package in sequence
dhlw-s1	5 DHLW/DOE SNF-SHORT	3.59	2.983	Hottest DHLW waste package in sequence
pwr1-2	21-PWR AP CSNF	5.165	11.528	"Hottest" waste package in sequence, but average PWR waste package with respect to heat output
bwr1-2	44-BWR CSNF	2.5825	3.689*	Half waste package in model; coolest BWR waste package in sequence, but "average" BWR waste package with respect to heat output

Source: Waste package lengths are based on information from BSC 2003f.
Heat generation rates are based on information from BSC 2004f.

NOTE: *This is the heat-generation rate for a half waste package.

Table 6.3-11. The range of peak temperatures (resulting from waste-package-to-waste-package heat-generation variability) for the mean infiltration flux case is summarized for five locations in the repository (Figure 6.3-1 for locations).

LDTH-SDT-Submodel Location	Host-Rock Unit	Peak Drift-Wall Temperature (°C)			Peak Waste Package Temperature (°C)		
		Lowest	Highest	Range	Lowest	Highest	Range
P2ER8C6	Tptpul (tsw33)	122.3	135.5	13.2	132.0	163.2	31.2
P2WR8C8	Tptpmn (tsw34)	109.7	123.0	13.3	118.9	150.6	31.7
P2WR5C10	Tptpll (tsw35)	126.8	140.8	14.0	136.7	168.8	32.1
P3R7C12	Tptpll (tsw35)	126.8	140.0	13.2	136.3	167.3	31.0
P3R8C13	Tptpln (tsw36)	106.6	120.2	13.6	116.1	148.2	32.1

Table 6.3-12. The range of the time when boiling at the drift wall ceases (resulting from waste-package-to-waste-package heat-generation variability) for the mean infiltration flux case is summarized for five locations in the repository (Figure 6.3-1 for locations).

LDTH-SDT-Submodel Location	Host-Rock Unit	Time When Boiling at the Drift Wall Ceases (years)			
		Shortest	Longest	Range	Range*
P2ER8C6	Tptpul (tsw33)	284.2	364.8	80.6	24.8%
P2WR8C8	Tptpmn (tsw34)	166.1	242.8	76.7	37.5%
P2WR5C10	Tptpll (tsw35)	340.7	623.0	282.3	58.6%
P3R7C12	Tptpll (tsw35)	1,072.3	1,200.1	127.8	11.3%
P3R8C13	Tptpln (tsw36)	140.4	195.2	54.8	32.7%

NOTE: * The range (%) is the range (years) divided by the average time when drift-wall boiling ceases [(shortest + longest)/2].

The influence of waste-package-to-waste-package heat-generation variability on peak drift-wall temperatures is virtually the same for all five locations (Table 6.3-11); similarly the influence of heat-generation variability on peak waste package temperatures is virtually the same for all five locations. Notice that the range of peak drift-wall temperatures is considerably less than the range of peak waste package temperatures. Thermal radiation in the drift is a very efficient heat-transfer mechanism for limiting the extent of temperature variability along the axis of the drift. The influence of heat-generation variability on boiling duration varies considerably among the five locations (Table 6.3-12). The greatest degree of boiling-duration variability is at location P2WR5C10, while location P3R7C12 has the least degree of boiling-duration variability.

The influence of heat-generation variability on dryout/rewetting is illustrated by the drift-wall and invert liquid-phase saturation histories (Figures 6.3-12c, 6.3-12e, 6.3-13c, 6.3-13e, 6.3-14c, 6.3-14e, 6.3-15c, 6.3-15e, 6.3-16c, and 6.3-16e). Dryout/rewetting at locations P2ER8C6, P2WR8C8, and P3R8C13 (Figures 6.3-12c 6.3-12e, 6.3-13c, 6.3-13e, 6.3-16c, and 6.3-16e), which are close to the repository edges, exhibit more sensitivity to heat-generation variability than at locations P2WR5C10 and P3R7C12 (Figures 6.3-14c, 6.3-14e, 6.3-15c, and 6.3-15e), which are farther away from the repository edges. Note that location P3R7C12 has by far the least degree of dryout/rewetting variability. For all locations, the invert exhibits less dryout/rewetting variability than the drift wall.

The key factor influencing the relationship between dryout/rewetting variability and heat-generation variability is the duration of boiling. Initially, the radial extent of the rock dryout zone is very undulating, with wider zones adjacent to hotter waste packages and narrower zones adjacent to cooler waste packages. Locations (within the repository area) with a longer boiling duration have a greater opportunity for the rock dryout zones around the respective cooler and hotter waste packages to coalesce along the drift, smoothing out the undulating shape and forming a more uniform cylindrical rock-dryout zone. Locations (within the repository area) with a shorter boiling duration have less of an opportunity for the rock dryout zones to coalesce along the drift and the undulating shape of the rock dryout zone remains.

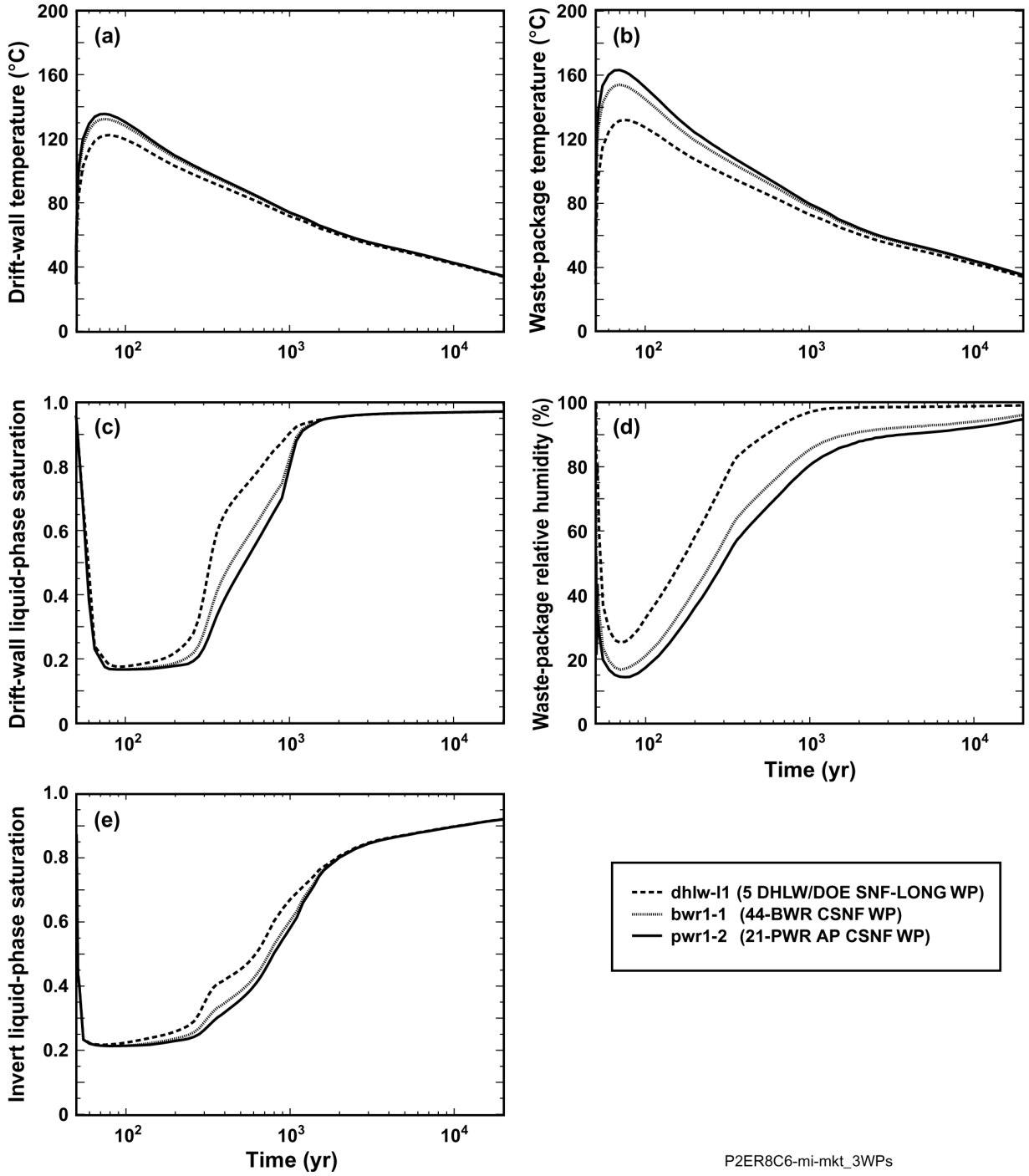

Figure 6.3-12. Thermohydrologic conditions for the mean infiltration flux case are plotted for a range of waste packages at the P2ER8C6 location, which is in the Tptpul (tsw33) unit (see Figure 6.3-1 for location). The plotted thermohydrologic variables are (a) drift-wall temperature, (b) waste package temperature, (c) drift-wall liquid-phase saturation, (d) waste package relative humidity, and (e) invert liquid-phase saturation. These waste packages bracket the entire range of temperature at this location.

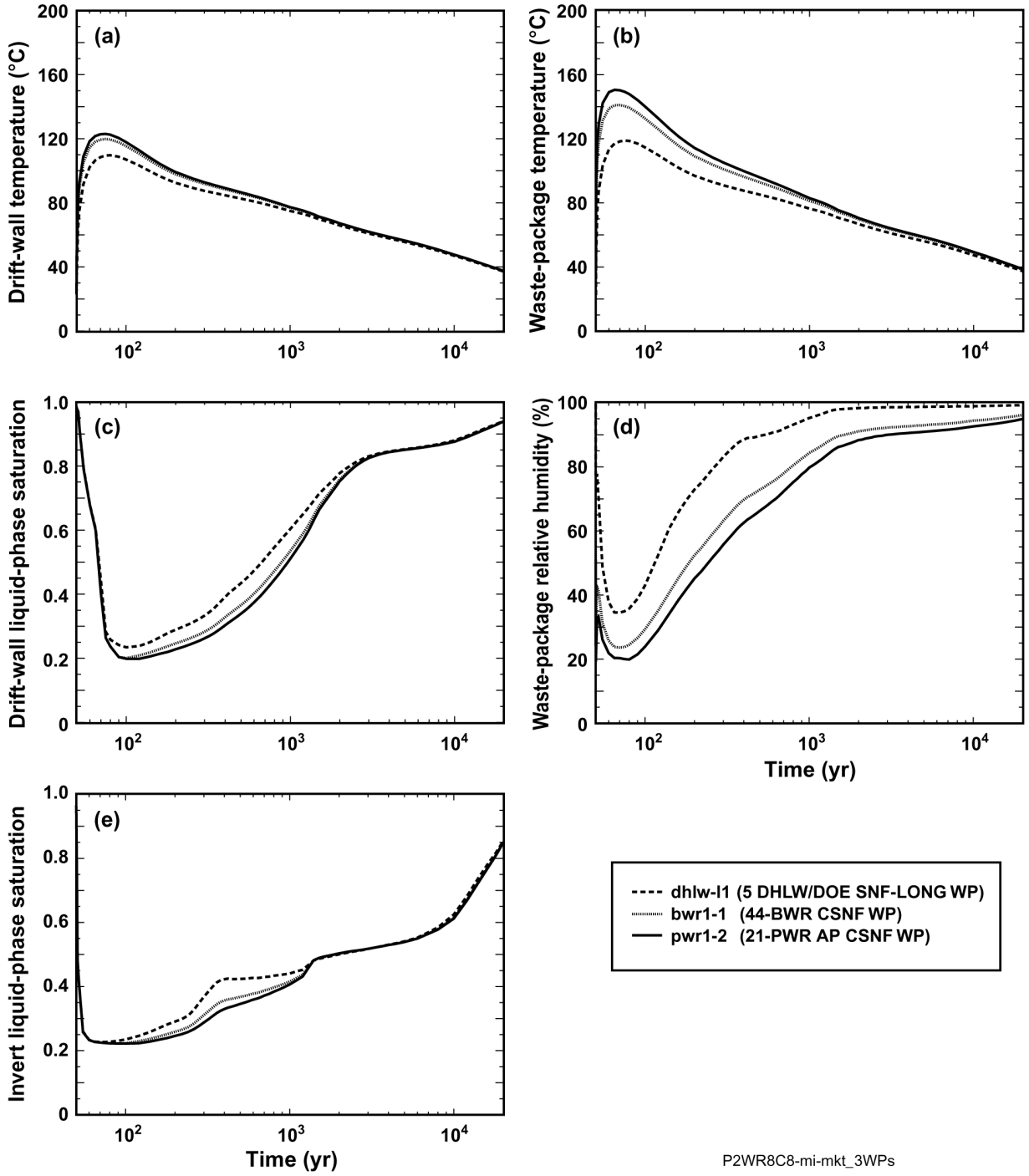

NOTE: WP = waste package.

Figure 6.3-13. Thermohydrologic conditions for the mean infiltration flux case are plotted for a range of waste packages at the P2WR8C8 location, which is in the Tptpmn (tsw34) unit (see Figure 6.3-1 for location). The plotted thermohydrologic variables are (a) drift-wall temperature, (b) waste package temperature, (c) drift-wall liquid-phase saturation, (d) waste package relative humidity, and (e) invert liquid-phase saturation. These waste packages bracket the entire range of temperature at this location.

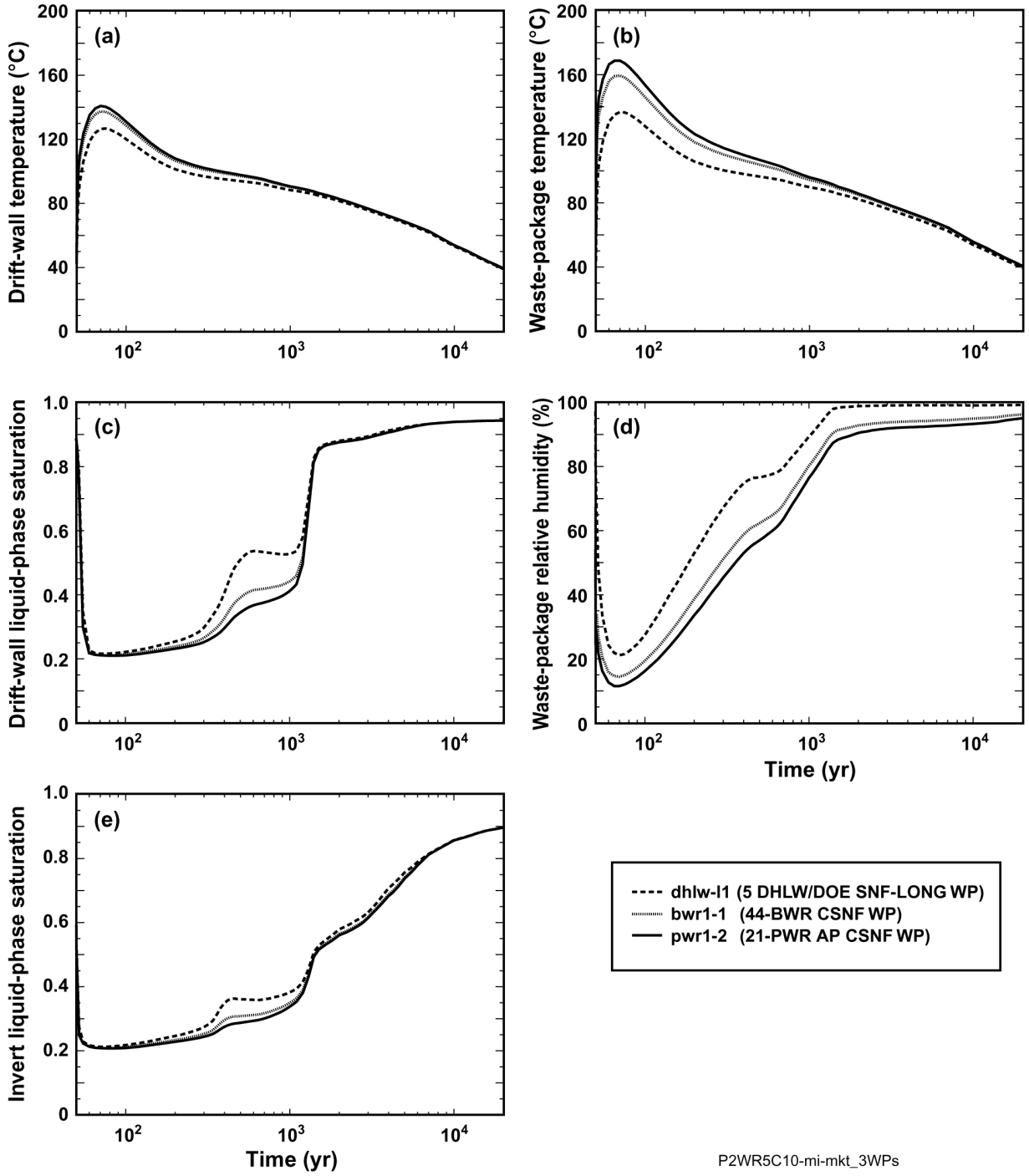

NOTE: WP = waste package.

Figure 6.3-14. Thermohydrologic conditions for the mean infiltration flux case are plotted for a range of waste packages at the P2WR5C10 location, which is in the Tptpll (tsw35) unit (see Figure 6.3-1 for location). The plotted thermohydrologic variables are (a) drift-wall temperature, (b) waste package temperature, (c) drift-wall liquid-phase saturation, (d) waste package relative humidity, and (e) invert liquid-phase saturation. These waste packages bracket the entire range of temperature at this location.

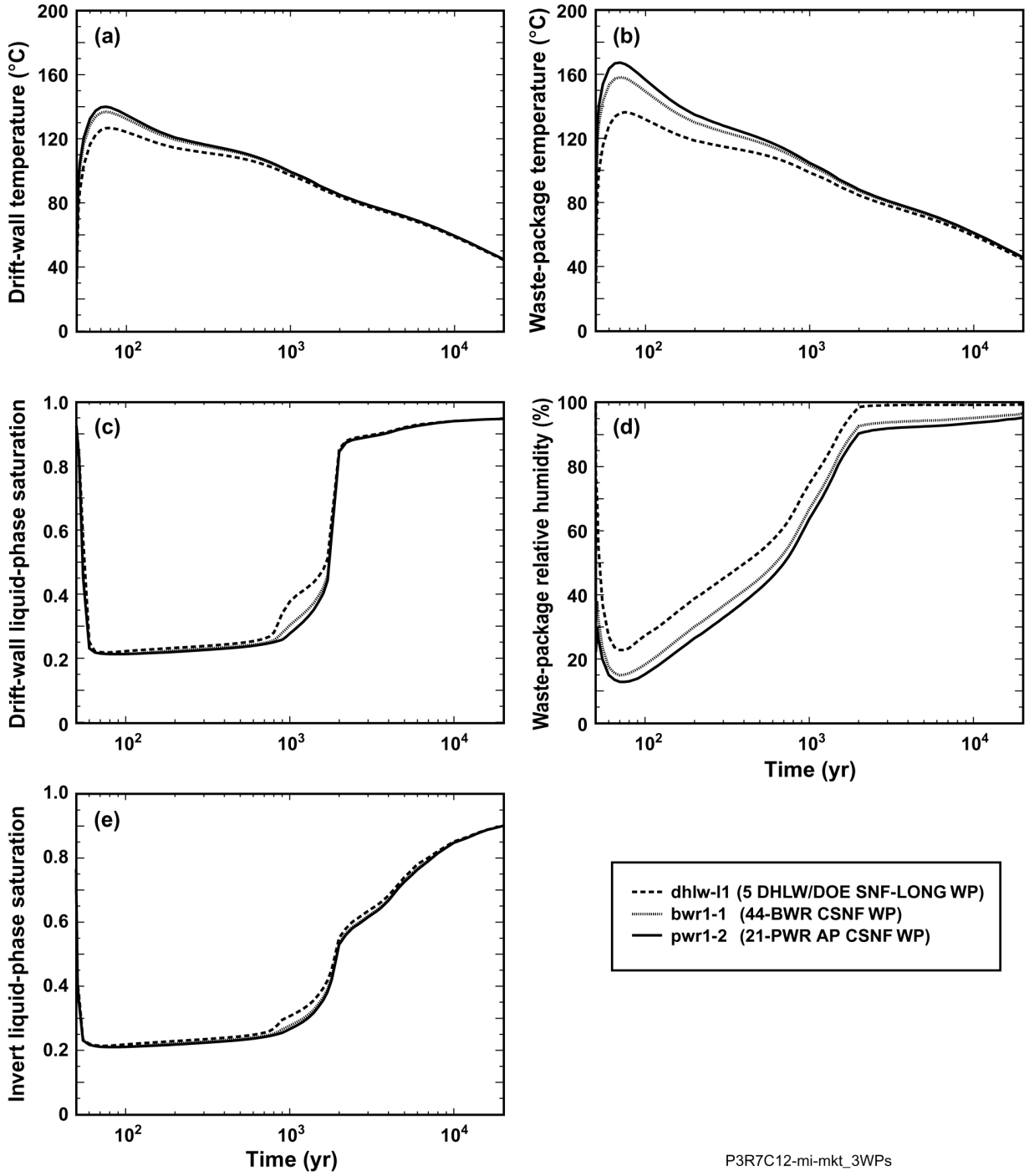

NOTE: WP = waste package.

Figure 6.3-15. Thermohydrologic conditions for the mean infiltration flux case are plotted for a range of waste packages at the P3R7C12 location, which is in the Tptpll (tsw35) unit (see Figure 6.3-1 for location). The plotted thermohydrologic variables are (a) drift-wall temperature, (b) waste package temperature, (c) drift-wall liquid-phase saturation, (d) waste package relative humidity, and (e) invert liquid-phase saturation. These waste packages bracket the entire range of temperature at this location.

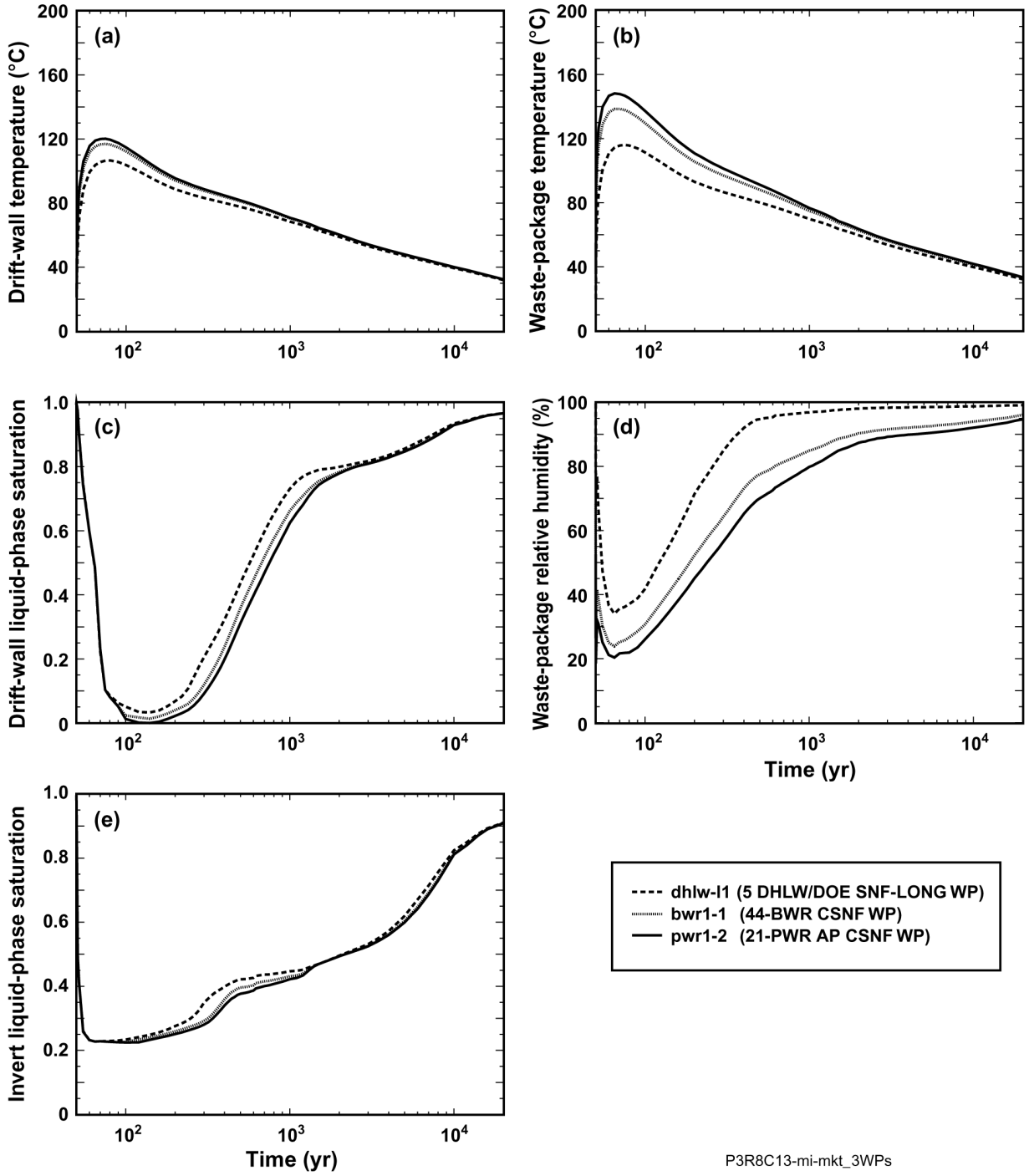

NOTE: WP = waste package.

Figure 6.3-16. Thermohydrologic conditions for the mean infiltration flux case are plotted for a range of waste packages at the P3R8C13 location, which is in the Tptpln (tsw36) unit (see Figure 6.3-1 for location). The plotted thermohydrologic variables are (a) drift-wall temperature, (b) waste package temperature, (c) drift-wall liquid-phase saturation, (d) waste package relative humidity, and (e) invert liquid-phase saturation. These waste packages bracket the entire range of temperature at this location.

The influence of heat-generation variability on waste package relative humidity variability is similar to the influence on dryout/rewetting. Because the relative humidity at the drift wall strongly depends on the liquid-phase saturation (as well as on temperature) at the drift wall, the variability of drift-wall relative humidity is similar to that of drift-wall liquid-phase saturation. Relative humidity on a given waste package depends on two factors. The first is the adjacent drift-wall relative humidity. The second factor is the temperature difference between the waste package and adjoining drift-wall surface; relative humidity reduction (relative to the adjacent drift wall) depends on this temperature difference (Section 6.1.4). Waste packages with higher heat-generation rates result in a greater relative humidity reduction than those with lower heat-generation rates. The large difference in heat-generation rate between the coolest and hottest waste packages results in a large difference in the respective relative humidity histories.

From a heat-transfer perspective, the drip shield functions like a thermal-radiation shield (between the waste package and the drift wall) that causes the waste package to be hotter than it would have been without the presence of the drip shield. The increased temperature difference between the waste package and the drift wall reduces the relative humidity on the waste package in a fashion that is analogous to that given in Equation 24 (Section 6.2.4) for the drip shield itself. For waste packages with higher heat-generation rates (i.e., the pwr1-2 waste package in Figure 6.3-16), the influence of the thermal-radiation shield on waste package temperature and relative humidity is much greater than it is for waste packages with lower heat-generation rates (i.e., the dhlw-l1 waste package in Figure 6.3-16). This effect is exhibited by comparing the range in drift-wall temperatures (Figure 6.3-16a) with the range in waste package temperatures (Figure 6.3-16b). The larger range in waste package temperatures, compared to the corresponding range in drift-wall temperatures results in a wide range in waste package relative humidities (Figure 6.3-16d).

6.3.1.3 Alternative MSTHM with Vertically Extended LDTH/SDT Submodels

The standard MSTHM utilizes LDTH and SDT submodels that have a constant-temperature boundary at the water table. To test an alternative approach, MSTHM calculations were conducted with vertically extended LDTH and SDT submodels. In these submodels, the lower boundary of the LDTH and SDT submodels is set 1,000 m below the water table (as is done in the SMT submodel). A series of initialization runs are conducted with the SDT submodel where the lower boundary temperature is iteratively adjusted until the temperature at the water is equal to that of the SDT submodel with the lower boundary at the water table. The vertically extended SDT submodel is then run with the appropriate heat-generation-rate-versus-time table and the temperature at the water table is saved as output. The water-table temperature history is then applied as the lower boundary temperature (at the water table) in the corresponding LDTH submodel. Applying the SDT-submodel water-table temperature history to the lower (water-table) boundary of the LDTH submodel is equivalent to having extended the LDTH submodel 1,000 m below the water table. This alternative MSTHM approach, with vertically extended LDTH and SDT submodels, was applied to four of the five locations (Figure 6.3-1) discussed in previous sections. The alternative MSTHM approach is compared to the standard MSTHM approach in Figures 6.3-17 through 6.3-20. Overall, the two approaches predict nearly the same thermohydrologic conditions at the four locations. The small differences between the two approaches occur only at later time (e.g., Figures 6.3-19a, 6.3-19b, 6.3-20a, 6.3-20b, 6.3-20c, and 6.3-20e). At early time, the two approaches predict virtually identical

thermohydrologic conditions. Peak temperatures (Table 6.3-13) are exactly the same for the two approaches and the duration of boiling (Table 6.3-14) is nearly the same for the two approaches. Waste package relative humidity is virtually the same for all time (Figures 6.3-17d, 6.3-18d, 6.3-19d, and 6.3-20d). The alternative MSTHM approach is applied to the low percolation flux cases described in Sections 6.3.2.1 and 6.3.2.3.

Table 6.3-13. Peak temperatures are compared between an alternative MSTHM with vertically extended LDTH and SDT submodels with the standard MSTHM results for the pwr1-2 at four locations in the repository (see Figure 6.3-1 for locations).

LDTH-SDT-Submodel Location	Host-Rock Unit	Peak Drift-Wall Temperature (°C)			Peak Waste Package Temperature (°C)		
		Standard MSTHM	Alternative MSTHM	Difference	Standard MSTHM	Alternative MSTHM	Difference
P2ER8C6	Tptpul (tsw33)	135.5	135.5	0.0	163.2	163.2	0.0
P2WR8C8	Tptpmn (tsw34)	123.0	123.0	0.0	150.6	150.6	0.0
P2WR5C10	Tptpll (tsw35)	140.8	140.8	0.0	168.8	168.8	0.0
P3R8C13	Tptpln (tsw36)	120.2	120.2	0.0	148.2	148.2	0.0

Table 6.3-14. The time when boiling at the drift wall ceases is compared between an alternative MSTHM with vertically extended LDTH and SDT submodels with the standard MSTHM results for the pwr1-2 at four locations in the repository (see Figure 6.3-1 for locations).

LDTH-SDT-Submodel Location	Host-Rock Unit	Time When Boiling at the Drift Wall Ceases (years)			
		Standard MSTHM	Alternative MSTHM	Difference	Range*
P2ER8C6	Tptpul (tsw33)	364.8	364.9	0.1	0.027%
P2WR8C8	Tptpmn (tsw34)	242.8	242.6	-0.2	0.082%
P2WR5C10	Tptpll (tsw35)	623.0	622.0	-1.0	0.161%
P3R8C13	Tptpln (tsw36)	195.2	195.1	-0.1	0.051%

NOTE: * The range (%) is the range (years) divided by the average time when drift-wall boiling ceases [(shortest + longest)/2].

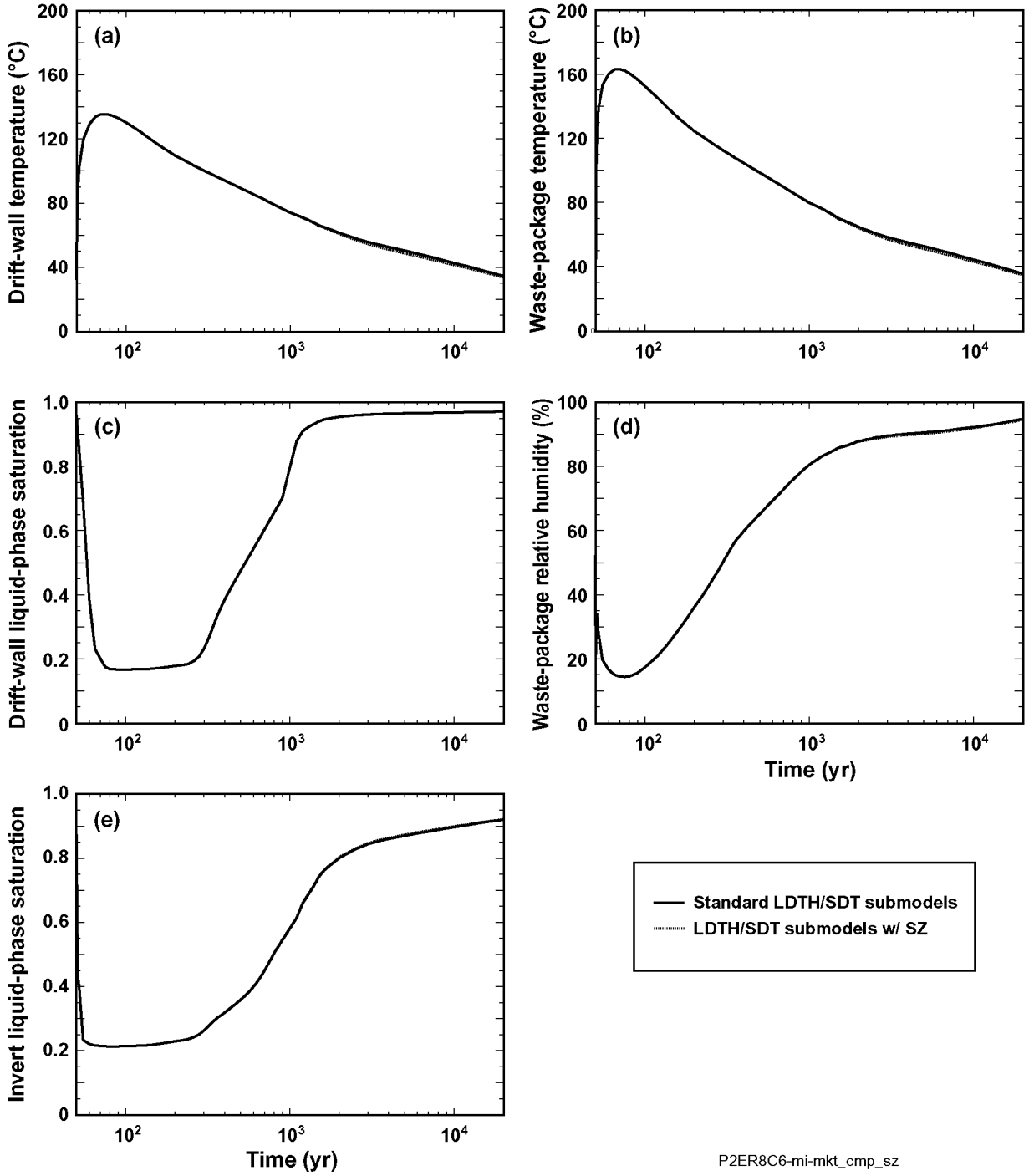

NOTE: SZ = saturated zone.

Figure 6.3-17. Thermohydrologic conditions for the mean infiltration flux case are plotted for the pwr1-2 waste package at the P2ER8C6 location, which is in the Tptpul (tsw33) unit (see Figure 6.3-1 for location). The plotted thermohydrologic variables are (a) drift-wall temperature, (b) waste package temperature, (c) drift-wall liquid-phase saturation, (d) waste package relative humidity, and (e) invert liquid-phase saturation. The standard MSTHM calculation is compared with an alternative MSTHM calculation in which the LDTH and SDT submodels are vertically extended to include the upper 1 km of the saturated zone.

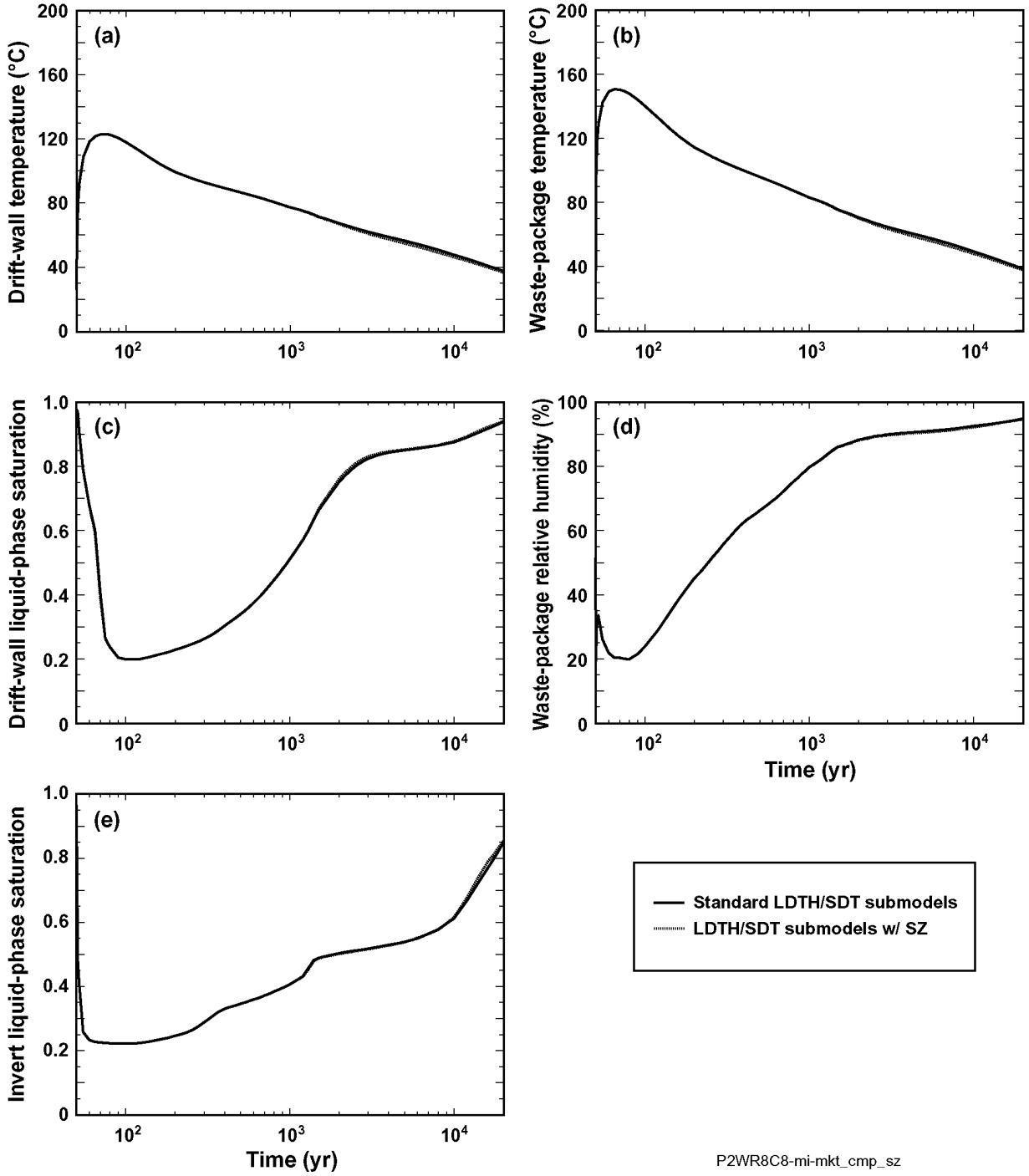

NOTE: SZ = saturated zone.

Figure 6.3-18. Thermohydrologic conditions for the mean infiltration flux case are plotted for the pwr1-2 waste package at the P2WR8C8 location, which is in the Tptpmn (tsw34) unit (see Figure 6.3-1 for location). The plotted thermohydrologic variables are (a) drift-wall temperature, (b) waste package temperature, (c) drift-wall liquid-phase saturation, (d) waste package relative humidity, and (e) invert liquid-phase saturation. The standard MSTHM calculation is compared with an alternative MSTHM calculation in which the LDTH and SDT submodels are vertically extended to include the upper 1 km of the saturated zone.

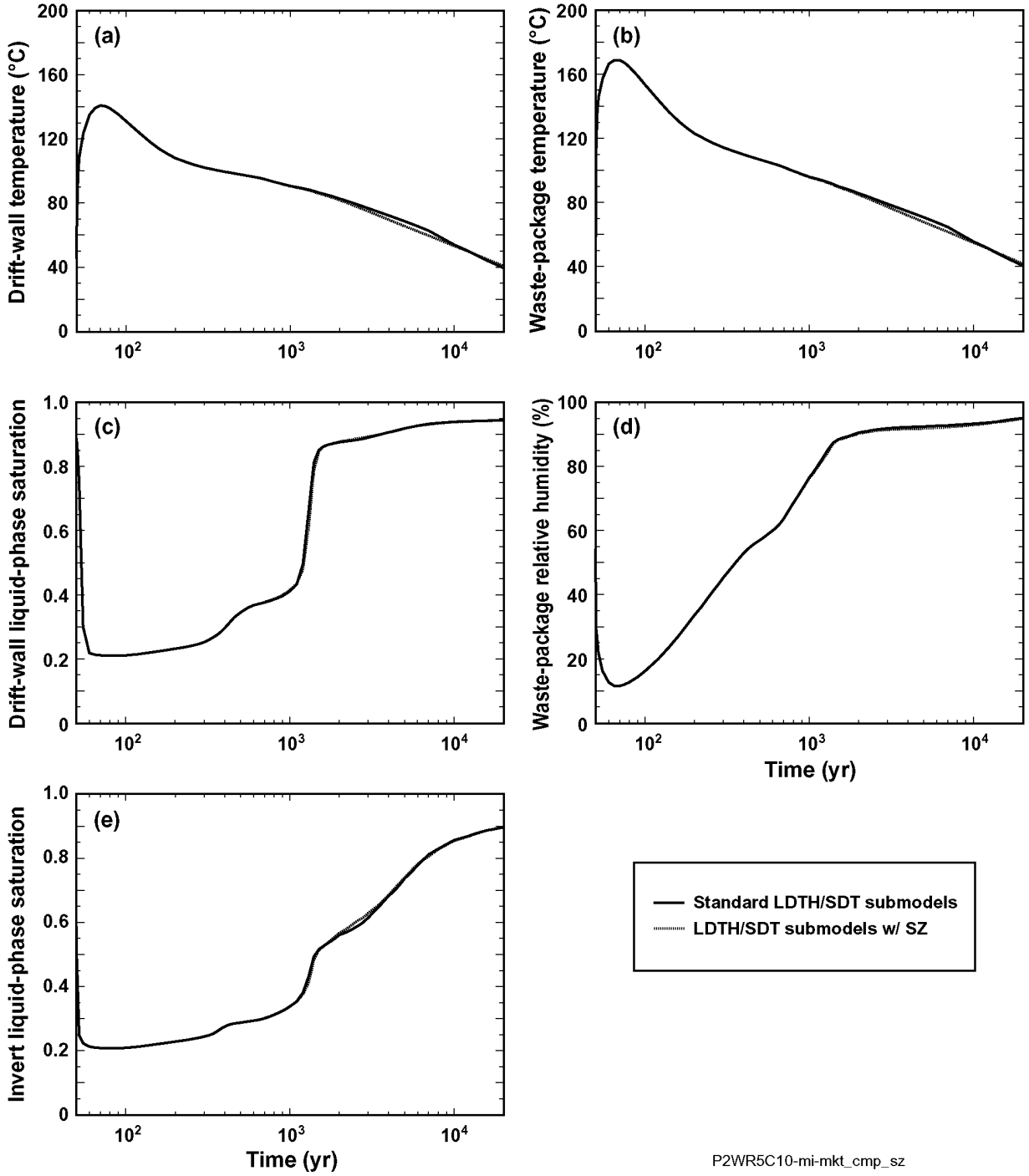

NOTE: SZ = saturated zone.

Figure 6.3-19. Thermohydrologic conditions for the mean infiltration flux case are plotted for the pwr1-2 waste package at the P2WR5C10 location, which is in the Tptpll (tsw35) unit (see Figure 6.3-1 for location). The plotted thermohydrologic variables are (a) drift-wall temperature, (b) waste package temperature, (c) drift-wall liquid-phase saturation, (d) waste package relative humidity, and (e) invert liquid-phase saturation. The standard MSTHM calculation is compared with an alternative MSTHM calculation in which the LDTH and SDT submodels are vertically extended to include the upper 1 km of the saturated zone.

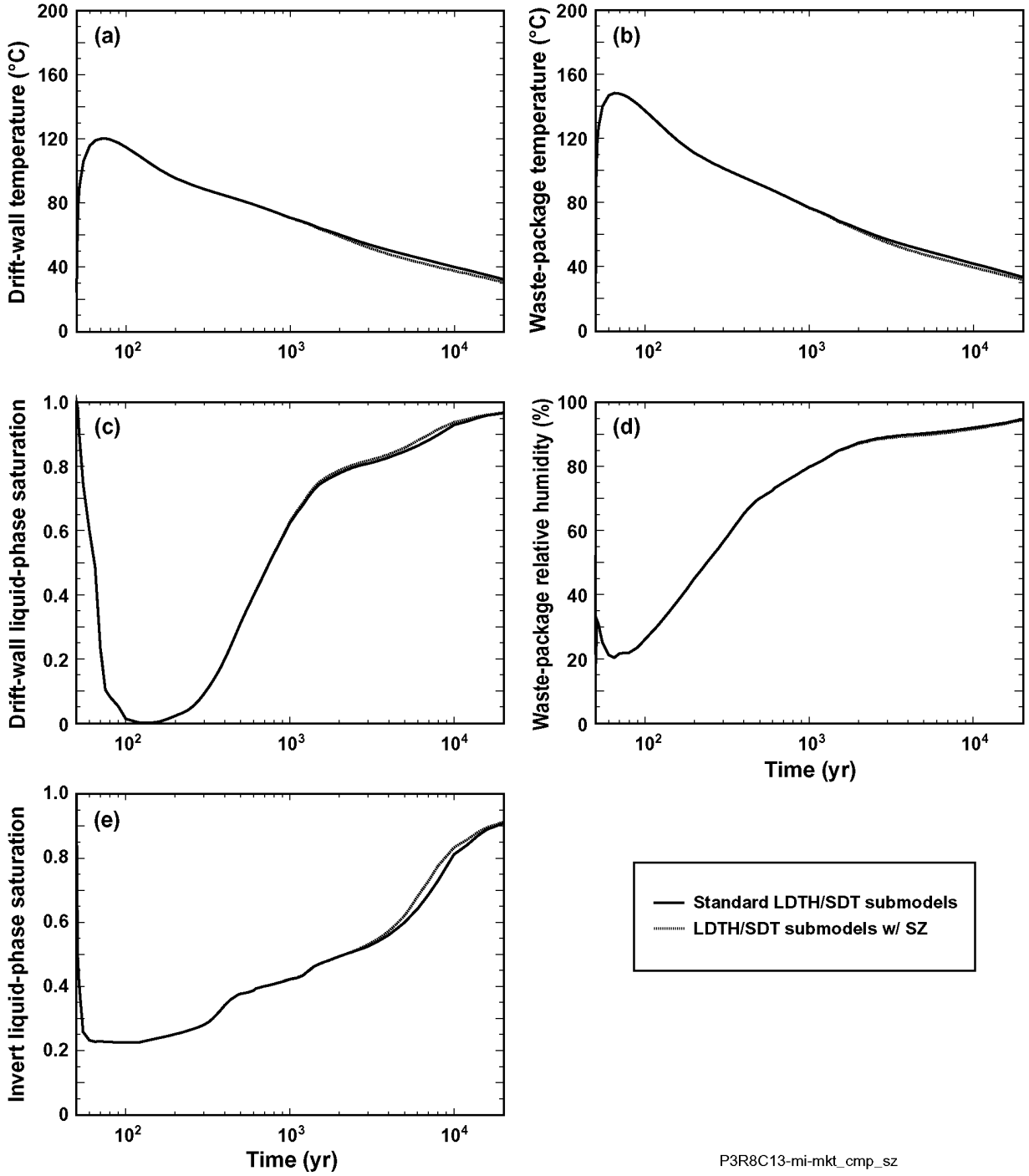

NOTE: SZ = saturated zone.

Figure 6.3-20. Thermohydrologic conditions for the mean infiltration flux case are plotted for a range of waste packages at the P3R8C13 location, which is in the Tptpln (tsw36) unit (see Figure 6.3-1 for location). The plotted thermohydrologic variables are (a) drift-wall temperature, (b) waste package temperature, (c) drift-wall liquid-phase saturation, (d) waste package relative humidity, and (e) invert liquid-phase saturation. The standard MSTHM calculation is compared with an alternative MSTHM calculation in which the LDTH and SDT submodels are vertically extended to include the upper 1 km of the saturated zone.

6.3.2 Parameter-Uncertainty-Sensitivity Analyses

For the MSTHM predictions of thermohydrologic conditions within the emplacement drifts and in the adjoining host rock, the key uncertain parameters (Table 6.3-15) fall into three categories: (1) thermal properties, (2) hydrologic properties, and (3) percolation flux. For thermal and hydrologic properties, the primary focus concerns the properties of the host rock and of the materials within the emplacement drifts and the ambient percolation flux at the repository horizon.

The primary thermal properties are heat capacity and thermal conductivity. The sensitivity of MSTHM predictions of in-drift and host-rock thermohydrologic conditions to host-rock heat capacity was found to be negligible in Section 5.3.1.4.10 of *FY 01 Supplemental Science and Performance Analyses, Volume 1: Scientific Bases and Analyses* (BSC 2001b), the sensitivity to invert thermal conductivity was found also to be negligible in Section 5.3.1.4.10 of that report. Note that the host-rock thermal conductivity was found to be a significant parameter (BSC 2001b, Section 5.3.1.4.8); consequently, it is addressed in Sections 6.3.2.2 and 6.3.2.3.

The primary hydrologic property of interest is the bulk permeability of the host rock, which is primarily affected by the permeability of the fracture network. A sensitivity study of host-rock bulk permeability (BSC 2001b, Section 5.3.1.4.7) found the influence to be primarily confined to temperature. Host-rock bulk permeability was found to modestly influence peak temperatures and boiling-period duration. Because the effect of host-rock bulk permeability on temperatures is small compared to that of host-rock thermal-conductivity uncertainty (which is addressed in Sections 6.3.2.2 and 6.3.2.3), it is unnecessary to further investigate the influence of bulk-permeability uncertainty in this report.

Percolation flux uncertainty at the repository horizon can result from at least two sources. The first source is the uncertainty concerning the magnitude of infiltration flux, which is addressed by way of lower-bound, mean, and upper-bound infiltration flux cases in Section 6.3.1.1. It was also addressed in the previous revision of *Multiscale Thermohydrologic Model* (BSC 2001c, Sections 6.11 and 6.12) by way of lower-bound, mean, and upper-bound infiltration flux cases. The three infiltration flux cases result in a wide range of percolation flux that might occur at any location within the repository.

The second source of percolation flux uncertainty concerns the possibility of flow focusing in the UZ Model Layers between the base of the PTn sequence of units and the repository horizon. The liquid-phase flux distribution applied at the upper boundary of the LDTH submodels of the MSTHM is the percolation flux distribution (from the base of the PTn unit into the top of the TSw sequence of units) calculated by *UZ Flow Models and Submodels* (BSC 2003h). Flow focusing is the term used to denote the potential concentration of percolation flux from the large-scale distribution of percolation flux, as simulated by the relatively coarsely gridded three-dimensional UZ Flow Model, to the drift scale, as simulated by the MSTHM and by *Drift-Scale Coupled Processes (DST and TH Seepage) Models* (BSC 2003j). Thus, flow focusing uncertainty is the result of the relatively coarsely gridded three-dimensional mesh in the UZ Flow Model not fully capturing the potential for heterogeneity between the base of the PTn sequence and the repository horizon to generate focused percolation flux into the repository

horizon. The impact of flow focusing of ambient percolation flux at the repository horizon is addressed in Sections 6.3.2.1 and 6.3.2.3.

Table 6.3-15. Potentially important parameters to thermohydrologic conditions in emplacement drifts are listed for consideration in the parameter-uncertainty sensitivity analysis.

Parameter	Previous Parameter-Uncertainty-Sensitivity Analyses	Importance to In-drift Thermohydrologic Conditions	Parameter Uncertainty-Sensitivity Analyses in This Report
Host-rock heat capacity (which includes influence of specific heat and bulk density)	BSC 2001b, Section 5.3.1.4.10	Negligible	None
Host-rock thermal conductivity	BSC 2001b, Section 5.3.1.4.8	Very important	Sections 6.3.2.2 and 6.3.2.3
Invert thermal conductivity	BSC 2001b, Section 5.3.1.4.10	Negligible	None
Host-rock bulk permeability	BSC 2001b, Section 5.3.1.4.7	Minor influence on temperature, which is small compared to that of host rock thermal-conductivity uncertainty (Sections 6.3.2.2 and 6.3.2.3)	None
Percolation flux	BSC 2001c, Sections 6.11 and 6.12	Very important	Sections 6.3.1.1, 6.3.2.1, and 6.3.2.3

6.3.2.1 Percolation Flux Uncertainty at the Repository Horizon, Including the Influence of Flow Focusing

The uncertainty of ambient percolation flux at the repository horizon is addressed in Section 6.3.1.1 by way of lower-bound, mean, and upper-bound infiltration flux cases. For each of these infiltration flux cases, the host-rock percolation flux in the MSTHM corresponds to the distribution of percolation flux just below the base of the PTn unit; this data is generated by the three-dimensional UZ Flow Model for the three climate states: present-day, monsoonal, and glacial-transition. Thus, the MSTHM accounts for the influence of lateral diversion in the PTn as represented in the three-dimensional UZ Flow Model. Between the base of the PTn unit and the repository horizon, ambient percolation flux is assumed to be one-dimensional vertically downward with neither lateral diversion nor flow focusing caused by layering or heterogeneity in the hydrologic-property distributions. Section 6.2.1.4 of *Drift-Scale Coupled Processes (DST and TH Seepage) Models* (BSC 2003j) discusses the need to address the potential for flow focusing of percolation flux in the hydrogeologic units above the repository horizon. Flow focusing is the term used to denote the potential concentration of percolation flux from the large-scale distribution of percolation flux, as simulated by the relatively coarsely gridded three-dimensional UZ Flow Model, to the drift scale, as simulated by the MSTHM and by *Drift-Scale Coupled Processes (DST and TH Seepage) Models* (BSC 2003j). Stochastic modeling analyses discussed in Section 4.3.2 of *FY 01 Supplemental Science and Performance Analyses, Volume 1: Scientific Bases and Analyses* (BSC 2001b), using a two-dimensional, finely gridded vertical cross section of the unsaturated zone, resulted in maximum flow-focusing factors between 5 and 6. In Section 6.2.2.2.4 of *Drift-Scale Coupled Processes (DST and TH Seepage)*

Models (BSC 2003j) flow-focusing factors of 5 and 10 were considered in the sensitivity study to percolation flux, resulting in percolation fluxes of 30, 80, and 125 mm/yr for the present-day, monsoonal, and glacial-transition climate states, respectively.

Table 6.3-16 summarizes the percolation fluxes for the low- and high-percolation flux cases considered in this study. To better discern the influence of the local host-rock unit on thermohydrologic behavior, it was decided to use the same value of present-day percolation flux (25 mm/yr) for the high-percolation flux case at all four locations, thus resulting in an effective flow focusing factor of close to 5 at all locations. To obtain the monsoonal and glacial-transition high-percolation flux values at a given location (Table 6.3-16), the corresponding percolation flux values in Table 6.3-7a are multiplied by the corresponding effective focus factor. Note that the present-day, monsoonal, and glacial-transition high-percolation flux values are similar to those used in Section 6.2.2.2.4 of *Drift-Scale Coupled Processes (DST and TH Seepage) Models* (BSC 2003j) for the case with a focus factor of 5 (that case used percolation flux values of 30, 80, and 125 mm/yr for the three climate states, respectively).

The low-percolation flux case in Table 6.3-16 corresponds to the possibility of a region of the repository experiencing "flow defocusing," which is the opposite of "flow focusing." Thus, for flow focusing to be able to occur in one region of the repository, it is necessary for adjoining regions to receive less percolation flux than would have occurred without flow focusing. To discern the influence of the local host-rock unit on thermohydrologic behavior, it was decided to apply the same value (0.025 mm/yr) to all four locations. Because the low-percolation flux cases are meant to correspond to regions that are, in effect, shielded from significant percolation flux, regardless of the magnitude of repository-wide percolation flux, it was decided to use the same small value of percolation flux for all (three) climate states. Thus, this "percolation-shielding" effect persists during all (three) climate states. It is worth noting that for all four locations (P2ER8C6, P2WR8C8, P2WR5C10, and P3R8C13) considered in this section, the lower-bound infiltration flux case results in a moderately high values of percolation flux during the monsoonal climate (Table 6.3-7b). Consequently, the low-percolation flux case considered in this section corresponds to more persistent low-percolation flux values (than in the lower-bound infiltration flux case), thereby allowing the effects of low percolation flux to develop (in a thermohydrologic sense) in a more persistent fashion. Note that values of present-day percolation flux vary by a factor of 1,000 between the low- and high-percolation flux cases.

Table 6.3-16. The percolation flux for the low-, mean, and high-percolation flux cases is summarized for four locations in the repository used to examine thermohydrologic conditions in the repository (Figure 6.2-2). The values for the mean percolation flux case are given in Table 6.3-7a.

LDTH-SDT-Submodel Location	Percolation Flux for the Low-Percolation Flux (defocused flow) Case (mm/yr)			Percolation Flux for the High-Percolation Flux (focused flow) Case (mm/yr)			
	Present-Day	Monsoonal	Glacial-Transition	Present-Day	Monsoonal[1]	Glacial-Transition[1]	Effective Focus Factor[2]
P2ER8C6	0.025	0.025	0.025	25.00	54.04	106.3	4.62
P2WR8C8	0.025	0.025	0.025	25.00	58.41	87.47	5.59
P2WR5C10	0.025	0.025	0.025	25.00	77.49	117.18	5.31
P3R8C13	0.025	0.025	0.025	25.00	77.57	111.89	3.54

NOTE: [1] The monsoonal and glacial-transition percolation flux values for the high-percolation flux case are obtained by multiplying the corresponding percolation flux values in Table 6.3-7a by the effective focus factor for that location.

[2] The effective focus factor is obtained by dividing 25.00 mm/yr by the present-day percolation flux listed for the given location in Table 6.3-7a.

The influence of percolation flux uncertainty on thermohydrologic behavior at four locations (P2ER8C6, P2WR8C8, P2WR5C10, and P3R8C13) in the repository (see Figure 6.3-1 for locations) is shown in time histories of drift-wall temperature and liquid-phase saturation, waste package temperature and relative humidity, and invert liquid-phase saturation (Figures 6.3-21 through 6.3-24) for a 21-PWR AP CSNF waste package. Percolation flux uncertainty is seen to have a small influence on peak drift-wall temperature (Table 6.3-17) and on peak waste package temperature (Table 6.3-18). Peak drift-wall temperatures only vary by 3.7 to 5.2 percent and peak waste package temperatures only vary by 2.9 to 4.3 percent for a 1,000-fold range of percolation flux. Compared to its influence on peak temperatures, percolation flux uncertainty has a much stronger influence on the duration of boiling (Table 6.3-19). The sensitivity of boiling-period duration to percolation flux uncertainty is greatest for those locations with the longest boiling-period duration, which correspond to locations furthest away from the repository edges where differences in the spatial (and temporal) extent of rock dryout (resulting from differences in percolation flux) have more time to develop. Thus locations P2ER8C6 and P3R8C13, which are at the repository edges have the smallest sensitivity to percolation flux uncertainty, while location P2WR5C10, which is close to the center of the repository, has the greatest sensitivity to percolation flux uncertainty.

Percolation flux uncertainty has a strong influence on dryout/rewetting behavior, as shown in the drift-wall and invert liquid-phase saturation histories (Figures 6.3-21c, 6.3-21e, 6.3.22c, 6.3.22e, 6.3-23c, 6.3-23e, 6.3-24c, and 6.3-24e). Similarly, it also has a strong influence on the waste package relative humidity histories (Figures 6.3-21d, 6.3-22d, 6.3-23d, and 6.3-24d). Because the relative humidity at the drift wall strongly depends on the liquid-phase saturation (as well as on temperature) at the drift wall, the variability of drift-wall relative humidity is similar to that of drift-wall liquid-phase saturation. Relative humidity on a given waste package depends on relative humidity at the adjoining drift wall. The large differences in drift-wall liquid-phase saturation histories (between the low- and high-percolation flux cases) result in large differences in waste package relative humidity histories between the flux cases.

Table 6.3-17. The range of peak drift-wall temperatures for the pwr1-2 waste package (resulting from percolation flux uncertainty) is summarized for four locations in the repository (see Figure 6.3-1 for locations). The pwr1-2 (21-PWR AP CSNF) waste package is the hottest waste package in the sequence (Figure 6.2-2).

LDTH-SDT-Submodel Location	Host-Rock Unit	Peak Drift-Wall Temperature (°C)				
		Low Percolation Flux	Mean Percolation Flux	High Percolation Flux	Low to High Range	Low to High Range*
P2ER8C6	Tptpul (tsw33)	138.9	135.5	131.9	7.0	5.2%
P2WR8C8	Tptpmn (tsw34)	124.5	123.0	119.4	5.1	4.2%
P2WR5C10	Tptpll (tsw35)	144.1	140.8	137.2	6.9	4.9%
P3R8C13	Tptpln (tsw36)	121.9	120.2	117.5	4.4	3.7%

NOTE: *The range (%) is the range (°C) divided by the peak drift-wall temperature [(low + high)/2].

Table 6.3-18. The range of peak waste package temperatures for the pwr1-2 waste package (resulting from percolation flux uncertainty) is summarized for four locations in the repository (see Figure 6.3-1 for locations). The pwr1-2 (21-PWR AP CSNF) waste package is the hottest waste package in the sequence (Figure 6.2-2).

LDTH-SDT-Submodel Location	Host-Rock Unit	Peak Waste Package Temperature (°C)				
		Low Percolation Flux	Mean Percolation Flux	High Percolation Flux	Low to High Range	Low to High Range*
P2ER8C6	Tptpul (tsw33)	166.5	163.2	159.5	7.0	4.3%
P2WR8C8	Tptpmn (tsw34)	151.7	150.6	147.4	4.3	2.9%
P2WR5C10	Tptpll (tsw35)	172.4	168.8	165.4	7.0	4.1%
P3R8C13	Tptpln (tsw36)	149.9	148.2	145.9	4.0	2.7%

NOTE: *The range (%) is the range (°C) divided by the peak drift-wall temperature [(low + high)/2].

Table 6.3-19. The range of the time when boiling at the drift wall ceases for the pwr1-2 waste package (resulting from percolation flux uncertainty) is summarized for four locations in the repository (see Figure 6.3-1 for locations). The pwr1-2 (21-PWR AP CSNF) waste package is the hottest waste package in the sequence (Figure 6.2-2).

LDTH-SDT-Submodel Location	Host-Rock Unit	Time When Boiling at the Drift Wall Ceases (years)				
		Low Percolation Flux	Mean Percolation Flux	High Percolation Flux	Low to High Range	Low to High Range*
P2ER8C6	Tptpul (tsw33)	438.1	364.8	313.3	124.8	33.2%
P2WR8C8	Tptpmn (tsw34)	286.1	242.8	197.7	88.4	36.5%
P2WR5C10	Tptpll (tsw35)	896.9	623.0	385.4	484.5	75.6%
P3R8C13	Tptpln (tsw36)	224.2	195.2	175.2	49.0	24.5%

NOTE: *The range (%) is the range (years) divided by the average time when drift-wall boiling ceases [(shortest + longest)/2].

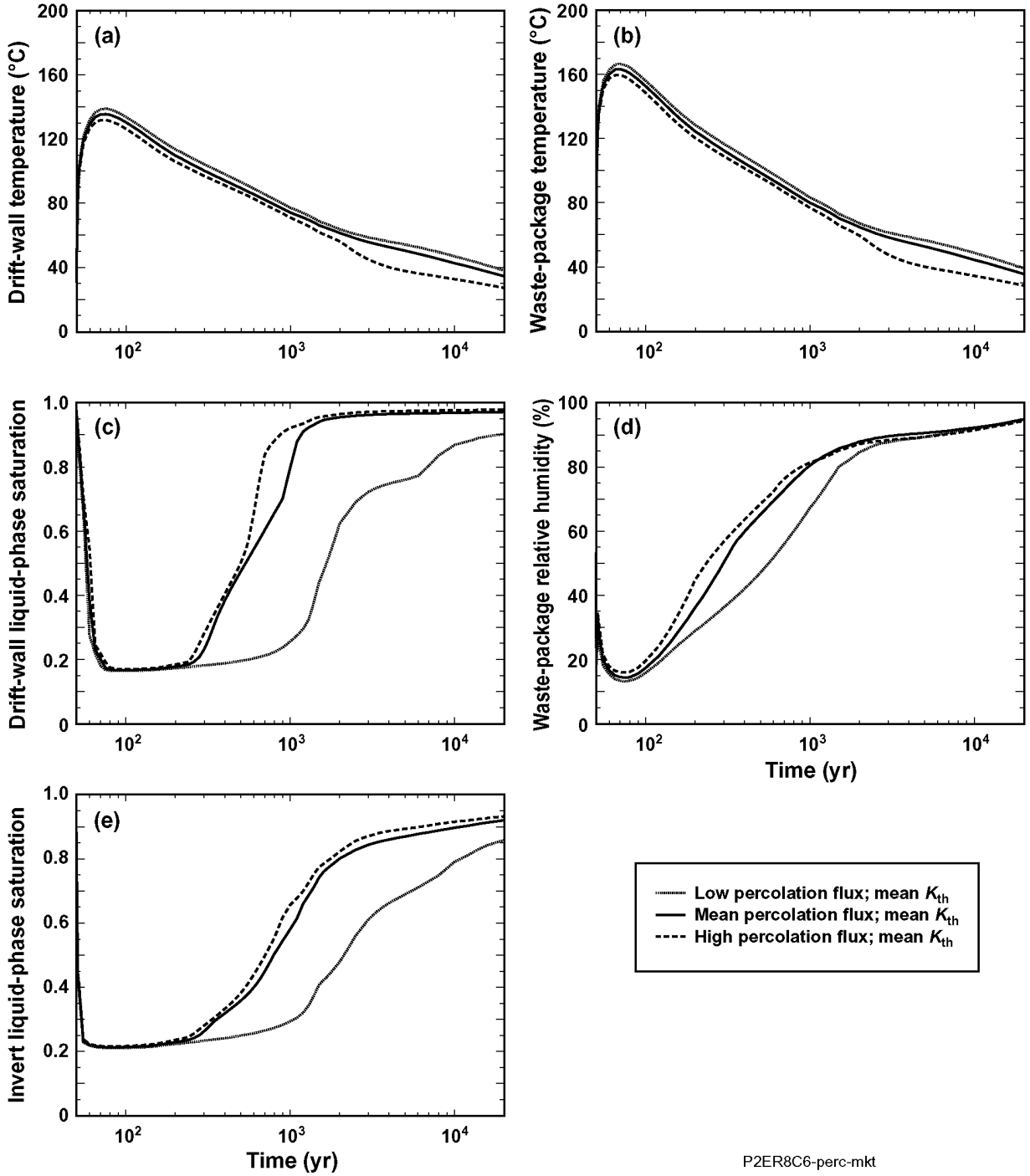

Figure 6.3-21. Thermohydrologic conditions for the pwr1-2 waste package are plotted for lower-bound, mean, and upper-bound infiltration flux cases at the P2ER8C6 location, which is in the Tptpul (tsw33) unit (see Figure 6.3-1 for location). The plotted thermohydrologic variables are (a) drift-wall temperature, (b) waste package temperature, (c) drift-wall liquid-phase saturation, (d) waste package relative humidity, and (e) invert liquid-phase saturation. The pwr1-2 (21-PWR AP CSNF) waste package is the hottest waste package in the sequence (Figure 6.2-2).

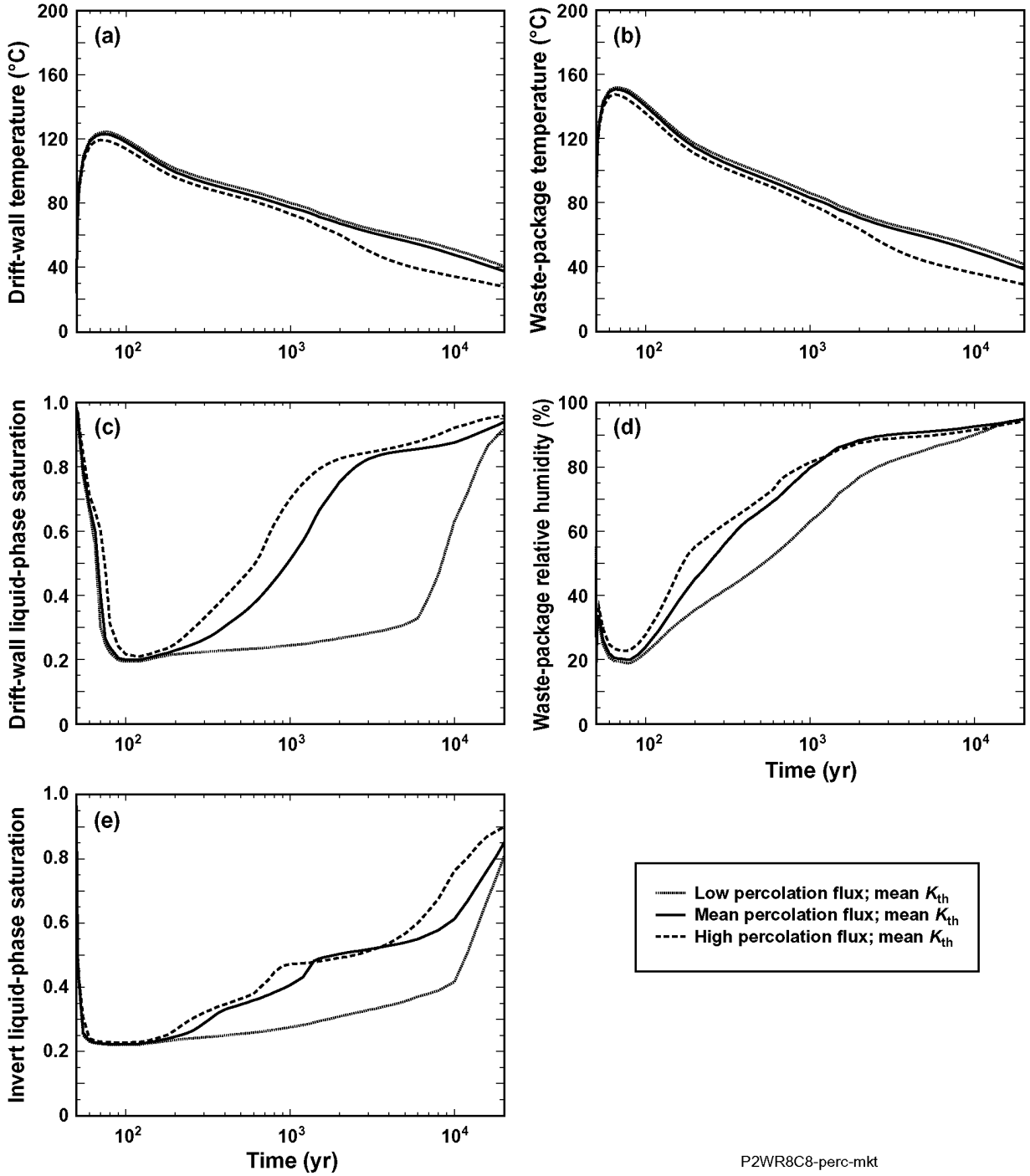

Figure 6.3-22. Thermohydrologic conditions for the pwr1-2 waste package are plotted for the low-, mean, and high-percolation flux cases at the P2WR8C8 location, which is in the Tptpmn (tsw34) unit (see Figure 6.3-1 for location). The plotted thermohydrologic variables are (a) drift-wall temperature, (b) waste package temperature, (c) drift-wall liquid-phase saturation, (d) waste package relative humidity, and (e) invert liquid-phase saturation. The pwr1-2 (21-PWR AP CSNF) waste package is the hottest waste package in the sequence (Figure 6.2-2).

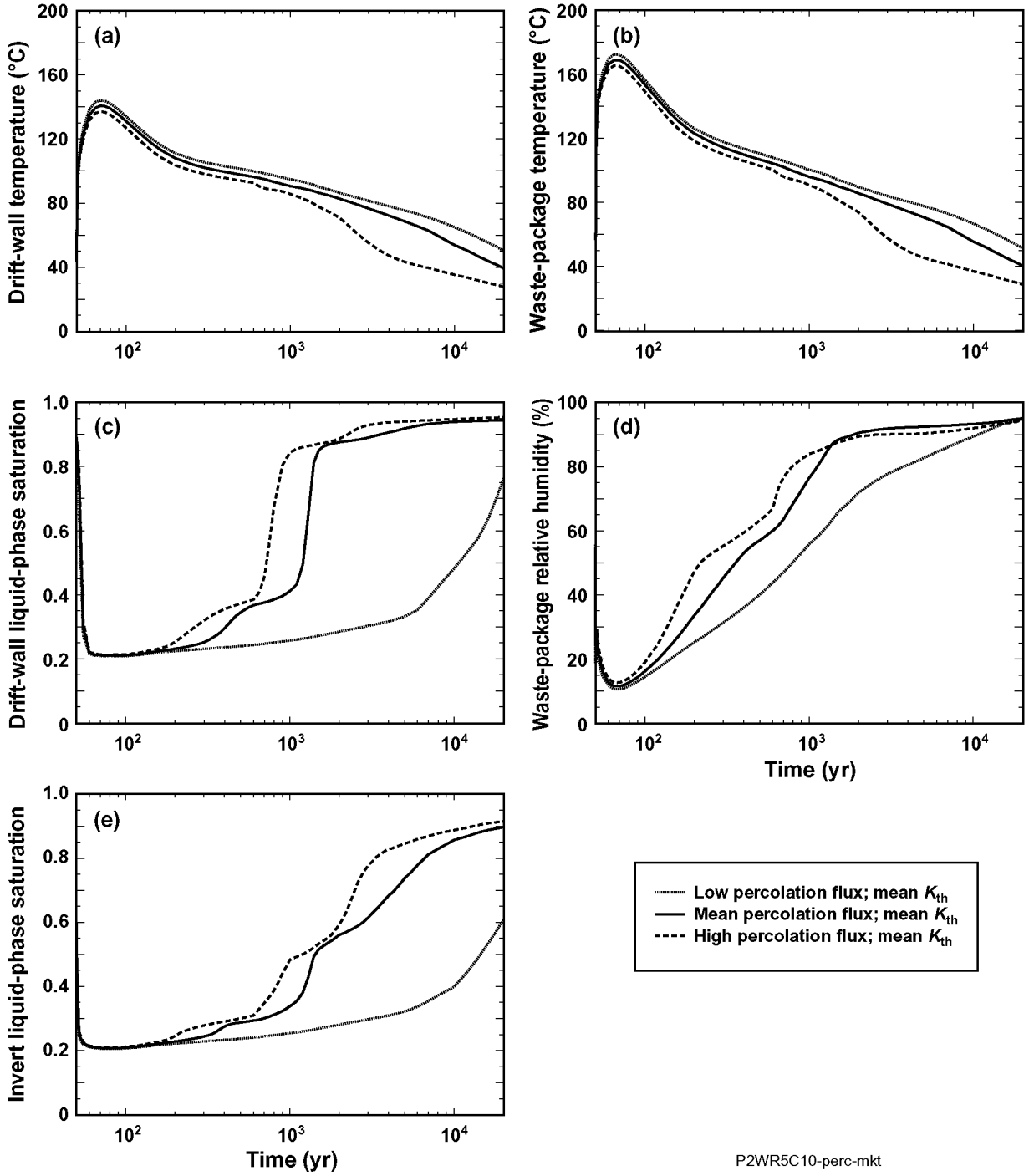

Figure 6.3-23. Thermohydrologic conditions for the pwr1-2 waste package are plotted for the low-, mean, and high-percolation flux cases at the P2WR5C10 location, which is in the Tptpll (tsw35) unit (see Figure 6.3-1 for location). The plotted thermohydrologic variables are (a) drift-wall temperature, (b) waste package temperature, (c) drift-wall liquid-phase saturation, (d) waste package relative humidity, and (e) invert liquid-phase saturation. The pwr1-2 (21-PWR AP CSNF) waste package is the hottest waste package in the sequence (Figure 6.2-2).

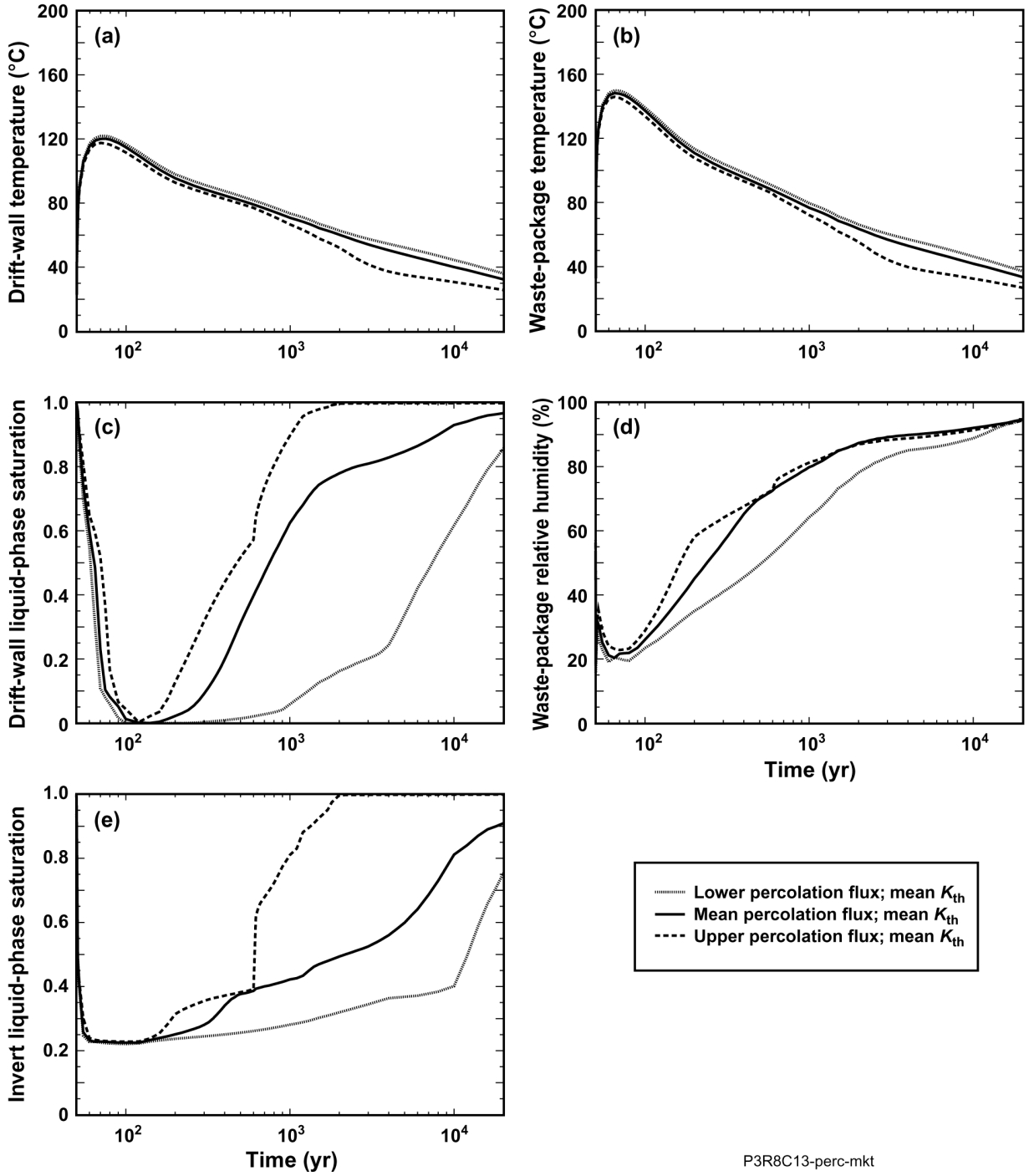

Figure 6.3-24. Thermohydrologic conditions for the pwr1-2 waste package are plotted for the low-, mean, and high-percolation flux cases at the P3R8C13 location, which is in the Tptpln (tsw36) unit (see Figure 6.3-1 for location). The plotted thermohydrologic variables are (a) drift-wall temperature, (b) waste package temperature, (c) drift-wall liquid-phase saturation, (d) waste package relative humidity, and (e) invert liquid-phase saturation. The pwr1-2 (21-PWR AP CSNF) waste package is the hottest waste package in the sequence (Figure 6.2-2).

6.3.2.2 Host-Rock Thermal-Conductivity Uncertainty

The sensitivity of thermohydrologic behavior to host-rock thermal-conductivity uncertainty is addressed for plus and minus one standard deviation about the mean value (Table 6.3-20). The thermal-conductivity data from Table 7-10 of *Thermal Conductivity of the Potential Repository Horizon Model Report* (BSC 2002a) is used to determine plus and minus one standard deviation about the mean for the wet and dry thermal conductivity values for the four host-rock units. Note that the mean values of K_{th} of the Tptpul (tsw33) unit are slightly different from those in Table 7-10 of *Thermal Conductivity of the Potential Repository Horizon Model Report* (BSC 2002a). To be consistent with the other thermohydrologic models, such as those in *Drift-Scale Coupled Processes (DST and TH Seepage) Models* (BSC 2003j), K_{th} for the Tptpul (tsw33) unit is computed as a straight arithmetic average of K_{th} for the Tptpul from Table 7-10 of *Thermal Conductivity of the Potential Repository Horizon Model Report* (BSC 2002a) and the K_{th} of the Tptrl from DTN: SN0303T0503102.008. This averaging for the Tptpul (tsw33) unit is also applied to the other thermal properties to be consistent with *Drift-Scale Coupled Processes (DST and TH Seepage) Models* (BSC 2003j), which computes the thermal properties (including K_{th}) of the Tptpul (tsw33) unit to be the average of the thermal properties of the Tptpul from Table 7-10 of *Thermal Conductivity of the Potential Repository Horizon Model Report* (BSC 2002a) and the thermal properties of the Tptrl unit from DTN: SN0303T0503102.008. Note that Table 7-10 of *Thermal Conductivity of the Potential Repository Horizon Model Report* (BSC 2002a) is a summary of data from DTN: SN0208T0503102.007.

For all locations, host-rock thermal-conductivity uncertainty has a very strong influence on boiling duration (Table 6.3-23), with the influence being stronger for locations further removed from the repository edges. Thus, the P2WR5C10 location, which is located close to the center of the repository, has the widest range (114.3 percent) of the time when boiling at the drift wall ceases. Locations P2ER8C6 and P3R8C13, which are at the edge of the repository, have somewhat smaller ranges (65.2 percent and 75.4 percent, respectively) of the time when boiling ceases at the drift wall. The reason for the strong dependence of boiling-period duration on host-rock thermal conductivity is the result of strong feedback between temperature rise and rock dryout. Where host-rock thermal conductivity is lower, the resulting temperature rise in the host rock is greater, which, in turn, creates a larger rock-dryout zone. This larger rock-dryout zone results in a larger region in which the dry value of thermal conductivity (which is less than the wet value) applies. This larger zone of low (dry) thermal conductivity creates an even greater temperature rise, which, in turn, drives the dryout zone farther out into the host rock. The feedback between increased temperature rise and increased dryout-zone volume, and vice versa, continues.

Host-rock thermal-conductivity uncertainty has a strong influence on dryout/rewetting behavior for the first one-to-two thousand years, as shown in the drift-wall and invert liquid-phase saturation histories (Figures 6.3-25c, 6.3-25e, 6.3.26c, 6.3.26e, 6.3-27c, 6.3-27e, 6.3-28c, and 6.3-28e). Similarly, host-rock thermal-conductivity uncertainty also has a strong influence on the waste package relative humidity histories for the first one-to-two thousand years (Figures 6.3-21d, 6.3-22d, 6.3-23d, and 6.3-24d).

Table 6.3-20. The wet and dry thermal-conductivity values used in the host-rock thermal-conductivity uncertainty study are summarized. Low, mean, and high thermal-conductivity cases are considered for a range of plus and minus one standard deviation about the mean value.

Host-Rock Unit	Dry Thermal Conductivity (W/m^2 °C)			Wet Thermal Conductivity (W/m^2 °C)		
	Low	Mean	High	Low	Mean	High
Tptpul (tsw33)	0.9842	1.24	1.4958	1.5405	1.79	2.0395
Tptpmn (tsw34)	1.1544	1.42	1.6856	1.8188	2.07	2.3212
Tptpll (tsw35)	1.0286	1.28	1.5314	1.6415	1.89	2.1385
Tptpln (tsw36)	1.2056	1.49	1.7744	1.8624	2.13	2.3976

Source: BSC 2002a

Table 6.3-21. The range of peak drift-wall temperatures for the pwr1-2 waste package (resulting from thermal-conductivity uncertainty) is summarized for four locations in the repository (see Figure 6.3-1 for locations). The pwr1-2 (21-PWR AP CSNF) waste package is the hottest waste package in the sequence (Figure 6.2-2). Low, mean, and high thermal-conductivity cases are considered for a range of plus and minus one standard deviation about the mean value.

LDTH-SDT-Submodel Location	Host-Rock Unit	Peak Drift-Wall Temperature (°C)				
		Low Thermal Conductivity	Mean Thermal Conductivity	High Thermal Conductivity	Low to High Range	Low to High Range*
P2ER8C6	Tptpul (tsw33)	153.3	135.5	123.2	30.1	21.8%
P2WR8C8	Tptpmn (tsw34)	136.5	123.0	113.8	22.7	18.1%
P2WR5C10	Tptpll (tsw35)	158.9	140.8	127.4	31.5	22.0%
P3R8C13	Tptpln (tsw36)	132.7	120.2	110.8	21.9	18.0%

NOTE: The range (%) is the range (°C) divided by the peak drift-wall temperature [(low + high)/2].

Table 6.3-22. The range of peak waste package temperatures for the pwr1-2 waste package (resulting from thermal-conductivity uncertainty) is summarized for four locations in the repository (see Figure 6.3-1 for locations). The pwr1-2 (21-PWR AP CSNF) waste package is the hottest waste package in the sequence (Figure 6.2-2). Low, mean, and high thermal-conductivity cases are considered for a range of plus and minus one standard deviation about the mean value.

LDTH-SDT-Submodel Location	Host-Rock Unit	Peak Waste Package Temperature (°C)				
		Low Thermal Conductivity	Mean Thermal Conductivity	High Thermal Conductivity	Low to High Range	Low to High Range*
P2ER8C6	Tptpul (tsw33)	181.2	163.2	151.4	29.8	17.9%
P2WR8C8	Tptpmn (tsw34)	163.8	150.6	141.9	21.9	14.3%
P2WR5C10	Tptpll (tsw35)	187.2	168.8	155.8	31.4	18.3%
P3R8C13	Tptpln (tsw36)	160.6	148.2	139.2	21.4	14.3%

NOTE: The range (%) is the range (°C) divided by the peak drift-wall temperature [(low + high)/2].

Table 6.3-23. The range of the time when boiling at the drift wall ceases for the pwr1-2 waste package (resulting from host-rock thermal-conductivity uncertainty) is summarized for four locations in the repository (see Figure 6.3-1 for locations). The pwr1-2 (21-PWR AP CSNF) waste package is the hottest waste package in the sequence (Figure 6.2-2). Low, mean, and high thermal-conductivity cases are considered for a range of plus and minus one standard deviation about the mean value.

LDTH-SDT-Submodel Location	Host-Rock Unit	Time When Boiling at the Drift Wall Ceases (years)				
		Low Thermal Conductivity	Mean Thermal Conductivity	High Thermal Conductivity	Low to High Range	Low to High Range*
P2ER8C6	Tptpul (tsw33)	508.9	364.8	258.9	250.0	65.2%
P2WR8C8	Tptpmn (tsw34)	412.8	242.8	163.8	249.0	86.4%
P2WR5C10	Tptpll (tsw35)	963.8	623.0	263.0	700.8	114.3%
P3R8C13	Tptpln (tsw36)	309.0	195.2	139.8	169.2	75.4%

NOTE: * The range (%) is the range (years) divided by the average time when drift-wall boiling ceases [(shortest + longest)/2].

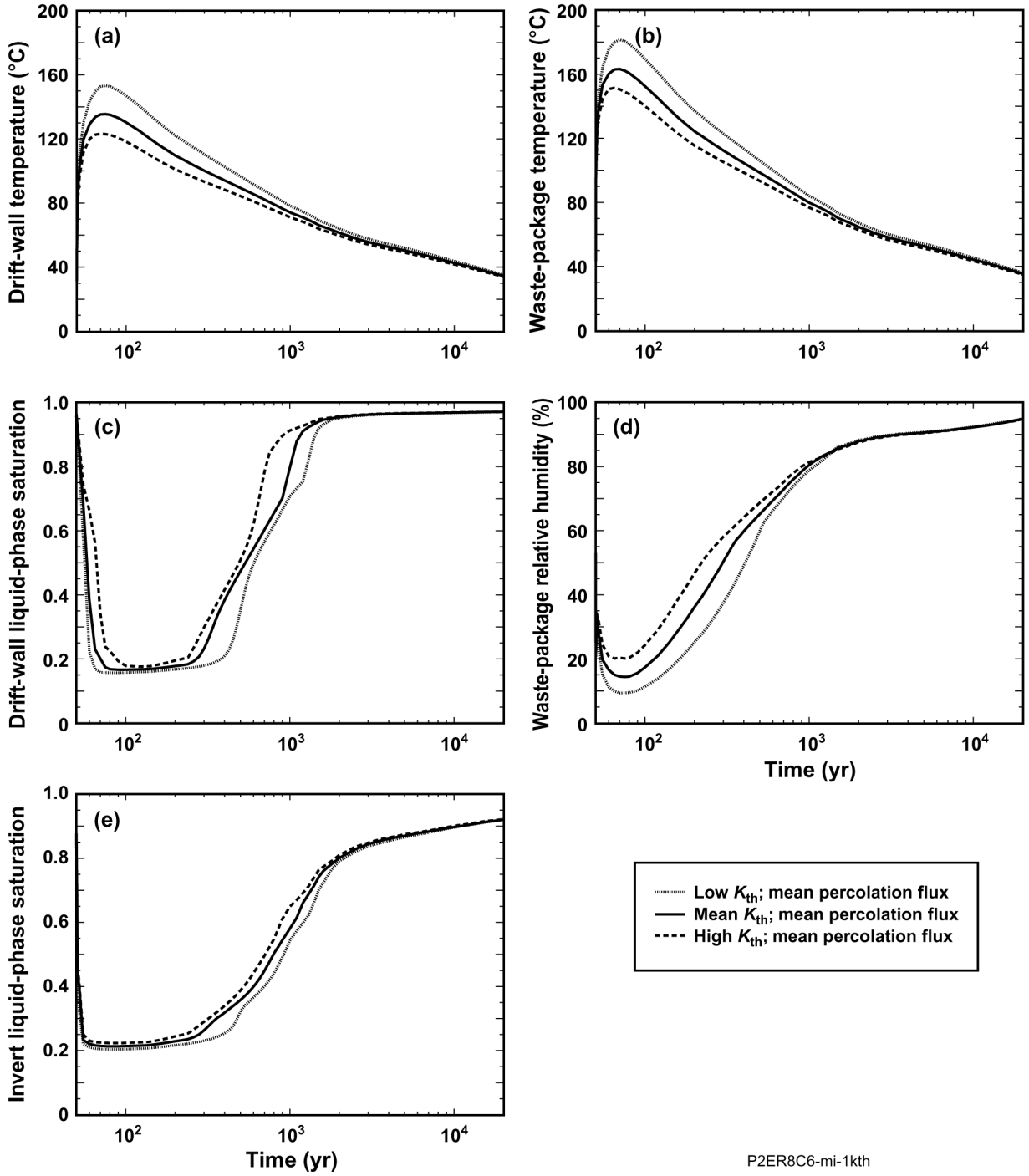

Figure 6.3-25. Thermohydrologic conditions for the pwr1-2 waste package are plotted for the mean infiltration flux case at the P2ER8C6 location, which is in the Tptpul (tsw33) unit (see Figure 6.3-1 for location). Low, mean, and high thermal-conductivity cases are considered for a range of plus and minus one standard deviation about the mean value. The plotted thermohydrologic variables are (a) drift-wall temperature, (b) waste package temperature, (c) drift-wall liquid-phase saturation, (d) waste package relative humidity, and (e) invert liquid-phase saturation. The pwr1-2 (21-PWR AP CSNF) waste package is the hottest waste package in the sequence (Figure 6.2-2).

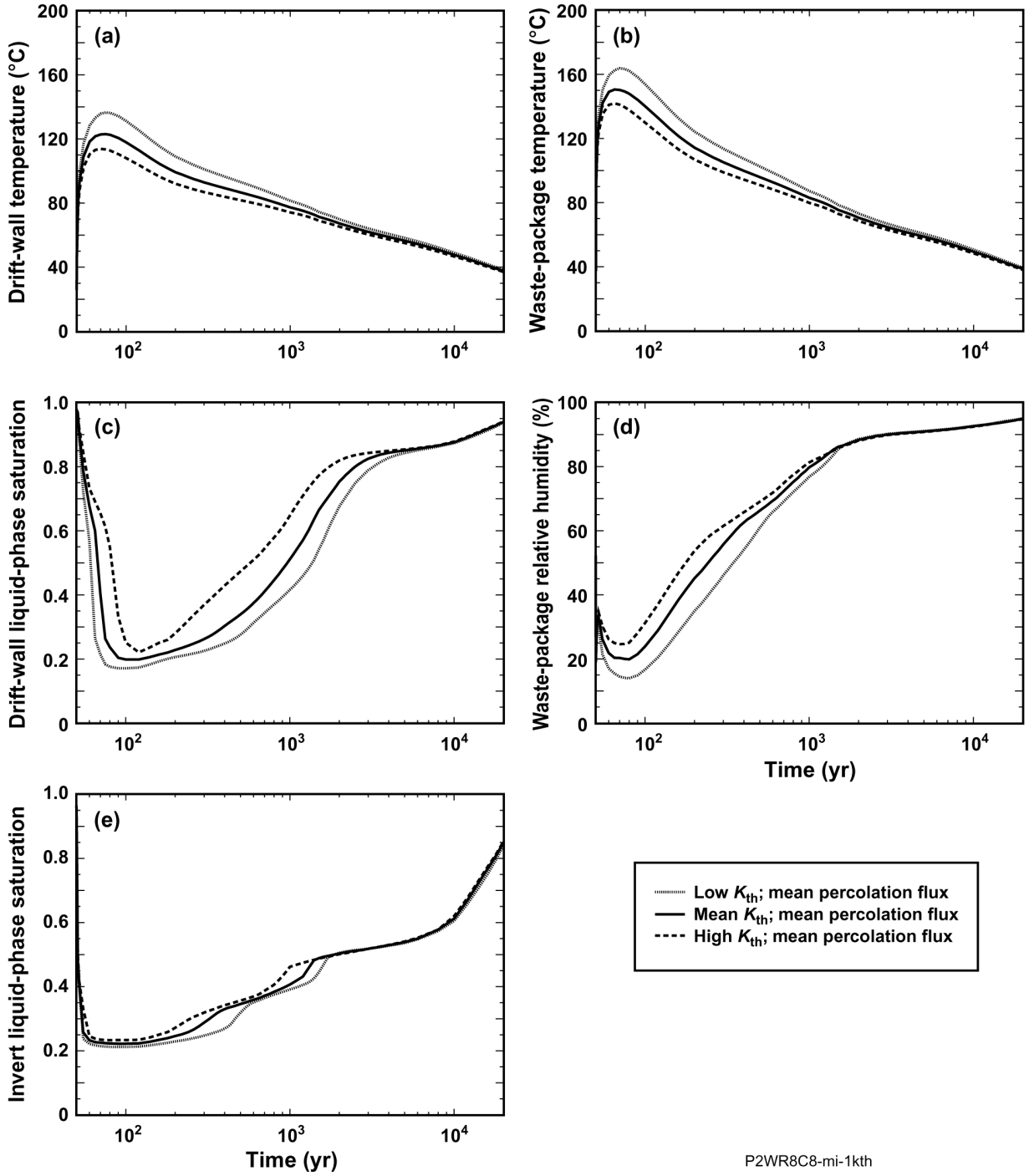

Figure 6.3-26. Thermohydrologic conditions for the pwr1-2 waste package are plotted for the mean infiltration flux case at the P2WR8C8 location, which is in the Tptpmn (tsw34) unit (see Figure 6.3-1 for location). Low, mean, and high thermal-conductivity cases are considered range of plus and minus one standard deviation about the mean value. The plotted thermohydrologic variables are (a) drift-wall temperature, (b) waste package temperature, (c) drift-wall liquid-phase saturation, (d) waste package relative humidity, and (e) invert liquid-phase saturation. The pwr1-2 (21-PWR AP CSNF) waste package is the hottest waste package in the sequence (Figure 6.2-2).

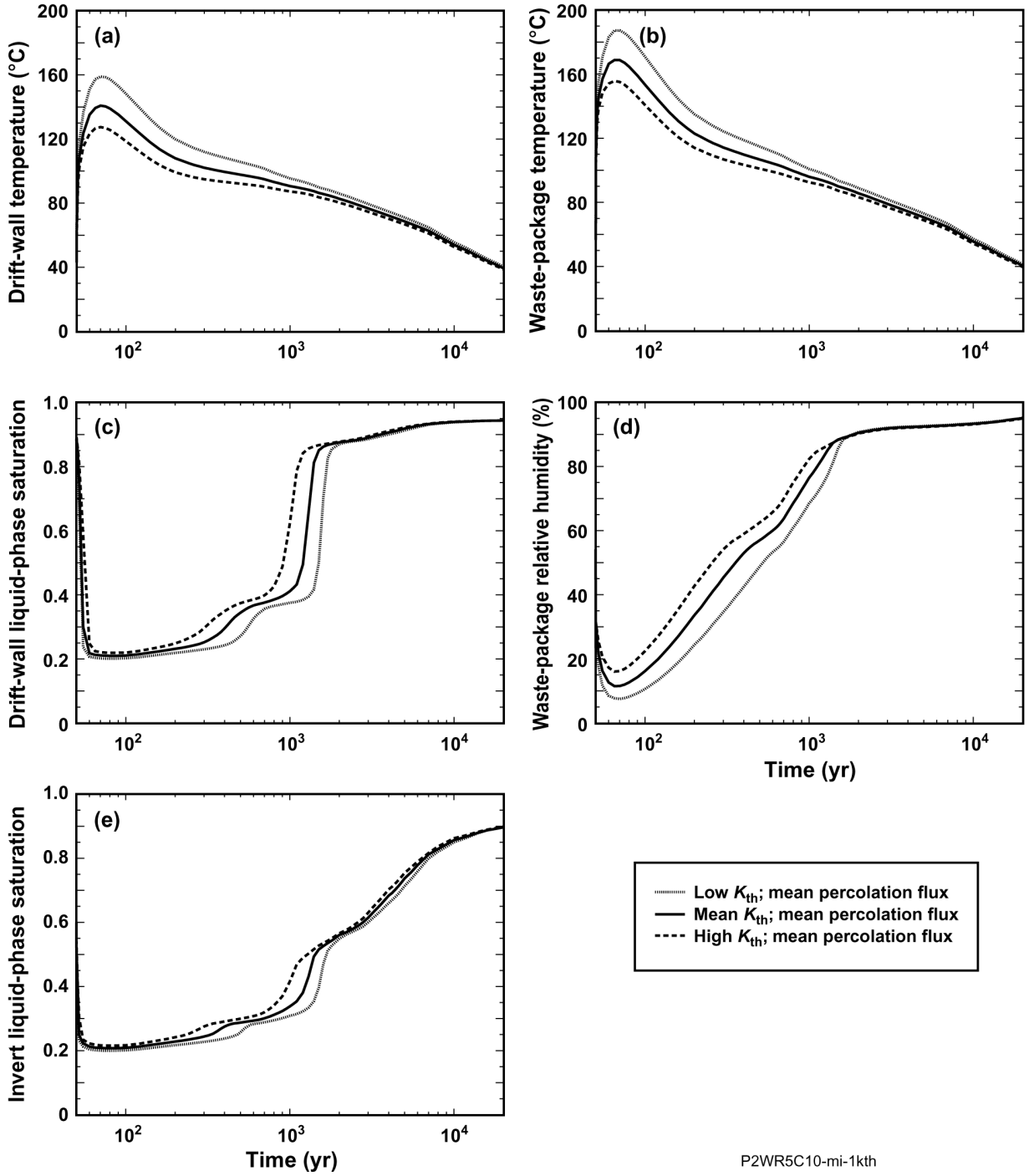

Figure 6.3-27. Thermohydrologic conditions for the pwr1-2 waste package are plotted for the mean infiltration flux case at the P2WR5C10 location, which is in the Tptpll (tsw35) unit (see Figure 6.3-1 for location). Low, mean, and high thermal-conductivity cases are considered for a range of plus and minus one standard deviation about the mean value. The plotted thermohydrologic variables are (a) drift-wall temperature, (b) waste package temperature, (c) drift-wall liquid-phase saturation, (d) waste package relative humidity, and (e) invert liquid-phase saturation. The pwr1-2 (21-PWR AP CSNF) waste package is the hottest waste package in the sequence (Figure 6.2-2).

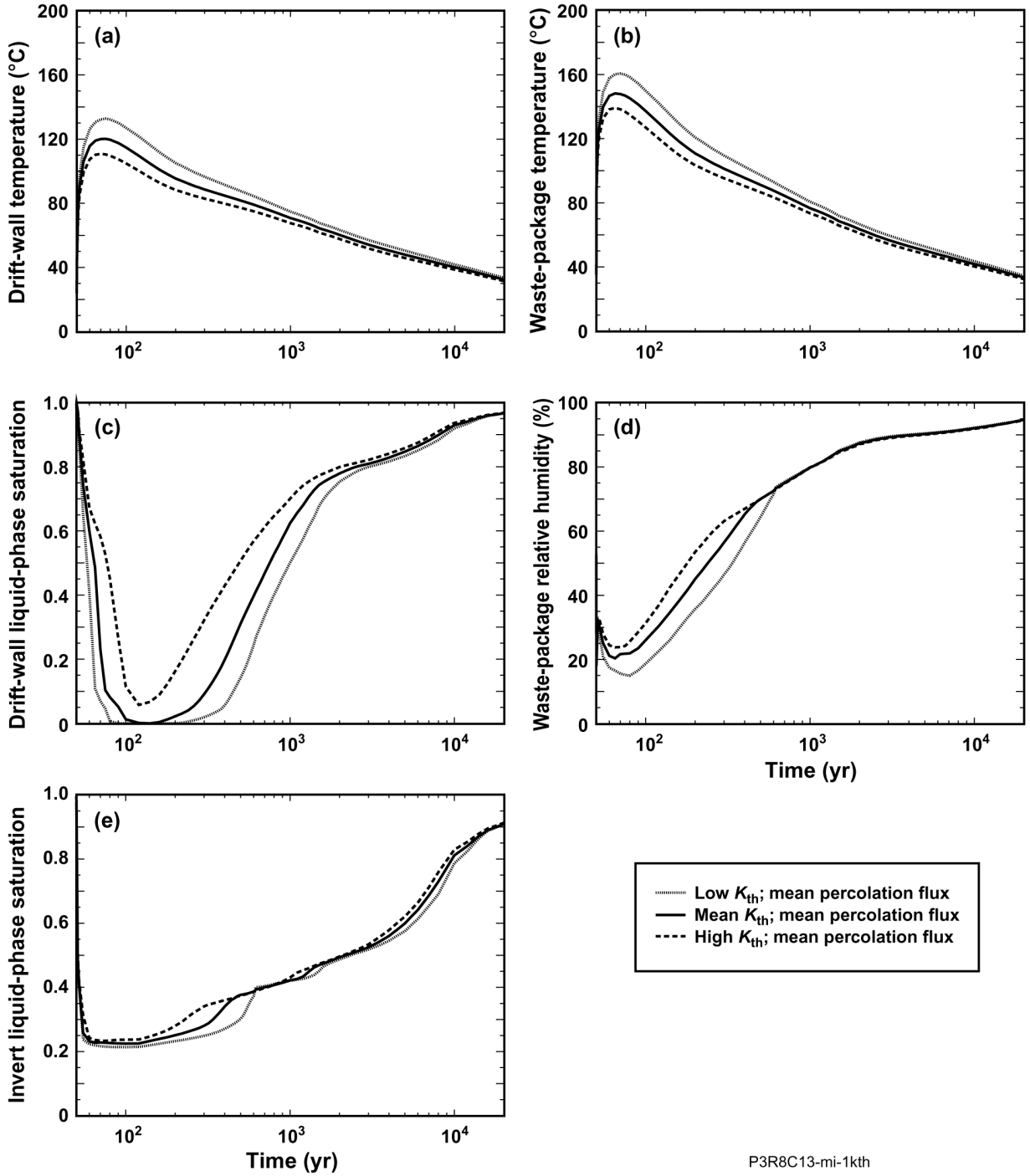

Figure 6.3-28. Thermohydrologic conditions for the pwr1-2 waste package are plotted for the mean infiltration flux case at the P3R8C13 location, which is in the Tptpln (tsw36) unit (see Figure 6.3-1 for location). Low, mean, and high thermal-conductivity cases are considered for a range of plus and minus one standard deviation about the mean value. The plotted thermohydrologic variables are (a) drift-wall temperature, (b) waste package temperature, (c) drift-wall liquid-phase saturation, (d) waste package relative humidity, and (e) invert liquid-phase saturation. The pwr1-2 (21-PWR AP CSNF) waste package is the hottest waste package in the sequence (Figure 6.2-2).

6.3.2.3 Combined Influence of Percolation Flux and Host-Rock Thermal-Conductivity Uncertainty, Including the Influence of Flow Focusing

In this section, the combined influence of percolation flux uncertainty and host-rock thermal-conductivity uncertainty on thermohydrologic behavior at four locations (P2ER8C6, P2WR8C8, P2WR5C10, and P3R8C13) in the repository (Figure 6.3-1) is shown in time histories of drift-wall temperature and liquid-phase saturation, waste package temperature and relative humidity, and invert liquid-phase saturation (Figures 6.3-29 through 6.3-32) for a 21-PWR AP CSNF waste package. Three cases are considered: (1) low percolation flux and low host-rock thermal conductivity, (2) mean percolation flux and mean host rock thermal-conductivity, and (3) high percolation flux and high host-rock thermal conductivity. The values of present-day, monsoonal, and glacial-transition percolation flux values for the low and high percolation flux cases are summarized in Table 6.3-16; the mean percolation flux values are summarized in Table 6.3-7a. The values of dry and wet host-rock thermal conductivity for the low, mean, and high thermal-conductivity cases are summarized in Table 6.3-20. Note that the values of percolation flux for these cases are the same as those considered in Section 6.3.2.1 and that the values of host-rock thermal conductivity are the same as those considered in Section 6.3.2.2. Low percolation flux and low host-rock thermal conductivity both result in higher peak temperatures and longer boiling durations. High percolation flux and high host-rock thermal conductivity both result in lower peak temperatures and shorter boiling durations. The range of peak drift-wall and waste package temperatures that result from the two extreme combinations of percolation flux and host-rock thermal conductivity are summarized in Tables 6.3-24 and 6.3-25, respectively; the range of the time when boiling on the drift wall ceases that result from the two extreme combinations is summarized in Table 6.3-26.

Table 6.3-24. The range of peak drift-wall temperatures for the pwr1-2 waste package (resulting from a combination of percolation flux Q_{perc} and thermal-conductivity K_{th} uncertainty) is summarized for four locations in the repository (see Figure 6.3-1 for locations). The pwr1-2 (21-PWR AP CSNF) waste package is the hottest waste package in the sequence (Figure 6.2-2). Low, mean, and high thermal-conductivity cases are considered for a range of plus and minus one standard deviation about the mean.

LDTH-SDT-Submodel Location	Host-Rock Unit	Peak Drift-Wall Temperature (°C)				
		Low Q_{perc} Low K_{th}	Mean Q_{perc} Mean K_{th}	High Q_{perc} High K_{th}	Low to High Range	Low to High Range*
P2ER8C6	Tptpul (tsw33)	156.9	135.5	120.4	36.5	26.3%
P2WR8C8	Tptpmn (tsw34)	138.0	123.0	111.4	26.6	21.3%
P2WR5C10	Tptpll (tsw35)	162.8	140.8	124.5	38.3	26.7%
P3R8C13	Tptpln (tsw36)	136.1	120.2	108.8	27.3	22.3%

NOTE: *The range (%) is the range (°C) divided by the peak drift-wall temperature [(low + high)/2].

Table 6.3-25. The range of peak waste package temperatures for the pwr1-2 waste package (resulting from a combination of percolation flux Q_{perc} and thermal-conductivity K_{th} uncertainty) is summarized for four locations in the repository (see Figure 6.3-1 for locations). The pwr1-2 (21-PWR AP CSNF) waste package is the hottest waste package in the sequence (Figure 6.2-2). Low, mean, and high thermal-conductivity cases are considered for a range of plus and minus one standard deviation about the mean.

LDTH-SDT-Submodel Location	Host-Rock Unit	Peak Waste Package Temperature (°C)				
		Low Q_{perc} Low K_{th}	Mean Q_{perc} Mean K_{th}	High Q_{perc} High K_{th}	Low to High Range	Low to High Range*
P2ER8C6	Tptpul (tsw33)	185.1	163.2	148.7	36.4	21.8%
P2WR8C8	Tptpmn (tsw34)	165.4	150.6	139.5	25.9	17.0%
P2WR5C10	Tptpll (tsw35)	191.0	168.8	152.7	38.3	22.3%
P3R8C13	Tptpln (tsw36)	163.9	148.2	137.3	26.6	17.7%

NOTE: *The range (%) is the range (°C) divided by the peak drift-wall temperature [(low + high)/2].

Table 6.3-26. The range of the time when boiling at the drift wall ceases for the pwr1-2 waste package (resulting from a combination of percolation flux Q_{perc} and thermal-conductivity K_{th} uncertainty) is summarized for four locations in the repository (see Figure 6.3-1 for location). The pwr1-2 (21-PWR AP CSNF) waste package is the hottest waste package in the sequence (Figure 6.2-2). Low, mean, and high thermal-conductivity cases are considered for a range of plus and minus one standard deviation about the mean.

LDTH-SDT-Submodel Location	Host-Rock Unit	Time When Boiling at the Drift Wall Ceases (years)				
		Low Q_{perc} Low K_{th}	Mean Q_{perc} Mean K_{th}	High Q_{perc} High K_{th}	Low to High Range	Low to High Range*
P2ER8C6	Tptpul (tsw33)	615.5	364.8	222.5	393.0	93.8%
P2WR8C8	Tptpmn (tsw34)	514.1	242.8	144.7	369.4	112.1%
P2WR5C10	Tptpll (tsw35)	1,415.8	623.0	207.4	1,208.4	148.9%
P3R8C13	Tptpln (tsw36)	377.2	195.2	129.8	247.4	97.6%

NOTE: *The range (%) is the range (years) divided by the average time when drift-wall boiling ceases [(shortest + longest)/2].

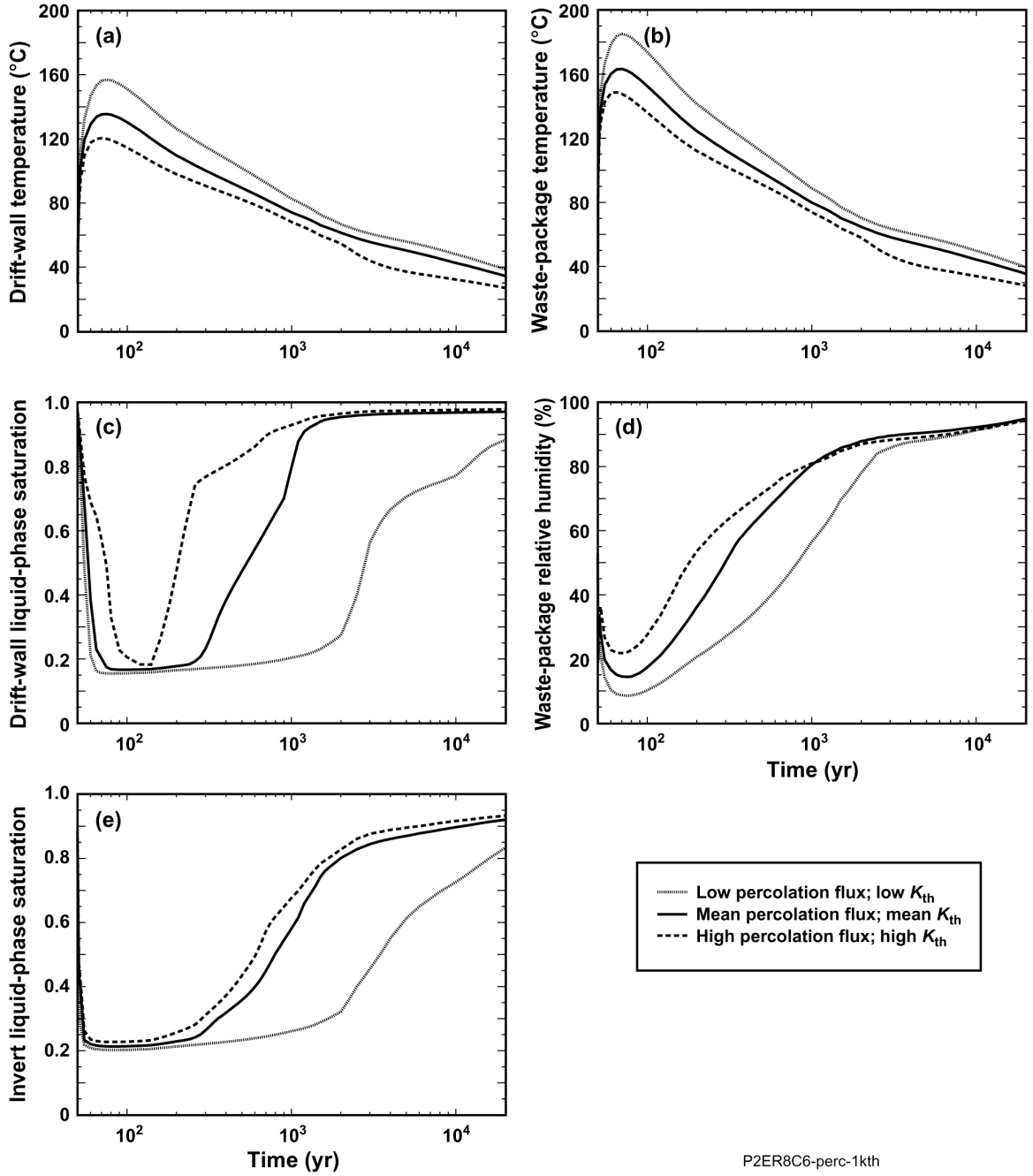

Figure 6.3-29. Thermohydrologic conditions for the pwr1-2 waste package are plotted for three cases at the P2ER8C6 location, which is in the Tptpul (tsw33) unit (see Figure 6.3-1 for location). These cases are: (1) low percolation flux and low thermal-conductivity, (2) mean percolation flux and mean thermal conductivity, and (3) high percolation flux and high thermal conductivity, where the thermal conductivity is varied by plus and minus one standard deviation about the mean. The plotted thermohydrologic variables are (a) drift-wall temperature, (b) waste package temperature, (c) drift-wall liquid-phase saturation, (d) waste package relative humidity, and (e) invert liquid-phase saturation. The pwr1-2 (21-PWR AP CSNF) waste package is the hottest waste package in the sequence (Figure 6.2-2).

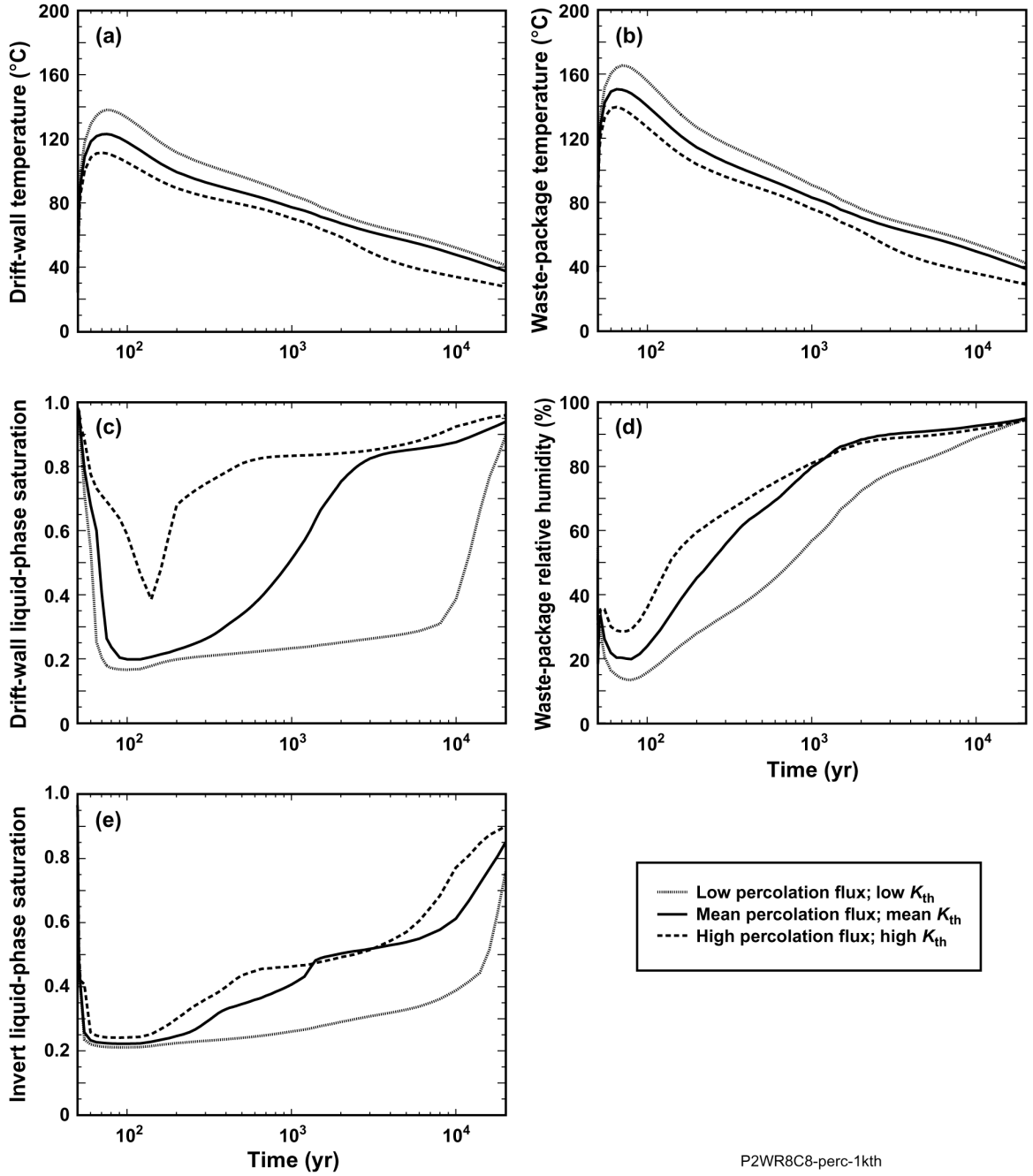

Figure 6.3-30. Thermohydrologic conditions for the pwr1-2 waste package are plotted for three cases at the P2WR8C8 location, which is in the Tptpmn (tsw34) unit (see Figure 6.3-1 for location). These cases are: (1) low percolation flux and low thermal conductivity, (2) mean percolation flux and mean thermal conductivity, and (3) high percolation flux and high thermal conductivity, where the thermal conductivity is varied by plus and minus one standard deviation about the mean. The plotted thermohydrologic variables are (a) drift-wall temperature, (b) waste package temperature, (c) drift-wall liquid-phase saturation, (d) waste package relative humidity, and (e) invert liquid-phase saturation. The pwr1-2 (21-PWR AP CSNF) waste package is the hottest waste package in the sequence (Figure 6.2-2).

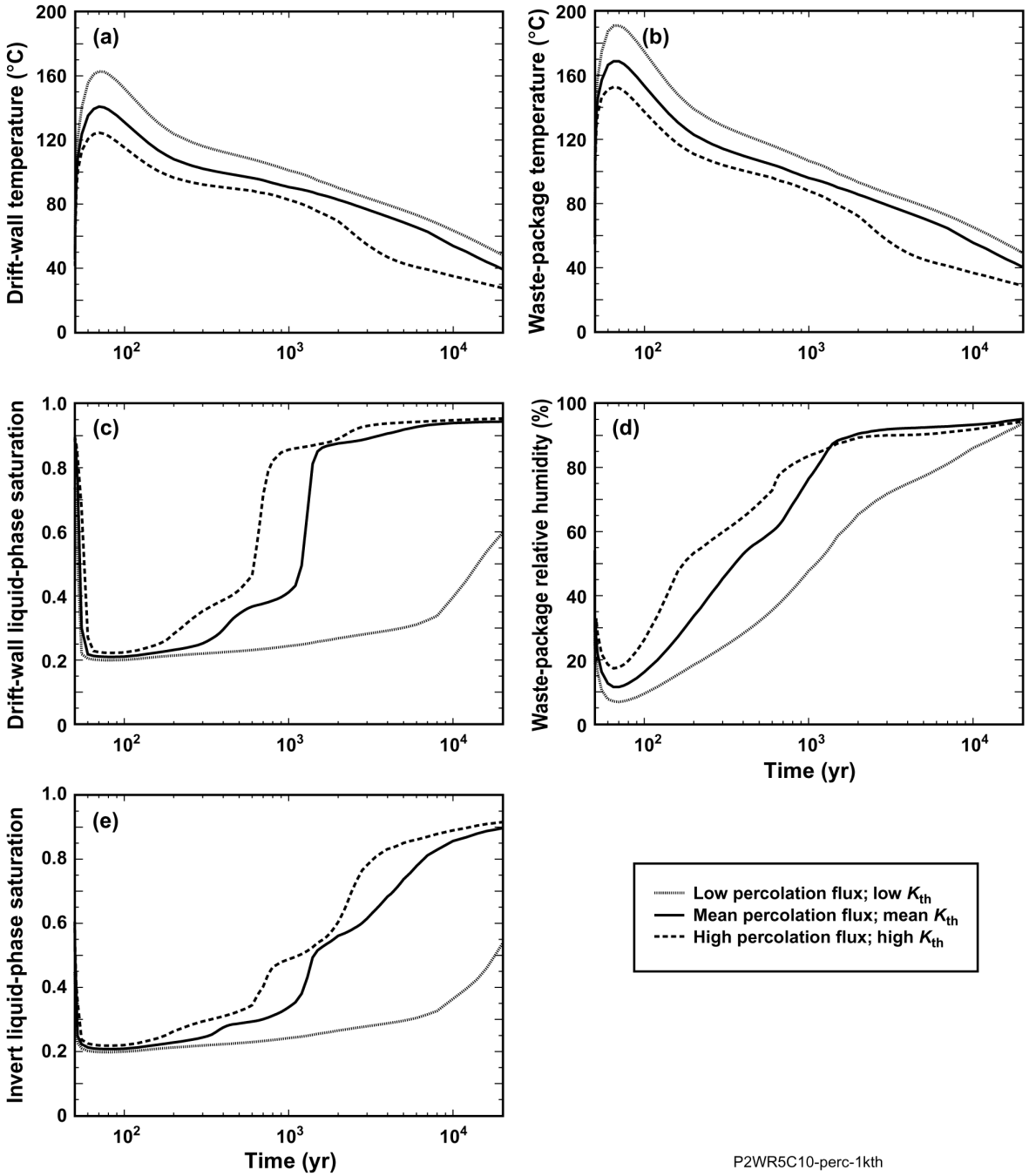

Figure 6.3-31. Thermohydrologic conditions for the pwr1-2 waste package are plotted for three cases at the P2WR5C10 location, which is in the Tptpll (tsw35) unit (see Figure 6.3-1 for location). These cases are: (1) low percolation flux and low thermal conductivity, (2) mean percolation flux and mean thermal conductivity, and (3) high percolation flux and high thermal conductivity, where the thermal conductivity is varied by plus and minus one standard deviation about the mean. The plotted thermohydrologic variables are (a) drift-wall temperature, (b) waste package temperature, (c) drift-wall liquid-phase saturation, (d) waste package relative humidity, and (e) invert liquid-phase saturation. The pwr1-2 (21-PWR AP CSNF) waste package is the hottest waste package in the sequence (Figure 6.2-2).

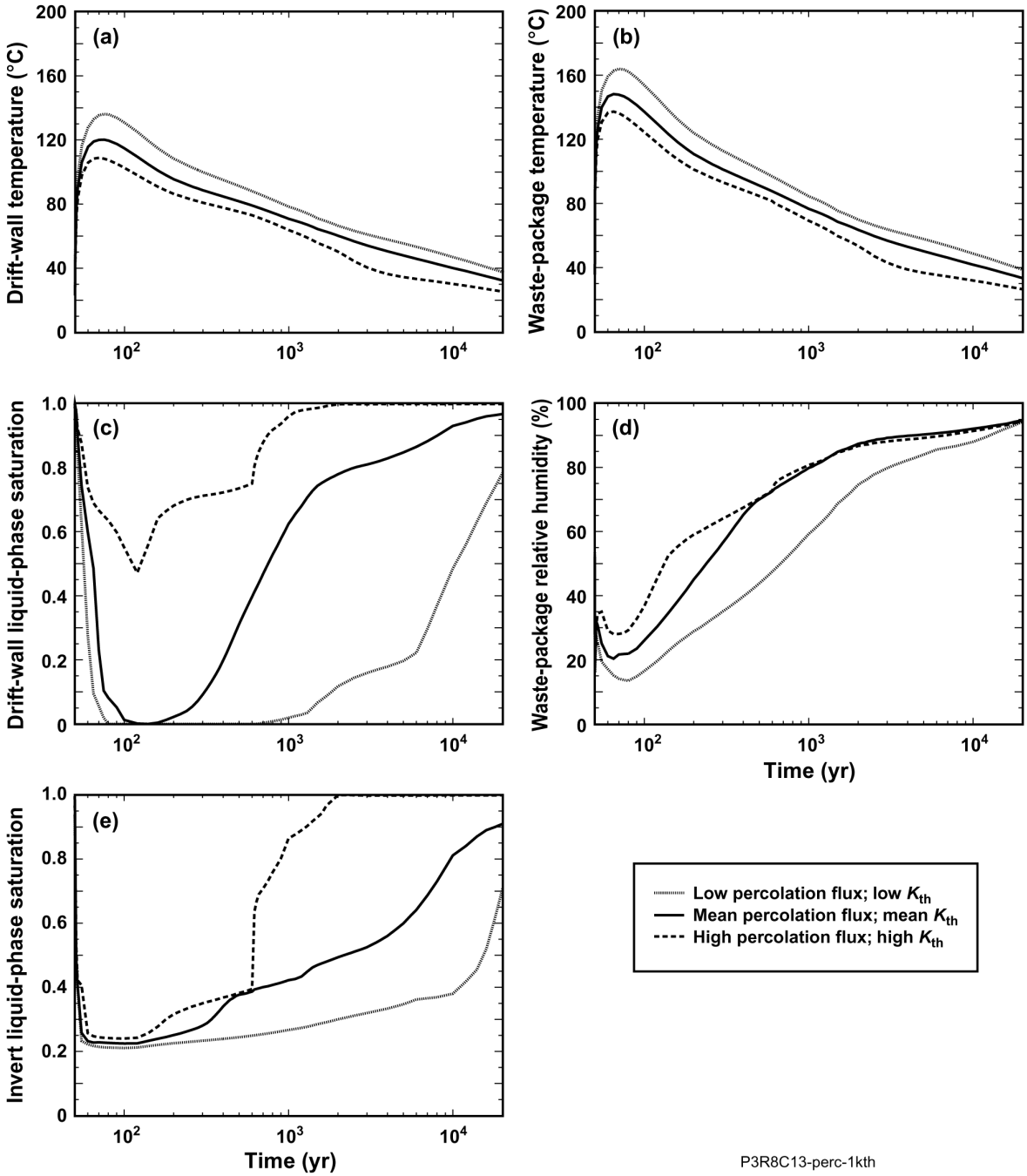

Figure 6.3-32. Thermohydrologic conditions for the pwr1-2 waste package are plotted for three cases at the P3R8C13 location, which is in the Tptpln (tsw36) unit (see Figure 6.3-1 for location). These cases are: (1) low percolation flux and low thermal-conductivity, (2) mean percolation flux and mean thermal conductivity, and (3) high percolation flux and high thermal conductivity, where the thermal conductivity is varied by plus and minus one standard deviation about the mean. The plotted thermohydrologic variables are (a) drift-wall temperature, (b) waste package temperature, (c) drift-wall liquid-phase saturation, (d) waste package relative humidity, and (e) invert liquid-phase saturation. The pwr1-2 (21-PWR AP CSNF) waste package is the hottest waste package in the sequence (Figure 6.2-2).

An important question to ask is whether the combined influence of percolation flux uncertainty and host-rock thermal-conductivity on peak temperatures is simply the sum of the individual contributions to peak-temperature uncertainty. Table 6.3-27 compares the ranges of peak temperatures resulting from (1) percolation flux uncertainty, (2) host-rock thermal-conductivity uncertainty, and (3) a combination of percolation flux and host-rock thermal-conductivity uncertainty; Table 6.3-28 makes the same comparison for peak waste package temperatures. Note that when one adds the range of peak temperatures resulting from percolation flux uncertainty to that resulting from host-rock thermal-conductivity uncertainty, it is nearly identical to the range of peak temperatures resulting from a combination of percolation flux uncertainty and host-rock thermal-conductivity. Taking location P2WR5C10 in Table 6.3-27 as an example: adding the peak-temperature range resulting from percolation flux uncertainty (6.9°C) to that resulting from host-rock thermal-conductivity uncertainty (31.5°C) yields a total of 38.4°C, which is extremely close to the peak-temperature range (38.3°C) that results when the influence of percolation flux and host-rock thermal-conductivity uncertainty is combined. This principal has extremely useful implications to engineered barrier system performance assessments because (1) percolation flux and host-rock thermal-conductivity are the two most important natural system parameters influencing peak temperatures in the emplacement drifts and (2) it is possible to use superposition to quantify the influence of percolation flux and host-rock thermal-conductivity uncertainty on peak temperatures within emplacement drifts.

A related important question is whether the combined influence of percolation flux uncertainty and host-rock thermal-conductivity on boiling duration is simply the sum of the individual contributions to boiling-duration uncertainty. Table 6.3-29 compares the ranges of the time when boiling at the drift wall ceases resulting from (1) percolation flux uncertainty, (2) host-rock thermal-conductivity uncertainty, and (3) a combination of percolation flux and host-rock thermal-conductivity uncertainty. When one adds the range of time when drift-wall boiling ends resulting from percolation flux uncertainty to that resulting from host-rock thermal-conductivity uncertainty, it is nearly equal to the range of boiling duration resulting from a combination of percolation flux uncertainty and host-rock thermal-conductivity. Taking location P2WR5C10 in Table 6.3-29 as an example: adding the range of the time when boiling at the drift wall ends resulting from percolation flux uncertainty (484.5 years) to that resulting from host-rock thermal-conductivity uncertainty (700.8 years) yields a total of 1,185.3 years, which is only slightly less than the range (1,208.4 years) that results when the influence of percolation flux and host-rock thermal-conductivity uncertainty is combined. In general, range resulting from the combined uncertainties is always slightly greater than the sum of the individual contributions to boiling-duration uncertainty. The important distinction between peak temperatures and the time when boiling at the drift wall ceases is that peak temperatures occur relatively early (usually during the first 10 years following the end of the ventilation period), while boiling at the drift wall persists from several hundred years up to nearly two thousand years. Consequently, there is more time for feedback between the influence of host-rock thermal conductivity and that of percolation flux. For example, lower values of thermal conductivity enhance the significance of the larger rock-dryout zone that is inherent to lower values of percolation flux. Because peak temperatures occur only about ten years into the boiling period and because significant rock dryout only occurs during the boiling period, there is much less time for feedback between the influence of host-rock thermal conductivity and that of percolation flux.

Table 6.3-27. The range of peak drift-wall temperatures for the pwr1-2 waste package resulting from various combinations of percolation flux Q_{perc} and thermal-conductivity K_{th} uncertainty is summarized for four locations in the repository (see Figure 6.3-1 for locations). The pwr1-2 (21-PWR AP CSNF) waste package is the hottest waste package in the sequence (Figure 6.2-2).

LDTH-SDT-Submodel Location	Host-Rock Unit	Influence of Percolation Flux Uncertainty on Peak Drift-Wall Temperature		Influence of Host-Rock Thermal-Conductivity Uncertainty on Peak Drift-Wall Temperature		Influence of Combined Percolation Flux and Host-Rock Thermal-Conductivity Uncertainty on Peak Drift-Wall Temperature	
		Range (°C)	Range (%)	Range (°C)	Range (%)	Range (°C)	Range (%)
P2ER8C6	Tptpul (tsw33)	7.0	5.2%	30.1	21.8%	36.5	26.3%
P2WR8C8	Tptpmn (tsw34)	5.1	4.2%	22.7	18.1%	26.6	21.3%
P2WR5C10	Tptpll (tsw35)	6.9	4.9%	31.5	22.0%	38.3	26.7%
P3R8C13	Tptpln (tsw36)	4.4	3.7%	21.9	18.0%	27.3	22.3%

Table 6.3-28. The range of peak waste package temperatures for the pwr1-2 waste package resulting from various combinations of percolation flux Q_{perc} and thermal-conductivity K_{th} uncertainty is summarized for four locations in the repository (see Figure 6.3-1 for locations). The pwr1-2 (21-PWR AP CSNF) waste package is the hottest waste package in the sequence (Figure 6.2-2).

LDTH-SDT-Submodel Location	Host-Rock Unit	Influence of Percolation Flux Uncertainty on Peak Waste Package Temperature		Influence of Host-Rock Thermal Conductivity Uncertainty on Peak Waste Package Temperature		Influence of Combined Percolation Flux and Host-Rock Thermal-Conductivity Uncertainty on Peak Waste Package Temperature	
		Range (°C)	Range (%)	Range (°C)	Range (%)	Range (°C)	Range (%)
P2ER8C6	Tptpul (tsw33)	7.0	4.3%	29.8	17.9%	36.4	21.8%
P2WR8C8	Tptpmn (tsw34)	4.3	2.9%	21.9	14.3%	25.9	17.0%
P2WR5C10	Tptpll (tsw35)	7.0	4.1%	31.4	18.3%	38.3	22.3%
P3R8C13	Tptpln (tsw36)	4.0	2.7%	21.4	14.3%	26.6	17.7%

The combined influence of percolation flux uncertainty and host-rock thermal conductivity uncertainty on dryout/rewetting is illustrated by the drift-wall and invert liquid-phase saturation histories (Figures 6.3-29c, 6.3-29e, 6.3-30c, 6.3-30e, 6.3-31c, 6.3-31e, 6.3-32c, and 6.3-32e). The time for liquid-phase saturation to rewet back to ambient values ranges by two orders of magnitude for these cases. The combined influence of percolation flux uncertainty and host-rock thermal conductivity uncertainty on waste package relative humidity histories is shown in Figures 6.3-29d, 6.3-30d, 6.3-31d, and 6.3-32d. Because of the contribution of the temperature difference between the waste package and the drift wall on relative humidity reduction on waste packages, the combined influence on percolation flux and host-rock thermal-conductivity uncertainty on waste package relative humidity, while strong, is not as strong as it is for liquid-phase saturation histories.

Table 6.3-29. The range of the time when boiling at the drift wall ceases for the pwr1-2 waste package resulting from various combinations of percolation flux Q_{perc} and thermal-conductivity K_{th} uncertainty is summarized for four locations in the repository (see Figure 6.3-1 for locations). The pwr1-2 (21-PWR AP CSNF) waste package is the hottest waste package in the sequence (Figure 6.2-2).

LDTH-SDT-Submodel Location	Host-Rock Unit	Influence of Percolation Flux Uncertainty on Time When Boiling at the Drift Wall Ceases		Influence of Host-Rock Thermal-Conductivity Uncertainty on Time When Boiling at the Drift Wall Ceases		Influence of Combined Percolation Flux and Host-Rock Thermal-Conductivity Uncertainty on Time When Boiling at the Drift Wall Ceases	
		Range (years)	Range (%)	Range (years)	Range (%)	Range (years)	Range (%)
P2ER8C6	Tptpul (tsw33)	124.8	33.2%	250.0	65.2%	393.0	93.8%
P2WR8C8	Tptpmn (tsw34)	88.4	36.5%	249.0	86.4%	369.4	112.1%
P2WR5C10	Tptpll (tsw35)	484.5	75.6%	700.8	114.3%	1,208.4	148.9%
P3R8C13	Tptpln (tsw36)	49.0	24.5%	169.2	75.4%	247.4	97.6%

6.3.2.4 Influence of Hydrologic-Property Uncertainty on In-Drift Temperature and Relative Humidity

The primary purpose of this section is to help determine whether it is necessary to propagate hydrologic-property uncertainty in the MSTHM calculations for TSPA-LA. The primary hydrologic property of interest is the bulk permeability of the host rock; this parameter is primarily affected by the permeability of the fracture network. As discussed in Section 6.3.2, a sensitivity study (BSC 2001b, Section 5.3.1.4.7) found that host-rock bulk permeability has a minor influence on peak temperatures and boiling-period duration. Therefore, host-rock bulk permeability uncertainty does not need to be propagated in the MSTHM calculations for TSPA-LA. In this section, the influence of hydrologic-property uncertainty is further addressed by investigating the impact of utilizing various hydrologic-property sets that have differing values of matrix and fracture properties in the four host-rock units (Tptpul, Tptpmn, Tptpll, and Tptpln).

The influence of hydrologic-property uncertainty on in-drift temperature and relative humidity at four locations (P2ER8C6, P2WR8C8, P2WR5C10, and P3R8C13) in the repository (Figure 6.3-1) is illustrated in time histories of drip-shield temperature and relative humidity (Figures 6.3-33 through 6.3-36). These time histories were generated with the use of the LDTH submodel (Section 6.2.6), which is the primary thermohydrologic submodel in the MSTHM family of submodels. Because the LDTH submodel is the only MSTHM submodel that uses hydrologic-property information as input, it is reasonable to use the results of the LDTH submodel to investigate the degree of sensitivity of in-drift temperature and relative humidity to hydrologic-property uncertainty. The LDTH-submodel calculations in this section were conducted for an Areal Mass Loading (AML) of 55 MTU/acre. Thus, these results correspond to line-average heat-generation conditions for a repository location far enough away from the repository edges not to be influenced by the edge-cooling effect. For these four locations in the repository, four different cases are investigated: (1) lower-bound infiltration flux case with lower-bound infiltration flux property set, (DTN: LB0208UZDSCPLI.002), (2) lower-bound infiltration flux case with modified-mean infiltration flux property set, (3) upper-bound infiltration flux case with upper-bound infiltration flux property set (DTN: LB0302UZDSCPUI.002), and (4) upper-bound

infiltration flux case with modified-mean infiltration flux property set. The modified-mean infiltration flux property set is used in all of the MSTHM calculations discussed in Sections 6.3.2.1 through 6.3.2.3 and in Section 6.3.3. These pairs of cases were chosen to be able to discern the influence of hydrologic properties on in-drift temperature and relative humidity. Because temperature and relative humidity on the drip shield are key measures of in-drift thermohydrologic conditions, this section focuses on those parameters.

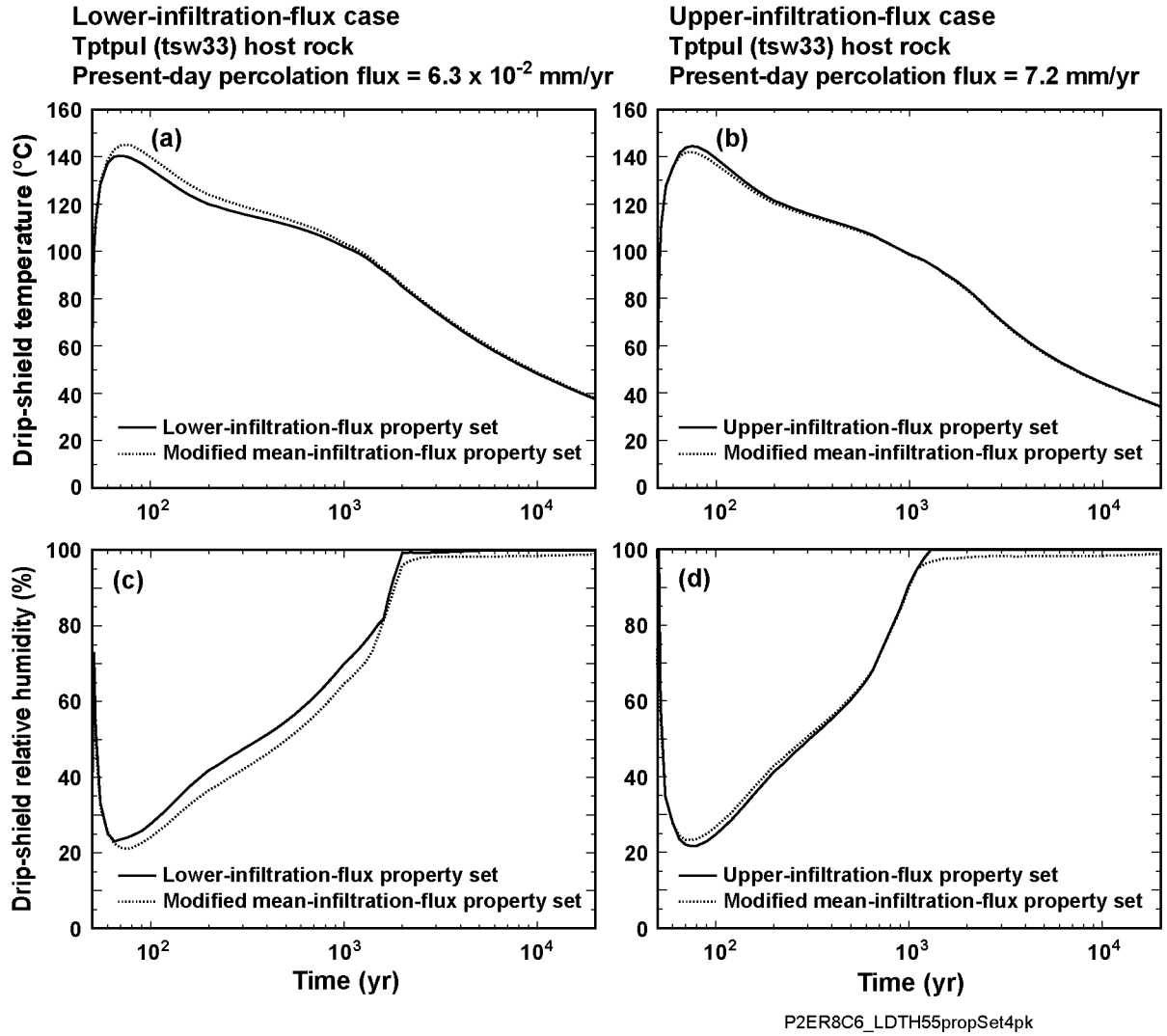

Figure 6.3-33. Drip-shield temperature (a,b) and relative humidity (c,d) for line-averaged heating conditions are plotted for four cases at the P2ER8C6 location, which is in the Tptpul (tsw33) unit (see Figure 6.3-1 for location). These cases are: (1) lower-bound infiltration flux case with lower-bound infiltration flux property set, (2) lower-bound infiltration flux case with modified-mean infiltration flux property set, (3) upper-bound infiltration flux case with upper-bound infiltration flux property set, and (4) upper-bound infiltration flux case with modified-mean infiltration flux property set.

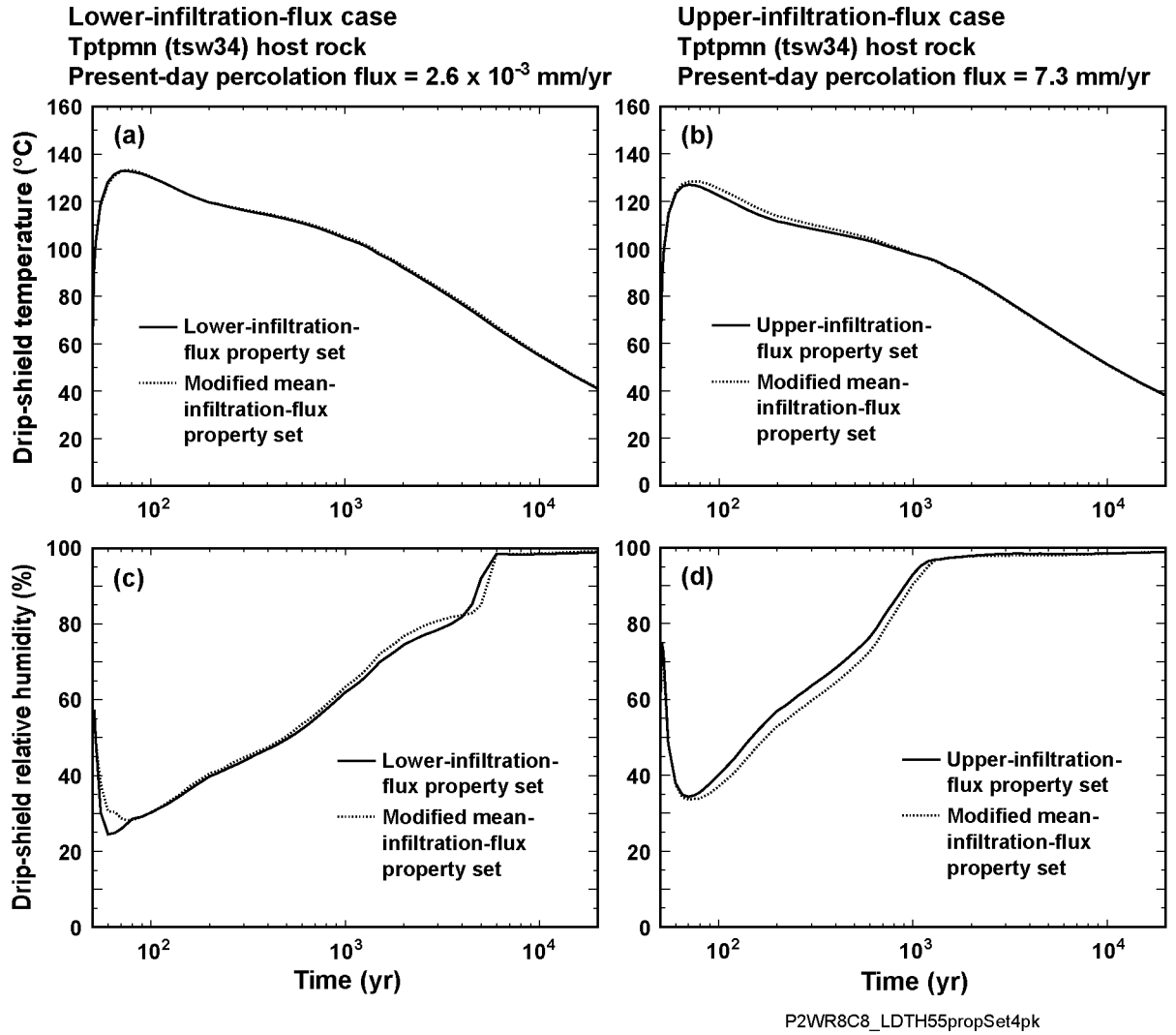

Figure 6.3-34. Drip-shield temperature (a,b) and relative humidity (c,d) for line-averaged heating conditions are plotted for four cases at the P2WR8C8 location, which is in the Tptpmn (tsw34) unit (see Figure 6.3-1 for location). These cases are: (1) lower-bound infiltration flux case with lower-bound infiltration flux property set, (2) lower-bound infiltration flux case with modified-mean infiltration flux property set, (3) upper-bound infiltration flux case with upper-bound infiltration flux property set, and (4) upper-bound infiltration flux case with modified-mean infiltration flux property set.

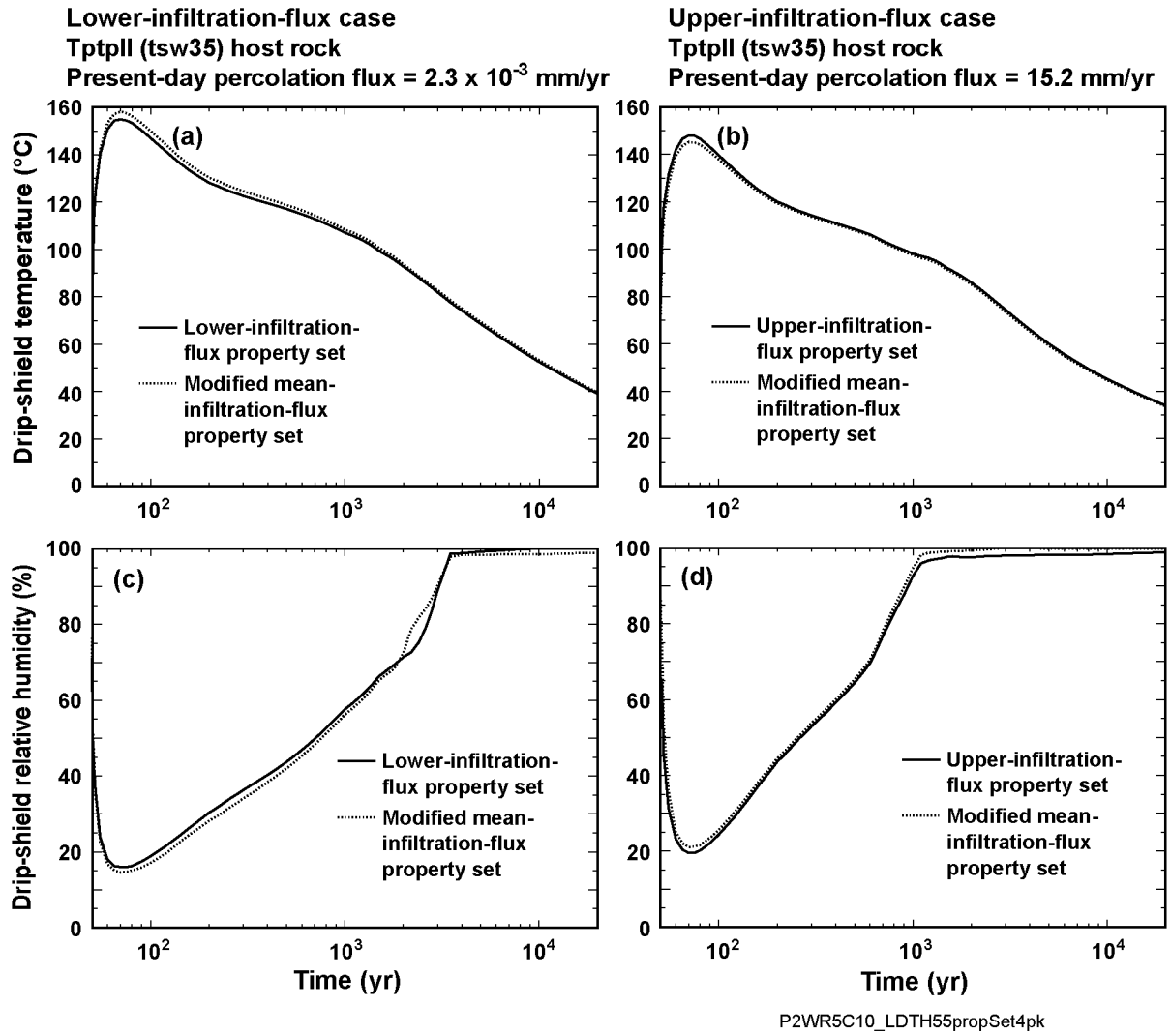

Figure 6.3-35. Drip-shield temperature (a,b) and relative humidity (c,d) for line-averaged heating conditions are plotted for four cases at the P2WR5C10 location, which is in the Tptpll (tsw35) unit (see Figure 6.3-1 for location). These cases are: (1) lower-bound infiltration flux case with lower-bound infiltration flux property set, (2) lower-bound infiltration flux case with modified-mean infiltration flux property set, (3) upper-bound infiltration flux case with upper-bound infiltration flux property set, and (4) upper-bound infiltration flux case with modified-mean infiltration flux property set.

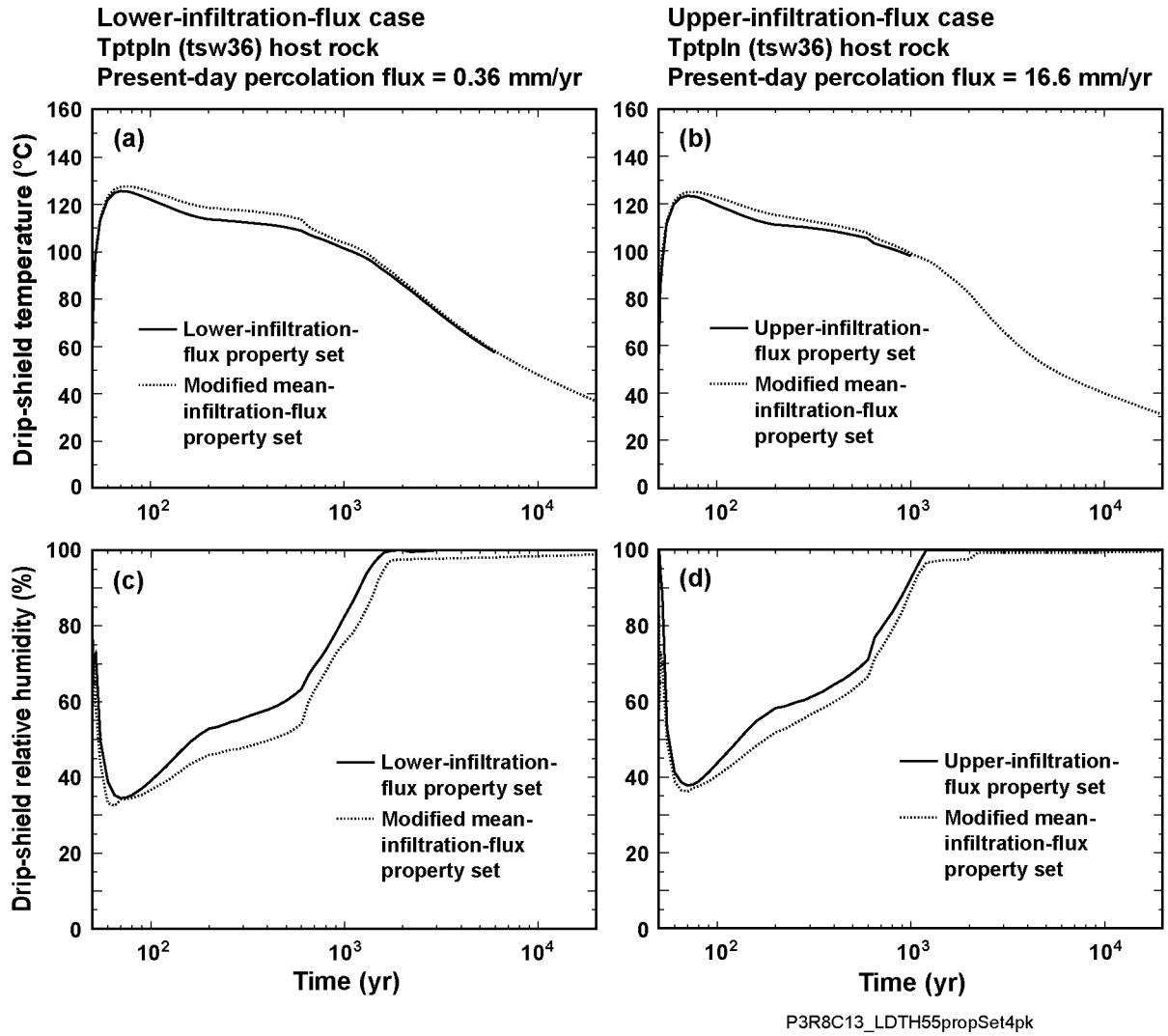

Figure 6.3-36. Drip-shield temperature (a,b) and relative humidity (c,d) for line-averaged heating conditions are plotted for four cases at the P3R8C13 location, which is in the Tptpln (tsw36) unit (see Figure 6.3-1 for location). These cases are: (1) lower-bound infiltration flux case with lower-bound infiltration flux property set, (2) lower-bound infiltration flux case with modified-mean infiltration flux property set, (3) upper-bound infiltration flux case with upper-bound infiltration flux property set, and (4) upper-bound infiltration flux case with modified mean infiltration flux property set.

Figures 6.3-33 through 6.3-36 indicate that in-drift temperature and relative humidity are insensitive to hydrologic-property uncertainty. For drifts located in the Tptpul (tsw33) unit (Figure 6.3-33) and the Tptpmn (tsw34) unit (Figure 6.3-34), which comprise 6.0 percent and 16.1 percent of the repository area, respectively (Table 6.3-2), drip-shield temperature and relative humidity are weakly sensitive to hydrologic properties. For drifts located in the Tptpll (tsw35) unit (Figure 6.3-35), which comprise 75.1 percent of the repository area (Table 6.3-2), drip-shield temperature and relative humidity are extremely insensitive to hydrologic properties. For drifts located in the Tptpln (tsw36) unit (Figure 6.3-36), which comprise only 1.6 percent of the repository area (Table 6.3-2), drip-shield temperature and relative humidity are relatively insensitive to hydrologic properties. The results support the conclusion that hydrologic-property

uncertainty does not need to be propagated in the MSTHM calculations of in-drift temperature and relative humidity.

6.3.3 Summary of the Range of Thermohydrologic Conditions for the TSPA-LA Base Case

Section 6.3.1.1 summarizes thermohydrologic conditions across the repository for the lower-bound, mean, and upper-bound infiltration flux cases. Figure 6.3-37 gives the corresponding ranges of temperature and relative–humidity histories for all waste packages. The plots in Figure 6.3-37, which are sometimes referred to as "horsetail" plots, also break down the ranges in temperature and relative–humidity histories into CSNF and DHLW groupings. The peak temperatures are 182.9°C and 169.2°C for the hottest CSNF and DHLW waste packages, respectively. The peak temperatures are 114.3°C and 108.6°C for the coolest CSNF and DHLW waste packages, respectively. Table 6.3-5 shows that the range in the time when boiling at the drift wall ceases ranges from 97.7 years to 1,734.6 years. The range in thermohydrologic conditions shown in Figure 6.3-37 incorporate the influence of percolation flux uncertainty, as it is represented in the lower, mean, and upper infiltration flux cases. It is important to note that these results pertain to the mean thermal-conductivity case; thus, the influence of thermal-conductivity uncertainty is not incorporated in Figure 6.3-37.

It is possible to approximate the combined influence of percolation flux uncertainty and thermal-conductivity uncertainty on peak temperatures. Section 6.3.2.3 shows that for determining peak temperatures it is possible to superpose the influence of percolation flux uncertainty and thermal-conductivity uncertainty. Section 6.3.2.2 addresses the influence of thermal-conductivity uncertainty on thermohydrologic conditions for each of the four host-rock units. Table 6.3-22 summarizes the influence of thermal-conductivity uncertainty on peak waste package temperature for each of the four host-rock units. It should be noted that the maximum peak waste package temperature occurs in the Tptpll (tsw35), while the minimum peak waste package temperature occurs in the Tptpln (tsw36) unit. For the P2WR5C10 location, which is in the Tptpll (tsw35) host-rock unit, the peak waste package temperature is 18.4°C higher for the low thermal-conductivity case than it is for the mean thermal-conductivity case (Table 6.3-22). For the P3R8C13 location, which is in the Tptpln (tsw36) unit, the peak waste package temperature is 9.0°C lower for the high thermal-conductivity case than it is for the mean thermal-conductivity case. Combining the influence of thermal-conductivity uncertainty (as given in Table 6.3-22) onto that of percolation flux uncertainty (as given in Table 6.3-4), results in a maximum peak waste package temperature of 201.3°C (182.9°C plus 18.4°C), while resulting in a minimum peak waste package temperature of 99.6°C (108.6°C minus 9.0°C). Thus, the combined influence of percolation flux uncertainty and thermal-conductivity uncertainty results in a peak waste package temperature range of approximately 100°C to 200°C across the repository.

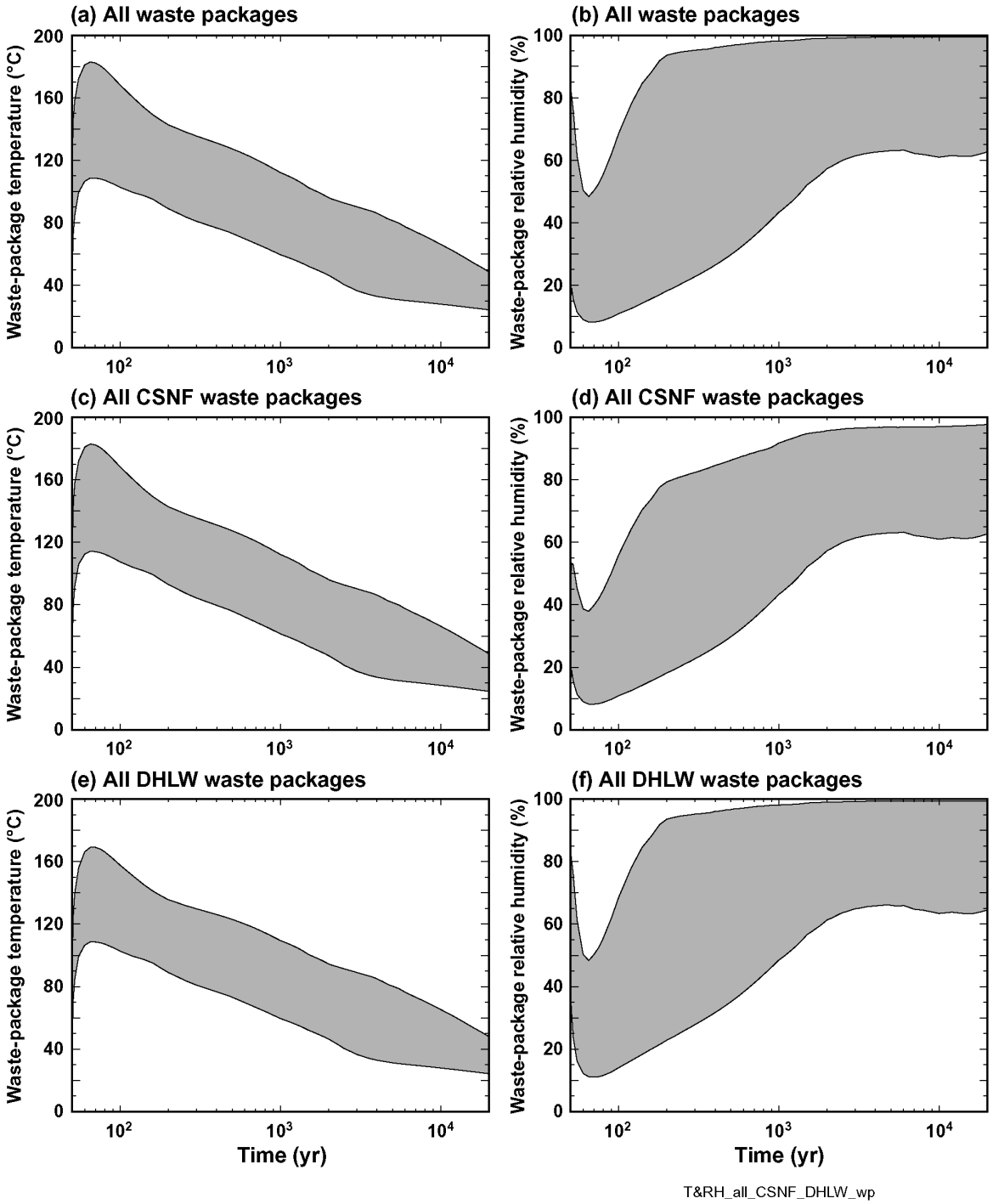

Figure 6.3-37. The range of waste package temperature and relative humidity histories are given for all waste packages (a, b), for all CSNF waste packages (c, d), and for all DHLW waste packages (e, f). The ranges include the lower-bound, mean, and upper-bound infiltration flux cases and use the mean thermal-conductivity values for all UZ Model Layer units, including the host-rock units.

It is also possible to approximate the combined influence of percolation flux uncertainty and thermal-conductivity uncertainty on the duration of boiling at the drift wall. Section 6.3.2.3 shows that for determining the duration of boiling, it is possible to superpose the influence of

percolation flux uncertainty and thermal-conductivity uncertainty. Table 6.3-23 summarizes the influence of thermal-conductivity uncertainty on the time when boiling at the drift wall ceases for the four host-rock units. It should be noted that the maximum duration of boiling at the drift wall occurs in the Tptpll (tsw35) unit, while the minimum duration of boiling occurs in the Tptpln (tsw36). For the P2WR5C10 location, which is in the Tptpll (tsw35) unit, the low thermal-conductivity case has a boiling-period duration that is 340.8 years longer than that of the mean thermal-conductivity case (Table 6.3-23). For the P3R8C13 location, which is in the Tptpln (tsw36) unit, the high thermal-conductivity case has a boiling-period duration that is 105.9 years shorter than that of the mean thermal-conductivity case (Table 6.3-23). Combining the influence of thermal-conductivity uncertainty (as given in Table 6.3-23) onto that of percolation flux uncertainty (as given in Table 6.3-5), results in a repository-wide maximum time when boiling ceases at the drift wall of 2,075.4 years (1,734.6 years plus 340.8 years). Because the high thermal-conductivity case resulted in a boiling-period duration that is 105.9 years shorter than that of the mean thermal-conductivity case and because the minimum boiling-period duration in Table 6.3-5 is 97.7 years (which pertains to the mean thermal-conductivity case), the repository-wide minimum time when boiling ceases at the drift wall is effectively zero (i.e., no boiling at the drift wall at all). Note that this situation with no boiling at the drift wall pertains only to a very small percentage of the waste package locations in the repository. Thus, the combined influence of percolation flux uncertainty and thermal-conductivity uncertainty results in an approximate range of no boiling at the drift wall to 2,100 years for the time when boiling at the drift wall ceases.

6.4 COMPARISON AGAINST AN ALTERNATIVE CONCEPTUAL MODEL

An alternative conceptual model to the MSTHM is a mountain-scale thermohydrologic model developed by LBNL (Haukwa et al. 1998). The LBNL model is a monolithic thermohydrologic model. Note that the three-drift repository MSTHM model-validation test case (Section 7.3) also used a monolithic thermohydrologic model to compare against the MSTHM. There is an important distinction between how the monolithic thermohydrologic model was used in Section 7.3 and how the LBNL monolithic thermohydrologic model is being used in this section (Section 6.4). In Section 7.3, the MSTHM and monolithic thermohydrologic model representation of the model-validation test problem are essentially exactly equivalent in a number of important respects, including (1) gridblock discretization at the drift scale, (2) heat-generation-rate-versus-time tables, (3) representation of in-drift heat-flow processes, and (4) hydrologic and thermal properties used in the respect models. In Section 6.4, the MSTHM and corresponding LBNL thermohydrologic model were similar, but not identical in any of these aspects. As discussed below, the LBNL thermohydrologic model used (1) coarser grid discretization at the drift scale than the MSTHM, (2) a line-averaged approximation of the heat-generation-rate-versus-time table (whereas the MSTHM represented the waste packages as discrete heat sources), and (3) a lumped heat source that filled the entire cross section of the emplacement drift.

Figure 6.4-1 compares the drift-wall temperature predicted by the MSTHM (Buscheck et al. 1998) with those predicted by an east-west cross-sectional mountain-scale thermohydrologic model (Haukwa et al. 1998). Because the east-west thermohydrologic model does not predict in-drift thermohydrologic conditions and because relative humidity and

liquid-phase saturation was not provided from that model, the comparison is restricted to predictions of drift-wall temperatures by the respective modeling approaches.

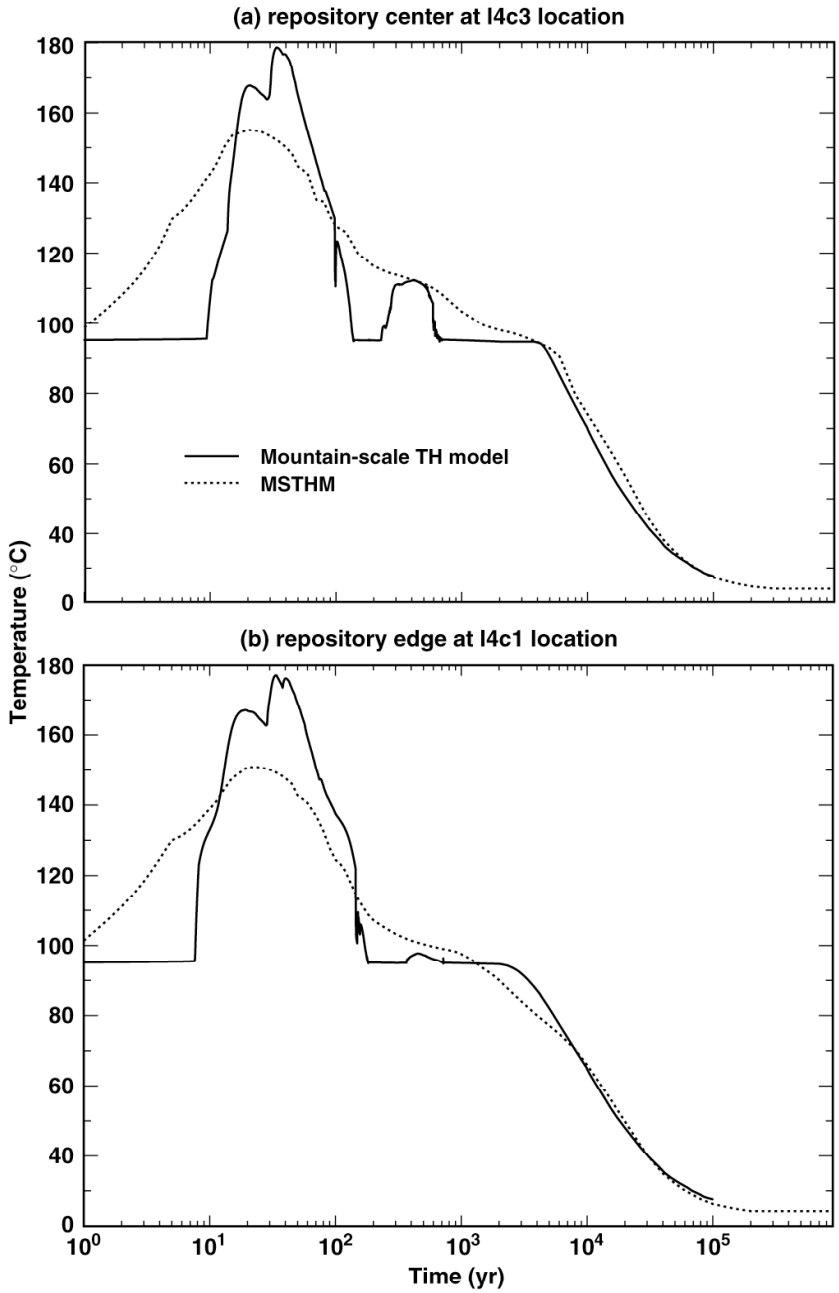

Figure 6.4-1. Comparison of predicted temperatures at (a) center of the repository (l4c3 location in Buscheck et al. 1998, Table 2-2) and (b) 100 m from the edge of the repository (l4c1 location) for the 12/97 TSPA-VA base-case I1 × 1 $\alpha_{f,mean}$ parameter set, where the symbol I stands for the nominal infiltration flux map (q_{inf} map (average q_{inf} = 7.8 mm/yr) for the present-day climate and the variable α_f is the van Genuchten "alpha" parameter for fractures. The MSTHM is used to predict drift-wall temperature adjacent to an "average" 21-PWR medium-heat CSNF waste package. The east-west cross-sectional mountain-scale thermohydrologic model (Haukwa et al. 1998) is used to predict the drift temperature, which is averaged over the cross section of the drift, arising from a line-averaged heat-source representation of waste package decay heat.

Before discussing the differences in the temperatures predicted by the two approaches (Figure 6.4-1), it is important to discuss the differences in the models. The temperature predicted by the MSTHM is the perimeter-averaged drift-wall temperature adjacent to an "average" 21-PWR medium-heat CSNF waste package. MSTHM discretely represents the decay-heat source from individual waste packages; therefore, some of the drift-wall locations are hotter than that shown in Figure 6.4-1, while some are considerably cooler. The drift-wall gridblocks over which the temperature is averaged extend 0.5 m into the host rock surrounding the drift. The temperature prediction in the east-west cross-sectional mountain-scale thermohydrologic model is for a gridblock that occupies the entire cross section of the drift; therefore, it is a lumped representation of the drift temperature. Moreover, because the east-west cross-sectional mountain-scale model uses a line-averaged heat source, it axially smears out the differences between "hot" and "cold" waste package locations along the drift.

Another difference between the modeling approaches concerns the mountains-scale dimensionality. The MSTHM represents three-dimensional mountain-scale heat flow for entire extent of the heated repository footprint, while the east-west cross-sectional mountain-scale thermohydrologic model has a reflected boundary at the east-west midpoint of the repository. Thus, the east-west model assumes that the overburden thickness of the entire repository area can be approximated with the overburden thickness between the western repository boundary and the midpoint of the repository. Because the eastern half of the repository has much less overburden thickness than the western half, this east-west symmetry approximation effectively over represents the effective overburden thickness for the eastern half of the repository. The cross-sectional geometry of the east-west mountain-scale model implicitly assumes that mountain-scale heat loss in the north-south dimension is negligible, which is a reasonable assumption given the large north-south dimension of the repository.

Another difference between the two modeling approaches concerns the areal power density applied in the respective models. The initial areal power density in the MSTHM is 92.3 kW/acre, while it is 99.4 kW/acre in the east-west cross-sectional mountain-scale model. Thus, the east-west model has a 7.7 percent larger areal power density than does the MSTHM (Buscheck et al. 1998, p. 3-10).

At the center of the repository (the l4c3 location in Buscheck et al. 1998, Table 2-2) the respective modeling approaches predict almost an identical duration of boiling (Figure 6.4-1a). At the edge repository location, which is 100 m from the western edge of the repository in the MSTHM (the l4c1 location in Buscheck et al. 1998, Table 2-2), the east-west cross-sectional mountain-scale model predicts a longer duration of boiling than does the MSTHM (Figure 6.4-1b). One reason for this difference is that the east-west model representation of the heated repository footprint extends slightly further to the west than in the MSTHM.

During the postboiling period, the temperatures predicted by the respective modeling approaches are in good agreement. During the early time heat-up period, the coarse (lateral and axial) grid-block spacing in the east-west cross-sectional mountain-scale model does not capture the rapid drift-wall temperature rise that the more finely gridded MSTHM predicts. Because of the coarse lateral grid-block spacing in the east-west model, it smears out the lateral temperature gradient between the drift and the mid-pillar location. Therefore, it tends to overpredict the temperature at the mid-pillar location and thereby prevent condensate from shedding between

drifts. The fine lateral grid-block spacing in the MSTHM captures the influence that the lateral temperature gradient has on allowing condensate to shed between drifts. The tendency for the east-west cross-sectional mountain-scale model to underrepresent condensate shedding results in a more substantial condensate buildup above the repository horizon. Also, the line-averaged heat-source approximation smears out differences in temperature between otherwise "hot" and "cold" waste package locations and thereby preventing condensate from breaking through "cold" waste package locations along the drift. Altogether, the underprediction of condensate shedding between drifts and condensate breakthrough at "cold" waste package locations causes the east-west cross-sectional mountain-scale model to build up more condensate above the repository horizon that leads to unstable heat-pipe behavior. This unstable behavior is exhibited by the rapid decline from superheated conditions to heat-pipe conditions (Figure 6.4-1a) and the rapid rise once again to superheated conditions at about 400 years. Notice that during the second superheated period predicted by the east-west model, the temperature climbs to be almost exactly that predicted by the MSTHM.

Given the differences between the MSTHM and the east-west cross-sectional mountain-scale model, the agreement between the two models is adequate. Moreover, the differences in predicted temperatures between the MSTHM and the east-west cross-sectional mountain-scale model are within the range of temperature differences resulting from parametric uncertainty (Tables 6.3-27 and 6.3-28). Therefore, the impact of conceptual-model uncertainty is no larger than that of parametric uncertainty. On the basis of this comparison, it is determined that the MSTHM is validated for its intended use.

6.5 FEPS

The development of a comprehensive list of features, events, and processes (FEPs) potentially relevant to postclosure performance of the potential Yucca Mountain repository is an ongoing, iterative process based on site-specific information, design, and regulations. The approach for developing an initial list of FEPs in support of TSPA-SR (CRWMS M&O 2000a) was documented by Freeze et al. (2001). The initial FEP list contained 328 FEPs, of which 176 were included in the TSPA-SR models (CRWMS M&O 2000a, Tables B-9 to B-17). To support TSPA-LA, the FEP list was re-evaluated in accordance with *The Enhanced Plan for Features, Events, and Processes (FEPs) at Yucca Mountain* (BSC 2002b, Section 3.2). Table 6.5-1 provides a listing of FEPs included in TSPA-LA models described and addressed in this document. *Technical Work Plan for: Engineered Barrier System Department Modeling and Testing FY03 Work Activities* (BSC 2003a) lists an additional five FEPs that are beyond the scope of the MSTHM and have either been assigned to other disciplines, or are addressed in other reports, as shown in Table 6.5-2.

Table 6.5-1. Included FEPs Addressed by This Model Report

FEP	Name	Description	Section Where Disposition is Described	Summary of Disposition in TSPA-LA
2.1.06.06.0A	Effects of drip shield on flow	The drip shield will affect the amount of water reaching the waste package. Effects of the drip shield on the disposal region environment (for example, changes in relative humidity and temperature below the shield) should be considered for both intact and degraded conditions.	6.3	*Multiscale Thermohydrologic Model* (ANL-EBS-MD-000049 REV 01) partially addresses this FEP. The MSTHM includes an intact drip shield in the thermohydrologic model of the repository. Based on inputs described in Section 4 and the modeling methodology described in Section 6.2, the MSTHM models flow around the drip shield and predicts the temperature and relative humidity of the in-drift environment both outside and inside the intact drip shield. These MSTHM outputs are direct feeds to the TSPA-LA. *In-Drift Natural Convection and Condensation Model Report* (MDL-EBS-MD-000001) (BSC 2003l) and *EBS Radionuclide Transport Abstraction* (ANL-WIS-PA-000001) (BSC 2003m) further address this FEP by modeling flow both around an intact drip shield and through a degraded drip shield. These reports investigate the environment between the waste package and the drip shield (including relative humidity and temperature), and amount of water reaching the waste package due to drip shield degradation.

Table 6.5-1. Included FEPs Addressed by This Model Report

FEP	Name	Description	Section Where Disposition is Described	Summary of Disposition in TSPA-LA
2.1.08.03.0A	Repository dry-out due to waste heat	Repository heat evaporates water from the UZ rocks near the drifts, as the temperature exceeds the vaporization temperature. This zone of reduced water content (reduced saturation) migrates outward during the heating phase and then migrates back to the containers as heat diffuses throughout the mountain and the radioactive heat sources decay. This FEP addresses the effects of dry-out within the repository drifts.	6.3	*Multiscale Thermohydrologic Model* (ANL-EBS-MD-000049 REV 01) models two-phase flow in the host rock and calculates postclosure thermohydrologic conditions, including dryout during the heating phase and rewetting during the cooling phase. Based on inputs described in Section 4 and the modeling methodology described in Section 6.2, the repository dryout is characterized by the model output variables of temperature and liquid-phase flux in the near field host rock. These MSTHM output variables are direct feeds to the TSPA-LA. In the host rock, the tendency for rock dryout is dominated by whether a location is inside or outside of the zone of boiling temperatures, 96°C at the elevation of the repository horizon at Yucca Mountain ~1100 m above mean sea level. Although evaporation, vapor flow (away from the heat source), and condensation occur at below-boiling temperatures, the thermally driven vaporization rates and vapor fluxes in the repository horizon are generally not great enough to result in significant dryout (and relative humidity reduction) in the rock unless temperatures are well above the boiling point. The boiling zone evolves with time. Because the majority of the decay heat is removed with the ventilation air during the preclosure period, boiling does not occur during this period. After drift ventilation ceases (which occurs at the onset of the postclosure period), a small zone of boiling-to-above-boiling temperatures forms in the volume immediately encircling each individual emplacement drift. This zone increases until reaching a maximum lateral extent in several hundred years. For the TSPA-LA design the maximum lateral extent of the boiling zone (relative to the centerline of the emplacement drift) ranges from 5.1 to 17.8 m, with a median maximum lateral extent of 7.9 m. A portion the rock within this zone will dry out to a varying degree, from nearly completely dry immediately adjacent to the emplacement drift to close to ambient liquid-phase saturation at the boiling front (which varies, but generally is of the order of 90 percent). Barometric pumping is not a significant contributor to the removal of water vapor from emplacement drifts or from the adjoining host rock.

Table 6.5-1. Included FEPs Addressed by This Model Report

FEP	Name	Description	Section Where Disposition is Described	Summary of Disposition in TSPA-LA
2.1.08.04.0A	Condensation forms on roofs of drifts (drift-scale cold traps)	Emplacement of waste in drifts creates thermal gradients within the repository. Such thermal gradients can lead to drift-scale cold traps characterized by latent heat transfer from warmer to cooler locations. This mechanism can result in condensation forming on the roof or other parts of the drifts, leading to enhanced dripping on the drip shields, waste packages, or exposed waste material.	7.3 and 6.3	*Multiscale Thermohydrologic Model* (ANL-EBS-MD-000049 REV 01) calculates the in-drift thermohydrologic environment, including the temperature of the in-drift components (i.e. drift wall, invert, drip shield, and waste package), relative humidity of the in-drift air, and liquid- and gas-phase saturations and pressures. The input parameters significant to this FEP are shown in Table 4-1, and generally include the thermophysical and hydrologic properties of the host rock units, and the waste package heat generation/decay. Section 7.3 describes an analysis that addresses the potential importance of the cold-trap effect on thermohydrologic behavior in the drift and in the adjoining host rock. It was found that sufficient rock dryout occurs along the entire length of the emplacement drift (center to edge) to cause the adjoining host rock to function as an effective desiccant that fully imbibes (by capillary forces) all potential condensate at the drift wall (including the drift roof). It was also found that no condensation occurs within the drift, with the only exception being the coolest (DHLW) waste package at the very outer edge of the drift; at only this cool waste package location, condensation occurred on the outside of the drip shield for as long as boiling conditions occurred at the center location (i.e., hottest) location within the emplacement drift. The impact of this condensation on the predicted temperature and relative humidity for this cool DHLW waste package is smaller than that caused by parametric uncertainty. Therefore, the impact of cold traps does not need to be directly incorporated in the MSTHM output.

Table 6.5-1. Included FEPs Addressed by This Model Report

FEP	Name	Description	Section Where Disposition is Described	Summary of Disposition in TSPA-LA
2.1.08.04.0B	Condensation forms at repository edges (repository-scale cold traps)	Emplacement of waste in drifts creates thermal gradients within the repository. Such thermal gradients can lead to repository-scale cold traps characterized by latent heat transfer from warmer to cooler locations. This mechanism can result in condensation forming at repository edges or elsewhere in the engineered barrier system, leading to enhanced dripping on the drip shields, waste packages, or exposed waste material.	7.3	*Multiscale Thermohydrologic Model* (ANL-EBS-MD-000049 REV 01) calculates the repository thermohydrologic environment, including thermal gradients from the middle to the edges and corners of the repository. The input parameters significant to this FEP are shown in Table 4-1, and generally include the thermophysical and hydrologic properties of the host rock units, and the waste package heat generation/decay. Section 7.3 describes an analysis that addresses the potential importance of the cold-trap effect on thermohydrologic behavior in the drift and in the adjoining host rock. It was found that sufficient rock dryout occurs along the entire length of the emplacement drift (center to edge) to cause the adjoining host rock to function as an effective desiccant that fully imbibes (by capillary forces) all potential condensate at the drift wall (including the drift roof). It was also found that no condensation occurs within the drift, with the only exception being the coolest (DHLW) waste package at the very outer edge of the drift; at only this cool waste package location, condensation occurred on the outside of the drip shield for as long as boiling conditions occurred at the center location (i.e., hottest) location within the emplacement drift. The impact of this condensation on the predicted temperature and relative humidity for this cool DHLW waste package is smaller than that caused by parametric uncertainty. Therefore, the impact of cold traps does not need to be directly incorporated in the MSTHM output.
2.1.08.05.0A	Flow through invert	The invert, a porous material consisting of crushed tuff, separates the waste package from the bottom of the drift. Flow and transport through and bypassing the invert can influence radionuclide release to the UZ.	6.3	*Multiscale Thermohydrologic Model* (ANL-EBS-MD-000049 REV 01) partially addressed this FEP. The MSTHM calculates the matrix saturation of the invert based on the inputs described in Table 4-1. These inputs include the hydrologic properties of the invert which are, in part, calculated by Table 6-2 of *Advection Versus Diffusion in the Invert* (ANL-EBS-MD-000063 REV 00) (BSC 2003n). This calculation develops the retention and unsaturated flow properties of the invert using a Non-Dimensionalized Van Genuchten Retention Relation. Invert matrix saturations are passed on to *EBS Radionuclide Transport Abstraction* (ANL-WIS-PA-000001 REV 00 ICN 03) (BSC 2003m) where the flow and transport in and around the invert is investigated and this FEP is more directly addressed for the TSPA-LA.

Table 6.5-1. Included FEPs Addressed by This Model Report

FEP	Name	Description	Section Where Disposition is Described	Summary of Disposition in TSPA-LA
2.1.08.06.0A	Capillary effects (wicking) in EBS	Capillary rise, or wicking, is a potential mechanism for water to move through the waste and engineered barrier system.	6.3	*Multiscale Thermohydrologic Model* (ANL-EBS-MD-000049 REV 01) partially addressed this FEP. The MSTHM calculates wicking from the host rock to the invert. This effect is captured by predicting the matrix saturation of the invert based on the inputs described in Table 4-1. These inputs include the hydrologic properties of the invert which are, in part, calculated by Table 6-2 of *Advection Versus Diffusion in the Invert* (ANL-EBS-MD-000063 REV 00) (BSC 2003n). This calculation develops the retention and unsaturated flow properties of the invert using a Non-Dimensionalized Van Genuchten Retention Relation. The other relevant inputs to this FEP include the hydrologic properties of the host rock at the repository horizon. Invert matrix saturations are passed on to *EBS Radionuclide Transport Abstraction* (ANL-WIS-PA-000001 REV 00 ICN 03) (BSC 2003m) where the flow and transport in and around the invert is actually investigated and this FEP is more directly addressed for the TSPA-LA. *EBS Radionuclide Transport Abstraction* (ANL-WIS-PA-000001 REV 00 ICN 03) (BSC 2003m) also addresses additional mechanisms for water to move through the engineered barrier system and waste.
2.1.08.11.0A	Repository desaturation due to waste cooling	Following the peak thermal period, water in the condensation cap may flow downward, resaturating the geosphere dry-out zone and flowing into the drifts. This may lead to an increase in water content and/or resaturation in the repository.	6.3	*Multiscale Thermohydrologic Model* (ANL-EBS-MD-000049 REV 01) models two-phase flow in the host rock and calculates postclosure thermohydrologic conditions, including relative humidity and rewetting and unsaturated flow back toward the drift. Based on inputs described in Section 4 and the modeling methodology described in Section 6.2, these effects are characterized by the MSTHM output of liquid-phase flux in the near field host rock. The resaturation of the dry-out zone is captured by the TSPA-LA using the MSTHM output of liquid-phase flux as a direct feed. A key thermohydrologic parameter is the maximum lateral extent of the boiling zone relative to the centerline of the emplacement drifts because this is a strong indication of the likelihood of continuous condensate and percolation flux drainage around emplacement drifts. For the three infiltration flux data sets considered in this report, the maximum lateral extent of boiling ranges from 5.1 to 17.8 m, with a median maximum lateral extent of 7.9 m. It is important to note that the lateral extent of boiling is

Table 6.5-1. Included FEPs Addressed by This Model Report

FEP	Name	Description	Section Where Disposition is Described	Summary of Disposition in TSPA-LA
				always much smaller than the half spacing between emplacement drifts. Therefore, the majority of the host rock between the emplacement drifts always remains below the boiling point, thereby enabling condensate and percolation flux to continuously drain between emplacement drifts. Because of this continuous drainage of condensate around a relatively narrow cylindrically shaped boiling zone, the condensate cap above the emplacement drifts is of very limited spatial extent. Therefore, it is extremely unlikely that the condensate cap could augment liquid-phase saturation during postboiling rewetting period. Therefore, the return flow of liquid from the condensate zone to the dryout zone does not cause the liquid-phase saturation around the emplacement drifts to be greater than that which would occur under ambient (unheated) conditions.
2.1.11.01.0A	Heat generation in EBS	Temperature in the waste and engineered barrier system will vary through time. Heat from radioactive decay will be the primary cause of temperature change, but other factors to be considered in determining the temperature history include the in-situ geothermal gradient, thermal properties of the rock, engineered barrier system, and waste materials, hydrological effects, and the possibility of exothermic reactions. Considerations of the heat generated by radioactive decay should take different properties of different waste types, including defense spent nuclear fuel, into account.	6.3	*Multiscale Thermohydrologic Model* (ANL-EBS-MD-000049 REV 01) partially addressed this FEP. The MSTHM calculates the temperature history of the waste and engineered barrier system through time. The temperatures as predicted by the MSTHM are influenced by not only the heat of radionuclide decay, but the geothermal gradient from the ground surface to the water table, and the thermophysical properties of the rock and engineered barrier system components, which are described in Table 4.1. Temperatures for different types of waste forms are captured in the DDT model of the MSTHM. These waste forms include the 21-PWR, the DHLW long and short, and the 44-BWR, all of which produce heat at different rates. These effects are captured in the TSPA-LA by providing the temperature as a direct input. Section 6.3.1.2 investigates the influence of waste-package-to-waste-package heat-generation variability on thermohydrologic conditions in the emplacement drifts. The eight different waste packages considered in all of the MSTHM calculations (Figure 6.2-2) are summarized in Table 6.3-10. Table 6.3-11 summarizes the impact of heat-generation variability on peak temperatures. Table 6.3-12 summarizes the impact of this variability on the time when boiling at the drift wall ceases. *Engineered Barrier System: Physical and Chemical Environment Model* (ANL-EBS-MD-000033 REV 02) (BSC 2004g) addressed the possibility of exothermic reactions on the waste package surfaces.

Table 6.5-1. Included FEPs Addressed by This Model Report

FEP	Name	Description	Section Where Disposition is Described	Summary of Disposition in TSPA-LA
2.1.11.02.0A	Non-uniform heat distribution in EBS	Uneven heating and cooling at edges of the repository lead to non-uniform thermal effects during both the thermal peak and the cool-down period.	6.3	*Multiscale Thermohydrologic Model* (ANL-EBS-MD-000049 REV 01) calculates the repository thermohydrologic environment, including thermal gradients from the repository center to the edges and corners of the repository. The impact of uneven heating and cooling is captured in the MSTHM and passed to the TSPA-LA by providing temperatures as a direct feed. For the three infiltration flux sets, the range in peak drift-wall temperature is from 98.6 to 154.8°C, with a median drift-wall temperature of 133.0°C; the range in peak waste package temperature is from 109.6 to 182.9°C, with a median waste package temperature of 153.3°C. Another key thermohydrologic parameter is the time when boiling ceases at the drift wall because this is an indication of how long seepage into the emplacement drifts is extremely unlikely. For the three data sets, the time when drift-wall boiling ceases ranges from 97.7 to 1,734.6 years, with a median time of 721.0 years.
2.1.11.09.0A	Thermal effects on flow in the EBS	High temperatures in the engineered barrier system may influence seepage into and flow within the waste and engineered barrier system. Thermally induced changes to fluid saturation and/or relative humidity could influence in-package chemistry. Thermal gradients in the repository lead to localized accumulation of moisture. Wet zones form below the areas of moisture accumulation.	6.3 and 7.3	*Multiscale Thermohydrologic Model* (ANL-EBS-MD-000049 REV 01) calculates the thermohydrologic environment within and around the emplacement drifts. Based on inputs described in Section 4 and the modeling methodology described in Section 6.2, the MSTHM predicts the temperature, relative humidity, gas- and liquid-phase fluxes, and gas- and liquid-phase saturations in the near-field host rock, as well as within the emplacement drifts. These MSTHM outputs indirectly effect the in-drift chemical environment through the TSPA-LA. A key thermohydrologic parameter is the maximum lateral extent of the boiling zone relative to the centerline of the emplacement drifts because this is a strong indication of the likelihood of continuous condensate and percolation flux drainage around emplacement drifts. For the three infiltration flux data sets considered in this report, the maximum lateral extent of boiling ranges from 5.1 to 17.8 m, with a median maximum lateral extent of 7.9 m. It is important to note that the lateral extent of boiling is always much smaller than the half spacing between emplacement drifts. Therefore, the majority of the host rock between the emplacement drifts always remains below the boiling point, thereby enabling condensate and percolation flux to continuously drain

Table 6.5-1. Included FEPs Addressed by This Model Report

FEP	Name	Description	Section Where Disposition is Described	Summary of Disposition in TSPA-LA
				between emplacement drifts. Because of this continuous drainage of condensate around a relatively narrow, cylindrically shaped boiling zone, the condensate cap above the emplacement drifts is of very limited spatial extent. Therefore, it is extremely unlikely that the condensate cap could augment liquid-phase saturation during postboiling rewetting period. Therefore, the return flow of liquid from the condensate zone to the dryout zone does not cause the liquid-phase saturation around the emplacement drifts to be greater than that which would have occur under ambient (unheated) conditions. Section 7.3 describes an analysis that addresses the potential importance of the cold-trap effect on thermohydrologic behavior in the drift and in the adjoining host rock. It was found that sufficient rock dryout occurs along the entire length of the emplacement drift (center to edge) to cause the adjoining host rock to function as an effective desiccant that fully imbibes (by capillary forces) all potential condensate at the drift wall (including the drift roof). It was also found that no condensation occurs within the drift, with the only exception being the coolest (DHLW) waste package at the very outer edge of the drift; at only this cool waste package location, condensation occurred on the outside of the drip shield for as long as boiling conditions occurred at the center location (i.e., hottest) location within the emplacement drift. The impact of this condensation on the predicted temperature and relative humidity for this cool DHLW waste package is smaller than that caused by parametric uncertainty. Therefore, the impact of cold traps does not need to be directly incorporated in the MSTHM output.

Table 6.5-2. Engineered Barrier System Features, Events, and Processes Not Covered in this Model Report

FEP Number	FEP Subject	Addressed By:
1.2.02.01.0A	Fractures	BSC 2003h; BSC 2003j
2.1.08.01.0B	Effects of rapid influx into the repository	BSC 2003m
2.1.08.02.0A	Enhanced influx at the repository	BSC 2003j
2.1.08.07.0A	Unsaturated flow in the EBS	BSC 2003m
2.1.08.14.0A	Condensation (cold traps) on underside of drip shield	BSC 2004g; BSC 2003m

INTENTIONALLY LEFT BLANK

7. MODEL VALIDATION

The validation of the MSTHM involves the validation of both the MSTHM methodology and the submodels used in the MSTHM. Note that all MSTHM submodels are executed with the NUFT v3.0s code (Section 3.1.1). The primary MSTHM submodel type (called the LDTH submodel) is validated using field-scale thermal tests. The other three MSTHM submodel types (called the SDT, SMT and DDT submodels) are thermal conduction models. Given the manner in which the MSTHM utilizes the SDT, SMT, and DDT submodels, this assumption is justified (Sections 5.3.2.1 and 6.2.4). The DDT submodel represents thermal radiation inside the emplacement drifts and also represents the influence of natural convective heat flow in the drifts through the use of an equivalent thermal conductivity that is based on a correlation (Francis et al. 2003, Table 6) (Section 6.2.8.5). The software qualification of NUFT v3.0s includes test problems that demonstrate the validity of NUFT in modeling three-dimensional thermal-conduction and thermal-radiation problems. The NUFT code uses an industry-standard finite-difference method that solves the mass balance of water and air and an energy balance. In addition to the NUFT v3.0s validation test suite, the MSTHM validation includes the following activities:

- **Comparison of NUFT LDTH submodel results against the Large Block Test**–*Thermal Tests Thermal-Hydrological Analyses/Model Report* (CRWMS M&O 2000b, Section 6.2.3) documents the comparison of NUFT thermohydrologic model calculations against measurements made in the Large Block Test. The adequacy of the agreement between the modeled and field-measured thermohydrologic behavior is judged in light of the impact of parameter uncertainty on thermohydrologic behavior. A summary of this comparison is given in Section 7.1. The NUFT thermohydrologic model used in this validation study is a three-dimensional equivalent to the LDTH submodels used in the MSTHM. These thermohydrologic calculations used NUFT v3.0s (Section 3.1.1).

- **Comparison of NUFT LDTH submodel results against the Drift Scale Test**–Section 7.2 documents the comparison of NUFT thermohydrologic model calculations against measurements made in the Drift Scale Test. The adequacy of the agreement between the modeled and field-measured thermohydrologic behavior is judged in light of the impact of parameter uncertainty on thermohydrologic behavior. The NUFT thermohydrologic model used in this validation study is a three-dimensional equivalent to the LDTH submodels used in the MSTHM. These thermohydrologic calculations used NUFT v3.0.1s (Section 3.1.2), which is essentially identical to NUFT v3.0s except that NUFT v3.0.1s is able to address nested-mesh problems having a large number of nests, while NUFT v3.0s can handle nested meshes with two nests.

- **Comparison of the MSTHM results against a monolithic three-dimensional thermohydrologic model**–Using a three-drift repository example (which is a scaled-down version of the repository), the validity of the MSTHM approach is demonstrated by comparing the results of the MSTHM against a corresponding monolithic three-dimensional thermohydrologic model that uses a nested mesh. This validation test case is similar to that reported by Buscheck, Glascoe et al. (2003). A summary of this comparison is given in Section 7.3. The adequacy of the agreement between the MSTHM and the monolithic three-dimensional thermohydrologic model is

judged in light of the impact of parameter uncertainty on thermohydrologic behavior. For this comparison NUFT v3.0s is used for the MSTHM calculations, while NUFT v3.0.1s is used in the corresponding monolithic three-dimensional thermohydrologic model that uses a nested mesh.

- **Comparison of MSTHM results against alternative numerical models**–Buscheck et al. (1998) document a comparison between the results of the MSTHM against a three-dimensional east-west cross-sectional mountain-scale thermohydrologic model developed at Lawrence Berkeley National Laboratory (Haukwa et al. 1998). The adequacy of the agreement between these two models is judged in light of the impact of parameter uncertainty on thermohydrologic behavior. A brief summary of this comparison is given in Section 6.4.

7.1 COMPARISON OF NUFT THERMOHYDROLOGIC MODEL AGAINST THE LARGE BLOCK TEST

The NUFT thermohydrologic model used to model the Large Block Test (LBT) is described in Section 6.1.4 of *Thermal Tests Thermal-Hydrological Analyses/Model Report* (CRWMS M&O 2000b). As in the case of the Drift-Scale Test (DST), the LBT is located in the Tptpmn (tsw34) unit. In the LBT, a block of excavated rock (3 by 3 by 4.5) is heated for one year with five heaters placed in an array of horizontal boreholes 2.75 m from the top of the block. Temperatures were constantly monitored during the test, while liquid-phase saturations are measured on a regular basis. The source DTN for the heater power history is listed in Table 4-2.

7.1.1 Comparison of Simulated and Field-Measured Temperatures

Figure 7.1-1 shows the NUFT-simulated versus measured temperature profile along Borehole TT1 at five times from 30 to 400 days. The source DTNs for all field measurements of temperatures are listed in Table 4-2. Because the LBT is in the Tptpmn (tsw34) unit, the NUFT thermohydrologic models apply the thermal and hydrologic properties for that unit. Two cases are considered: (1) the mean infiltration flux hydrologic property set used in the TSPA-SR base-case MSTHM calculations (BSC 2001c) and (2) the modified-mean infiltration flux hydrologic property set used in the TSPA-LA base-case MSTHM calculations. The source of the mean infiltration flux hydrologic property set used in the TSPA-SR base-case MSTHM calculations is DTN: LB990861233129.001 (Table 4-2). For the Tptpmn (tsw34) unit, the modified-mean infiltration flux property set used in the TSPA-LA base-case MSTHM calculations are the same as those in the mean infiltration flux property set (DTN: LB0208UZDSCPMI.002). Both the TSPA-SR and TSPA-LA cases are in good agreement with the field-measured temperature data. However, both cases predict slightly higher temperatures than the field-measured values, with the TSPA-LA case resulting in the highest temperatures. As is discussed below, the primary cause for the higher simulated temperatures for the TSPA-LA case is the large gas-phase pressure buildup in the matrix (Figure 7.1-2b, d, and f).

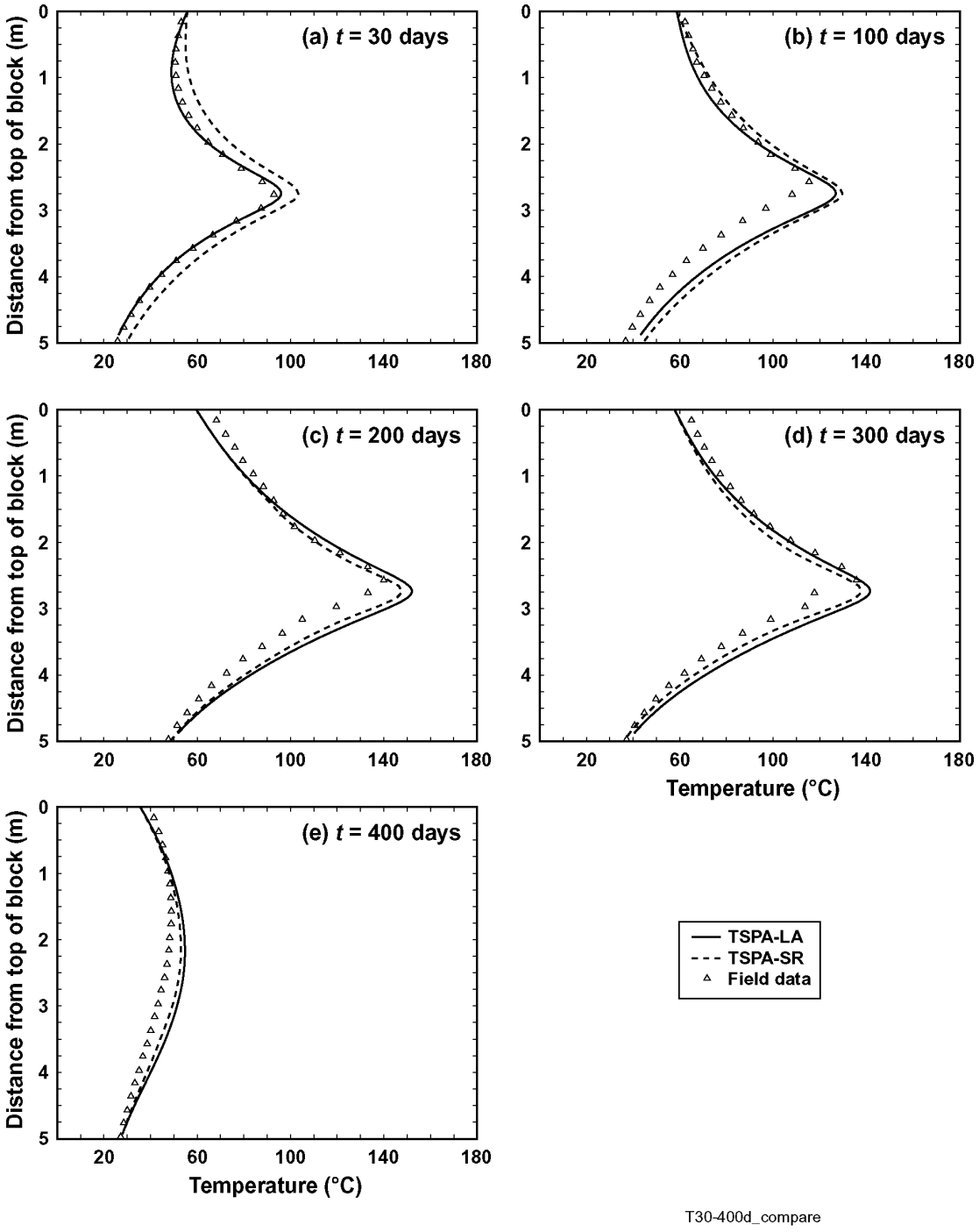

Figure 7.1-1. Comparison of the NUFT-simulated and measured temperatures along Borehole TT1 in the Large Block Test is given at (a) 30 days, (b) 100 days, (c) 200 days, (d) 300 days, and (e) 400 days. The NUFT simulations include two cases. The TSPA-LA case uses the modified-mean infiltration flux hydrologic property values for the Tptpmn (tsw34) unit that are used in the MSTHM calculations for the TSPA-LA base case (Section 6.3). Note that for the Tptpmn (tsw34) unit, the mean and modified-mean property sets (discussed in Section 6.3.1) are the same. The TSPA-SR case uses the mean infiltration flux property values for the Tptpmn (tsw34) unit that are used in the MSTHM calculations for the TSPA-SR base case (BSC 2001c).

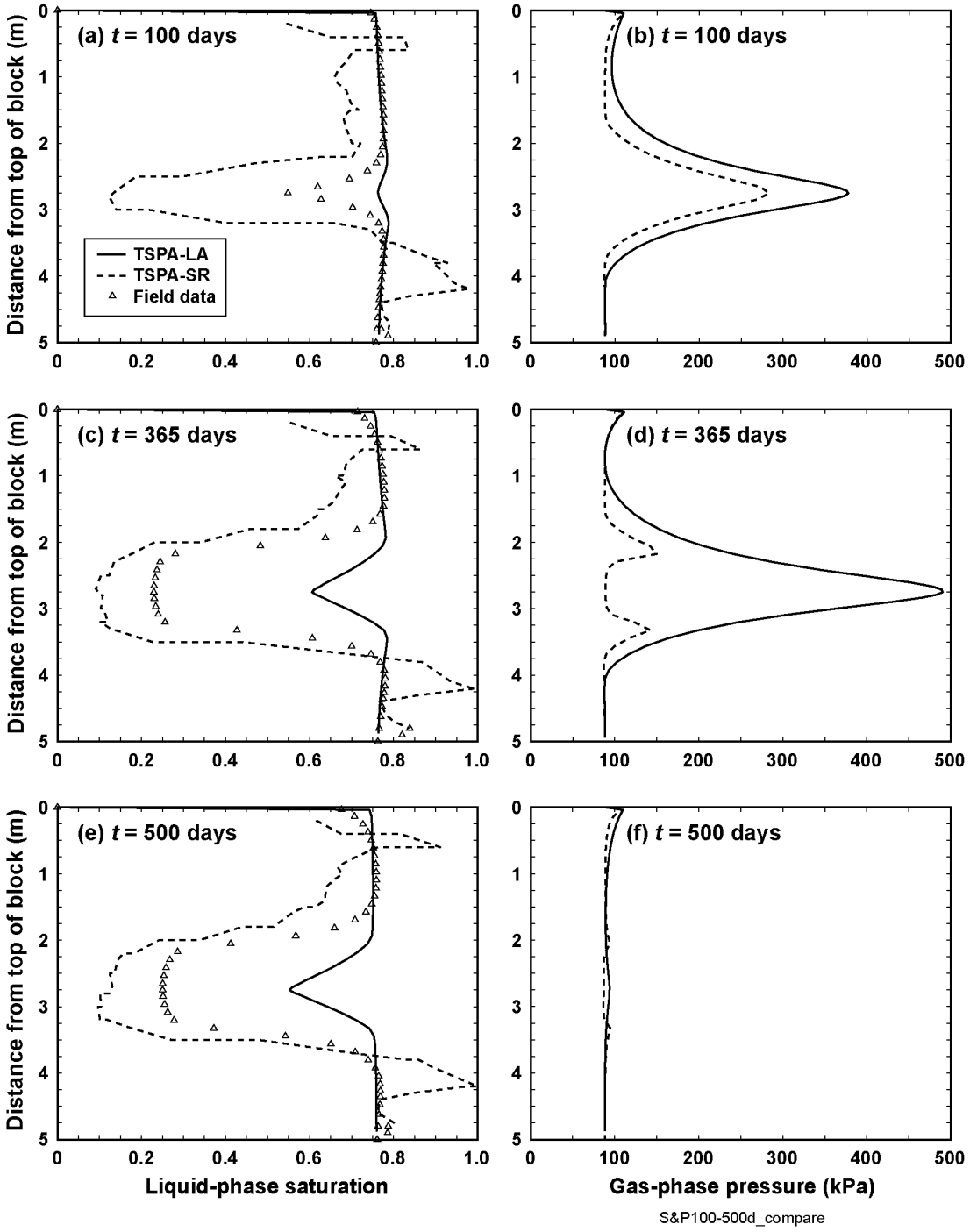

Figure 7.1-2. Comparison of the NUFT-simulated and measured liquid-phase saturations along Borehole TN3 is given at (a) 100 days, (c) 365 days, and (e) 500 days. The NUFT-simulated gas-phase pressures in the matrix are also plotted at (b) 100 days, (d) 365 days, and (f) 500 days. Note that there are no field measurements of gas-phase pressure in the matrix. The NUFT simulations include two cases. The TSPA-LA case uses the modified-mean infiltration flux hydrologic property values for the Tptpmn (tsw34) unit that are used in the MSTHM calculations for the TSPA-LA base case (Section 6.3). Note that for the Tptpmn (tsw34) unit, the mean and modified-mean property sets (discussed in Section 6.3.1) are the same. The TSPA-SR case uses the mean infiltration flux property values for the Tptpmn (tsw34) unit that are used in the MSTHM calculations for the TSPA-SR base case.

7.1.2 Comparison of Simulated and Field-Measured Liquid-Phase Saturations

Figure 7.1-2 shows the NUFT-simulated and measured liquid-phase saturation profile along TN3, which is a vertical borehole used for neutron probe measurements of water content. The source DTNs for all liquid-phase saturation measurements are listed in Table 4-2. Figure 7.1-2 also shows are the NUFT-simulated gas-phase pressures in the matrix; note that there are no field measurements of gas-phase pressure in the matrix. At 100 days, the NUFT simulation for the TSPA-SR case shows a well-developed dryout zone, while the TSPA-LA case shows almost no dryout. An important distinction between these two cases is that the matrix permeability for the TSPA-SR case is 23 times greater than it is for the TSPA-LA case. The small matrix permeability in the TSPA-LA case causes more gas-phase pressure buildup, which drives the saturation (or boiling) temperature to be higher, thereby throttling the rate of vaporization and rock dryout. The difference in gas-phase pressure buildup is very pronounced at 365 days (Figure 7.1-2d), which causes a large difference in the dryout zones for these two cases (Figure 7.1-2c). The simulated dryout zone for the TSPA-SR case is in close agreement with the measured dryout zone, which the TSPA-LA case results in very little dryout. At 365 days the gas-phase pressure nearly reaches 5 atm for the TSPA-LA case, while for the TSPA-SR case it is less than 1.5 atm (Figure 7.1-2d). Notice that the TSPA-SR case produces two zones of increased gas-phase pressure with each zone corresponding to the boiling zones above and below the heater horizon. A comparison of the field-measured liquid-phase saturations at 365 days (when heating ceased) and at 500 days (Figure 7.1-2c and e) indicate that rewetting of the dryout zone in the LBT progresses at a very slow rate. Similarly, a comparison of the NUFT-simulated liquid-phase saturations for 365 and 500 days indicates that rewetting progresses at a very slow rate. Therefore, the NUFT thermohydrologic model, for both the TSPA-SR and TSPA-LA hydrologic property sets, provides a valid representation of rewetting behavior observed in the LBT.

7.1.3 Summary of Model Validation Using LBT Data

The good agreement between the NUFT-simulated and measured temperatures demonstrates that the thermal conductivity values in the TSPA-SR and TSPA-LA property sets are appropriate. Moreover, this agreement demonstrates that the NUFT thermohydrologic model provides a valid representation of heat flow in the LBT. Moreover, the differences between the predicted and field-measured temperatures are well within the relative impact resulting from parametric uncertainty (Tables 6.3-27 and 6.3-28). The agreement between the simulated and measured dryout behavior demonstrates that the NUFT thermohydrologic model provides a valid representation of dryout behavior for the TSPA-SR hydrologic property set. The NUFT thermohydrologic model, using both the TSPA-SR and TSPA-LA hydrologic property sets, also provides a valid representation of rewetting behavior observed in the LBT. The cause for the differences between the NUFT-simulated dryout (using the TSPA-LA hydrologic property set) and the measured dryout data is well understood and does not affect the conclusion that the NUFT thermohydrologic model of the LBT provides a valid representation of dryout behavior.

7.2 VALIDATION OF THE LDTH SUBMODEL USING THE DRIFT SCALE TEST

The three-dimensional model thermohydrologic model of the Drift-Scale Test (DST) is a three-dimensional equivalent of the two-dimensional LDTH submodel used in the MSTHM. Both the three-dimensional thermohydrologic model of the DST and the two-dimensional LDTH

submodel use the NUFT code. Both models use the same cross-sectional approximation of the emplacement (or heater) drift and both use the same grid refinement within the drift and in the near-field host rock. Both models use the same representation of thermal-radiative heat transfer in the drift. They both use the same effective thermal-conductivity approach to representing the influence of natural convective heat flow in the drifts, which is based on a correlation by Francis et al. (2003, Table 6) (Section 6.2.8.5). Both models use the same thermal and hydrologic property set. Both models use the same boundary conditions at the ground surface and at the water table. The only difference between the three-dimensional thermohydrologic model of the DST and the two-dimensional LDTH submodel is the dimensionality of the respective models. Therefore, the validation of the three-dimensional thermohydrologic model of the DST is effectively equivalent to validating the two-dimensional LDTH submodels in the MSTHM.

7.2.1 Design and Geometry of the DST

The DST is the largest (and longest duration) in situ heater test of its kind (Figure 7.2-1). At the center of the DST is the Heated Drift, which is 47.5-m long with a 5.0-m diameter (which is very similar to the 5.5-m-diameter emplacement drifts in the repository). The thermal load comes from two kinds of heat sources. The Heated Drift has nine waste-package-sized heat sources. Emanating from either side of the Heated Drift are 50 horizontal boreholes (25 on each side), containing "wing heaters" that provide additional heating to simulate (in an accelerated fashion) the influence of heating from neighboring emplacement drifts. Each wing heater is composed of two 4.44-m-long segments separated by a 0.66-m gap. The outside of each wing heater is 14 m from the centerline of the heater drift, while the inside of each wing heater is 4.46 m from the centerline. The "hot" side of the Heated Drift is separated from the cold side with a thermally insulated bulkhead. The DST heating began on December 3, 1997 and continued for 1,503 days (4.1 years) until January 14, 2002. The DST is now in the cooldown phase and continues to be monitored. The source DTN for the heater power history is listed in Table 4-3.

The purpose of large-scale thermal testing at Yucca Mountain is discussed in Section II.E of *Thermal-Hydrological Analysis of Large-Scale Thermal Tests in the Exploratory Studies Facility at Yucca Mountain* (Buscheck and Nitao 1995). Sections II.F and II.G of that report discuss the rationale and criteria for the design of large-scale thermal tests. A thermohydrologic modeling study (Buscheck and Nitao 1995, Section IV) helped determine the recommended size and duration of the DST. A comprehensive description of the design and geometry of the DST is documented in Sections 7.2.1 and 7.2.2 of *Drift-Scale Coupled Processes (DST and TH Seepage) Models* (BSC 2003j). Section 7.4 of that report gives a very detailed and thorough discussion of a thermohydrologic-model-validation study.

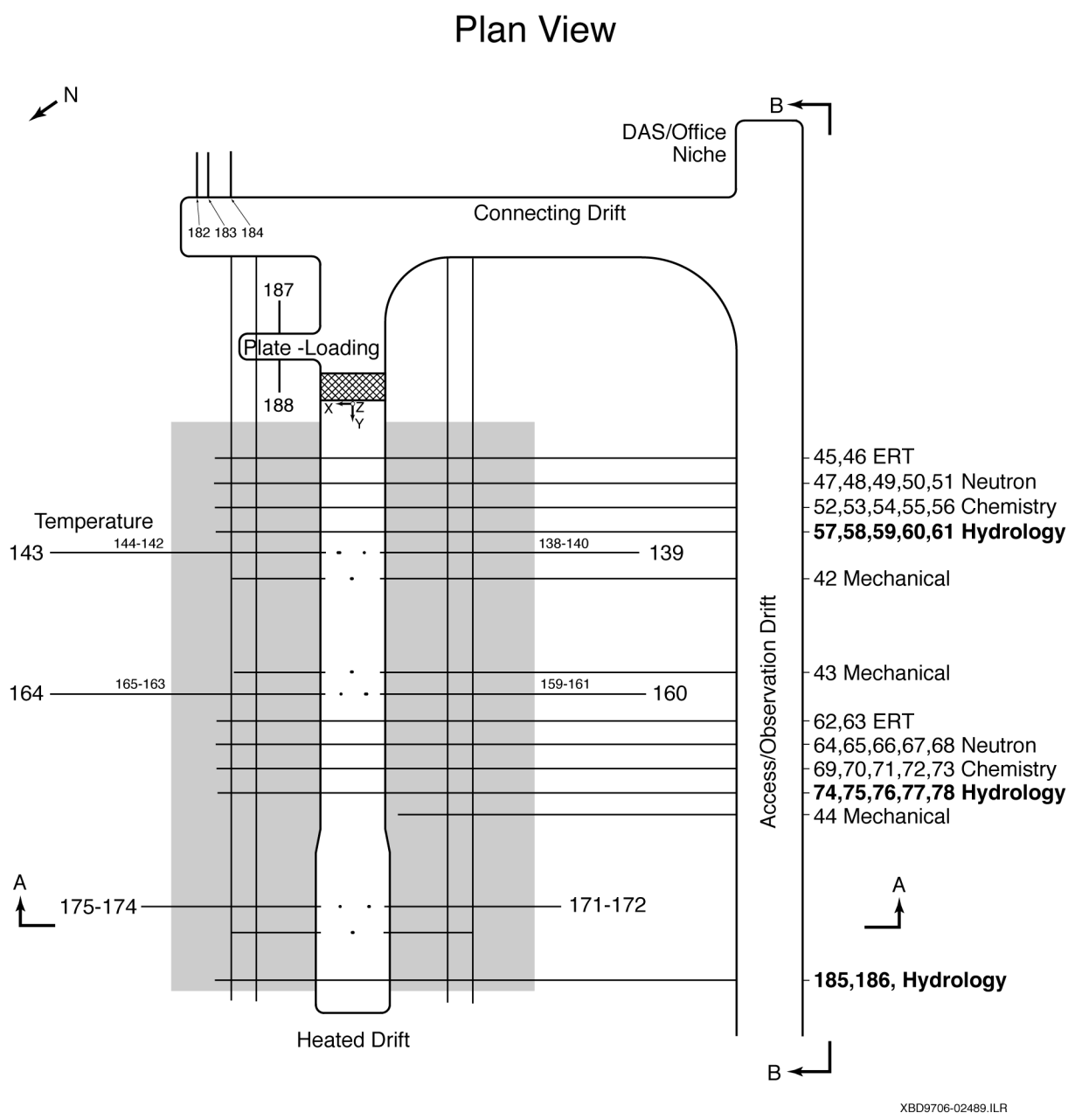

Source: BSC 2003j, Figure 7.2.1-1

Figure 7.2-1. Plan View of the Drift Scale Test Area

7.2.2 Description of Three-Dimensional Thermohydrologic Model of the DST

The model is designed to accurately represent the test domain and the processes governing heat and mass transport in the system. The test geometry, including the dimensions of the stratigraphic units from the water table to the ground surface, is adequately represented in this full three-dimensional model. Fracture and matrix interaction is handled using the dual-permeability model employing the active-fracture concept. The thermohydrologic simulation code NUFT v3.0.1s (Section 3.1.2) is used because of its ability to handle nested meshes containing many levels of nesting. The model handles heat transfer by conduction,

convection, and radiation. The simulation time is 6 years, which includes the 4.1-year heating phase, and 1.9 years of the ongoing cooldown phase.

The thicknesses of hydrogeologic units in the model were obtained by using YMESH v1.54 (Section 3.1.7) to extract a profile of the units located at the origin of the DST field coordinate system, E171432, N234060 (CRWMS M&O 1998a). The model extends from the ground surface to the water table 576 m below the surface, 278 m in the x-direction, and 478 m in the y-direction. The center of the bulkhead is located at elevation 1,053 m, 253 m below the ground surface, and 323 m above the water table. The test configuration geometry allows use of a half-symmetry model since the test is approximately symmetrical about the axis of the Heated Drift. The Connecting Drift, Access Observation Drift, and Plate-Loading Niche are not included in the model. Field data show that these structures have limited effect on the thermohydrologic response of the system within a radius of about 25 m from the Heated Drift.

The half-symmetry model has x-coordinate origin at the center of the bulkhead, and x positive in the direction away from the access drift (Northward). The y-coordinate axis is parallel to the axis of the Heated Drift with origin 215.9 m from the bulkhead, and positive in a general westerly direction. The z-direction is positive downward, with origin at the ground surface 252.9 m above the center of the bulkhead. The root mesh contains four levels of nesting, permitting sufficiently fine discretization in the Heated Drift and wing heater areas, while limiting memory requirements and computation time for the relatively large model. Element dimension varies from 6 cm in the bulkhead to tens of meters away from the heated areas of the test. The model has a total of 58,258 active elements, 29,129 elements in each of the two continua.

The origin of field coordinates is located at the center of the cold side of the bulkhead that separates the Heated Drift from an unheated and ventilated section of the drift. The y-axis extends from the origin through the bulkhead towards the back end of the Heated Drift (positive to west). X is positive in a direction away from the access drift (approximately north) and z is positive upward. The origin of field coordinates is located at approximately (0, 216, 253) with respect to the computational mesh.

The Heated Drift section in the x-z plane is stair-stepped to approximate the 5-m diameter circular drift using a rectangular Cartesian coordinate system. The surface of the invert is 1.3 m below the center of the drift. Since no thermal and hydrologic properties are available for the invert, material properties of the host rock, Tptpmn (tsw34), are assumed to be applicable to the invert for the DST thermohydrologic calculation (Sections 5.3.1.3 and 5.3.2.5).

The nine cylindrical heaters along the Heated Drift are modeled as having a square cross section with area equal to that of the 1.7-m diameter of the cylinder. There are no gaps between the heaters in the model; however, the thermal influence of the gaps is represented by removing conductive heat transfer between the ends of the heaters and by adding thermal-radiative heat transfer between the ends of the heaters. Thermal-radiative heat transfer between heater and rock wall elements and across rock wall elements is handled in the model. No fluid flow between canisters is permitted. Wing heater arrays are treated as a separate smeared heat sources.

7.2.2.1 Wing-Heater Arrays

Because the wing-heater boreholes are open to the Heated Drift and because they reside in the area of intensive boiling they are preferential conduits for the flow of water vapor into the Heated Drift. Once the water vapor enters the Heated Drift it then tends to flow towards and through the leaky bulkhead. The NUFT thermohydrologic model of the DST does not discretely represent the wing-heater boreholes. However, it is important to include the influence of the wing-heater boreholes on the preferential flow of water vapor. To include the influence of these conduits, the fracture permeability is treated as being anisotropic over the volume of rock occupied by the wing-heater boreholes. The fracture permeability in the x-direction (which is lateral to the Heated Drift axis) is increased by a factor of 1,000 relative to the value of fracture permeability for the Tptpmn (tsw34) unit (Section 5.3.1.4).

7.2.2.2 Bulkhead

The bulkhead, which separates the hot and cold sides of the Heated Drift, is treated as being highly permeable (Section 5.3.1.5). This was necessary because gas-phase pressure measurements across the bulkhead suggest that the structure acts as a nearly open boundary that allows substantial vapor loss from the Heated Drift. As described in *Drift Scale Test As-Built Report* (CRWMS M&O 1998a), the bulkhead consists of a complex mix of steel, glass, and fiberglass. The thermal conductivity of the bulkhead is assumed to be very large (Section 5.3.2.6) because portions of the bulkhead (such as the glass window) are not insulated and because the bulkhead is penetrated by a large array of metal conduit containing instrument cables and power lines.

7.2.2.3 Initial and Boundary Conditions

One-dimensional initialization models with the stratigraphic profile developed from YMESH were used to establish initial conditions for the full three-dimensional models. Boundary conditions were obtained using the boundary_conditions v1.0 (Section 3.1.8), a code developed for calculating boundary conditions for Multiscale submodels based on location on Yucca Mountain. For the medium infiltration present day percolation flux of 5.922 mm/yr, at the Easting and Northing of the center of the bulkhead, the surface and water table boundary conditions were obtained from boundary_conditions v1.0 (Section 3.1.8). Surface boundary variables calculated were temperature, pressure, air mass fraction, and specific enthalpy of water. Water table variables were temperature and pressure. The simulation time used for one-dimensional initialization run is 1.0×10^9 years. The initialization process is equivalent to that of the LDTH submodels.

7.2.3 Comparison of Simulated and Field-Measured Temperatures

Temperatures are monitored in the DST area on a continuous basis by thermocouple Resistance Temperature Device (RTD) sensors along 28 boreholes; thus the boreholes containing the thermocouples are called RTD boreholes. The source DTNs for all field measurements of temperatures in the DST are listed in Table 4-3. The spatial layout of the 28 RTD boreholes is shown in Figure 7.2.2-1 of *Drift-Scale Coupled Processes (DST and TH Seepage) Models* (BSC 2003j). For the purpose of comparison with the simulated temperatures, a daily temperature value is taken at 00:00 Greenwich Mean Time. Table 7.2-1 summarizes the RTD

boreholes that were used to compare against the NUFT-simulated temperatures. The NUFT simulations considered three cases. The base case represents the bulkhead as being thermally insulated and permeable, thereby being leaky to gas flow. The sealed bulkhead case represents the bulkhead as being thermally insulated and impermeable, thereby allowing no gas flow across it. The high thermal conductivity K_{th} case is the same as the base case with K_{th} being one standard deviation above the mean, based on Table 7-10 of *Thermal Conductivity of the Potential Repository Horizon Model Report* (BSC 2002a).

Table 7.2-1. Summary of thermocouple (RTD) boreholes used to compare field-measured temperatures with NUFT-simulated temperatures. The indicated orientation is relative to the Heated Drift. The source of the coordinates is given in Tables S00085_001 and S00085_002 of DTN: MO0002ABBLSLDS.000.

Borehole Number	Figure	Orientation	Collar X Coordinate	Collar Y Coordinate	Collar Z Coordinate
137	7.2-3, 7.2-4	Vertical above HD (+Z)	0.775	11.918	2.510
141	7.2-3, 7.2-4	Vertical below HD (-Z)	0.764	11.893	-1.637
168	7.2-5, 7.2-6	Vertical above HD (+Z)	-0.071	31.952	2.451
169	7.2-5, 7.2-6	Vertical below HD (-Z)	-0.003	32.007	-1.629
170	7.2-7, 7.2-8	Vertical above HD (+Z)	0.751	39.306	2.488
173	7.2-7, 7.2-8	Vertical below HD (-Z)	0.758	39.324	-1.623
139	7.2-9, 7.2-10	Lateral (-X)	-2.569	11.891	-0.017
143	7.2-9, 7.2-10	Lateral (+X)	2.665	11.890	-0.008
79	7.2-11, 7.2-12	Longitudinal (+Y)	9.460	-11.022	3.752
80	7.1-11, 7.2-12	Longitudinal (+Y)	-9.486	-11.059	3.228

NOTE: HD = Heated Drift

Figure 7.2-2 shows the temperature contours near the end of the heating phase (1,500 days) in plan view through a plane at the elevation of the wing-heater array and for a vertical cross-section midway along the length of the Heated Drift. Note that the heaters are turned off at 1,503 days. Notice that the highest temperatures are located close to the wing heaters and that the temperature contours are very vertically symmetrical about the heater horizon, which indicates that heat flow there is dominated by heat conduction. Because the bulk permeability k_b of the DST area is less than the threshold k_b value at which buoyant gas-phase convection begins to significantly influence heat flow (Buscheck and Nitao 1994, pp. 2,457 to 2,459), heat flow in the subboiling region is dominated by heat conduction.

Figures 7.2-3 through 7.2-8 compare NUFT-simulated temperatures (for three cases) with measured temperatures along vertically oriented RTD boreholes. Several general observations can be made about the temperature comparisons in the vertical RTD boreholes.

- NUFT-simulated temperatures are higher than the measured temperatures in the zone where temperatures exceed 96°C.
- NUFT-simulated temperatures agree fairly well with measured temperatures for the lower temperature range (less than 80°C) during the heating phase.
- The high-K_{th} case, which results in the lowest NUFT-simulated temperatures, is in best agreement with the measured temperatures during both the heating and cooldown phases.

- The sealed-bulkhead case results in slightly higher NUFT-simulated temperatures than the base case (which had a leaky bulkhead). The influence of the leaky bulkhead (versus the case with a sealed bulkhead) on simulated temperatures is much less than that resulting from a one standard-deviation range in thermal conductivity (which is evident in the temperature differences between the high- K_{th} case and the base case).

- The distinctive "plateau" in temperature (close to 96°C) develops (early on) in virtually all of the measured temperature profiles; however, they only appear in a few of the NUFT-simulated temperature profiles at later times. The underlying cause for the limited occurrences of NUFT-simulated temperature plateaus (at 96°C) is the very low value of matrix permeability in the Tptpmn (tsw34) in the TSPA-LA base-case hydrologic property set, which results in a very large gas-phase pressure buildup in the matrix. The impact of the large gas-phase pressure buildup is discussed in more detail in Section 7.2.4.

- The measured temperatures appear to indicate a more rapid cooldown than the NUFT-simulated cooldown.

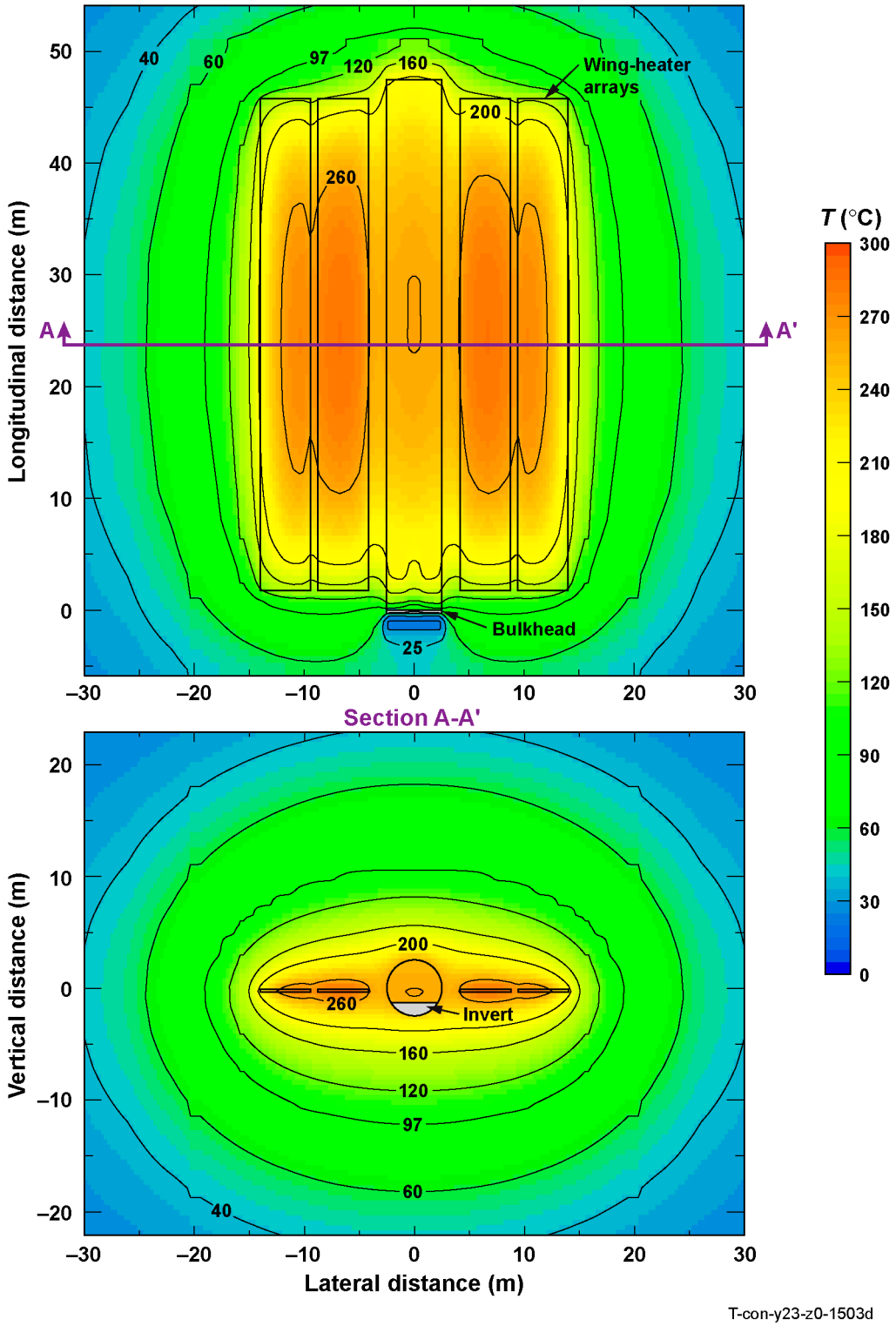

Figure 7.2-2. Contours of temperature (for the base case) at the end of the heating phase (1,503 days) are plotted in (a) plan view through a horizontal plane at the elevation of the wing-heater array and (b) for a vertical cross-section midway along the Heated Drift (y = 22.9 m). Note that the heaters are turned off at 1,503 days.

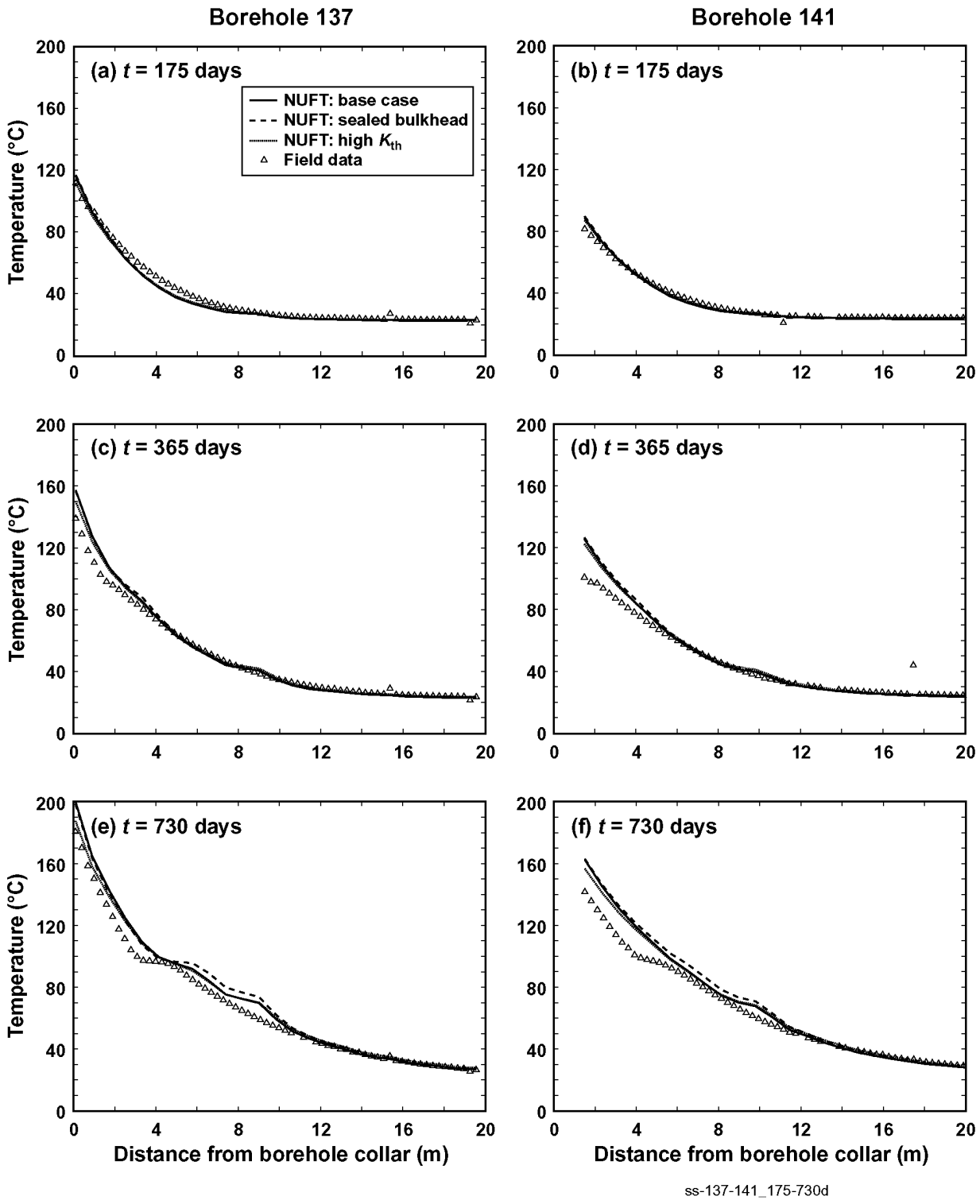

Figure 7.2-3. NUFT-simulated and measured temperatures are compared along Borehole 137 (a, c, e) and Borehole 141 (b, d, f) at 175, 365, and 730 days. The NUFT simulations are for the three indicated cases. The base case represents gas leakage through the bulkhead, while the sealed-bulkhead case does not allow gas leakage through the bulkhead. The high-K_{th} case is the same as the base case except with the host-rock thermal conductivity K_{th} being one standard deviation higher than the mean.

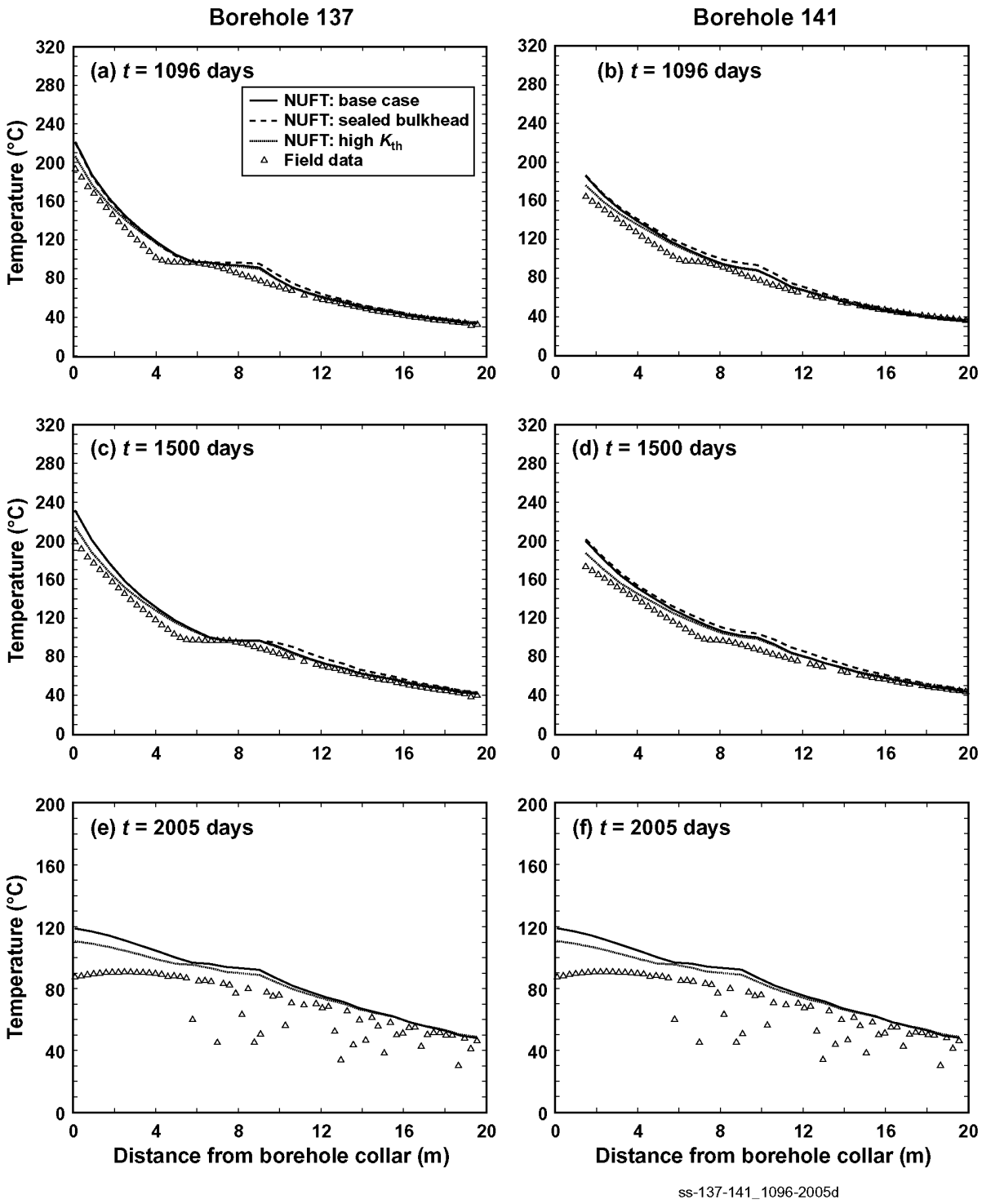

Figure 7.2-4. NUFT-simulated and measured temperatures are compared along Borehole 137 (a, c, e) and Borehole 141 (b, d, f) at 1,096, 1,500, and 2,005 days. The NUFT simulations are for the three indicated cases. The base case represents gas leakage through the bulkhead, while the sealed-bulkhead case does not allow gas leakage through the bulkhead. The high-K_{th} case is the same as the base case except with the host-rock thermal conductivity K_{th} being one standard deviation higher than the mean. Note that the heaters are turned off at 1,503 days.

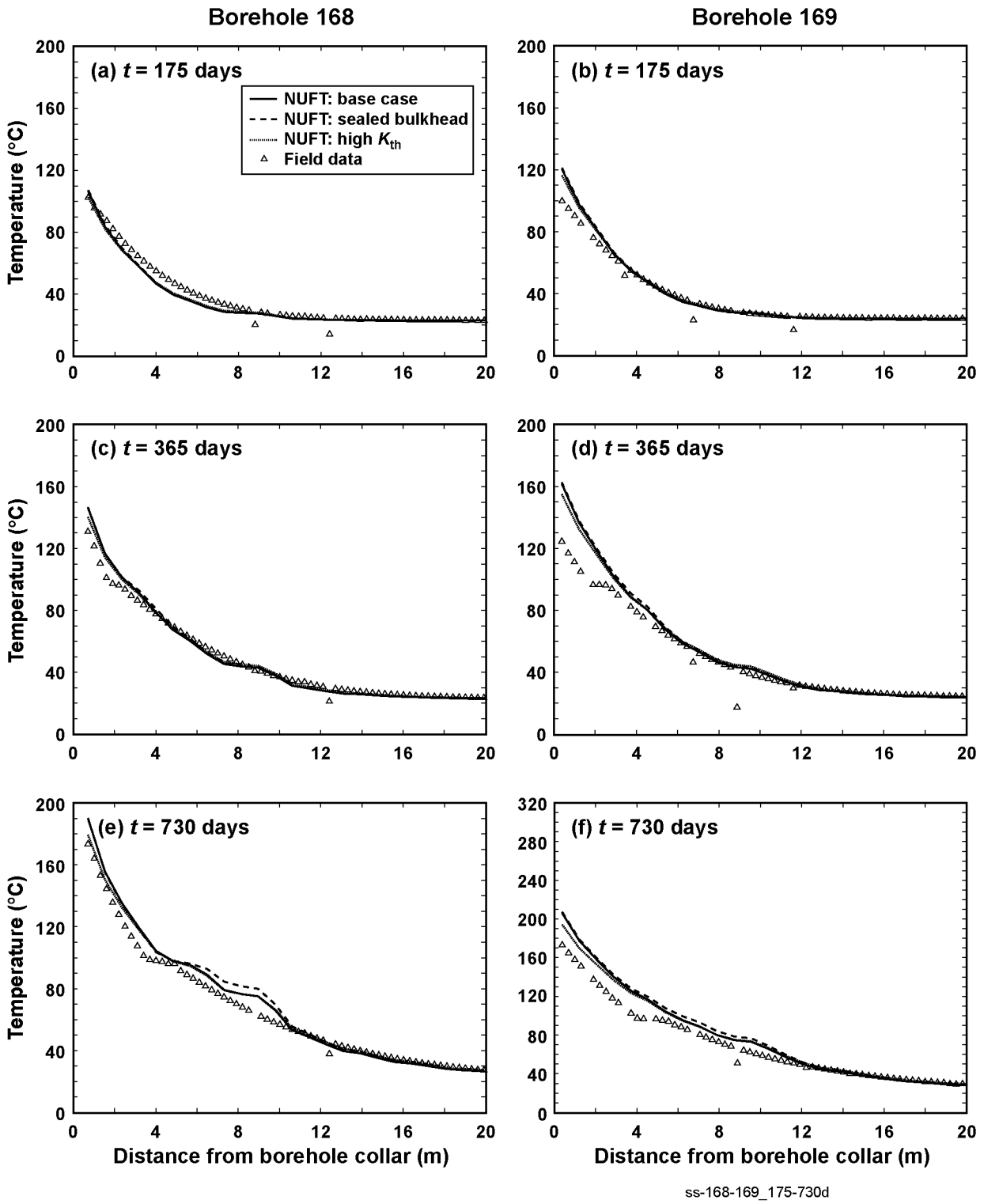

Figure 7.2-5. NUFT-simulated and measured temperatures are compared along Borehole 168 (a, c, e) and Borehole 169 (b, d, f) at 175, 365, and 730 days. The NUFT simulations are for the three indicated cases. The base case represents gas leakage through the bulkhead, while the sealed-bulkhead case does not allow gas leakage through the bulkhead. The high-K_{th} case is the same as the base case except with the host-rock thermal conductivity K_{th} being one standard deviation higher than the mean.

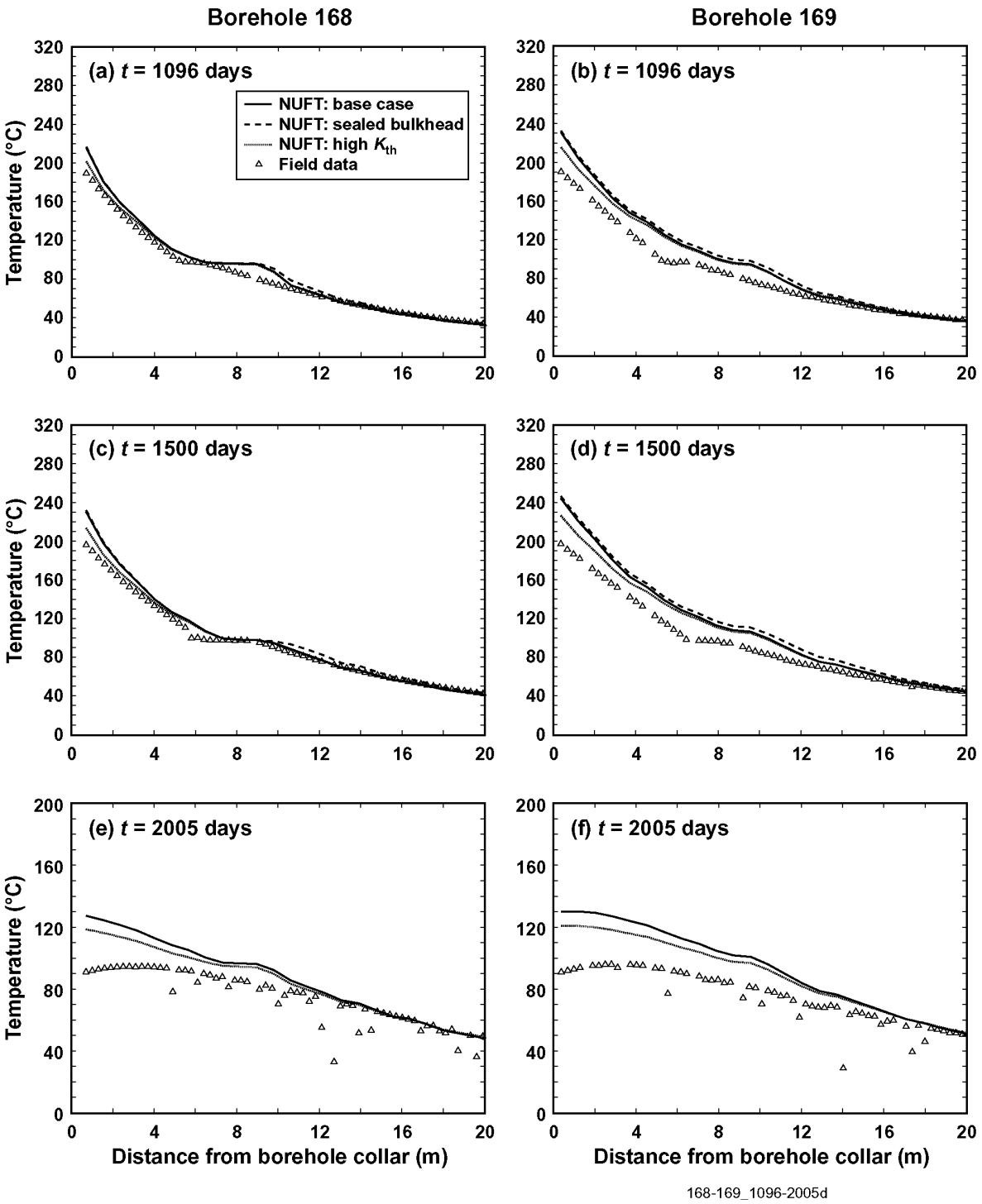

Figure 7.2-6. NUFT-simulated and measured temperatures are compared along Borehole 168 (a, c, e) and Borehole 169 (b, d, f) at 1,096, 1,500, and 2,005 days. The NUFT simulations are for the three cases. The base case represents gas leakage through the bulkhead, while the sealed-bulkhead case does not allow gas leakage through the bulkhead. The high-Kth case is the same as the base case except with the host-rock thermal conductivity K_{th} being one standard deviation higher than the mean. Note that the heaters are turned off at 1,503 days.

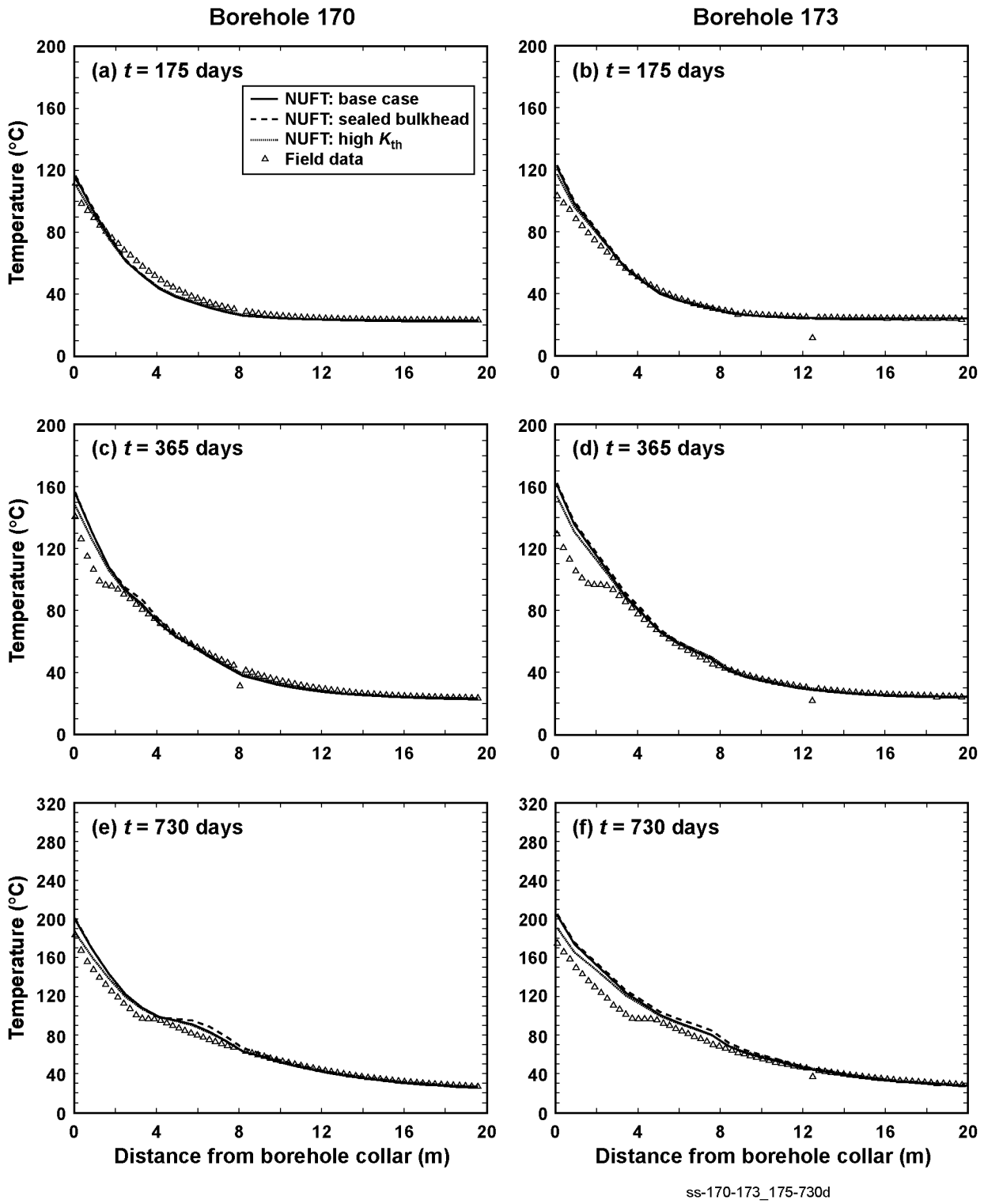

Figure 7.2-7. NUFT-simulated and measured temperatures are compared along Borehole 170 (a, c, e) and Borehole 173 (b, d, f) at 175, 365, and 730 days. The NUFT simulations are for the three indicated cases. The base case represents gas leakage through the bulkhead, while the sealed-bulkhead case does not allow gas leakage through the bulkhead. The high-K_{th} case is the same as the base case except with the host-rock thermal conductivity K_{th} being one standard deviation higher than the mean.

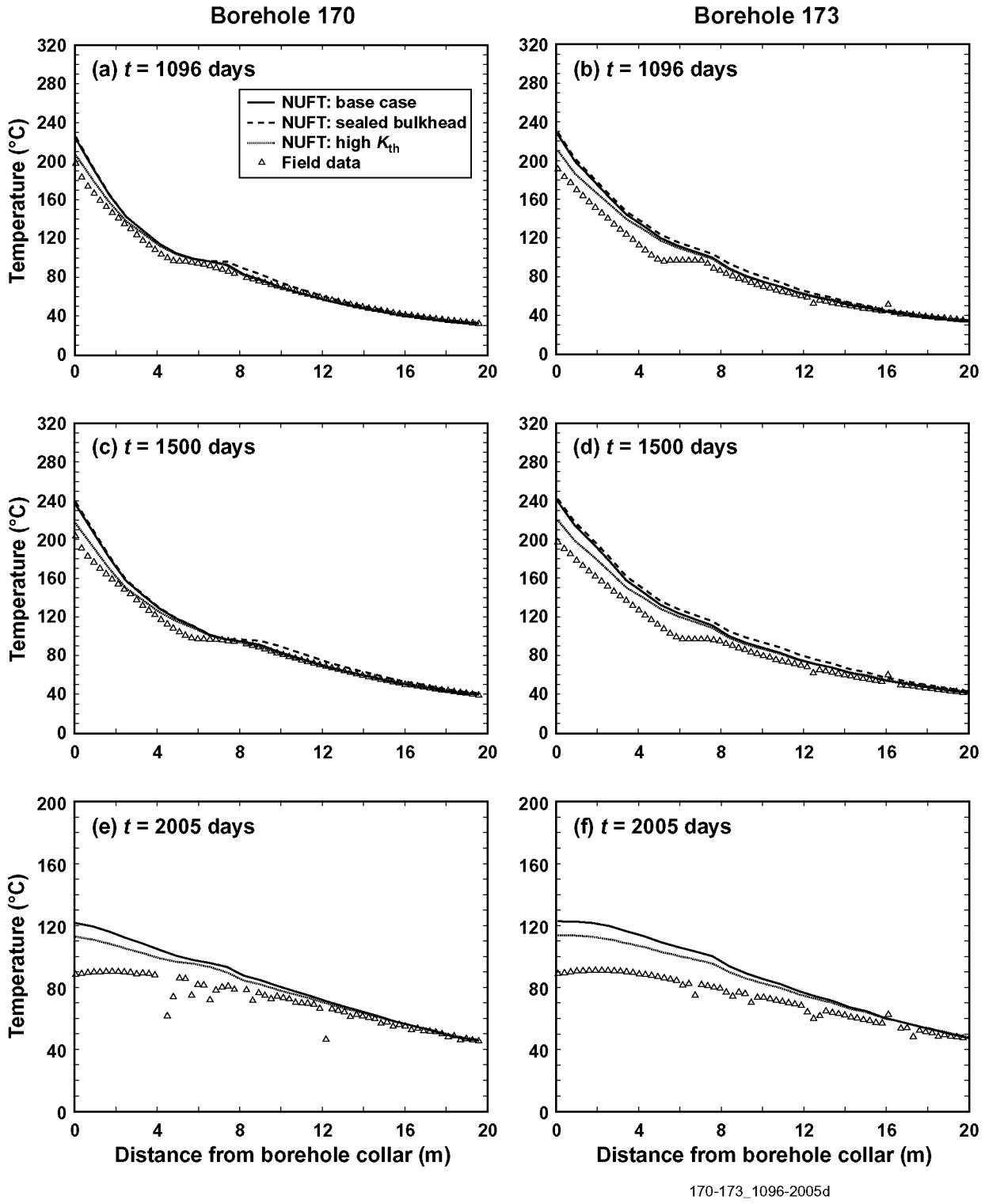

Figure 7.2-8. NUFT-simulated and measured temperatures are compared along Borehole 170 (a, c, e) and Borehole 173 (b, d, f) at 1,096, 1,500, and 2,005 days. The NUFT simulations are for the three indicated cases. The base case represents gas leakage through the bulkhead, while the sealed bulkhead case does not allow gas leakage through the bulkhead. The high-K_{th} case is the same as the base case except with the host-rock thermal conductivity K_{th} being one standard deviation higher than the mean. Note that the heaters are turned off at 1,503 days.

Figures 7.2-9 and 7.2-10 compare NUFT-simulated temperatures (for the three cases) with measured temperatures along horizontal (lateral) RTD boreholes. Several general observations can be made about the temperature comparisons in the horizontal (lateral) boreholes.

- NUFT-simulated temperatures are higher than the measured temperatures in the zone where temperatures exceed 96°C.
- NUFT-simulated temperatures agree fairly well with measured temperatures for the lower temperature range (less than 80°C) during the heating phase.
- The high-K_{th} case, resulting in the lowest NUFT-simulated temperatures, is in best agreement with the measured temperatures during the heating and cooldown phases.
- The sealed-bulkhead case results in slightly higher NUFT-simulated temperatures than the base case (which had a leaky bulkhead). The influence of the leaky bulkhead (versus the case with a sealed bulkhead) on simulated temperatures is much less than that resulting from a one standard-deviation range in thermal conductivity (which is evident in the temperature differences between the high- K_{th} case and the base case).
- At early time (175, 365, and 730 days), the NUFT-simulated temperature profiles develop more of a plateau than the measured temperature profiles within the zone of likely condensate shedding.
- At later time (1,096 and 1,500 days), the distinctive plateau in temperature (close to 96°C) appears in the measured temperature profiles. However, the NUFT-temperature profiles show a plateau at much higher temperatures. The underlying cause NUFT-simulated temperature plateau occurring at temperatures greater than 96°C is the low value of matrix permeability in the Tptpmn (tsw34) in the TSPA-LA base-case hydrologic property set, which results in a very large gas-phase pressure buildup in the matrix. Saturation (boiling) temperature increases with gas-phase pressure. Consequently, high gas-phase pressures in the matrix throttle both the boiling and rock dryout rates. The impact of the large gas-phase pressure buildup is discussed in more detail in Section 7.2.4.
- The measured temperatures appear to indicate a more rapid cooldown than the NUFT-simulated cooldown.
- For distances greater than 12 m from the borehole collar, there is a pronounced "scattering" of the measured temperature profile during the cooldown phase is indicative of preferential condensate drainage down fractures into the boreholes, resulting in local convective cooling. Note that the outer portions of Boreholes 139 and 143 are the intervals where condensate shedding is most likely to occur.

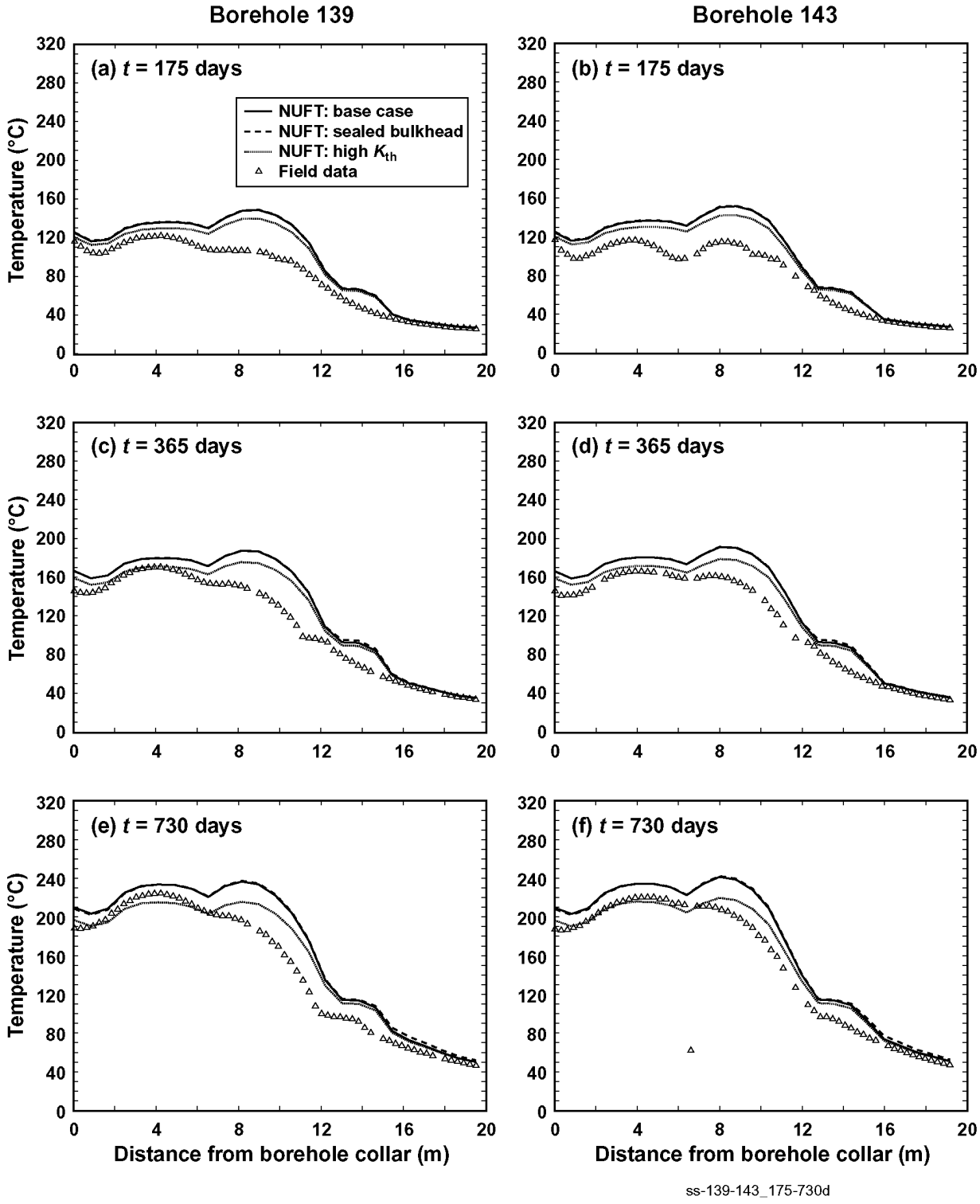

Figure 7.2-9. NUFT-simulated and measured temperatures are compared along Borehole 139 (a, c, e) and Borehole 143 (b, d, f) at 175, 365, and 730 days. The NUFT simulations are for the three indicated cases. The base case represents gas leakage through the bulkhead, while the sealed-bulkhead case does not allow gas leakage through the bulkhead. The high-K_{th} case is the same as the base case except with the host-rock thermal conductivity K_{th} being one standard deviation higher than the mean.

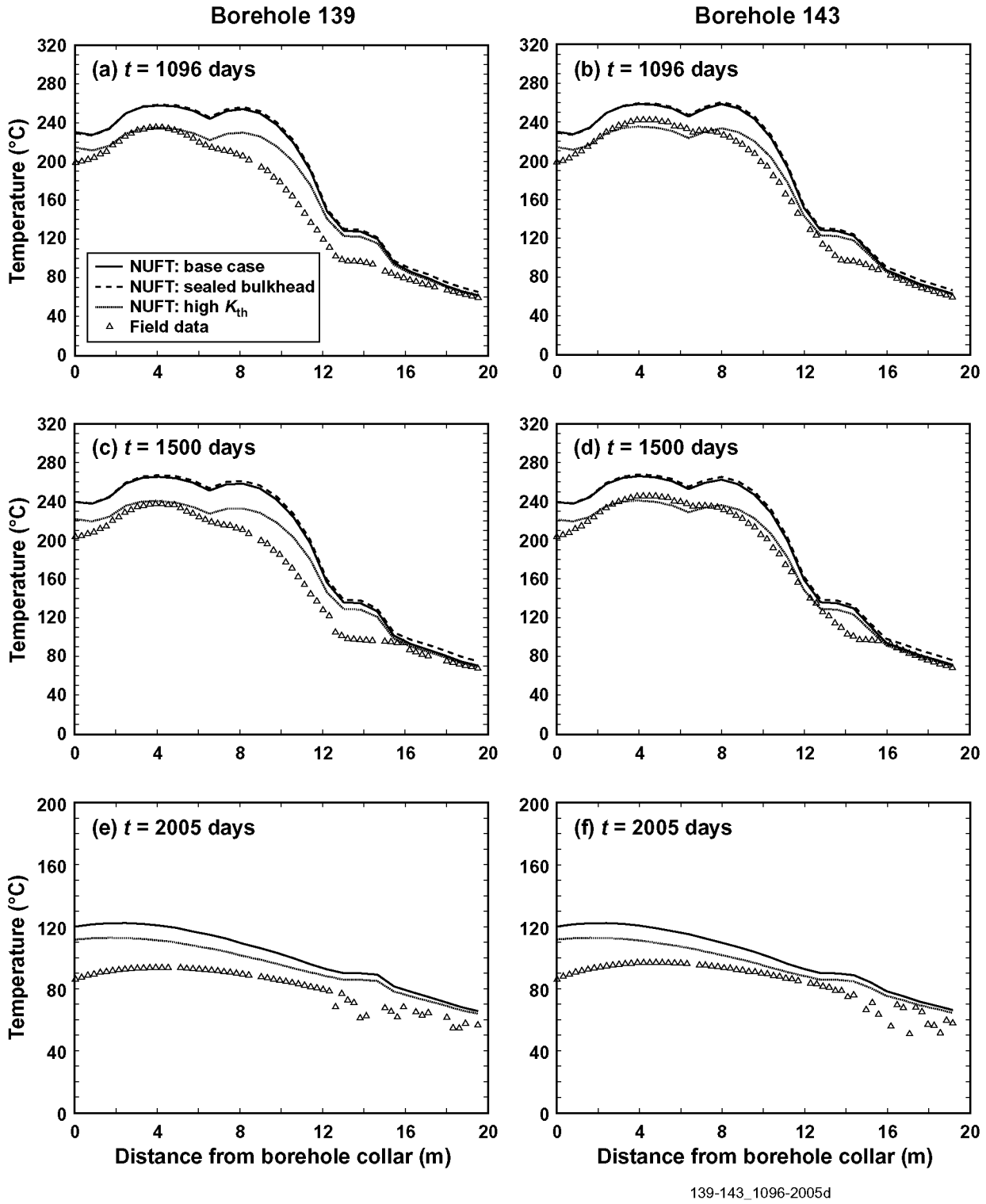

Figure 7.2-10. NUFT-simulated and measured temperatures are compared along Borehole 139 (a, c, e) and Borehole 143 (b, d, f) at 1,096, 1,500, and 2,005 days. The NUFT simulations are for the three indicated cases. The base case represents gas leakage through the bulkhead, while the sealed-bulkhead case does not allow gas leakage through the bulkhead. The high-K_{th} case is the same as the base case except with the host-rock thermal conductivity K_{th} being one standard deviation higher than the mean. Note that the heaters are turned off at 1,503 days.

Figures 7.2-11 and 7.2-12 compare NUFT-simulated temperatures (for the three cases) with measured temperatures along horizontal (longitudinal) RTD boreholes. Several general observations can be made about the temperature comparisons in the horizontal (longitudinal) boreholes.

- At early time (175 and 365 days) the NUFT-simulated temperatures agree closely with the measured temperatures. Good temperature agreement persists in Borehole 79 throughout the heating phase.

- At later time (730, 1,096, and 1,500 days) the NUFT-simulated temperatures are higher than the measured temperatures in Borehole 80 for the interval of 15 to 50 m from the borehole collar. For the interval of 0 to 15 m from the borehole collar, the measured temperatures are higher than the NUFT-simulated temperatures. The measured-temperature profile is strongly indicative the "cold-trap" effect whereby water vapor flows towards the borehole collar, condenses, and deposits the latent heat of condensation. The cold-trap effect removes the latent heat of evaporation from the interval of 15 to 50 m from the borehole collar and deposits this latent heat along the interval 0 to 15 m.

- The high-K_{th} case, which results in the lowest NUFT-simulated temperatures, is in best agreement with the measured temperatures during both the heating and cooldown phases.

- The measured temperatures appear to indicate a more rapid cooldown than the NUFT-simulated cooldown.

- The scattering of the measured temperature profile during the cooldown phase is indicative of preferential condensate drainage down fractures into the boreholes, resulting in local convective cooling. Note that Boreholes 79 and 80 are located in a region where condensate shedding is more likely to occur.

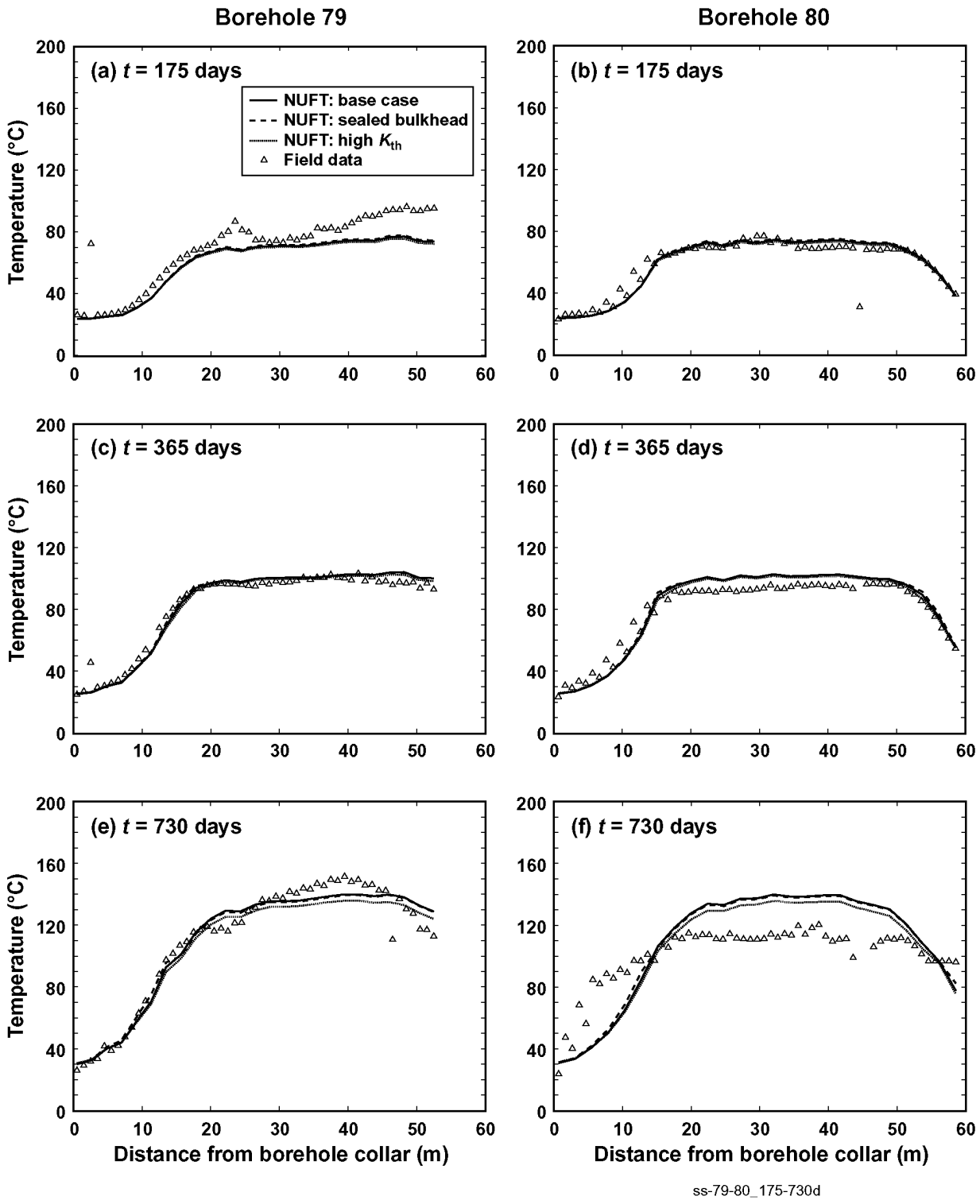

Figure 7.2-11. NUFT-simulated and measured temperatures are compared along Borehole 79 (a, c, e) and Borehole 80 (b, d, f) at 175, 365, and 730 days. The NUFT simulations are for the three indicated cases. The base case represents gas leakage through the bulkhead, while the sealed-bulkhead case does not allow gas leakage through the bulkhead. The high-K_{th} case is the same as the base case except with the host-rock thermal conductivity K_{th} being one standard deviation higher than the mean.

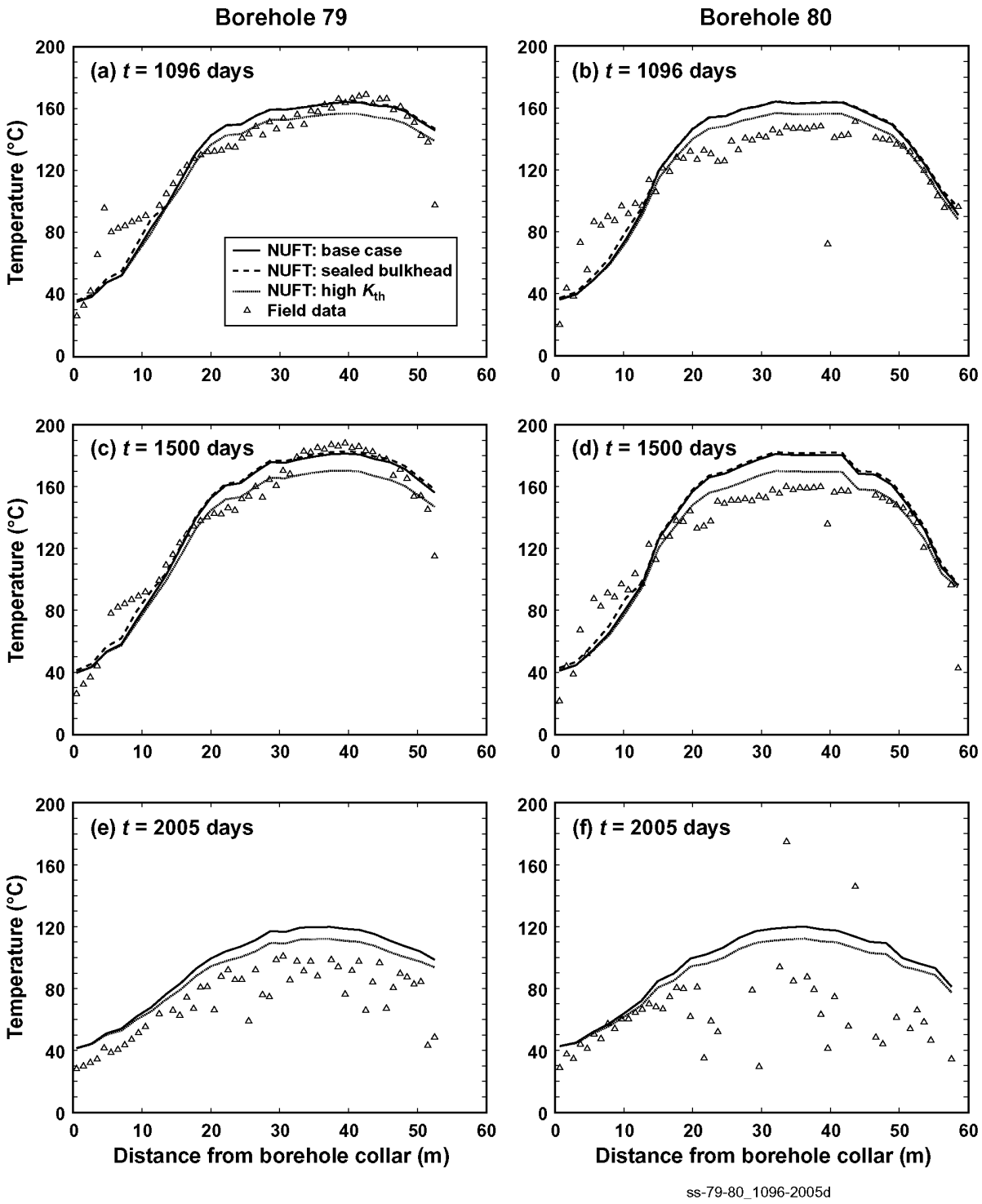

Figure 7.2-12. NUFT-simulated and measured temperatures are compared along Borehole 79 (a, c, e) and Borehole 80 (b, d, f) at 1,096, 1,500, and 2,005 days. The NUFT simulations are for the three indicated cases. The base case represents gas leakage through the bulkhead, while the sealed-bulkhead case does not allow gas leakage through the bulkhead. The high-K_{th} case is the same as the base case except with the host-rock thermal conductivity K_{th} being one standard deviation higher than the mean. Note that the heaters are turned off at 1,503 days.

Table 7.2-2 summarizes the information for the thermocouple sensors used to compare NUFT-simulated and field-measured temperature histories. Figures 7.2-13 through 7.2-16 compare NUFT-simulated temperature histories (for the three cases) with measured temperature histories. Several general observations can be made about the temperature-history comparisons.

- The measured temperature histories generally show a very pronounced plateau close to 96°C whereas the NUFT-measured temperature histories do not show plateau. The underlying cause for the absence of a NUFT-simulated temperature plateau is the very low value of matrix permeability in the Tptpmn (tsw34) in the TSPA-LA base-case hydrologic property set, which results in a very large gas-phase pressure buildup in the matrix. The impact of the large gas-phase pressure buildup is discussed in more detail in Section 7.2.4.

- The high-K_{th} case, which results in the lowest NUFT-simulated temperatures, is in best agreement with the measured temperatures during both the heating and cooldown phases.

- The sealed-bulkhead case results in slightly higher NUFT-simulated temperatures than the base case (which had a leaky bulkhead). The influence of the leaky bulkhead (versus the case with a sealed bulkhead) on simulated temperatures is much less than that resulting from a one standard-deviation range in thermal conductivity (which is evident in the temperature differences between the high-K_{th} case and the base case). The only exception to this observation is for Borehole 133: Sensor 23 (Figure 7.2-13b), which remains entirely within the subboiling zone. The significance of the lack of heat loss (through the bulkhead) for the sealed-bulkhead case is greatest for locations furthest removed from the center of heating.

The underlying cause for the absence of a NUFT-simulated temperature plateau (at 96°C) is the very low value of matrix permeability in the Tptpmn (tsw34) in the TSPA-LA base-case hydrologic property set, which results in a very large gas-phase pressure buildup in the matrix. The impact of the large gas-phase pressure buildup is discussed in more detail in Section 7.2.4. The absence of a temperature plateau at 96°C is the primary reason the NUFT-simulated temperatures are generally higher than the field-measured temperatures for temperatures exceeding 96°C; a secondary reason is uncertainty in thermal conductivity of the host rock in the DST. For temperatures less than about 80°C, the NUFT-simulated and field-measured temperatures are in good agreement for all three cases: (1) base case, (2) sealed bulkhead, and (3) high K_{th}. Overall, the comparison of NUFT-simulated and measured temperatures demonstrate that the NUFT thermohydrologic model provides a valid representation of heat flow in the DST.

Table 7.2-2. Coordinates of thermocouple sensors used in Figures 7.2-13, 7.2-14, and 7.2-15. The source of the coordinates is given in Table 4-3.

Borehole	Sensor	Figure	X Coordinate	Y Coordinate	Z Coordinate
133	52	7.2-13	0.85	2.81	17.85
133	23	7.2-13	0.79	2.77	9.12
141	20	7.2-13	0.70	11.94	-8.87
138	23	7.2-13	-6.39	11.77	6.36
134	8	7.2-14	0.73	2.74	-3.13
144	21	7.2-14	6.31	11.96	6.27
162	26	7.2-14	0.79	22.9	-8.85
163	24	7.2-14	6.39	22.72	-6.49
138	3	7.2-15	-2.15	11.88	2.12
139	23	7.2-15	-8.9	11.91	0.04
144	1	7.2-15	2.07	11.92	2.04
164	24	7.2-15	9.01	22.77	0.11

Source: CRWMS M&O 1998a

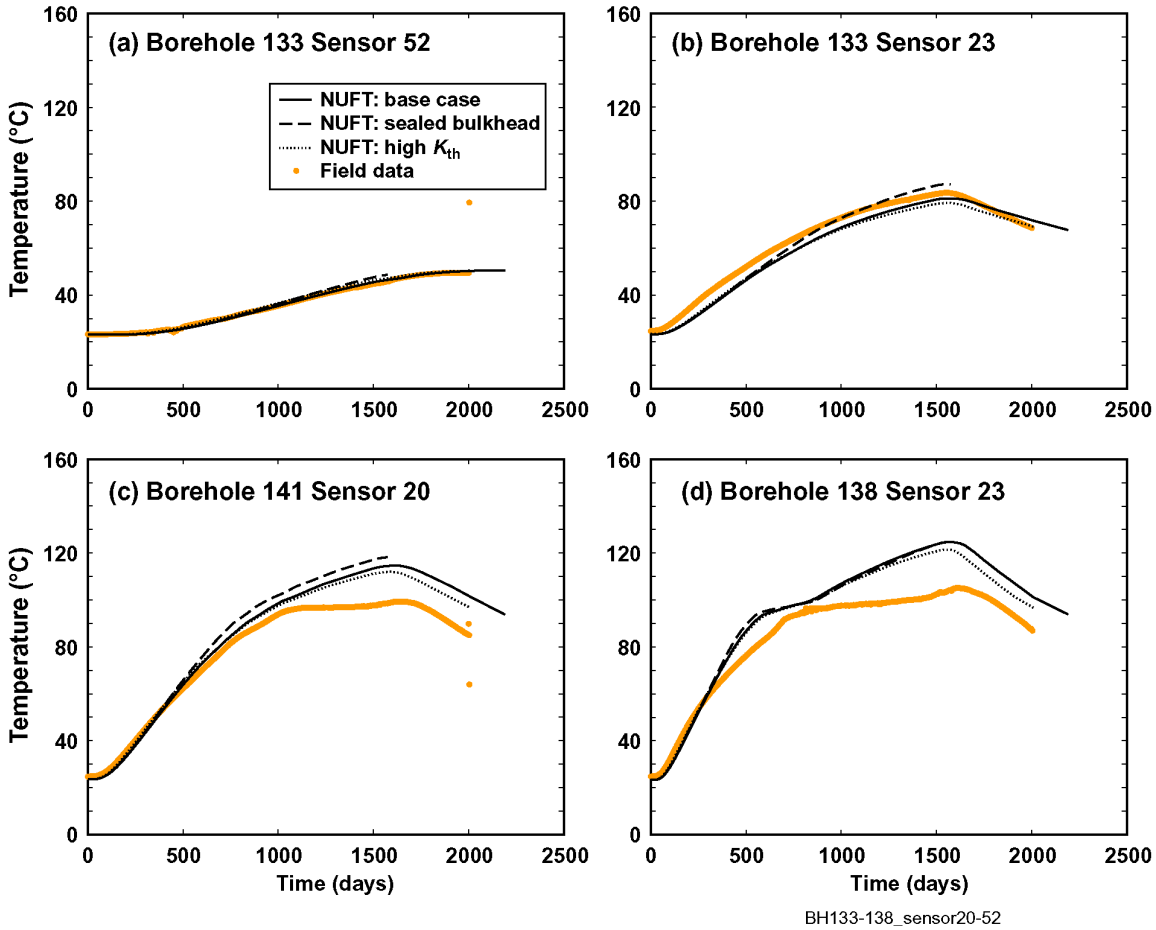

Figure 7.2-13. NUFT-simulated and measured temperature histories are compared at Borehole 133: Sensor 52 (a) and Sensor 23 (b), Borehole 141: Sensor 20 (c), and Borehole 138: Sensor 23 (d). The NUFT simulations are for the three indicated cases. The base case represents gas leakage through the bulkhead, while the sealed-bulkhead case does not allow gas leakage through the bulkhead. The high-K_{th} case is the same as the base case except with the host-rock thermal conductivity K_{th} being one standard deviation higher than the mean. Note that the heaters are turned off at 1,503 days.

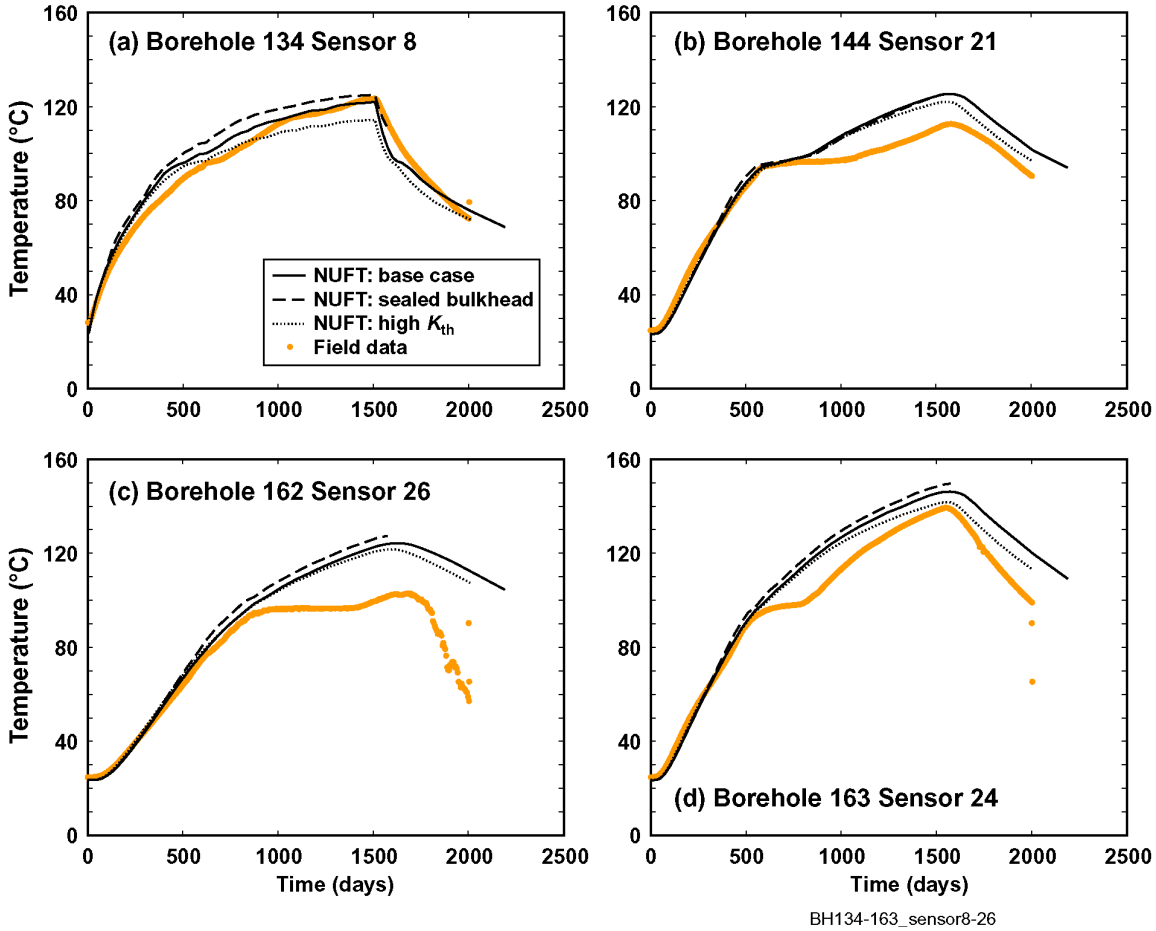

Figure 7.2-14. NUFT-simulated and measured temperature histories are compared at Borehole 134: Sensor 8 (a), Borehole 144: Sensor 21 (b), Borehole 162: Sensor 26 (c), and Borehole 163: Sensor 24 (d). The NUFT simulations are for the three indicated cases. The base case represents gas leakage through the bulkhead, while the sealed-bulkhead case does not allow gas leakage through the bulkhead. The high-K_{th} case is the same as the base case except with the host-rock thermal conductivity K_{th} being one standard deviation higher than the mean. Note that the heaters are turned off at 1,503 days.

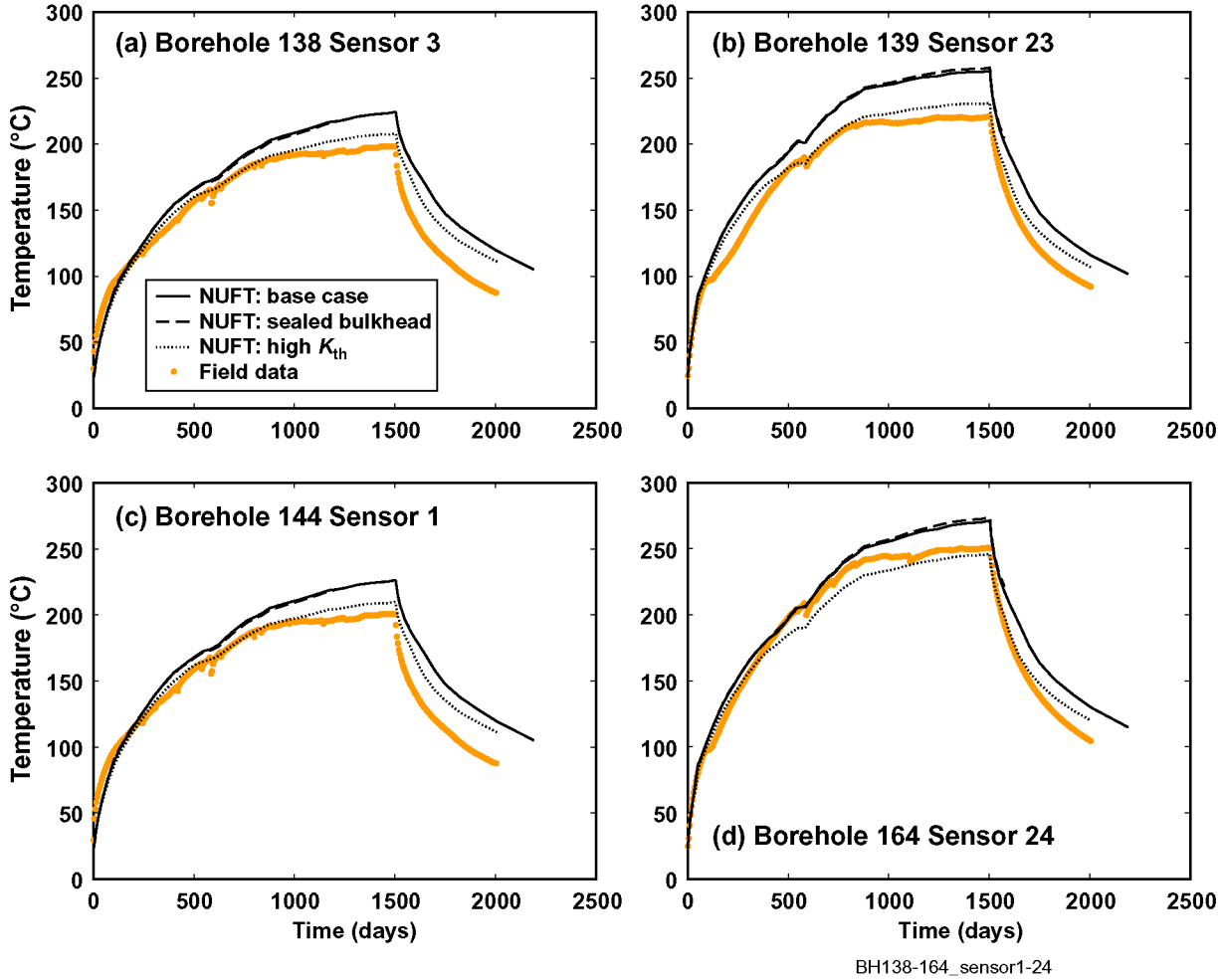

Figure 7.2-15. NUFT-simulated and measured temperature histories are compared at Borehole 138: Sensor 3 (a), Borehole 139: Sensor 23 (b), Borehole 144: Sensor 1 (c), and Borehole 164: Sensor 24 (d). The NUFT simulations are for the three indicated cases. The base case represents gas leakage through the bulkhead, while the sealed-bulkhead case does not allow gas leakage through the bulkhead. The high-K_{th} case is the same as the base case except with the host-rock thermal conductivity K_{th} being one standard deviation higher than the mean. Note that the heaters are turned off at 1,503 days.

7.2.4 Comparison of Simulated and Field-Measured Liquid-Phase Saturations

The source DTNs for all field measurements of liquid-phase saturations in the DST are listed in Table 4-3. Figure 7.2-16 shows the liquid-phase saturation contours near the end of the heating phase (1,500 days) in plan view through a plane at the elevation of the wing-heater array and for a vertical cross-section midway along the length of the Heated Drift. Note that the heaters are turned off at 1,503 days. The maximum spatial extent of rock dryout occurs at the end of the heating phase. The dryout zones have coalesced between the wing-heater arrays and the Heated Drift. Also, rock dryout is fairly vertically symmetrical about the heater horizon, indicating that condensate shedding is occurring efficiently around the edges of the boiling/rock-dryout zone.

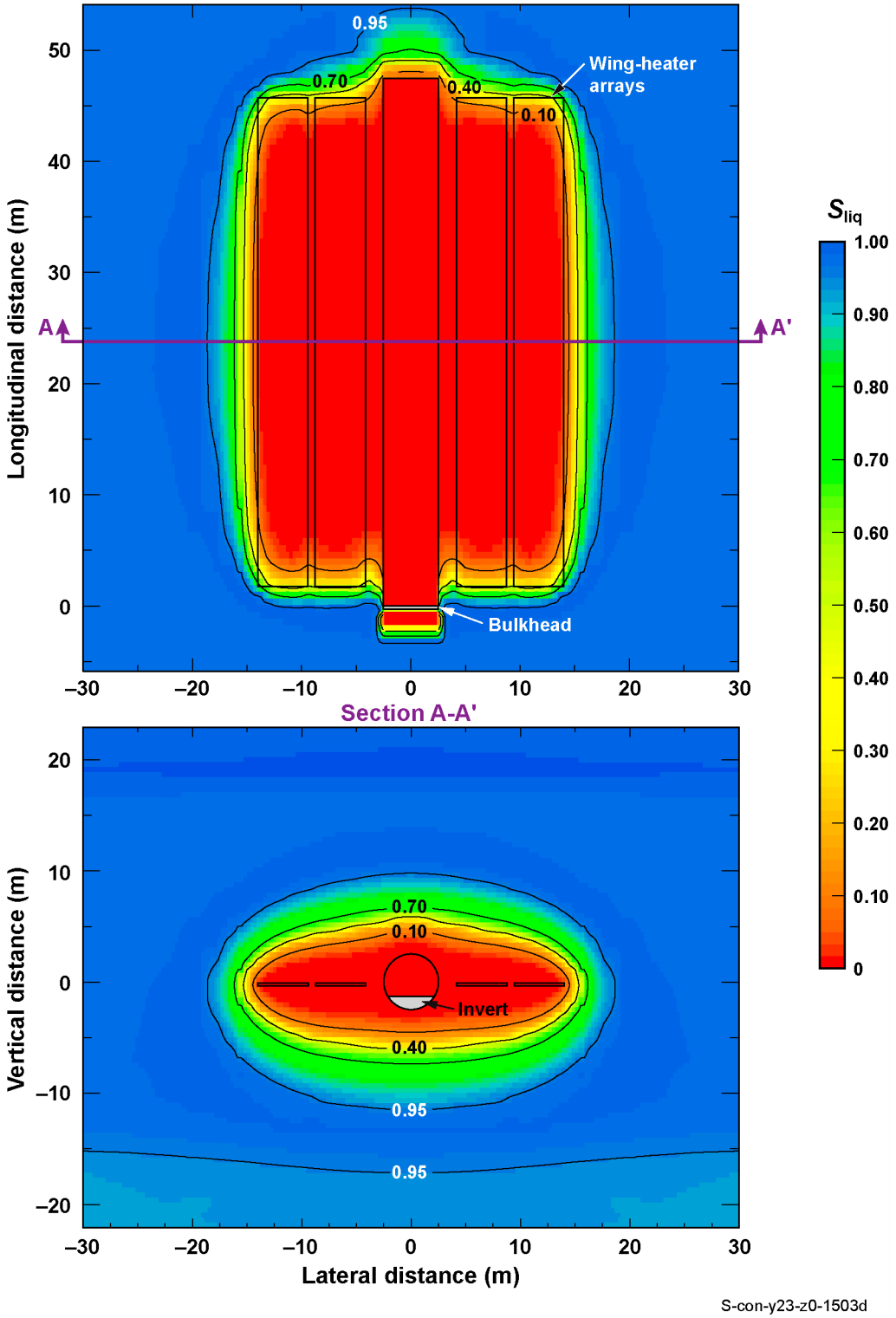

Figure 7.2-16 Contours of liquid-phase saturation (for the base case) at the end of the heating phase (1,503 days) are plotted in (a) plan view through a horizontal plane at the elevation of the wing-heater array and (b) for a vertical cross-section midway along the Heated Drift (y = 22.9 m). Note that the heaters are turned off at 1,503 days.

Figures 7.2-17 through 7.2-19 compare NUFT-simulated and measured liquid-phase saturation profiles along the Neutron Probe boreholes. Boreholes 79 and 80 are described in Table 7.2-1,

while Borehole 68 is an inclined borehole passing below the Heated Drift, as is shown in Figure 7.2.2-3 of *Drift-Scale Coupled Processes (DST and TH Seepage) Models* (BSC 2003j). All of the comparisons of liquid-phase saturation profiles clearly indicate that the NUFT-simulated rock dryout lags far behind the dryout measured in the field. Figure 7.2-20 shows the NUFT-simulated time histories of temperature, liquid-phase saturation, and gas-phase pressure in the matrix at two locations: 20 and 27 m from the collar in Borehole 68. An inspection of Table 7.2-3, which summarizes NUFT-simulated temperature, liquid-phase saturation, and gas-phase pressure in the matrix at those locations, clearly indicates that high gas-phase pressures in the matrix is throttling vaporization and delaying rock dryout (indicated by the NUFT-simulated liquid-phase saturation) compared to the observed dryout rate in the DST (indicated by field measurements of liquid-phase saturation). The implication is that the use of a larger value of matrix permeability in the NUFT thermohydrologic model would result in less of a delay in NUFT-simulated rock dryout compared to the observed dryout rate in the DST. This conclusion is supported by the comparison of NUFT-simulated and observed rock dryout for the Large Block Test (Figure 7.1-2), which showed that the use of a larger value of matrix permeability resulted in a larger dryout zone.

Table 7.2-3. NUFT-simulated (base-case) temperature, liquid-phase saturation, and gas-phase pressure in the matrix is summarized at 20 and 27 m from the collar of Borehole 68.

Distance (m) From Collar of Borehole 68	Time (days)	Temperature (°C)	Liquid-Phase Saturation	Gas-Phase Pressure in Matrix (atm)	Saturation Temperature from Steam Tables (°C)
20	877	128.7	0.806	2.600	128.7
20	1,242	143.9	0.684	4.032	143.9
20	1,500	150.9	0.560	4.864	150.9
20	1,917	118.2	0.376	1.946	118.2
27	877	121.8	0.847	2.100	121.8
27	1,242	139.7	0.721	3.582	139.7
27	1,500	147.8	0.632	4.476	147.8
27	1,917	128.0	0.462	2.562	128.0

The underlying cause for the NUFT-simulated dryout behavior lagging behind the dryout behavior observed in the DST is the very low value of matrix permeability in the Tptpmn (tsw34) in the TSPA-LA base-case hydrologic property set, which results in a very large gas-phase pressure buildup in the matrix. This large gas-phase pressure buildup throttles the rate of vaporization and delays dryout of the host rock in the DST. Eventually, the spatial extent of the NUFT-simulated dryout zones approaches that of the measured dryout zones. A comparison of the measure liquid-phase saturation profiles at 1,510 days (approximately when heating ceased) and 1,917 days shows that the dryout zone continues to expand during the cooldown phase. Thus, the DST measurements indicate that no rewetting has commenced prior to 1,917 days. Similarly, the NUFT-simulated liquid-phase saturations continue to decrease during the cooldown phase. Thus, the NUFT thermohydrologic model agrees with the field measurements of rewetting behavior in the DST.

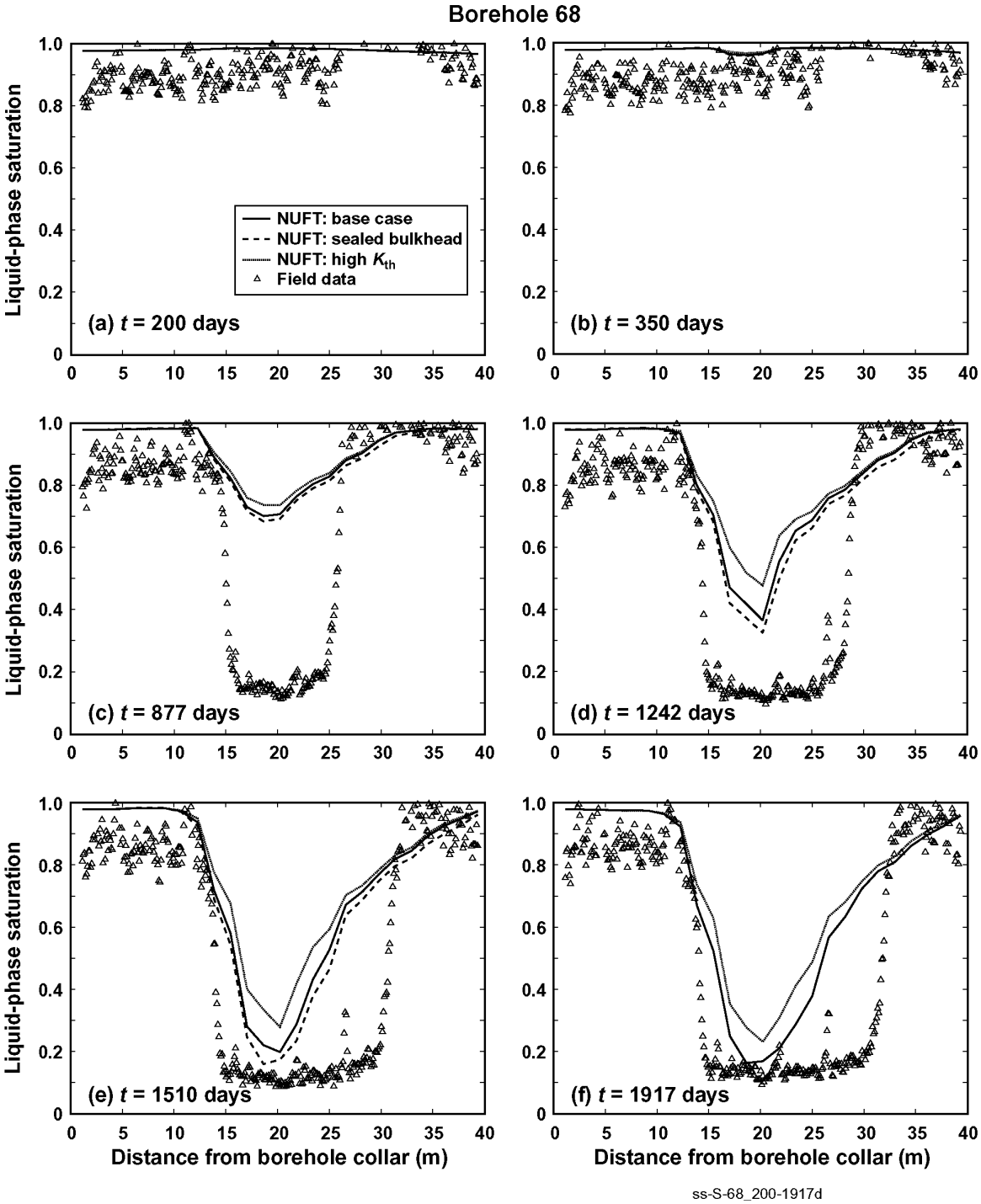

Figure 7.2-17. NUFT-simulated and measured liquid-phase saturations are compared along Borehole 68 at (a) 200 days, (b) 350 days, (c) 877 days, (d) 1,242 days, (e) 1,510 days, and (f) 1,917 days. The NUFT simulations are for the three indicated cases. The base case represents gas leakage through the bulkhead, while the sealed-bulkhead case does not allow gas leakage through the bulkhead. The high-K_{th} case is the same as the base case except with the host-rock thermal conductivity K_{th} being one standard deviation higher than the mean. Note that the heaters are turned off at 1,503 days.

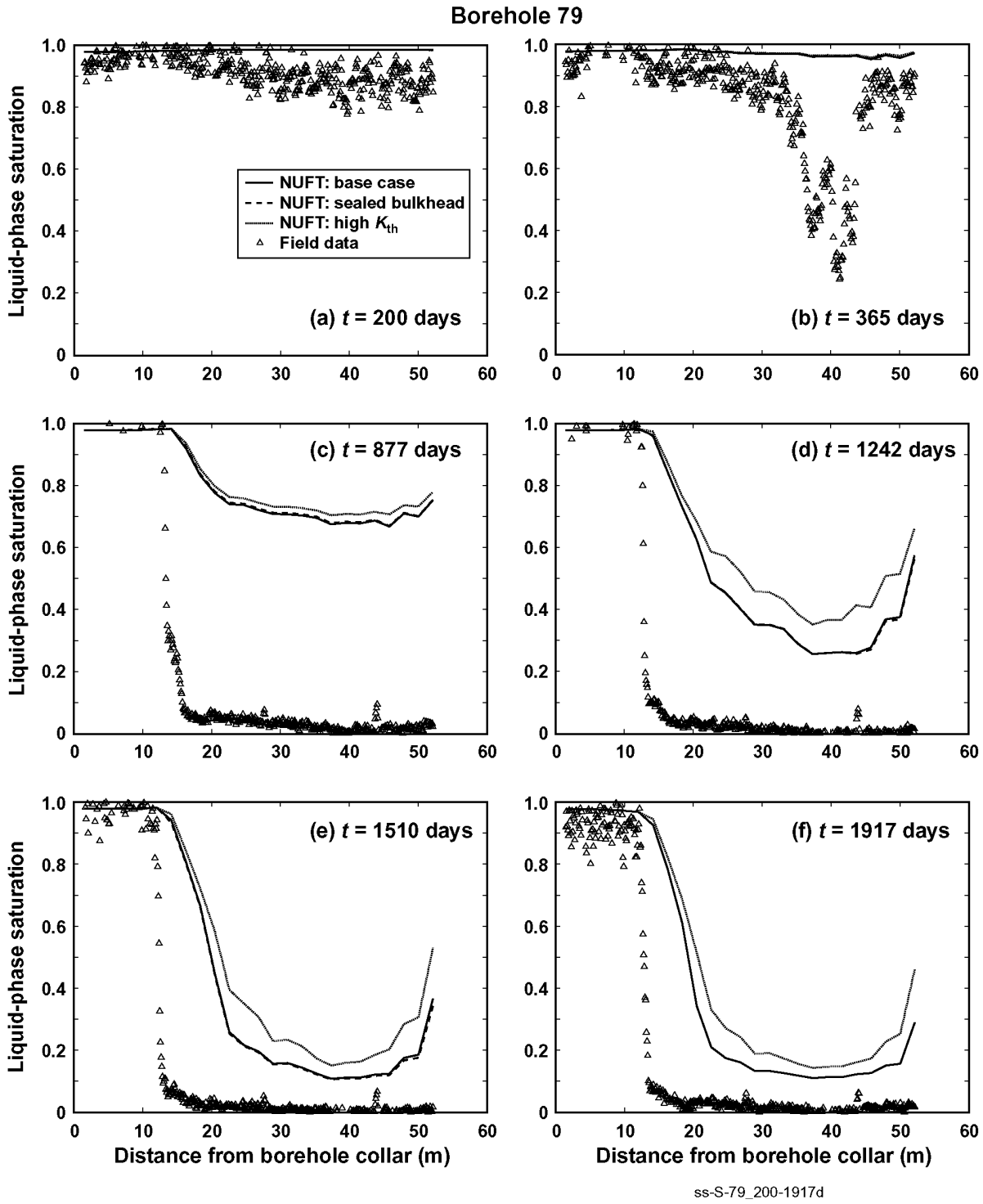

Figure 7.2-18. NUFT-simulated and measured liquid-phase saturations are compared along Borehole 79 at (a) 200 days, (b) 365 days, (c) 877 days, (d) 1,242 days, (e) 1,510 days, and (f) 1,917 days. The NUFT simulations are for the three indicated cases. The base case represents gas leakage through the bulkhead, while the sealed-bulkhead case does not allow gas leakage through the bulkhead. The high-K_{th} case is the same as the base case except with the host-rock thermal conductivity K_{th} being one standard deviation higher than the mean. Note that the heaters are turned off at 1,503 days.

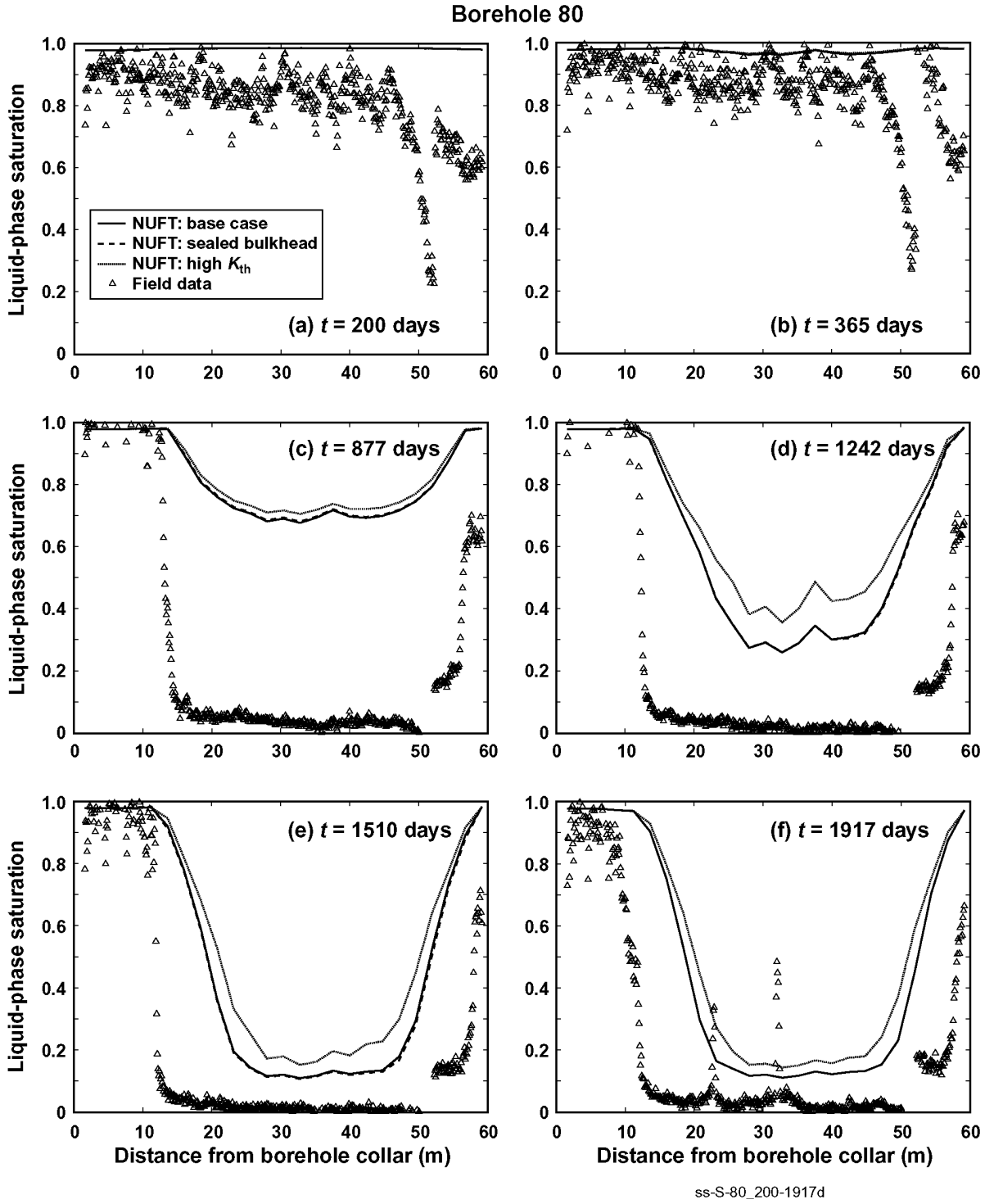

Figure 7.2-19. NUFT-simulated and measured liquid-phase saturations are compared along Borehole 80 at (a) 200 days, (b) 365 days, (c) 877 days, (d) 1,242 days, (e) 1,510 days, and (f) 1,917 days. The NUFT simulations are for the three indicated cases. The base case represents gas leakage through the bulkhead, while the sealed-bulkhead case does not allow gas leakage through the bulkhead. The high-K_{th} case is the same as the base case except with the host-rock thermal conductivity K_{th} being one standard deviation higher than the mean. Note that the heaters are turned off at 1,503 days.

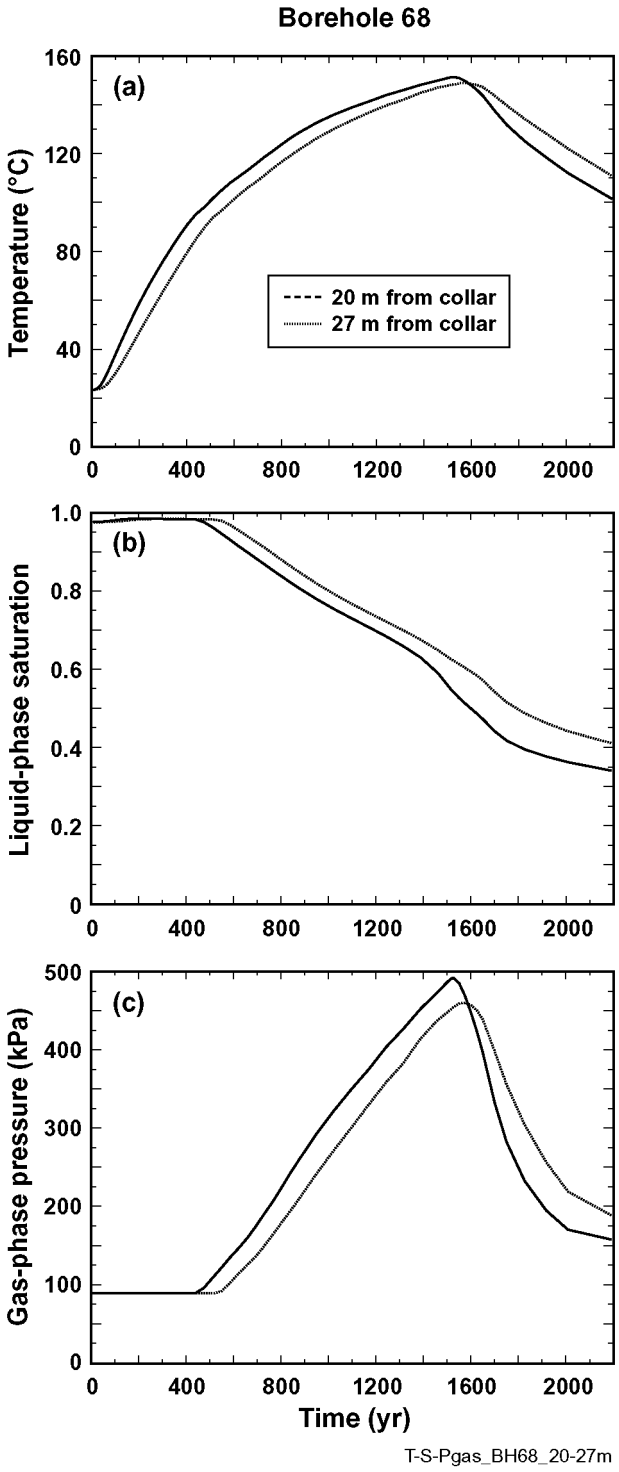

Figure 7.2-20. NUFT-simulated time histories of (a) temperature, (b) liquid-phase saturation, and (c) gas-phase pressure are plotted at distances of 20 m and 27 m from the collar of Borehole 68.

7.2.5 Summary of Model Validation Using DST Data

The underlying cause for the absence of a NUFT-simulated temperature plateau (at 96°C) is the low value of matrix permeability in the Tptpmn (tsw34) in the TSPA-LA base-case hydrologic

property set, which results in a large gas-phase pressure buildup in the matrix. The absence of a temperature plateau at 96°C is the primary reason the NUFT-simulated temperatures are generally higher than field-measured temperatures for temperatures exceeding 96°C; a secondary reason is the uncertainty in host-rock thermal conductivity K_{th} in the DST. For the high-K_{th} case (one standard deviation above the mean), the NUFT-simulated temperatures were in better agreement with the measured temperatures than the cases that used the mean K_{th} values. For temperatures less than about 80°C, the NUFT-simulated and field-measured temperatures are in good agreement for all three cases: (1) base case, (2) sealed bulkhead, and (3) high K_{th}. Overall, the comparison of NUFT-simulated and measured temperatures demonstrate that the NUFT thermohydrologic model provides a valid representation of heat flow in the DST.

The underlying cause for the NUFT-simulated throttled vaporization and delayed dryout (compared to dryout observed in the DST) is the high gas-phase pressure buildup in the matrix, which is caused by the low matrix permeability in the Tptpmn (tsw34) in the TSPA-LA hydrologic property set. Thus, the cause of the difference between the NUFT-simulated and observed rock-dryout rate is well understood. Eventually, the spatial extent of the NUFT-simulated dryout zone approaches that of the dryout zone observed in the DST. Therefore, the ultimate spatial extent of rock dryout simulated by the NUFT thermohydrologic model agrees with that measured in the DST. Therefore, it can be concluded that the NUFT thermohydrologic model provides a valid representation of rock dryout in the DST. To the extent that the observations in the DST allow, the NUFT thermohydrologic model provides a valid representation of rewetting behavior in the DST.

The overall impact of the modeling and parametric uncertainties in the DST is that the modeled behavior is somewhat higher in temperature and somewhat wetter than the field-measured conditions. The conclusion is that the MSTHM simulations of thermohydrologic behavior within emplacement drifts and in the adjoining host rock may be slightly biased on the high side for temperature, liquid-phase saturation, and relative humidity, all of which are conservative with respect to engineered barrier system performance.

Another key conclusion from the DST model-validation study is that the sealed-bulkhead case results in slightly higher NUFT-simulated temperatures than the base case (which had a very leaky bulkhead). The influence of the leaky bulkhead (versus the case with a sealed bulkhead) on simulated temperatures is much less than that resulting from one a one standard-deviation range in thermal conductivity. This conclusion is important with respect to the potential significance of whether the ends of the emplacement drifts are sealed with bulkheads or simply backfilled with highly permeable crushed tuff. The conclusion of the insensitivity of the DST thermohydrologic simulations to the treatment of the bulkhead (leaky versus sealed) clearly demonstrates that the MSTHM representation of thermohydrologic behavior in the emplacement drifts will not be significantly affected by whether the ends of the emplacement drifts are sealed.

7.3 COMPARISON OF THE MSTHM RESULTS AGAINST A MONOLITHIC THREE-DIMENSIONAL THERMOHYDROLOGIC MODEL

This model-validation test case is similar to that conducted by Buscheck, Glascoe et al. (2003). Using a three-drift repository as a model-validation test case, the MSTHM is applied along with a corresponding monolithic three-dimensional thermohydrologic model for calculating drift-scale thermohydrologic conditions. The monolithic thermohydrologic model, which is called a

Discrete-/Line-Averaged-Heat-Source Mountain-Scale Thermohydrologic (D/LMTH) model (Table 1-2), uses a nested mesh to represent detailed thermohydrologic behavior in the vicinity of the emplacement drifts as well as mountain-scale thermohydrologic behavior. Both the MSTHM and the corresponding monolithic three-dimensional D/LMTH model discretely represent eight individual waste packages down to the surface of the drip shield. Results from these two models are compared at the drift wall, drip shield, and invert. This comparison is the basis for the validation of the MSTHM methodology.

7.3.1 Description of the MSTHM Validation Test Case

The test case used to validate the MSTHM approach represents a scaled-down repository, consisting of three 243-m long drifts (Figure 7.3-1 and Table 7.3-1). The total heat output from these three drifts is 986.6 kW, representing approximately 143 average waste packages (Buscheck, Glascoe et al. 2003). This heat output is modeled in the three drifts as a line-averaged heat source everywhere except at the center of Drift #2 where 15 discrete waste packages are modeled: 7 at the center of Drift #2 and 4 at either end of Drift #2. Because the test case is symmetric, the 15 discrete waste packages can be modeled as the 7.5 discrete waste packages described in Table 7.3-2. The thermal-operating parameters of the three-drift repository system are equivalent to those being considered for the TSPA-LA except for the total inventory of waste packages. The waste packages are spaced end to end along the drift with a gap of 10.6 cm, which is similar to 10 cm gap that is being considered for the TSPA-LA (Table 4-1). Preclosure ventilation of the drifts is assumed to remove 70 percent of the heat generated during the 50-year ventilation period. Note that at the time this validation test case was developed, a heat-removal efficiency of 70 percent was being used in the MSTHM calculations in support of *FY 01 Supplemental Science and Performance Analyses, Volume 1: Scientific Bases and Analyses* (BSC 2001b). The initial heat output is 986.6 kW for the entire three-drift system, which is equivalent to about 1.18 percent of the 63,000-MTU thermal load (83,346 kW) for the repository. Note that the total repository thermal load is obtained by multiplying the initial linear power density of 1.45 kW/m (Table 4-1) by 57,480 m of heated emplacement drift (Table 6.2-1). Four different types of waste packages are represented in the test case and are described in Table 7.3-2.

Table 7.3-1. Design and Operating Parameters Used in MSTHM Validation Test Case

Parameter	Parameter Value
Drift spacing	81 m
Drift length	243 m
Drift diameter	5.5 m
Drip-shield diameter	2.512 m
Areal Mass Loading (AML)	54.5 MTU/acre*
Heated repository footprint	59,049 m2
Lineal Power Density	1.3534 kW/m
Total heat output	986.6 kW
Approximate number of waste packages represented in entire three-drift model	143
Heat removal by ventilation	70% for 50 years
Waste package configuration and spacing	Line load with10.6-cm gaps

Source: Buscheck, Glascoe et al. 2003, Table 4

*Note that this value is rounded to 55 MTU/acre elsewhere in Section 7.3.

Table 7.3-2. Waste Package Types Used in the MSTHM Validation Test Case

Waste Package Type	Waste Package Description	Number of Waste Packages*	Length (m)	Initial Heat Output (kW)
PWR1	Average 21-PWR CSNF	1.5	5.17	11.53
DHLW	Long DHLW	2	5.22	0.282
PWR2	Design-Basis 21-PWR CSNF	2	5.17	11.80
BWR	Average 44-BWR CSNF	2	5.17	7.377

Source: Buscheck, Glascoe et al. 2003

*The number of discrete waste packages in the quarter-symmetry element test case (Figure 7.3-1).

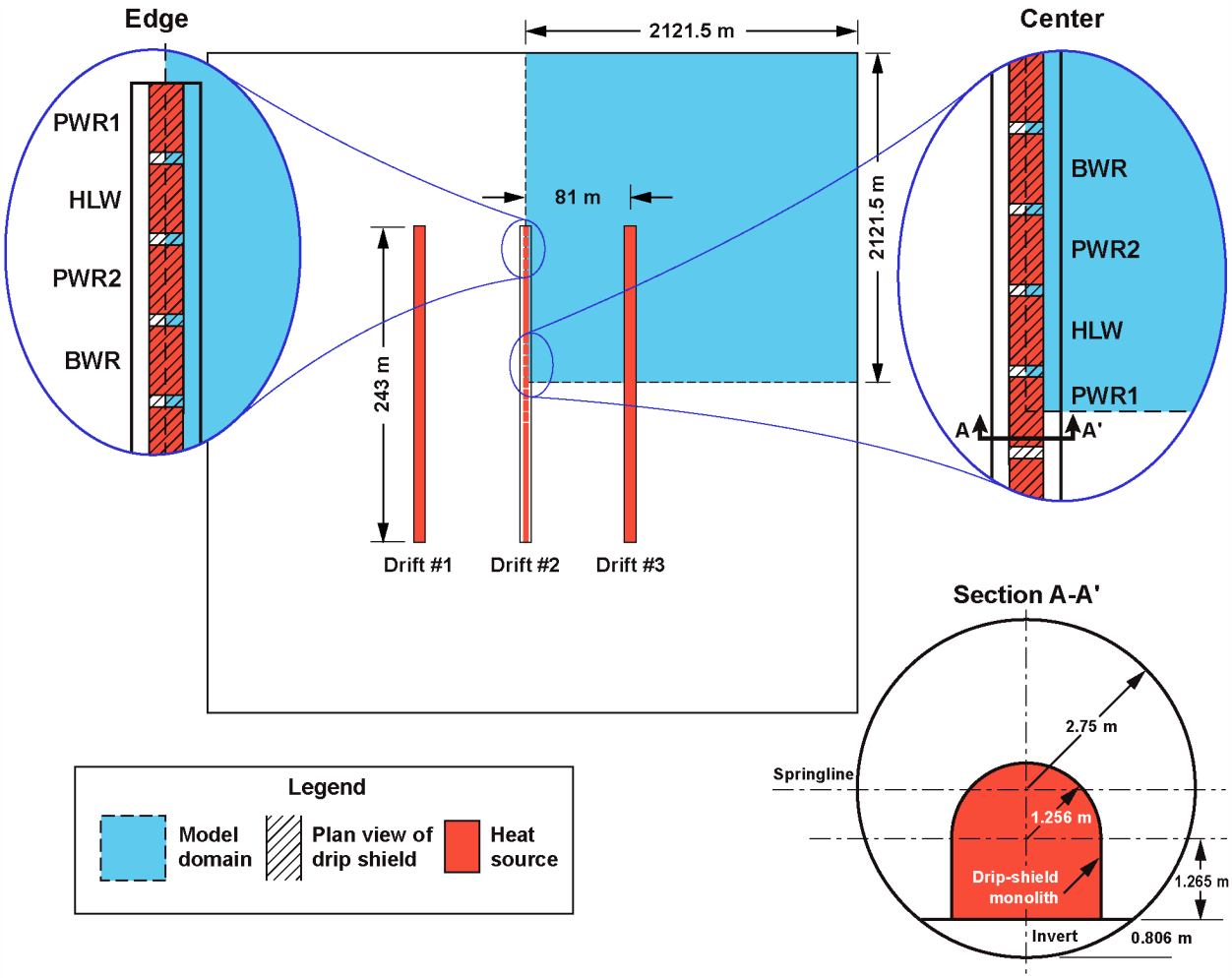

Figure 7.3-1. Drift-scale conceptual schematic is shown for the model-validation test case. To the upper left is the plan view of the three-drift repository system; highlighted in blue is the zone of symmetry. To the upper right is a close-up of the Drift #2 waste package sequencing. To the bottom right is the vertical cross-section of the modeled drift with the drip shield and waste package lumped together as a heat source.

The validation test case focuses on two locations: at the center and edge of the repository. At the center of the repository, four waste package types are discretely represented (Figure 7.3-1) in Drift #2, which is the central drift. At the edge of the repository, the same four waste package types are discretely represented; these four waste packages are also in Drift #2. In this test case,

the waste packages are not represented distinctly from the drip shield. Instead, the waste package and drip shield are lumped together and treated as a monolithic heat source. This simplification was made because of the computational expense of representing waste packages in a relatively complex thermohydrologic model like the D/LMTH model used in this test case. No further simplification of the drift was made (i.e., the conductive, convective, and radiative heat transfer occurring from the monolithic heat source to other generic locations within the drift are still modeled). The remainder of Drift #2, beyond the discretely represented waste package locations, has a line-averaged heat source within the drip-shield/waste package monolith (Figure 7.3-1). For Drifts #1 and #3, the heat-source representation is a line-averaged heat source distributed over the entire 5.5-m diameter cross section of the drift. Because heat is delivered directly to the host rock (with a line-averaged heat source) in Drifts #1 and #3, the contribution of thermal radiation and convection inside of those drifts is irrelevant. Within Drift #2, thermal radiation and natural convection are approximated with a time-dependent effective thermal conductivity for the drift cavity between the drip shield and the drift wall (CRWMS M&O 2001). Note that this approximation is different from that being used in the MSTHM calculations in support of the TSPA-LA (Section 6.3). However, for the purpose of the MSTHM validation problem it is only necessary that the MSTHM and the corresponding D/LMTH model both use the same approximation for thermal radiation and convection in the drift. Permeability in the drift cavity of Drift #2 (which is the central drift in Figure 7.3-1) is 1.0×10^{-8} m^2 in all three principal directions. Because advective and diffusive transport of gas can occur in the longitudinal direction along the drift axis, this model allows the cold-trap effect to occur. This D/LMTH model also allows liquid-phase flow in the invert to occur in the longitudinal direction along the drift axis. Note that in the MSTHM calculations in support of the TSPA-LA (Section 6.3) the permeability in the drift is 1.0×10^{-8} m^2 in the vertical and lateral directions. However, the MSTHM calculations in support of the TSPA-LA assume that gas- and liquid-phase flow in the longitudinal direction along the drift is negligible (Section 5.7). This assumption is equivalent to assuming that the cold-trap effect is negligible. A leaky bulkhead is placed at the very end of the heated portion of Drift #2 in the D/LMTH model. This leaky bulkhead is assumed to have the same bulk permeability as that of the adjoining host rock (Section 5.3.1.6).

A second set of D/LMTH model calculations were conducted in which the permeability in the drift cavity and in the invert of Drift #2 is set to zero in the longitudinal direction. Because this D/LMTH model prevents the cold-trap effect from occurring, it corresponds to the assumption in the MSTHM calculations in support of the TSPA-LA. The differences in thermohydrologic behavior in the drift between the D/LMTH model that allows gas-phase and liquid-phase flow in the longitudinal direction along the drift axis and the D/LMTH model that does not allow this longitudinal flow, quantifies the relative influence of the cold-trap effect in this three-drift repository system.

The D/LMTH model assumes the stratigraphy and boundary conditions, including infiltration flux that pertain to the center of the repository modeled in supplemental analyses (BSC 2001b; BSC 2001c) in the MSTHM. The assumption in this test case is that the conditions at this location apply to the entire model domain, that is, there is no lateral variation of stratigraphy in the test model. At this location, the repository is 372.9 m below the ground surface and 344.7 m above the water table. The host-rock unit at this location, which is a fractured welded tuff, is called the Topopah Spring lower lithophysal tuff Tptpll (tsw35) unit (Bandurraga and Bodvarsson 1999). The Tptpll unit, which is the host-rock unit for the majority of the repository

area, is modeled with a matrix porosity of 0.131, a matrix permeability of 3.04×10^{-17} m^2, a fracture porosity of 0.018 and a fracture permeability of 2.38×10^{-11} m^2; thermal parameters for the welded tuff are modeled using 900 J/kg°C for specific heat capacity, and 1.84 and 1.25 W/m/°C for wet and dry thermal conductivity, respectively. The time-dependent infiltration rates at this location are 5.7 mm/yr for the present-day climate (0 to 600 years), 15.1 mm/yr for the monsoonal climate (600 to 2,000 years), and 23.2 mm/yr for the glacial-transition climate (beyond 2,000 years) (Flint et al. 2001; BSC 2001c). Parameter values used here are the same as used for *FY 01 Supplemental Science and Performance Analyses, Volume 1: Scientific Bases and Analyses* (BSC 2001b).

The numerical mesh in the D/LMTH model includes four nested regions: (1) the very-fine-gridded inner nest surrounding Drift #2 with grid-block dimensions of approximately 0.2 m in the horizontal and the vertical directions; (2) the fine-gridded intermediate mesh, surrounding the inner nest, with grid-block dimensions of approximately 1 m in the horizontal and the vertical directions; (3) the medium-gridded intermediate nest surrounding the fine-gridded intermediate nest, as well as Drifts #1 and #3, with grid-block dimensions of approximately 5 m in the horizontal and the vertical directions; and (4) the coarse-gridded mountain-scale mesh, surrounding the medium-gridded intermediate nest with grid-block dimensions of approximately 50 m in the horizontal direction and approximately 20 m in the vertical direction, and which extends 2 km laterally to the model boundaries. Because of symmetry, it is only necessary to explicitly model one-quarter of the model domain (Figure 7.3-1).

All of the MSTHM submodels used in the model-validation test case used the same stratigraphy and boundary conditions as in the D/LMTH model. The SMT submodel has a heated repository footprint of 59,049 m^2 and the same total initial heat output (986.6 kW or 829 MTU) as in the D/LMTH model (Buscheck, Glascoe et al. 2003, p. 434, Table 4). Recent MSTHM calculations of the repository at Yucca Mountain have required running the LDTH and SDT submodels at four different AMLs. Because of the very small heated footprint of the repository in this example, the influence of the edge-cooling effect occurs more abruptly and in a more pronounced manner, which requires that the LDTH-SDT-submodel pairs be run at six different AMLs, rather than at just four. The DDT submodels are also run for the same six AMLs.

An important distinction between the MSTHM and the D/LMTH model concerns the treatment of air and vapor flow along the emplacement drift. The MSTHM effectively sets the axial permeability along the emplacement drift to zero, preventing axial air and vapor flow along the drift. For the D/LMTH model, the axial permeability is the same as that in the lateral and vertical directions (1×10^{-8} m^2, which is about three orders of magnitude greater than the bulk permeability of the host rock). Consequently, axial vapor flow (and the resulting cold-trap effect) occurs in the D/LMTH model, but does not occur in the MSTHM. It is also worth noting that the D/LMTH model includes the effect of a leaky bulkhead (with a permeability of 2.38×10^{-11} m^2) just beyond the last waste package (the PWR1 waste package in Figure 7.3-1) at the outer edge of the emplacement drift. The comparison of the MSTHM-simulated thermohydrologic behavior with that of the D/LMTH model, in part, test the relative importance of axial vapor flow (and the resulting cold-trap effect) on thermohydrologic behavior in the emplacement drifts.

7.3.2 Results of the MSTHM Validation Test Case

The results of the nested D/LMTH model and the MSTHM are compared at the four waste package locations at the center of the three-drift repository. The results from the D/LMTH model are shown for two cases: (1) the case with longitudinal gas- and liquid-phase flow along the drift axis and (2) the case without that longitudinal flow; a comparison of the results for these two cases shows the influence of that longitudinal flow. Predictions of temperature, relative humidity, and liquid-phase saturation are compared between the two models.

7.3.2.1 Temperature at the Center of the Three-Drift Repository

Drift-wall and drip-shield temperatures predicted by the nested D/LMTH model and the MSTHM are in good agreement at all four waste package locations at the center of Drift #2 (Figure 7.3-2). Longitudinal gas- and liquid-phase flow along the drift axis is seen to have a negligible influence on temperatures at the center of the three-drift repository. Table-7.3-3 summarizes the peak drift-wall and drip-shield temperatures predicted by the MSTHM and the nested D/LMTH model at the center of the three-drift repository. Differences in peak drift-wall temperature between the MSTHM and the D/LMTH model with longitudinal gas- and liquid-phase flow along the drift axis range from 0.5°C to 2.3°C; differences in peak drip-shield temperature range from –1.7°C to 2.7°C. Table 7.3-4 summarizes the time when boiling at the drift wall ceases; differences between the two models are minimal (generally 3 percent).

There is similar good agreement in temperature at other generic locations, such as in the invert. The nested D/LMTH-predicted temperatures tend to be slightly lower than the MSTHM-predicted temperatures. This is most likely because the MSTHM does not consider mountain-scale buoyant gas-phase convection, nor does it consider vapor (and latent heat) flow along the axis of the drift from the center to the edge of the repository (and beyond). The nested D/LMTH model considers both of these cooling mechanisms and, therefore, would be expected to predict slightly cooler temperature histories than the MSTHM.

Table 7.3-3. Summary of Peak Temperatures for the Four Waste Package Locations at the Center of the Three-Drift Repository

Waste package	Peak Drift-Wall Temperature (°C)			Peak Drip Shield Temperature (°C)		
	MSTHM	D/LMTH model	Difference	MSTHM	D/LMTH model	Difference
PWR1	140.4	138.8 (139.3)	1.6 (1.1)	160.0	160.5 (160.9)	-0.5 (-0.9)
DHLW	135.5	133.2 (133.8)	2.3 (1.7)	145.1	142.4 (142.9)	2.7 (2.2)
PWR2	146.4	145.9 (146.3)	0.5 (0.1)	168.0	169.7 (170.1)	-1.7 (-2.1)
BWR	145.5	144.9 (145.3)	0.6 (0.2)	163.1	163.1 (164.4)	0.0 (-1.3)

NOTE: The D/LMTH-model results are for the cases with and without longitudinal gas- and liquid-phase flow along the drift axis; the latter case is given in the parentheses.

7.3.2.2 Relative Humidity at the Center of the Three-Drift Repository

Drift-wall relative humidity predicted by the nested D/LMTH model and the MSTHM are in good agreement at all four center waste package locations. Given in Figure 7.3-3 is drift-wall relative humidity for the four waste packages. The agreement is closest up until the very end of the rock dryout period when the MSTHM predicts slightly greater relative humidity reduction in the host rock at the drift wall. The agreement in the predicted drip-shield relative humidity

between the two models is best for the PWR2 and BWR waste package (Figure 7.3-3f and h). The MSTHM predicts slightly greater relative humidity reduction than the D/LMTH model for the relatively cool DHLW waste package (Figure 7.3-3d). It is worth noting that the DHLW waste package location has temperature and relative humidity gradients within the drip shield in the axial direction (not shown). The DHLW waste package is warmer (and drier) at its end than at its center because it is being heated by its neighboring waste packages that generate considerably more heat (Table 7.3-2). Longitudinal gas- and liquid-phase flow along the drift axis is seen to have a negligible influence on relative humidity at the center of the three-drift repository.

Table 7.3-4. Summary of Time When Boiling Ceases at the Drift Wall for the Four Waste Package Locations at the Center of the Three-Drift Repository

Waste package	Time When Boiling at Drift Wall Ceases (years)			
	MSTHM	D/LMTH model	Difference	Difference*
PWR1	291.2	283.1	8.1	2.82%
DHLW	269.7	259.6	10.1	3.82%
PWR2	312.0	303.3	8.7	2.83%
BWR	304.0	294.4	9.6	3.21%

NOTE: *The difference (%) is the difference (years) divided by the average time when drift-wall boiling ceases [(shortest + longest)/2]. The D/LMTH-model results are for the case with longitudinal gas- and liquid-phase flow along the drift axis.

7.3.2.3 Liquid-Phase Saturation at the Center of the Three-Drift Repository

Drift-wall liquid-phase saturation $S_{dw,j,DMTH}$ predicted by the D/LMTH model and MSTHM are in good agreement at all four center waste package locations (Figure 7.3-4a, c, e, and g). This good agreement is obtained regardless of whether longitudinal gas- and liquid-phase flow is allowed to occur along the drift axis in the D/LMTH model. The minimum $S_{dw,j,DMTH}$, which occurs during the boiling period, is virtually identical for the two models. The MSTHM predicts a slightly longer duration of dryout for the PWR1, PWR2, and BWR waste packages; for the DHLW waste package, the two models predict virtually the same dryout duration (Figure 7.3-4c). Longitudinal gas- and liquid-phase flow along the drift axis is seen to have a negligible influence on drift-wall liquid-phase saturation. The agreement between the MSTHM and the D/LMTH model for the invert liquid-phase saturation, $S_{inv,j,DMTH}$, is good for the CSNF waste packages (Figure 7.3-4b, f, and h) and it is adequate for the relatively cool DHLW waste package (Figure 7-3-4d). The influence of the cold-trap effect is exhibited by the slightly higher values of $S_{inv,j,DMTH}$ for the DHLW waste package in the D/LMTH model with longitudinal gas- and liquid-phase flow along the drift axis, compared to the D/LMTH model that does not allow that longitudinal flow. The cold-trap effect causes the advection of water vapor from the relatively hot CNSF waste package locations to the relatively cool DHLW waste package location, where it condenses, causing an increase in $S_{in,j,DMTH}$. The two hot CSNF waste packages next to the DHLW waste package have slightly reduced $S_{in,j,DMTH}$ for the D/LMTH model with longitudinal gas- and liquid-phase flow along the drift axis compared to the D/LMTH model that does not allow that longitudinal flow.

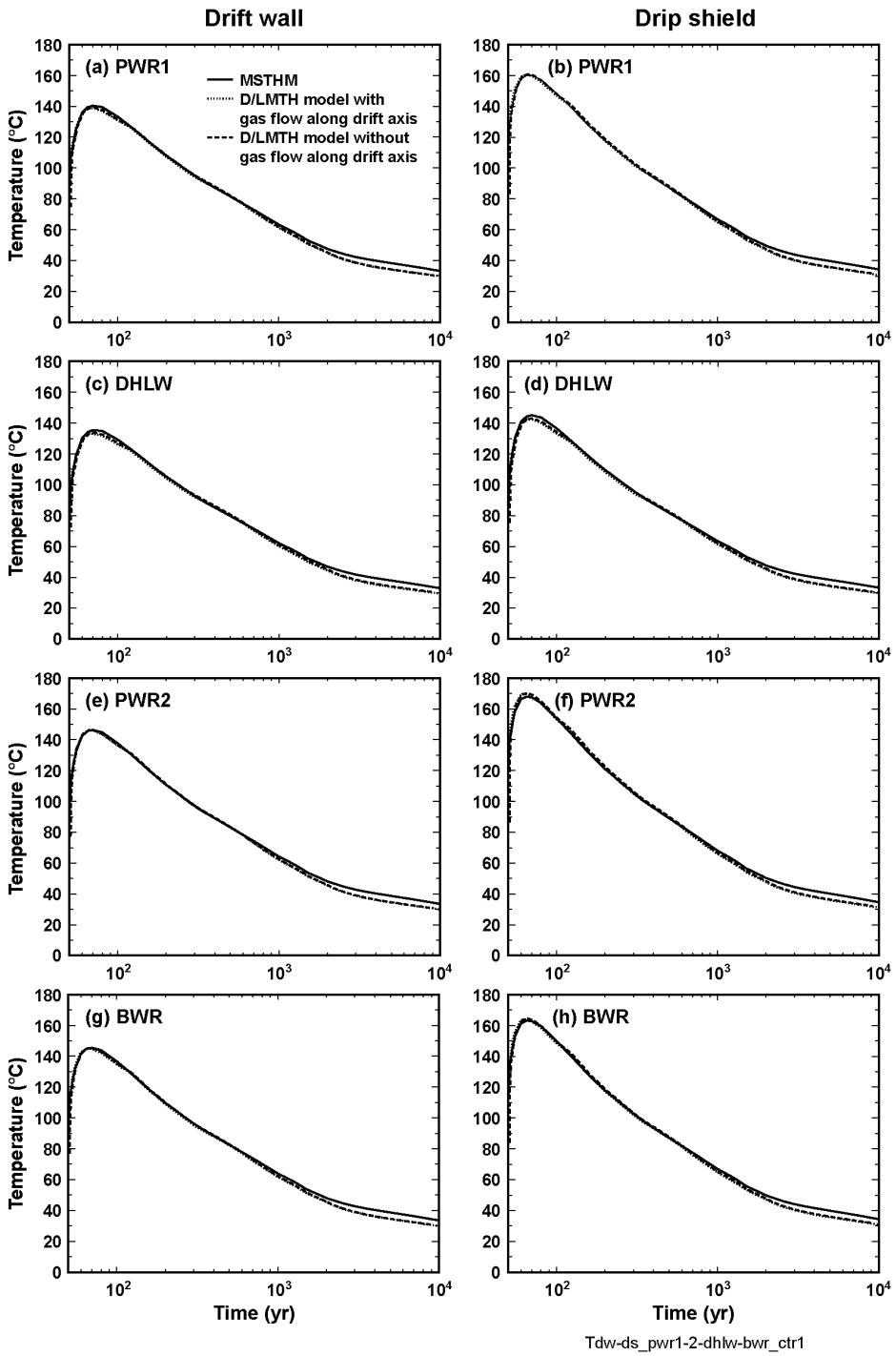

Figure 7.3-2. Drift-wall temperature ($T_{dw,j,DMTH}$) vs. time (a, c, e, g) and the drip-shield temperature ($T_{ds,j,DMTH}$) vs. time (b, d, f, h), determined by the MSTHM and the nested D/LMTH model, for the (a,b) PWR1, (c,d) DHLW, (e, f) PWR2, and (g, h) BWR waste packages at the center of the three-drift repository. The D/LMTH-model results are given for the cases with and without longitudinal gas- and liquid-phase flow along the drift axis.

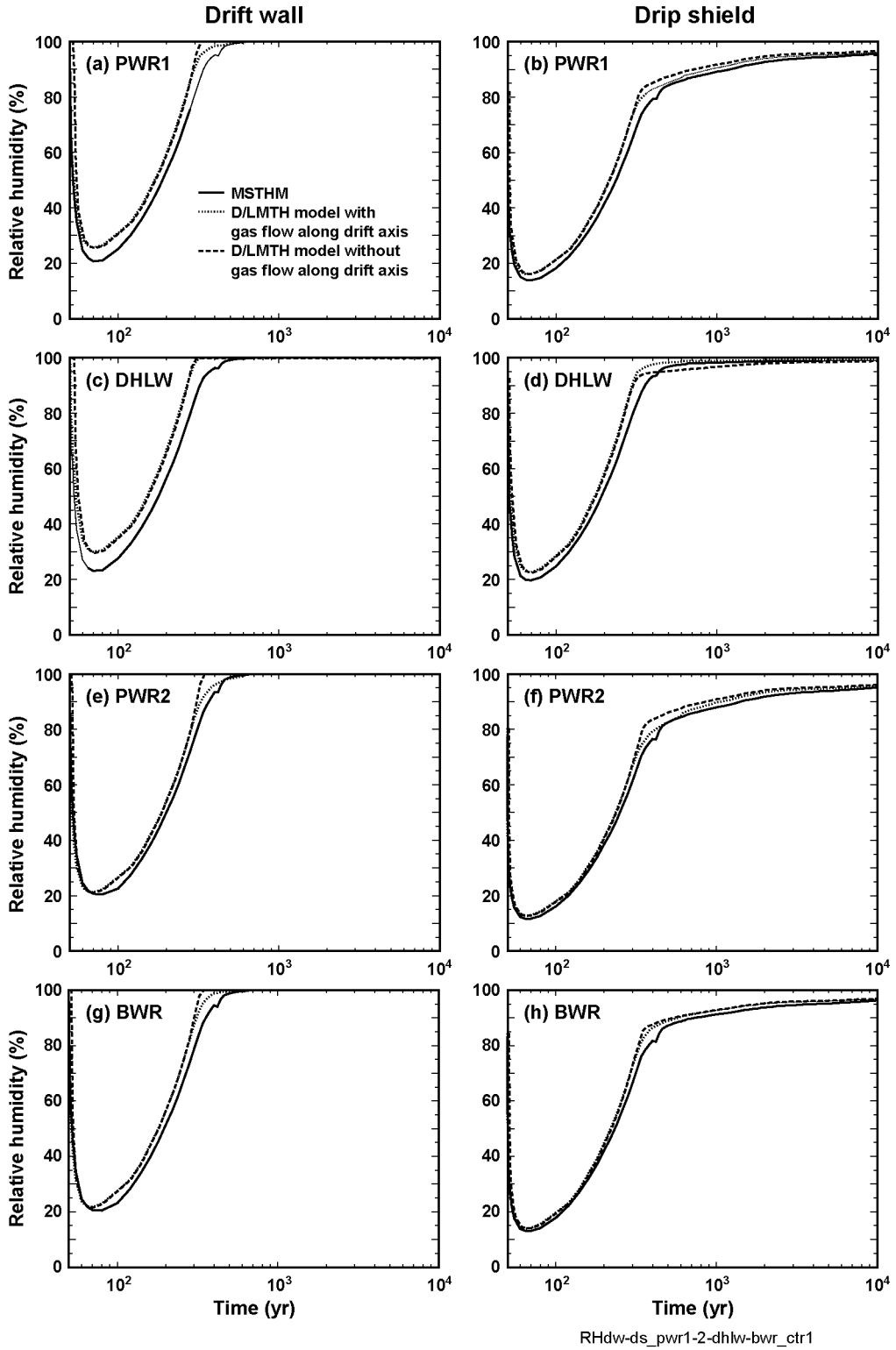

Figure 7.3-3. Drift-wall relative humidity ($_{RHdw,j,DMTH}$) vs. time (a, c, e, g) and drip-shield relative humidity ($RH_{ds,j,DMTH}$) vs. time (b, d, f, h), determined by the MSTHM and the nested D/LMTH model, for the (a,b) PWR1, (c,d) DHLW, (e, f) PWR2, and (g, h) BWR waste packages at the center of the three-drift repository. The D/LMTH-model results are given for the cases with and without longitudinal gas- and liquid-phase flow along the drift axis.

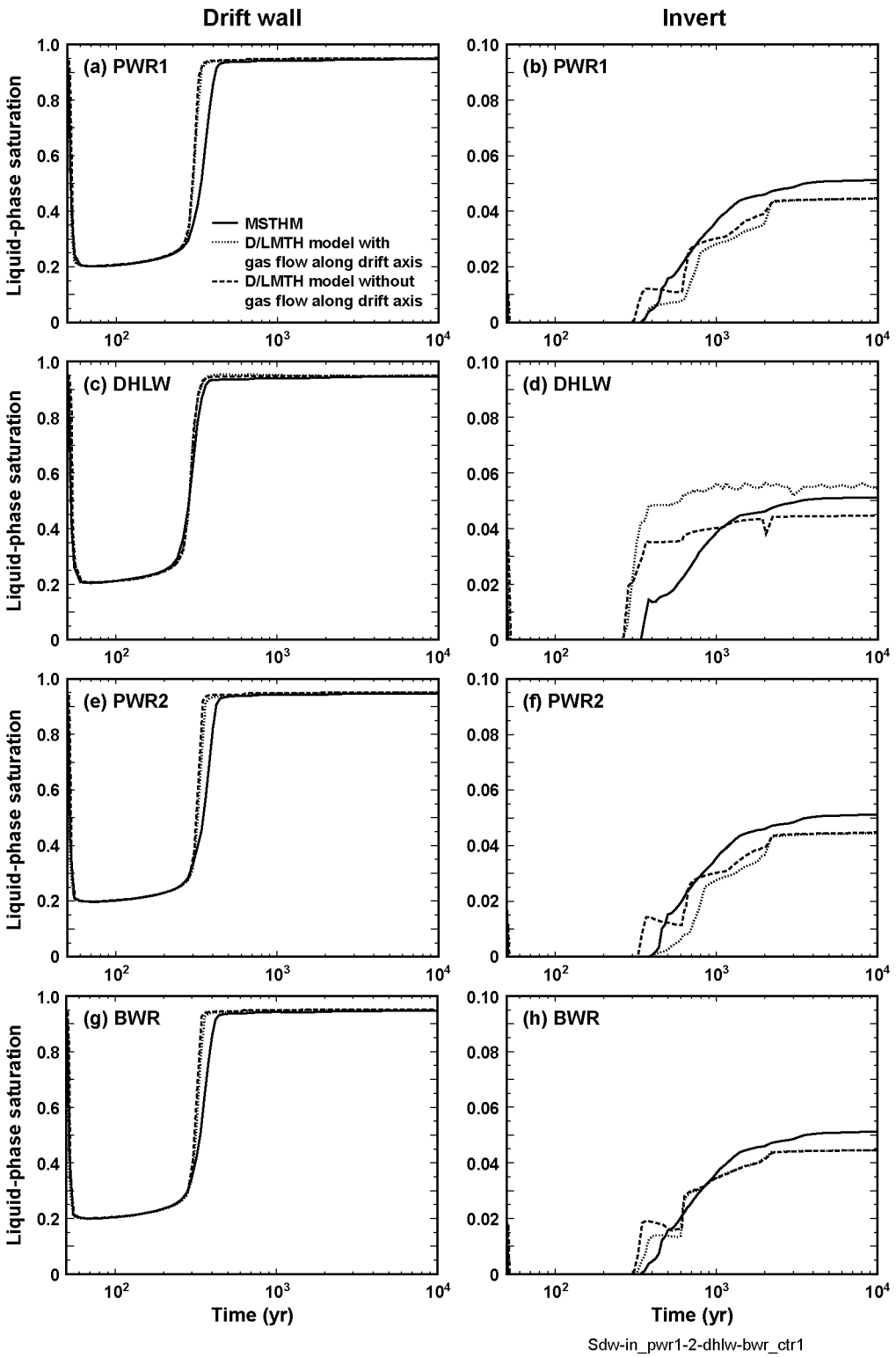

Figure 7.3-4. Drift-wall liquid-phase saturation ($S_{dw,j,DMTH}$) vs. time (a, c, e, g) and invert liquid-phase saturation ($S_{in,j,DMTH}$) vs. time (b, d, f, h) determined by the MSTHM and the nested D/LMTH for the (a, b) PWR1, (c, d) DHLW, (e, f) PWR2, and (g, h) BWR waste packages at the center of the three-drift repository. The D/LMTH-model results are given for the cases with and without longitudinal gas- and liquid-phase flow along the drift axis.

7.3.2.5 Temperature at the Edge of the Three-Drift Repository

At the edge of the three-drift repository, the longitudinal waste package order from the end of the drift is the following: PWR1, DHLW, PWR2, BWR. The drift-wall temperatures predicted by the nested D/LMTH model and the MSTHM are in reasonably good agreement at the four waste package locations at the edge of Drift #2 (Figure 7.3-5). This agreement is achieved regardless of whether longitudinal gas- and liquid-phase flow along the drift axis is allowed to occur in the D/LMTH model. Table 7.3-5 summarizes the peak drift-wall and drip-shield temperatures predicted by the MSTHM and the nested D/LMTH model at the edge of the three-drift repository. When the MSTHM is compared with the D/LMTH model that allows longitudinal gas- and liquid-phase flow along the drift axis, differences in peak drip-shield temperature range from 5.0°C for BWR package to 15.7°C for the PWR1 package. Notice that the agreement between the two models improves with distance from the edge of the repository. The current implementation of the MSTHM has an SMT submodel that discretizes the emplacement drifts into 20-m intervals (Section 6.2.5.1). Thus, the edge of the repository is represented by an SMT-submodel temperature history that is 10 m from the repository edge. Finer gridding in the longitudinal direction would likely result in better distinguishing the relative rate of temperature decline for the outermost waste packages in the drift. It needs to be noted that even while MSTHM overpredicts temperatures for packages nearest the end of the drift, these temperature differences between the MSTHM and D/LMTH are well within the range of temperature differences resulting from parametric uncertainty (Tables 6.3-27 and 6.3-28). Therefore, the impact of conceptual-model uncertainty is smaller than that of parametric uncertainty.

Table 7.3-5. Peak temperatures are summarized for the four waste package locations at the edge of the three-drift repository. The D/LMTH-model results are for the cases with and without longitudinal gas- and liquid-phase flow along the drift axis; the latter case is given in the parentheses.

Waste Package	Peak Drift-Wall Temperature (°C)			Peak Drip Shield Temperature (°C)		
	MSTHM	D/LMTH model	Difference	MSTHM	D/LMTH model	Difference
PWR1	136.3	117.5 (115.8)	18.8 (20.5)	156.7	141.0 (139.2)	15.7 (17.5)
DHLW	131.3	115.8 (114.3)	15.5 (17.0)	141.0	125.5 (124.0)	15.5 (17.0)
PWR2	142.3	133.5 (132.2)	8.8 (10.1)	164.7	158.0 (156.6)	6.7 (8.1)
BWR	141.4	135.5 (134.5)	5.9 (6.9)	159.9	154.9 (153.9)	5.0 (6.0)

When the D/LMTH model that allows longitudinal flow along the drift is compared with the D/LMTH model that does not, the small influence of the cold-trap effect on temperatures is evident. The influence of the cold-trap effect is to slightly increase temperatures at the edge of the repository. Water vapor from the hotter central portion of the repository is transported to the edge where it condenses, thereby depositing the latent heat of condensation, which increases temperatures at the repository edge.

A useful way of examining the differences between the MSTHM and D/LMTH models is to consider the center-to-edge temperature differences predicted by the two models (Table 7.3-6). Note that the MSTHM predicts the same center-to-edge differences for all four waste packages, whereas the D/LMTH model predicts a progressively smaller center-to-edge difference with increasing distance from the repository edge. The MSTHM methodology utilizes an SMT submodel that discretizes the emplacement drifts into 20-m intervals; thus, the outer 20 m of the

MSTHM is treated in the same fashion insofar as the influence of the edge-cooling effect is concerned. Similarly, the four waste packages at the center of the three-drift repository are treated in the same fashion insofar as their proximity to the repository edge is concerned. In a sense, the MSTHM does not distinguish which of the four waste packages is actually the outermost waste package over the outermost 20 m of the emplacement drift. All four waste packages are treated as though their respective centers are located 10 m from the edge of the heated footprint of the repository. Similarly, all four waste packages at the center of the three-drift repository are treated as though their centers are located 111.5 m from the edge of the heated repository footprint. Consequently, all four waste packages have virtually the same center-to-edge temperature difference. Conversely, the D/LMTH model does distinguish the respective distances from the repository edge for each of the four waste packages.

Table 7.3-6. The drip-shield temperature difference between the center and edge of the three-drift repository is compared for the D/LMTH model and MSTHM. The temperature differences are based upon Tables 7.3-3 and 7.3-5. The center-to-edge distances are based upon Figure 7.3-1. The D/LMTH-model results are for the case with longitudinal gas- and liquid-phase flow along the drift axis.

Waste Package	Center-to-Edge Distance (m)		Center-to-Edge Drip Shield Temperature Difference (°C)	
	MSTHM	D/LMTH model	MSTHM	D/LMTH model
PWR1	101.5	118.862	3.3	19.5
DHLW	101.5	108.260	4.1	16.9
PWR2	101.5	97.658	3.3	11.7
BWR	101.5	87.106	3.2	8.2

Table 7.3-6 indicates that the center-to-edge temperature difference in the D/LMTH model approaches that of the MSTHM for increasing distance from the repository edge. The primary reason that the center-to-edge temperature differences are smaller for the MSTHM is because the D/LMTH model accounts for the influence of axial vapor (and latent heat) flow towards (and beyond) the edge of the emplacement drift, while the MSTHM does not. The influence of this loss of latent heat is greatest for the waste packages closest to the edge. Tables 7.3-5 and 7.3-6 indicate that for waste packages located 20 m or more from the repository edge, the influence of axial vapor (and latent heat) loss along the drift is small (less than 5°C for peak waste package temperatures). The MSTHM discretizes thermohydrologic behavior for 2,874 20-m intervals (Figure 6.2-3); of these intervals, only 92 are potentially affected by the axial vapor (and latent heat) loss at the edge of the repository, constituting only 3.2 percent of the repository area. Consequently, 96.8 percent of the repository should not be influenced by this effect. For the outermost 3.2 percent of the repository, the influence of axial vapor (and latent heat) loss on MSTHM-predicted temperatures is well within the range of temperature differences resulting from parametric uncertainty (Tables 6.3-27 and 6.3-28).

Table 7.3-7 summarizes the time when boiling at the drift wall ceases; differences between the two models range from 17.3 to 44.9 percent. Again, the agreement between the two models improves with distance from the edge of the repository. Because the differences between the two models are within the range of differences arising from parametric uncertainty (Table 6.3-29), the impact of conceptual-model uncertainty is less than that of parametric uncertainty.

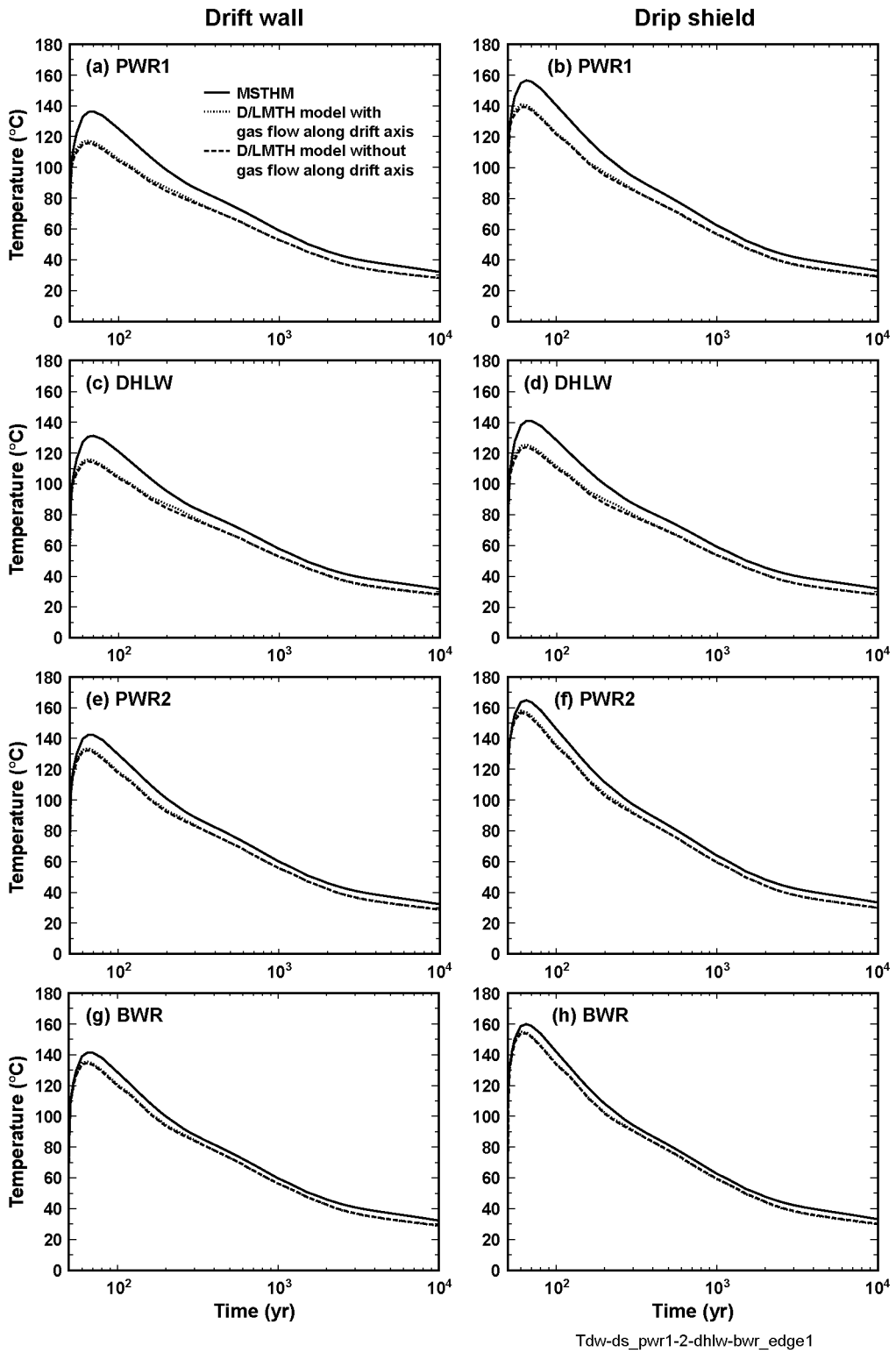

Figure 7.3-5. Drift-wall temperature ($T_{dw,j,DMTH}$) vs. time (a, c, e, g) and the drip-shield temperature ($T_{ds,j,DMTH}$) vs. time (b, d, f, h), determined by the MSTHM and the nested D/LMTH model, for the (a, b) PWR1, (c, d) DHLW, (e, f) PWR2, and (g, h) BWR waste packages at the edge of the three-drift repository. The D/LMTH-model results are given for the cases with and without longitudinal gas- and liquid-phase flow along the drift axis.

Table 7.3-7. Summary of Time When Boiling Ceases at the Drift Wall for the Four Waste Package Locations at the Edge of the Three-Drift Repository

Waste Package	Time When Boiling at Drift Wall Ceases (years)			
	MSTHM	D/LMTH Model	Difference	Difference*
PWR1	215.0	136.1	78.9	44.9%
DHLW	195.9	136.0	59.9	36.1%
PWR2	233.2	184.2	49.0	23.5%
BWR	226.6	190.6	36.0	17.3%

NOTE: *The difference (%) is the difference (years) divided by the average time when drift-wall boiling ceases [(shortest + longest)/2]. The D/LMTH model results are for the case with longitudinal gas- and liquid-phase flow along the drift axis.

7.3.2.6 Relative Humidity at the Edge of the Three-Drift Repository

Drift-wall relative humidity predicted by the nested D/LMTH model and the MSTHM are in reasonable agreement at the four "edge" waste package locations. This agreement is achieved regardless of whether longitudinal gas- and liquid-phase flow along the drift axis is allowed to occur in the D/LMTH model. Figure 7.3-6 gives the drift-wall relative humidity for the four waste packages at the edge of the repository. The agreement between the two models improves with distance from the repository edge. The agreement in the predicted drift-wall relative humidity between the two models is best for the PWR2 and BWR waste package (Figure 7.3-6e and g). The agreement between the two models is better for drip-shield relative humidity (Figure 7.3-6b, d, f, and h) than it is for drift-wall relative humidity (Figure 7.3-6a, c, e, and g). The agreement is best during the postboiling period when relative humidity reduction resulting from rock dryout no longer plays a significant role in relative humidity reduction on the drip shield. During the boiling period, the agreement in drip-shield relative humidity improves with distance from the edge of the repository. The differences between the two models in drip-shield relative humidity are within the range of differences arising from parametric uncertainty (Section 6.3.2).

The influence of the cold-trap effect can be observed in Figure 7.3-6 by comparing the results from the D/LMTH model that allows longitudinal gas- and liquid-phase flow along the drift axis with those from the D/LMTH model that does not allow that longitudinal flow. The influence of the cold-trap effect is to slightly reduce the drift-wall relative humidity for the three CSNF waste packages. This reduction results because some of the water vapor generated in the rock at these locations is able to flow longitudinally along the drift axis beyond the outermost waste package, where it condenses and is imbibed into the host rock. This process results in a net reduction in moisture in the host rock adjoining the relatively hot CSNF waste packages. The relatively cool DHLW waste package location does not experience a net reduction in moisture in the host rock. The drift-wall temperature at the DHLW waste package location drops below the boiling point earlier than at the hotter CSNF waste package locations, resulting in preferential condensation and imbibition into the host-rock that adjoins the DHLW waste package. The preferential condensation at the DHLW waste package location also results in a sharp rise in drip-shield relative humidity at the end of the local boiling period (Figure 7.3-6d). For the D/LMTH model with no longitudinal gas- and liquid-phase flow along the drift axis, the drip-shield relative humidity at the DHLW waste package location does not increase sharply following the end of the boiling period; rather it gradually increases in much the same way as predicted by the MSTHM.

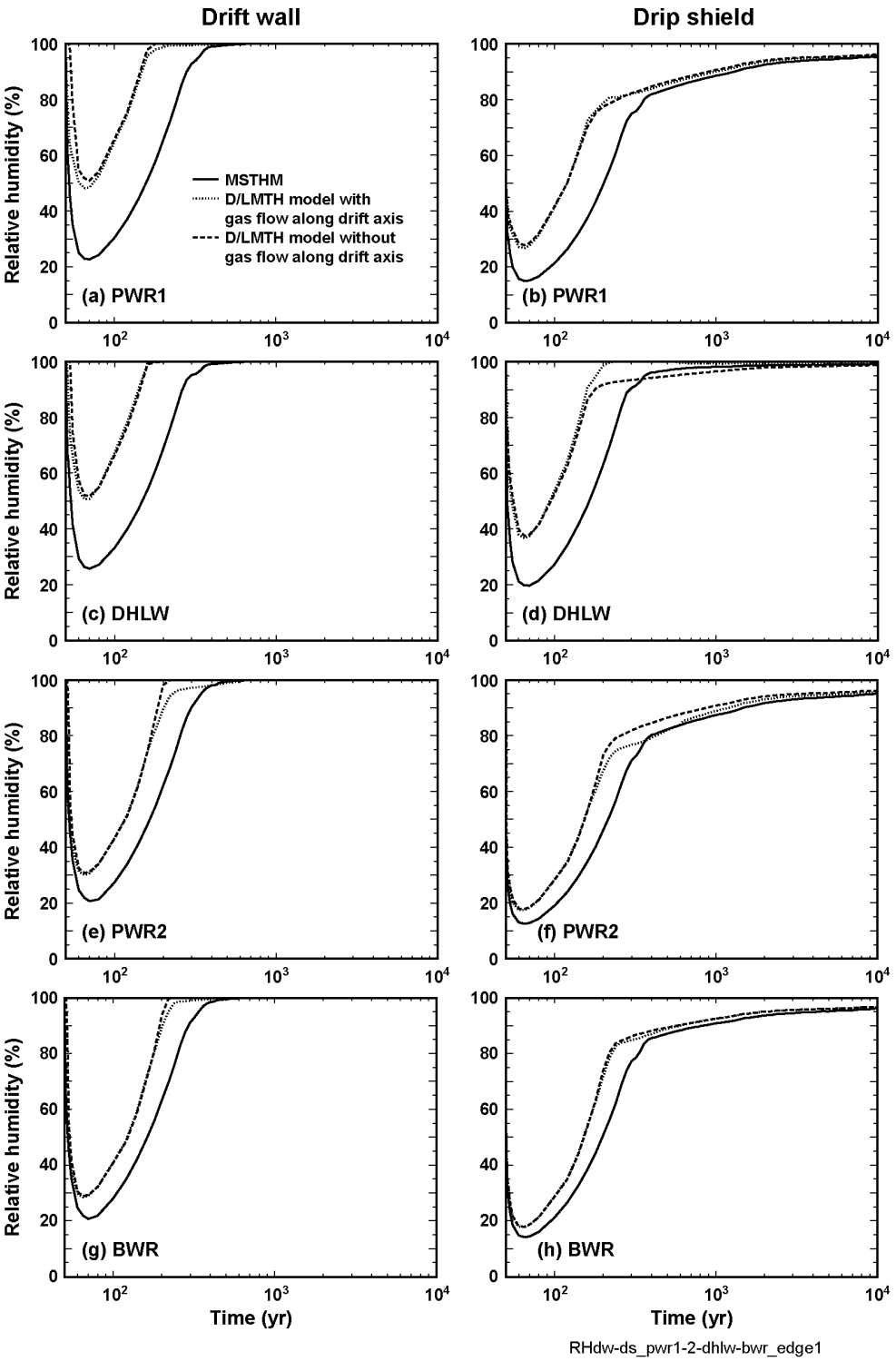

Figure 7.3-6. Drift-wall relative humidity ($RH_{dw,j,DMTH}$) vs. time (a, c, e, g) and drip-shield relative humidity ($RH_{ds,j,DMTH}$) vs. time (b, d, f, h), determined by the MSTHM and the nested D/LMTH model, for the (a, b) PWR1, (c, d) DHLW, (e, f) PWR2, and (g, h) BWR waste packages at the edge of the three-drift repository. The D/LMTH-model results are given for the cases with and without longitudinal gas- and liquid-phase flow along the drift axis.

7.3.2.7 Liquid-Phase Saturation at the Edge of the Three-Drift Repository

Drift-wall liquid-phase saturation $S_{dw,j,DMTH}$ predicted by the D/LMTH model and MSTHM are in reasonable agreement at the four "edge" center waste package locations (Figure 7.3-7a, c, e, and g). This agreement is achieved regardless of whether longitudinal gas- and liquid-phase flow along the drift axis is allowed to occur in the D/LMTH model. The minimum $S_{dw,j,DMTH}$, which occurs during the boiling period, is similar for the two models. The agreement in the prediction of dryout improves with distance from the edge of the repository. Invert liquid-phase saturation $S_{inv,j,DMTH}$ predicted by the D/LMTH model and MSTHM are in reasonable agreement at the four edge center waste package locations (Figure 7.3-7b, d, f, and h). The agreement in invert liquid-phase saturation, $S_{inv,j,DMTH}$, is better for the CSNF waste packages (Figure 7.3-7b, f, and h) than it is for the relatively cool DHLW waste package (Figure 7.3-7d).

The influence of the cold-trap effect can be observed in Figure 7.3-7, by comparing the results from the D/LMTH model that allows longitudinal gas- and liquid-phase flow along the drift axis with those from the D/LMTH model that does not allow that longitudinal flow. The influence of the cold-trap effect is exhibited by the rapid rise of $S_{inv,j,DMTH}$ for the DHLW waste package; it is also indicated by the anomalously high values of $S_{inv,j,DMTH}$ during the window of time that the cold-trap effect can occur in this three-drift repository example (136 to 312 years). At 136 years (Table 7.3-7), the drift-wall temperature at the DHLW waste package location at the edge of the repository drops below the boiling point, which corresponds to the earliest time that preferential condensation can commence on the drift wall at this location. At the center of the repository the drift-wall temperature at the hottest waste package location drops below the boiling point at 312 years (Table 7.3-4), which corresponds to the end of the period during which boiling in the host rock can generate a large flux of water vapor that can be longitudinally transported along the drift axis towards the edge of the repository. The window of time during which the cold trap can occur on the drip shield at the cool DHLW waste package location begins when boiling ceases on the DHLW drip shield and ends when boiling ceases at the drift wall at the center of the repository. It is during this time period that boiling at the center of the repository generates a significant enough source of water vapor that can condense on the relatively cold DHLW drip-shield surface. The reason that the other waste packages at the edge of the repository did not experience the cold trap is that the adjoining host rock was relatively dry during the potential window when the cold trap could occur. Because the adjoining host rock for the CSNF waste packages was sufficiently dry, it acted as a desiccant, thereby imbibing the water vapor condensing on the drift wall. The DHLW waste package, on the other hand, did not have a sufficiently dry condition on the adjoining drift-wall surfaces to function as a desiccant. It is important to note that the D/LMTH model did not account for the potential rock dryout during the preclosure ventilation period. Had preclosure dryout been accounted for, it is possible that the drift wall adjoining the DHLW waste package would have been sufficiently dry to function as a desiccant, which would have prevented the cold-trap effect from occurring on the DHLW drip-shield surface and in the underlying invert.

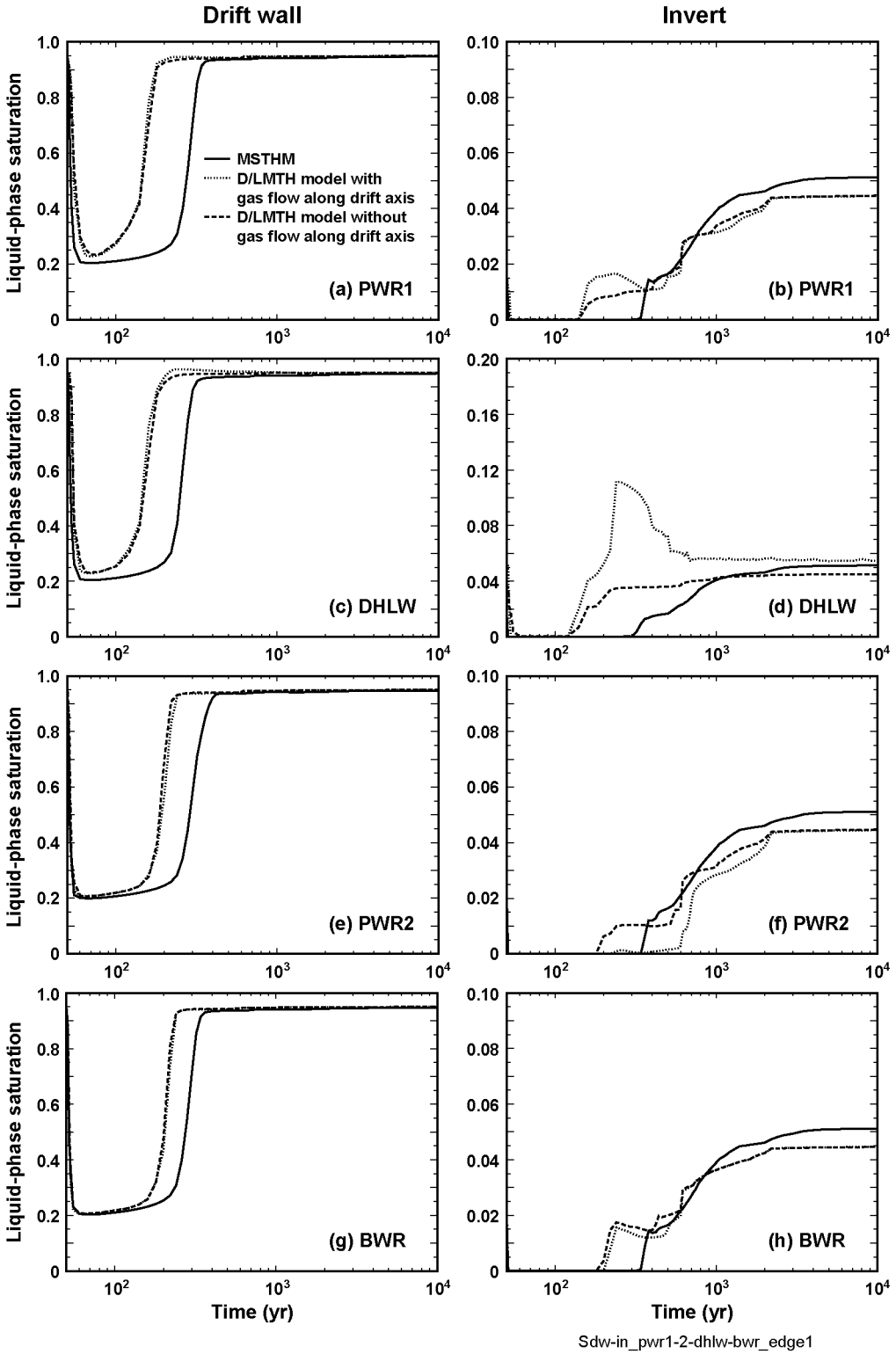

Figure 7.3-7. Drift-wall liquid-phase saturation ($S_{dw,j,DMTH}$) vs. time (a, c, e, g) and invert liquid-phase saturation ($S_{in,j,DMTH}$) vs. time (b, d, f, h) determined by the MSTHM and the nested D/LMTH model for the (a, b) PWR1, (c, d) DHLW, (e, f) PWR2, and (g, h) BWR waste packages at the edge of the three-drift repository. The D/LMTH-model results are given for the cases with and without longitudinal gas- and liquid-phase flow along the drift axis.

7.3.2.8 Summary of MSTHM Validation Test Case

A model-validation test case is developed that is a scaled-down three-drift version of the repository system. The results of a nested D/LMTH model were compared against those of the MSTHM at the drift wall, on the drip shield, and in the invert at four different waste package locations. Temperature and relative humidity predicted by the MSTHM closely agree with results from the D/LMTH model at all four waste package locations. Liquid-phase saturation at the drift wall predicted by the MSTHM is also in close agreement with results from the D/LMTH model at all four waste package locations. The MSTHM predictions of invert liquid-phase saturation are in good agreement with results from the D/LMTH model for three of the four center waste package locations. At the remaining waste package location, which corresponds to the coolest waste package, the agreement is qualitatively good. However, the D/LMTH model predicts higher values of liquid-phase saturation during both the ventilation period and the rewetting period. These higher values are attributed to the drift-scale cold-trap effect resulting in the advection of water vapor from the hotter waste package locations to the cooler waste package location, where it condenses.

This validation test case is a simplified example of the repository system because it only considers a spatially uniform percolation flux as well as a uniform overburden thickness. These test case results demonstrate the validity and soundness of the fundamental approach that the MSTHM uses to modify two-dimensional LDTH-submodel results with those of three-dimensional mountain- and drift-scale thermal models to predict thermohydrologic conditions in the Yucca Mountain repository system. The differences in the predicted thermohydrologic behavior between the MSTHM and the nested monolithic thermohydrologic (D/LMTH) model are small. Moreover, these small differences are negligible relative to the influence of parameter variability and uncertainty on predicted thermohydrologic behavior.

8. CONCLUSIONS

8.1 ANALYSIS AND MODELING CONCLUSIONS

This model report documents the Multiscale Thermohydrologic Model (MSTHM). An important phenomenological consideration for the licensing of the repository at Yucca Mountain is the generation of decay heat by the emplaced waste and the thermohydrologic consequences of this decay heat. Changes in temperature will affect the hydrologic and chemical environment at Yucca Mountain. A thermohydrologic-modeling tool is necessary to support the performance assessment of the engineered barrier system of the repository. This modeling tool must simultaneously account for processes occurring at a scale of a few tens of centimeters around individual waste packages, for processes occurring around the emplacement drifts themselves, and for processes occurring at the multikilometer scale of the mountain. Additionally, many other features must be considered including nonisothermal, multiphase-flow in fractured porous rock of variable liquid-phase saturation and thermal radiation and convection in open cavities.

The MSTHM calculates the following thermohydrologic variables: temperature, relative humidity, liquid-phase saturation, evaporation rate, air-mass fraction, gas-phase pressure, capillary pressure, and liquid- and gas-phase fluxes. The thermohydrologic variables are determined as a function of position along each of the emplacement drifts in the repository and as a function of waste package type. These variables are determined at various generic locations within the emplacement drifts, including the waste package and drip-shield surfaces and in the invert; they are also determined at various generic locations in the adjoining host rock; these variables are determined every 20 m for each emplacement drift in the repository. Each emplacement drift is represented with its precise coordinate location, as well as each of the emplacement panels in the repository area. The MSTHM also accounts for the manner in which the emplacement drifts are to be ventilated during the preclosure period, including how heat-removal efficiency from drift ventilation varies as a function of time and distance along each of the emplacement drifts. The MSTHM accounts for three-dimensional drift-scale and mountain-scale heat flow. The MSTHM captures the influence of the key engineering-design variables and natural system factors affecting thermohydrologic conditions in the emplacement drifts and adjoining host rock including the following:

- Repository-scale variability of percolation flux above the repository
- Temporal variability of percolation flux (as influenced by climate change)
- Uncertainty in percolation flux (as addressed by the low-, mean, and high-percolation flux cases)
- Uncertainty in percolation flux (resulting from flow focusing and flow diversion)
- Repository-scale variability of thermal conductivity (notably in host rock)
- Uncertainty in host-rock thermal conductivity (notably in the host rock)
- Repository-scale variability of bulk rock density and specific heat
- Repository-scale variability of hydrologic properties of the rock matrix
- Repository-scale variability of hydrologic properties of fractures

- Repository-scale variability in overburden thickness
- Overall areal heat-generation density of the waste inventory, which is quantified by the Areal Mass Loading (AML, expressed in MTU/acre)
- Line-averaged thermal load along emplacement drifts, which is quantified by the Lineal Power Density (LPD, expressed in kW/m)
- Distance between emplacement drifts (also called drift spacing)
- Age of spent-nuclear fuel at time of emplacement
- Location of the repository with respect to the stratigraphy
- Repository footprint shape, which influences the evolution of the edge-cooling effect that increases with proximity to the repository edges
- Dimensions of the in-drift design (waste packages, drip shield, and invert)
- Properties of the in-drift engineered barrier system components
- Waste package spacing along the drift (line-load versus point-load spacing)
- Waste package sequencing (particularly with respect to the heat output from the respective waste packages)
- Time- and distance-dependent heat-removal efficiency of preclosure drift ventilation
- Duration and heat-removal efficiency of drift ventilation.

This report describes MSTHM calculations conducted to support the Total System Performance Assessment for the License Application (TSPA-LA). The MSTHM simulations are conducted for three infiltration flux cases (lower-bound, mean, and upper-bound). The impact of parametric uncertainty of the key input variables: percolation flux and host-rock thermal conductivity are also addressed. Percolation flux and host-rock thermal conductivity are the two most important natural system parameters influencing peak temperatures and the time that the drift wall remains above the boiling point. It is found that the combined influence of percolation flux uncertainty and host-rock thermal-conductivity on peak temperatures is simply the sum of the individual contributions to peak-temperature uncertainty. It is also found that the combined influence of percolation flux uncertainty and host-rock thermal-conductivity on the duration of boiling at the drift wall is simply the sum of the individual contributions to drift-wall-boiling-duration uncertainty. These conclusions are extremely useful to engineered barrier system performance assessments because it is possible to use superposition to quantify the influence of these key sources of uncertainty.

8.2 MODEL VALIDATION, UNCERTAINTIES, AND LIMITATIONS

For the purpose of model-confidence building, results from the MSTHM are compared against those from a mountain-scale thermohydrologic model, which is an alternative conceptual model. The validation of the MSTHM is systematically addressed in multiple stages, including those utilizing results from field-scale thermal tests and those using a nested monolithic mountain-drift-scale thermohydrologic model of a three-drift repository example of the repository.

Three-dimensional NUFT thermohydrologic-model simulations are compared with temperatures and liquid-phase saturations measured in the Large Block Test (LBT). The good agreement between the simulated and measured temperatures in the LBT demonstrates that the NUFT thermohydrologic model provides a valid representation of heat flow in partially saturated fractured porous rock. Good agreement between the simulated and measured dryout and rewetting behavior in the LBT demonstrates that the NUFT thermohydrologic model provides a valid representation of dryout and rewetting behavior in partially saturated fractured porous rock.

Three-dimensional NUFT thermohydrologic model simulations were compared with temperatures and liquid-phase saturations measured in the Drift Scale Test (DST). Overall the agreement between simulated and measured temperatures was reasonable. While the field-measured temperature profiles and temperature histories showed a distinctive (or prolonged) plateau at 96°C, the NUFT-simulated temperature profiles and temperature histories either showed no plateau or showed a plateau at elevated temperatures. The underlying cause for this difference is the low value of matrix permeability in the Tptpmn (tsw34) in the TSPA-LA base-case hydrologic property set, which results in a large gas-phase pressure buildup in the matrix. The large gas-phase pressure buildup tends to throttle vaporization and delay rock dryout. The absence of a temperature plateau at 96°C is the primary reason the NUFT-simulated temperatures are generally higher than the field-measured temperatures for temperatures exceeding 96°C; a secondary reason is the uncertainty in host-rock thermal conductivity K_{th} in the DST. For the high-K_{th} case (one standard deviation above the mean), the NUFT-simulated temperatures are in better agreement with the measured temperatures than the cases that used the mean K_{th} values. For temperatures less than about 80°C, the NUFT-simulated and field-measured temperatures are in good agreement for all three cases considered: (1) base case, (2) sealed bulkhead, and (3) high K_{th}. Overall, the comparison of NUFT-simulated and measured temperatures demonstrate that the NUFT thermohydrologic model provides a valid representation of heat flow in the DST.

Although the NUFT-simulated dryout behavior lagged behind that observed in the DST, the spatial extent of the NUFT-simulated dryout zone eventually approaches that of the dryout zone observed in the DST. Therefore, the ultimate spatial extent of rock dryout simulated by the NUFT thermohydrologic model agrees reasonably well with that measured in the DST. Therefore, it can be concluded that the NUFT thermohydrologic model provides a valid representation of rock dryout in the DST. To the extent that the observations in the DST allow, the NUFT thermohydrologic model provides a valid representation of rewetting behavior in the DST. The overall impact of the modeling and parametric uncertainties in the DST is that the modeled behavior is somewhat higher in temperature and somewhat wetter than the field-measured conditions. The conclusion is that the MSTHM simulations of thermohydrologic behavior within emplacement drifts and in the adjoining host rock may be slightly biased on the high side for temperature, liquid-phase saturation, and relative humidity, all of which are conservative with respect to engineered barrier system performance.

Another key conclusion from the DST model-validation study is that the sealed-bulkhead case results in slightly higher NUFT-simulated temperatures than the base case (which had a very leaky bulkhead). The influence of the leaky bulkhead (versus the case with a sealed bulkhead) on simulated temperatures is much less than that resulting from a one standard-deviation range in thermal conductivity. This conclusion is important with respect to the potential significance of whether the ends of the emplacement drifts are sealed with bulkheads or simply backfilled with

highly permeable crushed tuff. The conclusion of the insensitivity of the DST thermohydrologic simulations to the treatment of the bulkhead (leaky versus sealed) clearly demonstrates that the MSTHM representation of thermohydrologic behavior in the emplacement drifts will not be significantly affected by whether the ends of the emplacement drifts are sealed.

The validation of the MSTHM methodology involves a three-drift test case. This test case represents a scaled-down repository, consisting of three 243-m long drifts. A nested monolithic mountain-/drift-scale thermohydrologic model of this three-drift test case discretely represents 15 waste packages: 7 at the center of the central drift and 4 at either end of the central drift. The MSTHM and the nested monolithic thermohydrologic model predict almost identical thermohydrologic conditions at all waste package locations at the center of the repository. At the edge of the repository, the MSTHM and nested monolithic thermohydrologic model also predict similar conditions. Differences between the two models are largest for the last two waste packages at the edge. However, because the differences are within the range of those caused by parametric uncertainty, the MSTHM is still valid for its intended purpose, which is to predict thermohydrologic conditions for all waste package locations throughout the repository.

The propagation of parametric uncertainty in the MSTHM involves two key natural system parameters: host-rock thermal conductivity and percolation flux. A sensitivity study of the influence of hydrologic-property uncertainty supports the conclusion that hydrologic-property uncertainty does not need to be propagated in the MSTHM calculations of in-drift temperature and relative humidity. The propagation of percolation flux uncertainty and host-rock thermal-conductivity uncertainty on MSTHM output is captured with the use of lower-bound, mean, and upper-bound infiltration flux MSTHM-output data sets for the following reasons. Because the MSTHM captures the influence of repository-scale variability of the influence of the edge-cooling effect and of the distribution of thermohydrologic properties and percolation flux (down to the scale of 20 m along each of the emplacement drifts), because it captures the influence of waste-package-to-waste-package variability of heat-generation output (down to the scale of individual waste packages), and because it captures the wide range in percolation flux (by virtue of incorporating three infiltration flux cases), the spectrum of MSTHM-calculated thermohydrologic conditions is extremely broad. For these three data sets, the range in peak drift-wall temperature is from 98.6°C to 154.8°C, with a median drift-wall temperature of 133.0°C; the range in peak waste package temperature is from 108.6°C to 182.9°C, with a median waste package temperature of 153.3°C (Table 6.3-4). Another key thermohydrologic parameter is the time when boiling ceases at the drift wall because this is an indication of how long seepage into the emplacement drifts is extremely unlikely. For the three data sets, the time when drift-wall boiling ceases ranges from 97.7 to 1,734.6 years, with a median time of 721.0 years (Table 6.3-5). A sensitivity study of the importance of thermal-conductivity uncertainty on thermohydrologic conditions in the emplacement drifts was conducted for selected locations in the repository, which included each of the four host-rock units. It is found that combined influence of percolation flux uncertainty and thermal-conductivity uncertainty results in a peak waste package temperature range of approximately 100°C to 200°C across the repository. The combined influence of percolation flux uncertainty and thermal-conductivity uncertainty results in an approximate range of no boiling at the drift wall to 2,100 years for the time when boiling at the drift wall ceases.

Another key thermohydrologic parameter is the maximum lateral extent of the boiling zone relative to the centerline of the emplacement drifts because this is a strong indication of the

likelihood of continuous condensate and percolation flux drainage around emplacement drifts. For the three infiltration flux data sets, the maximum lateral extent of boiling ranges from 5.1 to 17.8 m, with a median maximum lateral extent of 7.9 m. It is important to note that the lateral extent of boiling is always much smaller than the half spacing between emplacement drifts. Therefore, the majority of the host rock between emplacement drifts always remains below the boiling point, thereby enabling condensate and percolation flux to continuously drain between emplacement drifts. Because of this continuous drainage of condensate around a relatively narrow cylindrically shaped boiling zone, a condensate cap above the emplacement drifts is of very limited spatial extent. Therefore, it is extremely unlikely that any condensate cap could augment liquid-phase saturation during postboiling rewetting period.

8.3 MODEL OUTPUTS

The MSTHM results supplied to TSPA are summarized in Table 1-1. For each SMT-submodel location (2,874 locations distributed over the repository area, which is shown in Figure 6.2-3), bin indices are calculated based on the rank order of the percolation flux associated with the location. Bin 1 includes the 5 percent of locations with the smallest percolation flux. Bin 2 includes locations with percolation fluxes in the 5th to 30th percentile. Bin 3 includes locations with percolation fluxes in the 30th to 70th percentile. Bin 4 includes locations with percolation fluxes in the 70th to 95th percentile. Bin 5 includes locations with percolation fluxes above the 95th percentile. Note that the binning is based solely on the percolation fluxes for the glacial-transition climate of the mean infiltration flux case. Moreover, the lower- and upper-bound infiltration flux cases share the same areal binning as that determined for the mean infiltration flux case.

MSTHAC v7.0 micro-abstractions are performed at all 2,874 SMT-submodel locations, and the output from these calculations are postprocessed and written in a format required to satisfy TSPA-parameter requirements. Two sets of information are generated for the MSTHM-output-parameter DTNs. The first set, which is called the "WAPDEG binning" set, includes limited output variables at every SMT-submodel location and for each of the two waste package groups (CSNF and DHLW). The second set, which is called the "TSPA binning" set, includes complete output variable information for only typical bin locations and for typical waste packages (with respect to temperature and relative humidity histories) for each of the two waste package groups (CSNF and DHLW). Note that WAPDEG is a process model, which is downstream of the MSTHM (with respect to model-to-model parameter flow) and which directly uses MSTHM-output parameters.

For seepage modeling and engineered barrier system performance assessment (Seepage and WAPDEG models), all SMT-submodel locations and each of the eight waste package type (Table 6.3-10) are considered, therefore, there are 2,874 locations multiplied by 8 waste package types, which results in 22,992 waste package histories that are reported. For each SMT-submodel location and waste package type, a single file is produced that reports T_{wp}, RH_{wp}, T_{dw}, T_{ds}, and RH_{ds}, where T and RH are temperature and relative humidity and wp, dw, and ds stand for waste package, drift wall, and drip shield, respectively. Two waste package groups–DHLW and CSNF–are also defined, and for each SMT-submodel location, the most typical waste package in the grouping is selected and the same four variables reported. The DHLW group includes waste packages dhlw-l1 and dhlw-s1. The CSNF group includes waste packages

pwr1-1, pwr2-1, bwr1-1, bwr2-1, pwr1-2 and bwr1-2. Details of the determination of the typical waste package can be found in Attachment VIII.

Since the WAPDEG binning produces a large number of output files, the first set of files are concatenated using a UNIX shell script so that all locations falling within a bin and all waste packages of a given type (CSNF or DHLW) are included in a single file. This process creates 5 (the number of bins) multiplied by 2 (the number of waste package groups), which results in 10 output files. The second set of typical files is also concatenated so that there is one file for each bin and each waste package group. This produces another $5 \times 2 = 10$ files. Hence a total of 20 WAPDEG files are provided for each infiltration flux case.

The second process (TSPA binning) involves determining the most typical location given a set of locations that define a "bin." For TSPA purposes, the focus is the most typical waste package (see below) in a group or bin, therefore, there are 5 bins $\times$ 2 groups = 10 typical waste packages reported. TSPA binning uses the same waste package group definitions used in WAPDEG binning. For each bin, two output files are created, one for the most typical CSNF package and one for the most typical DHLW package. There are 5 (the number of bins) multiplied by 2 (the number of waste package groups) files created for this type of processing. The process of determining the typical waste packages is described in Attachment VIII. The TSPA files include all MSTHM output variables that are relevant to the modeled repository (43 in all) covering temperature, relative humidity, liquid-phase saturation, liquid-phase flux and other thermohydrologic parameters at generic locations within and adjacent to the emplacement drifts.

Table 8-1 is a list of data tracking numbers (DTNs) associated with the output produced by this report.

Table 8-1. Data Tracking Numbers Associated with the Output Produced by This Report

DTN	TDIF	Title	TDIF Submittal Date
LL030602723122.027	314920	Multiscale Thermohydrologic Model Output to TSPA and WAGDEG for Upper Infiltration Case	06/25/2003
LL030608723122.028	315021	Multiscale Thermohydrologic Model Output to TSPA and WAPDEG for the Lower Infiltration Case	06/27/2003
LL030610323122.029	315037	Multiscale Thermohydrologic Model Output to TSPA and WAPDEG for the Mean Infiltration Case	06/27/2003
LL030704523122.030	315142	NUFT Input File Data Development to Support LA Multi-Scale Analyses	07/17/2003
LL030704623122.031	315211	NUFT Input File Data Development to Support LA Multi-Scale Analyses	07/23/2003
LL030804023122.034	315470	Sensitivity Studies for Evaluating the Impact of Thermal Conductivity and Percolation Rate on LA Multi-Scale Analyses	09/11/2003
LL030808523122.035	315471	Input and Output Files Supporting MSTHM Micro-Abstractions for LA Multi-Scale Analyses	09/11/2003
LL030808623122.036	315472	Input and Output Files for NUFT MSTHM Submodels Supporting LA Multi-Scale Analyses	09/11/2003
LL030808723122.037	315473	Input and Output Files for the Creation of NUFT MSTHM Submodel Input Files Supporting LA Multi-Scale Analyses	09/11/2003
LL030808823122.038	315474	Input and Output Files for Building SMT, SDT, and LDTH Submodel Mesh Files in Support of LA Multi-Scale Analyses	09/11/2003
LL030808923122.039	315475	Input and Output Files Associated with the Large-Block and Drift Scale Tests in Support of LA Multi-Scale Analyses	09/11/2003
LL030906131032.002	315485	Output from the Multi-Scale AMR for the Lower Percolation Mean Thermal Conductivity Case including Drift Wall Temperatures	09/16/2003
LL030906531032.005	315488	Output from the Multi-Scale AMR for the Upper Percolation Mean Thermal Conductivity Case including Drift Wall Temperatures	09/16/2003
LL031206723122.041	316024	Output from the Multi-Scale AMR for the Mean Percolation Mean Thermal Conductivity Case including Drift Wall Temperatures	12/22/2003
LL040102223122.042	316066	Evaluation of the Sensitivity of In-Drift Temperature and Relative Humidity to Hydrologic-Property Uncertainty	01/12/2004

INTENTIONALLY LEFT BLANK

9. INPUTS AND REFERENCES

9.1 DOCUMENTS CITED

ASME (American Society of Mechanical Engineers) 1995. "Materials." Section II of *1995 ASME Boiler and Pressure Vessel Code*. New York, New York: American Society of Mechanical Engineers. TIC: 245287.

Bandurraga, T.M. and Bodvarsson, G.S. 1999. "Calibrating Hydrogeologic Parameters for the 3-D Site-Scale Unsaturated Zone Model of Yucca Mountain, Nevada." *Journal of Contaminant Hydrology*, *38*, (1-3), 25-46. New York, New York: Elsevier. TIC: 244160.

Bird, R.B.; Stewart, W.E.; and Lightfoot, E.N. 1960. *Transport Phenomena*. New York, New York: John Wiley & Sons. TIC: 208957.

BSC (Bechtel SAIC Company) 2001a. *Repository Multiple Waste Package Thermal Calculation*. CAL-WIS-TH-000010 REV 00. Las Vegas, Nevada: Bechtel SAIC Company. ACC: MOL.20010814.0330.

BSC 2001b. *FY 01 Supplemental Science and Performance Analyses, Volume 1: Scientific Bases and Analyses*. TDR-MGR-MD-000007 REV 00 ICN 01. Las Vegas, Nevada: Bechtel SAIC Company. ACC: MOL.20010801.0404; MOL.20010712.0062; MOL.20010815.0001.

BSC 2001c. *Multiscale Thermohydrologic Model*. ANL-EBS-MD-000049 REV 00 ICN 02. Las Vegas, Nevada: Bechtel SAIC Company. ACC: MOL.20020123.0279.

BSC 2002a. *Thermal Conductivity of the Potential Repository Horizon Model Report*. MDL-NBS-GS-000005 REV 00. Las Vegas, Nevada: Bechtel SAIC Company. ACC: MOL.20020923.0167.

BSC 2002b. *The Enhanced Plan for Features, Events, and Processes (FEPs) at Yucca Mountain*. TDR-WIS-PA-000005 REV 00. Las Vegas, Nevada: Bechtel SAIC Company. ACC: MOL.20020417.0385.

BSC 2003a. *Technical Work Plan for: Engineered Barrier System Department Modeling and Testing FY03 Work Activities*. TWP-MGR-MD-000015 REV 04 ICN 02. Las Vegas, Nevada: Bechtel SAIC Company. ACC: DOC.20031001.0008.

BSC 2003b. *Q-List*. TDR-MGR-RL-000005 REV 00. Las Vegas, Nevada: Bechtel SAIC Company. ACC: DOC.20030930.0002.

BSC 2003c. *Development of Numerical Grids for UZ Flow and Transport Modeling*. ANL-NBS-HS-000015 REV 01. Las Vegas, Nevada: Bechtel SAIC Company. ACC: DOC.20030404.0005.

BSC 2003d. *Repository Design, Repository/PA IED Subsurface Facilities*. 800-IED-EBS0-00402-000-00B. Las Vegas, Nevada: Bechtel SAIC Company. ACC: MOL.20030109.0146.

BSC 2003e. *Repository Design Project, Repository/PA IED Emplacement Drift Committed Materials (2)*. 800-IED-WIS0-00302-000-00A. Las Vegas, Nevada: Bechtel SAIC Company. ACC: ENG.20030627.0004.

BSC 2003f. *Design and Engineering, D&E/PA/C IED Typical Waste Package Components Assembly 1 of 9*. 800-IED-WIS0-00201-000-00C. Las Vegas, Nevada: Bechtel SAIC Company. ACC: ENG.20030917.0002.

BSC 2003g. *Interlocking Drip Shield*. 000-MW0-TED0-00101-000-00A, -00102-000-00A, and -00103-000-00A. 3 Sheets. Las Vegas, Nevada: Bechtel SAIC Company. ACC: ENG.20030205.0001; ENG.20030205.0002; ENG.20030205.0003.

BSC 2003h. *UZ Flow Models and Submodels*. MDL-NBS-HS-000006 REV 01. Las Vegas, Nevada: Bechtel SAIC Company. ACC: DOC.20030818.0002.

BSC 2003i. *Calibrated Properties Model*. MDL-NBS-HS-000003 REV 01. Las Vegas, Nevada: Bechtel SAIC Company. ACC: DOC.20030219.0001.

BSC 2003j. *Drift-Scale Coupled Processes (DST and TH Seepage) Models*. MDL-NBS-HS-000015 REV 00C. Las Vegas, Nevada: Bechtel SAIC Company. ACC: MOL.20030910.0160. TBV-5666

BSC 2003k. *Abstraction of Drift Seepage*. MDL-NBS-HS-000019 REV 00 ICN 01. Las Vegas, Nevada: Bechtel SAIC Company. ACC: DOC.20031112.0002.

BSC 2003l. *MR - In-Drift Natural Convection and Condensation. Working Draft as of 11 April 2003*. MDL-EBS-MD-000001 REV 00A. Las Vegas, Nevada: Bechtel SAIC Company. ACC: MOL.20030912.0050.

BSC 2003m. *EBS Radionuclide Transport Abstraction*. ANL-WIS-PA-000001 REV 01F. Las Vegas, Nevada: Bechtel SAIC Company. ACC: MOL.20031210.0361. TBV-5644

BSC 2003n. *Advection Versus Diffusion in the Invert*. ANL-EBS-MD-000063 REV 00. Las Vegas, Nevada: Bechtel SAIC Company. ACC: DOC.20030904.0007.

BSC 2003o. *Design and Engineering, Interlocking Drip Shield Configuration*. 000-M00-SSE0-00102-000-00A. Las Vegas, Nevada: Bechtel SAIC Company. ACC: ENG.20031028.0003.

BSC 2004a. *D&E / PA/C IED Emplacement Drift Configuration*. 800-IED-MGR0-00201-000-00A. Las Vegas, Nevada: Bechtel SAIC Company. ACC: ENG.20040113.0011.

BSC 2004b. *D&E/PA/C IED Typical Waste Package Components Assembly*. 800-IED-WIS0-00202-000-00B. Las Vegas, Nevada: Bechtel SAIC Company. ACC: ENG.20040202.0010.

BSC 2004c. *D&E / PA/C IED Interlocking Drip Shield and Emplacement Pallet*. 800-IED-WIS0-00401-000-00C. Las Vegas, Nevada: Bechtel SAIC Company. ACC: ENG.20040202.0022.

BSC 2004d. *D&E / PA/C IED Typical Waste Package Components Assembly*. 800-IED-WIS0-00205-000-00C. Las Vegas, Nevada: Bechtel SAIC Company. ACC: ENG.20040202.0013.

BSC 2004e. *D&E / PA/C IED Typical Waste Package Components Assembly*. 800-IED-WIS0-00204-000-00B. Las Vegas, Nevada: Bechtel SAIC Company. ACC: ENG.20040202.0012.

BSC 2004f. *D&E / PA/C IED Typical Waste Package Components Assembly*. 800-IED-WIS0-00203-000-00B. Las Vegas, Nevada: Bechtel SAIC Company. ACC: ENG.20040202.0011.

BSC 2004g. *Engineered Barrier System: Physical and Chemical Environment Model*. ANL-EBS-MD-000033 REV 02. Las Vegas, Nevada: Bechtel SAIC Company. ACC: DOC.20040212.0004.

Buscheck, T.A. and Nitao, J.J. 1994. *The Impact of Buoyant, Gas-Phase Flow and Heterogeneity on Thermo-Hydrological Behavior at Yucca Mountain*. UCRL-JC-115351. Livermore, California: Lawrence Livermore National Laboratory. ACC: NNA.19940524.0012.

Buscheck, T.A. and Nitao, J.J. 1995. *Thermal-Hydrological Analysis of Large-Scale Thermal Tests in the Exploratory Studies Facility at Yucca Mountain*. UCRL-ID-121791. Livermore, California: Lawrence Livermore National Laboratory. ACC: MOL.19960501.0392.

Buscheck, T.A.; Gansemer, J.; DeLorenzo, T.H.; Nitao, J.J.; and Shaffer, R.J. 1998. *Multiscale Thermohydrologic Model Sensitivity Analysis*. UCRL-ID-131489. Livermore, California: Lawrence Livermore National Laboratory. ACC: MOL.19980901.0245.

Buscheck, T.A. 1999. *Thermohydrologic Calculations for the Site Recommendation/License Application Design Selection, Phase 2*. UCRL-ID-133988. BB0000000-01717-0210-00009 REV 00. Livermore, California: Lawrence Livermore National Laboratory. ACC: MOL.20000606.0193.

Buscheck, T.A.; Gansemer, J.; Nitao, J.J.; and Delorenzo, T.H. 1999. "Multi-Scale Near-Field Thermohydrologic Analysis of Alternative Designs for the Potential Repository at Yucca Mountain." *Scientific Basis for Nuclear Waste Management XXII, Symposium held November 30-December 4, 1998, Boston, Massachusetts, U.S.A*. Wronkiewicz, D.J. and Lee, J.H., eds. *556*, 615-622. Warrendale, Pennsylvania: Materials Research Society. TIC: 246426.

Buscheck, T.A.; Rosenberg, N.D.; Gansemer, J.; and Sun, Y. 2002. "Thermohydrologic Behavior at an Underground Nuclear Waste Repository." *Water Resources Research*, *38*, (3), 10-1 through 10-19. Washington, D.C.: American Geophysical Union. TIC: 253566.

Buscheck, T.A.; Glascoe, L.G.; Lee, K.H.; Gansemer, J.; Sun, Y.; and Mansoor, K. 2003. "Validation of the Multiscale Thermohydrologic Model Used for Analysis of a Proposed Repository at Yucca Mountain." *Journal of Contaminant Hydrology*, *62-63*, 421-440. New York, New York: Elsevier. TIC: 254205.

Buscheck, T.A.; Rosenberg, N.D.; Blink, J.A.; Sun, Y.; and Gansemer, J. 2003. "Analysis of Thermohydrologic Behavior for Above-Boiling and Below-Boiling Thermal-Operating Modes for a Repository at Yucca Mountain." *Journal of Contaminant Hydrology*, *62-63*, 441-457. New York, New York: Elsevier. TIC: 254205.

Canori, G.F. and Leitner, M.M. 2003. *Project Requirements Document*. TER-MGR-MD-000001 REV 01. Las Vegas, Nevada: Bechtel SAIC Company. ACC: DOC.20030404.0003.

CRWMS M&O (Civilian Radioactive Waste Management System Management and Operating Contractor) 1998a. *Drift Scale Test As-Built Report*. BAB000000-01717-5700-00003 REV 01. Las Vegas, Nevada: CRWMS M&O. ACC: MOL.19990107.0223.

CRWMS M&O 1998b. *Total System Performance Assessment-Viability Assessment (TSPA-VA) Analyses Technical Basis Document*. Las Vegas, Nevada: CRWMS M&O. ACC: MOL.19981008.0001 through MOL.19981008.0011.

CRWMS M&O 2000a. *Total System Performance Assessment for the Site Recommendation*. TDR-WIS-PA-000001 REV 00 ICN 01. Las Vegas, Nevada: CRWMS M&O. ACC: MOL.20001220.0045.

CRWMS M&O 2000b. *Thermal Tests Thermal-Hydrological Analyses/Model Report*. ANL-NBS-TH-000001 REV 00. Las Vegas, Nevada: CRWMS M&O. ACC: MOL.20000505.0231.

CRWMS M&O 2000c. *Mountain-Scale Coupled Processes (TH) Models*. MDL-NBS-HS-000007 REV 00. Las Vegas, Nevada: CRWMS M&O. ACC: MOL.19990721.0528.

CRWMS M&O 2001. *Effective Thermal Conductivity for Drift-Scale Models Used in TSPA-SR*. CAL-EBS-HS-000001 REV 00. Las Vegas, Nevada: CRWMS M&O. ACC: MOL.20010301.0252.

de Marsily, G. 1986. *Quantitative Hydrogeology: Groundwater Hydrology for Engineers*. San Diego, California: Academic Press. TIC: 208450.

DOE (U.S. Department of Energy) 2003. *Quality Assurance Requirements and Description*. DOE/RW-0333P, Rev. 13. Washington, D.C.: U.S. Department of Energy, Office of Civilian Radioactive Waste Management. ACC: DOC.20030422.0003.

Flint, A.L.; Flint, L.E.; Bodvarsson, G.S.; Kwicklis, E.M.; and Fabryka-Martin, J. 2001. "Evolution of the Conceptual Model of Unsaturated Zone Hydrology at Yucca Mountain, Nevada." *Journal of Hydrology*, *247*, (1-2), 1-30. New York, New York: Elsevier. TIC: 250932.

Francis, N.D., Jr.; Webb, S.W.; Itamura, M.T.; and James, D.L. 2003. *CFD Modeling of Natural Convection Heat Transfer and Fluid Flow in Yucca Mountain Project (YMP) Enclosures*. SAND2002-4179. Albuquerque, New Mexico: Sandia National Laboratories. ACC: MOL.20030906.0165.

Freeze, G.A.; Brodsky, N.S.; and Swift, P.N. 2001. *The Development of Information Catalogued in REV00 of the YMP FEP Database*. TDR-WIS-MD-000003 REV 00 ICN 01. Las Vegas, Nevada: Bechtel SAIC Company. ACC: MOL.20010301.0237.

Hardin, E.L. 1998. *Near-Field/Altered-Zone Models Report*. UCRL-ID-129179 DR. Livermore, California: Lawrence Livermore National Laboratory. ACC: MOL.19980504.0577.

Haukwa, C.; Wu, Y.S.; Hinds, J.J.; Zhang, W.; Ritcey, A.C.; Pan, L.H.; Simmons, A.M.; and Bodvarsson, G.S. 1998. *Results of Sensitivity Studies of Thermo-Hydrologic Behavior Conducted on Hydrologic Parameter Sets*. Milestone SP3CK5M4. Berkeley, California: Lawrence Berkeley National Laboratory. ACC: MOL.19980918.0001.

Holman, J.P. 1990. *Heat Transfer*. 7th Edition. New York, New York: McGraw-Hill. TIC: 242477.

Incropera, F.P. and DeWitt, D.P. 1996. *Fundamentals of Heat and Mass Transfer*. 4th Edition. New York, New York: John Wiley & Sons. TIC: 243950.

Keenan, J.H.; Keyes, F.G.; Hill, P.G.; and Moore, J.G. 1969. *Steam Tables, Thermodynamic Properties of Water Including Vapor, Liquid, and Solid Phases (English Units)*. New York, New York: John Wiley & Sons. TIC: 246766.

Lichtner, P.C. and Walton, J.C. 1994. *Near-Field Liquid-Vapor Transport in a Partially Saturated High-Level Nuclear Waste Repository*. CNWRA 94-022. San Antonio, Texas: Center for Nuclear Waste Regulatory Analyses. TIC: 216007.

Lide, D.R., ed. 1995. *CRC Handbook of Chemistry and Physics*. 76th Edition. Boca Raton, Florida: CRC Press. TIC: 216194.

Liu, H.H.; Doughty, C.; and Bodvarsson, G.S. 1998. "An Active Fracture Model for Unsaturated Flow and Transport in Fractured Rocks." *Water Resources Research*, *34*, (10), 2633-2646. Washington, D.C.: American Geophysical Union. TIC: 243012.

Manteufel, R.D.; Ahola, M.P.; Turner, D.R.; and Chowdhury, A.H. 1993. *A Literature Review of Coupled Thermal-Hydrologic-Mechanical-Chemical Processes Pertinent to the Proposed High-Level Nuclear Waste Repository at Yucca Mountain*. NUREG/CR-6021. Washington, D.C.: U.S. Nuclear Regulatory Commission. TIC: 207771.

Montazer, P. and Wilson, W.E. 1984. *Conceptual Hydrologic Model of Flow in the Unsaturated Zone, Yucca Mountain, Nevada*. Water-Resources Investigations Report 84-4345. Lakewood, Colorado: U.S. Geological Survey. ACC: NNA.19890327.0051.

Mualem, Y. 1976. "A New Model for Predicting the Hydraulic Conductivity of Unsaturated Porous Media." *Water Resources Research*, *12*, (3), 513-522. Washington, D.C.: American Geophysical Union. TIC: 217339.

Nitao, J.J. 1998. *Reference Manual for the NUFT Flow and Transport Code, Version 2.0*. UCRL-MA-130651. Livermore, California: Lawrence Livermore National Laboratory. ACC: MOL.19980810.0391.

Nitao, J.J. 2000. *Documentation of the Thermal Energy Balance Equation Used in the USNT Module of the NUFT Flow and Transport Code*. UCRL-ID-139836. Livermore, California: Lawrence Livermore National Laboratory. ACC: MOL.20020711.0161.

NRC (U.S. Nuclear Regulatory Commission) 2003. *Yucca Mountain Review Plan, Final Report*. NUREG-1804, Rev. 2. Washington, D.C.: U.S. Nuclear Regulatory Commission, Office of Nuclear Material Safety and Safeguards. TIC: 254568.

Pollock, D.W. 1986. "Simulation of Fluid Flow and Energy Transport Processes Associated with High-Level Radioactive Waste Disposal in Unsaturated Alluvium." *Water Resources Research*, *22*, (5), 765-775. Washington, D.C.: American Geophysical Union. TIC: 253791.

van Genuchten, M.T. 1980. "A Closed-Form Equation for Predicting the Hydraulic Conductivity of Unsaturated Soils." *Soil Science Society of America Journal*, *44*, (5), 892-898. Madison, Wisconsin: Soil Science Society of America. TIC: 217327.

YMP (Yucca Mountain Site Characterization Project) 2001. *Yucca Mountain Site Characterization Project Requirements Document (YMP-RD)*. YMP/CM-0025, Rev. 4, DCN 02. Las Vegas, Nevada: Yucca Mountain Site Characterization Office. ACC: MOL.20010322.0491; MOL.20011107.0002.

9.2 CODES, STANDARDS, REGULATIONS, AND PROCEDURES

10 CFR 63. Energy: Disposal of High-Level Radioactive Wastes in a Geologic Repository at Yucca Mountain, Nevada. Readily available.

AP-2.14Q, Rev. 3, ICN 0. *Document Review*. Washington, D.C.: U.S. Department of Energy, Office of Civilian Radioactive Waste Management. ACC: DOC.20030827.0018.

AP-2.22Q, Rev. 1, ICN 0. *Classification Analyses and Maintenance of the Q-List*. Washington, D.C.: U.S. Department of Energy, Office of Civilian Radioactive Waste Management. ACC: DOC.20030807.0002

AP-2.27Q, Rev. 1, ICN 1. *Planning for Science Activities*. Washington, D.C.: U.S. Department of Energy, Office of Civilian Radioactive Waste Management. ACC: DOC.20030724.0001.

AP-3.15Q, Rev. 4, ICN 2. *Managing Technical Product Inputs*. Washington, D.C.: U.S. Department of Energy, Office of Civilian Radioactive Waste Management. ACC: DOC.20030627.0002.

AP-SI.1Q, Rev. 5, ICN 2. *Software Management*. Washington, D.C.: U.S. Department of Energy, Office of Civilian Radioactive Waste Management. ACC: DOC.20030902.0003.

AP-SIII.10Q, Rev. 2, ICN 1. *Models*. Washington, D.C.: U.S. Department of Energy, Office of Civilian Radioactive Waste Management. ACC: DOC.20031126.0002.

ASTM G 1-90 (Reapproved 1999). 1999. *Standard Practice for Preparing, Cleaning, and Evaluating Corrosion Test Specimens*. West Conshohocken, Pennsylvania: American Society for Testing and Materials. TIC: 238771.

9.3 SOURCE DATA, LISTED BY DATA TRACKING NUMBER

GS000483351030.003. Thermal Properties Measured 12/01/99 to 12/02/99 Using the Thermolink Soil Multimeter and Thermal Properties Sensor on Selected Potential Candidate Backfill Materials Used in the Engineered Barrier System. Submittal date: 11/09/2000.

GS020183351030.001. Uncompacted Bulk Density for Analyses Performed 02/02/00 to 05/23/00 on Potential Backfill Materials Used in the Engineered Barrier System. Submittal date: 01/22/2002.

LB0205REVUZPRP.001. Fracture Properties for UZ Model Layers Developed from Field Data. Submittal date: 05/14/2002.

LB0208UZDSCPMI.002. Drift-Scale Calibrated Property Sets: Mean Infiltration Data Summary. Submittal date: 08/26/2002.

LB0208UZDSCPLI.002. Drift-Scale Calibrated Property Sets: Lower Infiltration Data Summary. Submittal date: 08/26/2002.

LB03023DKMGRID.001. UZ 3-D Site Scale Model Grids. Submittal date: 02/26/2003.

LB0302PTNTSW9I.001. PTN/TSW Interface Percolation Flux Maps for 9 Infiltration Scenarios. Submittal date: 02/28/2003.

LB0302UZDSCPUI.002. Drift-Scale Calibrated Property Sets: Upper Infiltration Data Summary. Submittal date: 02/05/2003.

LB990701233129.001. 3-D UZ Model Grids for Calculation of Flow Fields for PA for AMR U0000, “Development of Numerical Grids for UZ Flow and Transport Modeling”. Submittal date: 09/24/1999.

LB990861233129.001. Drift Scale Calibrated 1-D Property Set, FY99. Submittal date: 08/06/1999.

LB991091233129.006. Thermal Properties and Tortuosity Factor for the UZ Model Layers for AMR U0090, "Analysis of Hydrologic Properties Data". Submittal date: 10/15/1999.

LB991201233129.001. The Mountain-Scale Thermal-Hydrologic Model Simulations for AMR U0105, “Mountain-Scale Coupled Processes (TH) Models”. Submittal date: 03/11/2000.

LL020710223142.024. Moisture Content of Rock from Neutron Logging Activities in the Drift Scale Test (DST): August 1997 through May 2002. Submittal date: 08/20/2002.

LL030709023122.032. Moisture Content of Rock from Neutron Logging Activities in the Drift Scale Test (DST): January 2003 through May 2003. Submittal date: 07/24/2003.

LL980918904244.074. Temperature, Relative Humidity and Gas Pressure Results During the Large Block Test FY 98. Submittal date: 09/29/1998.

LL980919304244.075. Neutron Logging Activities at the Large Block Test (LBT). Submittal date: 09/30/1998.

MO0001SEPDSTPC.000. Drift Scale Test (DST) Temperature, Power, Current, and Voltage Data for June 1, 1999 through October 31, 1999. Submittal date: 01/12/2000.

MO0002ABBLSLDS.000. As-Built Borehole Locations and Sensor Locations for the Drift Scale Test Given in Local (DST) Coordinates. Submittal date: 02/01/2000.

MO0003RIB00071.000. Physical and Chemical Characteristics of Alloy 22. Submittal date: 03/13/2000.

MO0007SEPDSTPC.001. Drift Scale Test (DST) Temperature, Power, Current, and Voltage Data for November 1, 1999 through May 31, 2000. Submittal date: 07/13/2000.

MO0012SEPDSTPC.002. Drift Scale Test (DST) Temperature, Power, Current, and Voltage Data for June 1, 2000 through November 30, 2000. Submittal date: 12/19/2000.

MO0107SEPDSTPC.003. Drift Scale Test (DST) Temperature, Power, Current, and Voltage Data for December 1, 2000 through May 31, 2001. Submittal date: 07/06/2001.

MO0202SEPDSTTV.001. Drift Scale Test (DST) Temperature, Power, Current, and Voltage Data for June 1, 2001 through January 14, 2002. Submittal date: 02/28/2002.

MO0208SEPDSTTD.001. Drift Scale Test (DST) Temperature Data for January 15, 2002 through June 30, 2002. Submittal date: 08/29/2002.

MO0303SEPDSTTM.000. Drift Scale Test (DST) Temperature Data for July 1, 2002 through December 31, 2002. Submittal date: 03/17/2003.

MO0306MWDASLCV.001. ANSYS-LA-Coarse Ventilation. Submittal date: 07/01/2003.

MO0307SEPDST31.000. Drift Scale Test (DST) Temperature Data for 01/01/2003 through 06/30/2003. Submittal date: 07/07/2003.

MO0307SPAVGSUM.000. van Genuchten Hydrologic Parameters. Submittal date: 07/26/2003.

MO0312SEPQ1997.001. Data Collected at Meteorological Monitoring Sites 1-9, Yucca Mountain, Area 25, Nevada Test Site, Las Vegas, Nevada, From 01/01/1997 Through 12/31/1997. Submittal date: 12/24/2003.

MO9807DSTSET01.000. Drift Scale Test (DST) Temperature, Power, Current, Voltage Data for November 7, 1997 through May 31, 1998. Submittal date: 07/09/1998.

MO9810DSTSET02.000. Drift Scale Test (DST) Temperature, Power, Current, Voltage Data for June 1 through August 31, 1998. Submittal date: 10/09/1998.

MO98METDATA114.000. Validated Meteorological Data for Ambient Air Monitoring Report Period 27, January - March 1998. Submittal date: 04/30/1998.

MO98METDATA117.000. Validated Meteorological Data for Ambient Air Monitoring Report Period 28, April - June 1998. Submittal date: 08/11/1998.

MO98METDATA120.000. Validated Meteorological Data for Ambient Air Monitoring Report Period 29, July - September 1998. Submittal date: 10/30/1998.

MO9906DSTSET03.000. Drift Scale Test (DST) Temperature, Power, Current, Voltage Data for September 1, 1998 through May 31, 1999. Submittal date: 06/08/1999.

SN0208T0503102.007. Thermal Conductivity of the Potential Repository Horizon Rev 3. Submittal date: 08/26/2002.

SN0303T0503102.008. Revised Thermal Conductivity of the Non-Repository Layers of Yucca Mountain. Submittal date: 03/19/2003.

SN0307T0510902.003. Updated Heat Capacity of Yucca Mountain Stratigraphic Units. Submittal date: 07/15/2003.

9.4 SOFTWARE SOURCES

Software Code: boundary_conditions. V 1.0. Sun, Sun OS 5.8. 11042-1.0-00.

Software Code: Chimney_interpolate. V1.0. Sun, Solaris 8. 11038-1.0-00.

Software Code: colCen. V1.0. Sun, Solaris 8. 11043-1.0-00.

Software Code: extractBlocks_EXT. V1.0. Sun, SUN O.S. 5.8. 11040-1.0-00.

Software Code: heatgen_ventTable_emplace. V1.0. Sun, Solaris 8. 11039-1.0-00.

Software Code: MSTHAC. V7.0. Sun, SUN O.S. 5.8. 10419-7.0-00.

Software Code: NUFT. V3.0s. Sun, SUN O.S. 5.8. 10088-3.0s-02.

Software Code: NUFT. V3.0.1s. Sun, SUN O.S. 5.8. 10130-3.0.1s-01.

Software Code: RADPRO. V4.0. Sun, SUN O.S. 5.8. 10204-4.0-00.

Software Code: readsUnits. V1.0. Sun, O.S. 5.5.1. 10602-1.0-00.

Software Code: reformat_EXT_to_TSPA. V1.0. Sun, Sun OS 5.8. 11061-1.0-00.

Software Code: repository_percolation_calculator. V1.0. Sun, SUN O.S. 5.8. 11041-1.0-00.

Software Code: rme6. v1.2. Sun, Solaris 8. 10617-1.2-00.

Software Routine: XTOOL V10.1. V10.1. Sun Ultra10. 10208-10.1-00.

Software Code: xw. V1.0. Sun, Solaris 8. 11035-1.0-00.

Software Code: YMESH. v1.54. SUN, SOLARIS 8. 10172-1.54-00.

10. ATTACHMENTS

A list of attachments can be found in Table 10-1.

Table 10-1. List of Attachments

Attachment Number	Number of Pages	Attachment Title
I	16	Building NUFT Submodels
II	6	Building Boundary Conditions for Submodels
III	4	Heat Generation for Submodels
IV	24	Building Submodel Material Property Files
V	20	Building Submodel Input Files
VI	4	LDTH- and DDT-Submodel Thermal-Radiation Connection Calculation
VII	6	Extraction / Microabstraction Process for MSTHAC (Building Virtual LDTH and SDT “Chimney” Submodels)
VIII	6	Binning Calculations
IX	14	Multiscale Model Approach to Thermohydrology at Yucca Mountain

ATTACHMENT I
BUILDING NUFT SUBMODELS

INTENTIONALLY LEFT BLANK

ATTACHMENT I
BUILDING NUFT SUBMODELS

To build the NUFT submodels, the following 14 steps must be completed:

Step 1 - Reformat the mesh from* UZ Flow Models and Submodels *(BSC 2003h) using rme6 v1.2.

The mesh of the three-dimensional Site-Scale UZ Flow Model requires some minor modifications to be able to be usable as input to YMESH v1.54. Note that the term "World Grid," which is used in the following description, refers to the three-dimensional mountain-scale mesh that is required as input to YMESH v1.54. The software code rme6 v1.2 is used to read the element and vertices files in DTN: LB03023DKMGRID.001 and to then create a single output file (called the World Grid), which contains the three-dimensional mountain-scale mesh in a format that can be ready by YMESH v1.54. The software code rme6 v1.2 renames the UZ blocks such that the substring "Ze" in the block name is replaced by "z". Likewise, "VI" is replaced by "v", and all trailing "_" characters are removed.

The three-dimensional mountain-scale mesh (called the World Grid) is built by taking the element/connection and vertices files in DTN: LB03023DKMGRID.001 and reformatting them into a YMESH-readable format using software code rme6 v1.2. Rename *__ to *, rename *Ze to *z, and rename *VI to *v.

software code:
rme6

inputs:
1) element/connection file (from DTN: LB03023DKMGRID.001)
   Grid_LA_3D.mesh
2) vertices file (from DTN: LB03023DKMGRID.001)
   grid2002.grd

output:
1) World Grid
   LBL2003-LA-YMESH (DTN: LL030808823122.038)

command line:
rme6 Grid_LA_3D.mesh grid2002.grd LBL2003-LA-YMESH

Step 2 - Expand the reformatted mountain-scale mesh using xw v1.0.

The three-dimensional mountain-scale mesh (file LBL2003-LA-YMESH, which is called the World Grid) created in the previous step needs to be expanded since it is not large enough to encompass the required SMT-submodel mesh. The software code xw v1.0 reads the three-dimensional mountain-scale mesh (LBL2003-LA-YMESH) and expands it in the easting direction such that the grid begins at 166,000 m easting and ends at 177,000 m easting in the Nevada Central coordinate system.

software code:
xw v1.0

inputs:
LBL2003-LA-YMESH (output from rme6 v1.2)

outputs:
1) Expanded World Grid
LBL2003-LA-YMESH-expand (DTN: LL030808823122.038)

command line:
xw LBL2003-LA-YMESH LBL2003-LA-YMESH-expand (DTN: LL030808823122.038)

Step 3 - Create the SDT-, LDTH-, DDT-submodel ".dat" files.

The first step in building the NUFT LDTH-, SDT-, and DDT-submodel (also called chimney submodels) input files is to create the files containing the vertical grid dimensions and associated UZ Model Layers at each LDTH/SDT-submodel location. This process begins with a file that gives the easting, northing, and repository elevation in Nevada Central coordinates for each LDTH/SDT-submodel location. There are two additional reference files (one for LDTH submodels and one for SDT submodels) that detail how the UZ Model Layers should be vertically descritized by YMESH v1.54. These files serve as a template for the ".dat" files, which are constructed by taking the relevant template (SDT or LDTH) and inserting the Nevada Central coordinates for the specified LDTH/SDT-submodel location. These files are in the format specified by the YMESH v1.54 user's manual for extracting LDTH/SDT-submodel (chimney-submodel) stratigraphies from the expanded World Grid.

inputs:

a. SDT and LDTH-submodel inputs:
chimneyLocation.dat (DTN: LL030808823122.038)
Contains name, easting, northing, and repository elevation for each "chimney" LDTH/SDT-submodel location

b. SDT-submodel inputs:
SDT_column_template_2003: Template for the SDT-submodel .dat files. The template gives instructions to YMESH v1.54 about how to discretize the grid vertically by defining the vertical gridblock dimensions. This is essentially a complete .dat file, except the easting, northing, and repository elevation for each LDTH/SDT-submodel (i.e., chimney-submodel) location (eg. P1R10C5) defined in the file "chimneyLocation.dat" have been inserted (by copying and pasting), which creates .DAT files for each of the respective SDT-submodel locations (DTN: LL030808823122.038).

c. LDTH-submodel inputs:
LDTH_column_template_2003: Template for the LDTH .dat files. The template gives instructions to YMESH v1.54 about how to discretize the grid vertically by defining the vertical gridblock dimensions. This is essentially a complete .dat file, except the easting, northing, and repository elevation for each chimney-submodel location (eg. P1R10C5) defined in the file "chimneyLocation.dat" have been inserted (by copying and pasting), which creates .DAT files for each of the respective LDTH-submodel locations (DTN: LL030808823122.038).

Step 4 - Create the SDT-, LDTH-, DDT-submodel ".col" and ".nft" files (software code YMESH v1.54).

Once the ".dat" files have been created, YMESH v1.54 is used to create the "User Column Description" files that contain the vertical dimensions of the grid, along with the vertical distribution of UZ Model Layers. This file contains the definition of each gridblocklayer including its thickness and material type (i.e., UZ Model Layer). To create these files, YMESH v1.54 is started and the expanded World Mesh is read. Next, a ".dat" file is opened and a ".col" file is saved by selecting the "User Column Description" save option in the YMESH File/Save menu. This process is repeated for each chimney-submodel location and for each of the SDT, LDTH, and DDT submodels.

The output ".nft" file is a NUFT genmsh table as defined in the NUFT user's manual (Nitao 1998). To create these files, YMESH v1.54 is started and the expanded World Mesh is read as input (using the "Open data file" command). Next, a ".dat" file is opened and a ".nft" file is saved by selecting the "User NUFT genmsh" save option in the YMESH v1.54 File/Save menu. This process is repeated for each chimney-submodel location and for each of the SDT, LDTH, and DDT submodels.

software code:
YMESH v1.54

inputs:
LBL2003-LA-YMESH-expand (output from xw v1.0) (DTN: LL030808823122.038)
.dat files for each SDT submodel (chimney-submodel) location
(DTN: LL030808823122.038)
.dat files for each LDTH-submodel (chimney-submodel) location
(DTN: LL030808823122.038)

outputs:
.col file for each SDT-submodel (chimney-submodel) location
(DTN: LL030808823122.038)
.nft file for each SDT-submodel (chimney-submodel) location
(DTN: LL030808823122.038)

.col file for each LDTH-submodel (chimney-submodel) location
(DTN: LL030808823122.038)
.nft file for each LDTH-submodel (chimney-submodel) location
(DTN: LL030808823122.038)

methodology:
1) Start YMESH v1.54
2) Open data file: World Grid (/LBL2003-LA-YMESH-expand)
3) Open data file: chimney.dat file (*.dat)
4) Save data file: User NUFT genmsh file (*.nft)
5) Save data file: User Column Description file (*.col)
6) Repeat Substeps 3 to 5 for all chimney-submodel locations and for each of the SDT, LDTH, and DDT submodels.

Step 5 - Create the SDT-submodel files.

Once the ".nft" files have been created for the SDT-submodel "chimney-submodel" files (Step 4), the following substeps are carried out. For each chimney-submodel location, two output files are created. The first output file is a ".nft.dkm" file that adds the atm, wt, and wp block to the input NUFT gensmsh ".nft" file; this file is used for the SDT-submodel runs with repository heating. A second file is also created that is a duplicate of the ".nft.dkm" file except there is no wp block present. The second file is called ".nft.dkm0"; this file is used for the SDT-submodel initialization runs that have no repository heating. Note that because the file-naming convention is parallel with that used for the LDTH submodels (discussed below), the suffix "dkm" is used for the SDT submodels, as well as for the LDTH submodels. This naming convention does not mean that the SDT submodels use the DKM.

inputs (DTN: LL030808823122.038)
.nft file for each SDT-submodel (chimney-submodel) location
the string "5.990" used to identify the block that is the heated repository element

output files: (DTN: LL030808823122.038)
.nft.dkm file: adds the atm, wt boundary gridblocks and wp gridblocks to the input .nft file for each chimney-submodel location

.nft.dkm0 file: adds the atm and wt block to the input .nft file for each chimney-submodel location

Step 6 - Create the LDTH-submodel DKM files.

Once the ".nft" files have been created, the DKM version of these files are created for each LDTH-submodel (chimney-submodel) location. There are five output files created for each chimney-submodel location. The input files are modified to include the atmosphere and water table boundary gridblocks, to define the gridblocks within the emplacement drifts that represent the engineered barrier system components (e.g., invert), and to define the matrix and fracture continua. The specific elements added to each of the five types of output files are detailed below. Note that the files with the string "dkm" are used in the LDTH-submodel runs with repository heating. The files with the string "dkm0") are used in the LDTH-submodel initialization runs that have no repository heating.

inputs: (DTN: LL030808823122.038)
.nft file for each LDTH-submodel (chimney-submodel) location
the string "0.403" used to identify the waste package block

output files (a total of 5: for each chimney-submodel location): (DTN: LL030808823122.038)
*.nft.msh.dkm0: adds the atm and wt boundary gridblocks to the input .nft file
*.nft.msh.dkm0.f: adds the atm and wt fracture boundary gridblocks to the input .nft file. All blocks are prepended with "f-" to represent the fractures.
*.nft.msh.dkm.f: adds the atm, wt, drift, wp, invert, and hstrk fracture gridblocks to the input .nft file. All blocks are prepended with "f-" to represent the fractures.
*.nft.msh.dkm0.m: adds the atm and wt matrix boundary gridblocks to the input .nft file. All blocks are prepended with "m-" to represent the matrix.

*.nft.msh.dkm.m: adds the atm, wt, drift, wp, invert, and hstrk matrix gridblocks to the input .nft file. All blocks are prepended with "m-" to represent the matrix.

Step 7 - Create DDT- and LDTH-submodel thermal-radiation connections.

Radiative heat transfer is an important component in the DDT and LDTH heat transfer models. To accommodate this mechanism, NUFT requires a list of all thermal-radiation connections between surfaces inside the drifts that are separated by air. Typical thermal-radiation connections are found between the waste package and the drift wall, the waste package and the drip shield, the drip shield and the drift wall, and the drift wall and other drift wall elements. These connections are generated by hand and verified visually using RADPRO v4.0.

Step 8 - Calculate LDTH-submodel percolation flux values.

1. Determine the "raw" percolation flux value for each LDTH-submodel (chimney-submodel) location

The LDTH-submodel ".col" files created in Step 4 include the name of the grid column (e.g. g_9) from the three-dimensional Site-Scale UZ Model grid (DTN: LB03023DKMGRID.001) that a given LDTH submodel resides within. For each of the respective LDTH-submodel locations, the identity of the three-dimensional Site-Scale UZ Model grid column is recorded; note that this grid column is called the "World Column" by YMESH v1.54). Note that the identity of the World Column is given after the string "WORLD COLUMN" in the LDTH-submodel input file. For each LDTH-submodel location, the identity of the World Column is used to find the corresponding the present-day-, monsoonal- and glacial-transition-climate PTn-to-TSw percolation fluxes calculated by the three-dimensional Site-Scale UZ Flow Model (DTN: LB0302PTNTSW9I.001). This is repeated for the lower-bound, mean, and upper-bound infiltration flux cases. Note that there are nine percolation flux maps produced by the three-dimensional Site-Scale UZ Flow Model, corresponding to the three climate states and three infiltration flux cases.

i. For each LDTH-submodel ".col" file generated above, grep for the string "WORLD COLUMN" and record the name of the World Column that the LDTH submodel resides within.

ii. From the three-dimensional Site-Scale UZ Flow Model (DTN: LB0302PTNTSW9I.001) and on the basis of the World Column that a given LDTH submodel resides within, find the PTn-to-TSw percolation flux values for the present-day, monsoonal, and glacial-transition climates and for the lower-bound, mean, and upper-bound infiltration flux cases.

2. Determine the average percolation flux value for each repository panel

The software code repository_percolation_calculator v1.0 is used, along with two input files to determine the repository-panel-averaged percolation flux for each repository panel (Panels 1, 2E, 2W, 3, and 5 in Figure 6.3-1). The first input file gives the coordinates of the vertices (i.e., corners) of a given repository panel. The second

file is one of nine PTn-to-TSw percolation flux maps calculated by the three-dimensional Site-Scale UZ Flow Model (DTN: LB0302PTNTSW9I.001). The output from repository_percolation_calculator v1.0 is a file that contains the percolation flux values for each of the World Columns (i.e., grid columns from the three-dimensional Site-Scale UZ Flow Model) that fall within the given repository panel footprint. The output file also contains the average percolation flux for that repository panel. This averaged panel flux is a simple arithmetic average of the percolation flux values falling within the repository-panel footprint. Because Panel 1 is relatively small, it was decided to group it with Panel 2W and to treat Panels 1 and 2W as a contiguous repository panel. Panels 2E, 3, and 5 are treated individually according to the procedure described above.

software code:

repository_percolation_calculator v1.0: given a set of coordinates defining the footprint of a repository panel and a PTn-to-TSw percolation flux map from the three-dimensional Site-Scale UZ Flow Model (DTN: LB0302PTNTSW9I.001), determine which World Columns lie within the polygon and do a simple average of the corresponding percolation values to determine the average panel percolation.

input files: (DTN: LL030808723122.037)

frameData1.dat: define the polygon for panel 1
frameData2e.dat: define the polygon for panel 2E
frameData2w.dat:define the polygon for panel 2W
frameData3.dat: define the polygon for panel 3
frameData5.dat: define the polygon for panel 5

preq_la_ptn.dat: the present-day-climate lower-bound infiltration flux case PTn-to-TSw percolation flux map (DTN: LB0302PTNTSW9I.001)
preq _ma_ptn.dat: the present-day-climate mean infiltration flux case PTn-to-TSw percolation flux map (DTN: LB0302PTNTSW9I.001)
preq _ua_ptn.dat: the present-day-climate upper-bound infiltration flux case PTn-to-TSW percolation flux map (DTN: LB0302PTNTSW9I.001)

monq_la_ptn.dat: the monsoonal-climate lower-bound infiltration flux case PTn-to-TSw percolation flux map (DTN: LB0302PTNTSW9I.001)
monq _ma_ptn.dat: the monsoonal-climate mean infiltration flux case PTn-to-TSw percolation flux map (DTN: LB0302PTNTSW9I.001)
monq _ua_ptn.dat: the monsoonal-climate upper-bound infiltration flux case PTn-to-TSw percolation flux map (DTN: LB0302PTNTSW9I.001)

glaq_la_ptn.dat: the glacial-transition-climate lower-bound infiltration flux case PTn-to-TSw percolation flux map (DTN: LB0302PTNTSW9I.001)
glaq _ma_ptn.dat: the glacial-transition-climate mean infiltration flux case PTn-to-TSw percolation flux map (DTN: LB0302PTNTSW9I.001)

glaq _ua_ptn.dat: the glacial-transition-climate upper-bound infiltration flux case PTn-to-TSw percolation flux map (DTN: LB0302PTNTSW9I.001)

command line

repository_percolation_calculator <percolation map> <panel outline> <output file>

output files: (DTN: LL030808723122.037)

glacial_la_frameData1.dat
glacial_la_frameData2e.dat
glacial_la_frameData2w.dat
glacial_la_frameData3.dat
glacial_la_frameData5.dat
modern_la_frameData1.dat
modern_la_frameData2e.dat
modern_la_frameData2w.dat
modern_la_frameData3.dat
modern_la_frameData5.dat
monsoon_la_frameData1.dat
monsoon_la_frameData2e.dat
monsoon_la_frameData2w.dat
monsoon_la_frameData3.dat
monsoon_la_frameData5.dat

glacial_ma_frameData1.dat
glacial_ma_frameData2e.dat
glacial_ma_frameData2w.dat
glacial_ma_frameData3.dat
glacial_ma_frameData5.dat
modern_ma_frameData1.dat
modern_ma_frameData2e.dat
modern_ma_frameData2w.dat
modern_ma_frameData3.dat
modern_ma_frameData5.dat
monsoon_ma_frameData1.dat
monsoon_ma_frameData2e.dat
monsoon_ma_frameData2w.dat
monsoon_ma_frameData3.dat
monsoon_ma_frameData5.dat

glacial_ua_frameData1.dat
glacial_ua_frameData2e.dat
glacial_ua_frameData2w.dat
glacial_ua_frameData3.dat
glacial_ua_frameData5.dat
modern_ua_frameData1.dat
modern_ua_frameData2e.dat
modern_ua_frameData2w.dat

modern_ua_frameData3.dat
modern_ua_frameData5.dat
monsoon_ua_frameData1.dat
monsoon_ua_frameData2e.dat
monsoon_ua_frameData2w.dat
monsoon_ua_frameData3.dat
monsoon_ua_frameData5.dat

Note: These files contain the PTn-to-TSw percolation flux values falling within a given repository panel footprint and average value for that repository panel.

3. Calculate panel averages for panels 1 and 2w

Panels 1 and 2W are grouped for the purpose of computing the LDTH-submodel percolation fluxes. This is an area-weighted average, using the respective areas of Panels 1 and 2W.

4. Calculate average percolation of all LDTH-submodels falling within a repository panel

A simple arithmetic average of the percolation flux values (Substep 2) for all LDTH-submodel locations that fall inside of a particular panel footprint is calculated. These values are scaled in the following step so that the average percolation flux of the LDTH-submodels lying within a repository panel is the same as the panel average calculated in Substeps 2 and 3.

5. Determine the scaled LDTH-submodel percolation flux values from the "raw" LDTH-submodel "chimney" percolation flux values

The "raw" LDTH-submodel (chimney-submodel) percolation values determined in Step 8, Substep 1 above are scaled so that the average "scaled" percolation flux of all LDTH submodels falling within a given repository panel is the same as the average percolation flux for that panel determined in Step 8, Substep 2 above. First, a simple arithmetic average of the "raw" LDTH-submodel percolation flux values is calculated for a given repository panel. Then a scaling factor is computed for that panel, which is equal to the average percolation flux for that panel (determined in Step 8, Substep 2 above) divided by the average "raw" percolation flux of all LDTH submodels (determined in Step 8, Substep 1) within that panel. Finally, for each of the LDTH submodels within a repository panel, the "raw" percolation flux values are multiplied by the scaling factor for that panel to obtain the scaled percolation flux values for each of the LDTH submodels. This process is repeated for each repository panel, for each of the three climate states and for each of the three infiltration flux cases. These calculations are performed using Microsoft Excel spreadsheets in DTN: LL030808723122.037:

scaled chimney percolation (base PTn)_la.xls
scaled chimney percolation (base PTn)_ma.xls
scaled chimney percolation (base PTn)_ua.xls

6. Create scaled SMT-submodel repository-gridblockpercolation flux values

Once the scaled percolation flux values have been calculated for each of the LDTH-submodel locations, the corresponding percolation flux values for each of the SMT-submodel gridblock locations can be calculated by interpolating the percolation fluxes between each of the LDTH-submodel locations. Note that each of the LDTH/SDT-submodel locations lies at the centers of SMT-submodel repository gridblocks (see Figure 6.2-3). The LDTH and SDT submodel pairs are more or less equally spaced along drifts in the SMT submodel, and are always located at the ends of the emplacement drifts, and typically at one or two other locations along the central portion of the drift. Also, LDTH and SDT submodel pairs are typically located along every fourth drift. It is important to note that the gridblocks representing the emplacement drifts in the SMT submodel are regularly spaced, with 20-m gridblock spacing along each drift and each drift being represented by a gridblock row that is 81-m wide (which represents the drift spacing). Thus, intermediate locations along a drift (between LDTH/SDT-submodel locations) can be linearly interpolated simply on the basis of the number of gridblocks separating that particular location from the pair of LDTH/SDT-submodel locations that straddle it, and for which the simple linear interpolation is based upon. Once the drifts that contain LDTH and SDT submodel pairs have been filled in with interpolated values, the drifts lying between these interpolated drifts can also be interpolated as well. The interpolation methodology interpolates linearly between drifts (north/south) such that the previously interpolated SMT submodel gridblock pairs submodel pairs are the same distance from the ventilation inlet as the target SMT submodel gridblock location. Again, because of the uniform gridblock spacing, the interpolation process is simply based upon the number of drifts between the drift for which the interpolation is being conducted and the previously-interpoloated emplacement drifts (which contain the LDTH-SDT-submodel locations) that straddle the target drift.

Step 9 - Determine the identity of the world column (from the three-dimensional Site-Scale UZ Flow Model) for each LDTH-SDT-submodel pair.

The ".col" files created in Step 4 include the name of the world column into which an LDTH/SDT-submodel pair falls. These world column names are recorded from the ".col" files for the LDTH and SDT submodels.

Step 10 - Compute SMT-, SDT-, and LDTH-submodel boundary conditions.

The software code boundary_conditions v1.0 generates upper and lower boundary conditions for the LDTH, SMT, and SDT submodels of the MSTHM. The boundary conditions are derived from the three-dimensional Site-Scale UZ Flow Model. Data are extracted from the three-dimensional Site-Scale UZ Flow Model grid (DTN: LB03023DKMGRID.001) and a file (DTN: LB991201233129.001) containing boundary conditions at the ground surface and at an elevation of 730 m, which was the location of the (horizontal) water table in the three-dimensional Site-Scale UZ Flow Model grid used in the TSPA-SR (DTN: LB990701233129.001). Interpolation is used to determine the boundary conditions at the sloping water table in the three-dimensional Site-Scale UZ Flow Model. The software code boundary_conditions v1.0 reads input files containing the following information, respectively:

(1) the SMT-submodel grid, (2) the grid (File: MESH_rep.VF of DTN: LB991201233129.001) and (3) the initial conditions (File: INCON_thm_s32.dat of DTN: LB991201233129.001) from *Mountain-Scale Coupled Processes (TH) Models* (CRWMS M&O 2000c), (4) the grid centers and ground-surface and water-table elevations of the World Columns in the three-dimensional Site-Scale UZ Flow Model, (5) coordinates of the LDTH/SDT-submodel locations, and (6) the values of wet thermal conductivity of the UZ Model Layers. Boundary conditions are generated at all World Columns (from the three-dimensional Site-Scale UZ Flow Model) and at all LDTH/SDT-submodel locations. For the LDTH submodels, boundary_conditions v1.0 generates a table of boundary conditions at the ground surface, including temperature, gas-phase pressure, air mass fraction, and specific enthalpy of water at the ground-surface conditions in NUFT-input format. Also generated for LDTH submodels are boundary conditions at the water table, including temperature and gas-phase pressure in NUFT-input format. For the SMT and SDT submodels, boundary_conditions v1.0 generates ground-surface and water-table temperatures in NUFT-input format. See Attachment II for details on the SMT-submodel boundary condition construction.

Step 11 - Compute SMT-, SDT-, LDTH- and DDT-submodel heat-generation curves.

Using a reference heat-generation-versus-time table, as well as a table of ventilation-heat-removal-efficiency as a function of time and distance from the ventilation inlet, heatgen_ventTable_emplace v1.0 produces files of heat-generation-versus-time tables in NUFT-heatgen format. These heat-generation files have the influence of reduced heat-generation rates during the 50-year ventilation preclosure period and full-power heating during the postventilation postclosure period. See Attachment III for details on building the heat generation curves. See Attachment V for the assembly of NUFT input files.

Step 12 - Compile natural- and engineered-system properties.

Using several DTNs containing material-property values of the natural system and several Information Exchange Drawings containing material-property values of the engineered system, material-property files (called NUFT rocktab files) are constructed. These files are in the NUFT rocktab format; these files are read in as “include” file in the SMT-, SDT-, LDTH- and DDT-submodel NUFT input files. See Attachment IV for details on assembling the rocktab files that contain the material property values for the respective submodels.

Step 13 - Compute effective thermal conductivity.

To account for heat transfer by natural convection in the emplacement drift, correlations have been developed (Francis et al. 2003, Table 6) for the relationship between drift wall, waste package, and drift air temperatures and an effective thermal conductivity K_{eff} of the air in the emplacement drift cavity that represents the influence of heat transfer by natural convection. This process is conducted for the cavity between the drip shield and drift wall in the LDTH submodels and DDT submodels. This process is also conducted for the cavity between the waste package and drip shield in the DDT submodels.

The effective thermal conductivity K_{eff} is determined by running a NUFT submodel (either LDTH or DDT) starting with an initial guess for K_{eff} for the gas-filled cavities in the drift. The appropriate formula from Table 6 of *CFD Modeling of Natural Convection Heat Transfer and*

Fluid Flow in Yucca Mountain Project (YMP) Enclosures (Francis et al. 2003) is used to compute K_{eff} in the gas-filled cavities and the NUFT submodel is rerun with the new value of K_{eff}. Each time a new NUFT-submodel run is completed, the value of K_{eff} is computed and compared with the previous iteration. After the value of K_{eff} has converged (between successive iterations), the iterative process is completed. The effective thermal conductivity K_{eff} is a time-varying parameter and the formula in Table 6 of *CFD Modeling of Natural Convection Heat Transfer and Fluid Flow in Yucca Mountain Project (YMP) Enclosures* (Francis et al. 2003) involves computing temperatures averaged over the gridblocks representing the gas-filled cavities in the emplacement drift. To carry out this iterative process, extractBlocks_EXT v1.0 is used. This software code takes a list of gridblocks, extracts the required information from the NUFT-submodel output, applies the appropriate formula from Table 6 of *CFD Modeling of Natural Convection Heat Transfer and Fluid Flow in Yucca Mountain Project (YMP) Enclosures* (Francis et al. 2003), and produces a time history of calculated K_{eff}.

software code:

extractBlocks_EXT v1.0

inputs:

The name of an input file that defines how to apply the formula from Table 6 of *CFD Modeling of Natural Convection Heat Transfer and Fluid Flow in Yucca Mountain Project (YMP) Enclosures* (Francis et al. 2003) (DTN: LL030808723122.037)

```
DDT_Keff_postclose_inside_0_wp1
DDT_Keff_postclose_inside_0_wp2
DDT_Keff_postclose_inside_0_wp3
DDT_Keff_postclose_inside_0_wp4
DDT_Keff_postclose_inside_0_wp5
DDT_Keff_postclose_inside_0_wp6
DDT_Keff_postclose_inside_0_wp7
DDT_Keff_postclose_inside_0_wp8
DDT_Keff_preclose_0_wp1
DDT_Keff_preclose_0_wp2
DDT_Keff_preclose_0_wp3
DDT_Keff_preclose_0_wp4
DDT_Keff_preclose_0_wp5
DDT_Keff_preclose_0_wp6
DDT_Keff_preclose_0_wp7
DDT_Keff_preclose_0_wp8
```

outputs:

A file with a time history of K_{eff} calculated from the NUFT input (DTN: LL030808723122.037)

```
DDT_Keff_postclose_inside_0_wp1.out
DDT_Keff_postclose_inside_0_wp2.out
DDT_Keff_postclose_inside_0_wp3.out
DDT_Keff_postclose_inside_0_wp4.out
DDT_Keff_postclose_inside_0_wp5.out
DDT_Keff_postclose_inside_0_wp6.out
DDT_Keff_postclose_inside_0_wp7.out
DDT_Keff_postclose_inside_0_wp8.out
DDT_Keff_preclose_0_wp1.out
DDT_Keff_preclose_0_wp2.out
```

```
DDT_Keff_preclose_0_wp3.out
DDT_Keff_preclose_0_wp4.out
DDT_Keff_preclose_0_wp5.out
DDT_Keff_preclose_0_wp6.out
DDT_Keff_preclose_0_wp7.out
DDT_Keff_preclose_0_wp8.out
```

Step 14 - Create SMT-submodel mesh.

To create the SMT-submodel mesh used for the MSTHM calculations in this report, one must carefully perform the following steps. Note one must be using the qualified version of YMESH v1.54 and Solaris OS 5.8 UNIX operating system.

a. Execute YMESH v1.54
ymesh

b. Pull down *File* tab on YMESH v1.54 to and *Open* the data file. In the *Select Input File* popup highlight the file "LBL2003-LA-YMESH-expand_qualified" (from NUFT-submodel Building Step 2) and click *OK*

c. Pull down *Edit* tab and highlight *Extend World Columns*. Make certain the *Above* tab is active. Enter the following:

Material *atm*
Thickness *200.*
click *OK* button

d. Remain in the *Extended World Columns* but now make the *Below* tab active. Enter the following:

Material *sz1*
Thickness *30.*
click *OK* button

Material *sz2*
Thickness *60.*
click *OK* button

Material *sz3*
Thickness *70.*
click *OK* button

Material *sz4*
Thickness *120.*
click *OK* button

Material *sz5*
Thickness *240.*
click *OK* button

Material *sz6*
Thickness *480.*
click *OK* button

Material *bsmnt*
Thickness *0.1*
click *OK* button

e. Click *CLOSE* button on *Extend World Columns* popup

f. Open *File* pulldown from YMESH v1.54 menu and select *Open data file*

g. In the *Select Input File* popup, select file "tspa03.grid03-150w" and click *OK* button

h. Highlight *Options* pulldown from YMESH v1.54menu and select *Trim Top Boundary*

i. In *Ending Conditions* popup menu, enter the following:

Material *atm*
Thickness *0.1*
click *Apply* button
click *Close* button

j. Highlight *Edit* pulldown from YMESH v1.54 menu and select *Element Names*

k. In *Rename Elements* popup window, follow these steps:

i. Select *Material* button and enter

Prefix *atm*
Material *atm*
Click *Apply* button

Prefix bsm

Material bsmnt

Click *Apply* button

ii. Select *PrefixIndexFile* button

In the PrefixIndexRangeFile space enter
heatBlockIndicesPanel1_2e_2w_3_5.data
Click Apply button
Click *Close* button

l. Highlight the *File* pulldown menu and select *Save data file*

In the Save File popup window type the *Selection* space enter "tspa03.mesh03-150w"
Click *OK* button
(Note that this saves the mesh)

m. Return to a UNIX command prompt and type the following UNIX commands

```
rm P1-UB_list P2E-UB_list P2W-UB_list P3-UB_list
 P5-UB_list
```
(respond "yes" to all queries)
```
grep P1 tspa03.mesh03-150w > P1-UB_list
grep P2E tspa03.mesh03-150w > P2E-UB_list
grep P2W tspa03.mesh03-150w > P2W-UB_list
grep P3 tspa03.mesh03-150w > P3-UB_list
grep P5 tspa03.mesh03-150w > P5-UB_list
```

n. Using a text editor, open the five files just created: P1-UB_list, P2E-UB_list, P2W-UB_list, P3-UB_list, and P5-UB_list (DTN: LL030808823122.038)

o. Edit the five files by removing all gridblock connections information (which is the last 70 percent of the file), saving only the element information (which is the first 30 percent of the file)

p. Save the five files with the above names

Note that any mistakes made by the user in executing the YMESH v1.54 steps forces the user to return to the beginning and redo the YMESH v1.54 steps.

ATTACHMENT II
BUILDING BOUNDARY CONDITIONS FOR SUBMODELS

INTENTIONALLY LEFT BLANK

ATTACHMENT II
BUILDING BOUNDARY CONDITIONS FOR SUBMODELS

The software code boundary_conditions v1.0 generates upper and lower boundary conditions for the LDTH, SMT, and SDT submodels (see Step 10 of Attachment I). The boundary conditions are derived from *Mountain-Scale Coupled Processes (TH) Models* (CRWMS M&O 2000c) (DTN: LB991201233129.001). Data are extracted from the three-dimensional Site-Scale UZ Flow Model grid being used in the TSPA-LA (DTN: LB03023DKMGRID.001), as well as from *Mountain-Scale Coupled Processes (TH) Models* (CRWMS M&O 2000c), including the boundary conditions (file INCON_thm_s32.dat in DTN: LB991201233129.001) and the corresponding three-dimensional mountain-scale grid (file MESH_rep.VF in DTN: LB991201233129.001). It should be noted that the three-dimensional mountain-scale grid used in *Mountain-Scale Coupled Processes (TH) Models* (CRWMS M&O 2000c) has a horizontal water table at an elevation of 730 m, while the three-dimensional Site-Scale UZ Flow Model grid used in the TSPA-LA (DTN: LB03023DKMGRID.001) has a sloping water table. The software code boundary_conditions v1.0 uses linear interpolation to determine the water-table boundary conditions at the sloping water-table surface in the three-dimensional Site-Scale UZ Flow Model grid used in the TSPA-LA (DTN: LB03023DKMGRID.001). The software code boundary_conditions v1.0 reads input files containing the following information, respectively: (1) the SMT-submodel grid, (2) the grid and (3) initial conditions from *Mountain-Scale Coupled Processes (TH) Models* (CRWMS M&O 2000c), (4) the grid centers and ground-surface and water-table elevations of the World Columns in the three-dimensional Site-Scale UZ Flow Model, (5) coordinates of the LDTH/SDT-submodel locations, and (6) the values of wet thermal conductivity of the UZ Model Layers.

For item (4) above, colCen v1.0 is used to determine the grid centers for all World Columns in the three-dimensional Site-Scale UZ Flow Model.

Boundary conditions are generated by boundary_conditions v1.0 at all World Columns (from the three-dimensional Site-Scale UZ Flow Model) and at all LDTH/SDT-submodel locations. For the LDTH submodels, boundary_conditions v1.0 generates a table of boundary conditions at the ground surface, including temperature, gas-phase pressure, air mass fraction, and specific enthalpy of water at the ground-surface conditions in NUFT-input format. Also generated for LDTH submodels are boundary conditions at the water table, including temperature and gas-phase pressure in NUFT-input format. For the SMT and SDT submodels, boundary_conditions generates ground-surface and water-table temperatures in NUFT-input format.

Prior to determining the boundary conditions, Steps 1 and 2 of Attachment I, which result in an expanded three-dimensional mountain-scale mesh (called the expanded World Grid for YMESH v1.54), must be executed. This expanded three-dimensional mountain-scale mesh (also called the expanded World Grid) is used as an input to boundary conditions v1.0, which subsequently outputs all of the boundary condition files to be used for all of the submodels (see Attachment V for the assembly of NUFT input files).

Create boundary condition files for all submodels.

The software code boundary_conditions v1.0 was used to create the boundary conditions for all submodels.

software code:

boundary_conditions

input files (DTN: LL030808723122.037)

smtMesh (SMT-submodel mesh file in NUFT meshfile input format)

MESH_rep.VF of DTN: LB991201233129.001 (Mesh file for *Mountain-Scale Coupled Processes (TH) Models* (CRWMS M&O 2000c))

INCON_thm_s32.dat of DTN: LB991201233129.001 (Initial conditions for *Mountain-Scale Coupled Processes (TH) Models* (CRWMS M&O 2000c))

grid_column_centers (Ground-surface and water-table elevations and coordinates of World Columns of the three-dimensional Site-Scale UZ Flow Model grid, which is the LBL2002-YMESH Expanded World Grid; this information is generated as output from colCen v1.0—see above**)**

chimneyLocation (For each LDTH-/SDT-submodel pair this file locates the corresponding World Column in the LBL2002-YMESH Expanded World Grid)

tcond.dat (Thermal conductivity of UZ Model Layers)

output files (DTN: LL030808723122.037)

chimSurfBC.out (LDTH-submodel surface boundary conditions: temperature, gas pressure, air mass fraction in gas phase, and specific enthalpy of water)

chimLowerBC.out (LDTH-submodel water table boundary conditions: temperature and gas pressure)

smtUpperBC.out (Surface boundary temperature for SMT submodel in NUFT input format)

smtLowerBC.out (Lower boundary temperature for SMT submodel in NUFT input format)

worldColBC.out (:LDTH/SDT-submodel-type boundary conditions for all World Columns in the LBL2002-YMESH Expanded World Grid)

smtWorldBC (Summary of SMT-submodel boundary conditions for columns in the LBL2002-YMESH Expanded World Grid)

execution process

To start, type:

boundary_conditions

Enter output file extension:

out

Enter thermal cond. of material below water table, SMT submodel:

1.2

Enter value of added thickness below water table, SMT submodel:

1000

Enter name of SMT-submodel mesh file:

Hit return with no entry to use default file, smtMesh

SMTMESHTEST

Enter name of the Mountain-Scale Coupled (TH) Models (CRWMS M&O 2000c) mesh file:

Hit return with no entry to use default file, MESH_rep.VF

MESH_rep.VF

Enter name of the Mountain-Scale Coupled (TH) Models (CRWMS M&O 2000c) file with init.cond.:

Hit return with no entry to use default file, INCON_thm_s32.dat

INCON_thm_s32.dat

Enter name of file with World Column data from the 3-D Site-Scale UZ Flow Model:

Hit return with no entry to use default file, grid_column_centers

GRID_COLUMN_CENTERS

Enter name of file with LDTH-/SDT-submodel "chimney" locations:

Hit return with no entry to use default file, chimneyLocation

CHIMNEYLOCATION

Enter name of file with thermal cond. data:

Hit return with no entry to use default file, tcond.dat

TCOND.DAT

INTENTIONALLY LEFT BLANK

ATTACHMENT III
HEAT GENERATION FOR SUBMODELS

INTENTIONALLY LEFT BLANK

ATTACHMENT III
HEAT GENERATION FOR SUBMODELS

To produce the heat generation for the SMT, SDT, DDT, and LDTH submodels (Step 11 in Attachment I) the following instructions must be followed. The software code heatgen_ventTable_emplace v1.0 is used for this purpose:

The software code heatgen_ventTable_emplace v1.0 is used to define the ventilation heat-removal efficiency as a function of time and distance from the ventilation inlet. This code requires a control file that provides names of the locations (within the repository) at which heat generation files should be created along with the distance of that location from the ventilation inlet. The output of heatgen_ventTable_emplace v1.0 is a series of files of heat-generation-rate-versus time tables that account for the heat-removal efficiency of forced-convection ventilation of the emplacement drifts during the preclosure period. The output files from heatgen_ventTable_emplace v1.0 are in NUFT heatgen format.

Creating Heat Generation Curves for the SDT and LDTH submodels

software code

heatgen_ventTable_emplace v1.0

inputs: (DTN: LL030808723122.037)

SDT: string indicating to the software code that this is an SDT/LDTH-submodel heatgen file

multi-package_7WP_Segment_Info_SDT_LDTH_TSPA03: default SDT/LDTH-submodel heat-generation table with nominal loading and no ventilation

LA_ventilation_table_50yr.rfm: ventilation table with ventilation efficiency as a function of time and distance from the ventilation inlet.

ventilation_time.reform: file giving the name and distance from the ventilation input for each LDTH-/SDT-submodel "chimney" location.

outputs: (heatgen file) (DTN: LL030808723122.037)

P*_LDTH-SDT output heatgen file for each LDTH-/SDT-submodel "chimney" location

Creating Heat Generation Curves for the DDT submodels

software code

heatgen_ventTable_emplace

inputs: (DTN: LL030808723122.037)

DDT: string indicating to the software code that this is a DDT heatgen file

DDT_TSPA03: default DDT heat generation table with nominal loading and no ventilation

LA_ventilation_table_50yr.rfm: ventilation table with ventilation efficiency as a function of time and distance from the ventilation inlet.

ventilation_time.reform: file giving the name and distance from the ventilation input for each LDTH-/SDT-submodel "chimney" location.

outputs: (heatgen file) (DTN: LL030808723122.037)
P*_DDT output heatgen file for each LDTH-/SDT-submodel "chimney" location

Creating Heat Generation Curves for the SMT submodel
software code
heatgen_ventTable_emplace

inputs: (DTN: LL030808723122.037)
SMT: string indicating to the software code that this is an SMT-submodel heatgen file
SMT_TSPA03: default SMT-submodel heat-generation-versus-time table with nominal loading and no ventilation

LA_ventilation_table_50yr.rfm: ventilation table with ventilation efficiency as a function of time and distance from the ventilation inlet.

ventilation_time.rfm: file giving the name and distance from the ventilation input for each LDTH-/SDT-submodel "chimney" location.

outputs: (heatgen file) (DTN: LL030808723122.037)
SMT_TSPA03_P* output heatgen file for each SMT-sub-model location

The heatgen files are then used as inputs to the NUFT input files; see Attachment V for details on the assembly of NUFT input files.

ATTACHMENT IV

BUILDING SUBMODEL MATERIAL PROPERTY FILES

INTENTIONALLY LEFT BLANK

ATTACHMENT IV
BUILDING SUBMODEL MATERIAL PROPERTY FILES

LDTH - Submodel DKM Properties

Hydrologic properties from DTN: LB0208UZDSCPMI.002 are used for all three infiltration flux cases (Table IV-4), which are documented in Sections 6.3.1, 6.3.2, 6.3.3. Hydrologic properties from DTN: LB0208UZDSCPLI.002 (Table IV-5) and from DTN: LB0302UZDSCPUI.002 (Table IV-6) are used for the sensitivity study to hydrologic-property uncertainty, which is discussed in Section 6.3.2.4. From each of the three Microsoft Excel spreadsheet files contained in the respective DTNs, the following parameters are obtained: permeability (matrix and fracture), porosity (matrix and fracture), van Genuchten properties (matrix and fracture) and residual saturation (matrix and fracture).

The thermal properties are taken from files of the following sources: DTN: SN0303T0503102.008, DTN: SN0307T0510902.003, and Table 7-10 of *Thermal Conductivity of the Potential Repository Horizon Model Report* (BSC 2002a). Bulk thermal conductivity K_{th} (for both wet and dry conditions) and bulk density (average, and 1 standard deviation above and below) of the nonrepository GFM2000 layers is contained in DTN: SN0303T0503102.008. The bulk thermal conductivity (for both wet and dry conditions) and bulk density ρ_b of the repository UZ Model Layers was obtained from Table 7-10 of *Thermal Conductivity of the Potential Repository Horizon Model Report* (BSC 2002a); this data includes mean values as well as one standard deviation above and below the mean. The specific heat capacity of the mineralogical model layers is taken from DTN: SN0307T0510902.003. The source input data for bulk density and bulk thermal-conductivity is summarized in Table IV-3a.

The following parameters were calculated by hand using parameters obtained in the files listed above: (1) grain density, (2) matrix density and fracture density, (3) matrix and fracture contact length factors, and (4) thermal conductivity relations for matrix and fracture. Table IV-3b shows the results of calculating the density and thermal conductivity for the matrix and fracture. It should be noted that the vitric units have no fractures, but in order for the DKM to work, values must be assigned to a pseudo-fracture continuum for vitric units. This is accomplished by simply assigning matrix properties to the fracture continuum for the vitric units (tsw9v, ch1v, ch2v, ch3v, ch4v, chv5, and ch6v). The specific details of the hand calculations are listed below.

1. The grain density ρ_g is calculated as:

$$\rho_g = \frac{\rho_b}{1-\phi_m}$$

where ϕ_m is matrix porosity and ρ_b is bulk density.

2. The grain density ρ_g is partitioned to the matrix and fracture continuum according to the fracture porosity, ϕ_f. The matrix and fracture densities, $\rho_{g,m}$ and $\rho_{g,f}$, are calculated as:

$$\rho_{g,m} = \rho_g \left(1 - \phi_f\right)$$
$$\rho_{g,f} = \rho_g \, \phi_f$$

Because the vitric units do not have fractures, the grain density for the fracture and matrix continuum is calculated slightly differently. The matrix porosity is portioned 50 percent to the matrix continuum and 50 percent to the "pseudo-fracture" continuum. The bulk density is portioned 50 percent to the matrix continuum and 50 percent to the pseudo-fracture continuum. Thus, the grain densities for the fracture and matrix continuum are calculated as:

$$\rho_{g,m} = \rho_{g,f} = \frac{\rho_b}{2\left(1 - \frac{\phi_m}{2}\right)}$$

where ϕ_m is the total matrix porosity and ρ_b is the total bulk density. Table IV-3b shows the result of this hand calculation for the vitric units.

3. The matrix-contact-length factor is calculated as 1/(6N) where N is the fracture frequency from DTN: LB0205REVUZPRP.001 (Table IV-7) and 6 accounts for the distance between the center of the matrix block and the fractures for Type #1 fractures as is described in Subsection 6.7 of *Development of Numerical Grids for UZ Flow and Transport Modeling* (BSC 2003c). The fracture-contact-length factor is always 0, which is obtained from Equation 4 of *Development of Numerical Grids for UZ Flow and Transport Modeling* (BSC 2003c, Section 6.7). The matrix-contact-length factor and the fracture-contact-length factor affect disequilibrium between the matrix and fracture continuum in the LDTH submodels.

4. The thermal conductivity for the matrix $K_{th,m}$ and fracture $K_{th,f}$ (both dry and wet) are calculated as a function of fracture porosity ϕ_f for the given wet and dry bulk thermal conductivities K_{th}:

$$K_{th,m}^{dry} = K_{th}^{dry}\left(1 - \phi_f\right)$$
$$K_{th,f}^{dry} = K_{th}^{dry}\phi_f$$
$$K_{th,m}^{wet} = K_{th}^{wet}\left(1 - \phi_f\right)$$
$$K_{th,f}^{wet} = K_{th}^{wet}\phi_f$$

These properties are written into a "rocktab" file (an example of which is listed at the bottom of this Attachment) for the NUFT input file (see Attachment V). All transport and partitioning parameters (e.g., Kd and Kd_{Factor}) are set to zero because transport is not considered for any of the calculations of this report.

The uncertainty of the wet and dry thermal conductivities of the repository UZ Model Layers was addressed with values from DTN: SN0303T0503102.008 and from Table 7-10 of *Thermal Conductivity of the Potential Repository Horizon Model Report* (BSC 2002a), which summarizes data from DTN: SN0208T0503102.007.

The tortuosity factor is 0.2 for the matrix continuum (de Marsily 1986, p. 233) and 0.7 for the fracture (DTN: LB991091233129.006). Note that de Marsily (1986) gives a range from 0.1 for clays to 0.7 for sands. The value of 0.2 for the matrix continuum is used because the pore sizes for matrix are closer to that of clays than to that of sands.

LDTH-Submodel In-Drift, DKM Properties

Invert Properties

The invert properties for the matrix continuum (i.e., the intragranular porosity) are obtained from DTN: LB0208UZDSCPMI.002 and for the fracture continuum (i.e., the intergranular porosity) are from DTN: MO0307SPAVGSUM.000 (BSC 2003n). Section 5.3.1.8 discusses the assumption about the intergranular permeability of the crushed-tuff invert material. The van Genuchten alpha for the fracture continuum from DTN: MO0307SPAVGSUM.000 is 624 bar^{-1}, which converted to SI units, is equal to 6.24×10^{-3} Pa^{-1}. The input parameters that require hand calculations are: (1) intragranular porosity (ϕ_m), (2) the thermal conductivity for the fracture and matrix continuum, and (3) the grain density of the matrix and of the fracture continuum. The thermal properties of the crushed-tuff invert are given in Tables IV-8 and IV-9.

Invert Porosity

The porosity of the crushed-tuff grains in the invert (ϕ_m) is taken from DTN: LB0208UZDSCPMI.002 and is equal to 0.131, which is the matrix porosity of the Tptpll (tsw35) unit. The intergranular porosity of the crushed-tuff invert material is obtained from DTN: MO0307SPAVGSUM.000 (also Table 6-2 of BSC 2003n) and is equal to 0.45. The porosity of the fracture continuum in the invert (ϕ_f), which is called the intergranular porosity, is a bulk quantity. Because the porosity of the matrix continuum in the invert, which is called the intragranular porosity ($\phi_{g,m}$) is also a bulk quantity, the intragranular porosity of the crushed-tuff invert material is given by:

$$\phi_{g,m} = \phi_m (1 - \phi_f)$$

Thus, the intragranular porosity (or matrix-continuum porosity) of the crushed-tuff invert material used in the LDTH submodels is equal to 0.0721.

Invert Thermal Conductivity

The bulk thermal conductivity of the crushed-tuff invert material is partitioned 99 percent to the matrix continuum and 1 percent to the fracture continuum, as follows:

$$K_{th,f} = K_{th} (0.01)$$
$$K_{th,m} = K_{th} (0.99)$$

This partitioning is done because the majority of the thermal mass in the invert resides in the matrix continuum.

Invert Grain Density

The bulk grain density of the crushed-tuff invert material is partitioned 99 percent to the matrix continuum and 1 percent to the fracture continuum, as follows:

$$\rho_{g,m} = (0.99)\rho_b/(1-\phi_m)$$
$$\rho_{g,f} = (0.01)\rho_b/(1-\phi_f)$$

where $\rho_{g,m}$ is the grain density of the matrix continuum, $\rho_{g,f}$ is the grain density of the fracture continuum, ρ_b is the bulk density of the crushed-tuff invert material obtained from DTN: GS020183351030.001 and given in Table IV-8, ϕ_m is the matrix-continuum porosity of the crushed-tuff invert material, and ϕ_f is the fracture-continuum porosity of the crushed-tuff invert. This partitioning is done because the majority of the thermal mass in the invert resides in the matrix continuum.

Waste Package and Drip Shield Properties

Due to grid resolution limitations in the drift, the geometry of the waste package and drip shield are lumped into a monolithic heat source (see Figure 6.2-6). Waste package density, drip shield density, and thermal conductivity should be averaged into this lumped approximation. The half-area (called $A_{1/2}$) of the waste package and drip shield as represented in the LDTH submodel as a group of finite difference blocks with an area calculated as:

$$A_{1/2} = 0.242\times0.58+0.40\times(0.58+0.37)+(0.759+0.760+0.425)\times(0.58+0.37+0.3025) = 2.9552\ m^2$$

These dimensions are obtained from the gridblock spacings in the LDTH submodels (see Figure 6.2-6). Table 4-1 gives the nominal number of waste packages in the repository: (1) 4,299 21-PWR AP waste packages, (2) 2,831 44-BWR AP waste packages, and (3) 11,184 total waste packages. Therefore, the majority of waste packages (64 percent) will be either 21-PWR AP waste packages or 44-BWR AP waste packages; both of these waste packages weigh 43,000 kg and are 5.165 m in length (Table 4-1). After adding 0.1 m for the waste-package spacing (Table 4-1) to the length of the waste package, the weight per unit length of the majority of waste packages is 43,000 kg divided by 5.265 m (5.165 m + 0.1 m), or 8,200 kg/m. This is taken to be representative of the average waste package in the repository. The lineal weight per unit length of drip shield is equal to the weight of the drip shield (5,000 kg, given in Table 4-1) divided by the drip-shield length (6.105 m, given in Table 4-1), which is equal to 820 kg/m.

The lineal weight per unit length of the average waste package and drip shield is 8,200 kg/m and 820 kg/m, respectively, yielding a total lineal weight of 9,020 kg/m. The equivalent density, ρ_{equiv}, of the LDTH waste package and drip shield is calculated as:

$$\rho_{equiv} = (9{,}020\ kg/m)/(2 \times A_{1/2}) = 1{,}526.1\ kg/m^3$$

The thermal conductivity of the waste package and drip shield is the sum of the thermal conductivities weighted by the relative weight of the respective materials:

$$K_{th,equiv} = K_{th,ds} \times (820/9{,}020) + K_{th,wp} \times (8{,}200/9{,}020)$$

SDT/DDT-Submodel Thermal Properties

The thermal properties are taken from files of the following sources: DTN: SN0303T0503102.008, DTN: SN0307T0510902.003, and Table 7-10 of *Thermal Conductivity of the Potential Repository Horizon Model Report* (BSC 2002a). Note that Table 7-10 of *Thermal Conductivity of the Potential Repository Horizon Model Report* (BSC 2002a) is a summary of data from DTN: SN0208T0503102.007. Bulk thermal conductivity and bulk density (average, and 1 standard deviation above and below) of the GFM2000 nonrepository layers is contained in DTN: SN0303T0503102.008. Bulk thermal conductivity and bulk density variation (mean, and 1 standard deviation above and below) of the repository horizon UZ Model Layers is contained in Table 7-10 of *Thermal Conductivity of the Potential Repository Horizon Model Report* (BSC 2002a). The specific heat capacity of the mineralogical model units was taken from DTN: SN0307T0510902.003. The input data from these DTNs are summarized in Table IV-3a. As discussed in the footnotes of Table IV-3a there are minor differences between the specific heat capacity used for several mineralogical model units and those given in the source DTN: SN0307T0510902.003. These differences are much smaller than the range of uncertainty for the affected layers (see column Z of the excel spreadsheet for DTN: SN0307T0510902.003). The affected mineralogic model units are well removed from the repository horizon; consequently, these small differences have no effect on thermohydrologic conditions within and adjacent to emplacement drifts. The SDT, DDT, and SMT submodels use the bulk density and bulk thermal conductivity values and do not require that these values be partitioned into the fracture and matrix continuum. Note that because NUFT uses the grain density (also called solid density), the matrix porosity, which is obtained from DTN: LB0208UZDSCPMI.002, is also required as input to the input files for the SDT, DDT, and SMT submodels.

The only parameter requiring a hand calculation for the SDT- and DDT-submodel near-field properties is the grain density (or solid density) ρ_g, which is calculates as:

$$\rho_g = \frac{\rho_b}{1-\phi_m}$$

DDT Submodel In-drift Thermal Properties

The material properties for the DDT submodel are the same as the corresponding bulk thermal properties in the drift for the LDTH submodel. There is a difference with how the waste package and drip shield are accounted for in the DDT submodel, however, as the DDT submodel represents each waste package separately and discretizes the drip shield.

Waste Package and Drip Shield Thermal Properties

For the DDT submodel the weights of each individual waste package is discretely represented, not lumped, into an average representation of the drip shield and waste package, as was done for the LDTH submodel. The mass density of each waste package type (21-PWR, 44-BWR, 5DHLW-long, and 5DHLW-short) is determined by taking volumetric average of the materials (outer shell, inner shell, internal cylinder):

$$\rho_{WP} = [\rho_{outer} (d_3^2 - d_2^2) + \rho_{inner} (d_2^2 - d_1^2) + \rho_{internal} (d_1^2)] / d_3^2$$

where d_3 is the outermost diameter of the waste package, d_2 is the inner diameter of the "outer shell," and d_1 is the diameter of the internal cylinder obtained. The mass densities, ρ_{WP}, ρ_{outer}, ρ_{inner}, and $\rho_{internal}$ are, respectively, the weighted waste package mass density, the outer-shell mass density, the inner-shell mass density, and the internal cylinder density. These diameters were obtained from *Design and Engineering, D&E/PA/C IED Typical Waste Package Components Assembly 1 of 9* (BSC 2003f). The density of the outer shell (Alloy 22) was obtained from DTN: MO0003RIB00071.000; the density of the inner shell (Stainless Steel Type 316) was obtained from Table XI of ASTM G 1-90; the density of the internal cylinder was obtained from Table 20 of *D&E / PA/C IED Typical Waste Package Components Assembly* (BSC 2004d).

The effective waste package specific heat, Cp_{WP}, of the DDT submodel are calculated for each waste package using a volumetric average of the corresponding materials:

$$Cp_{WP} = [Cp_{outer} (d_3^2 - d_2^2) + Cp_{inner} (d_2^2 - d_1^2) + Cp_{internal} (d_1^2)] / d_3^2$$

where d_3 is the outer diameter of the outer shell, d_2 is the outer diameter of the inner shell, and d_1 is the inner diameter of the inner shell; Cp_{outer} is the specific heat of the outer shell, Cp_{inner} is the specific heat of the inner shell, and $Cp_{internal}$ is the specific heat of the internal cylinder.

The effective waste package thermal conductivity, $K_{th,WP,}$ also uses a volumetric average:

$$K_{th,WP} = [K_{th,outer} (d_3^2 - d_2^2) + K_{th,inner} (d_2^2 - d_1^2) + K_{th,internal} (d_1^2)] / d_3^2$$

The waste package thermal conductivity only influences longitudinal heat flow along the axis of the drift in the DDT submodel. In other words, radial heat flow (from the center of the waste package to the outer surface) is not predicted in the DDT submodel. Therefore, only the axial component of $K_{th,WP}$ is required in the DDT submodel. Because the materials in the waste package are concentrically arranged, the volumetric average of $K_{th,WP}$ of the respective components of the waste package is the appropriate manner in which to determine the effective waste package thermal conductivity.

The thermal parameters for the drip shield (Table 4-1) were taken directly from Table TCD of *1995 ASME Boiler and Pressure Vessel Code* (ASME 1995, Section II). The thermal parameters required in the NUFT submodels necessitate the calculations described below for titanium.

Due to limitations of grid resolution in the drift of the DDT submodels, all waste packages are modeled as though they have the same diameter even though the actual diameters are not the same (Table 4-1). An effective density ρ_{eff} is calculated for each of the respective waste packages so that the mass of each waste package is properly represented in the DDT submodels. The effective density ρ_{eff} is equal to the mass of the waste package (Table 4-1) divided by volume of the waste package as it is represented in the DDT submodel.

Thermal Properties for Stainless Steel Type 316 and Titanium

Several of the direct inputs available for determining waste package and drip shield thermal properties require interpolation (to a reference temperature) and/or require simple calculations to

the input parameters required by the DDT submodel. The thermal conductivity of Stainless Steel Type 316, which is used in the inner cylinder of the waste packages, requires interpolation to 100°C. Furthermore, the specific heat for Stainless Steel Type 316 should be calculated on the basis of thermal diffusivity and thermal conductivity, which are direct inputs. Similarly, the thermal conductivity of titanium, which is used in the drip shield, require interpolation to a temperature of 100°C. Furthermore, the specific heat for titanium should be calculated on the basis of thermal diffusivity and thermal conductivity, which are direct inputs. The following steps were used to obtain the required parameter values.

1. Mass density of Stainless Steel Type 316

   7.98 g/cm^3 = 7,980 kg/m^3 = 498.175 lb/ft^3

   The bold value above is taken from Table XI of ASTM G 1-90.

2. Thermal conductivity of Stainless Steel Type 316 (T = 100°C)

Table IV-1. The interpolation of thermal diffusivity and thermal conductivity is outlined for Stainless Steel Type 316. The conversion of these parameters from English units to SI units is also shown. The bold values are from Table TCD of *1995 ASME Boiler and Pressure Vessel Code* (ASME 1995).

Temperature (°F)	Temperature (°C)	Thermal Diffusivity (ft^2/hr)	Thermal Conductivity (BTU/hr-ft-°F)	Thermal Conductivity (W/m·K)
200	93.33	**0.141**	**8.4**	14.54
250	121.11	**0.143**	**8.7**	15.06
212	100.00	*0.1415*	*8.472*	*14.665*
Conversion Factor			1.0	1.730734666

$$0.1415 = \mathbf{0.141} + (\mathbf{0.143} - \mathbf{0.141}) \times \frac{212 - 200}{250 - 200}$$

$$8.472 = \mathbf{8.4} + (\mathbf{8.7} - \mathbf{8.4}) \times \frac{212 - 200}{250 - 200}$$

$$14.665 = 14.54 + (15.06 - 14.54) \times \frac{212 - 200}{250 - 200}$$

$$14.663 = 1.730734666 \times 8.472$$

3. Specific heat of Stainless Steel Type 316 (T = 100°C)

$$\text{Specific Heat (BTU/lb-}^\circ\text{F)} = \frac{\text{Thermal Conductivity (BTU/hr-ft-}^\circ\text{F)}}{\text{Density (lb/ft}^3\text{) Thermal Diffusivity(ft}^2\text{/hr)}}$$

$$= \frac{8.472}{498.175 \times 0.1415} = 0.1202 \text{ (BTU/lb-}^\circ\text{F)}$$

$$= 503.19 \text{ (J/kg-}^\circ\text{K).}$$

4. Density of titanium

   0.163 lb/in^3 = *4512* kg/m^3 = *281.675* lb/ft^3

   The bold value above is taken from Section II, Table NF-2 of *1995 ASME Boiler and Pressure Vessel Code* (ASME 1995).

5. Thermal conductivity of titanium (T = 100°C)

Table IV-2. The interpolation of thermal diffusivity and thermal conductivity is outlined for titanium. The conversion of these parameters from English units to SI units is also shown. The bold values are taken from Section II, Table NF-2 of *1995 ASME Boiler and Pressure Vessel Code* (ASME 1995).

Temperature (°F)	Temperature (°C)	Thermal Diffusivity (ft^2/hr)	Thermal Conductivity (BTU/h-ft-°F)	Thermal Conductivity (W/m·K)
200	93.33	**0.331**	**12.00**	20.7688
250	121.11	**0.322**	**11.85**	20.5092
212	100.00	0.3288	11.964	20.7065

$$0.3288 = \mathbf{0.331} + (\mathbf{0.322} - \mathbf{0.331}) \times \frac{212 - 200}{250 - 200}$$

$$11.964 = \mathbf{12.0} + (\mathbf{11.8}5 - \mathbf{12.0}) \times \frac{212 - 200}{250 - 200}$$

6. Specific heat of titanium (T = 100°C)

$$\text{Specific Heat (BTU/lb-°F)} = \frac{\text{Thermal Conductivity (BTU/h-ft-°F)}}{\text{Density (lb/ft}^3\text{) Thermal Diffusivity(ft}^2\text{/h)}}$$
$$= \frac{11.964}{281.675 \times 0.3288} = 0.1292 \text{ (BTU/lb-°F)}$$
$$= 540.85 \text{ (J/kg-K).}$$

These simple calculations used the following conversion factors:

1. Heat Capacity: 1.0 Btu/(lb-°F) = 4186.8 J/(kg·K)
2. Thermal Conductivity 1.0 Btu/(h-ft-°F) = 1.730734666 W/(m·K)
3. Density 1.0 g/cm^3= 62.427960576 lb/ft^3
4. 1.0 lb/in^3 = 27,679.904710203 kg/m^3

Invert Thermal Properties

For the DDT submodels, the invert has the same bulk thermal properties as the bulk thermal properties in the LDTH submodels. That is to say that the thermal conductivity, specific heat, and mass density in the DDT submodels are the same as the bulk thermal conductivity, specific heat capacity, and bulk mass density of the invert in the LDTH submodels.

SMT–Submodel thermal properties

Only fault and saturated zone thermal properties need to be specifically calculated for the SMT-submodel thermal properties. Otherwise, the SMT submodel uses the same thermal properties as the SDT submodels.

Fault-Zone Thermal Properties

The density of the fault zone is simply the average of all of the units that make up the fault zone:

$$\rho_{tcwfl} = (\rho_{tcwl1} + \rho_{tcwl2} + \rho_{tcwl3})/3$$
$$\rho_{ptnfl} = (\rho_{ptn21} + \rho_{ptn22} + \rho_{ptn23} + \rho_{ptn24} + \rho_{ptn25} + \rho_{ptn26})/6$$
$$\rho_{tsw} = (\rho_{tsw31} + \rho_{tsw32} + \rho_{tsw33} + \rho_{tsw34} + \rho_{tsw35} + \rho_{tsw35} + \rho_{tsw37} + \rho_{tsw38} + \rho_{tsw9v} + \rho_{tsw9z})/10$$
$$\rho_{ch1fl} = (\rho_{ch1v} + \rho_{ch1z})/2 \text{ (similar for ch2fl, ch3fl, ch4fl, ch5fl, ch6fl)}$$
$$\rho_{pp4f}l = \rho_{pp4} \text{ (similar for pp3, pp2, pp1, bf3, bf2, tr3, tr2)}$$

The same process is used to determine the fault-zone properties for thermal conductivity, specific heat and porosity.

Saturated Zone Thermal Properties

The saturated zone intersects 14 UZ Model-Layers (ch1z, ch2z, ch3z ch4z, ch5z, ch6z, pp4, pp3, pp2, pp1, bf3, bf2, tr3, and tr2). The saturated-zone density, thermal conductivity, specific heat, and porosity are simply calculated as the sum of the properties for those units divided by 14.

Rocktab File Example

Listed below is a part of an example rocktab file (dkm-afc-1Dds-mc-mi-03) that would be called in a NUFT input file (see Attachment V). Of note is that several material properties are listed each delineated by the line ";; End of the material". Specific details of the rocktab file properties can be found in the NUFT user's manual (Nitao 1998).

```
;; dkm-afc-1Dds-mc-mi-03
;;  4/11/2003 @16:23:21
;; 0.50 Shared in matrix & 0.50 shared in fracture
;; atm
(atm
  (cont-len-fac 1.00e+00) (cont-area-fac 2.00e+00)
  (exfac-adv (liquid 1.00e+00) (gas 1.00e+00))
  (solid-density 1.00e+08) (porosity 0.99)
  (Kd        (water 0.0) (air 0.0))
  (KdFactor  (water 0.0) (air 0.0))
  (Cp 1.00e+08)
  (tcond tcondLin (solid 1.00e+02) (liquid 1.00e+02) (gas 1.00e+02))
  (K0 1.00e-08) (K1 1.00e-08) (K2 1.00e-08)
  (tort (gas 1.00e+00) (liquid 0.00e+00))
  (kr (liquid krlLinear (Sr 0.00e+00) (Smax 1.0))
      (gas krgLinear    (Sr 0.00e+00) (Smax 1.0)))
  (pc (liquid  0.0))
  (krMC (liquid  krMCintrinsic) (gas  krMCintrinsic))
) ;;End of the material
;;Matrix materials
(m-tcw11
  (cont-len-fac 1.81e-01) (cont-area-fac 1.56e+00)
```

```
  (exfac-adv (liquid 1.00e+00) (gas 1.00e+00))
  (solid-density 2820.64) (porosity 0.241)
  (Kd        (water 0.0) (air 0.0))
  (KdFactor  (water 0.0) (air 0.0))
  (Cp 9.30e+02)
  (tcond tcondLin (solid 1.26880) (liquid 1.76656) (gas 1.26880))
  (K0 3.74e-15) (K1 3.74e-15) (K2 3.74e-15)
  (tort (gas 2.00e-01) (liquid 0.00e+00))
  (kr (liquid krlVanGen (Sr 2.00e-02) (m 3.88e-01) (Smax 1.0))
      (gas krgModCorey (Srl 2.00e-02) (m 3.88e-01) (Slmax 1.0)))
  (pc (liquid pcVanGen (Sr 2.00e-02) (m 3.88e-01) (alpha 1.01e-05) (Smax 1.0)))
  (krMC (liquid  krMCintrinsic) (gas  krMCintrinsic))
) ;;End of the material
```

[SECTION SKIP]

```
 (f-ptn24
  (cont-len-fac 0.00e+00) (cont-area-fac 1.00e+00)
  (exfac-adv (liquid 1.00e+00) (gas 1.00e+00))
  (solid-density 24.90) (porosity 1.00e-02)
  (Kd        (water 0.0) (air 0.0))
  (KdFactor  (water 0.0) (air 0.0))
  (Cp 9.60e+02)
  (tcond tcondLin (solid 0.00490) (liquid 0.01060) (gas 0.00490))
  (K0 3.00e-12) (K1 3.00e-12) (K2 3.00e-12)
  (tort (gas 7.00e-01) (liquid 0.00e+00))
  (kr (liquid krlVanGen (Sr 1.00e-02) (m 6.33e-01) (Smax 1.0) (gamma 2.32e-01))
      (gas krgModCorey (Srl 1.00e-02) (m 6.33e-01) (Slmax 1.0)))
  (pc (liquid pcVanGen (Sr 1.00e-02) (m 6.33e-01)(alpha 1.86e-03)
                       (Smax 1.0) (gamma 2.32e-01)))
  (krMC (liquid  krMCactiveFrac (gamma 2.32e-01) (Sr 1.00e-02))
        (gas     krMCactiveFrac (gamma 2.32e-01) (Sr 0.0)))
) ;;End of the material
(f-ptn25
  (cont-len-fac 0.00e+00) (cont-area-fac 1.00e+00)
  (exfac-adv (liquid 1.00e+00) (gas 1.00e+00))
  (solid-density 16.00) (porosity 5.50e-03)
  (Kd        (water 0.0) (air 0.0))
  (KdFactor  (water 0.0) (air 0.0))
  (Cp 9.60e+02)
  (tcond tcondLin (solid 0.00269) (liquid 0.00583) (gas 0.00269))
  (K0 1.70e-13) (K1 1.70e-13) (K2 1.70e-13)
  (tort (gas 7.00e-01) (liquid 0.00e+00))
  (kr (liquid krlVanGen (Sr 1.00e-02) (m 6.33e-01) (Smax 1.0) (gamma 2.32e-01))
      (gas krgModCorey (Srl 1.00e-02) (m 6.33e-01) (Slmax 1.0)))
  (pc (liquid pcVanGen (Sr 1.00e-02) (m 6.33e-01)(alpha 1.33e-03)
                      (Smax 1.0) (gamma 2.32e-01)))
  (krMC (liquid  krMCactiveFrac (gamma 2.32e-01) (Sr 1.00e-02))
        (gas     krMCactiveFrac (gamma 2.32e-01) (Sr 0.0)))
) ;;End of the material
```

[SECTION SKIP]

```
 (f-tr2
  (cont-len-fac 0.00e+00) (cont-area-fac 1.00e+00)
  (exfac-adv (liquid 1.00e+00) (gas 1.00e+00))
  (solid-density 0.85) (porosity 3.70e-04)
  (Kd        (water 0.0) (air 0.0))
  (KdFactor  (water 0.0) (air 0.0))
  (Cp 9.40e+02)
  (tcond tcondLin (solid 0.00020) (liquid 0.00041) (gas 0.00020))
  (K0 2.50e-14) (K1 2.50e-14) (K2 2.50e-14)
  (tort (gas 7.00e-01) (liquid 0.00e+00))
```

```
  (kr (liquid krlVanGen (Sr 1.00e-02) (m 6.33e-01) (Smax 1.0) (gamma 3.70e-01))
      (gas krgModCorey (Srl 1.00e-02) (m 6.33e-01) (Slmax 1.0)))
  (pc (liquid pcVanGen (Sr 1.00e-02) (m 6.33e-01)(alpha 8.90e-04)
                       (Smax 1.0) (gamma 3.70e-01)))
  (krMC (liquid  krMCactiveFrac (gamma 3.70e-01) (Sr 1.00e-02))
        (gas     krMCactiveFrac (gamma 3.70e-01) (Sr 0.0)))
) ;;End of the material
```

Table IV-3a. Specific heat capacity, bulk thermal conductivity (dry and wet) and bulk density for the GFM2000 units. The values for the nonrespository layers are from DTN: SN0303T0503102.008. The bulk thermal conductivity and bulk density values for the repository layers (tsw33, tsw34, tsw35, tsw36, and tsw37) are from Table 7-10 of BSC 2002a, which is a summary of data from DTN: SN0208T0503102.007. The GFM2000 layers shown in italics pertain to data obtained from Table 7-10 of BSC 2002a. The specific heat capacity is from DTN: SN0307T0510902.003 for the temperature range of 25 to 325°C. The values of specific heat capacity, bulk thermal conductivity, and bulk density for the layers with multiple GFM2000 layers (e.g., pp1) are the arithmetic average of the corresponding GFM2000-layer values. Table IV-3b gives the result of this averaging for bulk density and bulk thermal conductivity.

Material Name Used in LDTH Submodels	GFM2000 Layer	Bulk Density kg/m^3	Bulk Thermal Conductivity, dry W/m°C	Bulk Thermal Conductivity, wet W/m°C	Specific Heat Capacity J/g·K
tcw11	Tpcp	2,190	1.30	1.81	0.93
tcw12	Tpcp	2,190	1.30	1.81	0.93
	TpcLD	2,190	1.30	1.81	0.93
tcw13	Tpcpv3	2,310	0.688	0.796	0.95
	Tpcpv2	1,460	0.490	1.06	0.95
ptn21	Tpcpv1	1,460	0.490	1.06	0.93
ptn22	Tpbt4	1,460	0.490	1.06	0.96
	Tpy (Yucca)	1,460	0.490	1.06	0.96
ptn23	Tpbt3	1,460	0.490	1.06	0.96
ptn24	Tpy	1,460	0.490	1.06	0.96
	Tpbt3	1,460	0.490	1.06	0.96
ptn25	Tpp (Pah)	1,460	0.490	1.06	0.96
ptn26	Tpb2	1,460	0.490	1.06	0.96
	Tptrv3	1,460	0.490	1.06	0.96
	Tptrv2	1,460	0.490	1.06	0.96
tsw31	Tptrv1	2,310	0.688	0.796	0.95
	Tptrn	2,190	1.30	1.81	0.93
tsw32	Tptrn	2,190	1.30	1.81	0.93
tsw33	Tptprl	2190	1.30	1.81	0.93
	Tptpul	1,830	1.1829	1.7749	0.93
tsw34	*Tptpmn*	2,150	1.4189	2.0741	0.93
tsw35	*Tptpll*	1,980	1.2784	1.8895	0.93
tsw36	*Tptpln*	2,210	1.4900	2.1303	0.93
tsw37	*Tptpln*	2,210	1.4900	2.1303	0.93
tsw38	Tptpv3	2,310	0.688	0.796	0.98
tsw9v	Tptpv2	1,460	0.490	1.06	0.98 [a]
tsw9z	Tptpv2	1,460	0.490	1.06	0.98
ch1v	Tptpv1	1,460	0.490	1.06	1.08 [b]
	Tpbt1	1,460	0.490	1.06	1.08
ch1z	Tptpv1	1,460	0.490	1.06	1.08
	Tpbt1	1,460	0.490	1.06	1.08
ch2v	Tac (Calico)	1,670	0.595	1.26	1.07 [c]
ch3v	Tac (Calico)	1,670	0.595	1.26	1.07 [c]
ch4v	Tac (Calico)	1,670	0.595	1.26	1.07 [c]

Table IV-3a. Specific heat capacity, bulk thermal conductivity (dry and wet) and bulk density for the GFM2000 units. The values for the nonrespository layers are from DTN: SN0303T0503102.008. The bulk thermal conductivity and bulk density values for the repository layers (tsw33, tsw34, tsw35, tsw36, and tsw37) are from Table 7-10 of BSC 2002a, which is a summary of data from DTN: SN0208T0503102.007. The GFM2000 layers shown in italics pertain to data obtained from Table 7-10 of BSC 2002a. The specific heat capacity is from DTN: SN0307T0510902.003 for the temperature range of 25 to 325°C. The values of specific heat capacity, bulk thermal conductivity, and bulk density for the layers with multiple GFM2000 layers (e.g., pp1) are the arithmetic average of the corresponding GFM2000-layer values. Table IV-3b gives the result of this averaging for bulk density and bulk thermal conductivity. (Continued)

Material Name Used in LDTH Submodels	GFM2000 Layer	Bulk Density kg/m^3	Bulk Thermal Conductivity, dry W/m°C	Bulk Thermal Conductivity, wet W/m°C	Specific Heat Capacity J/g·K
ch5v	Tac (Calico)	1,670	0.595	1.26	1.07 [c]
ch2z	Tac (Calico)	1,670	0.595	1.26	1.07
ch3z	Tac (Calico)	1,670	0.595	1.26	1.07
ch4z	Tac (Calico)	1,670	0.595	1.26	1.07
ch5z	Tac (Calico)	1,670	0.595	1.26	1.07
ch6v	Tacbt (Calicobt)	1,670	0.595	1.26	1.02 [d]
ch6z	Tacbt (Calicobt)	1,670	0.595	1.26	1.02
pp4	Tcpuv (Prowuv)	1,790	0.569	1.13	1.04
pp3	Tcpuc (Prowuc)	1,790	0.569	1.13	0.93
pp2	Tcpmd (Prowmd)	2,070	1.06	1.63	0.93
	Tcplc (Prowlc)	1,790	0.569	1.13	0.93
pp1	Tcplv (Prowlv)	1,790	0.569	1.13	1.05 [e]
	Tcpbt (Prowbt)	1,790	0.569	1.13	1.05 [e]
	Tcbuv (Bullfroguv)	1,880	0.658	1.19	1.05 [e]
bf3	Tcbuc (Bullfroguc)	1,880	0.658	1.19	0.93
	Tcbmd (Bullfrogmd)	2,260	1.30	1.81	0.93
	Tcblc (Bullfroglc)	1,880	0.658	1.19	0.93
bf2	Tcblv (Bullfroglv)	1,880	0.658	1.19	1.05
	Tcbbt (Bullfrogbt)	1,880	0.658	1.19	1.05
	Tctuv (Tramuv)	1,760	0.535	1.10	1.05
tr3	Tctuc (Tramuc)	1,760	0.535	1.10	0.94
	Tctmd (Trammd)	2,140	1.06	1.63	0.94
	Tctlc (Tramlc)	1,760	0.535	1.10	0.94
tr2	Tctlv (Tramlv)	1,760	0.535	1.10	0.94
	Tctbt (Trambt)	1,760	0.535	1.10	0.94

NOTES: [a] Zeolitic value of specific heat capacity (0.98 J/g·K) is used rather than the vitric value (0.96 J/g·K).
[b] Zeolitic value of specific heat capacity (1.08 J/g·K) is used rather than the vitric value (0.96 J/g·K).
[c] Zeolitic value of specific heat capacity (1.07 J/g·K) is used rather than the vitric value (0.96 J/g·K).
[d] Zeolitic value of specific heat capacity (1.02 J/g·K) is used rather than the vitric value (0.97 J/g·K).
[e] Specific heat capacity value for the Tcblv-Tctuv (1.05 J/g·K) is used rather than for the Tcplv-Tcbuv (1.10 J/g·K).

Table IV-3b. Thermal properties for the UZ Model Layers. The subscripts m, f, B, and g stand for matrix, fracture, bulk, and grain, respectively. The bulk density ρ_B and bulk thermal conductivity $K_{th,B}$ (wet and dry) for the repository units (tsw33, tsw34, tsw35, tsw36, and tsw37) are obtained from Table 7-10 of BSC 2002a, which summarizes data from DTN: SN0208T0503102.007. The density and thermal-conductivity for the matrix and fracture are calculated by hand.

	Porosity		Density				Thermal Conductivity					
Material Name	ϕ_m [a]	ϕ_f [a]	ρ_B [b] kg/m^3	ρ_G kg/m^3	$\rho_{G,m}$ kg/m^3	$\rho_{G,f}$ kg/m^3	$K_{th,B}$ [b] wet W/m°C	$K_{th,m}$ wet W/m°C	$K_{th,f}$ wet W/m°C	$K_{th,B}$ [b] dry W/m°C	$K_{th,m}$ dry W/m°C	$K_{th,f}$ dry W/m°C
tcw11	0.241	2.40E-02	2190	2890	2820.64	69.36	1.81	1.767	4.34E-02	1.30	1.269	3.12E-02
tcw12	0.088	1.70E-02	2190	2400	2359.20	40.80	1.81	1.779	3.08E-02	1.30	1.278	2.21E-02
tcw13	0.200	1.30E-02	1890	2360	2329.32	30.68	0.93	0.918	1.21E-02	0.59	0.582	7.67E-03
ptn21	0.387	9.20E-03	1460	2380	2358.10	21.90	1.06	1.050	9.75E-03	0.49	0.485	4.51E-03
ptn22	0.428	1.00E-02	1460	2550	2524.50	25.50	1.06	1.049	1.06E-02	0.49	0.485	4.90E-03
ptn23	0.233	2.10E-03	1460	1900	1896.01	3.99	1.06	1.058	2.23E-03	0.49	0.489	1.03E-03
ptn24	0.413	1.00E-02	1460	2490	2465.10	24.90	1.06	1.049	1.06E-02	0.49	0.485	4.90E-03
ptn25	0.498	5.50E-03	1460	2910	2894.00	16.00	1.06	1.054	5.83E-03	0.49	0.487	2.69E-03
ptn26	0.490	3.10E-03	1460	2860	2851.13	8.87	1.06	1.057	3.29E-03	0.49	0.488	1.52E-03
tsw31	0.054	5.00E-03	2250	2380	2368.10	11.90	1.30	1.294	6.50E-03	0.99	0.985	4.95E-03
tsw32	0.157	8.30E-03	2190	2600	2578.42	21.58	1.81	1.795	1.50E-02	1.30	1.289	1.08E-02
tsw33	0.155	5.80E-03	2010	2380	2366.20	13.80	1.79	1.780	1.04E-02	1.24	1.233	7.19E-03
tsw34	0.111	8.50E-03	2150	2420	2399.43	20.57	2.07	2.052	1.76E-02	1.42	1.408	1.21E-02
tsw35	0.131	9.60E-03	1980	2280	2258.11	21.89	1.89	1.872	1.81E-02	1.28	1.268	1.23E-02
tsw36	0.103	1.30E-02	2210	2460	2428.02	31.98	2.13	2.102	2.77E-02	1.49	1.471	1.94E-02
tsw37	0.103	1.30E-02	2210	2460	2428.02	31.98	2.13	2.102	2.77E-02	1.49	1.471	1.94E-02
tsw38	0.043	1.10E-02	2310	2410	2383.49	26.51	0.80	0.791	8.80E-03	0.69	0.682	7.59E-03
tsw9v	0.115[1]	0.115[1]	1460	1890[2]	824.39[3]	824.39[3]	1.06	1.060	N/A	0.49	0.490	N/A
tsw9z	0.275	4.30E-03	1460	2010	2001.36	8.64	1.06	1.055	4.56E-03	0.49	0.488	2.11E-03
ch1v	0.166[1]	0.166[1]	1460	2180[2]	874.78[3]	874.78[3]	1.06	1.060	N/A	0.49	0.490	N/A
ch1z	0.285	1.60E-04	1460	2040	2039.67	0.33	1.06	1.060	1.70E-04	0.49	0.490	8.00E-05
ch2v	0.173[1]	0.173[1]	1670	2550[2]	1009.67[3]	1009.67[3]	1.26	1.260	N/A	0.60	0.600	N/A
ch3v	0.173[1]	0.173[1]	1670	2550[2]	1009.67[3]	1009.67[3]	1.26	1.260	N/A	0.60	0.600	N/A
ch4v	0.173[1]	0.173[1]	1670	2550[2]	1009.67[3]	1009.67[3]	1.26	1.260	N/A	0.60	0.600	N/A
ch5v	0.173[1]	0.173[1]	1670	2550[2]	1009.67[3]	1009.67[3]	1.26	1.260	N/A	0.60	0.600	N/A
ch2z	0.322	3.70E-04	1670	2460	2459.09	0.91	1.26	1.260	4.70E-04	0.60	0.600	2.20E-04
ch3z	0.322	3.70E-04	1670	2460	2459.09	0.91	1.26	1.260	4.70E-04	0.60	0.600	2.20E-04
ch4z	0.322	3.70E-04	1670	2460	2459.09	0.91	1.26	1.260	4.70E-04	0.60	0.600	2.20E-04
ch5z	0.322	3.70E-04	1670	2460	2459.09	0.91	1.26	1.260	4.70E-04	0.60	0.600	2.20E-04
ch6v	0.166[1]	0.166[1]	1670	2550[2]	1000.60[3]	1000.60[3]	1.26	1.260	N/A	0.60	0.600	N/A
ch6z	0.271	1.60E-04	1670	2290	2289.63	0.37	1.26	1.260	2.00E-04	0.60	0.600	1.00E-04
pp4	0.321	3.70E-04	1790	2640	2639.02	0.98	1.13	1.130	4.20E-04	0.57	0.570	2.10E-04
pp3	0.318	9.70E-04	1790	2620	2617.46	2.54	1.13	1.129	1.10E-03	0.57	0.569	5.50E-04
pp2	0.221	9.70E-04	1930	2480	2477.59	2.41	1.38	1.379	1.34E-03	0.81	0.809	7.90E-04
pp1	0.297	3.70E-04	1820	2590	2589.04	0.96	1.15	1.150	4.30E-04	0.60	0.600	2.20E-04
bf3	0.175	9.70E-04	2010	2440	2437.63	2.37	1.40	1.399	1.36E-03	0.87	0.869	8.40E-04
bf2	0.234	3.70E-04	1840	2400	2399.11	0.89	1.16	1.160	4.30E-04	0.62	0.620	2.30E-04
tr3	0.175	9.70E-04	1890	2290	2287.78	2.22	1.28	1.279	1.24E-03	0.71	0.709	6.90E-04
tr2	0.234	3.70E-04	1760	2300	2299.15	0.85	1.10	1.100	4.10E-04	0.54	0.540	2.00E-04

NOTES: [1] Vitric units have matrix porosity portioned 50% to the matrix continuum and 50% to the pseudo-fracture continuum.
[2] Value not used in LDTH submodel.
[3] Vitric units have grain density patitioned 50% to the matrix continuum and 50% to the pseudo-fracture continuum.
[a] Values obtained from DTN: LB0208UZDSCPMI.002.
[b] Values obtained from DTN: SN0303T0503102.008.

Table IV-4. Matrix and fracture properties for the mean infiltration flux one-dimensional drift-scale hydrologic property set (DTN: LB0208UZDSCPMI.002). The prefix "m-" stands for matrix and "f-" stands for fracture.

Material name from DTN source	Material name used in LDTH submodels	Permeability [m^2]	Porosity [-]	Residual saturation [-]	α (alpha) [1/Pa]	m [-]	γ (gamma) [-]
tcwM1	m-tcw11	3.74E-15	0.241	0.02	1.01E-05	0.388	N/A[1]
tcwM2	m-tcw12	5.52E-20	0.088	0.20	3.11E-06	0.280	N/A[1]
tcwM3	m-tcw13	5.65E-17	0.200	0.31	3.26E-06	0.259	N/A[1]
ptnM1	m-ptn21	4.60E-15	0.387	0.24	1.62E-04	0.245	N/A[1]
ptnM2	m-ptn22	4.43E-12	0.428	0.13	1.46E-04	0.219	N/A[1]
ptnM3	m-ptn23	9.20E-15	0.233	0.07	2.47E-05	0.247	N/A[1]
ptnM4	m-ptn24	2.35E-12	0.413	0.14	7.90E-04	0.182	N/A[1]
ptnM5	m-ptn25	2.15E-13	0.498	0.06	1.04E-04	0.300	N/A[1]
ptnM6	m-ptn26	1.00E-11	0.490	0.05	9.83E-04	0.126	N/A[1]
tswM1	m-tsw31	2.95E-17	0.054	0.21	8.70E-05	0.218	N/A[1]
tswM2	m-tsw32	2.23E-16	0.157	0.07	1.14E-05	0.290	N/A[1]
tswM3	m-tsw33	6.57E-18	0.155	0.12	6.17E-06	0.283	N/A[1]
tswM4	m-tsw34	1.77E-19	0.111	0.19	8.45E-06	0.317	N/A[1]
tswM5	m-tsw35	4.48E-18	0.131	0.12	1.08E-05	0.216	N/A[1]
tswM6	m-tsw36	2.00E-19	0.103	0.20	8.32E-06	0.442	N/A[1]
tswM7	m-tsw37	2.00E-19	0.103	0.20	8.32E-06	0.442	N/A[1]
tswM8	m-tsw38	2.00E-18	0.043	0.42	6.23E-06	0.286	N/A[1]
tswMv	m-tsw9v	1.49E-13	0.229	0.13	4.86E-05	0.293	N/A[1]
tswMz	m-tsw9z	3.5E-17	0.275	0.36	4.61E-06	0.059	N/A[1]
ch1Mv	m-ch1v	6.65E-13	0.331	0.06	8.73E-05	0.240	N/A[1]
ch1Mz	m-ch1z	3.5E-17	0.285	0.38	2.12E-07	0.349	N/A[1]
ch2Mv	m-ch2v	2.97E-11	0.346	0.06	2.59E-04	0.158	N/A[1]
ch3Mv	m-ch3v	2.97E-11	0.346	0.06	2.59E-04	0.158	N/A[1]
ch4Mv	m-ch4v	2.97E-11	0.346	0.06	2.59E-04	0.158	N/A[1]
ch5Mv	m-ch5v	2.97E-11	0.346	0.06	2.59E-04	0.158	N/A[1]
ch2Mz	m-ch2z	5.2E-18	0.322	0.26	2.25E-06	0.257	N/A[1]
ch3Mz	m-ch3z	5.2E-18	0.322	0.26	2.25E-06	0.257	N/A[1]
ch4Mz	m-ch4z	5.2E-18	0.322	0.26	2.25E-06	0.257	N/A[1]
ch5Mz	m-ch5z	5.2E-18	0.322	0.26	2.25E-06	0.257	N/A[1]
ch6Mv	m-ch6v	2.35E-13	0.331	0.06	1.57E-05	0.147	N/A[1]
ch6Mz	m-ch6z	8.2E-19	0.271	0.36	1.56E-07	0.499	N/A[1]
pp4Mz	m-pp4	8.77E-17	0.321	0.29	4.49E-07	0.474	N/A[1]
pp3Md	m-pp3	7.14E-14	0.318	0.08	8.83E-06	0.407	N/A[1]
pp2Md	m-pp2	1.68E-15	0.221	0.10	2.39E-06	0.309	N/A[1]
pp1Mz	m-pp1	2.35E-15	0.297	0.30	9.19E-07	0.272	N/A[1]
bf3Md	m-bf3	4.34E-13	0.175	0.11	1.26E-05	0.193	N/A[1]
bf2Mz	m-bf2	8.1E-17	0.234	0.21	1.18E-07	0.617	N/A[1]
tr3Md	m-tr3	1.1E-15	0.175	0.11	1.12E-05	0.193	N/A[1]
tr2Mz	m-tr2	8.1E-17	0.234	0.21	1.18E-07	0.617	N/A[1]
tcwF1	f-tcw11	3.0E-11	2.4E-02	0.01	5.27E-03	0.633	0.587
tcwF2	f-tcw12	5.3E-12	1.7E-02	0.01	1.57E-03	0.633	0.587
tcwF3	f-tcw13	4.5E-12	1.3E-02	0.01	1.24E-03	0.633	0.587

Table IV-4. Matrix and fracture properties for the mean infiltration flux one-dimensional drift-scale hydrologic property set (DTN: LB0208UZDSCPMI.002). The prefix "m-" stands for matrix and "f-" stands for fracture. (Continued)

Material name from DTN source	Material name used in LDTH submodels	Permeability [m^2]	Porosity [-]	Residual saturation [-]	α (alpha) [1/Pa]	m [-]	γ (gamma) [-]
ptnF1	f-ptn21	3.2E-12	9.2E-03	0.01	8.70E-04	0.633	0.232
ptnF2	f-ptn22	3.0E-13	1.0E-02	0.01	1.57E-03	0.633	0.232
ptnF3	f-ptn23	3.0E-13	2.1E-03	0.01	5.18E-03	0.633	0.232
ptnF4	f-ptn24	3.0E-12	1.0E-02	0.01	1.86E-03	0.633	0.232
ptnF5	f-ptn25	1.7E-13	5.5E-03	0.01	1.33E-03	0.633	0.232
ptnF6	f-ptn26	2.2E-13	3.1E-03	0.01	1.34E-03	0.633	0.232
tswF1	f-tsw31	8.1E-13	5.0E-03	0.01	1.60E-05	0.633	0.129
tswF2	f-tsw32	7.1E-13	8.3E-03	0.01	1.00E-04	0.633	0.600
tswF3	f-tsw33	7.8E-13	5.8E-03	0.01	1.59E-03	0.633	0.600
tswF4	f-tsw34	3.3E-13	8.5E-03	0.01	1.04E-04	0.633	0.569
tswF5	f-tsw35	9.1E-13	9.6E-03	0.01	1.02E-04	0.633	0.569
tswF6	f-tsw36	1.3E-12	1.3E-02	0.01	7.44E-04	0.633	0.569
tswF7	f-tsw37	1.3E-12	1.3E-02	0.01	7.44E-04	0.633	0.569
tswF8	f-tsw38	8.1E-13	1.1E-02	0.01	2.12E-03	0.633	0.569
tswFv	f-tsw9v	N/A[2]	N/A[2]	N/A[2]	N/A[2]	N/A[2]	N/A[2]
tswFz	f-tsw9z	8.1E-13	4.3E-03	0.01	1.5E-03	0.633	0.370
ch1Fv	f-ch1v	N/A2	N/A2	N/A2	N/A2	N/A2	N/A2
ch1Fz	f-ch1z	2.5E-14	1.6E-04	0.01	1.4E-03	0.633	0.370
ch2Fv	f-ch2v	N/A[2]	N/A[2]	N/A[2]	N/A[2]	N/A[2]	N/A[2]
ch3Fv	f-ch3v	N/A[2]	N/A[2]	N/A[2]	N/A[2]	N/A[2]	N/A[2]
ch4Fv	f-ch4v	N/A[2]	N/A[2]	N/A[2]	N/A[2]	N/A[2]	N/A[2]
ch5Fv	f-ch5v	N/A[2]	N/A[2]	N/A[2]	N/A[2]	N/A[2]	N/A[2]
ch2Fz	f-ch2z	2.5E-14	3.7E-04	0.01	8.9E-04	0.633	0.370
ch3Fz	f-ch3z	2.5E-14	3.7E-04	0.01	8.9E-04	0.633	0.370
ch4Fz	f-ch4z	2.5E-14	3.7E-04	0.01	8.9E-04	0.633	0.370
ch5Fz	f-ch5z	2.5E-14	3.7E-04	0.01	8.9E-04	0.633	0.370
ch6Fv	f-ch6v	N/A[2]	N/A[2]	N/A[2]	N/A[2]	N/A[2]	N/A[2]
ch6Fz	f-ch6z	2.5E-14	1.6E-04	0.01	1.4E-03	0.633	0.370
pp4Fz	f-pp4	2.5E-14	3.7E-04	0.01	1.83E-03	0.633	0.370
pp3Fd	f-pp3	2.2E-13	9.7E-04	0.01	2.47E-03	0.633	0.199
pp2Fd	f-pp2	2.2E-13	9.7E-04	0.01	3.17E-03	0.633	0.199
pp1Fz	f-pp1	2.5E-14	3.7E-04	0.01	1.83E-03	0.633	0.370
bf3Fd	f-bf3	2.2E-13	9.7E-04	0.01	2.93E-03	0.633	0.199
bf2Fz	f-bf2	2.5E-14	3.7E-04	0.01	8.9E-04	0.633	0.370
tr3Fd	f-tr3	2.2E-13	9.7E-04	0.01	1.6E-03	0.633	0.199
tr2Fz	f-tr2	2.5E-14	3.7E-04	0.01	8.9E-04	0.633	0.370

[1]Gamma value does not apply to matrix continuum.

[2]Vitric units (those units ending with a "**v**") do not have fractures. The fracture continuum properties are the same as those of the matrix continuum for these units.

Table IV-5. Matrix and fracture properties for the lower-bound infiltration flux one-dimensional drift-scale hydrologic property set (DTN: LB0208UZDSCPLI.002). The prefix "m-" stands for matrix and "f-" stands for fracture.

Material name from DTN source	Material name used in LDTH submodels	Permeability [m^2]	Porosity [-]	Residual saturation [-]	α (alpha) [1/Pa]	m [-]	γ (gamma) [-]
tcwM1	m-tcw11	3.44E-15	0.241	0.02	1.16E-05	0.388	N/A[1]
tcwM2	m-tcw12	3.00E-20	0.088	0.20	2.67E-06	0.280	N/A[1]
tcwM3	m-tcw13	3.96E-17	0.200	0.31	1.64E-06	0.259	N/A[1]
ptnM1	m-ptn21	5.55E-15	0.387	0.24	6.38E-05	0.245	N/A[1]
ptnM2	m-ptn22	8.40E-12	0.428	0.13	1.67E-04	0.219	N/A[1]
ptnM3	m-ptn23	1.92E-14	0.233	0.07	4.51E-05	0.247	N/A[1]
ptnM4	m-ptn24	6.66E-13	0.413	0.14	2.52E-03	0.182	N/A[1]
ptnM5	m-ptn25	1.96E-14	0.498	0.06	1.24E-04	0.300	N/A[1]
ptnM6	m-ptn26	1.00E-11	0.490	0.05	1.63E-03	0.126	N/A[1]
tswM1	m-tsw31	1.42E-17	0.054	0.21	8.02E-05	0.218	N/A[1]
tswM2	m-tsw32	3.96E-16	0.157	0.07	9.46E-06	0.290	N/A[1]
tswM3	m-tsw33	1.60E-18	0.155	0.12	4.25E-06	0.283	N/A[1]
tswM4	m-tsw34	1.38E-19	0.111	0.19	1.19E-06	0.317	N/A[1]
tswM5	m-tsw35	2.33E-18	0.131	0.12	1.97E-06	0.216	N/A[1]
tswM6	m-tsw36	5.58E-19	0.103	0.20	4.22E-07	0.442	N/A[1]
tswM7	m-tsw37	5.58E-19	0.103	0.20	4.22E-07	0.442	N/A[1]
tswM8	m-tsw38	2.93E-18	0.043	0.42	1.43E-06	0.286	N/A[1]
tswMv	m-tsw9v	3.15E-13	0.229	0.13	1.86E-05	0.293	N/A[1]
tswMz	m-tsw9z	3.5E-17	0.275	0.36	4.61E-06	0.059	N/A[1]
ch1Mv	m-ch1v	3.15E-14	0.331	0.06	4.50E-05	0.240	N/A[1]
ch1Mz	m-ch1z	3.5E-17	0.285	0.38	2.12E-07	0.349	N/A[1]
ch2Mv	m-ch2v	1.13E-11	0.346	0.06	1.22E-04	0.158	N/A[1]
ch3Mv	m-ch3v	1.13E-11	0.346	0.06	1.22E-04	0.158	N/A[1]
ch4Mv	m-ch4v	1.13E-11	0.346	0.06	1.22E-04	0.158	N/A[1]
ch5Mv	m-ch5v	1.13E-11	0.346	0.06	1.22E-04	0.158	N/A[1]
ch2Mz	m-ch2z	5.2E-18	0.322	0.26	2.25E-06	0.257	N/A[1]
ch3Mz	m-ch3z	5.2E-18	0.322	0.26	2.25E-06	0.257	N/A[1]
ch4Mz	m-ch4z	5.2E-18	0.322	0.26	2.25E-06	0.257	N/A[1]
ch5Mz	m-ch5z	5.2E-18	0.322	0.26	2.25E-06	0.257	N/A[1]
ch6Mv	m-ch6v	2.54E-13	0.331	0.06	9.05E-06	0.147	N/A[1]
ch6Mz	m-ch6z	8.2E-19	0.271	0.36	1.56E-07	0.499	N/A[1]
pp4Mz	m-pp4	2.98E-16	0.321	0.29	2.88E-07	0.474	N/A[1]
pp3Md	m-pp3	5.37E-14	0.318	0.08	7.97E-06	0.407	N/A[1]
pp2Md	m-pp2	4.24E-16	0.221	0.10	2.41E-06	0.309	N/A[1]
pp1Mz	m-pp1	7.02E-16	0.297	0.30	1.36E-06	0.272	N/A[1]
bf3Md	m-bf3	2.97E-14	0.175	0.11	1.32E-05	0.193	N/A[1]
bf2Mz	m-bf2	8.1E-17	0.234	0.21	1.18E-07	0.617	N/A[1]
tr3Md	m-tr3	1.1E-15	0.175	0.11	1.12E-05	0.193	N/A[1]
tr2Mz	m-tr2	8.1E-17	0.234	0.21	1.18E-07	0.617	N/A[1]
tcwF1	f-tcw11	3.0E-11	2.4E-02	0.01	4.68E-03	0.633	0.483
tcwF2	f-tcw12	5.3E-12	1.7E-02	0.01	3.20E-03	0.633	0.483
tcwF3	f-tcw13	4.5E-12	1.3E-02	0.01	2.13E-03	0.633	0.483

Table IV-5. Matrix and fracture properties for the lower-bound infiltration flux one-dimensional drift-scale hydrologic property set (DTN: LB0208UZDSCPLI.002). The prefix "m-" stands for matrix and "f-" stands for fracture. (Continued)

Material name from DTN source	Material name used in LDTH submodels	Permeability [m^2]	Porosity [-]	Residual saturation [-]	α (alpha) [1/Pa]	m [-]	γ (gamma) [-]
ptnF1	f-ptn21	3.2E-12	9.2E-03	0.01	2.93E-03	0.633	0.065
ptnF2	f-ptn22	3.0E-13	1.0E-02	0.01	6.76E-04	0.633	0.065
ptnF3	f-ptn23	3.0E-13	2.1E-03	0.01	3.96E-03	0.633	0.065
ptnF4	f-ptn24	3.0E-12	1.0E-02	0.01	2.51E-03	0.633	0.065
ptnF5	f-ptn25	1.7E-13	5.5E-03	0.01	1.53E-03	0.633	0.065
ptnF6	f-ptn26	2.2E-13	3.1E-03	0.01	1.52E-03	0.633	0.065
tswF1	f-tsw31	8.1E-13	5.0E-03	0.01	1.58E-05	0.633	0.037
tswF2	f-tsw32	7.1E-13	8.3E-03	0.01	1.31E-04	0.633	0.528
tswF3	f-tsw33	7.8E-13	5.8E-03	0.01	1.94E-03	0.633	0.528
tswF4	f-tsw34	3.3E-13	8.5E-03	0.01	6.55E-04	0.633	0.476
tswF5	f-tsw35	9.1E-13	9.6E-03	0.01	1.35E-03	0.633	0.476
tswF6	f-tsw36	1.3E-12	1.3E-02	0.01	1.31E-03	0.633	0.476
tswF7	f-tsw37	1.3E-12	1.3E-02	0.01	1.31E-03	0.633	0.476
tswF8	f-tsw38	8.1E-13	1.1E-02	0.01	1.75E-03	0.633	0.476
tswFv	f-tsw9v	N/A[2]	N/A[2]	N/A[2]	N/A[2]	N/A[2]	N/A[2]
tswFz	f-tsw9z	8.1E-13	4.3E-03	0.01	1.5E-03	0.633	0.276
ch1Fv	f-ch1v	N/A[2]	N/A[2]	N/A[2]	N/A[2]	N/A[2]	N/A[2]
ch1Fz	f-ch1z	2.5E-14	1.6E-04	0.01	1.4E-03	0.633	0.276
ch2Fv	f-ch2v	N/A[2]	N/A[2]	N/A[2]	N/A[2]	N/A[2]	N/A[2]
ch3Fv	f-ch3v	N/A[2]	N/A[2]	N/A[2]	N/A[2]	N/A[2]	N/A[2]
ch4Fv	f-ch4v	N/A[2]	N/A[2]	N/A[2]	N/A[2]	N/A[2]	N/A[2]
ch5Fv	f-ch5v	N/A[2]	N/A[2]	N/A[2]	N/A[2]	N/A[2]	N/A[2]
ch2Fz	f-ch2z	2.5E-14	3.7E-04	0.01	8.9E-04	0.633	0.276
ch3Fz	f-ch3z	2.5E-14	3.7E-04	0.01	8.9E-04	0.633	0.276
ch4Fz	f-ch4z	2.5E-14	3.7E-04	0.01	8.9E-04	0.633	0.276
ch5Fz	f-ch5z	2.5E-14	3.7E-04	0.01	8.9E-04	0.633	0.276
ch6Fv	f-ch6v	N/A[2]	N/A[2]	N/A[2]	N/A[2]	N/A[2]	N/A[2]
ch6Fz	f-ch6z	2.5E-14	1.6E-04	0.01	1.4E-03	0.633	0.276
pp4Fz	f-pp4	2.5E-14	3.7E-04	0.01	1.88E-03	0.633	0.276
pp3Fd	f-pp3	2.2E-13	9.7E-04	0.01	1.32E-03	0.633	0.248
pp2Fd	f-pp2	2.2E-13	9.7E-04	0.01	2.80E-03	0.633	0.248
pp1Fz	f-pp1	2.5E-14	3.7E-04	0.01	6.39E-04	0.633	0.276
bf3Fd	f-bf3	2.2E-13	9.7E-04	0.01	1.91E-03	0.633	0.248
bf2Fz	f-bf2	2.5E-14	3.7E-04	0.01	8.9E-04	0.633	0.276
tr3Fd	f-tr3	2.2E-13	9.7E-04	0.01	1.6E-03	0.633	0.248
tr2Fz	f-tr2	2.5E-14	3.7E-04	0.01	8.9E-04	0.633	0.276

[1]Gamma value does not apply to matrix continuum.

[2]Vitric units (those units ending with a "v") do not have fractures. The fracture continuum properties are the same as those of the matrix continuum for these units.

Table IV-6. Matrix and fracture properties for the upper-bound infiltration flux one-dimensional drift-scale hydrologic property set (DTN: LB0302UZDSCPUI.002). The prefix "m-" stands for matrix and "f-" stands for fracture.

Material name from DTN source	Material name used in LDTH submodels	Permeability [m^2]	Porosity [-]	Residual saturation [-]	α (alpha) [1/Pa]	m [-]	γ (gamma) [-]
tcwM1	m-tcw11	3.90E-15	0.241	0.02	1.23E-05	0.388	N/A[1]
tcwM2	m-tcw12	1.16E-19	0.088	0.20	3.39E-06	0.280	N/A[1]
tcwM3	m-tcw13	4.41E-16	0.200	0.31	3.25E-06	0.259	N/A[1]
ptnM1	m-ptn21	2.14E-14	0.387	0.24	1.56E-04	0.245	N/A[1]
ptnM2	m-ptn22	1.29E-11	0.428	0.13	1.33E-04	0.219	N/A[1]
ptnM3	m-ptn23	4.07E-14	0.233	0.07	2.39E-05	0.247	N/A[1]
ptnM4	m-ptn24	4.27E-12	0.413	0.14	5.62E-04	0.182	N/A[1]
ptnM5	m-ptn25	1.01E-12	0.498	0.06	9.48E-05	0.300	N/A[1]
ptnM6	m-ptn26	1.00E-11	0.490	0.05	5.23E-04	0.126	N/A[1]
tswM1	m-tsw31	1.77E-17	0.054	0.21	4.85E-05	0.218	N/A[1]
tswM2	m-tsw32	2.13E-16	0.157	0.07	1.96E-05	0.290	N/A[1]
tswM3	m-tsw33	2.39E-17	0.155	0.12	5.22E-06	0.283	N/A[1]
tswM4	m-tsw34	2.96E-19	0.111	0.19	1.65E-06	0.317	N/A[1]
tswM5	m-tsw35	8.55E-18	0.131	0.12	5.03E-06	0.216	N/A[1]
tswM6	m-tsw36	7.41E-19	0.103	0.20	1.08E-06	0.442	N/A[1]
tswM7	m-tsw37	7.41E-19	0.103	0.20	1.08E-06	0.442	N/A[1]
tswM8	m-tsw38	7.40E-18	0.043	0.42	5.58E-06	0.286	N/A[1]
tswMv	m-tsw9v	2.24E-13	0.229	0.13	4.86E-05	0.293	N/A[1]
tswMz	m-tsw9z	3.5E-17	0.275	0.36	4.61E-06	0.059	N/A[1]
ch1Mv	m-ch1v	1.39E-12	0.331	0.06	8.82E-05	0.240	N/A[1]
ch1Mz	m-ch1z	3.5E-17	0.285	0.38	2.12E-07	0.349	N/A[1]
ch2Mv	m-ch2v	4.90E-11	0.346	0.06	2.73E-04	0.158	N/A[1]
ch3Mv	m-ch3v	4.90E-11	0.346	0.06	2.73E-04	0.158	N/A[1]
ch4Mv	m-ch4v	4.90E-11	0.346	0.06	2.73E-04	0.158	N/A[1]
ch5Mv	m-ch5v	4.90E-11	0.346	0.06	2.73E-04	0.158	N/A[1]
ch2Mz	m-ch2z	5.2E-18	0.322	0.26	2.25E-06	0.257	N/A[1]
ch3Mz	m-ch3z	5.2E-18	0.322	0.26	2.25E-06	0.257	N/A[1]
ch4Mz	m-ch4z	5.2E-18	0.322	0.26	2.25E-06	0.257	N/A[1]
ch5Mz	m-ch5z	5.2E-18	0.322	0.26	2.25E-06	0.257	N/A[1]
ch6Mv	m-ch6v	2.72E-13	0.331	0.06	1.67E-05	0.147	N/A[1]
ch6Mz	m-ch6z	8.2E-19	0.271	0.36	1.56E-07	0.499	N/A[1]
pp4Mz	m-pp4	1.02E-15	0.321	0.29	4.57E-07	0.474	N/A[1]
pp3Md	m-pp3	1.26E-13	0.318	0.08	9.50E-06	0.407	N/A[1]
pp2Md	m-pp2	1.70E-15	0.221	0.10	2.25E-06	0.309	N/A[1]
pp1Mz	m-pp1	2.57E-15	0.297	0.30	8.77E-07	0.272	N/A[1]
bf3Md	m-bf3	3.55E-14	0.175	0.11	3.48E-05	0.193	N/A[1]
bf2Mz	m-bf2	8.1E-17	0.234	0.21	1.18E-07	0.617	N/A[1]
tr3Md	m-tr3	1.1E-15	0.175	0.11	1.12E-05	0.193	N/A[1]
tr2Mz	m-tr2	8.1E-17	0.234	0.21	1.18E-07	0.617	N/A[1]
tcwF1	f-tcw11	3.0E-11	2.4E-02	0.01	5.01E-03	0.633	5.00E-01
tcwF2	f-tcw12	5.3E-12	1.7E-02	0.01	2.19E-03	0.633	5.00E-01
tcwF3	f-tcw13	4.5E-12	1.3E-02	0.01	1.86E-03	0.633	5.00E-01
ptnF1	f-ptn21	3.2E-12	9.2E-03	0.01	2.69E-03	0.633	1.00E-01

Table IV-6. Matrix and fracture properties for the upper-bound infiltration flux one-dimensional drift-scale hydrologic property set (DTN: LB0302UZDSCPUI.002). The prefix "m-" stands for matrix and "f-" stands for fracture. (Continued)

Material name from DTN source	Material name used in LDTH submodels	Permeability [m^2]	Porosity [-]	Residual saturation [-]	α (alpha) [1/Pa]	m [-]	γ (gamma) [-]
ptnF2	f-ptn22	3.0E-13	1.0E-02	0.01	1.38E-03	0.633	1.00E-01
ptnF3	f-ptn23	3.0E-13	2.1E-03	0.01	1.23E-03	0.633	1.00E-01
ptnF4	f-ptn24	3.0E-12	1.0E-02	0.01	2.95E-03	0.633	1.00E-01
ptnF5	f-ptn25	1.7E-13	5.5E-03	0.01	1.10E-03	0.633	1.00E-01
ptnF6	f-ptn26	2.2E-13	3.1E-03	0.01	9.55E-04	0.633	1.00E-01
tswF1	f-tsw31	8.1E-13	5.0E-03	0.01	1.58E-05	0.633	1.00E-01
tswF2	f-tsw32	7.1E-13	8.3E-03	0.01	1.00E-04	0.633	5.61E-01
tswF3	f-tsw33	7.8E-13	5.8E-03	0.01	1.58E-03	0.633	5.61E-01
tswF4	f-tsw34	3.3E-13	8.5E-03	0.01	1.00E-04	0.633	5.70E-01
tswF5	f-tsw35	9.1E-13	9.6E-03	0.01	5.78E-04	0.633	5.70E-01
tswF6	f-tsw36	1.3E-12	1.3E-02	0.01	1.10E-03	0.633	5.70E-01
tswF7	f-tsw37	1.3E-12	1.3E-02	0.01	1.10E-03	0.633	5.70E-01
tswF8	f-tsw38	8.1E-13	1.1E-02	0.01	8.91E-04	0.633	5.70E-01
tswFv	f-tsw9v	N/A[2]	N/A[2]	N/A[2]	N/A[2]	N/A[2]	N/A[2]
tswFz	f-tsw9z	8.1E-13	4.3E-03	0.01	1.5E-03	0.633	5.00E-01
ch1Fv	f-ch1v	N/A[2]	N/A[2]	N/A[2]	N/A[2]	N/A[2]	N/A[2]
ch1Fz	f-ch1z	2.5E-14	1.6E-04	0.01	1.4E-03	0.633	5.00E-01
ch2Fv	f-ch2v	N/A[2]	N/A[2]	N/A[2]	N/A[2]	N/A[2]	N/A[2]
ch3Fv	f-ch3v	N/A[2]	N/A[2]	N/A[2]	N/A[2]	N/A[2]	N/A[2]
ch4Fv	f-ch4v	N/A[2]	N/A[2]	N/A[2]	N/A[2]	N/A[2]	N/A[2]
ch5Fv	f-ch5v	N/A[2]	N/A[2]	N/A[2]	N/A[2]	N/A[2]	N/A[2]
ch2Fz	f-ch2z	2.5E-14	3.7E-04	0.01	8.9E-04	0.633	5.00E-01
ch3Fz	f-ch3z	2.5E-14	3.7E-04	0.01	8.9E-04	0.633	5.00E-01
ch4Fz	f-ch4z	2.5E-14	3.7E-04	0.01	8.9E-04	0.633	5.00E-01
ch5Fz	f-ch5z	2.5E-14	3.7E-04	0.01	8.9E-04	0.633	5.00E-01
ch6Fv	f-ch6v	N/A[2]	N/A[2]	N/A[2]	N/A[2]	N/A[2]	N/A[2]
ch6Fz	f-ch6z	2.5E-14	1.6E-04	0.01	1.4E-03	0.633	5.00E-01
pp4Fz	f-pp4	2.5E-12	3.7E-04	0.01	8.91E-04	0.633	5.00E-01
pp3Fd	f-pp3	2.2E-12	9.7E-04	0.01	1.66E-03	0.633	5.00E-01
pp2Fd	f-pp2	2.2E-13	9.7E-04	0.01	1.66E-03	0.633	5.00E-01
pp1Fz	f-pp1	2.5E-14	3.7E-04	0.01	8.91E-04	0.633	5.00E-01
bf3Fd	f-bf3	2.2E-13	9.7E-04	0.01	1.66E-03	0.633	5.00E-01
bf2Fz	f-bf2	2.5E-14	3.7E-04	0.01	8.9E-04	0.633	5.00E-01
tr3Fd	f-tr3	2.2E-13	9.7E-04	0.01	1.6E-03	0.633	5.00E-01
tr2Fz	f-tr2	2.5E-14	3.7E-04	0.01	8.9E-04	0.633	5.00E-01

[1]Gamma value does not apply to matrix continuum.

[2]Vitric units (those units ending with a "v") do not have fractures. The fracture continuum properties are the same as those of the matrix continuum for these units.

Table IV-7. Fracture Frequency and Fracture-to-Matrix Interface Area. In parentheses are the material names used in the LDTH submodels of this report.

Material Name	Fracture Frequency (m^{-1})	Interface Area [m^2/m^3]
tcw11	0.92	1.56
tcw12	1.91	13.39
tcw13	2.79	3.77
ptn21	0.67	1.00
ptn22	0.46	1.41
ptn23	0.57	1.75
ptn24	0.46	0.34
ptn25	0.52	1.09
ptn26	0.97	3.56
tsw31	2.17	3.86
tsw32	1.12	3.21
tsw33	0.81	4.44
tsw34	4.32	13.54
tsw35	3.16	9.68
tsw36	4.02	12.31
tsw37	4.02	12.31
tsw38	4.36	13.34
tsw39 (tsw9v)	NA[1]	NA[1]
tsw39 (tsw9z)	0.96	2.95
ch1Vl (ch1v)	NA[1]	NA[1]
ch1Ze (ch1z)	0.04	0.11
ch2Vl (ch2v)	NA[1]	NA[1]
ch3Vl (ch3v)	NA[1]	NA[1]
ch4Vl (ch4v)	NA[1]	NA[1]
ch5Vl (ch5v)	NA[1]	NA[1]
ch2Ze (ch2z)	0.14	0.43
ch3Ze (ch3z)	0.14	0.43
ch4Ze (ch4z)	0.14	0.43
ch5Ze (ch5z)	0.14	0.43
ch6Vl (ch6v)	NA[1]	NA[1]
ch6 (ch6z)	0.04	0.11
pp4	0.14	0.43
pp3	0.20	0.61
pp2	0.20	0.61
pp1	0.14	0.43
bf3	0.20	0.61
bf2	0.14	0.43
tr3	0.20	0.61
tr2	0.14	0.43

Source: DTN: LB0205REVUZPRP.001

NOTE: [1] Vitric units (those units ending with a “Vl” or a “v”) do not have fractures; therefore, fracture properties do not pertain to those units.

Table IV-8. Mass density of 4-10 crushed tuff. The average mass density for the 50 samples in 1.27 gm/cm^3, which is the value used for the crushed-tuff invert.

Row number	Mass density (gm/cm^3)
321	1.3
322	1.2
323	1.3
324	1.3
325	1.3
326	1.2
327	1.3
328	1.2
329	1.3
330	1.2
331	1.2
332	1.2
333	1.3
334	1.3
335	1.3
336	1.3
337	1.3
338	1.2
339	1.2
340	1.2
341	1.3
342	1.3
343	1.3
344	1.3
345	1.3
346	1.3
347	1.3
348	1.3
349	1.3
350	1.2
351	1.3
352	1.3
353	1.3
354	1.2
355	1.3
356	1.3
357	1.2
358	1.2
359	1.2
360	1.3
361	1.3
362	1.3
363	1.3
364	1.2
365	1.2
366	1.2
367	1.3
368	1.3
369	1.3
370	1.3

DTN: GS020183351030.001

Table IV-9. Specific heat and thermal conductivity of 4-10 crushed tuff. The average specific heat for the 11 samples is 0.93 J/cm^3-°C, which is the value used for the crushed-tuff invert. The average thermal conductivity for the 11 samples is 0.2 W/m-°C, which is the averaged valued rounded up to the nearest "tenths"; this rounded averaged value is used for the crushed-tuff invert.

Row number	Specific heat (J/cm^3-°C)	Thermal conductivity (W/m °C)
1	0.82	0.17
2	0.84	0.14
3	0.98	0.17
4	0.98	0.17
5	0.99	0.17
6	0.92	0.16
7	0.96	0.17
8	0.86	0.15
9	0.88	0.16
10	1.06	0.17
11	0.94	0.17

DTN: GS000483351030.003

ATTACHMENT V
BUILDING SUBMODEL INPUT FILES

INTENTIONALLY LEFT BLANK

ATTACHMENT V
BUILDING SUBMODEL INPUT FILES

SMT Submodel

The SMT submodel has the following information in this order:

1. Time information (starttime, stoptime, timestepsize)
2. Material properties (calls a rocktab file, see Attachment IV)
3. Output information (for ".ext" time-history output this is a readable by XTOOL v10.1)
4. Heat generation information (calls a heatgen file, see Attachment III)
5. Restart file information
6. Boundary-conditions
7. Initial conditions
8. SMT-submodel mesh file (calls an SMT-submodel mesh file, see Attachment I)
9. Run control parameters

All parameter values are taken directly from inputs or calculations described in other attachments. An example of an SMT-submodel NUFT usnt-option input file follows below. For more information, see the NUFT documentation (Nitao 1998).

```
 (usnt
  (title "* YMP Site-Scale 3D Model, Conduction-Only Post-Emplacement Run")
;; AML = 55 MTU/acre ;; ventilation + post-closure run for MSTHM for the License
Application
;; rotated mesh explicitly representing emplacement drifts
;; Western Model representing Panels 1, 2E, 2W, 3, and 5
;; conduction only
  (modelname usnt)
  (include-pkg "thermcon.pkg") ;; single-comp (air), single-phase (gas) pkg for cond-
only run
  (tstop 20100y)
  (time 0)
  (stepmax 1000000)
  (dtmax 1.0e25)
  (dt 1e2)
;; include thermal properties
 (rocktab
    (include "/data34/TSPA03/physical_properties/SDT-1Dds-03")     ;; read rocktab
data
    (include "/data34/TSPA03/physical_properties/SMT-1Dds-fl-03")     ;; read rocktab
data
    (include "/data34/TSPA03/physical_properties/SMT-1Dds-sz-03")     ;; read rocktab
data
)  ;; end rocktab
;;
**********************************************************************************
**
;; ********************************************************************

(output
    (XTOOL (variables T )  ;; repository node temperatures
            (file-ext ".lvl.ext")(range "*#*:*:1")
                (outtimes
                        (include "/data34/TSPA03/outputTimes/outputTimes-SMT-55-01")
        ))
   )  ;; end output
```

```
;; ************************************************************************
;;  include heat curves in srctab
;;   (srctab
          (include
"/data34/TSPA03/heatgen/SMT_blocks/preliminary_DTN2/SMT_LA_includes01")
;;   ) ;; end srctab
;; ************************************************************************
;; read restart file
   (read-restart
    (file  "/data34/TSPA03/SMT/SMT55/03-150w-i/SMT55-03-150w-i.rst")
    (time 1.0e6y))
;; ************************************************************************
   (bctab
    (top
        (range "at*")
        (clamped))
    (bottom
        (range "bs*")
        (clamped))
   )  ;; end bctab
;; ************************************************************************
;; set initial conditions
;; (state
;;  P by-key  ("*"  1.0e5))
;;  (T by-key
;;    (include "/data34/TSPA03/BoundaryConditions/preliminary_DTN/smtUpperBC.out")
;;    (include "/data34/TSPA03/BoundaryConditions/preliminary_DTN/smtLowerBC.out")
;;  )
;; )  ;; end state
;; ************************************************************************
   (mesh-file  "/data34/TSPA03/smt_mesh/preliminary_DTN/tspa03.mesh03-150w")   ;; read
mesh and connection data
;; ************************************************************************

(include "/data30/TSPA01/run_control_param/run_control_param_SMT-v01")
  )  ;; end of model
```

LDTH submodel

For the LDTH submodel input files, a calculation (in addition to those described in other attachments) must be made to convert the percolation flux from mm/yr to kg/m^2/sec. An example of this calculation is:

$$J=4.1884 \text{ mm/yr } (1 \text{ day}/86{,}400 \text{ sec})(1 \text{ yr}/365.25 \text{ days})(\text{m}/1{,}000 \text{ mm})(1{,}000 \text{ kg/m}^3) = 1.3274\times10^{-7} \text{ kg/m}^2\text{/sec}$$

The LDTH submodel has the following information in this order:

1. Header information (lines preceded by a semicolon)
2. Time information (start time, stop time, timestepsize)
3. Convergence tolerance information
4. Output file (for ".ext" time-history output; this is readable by XTOOL v10.1)
5. Material properties (calls a rocktab file, see Attachment IV)
6. Percolation flux information (see the flux conversion mm/yr to kg/m^2/sec noted above)

7. Heat generation information (calls a heatgen file, see Attachment III)
8. Boundary-conditions
9. Restart conditions
10. Initial conditions
11. Mesh information for matrix continuum
12. Radcon information for matrix continuum (calls file for doing thermal-radiation connections, see Attachment VI)
13. Mesh information for fracture continuum
14. Run control parameters

All parameter values are taken directly from inputs or calculations described in other attachments. An example of an DDT-submodel NUFT usnt-option input file (P1R10C8-LDTH14-1Dds_mc-mi-02.in) follows below. For more information, see the NUFT documentation (Nitao 1998). LDTH-submodel input files follow the naming convention P(x)R(y)C(z)-LDTH(aml)-1Dds_mc-(percolation)i-0(property set).in. For the three infiltration flux cases, there are 2,592 input files including 1,296 initialization runs and 1,296 postemplacement runs. These files can be found in DTN: LL030808623122.036.

```
;; This Model was produced on
;; Thu May 22 18:12:31 PDT 2003
;; Implicit DKM with active fracture concept (AFC)
;; NBS material properties from 1D drift-scale infiltration flux property set
;; AML = 13.705 MTU/acre; half drift spacing = 162.0 m

;;  P1R10C8.col.units

;;  COLUMN INFORMATION (x,y =   171232.891,   233883.719) WORLD COLUMN h44

;;  unitthickness (m)
;;  _________________

;;  tcw11        0.059
;;  tcw12       77.988
;;  tcw13        5.771
;;  ptn21        3.867
;;  ptn22        5.303
;;  ptn23        1.670
;;  ptn24        8.643
;;  ptn25       18.486
;;  ptn26       12.832
;;  tsw31        1.904
;;  tsw32       52.070
;;  tsw33       85.734
;;  tsw34       33.656
;;  tsw35      101.756
;;  tsw36       36.992
;;  tsw37       18.486
;;  tsw38       16.699
;;  tsw9v        1.904
;;  tsw9z        0.000
;;  ch1v         0.000
;;  ch1z        16.787
;;  ch2v         0.000
;;  ch3v         0.000
;;  ch4v         0.000
```

```
;;  ch5v        0.000
;;  ch2z       21.299
;;  ch3z       21.299
;;  ch4z       21.299
;;  ch5z       21.299
;;  ch6v        0.000
;;  ch6z       17.461
;;  pp4        12.949
;;  pp3         8.320
;;  pp2         0.000
;;  pp1         0.000
;;  bf3         0.000
;;  bf2         0.000
;;  tr3         0.000
;;  tr2         0.000

;;  repository elevation (m):                    1069.300
;;  host rock:                              tsw34

;;  meters of host rock (tsw34) above repository:              12.001
;;  meters of host rock (tsw34) below repository:              21.656

;;  overburden thickness (m):                       286.329
;;  distance from repository plane to top of chn (m):          197.494
;;  distance from repository plane to top of water table (m):      338.206

(usnt
  (title "4.1883590e+00mm_yr,line-load,AML=14mtu_acre,LDTH14_1Dds_mc-mi")
  (modelname usnt)

  (tstop  20100y)
  (time 0y)
  (stepmax 1000000)
  (dtmax 1.000e+25)
  (dt 1e2)

  (tolerconv (P 5000.)(S 0.005)(X 0.005)(T 0.5))
  ;; absolute NR conv. tolerance
  (reltolerconv (P 0.005)(S 0.0)(X 0.0)(T 1.e-3))

  (tolerdt (P 2.e4)(S 0.35)(X 0.25)(T 10.))
  (reltolerdt (P 0.1)(S 0.0)(X 0.0)(T 0.0))

  ;; trying with harmonic mean everywhere which means turning off the geometric before
vtough.pkg
  ;;  gets called.
  (diffusion-geo-mean off)
  ;; for imp-DKM do not have this so that it will default to harmonic for fract-matrix
interaction
  ;;(mult-cont-diff-harmonic off)
  ;; following has to come after tolerances
  (rmstolerconv 1e-4)
  (include-pkg "vtough.pkg")
  (check-mult-con off )

;;
*******************************************************************************
*************
  (output
        (XTOOL (continuum f)
               (variables T S.liquid X.air.gas RH Pc.liquid P.gas qPhChg.water.gas
QPhChg.water.gas q.liquid q.water.gas q.air.gas)
               (file-ext ".f.EBS.ext")(range "*hstrk*.f*" "dr*.f*" "*in*.f*"
"*wp*.f*")
               (outtimes
                       (include "/data34/TSPA03/outputTimes/outputTimes-LDTH-SDT-DDT-
14-01")
               )
        )
        (XTOOL (continuum m)
               (variables T S.liquid X.air.gas RH Pc.liquid P.gas qPhChg.water.gas
QPhChg.water.gas q.liquid q.water.gas q.air.gas)
```

```
                (file-ext ".m.EBS.ext")(range "*hstrk*.m*" "dr*.m*" "*in*.m*"
"*wp*.m*")
                (outtimes
                        (include "/data34/TSPA03/outputTimes/outputTimes-LDTH-SDT-DDT-
14-01")
                )
        )

    ) ;; end output

;;
**********************************************************************************
***********
(rocktab
        (include "/data34/TSPA03/physical_properties/dkm-afc-1Dds-mc-mi-04")
        (include "/data34/TSPA03/physical_properties/dkm-afc-EBS-mi-03")
) ;; close rocktab
        (include "/data34/TSPA03/physical_properties/modpropTSPA03_01_14")
;;
**********************************************************************************
***********

;;  This srctab is adjusted to allocate percolation to just the fracture.
  (srctab
        (compflux
                (comp water)
                (name infil)
                (range "*.f*:*:2")
                (mult-by-area z)
                (allocate-by-element ("*" 1.0))
                (table    0.0     1.3274464e-07  600.00y  1.3274464e-07  ;;
4.1883590e+00  mm/yr
                         600.001y  2.4720940e-07  2000.00y 2.4720940e-07  ;;
7.7999510e+00  mm/yr
                        2000.001y  3.6606447e-07  1.0e30   3.6606447e-07) ;;
1.1550066e+01  mm/yr
                (enthalpy  0.0   7.1314900e+04  1E+30   7.1314900e+04 )
        )

        (include "/data34/TSPA03/heatgen/SDT_LDTH_blocks/preliminary_DTN/P1R10C8_LDTH-
SDT")
  ) ;; end srctab

     ;; set boundary conditions
    (bctab
    (atmos
        (range  "at*")
        (basephase gas)
        (tables
            (T        0.0  1.6984000e+01   1.0e30  1.6984000e+01 )
            (S.liquid 0.0  0.0    1.0e30  0.0  )
            (P        0.0  8.5705180e+04   1.0e30  8.5705180e+04 )
            (X.air    0.0  9.8582710e-01   1.0e30  9.8582710e-01 )
        )
    )

    (gwater
        (range  "wt*")
        (basephase liquid)
        (tables
            (T          0  3.2083000e+01      1.0e30   3.2083000e+01)
            (S.liquid   0  1.0      1.0e30   1.0)
            (P          0  9.1988930e+04      1.0e30   9.1988930e+04)
            (X.air      0  1.0e-6   1.0e30  1.0e-6)
        )

;;  SET PHASEFACTOR GAS TO 0, AND LIQUID TO 1
        (phasefactor
            (gas      0  0.0   1.0e30  0.0)
            (liquid   0  1.0   1.0e30  1.0)
        )

    )
```

```
    ) ;; end bctab

;; set initial conditions.
    (read-restart (time 3.15576e20)
    (file "/data33/TSPA03/LDTH/LDTH14/1Dds_mc-mi/02i/P1R10C8-LDTH14-1Dds_mc-mi-
02i.res"))
    (overwrite-restart
         (X.air by-key     ("dr*" 1.0)("*wp*" 1.0)("*in*" 1.0))
         (S.liquid  by-key ("dr*" 0.0)("*wp*" 0.0)("*in.m*" 0.9)("*in.f*" 0.1))
    ) ;; end overwrite

;;This is for a unit symmetry cell with a half drift and half pillar
;;between drifts.
  (genmsh
    (anisotropic)
    (down 0. 0. 1.0)
    (coord rect)
    (multi-continua
       (type rocktab)
       (continuum  (name m)
       ;; 13.705 MTU/acre
           (dx 0.580 0.370 0.3025 0.4222 0.4222 0.350 0.3031 0.35 0.5 0.9 1.0 1.5 2.5
4.0 7.0 13.0 24.00    42.0   62.5)
           (dy  1.0)
      (dz
        1.0e-30     0.059    17.988    30.000    30.000 ;;  1-  5:      atm     tcw11
tcw12     tcw12     tcw12
         5.771     3.867     5.303     1.670     8.643 ;;  6- 10:    tcw13     ptn21
ptn22     ptn23     ptn24
        18.486    12.832     1.904    17.070    15.000 ;; 11- 15:    ptn25     ptn26
tsw31     tsw32     tsw32
        10.000    10.000     7.734     6.000     6.000 ;; 16- 20:    tsw32     tsw32
tsw33     tsw33     tsw33
         6.000     6.000     6.000     6.000     6.000 ;; 21- 25:    tsw33     tsw33
tsw33     tsw33     tsw33
         6.000     6.000     6.000     6.000     3.000 ;; 26- 30:    tsw33     tsw33
tsw33     tsw33     tsw33
         3.000     3.000     3.000     1.500     2.000 ;; 31- 35:    tsw33     tsw33
tsw33     tsw34     tsw34
         1.000     1.000     0.500     0.300     0.200 ;; 36- 40:    tsw34     tsw34
tsw34     tsw34     tsw34
         0.200     0.200     0.200     0.200     0.200 ;; 41- 45:    tsw34     tsw34
tsw34     tsw34     tsw34
         0.200     0.200     0.200     0.200     0.200 ;; 46- 50:    tsw34     tsw34
tsw34     tsw34     tsw34
         0.108     0.242     0.400     0.759     0.760 ;; 51- 55:    tsw34     tsw34
tsw34     tsw34     tsw34
         0.425     0.403     0.403     0.800     1.200 ;; 56- 60:    tsw34     tsw34
tsw34     tsw34     tsw34
         1.500     2.500     3.000     3.000     6.000 ;; 61- 65:    tsw34     tsw34
tsw34     tsw34     tsw34
         3.656     6.000     6.000     6.000     6.000 ;; 66- 70:    tsw34     tsw35
tsw35     tsw35     tsw35
         6.000     6.000     6.000     6.000     6.000 ;; 71- 75:    tsw35     tsw35
tsw35     tsw35     tsw35
         6.000     6.000     6.000    10.000    10.000 ;; 76- 80:    tsw35     tsw35
tsw35     tsw35     tsw35
         9.756    15.000    20.000     1.992    18.486 ;; 81- 85:    tsw35     tsw36
tsw36     tsw36     tsw37
        16.699     1.904    16.787    21.299    21.299 ;; 86- 90:    tsw38     tsw9v
ch1z      ch2z      ch3z
        21.299    21.299    17.461    12.949     8.320 ;; 91- 95:     ch4z      ch5z
ch6z       pp4       pp3
        1.0e-30                                        ;; 96- 96:       wt
      )
      (mat
         (atm           atm           1  nx  1  ny   1   1)
         (tcw11         m-tcw11       1  nx  1  ny   2   2)
         (tcw12         m-tcw12       1  nx  1  ny   3   5)
         (tcw13         m-tcw13       1  nx  1  ny   6   6)
         (ptn21         m-ptn21       1  nx  1  ny   7   7)
         (ptn22         m-ptn22       1  nx  1  ny   8   8)
         (ptn23         m-ptn23       1  nx  1  ny   9   9)
```

```
         (ptn24         m-ptn24       1  nx  1  ny  10  10)
         (ptn25         m-ptn25       1  nx  1  ny  11  11)
         (ptn26         m-ptn26       1  nx  1  ny  12  12)
         (tsw31         m-tsw31       1  nx  1  ny  13  13)
         (tsw32         m-tsw32       1  nx  1  ny  14  17)
         (tsw33         m-tsw33       1  nx  1  ny  18  33)
         (tsw34         m-tsw34       1  nx  1  ny  34  66)
         (tsw35         m-tsw35       1  nx  1  ny  67  81)
         (tsw36         m-tsw36       1  nx  1  ny  82  84)
         (tsw37         m-tsw37       1  nx  1  ny  85  85)
         (tsw38         m-tsw38       1  nx  1  ny  86  86)
         (tsw9v         m-tsw9v       1  nx  1  ny  87  87)
         (ch1z          m-ch1z        1  nx  1  ny  88  88)
         (ch2z          m-ch2z        1  nx  1  ny  89  89)
         (ch3z          m-ch3z        1  nx  1  ny  90  90)
         (ch4z          m-ch4z        1  nx  1  ny  91  91)
         (ch5z          m-ch5z        1  nx  1  ny  92  92)
         (ch6z          m-ch6z        1  nx  1  ny  93  93)
         (pp4           m-pp4         1  nx  1  ny  94  94)
         (pp3           m-pp3         1  nx  1  ny  95  95)
         (wt            m-pp3         1  nx  1  ny  96  96)
         (hstrk         m-tsw34       1  nx  1  ny  34  61)
         (dr            m-dr          1   1  1  ny  41  41)
         (dr            m-dr          1   3  1  ny  42  42)
         (dr            m-dr          1   4  1  ny  43  44)
         (dr            m-dr          1   5  1  ny  45  46)
         (dr            m-dr          1   6  1  ny  47  49)
         (dr            m-dr          1   7  1  ny  50  54)
         (dr            m-dr          1   6  1  ny  55  55)
         (dr            m-dr          1   5  1  ny  56  56)
         (wp            lsnf          1   1  1  ny  52  52)
         (wp            lsnf          1   2  1  ny  53  53)
         (wp            lsnf          1   3  1  ny  54  56)
         ;; invert
         (in            m-invert1 1   4  1  ny  57  57)
         (in            m-invert2 1   2  1  ny  58  58) ;; bottom of invert
      )

 (radcon
        (surface-offset 0 0  -3)
        (include "/data34/TSPA03/radcon/LDTH/preliminary_DTN/ldth0_300m.radcon")
) ;; close radcon

) ;; end continuum
       (continuum  (name f)
           (flow-area-density ("*.f*" 1.0))
           (LenFirst  ("*.f*" 1.0))    ;; same as y-direction
                                       ;; half-width of matrix block
           (Len  ("*.f*" 1.0))         ;; same as y-direction
                                       ;; half-width of fracture
                      ;; LenFirst and Len values are doubled here since 50% of cont-
len-fac
                      ;; is used in rocktab file
       ;; 13.705 MTU/acre
           (dx 0.580 0.370 0.3025 0.4222 0.4222 0.350 0.3031 0.35 0.5 0.9 1.0 1.5 2.5
4.0 7.0 13.0 24.00    42.0   62.5)
           (dy  1.0)
      (dz
        1.0e-30     0.059    17.988    30.000    30.000 ;;  1-  5:      atm     tcw11
tcw12     tcw12     tcw12
          5.771     3.867     5.303     1.670     8.643 ;;  6- 10:    tcw13     ptn21
ptn22     ptn23     ptn24
         18.486    12.832     1.904    17.070    15.000 ;; 11- 15:    ptn25     ptn26
tsw31     tsw32     tsw32
         10.000    10.000     7.734     6.000     6.000 ;; 16- 20:    tsw32     tsw32
tsw33     tsw33     tsw33
          6.000     6.000     6.000     6.000     6.000 ;; 21- 25:    tsw33     tsw33
tsw33     tsw33     tsw33
          6.000     6.000     6.000     6.000     3.000 ;; 26- 30:    tsw33     tsw33
tsw33     tsw33     tsw33
          3.000     3.000     3.000     1.500     2.000 ;; 31- 35:    tsw33     tsw33
tsw33     tsw34     tsw34
```

```
          1.000     1.000     0.500     0.300     0.200 ;; 36- 40:    tsw34     tsw34
tsw34     tsw34     tsw34
          0.200     0.200     0.200     0.200     0.200 ;; 41- 45:    tsw34     tsw34
tsw34     tsw34     tsw34
          0.200     0.200     0.200     0.200     0.200 ;; 46- 50:    tsw34     tsw34
tsw34     tsw34     tsw34
          0.108     0.242     0.400     0.759     0.760 ;; 51- 55:    tsw34     tsw34
tsw34     tsw34     tsw34
          0.425     0.403     0.403     0.800     1.200 ;; 56- 60:    tsw34     tsw34
tsw34     tsw34     tsw34
          1.500     2.500     3.000     3.000     6.000 ;; 61- 65:    tsw34     tsw34
tsw34     tsw34     tsw34
          3.656     6.000     6.000     6.000     6.000 ;; 66- 70:    tsw34     tsw35
tsw35     tsw35     tsw35
          6.000     6.000     6.000     6.000     6.000 ;; 71- 75:    tsw35     tsw35
tsw35     tsw35     tsw35
          6.000     6.000     6.000    10.000    10.000 ;; 76- 80:    tsw35     tsw35
tsw35     tsw35     tsw35
          9.756    15.000    20.000     1.992    18.486 ;; 81- 85:    tsw35     tsw36
tsw36     tsw36     tsw37
         16.699     1.904    16.787    21.299    21.299 ;; 86- 90:    tsw38     tsw9v
ch1z       ch2z      ch3z
         21.299    21.299    17.461    12.949     8.320 ;; 91- 95:     ch4z      ch5z
ch6z        pp4       pp3
       1.0e-30                                          ;; 96- 96:       wt
      )
      (mat
         (atm       atm       1  nx  1  ny   1   1)
         (tcw11         f-tcw11       1  nx  1  ny   2   2)
         (tcw12         f-tcw12       1  nx  1  ny   3   5)
         (tcw13         f-tcw13       1  nx  1  ny   6   6)
         (ptn21         f-ptn21       1  nx  1  ny   7   7)
         (ptn22         f-ptn22       1  nx  1  ny   8   8)
         (ptn23         f-ptn23       1  nx  1  ny   9   9)
         (ptn24         f-ptn24       1  nx  1  ny  10  10)
         (ptn25         f-ptn25       1  nx  1  ny  11  11)
         (ptn26         f-ptn26       1  nx  1  ny  12  12)
         (tsw31         f-tsw31       1  nx  1  ny  13  13)
         (tsw32         f-tsw32       1  nx  1  ny  14  17)
         (tsw33         f-tsw33       1  nx  1  ny  18  33)
         (tsw34         f-tsw34       1  nx  1  ny  34  66)
         (tsw35         f-tsw35       1  nx  1  ny  67  81)
         (tsw36         f-tsw36       1  nx  1  ny  82  84)
         (tsw37         f-tsw37       1  nx  1  ny  85  85)
         (tsw38         f-tsw38       1  nx  1  ny  86  86)
         (tsw9v         f-tsw9v       1  nx  1  ny  87  87)
         (ch1z          f-ch1z        1  nx  1  ny  88  88)
         (ch2z          f-ch2z        1  nx  1  ny  89  89)
         (ch3z          f-ch3z        1  nx  1  ny  90  90)
         (ch4z          f-ch4z        1  nx  1  ny  91  91)
         (ch5z          f-ch5z        1  nx  1  ny  92  92)
         (ch6z          f-ch6z        1  nx  1  ny  93  93)
         (pp4           f-pp4         1  nx  1  ny  94  94)
         (pp3           f-pp3         1  nx  1  ny  95  95)
         (wt        f-pp3          1  nx  1  ny  96  96)
         (hstrk     f-tsw34   1  nx  1  ny  34  61)
         (dr        f-dr      1   1  1  ny  41  41)
         (dr        f-dr      1   3  1  ny  42  42)
         (dr        f-dr      1   4  1  ny  43  44)
         (dr        f-dr      1   5  1  ny  45  46)
         (dr        f-dr      1   6  1  ny  47  49)
         (dr        f-dr      1   7  1  ny  50  54)
         (dr        f-dr      1   6  1  ny  55  55)
         (dr        f-dr      1   5  1  ny  56  56)
         (wp        lsnf      1   1  1  ny  52  52)
         (wp        lsnf      1   2  1  ny  53  53)
         (wp        lsnf      1   3  1  ny  54  56)
         ;; invert
         (in        f-invert1 1   4  1  ny  57  57)
         (in        f-invert2 1   2  1  ny  58  58) ;; bottom of invert
      )
       ) ;; end continuum
    ) ;; end multi-continua
```

```
  ) ;; end genmsh

;; ************************Down stream
weighting*****************************************************
;;  (downstream-mob
;;       (liquid
;;           (crange ("ptn*.m#*" "tsw*.m#*"))
;;       ) ;; end liquid
;;  ) ;; end downstream-mob

;; ********************** Solver options
************************************************************
(include "/data30/TSPA01/run_control_param/run_control_param_LDTH-v09")

);; end of model input

;; ******************** Done
!************************************************************
```

SDT submodel

The SDT submodel has the following information in this order:

1. Header information (lines preceded by a semicolon)
2. Time information (start time, stop time, timestepsize)
3. Output information (for ".ext" time-history output this is a readable by XTOOL v10.1)
4. Material properties (calls a rocktab file, see Attachment IV)
5. Heat generation information (calls a heatgen file, see Attachment III)
6. Boundary-conditions
7. Initial conditions ("state" command)
8. SDT-submodel mesh file (calls an SDT-submodel mesh file, see Attachment I)

All parameter values are taken directly from inputs or calculations described in other attachments. An example of an SDT-submodel NUFT input file (P5415C8-SDT27-00-01.in) follows. For more information, see the NUFT documentation (Nitao 1998). SDT submodel input files follow the naming convention P(x)R(y)C(z)-SDT(aml)-00-01.in. Note that only one set of SDT submodels to cover all three infiltration flux cases (lower-bound, mean, and upper-bound), thus, there are 540 input files, which includes 108 initialization runs and 324 postemplacement runs. These files can be found in DTN: LL030808623122.036.

```
;; /data34/TSPA03/chimney_mesh/SDT/preliminary_DTN/P5R16C8-SDT27-00-01.in was produced
on
;; Wed Apr 23 09:48:11 PDT 2003
;; Conduction-only for smeared-heat-source cases
;; AML = 27 MTU/acre; half drift spacing = 81.00 m
;; use tcond_wet for both solid and gas pgases.

;;  P5R16C8.col.units

;;  COLUMN INFORMATION (x,y =   171137.797,   232234.609) WORLD COLUMN q47

;;  unitthickness (m)
;;  _________________

;;  tcw11        0.000
;;  tcw12       68.320
;;  tcw13        5.039
;;  ptn21        3.105
;;  ptn22        0.000
;;  ptn23        0.000
```

```
;;  ptn24        3.809
;;  ptn25        3.867
;;  ptn26       10.195
;;  tsw31        1.992
;;  tsw32       32.041
;;  tsw33       69.281
;;  tsw34       35.906
;;  tsw35       86.696
;;  tsw36       43.164
;;  tsw37       21.553
;;  tsw38        9.082
;;  tsw9v        9.023
;;  tsw9z        0.000
;;  ch1v    22.529
;;  ch1z     0.000
;;  ch2v    14.326
;;  ch3v    14.326
;;  ch4v     0.000
;;  ch5v    14.326
;;  ch2z     0.000
;;  ch3z     0.000
;;  ch4z    14.355
;;  ch5z     0.000
;;  ch6v     0.000
;;  ch6z    14.971
;;  pp4      8.643
;;  pp3     33.545
;;  pp2     23.760
;;  pp1     25.049
;;  bf3      0.000
;;  bf2      0.000
;;  tr3      0.000
;;  tr2      0.000

;;  repository elevation (m):                    1091.500
;;  host rock:                               tsw34

;;  meters of host rock (tsw34) above repository:              29.906
;;  meters of host rock (tsw34) below repository:               6.000

;;  overburden thickness (m):                      227.556
;;  distance from repository plane to top of chn (m):          175.518
;;  distance from repository plane to top of water table (m):      361.347

 (usnt
  (title "AML=27mtu_acre,SDT27,00")
  (modelname usnt)

(include-pkg "thermcon.pkg") ;; single-comp (air), single-phase (gas) pkg for cond-
only run
  (tstop 20100y)
  (time 0)
  (stepmax 1000000)
  (dtmax 1.728e+18)
  (dt 1e2)

;;
*******************************************************************************
*************

(output
    (XTOOL (variables T)
            (file-ext ".ext")(range "*")
        (outtimes
```

```
                        (include "/data34/TSPA03/outputTimes/outputTimes-LDTH-SDT-DDT-
27-01")

             )
        )
  )

;;*****************************************************************************
***************
  (rocktab
        (include "/data34/TSPA03/physical_properties/SDT-1Dds-03")
;;      (include "noSubUnits")
  ) ;; close rocktab
;;*****************************************************************************
***************

;;   There is no percolation for the conduction-only case
  (srctab
       (include "/data34/TSPA03/heatgen/SDT_LDTH_blocks/preliminary_DTN/P5R16C8_LDTH-
SDT")
  ) ;; end srctab
;;*****************************************************************************
***************

;; set boundary conditions
  (bctab
    (atmos
        (range  "at*")
                (clamped)
    )
    (gwater
        (range  "wt*")
                (clamped)
    )
    ) ;; end bctab

;;*****************************************************************************
*****************
   (state
        (include "/data34/TSPA03/SDT/SDT66/00/00i/P5R16C8-SDT-00i.ztable")
   )  ;; end state
;;*****************************************************************************
***************
   (genmsh
      (down 0. 0. 1.0)
      (coord rect)
      (dx    81.00)
      (dy    1.0)
      (dz
    1.0e-30   8.320  30.000  30.000   5.039 ;; 1 - 5:   atm tcw12   tcw12   tcw12
    tcw13
      3.105   3.809   3.867  10.195   1.992 ;; 6 - 10:  ptn21   ptn24   ptn25   ptn26
    tsw31
     12.041  10.000  10.000   3.281   6.000 ;; 11 - 15: tsw32   tsw32   tsw32   tsw33
    tsw33
      6.000   6.000   6.000   6.000   6.000 ;; 16 - 20: tsw33   tsw33   tsw33   tsw33
    tsw33
      6.000   6.000   6.000   6.000   6.000 ;; 21 - 25: tsw33   tsw33   tsw33   tsw33
    tsw33
      5.906   6.000   6.000   6.010   5.990 ;; 26 - 30: tsw34   tsw34   tsw34   tsw34
    tsw34
      6.000   6.000   6.000   6.000   6.000 ;; 31 - 35: tsw34   tsw35   tsw35   tsw35
    tsw35
      6.000   6.000   6.000   6.000   6.000 ;; 36 - 40: tsw35   tsw35   tsw35   tsw35
    tsw35
```

```
      6.000   6.000   6.000   6.000   4.348 ;; 41 - 45: tsw35   tsw35   tsw35   tsw35
    tsw35
      4.348  10.000  10.000  15.000   8.164 ;; 46 - 50: tsw35   tsw36   tsw36   tsw36
    tsw36
     20.000   1.553   9.082   9.023  22.529 ;; 51 - 55: tsw37   tsw37   tsw38   tsw9v
    ch1v
     14.326  14.326  14.355  14.326  14.971 ;; 56 - 60: ch2vch3vch4zch5vch6z
      8.643  30.000  30.000  30.000  30.000 ;; 61 - 65: pp4 pp3 pp3 pp2 pp1
    1.0e-30                  ;; 66 - 66:wt
)
(mat
    (    atm    atm 1   nx  1   ny  1   1)
    (  tcw12  tcw12 1   nx  1   ny  2   4)
    (  tcw13  tcw13 1   nx  1   ny  5   5)
    (  ptn21  ptn21 1   nx  1   ny  6   6)
    (  ptn24  ptn24 1   nx  1   ny  7   7)
    (  ptn25  ptn25 1   nx  1   ny  8   8)
    (  ptn26  ptn26 1   nx  1   ny  9   9)
    (  tsw31  tsw31 1   nx  1   ny  10  10)
    (  tsw32  tsw32 1   nx  1   ny  11  13)
    (  tsw33  tsw33 1   nx  1   ny  14  25)
    (  tsw34  tsw34 1   nx  1   ny  26  31)
    (  tsw35  tsw35 1   nx  1   ny  32  46)
    (  tsw36  tsw36 1   nx  1   ny  47  50)
    (  tsw37  tsw37 1   nx  1   ny  51  52)
    (  tsw38  tsw38 1   nx  1   ny  53  53)
    (  tsw9v  tsw9v 1   nx  1   ny  54  54)
    (   ch1v   ch1v 1   nx  1   ny  55  55)
    (   ch2v   ch2v 1   nx  1   ny  56  56)
    (   ch3v   ch3v 1   nx  1   ny  57  57)
    (   ch4z   ch4z 1   nx  1   ny  58  58)
    (   ch5v   ch5v 1   nx  1   ny  59  59)
    (   ch6z   ch6z 1   nx  1   ny  60  60)
    (    pp4    pp4 1   nx  1   ny  61  61)
    (    pp3    pp3 1   nx  1   ny  62  63)
    (    pp2    pp2 1   nx  1   ny  64  64)
    (    pp1    pp1 1   nx  1   ny  65  65)
    (     wt    pp1 1   nx  1   ny  66  66)
    (wp       tsw34 1   nx  1   ny  30  30)
  )
   ) ;; end genmsh

;;   Use this for the 1-D, 2-D cases
        (linear-solver d4vband)

);; end of model input
```

DDT submodel

The DDT submodel has the following information in this order:

1. header information (lines preceded by a semicolon)
2. time information (start time, stop time, timestepsize)
3. output information (for ".ext" time-history output this is a readable by XTOOL v10.1)
4. material properties (calls a rocktab file, see Attachment IV)
5. heat generation information (calls a heatgen file, see Attachment III)
6. boundary-conditions
7. restart file information
8. initial conditions
9. DDT mesh file

10. radcon information (calls file for doing thermal-radiation connections, see Attachment VI)
11. run control parameters

All parameter values are taken directly from inputs or calculations described in other attachments. An example of an DDT-submodel NUFT input file (P2WR5C10-DDT55-01-1e11.in) follows below. The interested reader is referred to the NUFT documentation (Nitao 1998) for specific details of this input file.

DDT submodel input files can be found in DTN: LL030808623122.036. The names of these files are:

```
P2WR5C10-DDT14-01v.in
P2WR5C10-DDT27-01v.in
P2WR5C10-DDT55-01v.in
P2WR5C10-DDT66-01v.in
P2WR5C10-DDT66-03.in
P2WR5C10-DDT55-03.in
P2WR5C10-DDT27-03.in
P2WR5C10-DDT14-03.in
```

```
;; Implicit DKM with active fracture concept (AFC)
;; NBS material properties from 1D drift-scale mean infiltration flux property set
;; AML = 54.82 MTU/acre; half drift spacing = 40.5 m
;; represents 8 WPs: 6 full WPs and 2 half WPs

;;  P2WR5C10.col.units

;;  COLUMN INFORMATION (x,y =   170730.297,   234912.719) WORLD COLUMN g_9

;;  unitthickness (m)
;;  ___________________

;;  tcw11        0.000
;;  tcw12       20.244
;;  tcw13        4.014
;;  ptn21        7.207
;;  ptn22        5.596
;;  ptn23        2.021
;;  ptn24       12.510
;;  ptn25       36.504
;;  ptn26       11.279
;;  tsw31        1.992
;;  tsw32       45.586
;;  tsw33       85.252
;;  tsw34       32.954
;;  tsw35      104.719
;;  tsw36       25.828
;;  tsw37       12.914
;;  tsw38       21.904
;;  tsw9v        0.000
;;  tsw9z        6.592
;;  ch1v     0.000
;;  ch1z    15.039
;;  ch2v     0.000
;;  ch3v     0.000
;;  ch4v     0.000
;;  ch5v     0.000
;;  ch2z    20.293
;;  ch3z    20.303
;;  ch4z    20.273
;;  ch5z    20.303
;;  ch6v     0.000
;;  ch6z    17.578
;;  pp4     19.688
```

```
;;  pp3     14.326
;;  pp2      4.102
;;  pp1      0.000
;;  bf3      0.000
;;  bf2      0.000
;;  tr3      0.000
;;  tr2      0.000

;;  repository elevation (m):                    1052.901
;;  host rock:                              tsw35

;;  meters of host rock (tsw35) above repository:              45.328
;;  meters of host rock (tsw35) below repository:              59.391

;;  overburden thickness (m):                     310.485
;;  distance from repository plane to top of chn (m):         126.629
;;  distance from repository plane to top of water table (m):      278.533

 (usnt
  (title "line-load,AML=55mtu_acre,P2WR5C10-DDT55-01")
  (modelname usnt)

(include-pkg "thermcon.pkg") ;; single-comp (air), single-phase (gas) pkg for cond-
only run

  (tstop  20100y)
  (time 50y)
  (stepmax 1000000)
  (dtmax 1.000e+25)
  (dt 1e2)
  (check-mult-con off)

;;
*******************************************************************************
*************
  (output
        (XTOOL (variables T )
                (file-ext ".EBS.ext")(range "hstrk*" "dr*" "dhlw*" "bwr*" "pwr*" "in*"
"ds*")
                (outtimes
                        (include "/data34/TSPA03/outputTimes/outputTimes-LDTH-SDT-DDT-
55-01")
                )
        )
   ) ;; end output

;;
*******************************************************************************
***********
(rocktab
      (include "/data34/TSPA03/physical_properties/SDT-1Dds-03")
      (include "/data34/TSPA03/physical_properties/DDT-EBS_Rev500")
) ;; close rocktab
;;
*******************************************************************************
***********

;;   There is no percolation for the conduction-only case
  (srctab
;;      (include "/data34/TSPA03/heatgen/multi-
package_7WP_Segment_Info_DDT_TSPA03_vent50y_remove93.2")
        (include "/data34/TSPA03/heatgen/DDT_blocks/preliminary_DTN/P2WR5C10_DDT")
  ) ;; end srctab

;;*****************************************************************************
***************

;; set boundary conditions
  (bctab
    (atmos
        (range  "at*")
                (clamped)
    )
```

```
    (gwater
        (range  "wt*")
                (clamped)
    )
    ) ;; end bctab

;;*************************************************************************************
*****************
   ;; set initial conditions.
    (read-restart (time 50y)
    (file "/data34/TSPA03/DDT/DDTlab/01v/P2WR5C10-DDT55-01v.res"))

;;*************************************************************************************
****************
;;This is for a unit symmetry cell with a half drift and half pillar
;;between drifts.
  (genmsh
    (down 0. 0. 1.0)
    (coord rect)
       ;; 54.82 MTU/acre
          (dx 0.7285 0.5125 0.015 0.4187 0.4222 0.350 0.3031 0.35 0.5 0.9 1.0 1.5 2.5
3.0 5.0  7.0  9.250)
          ;; the WP cross-sectional area is the same as for a 21-PWR AP WP with a
diameter of 1.644 m
          ;; the drip-shield width is 2.512 m ;; the drip-shield half-width is 1.256
m
          (dy     1.29125 1.29125  ;; 1/2 21-PWR AP    2.5825 m j = 1-2
                            0.1  ;; gap               0.1 m    j = 3
          1.30425 2.60850 1.30425  ;; 5-DHLW Long       5.217 m  j = 4-6
                            0.1  ;; gap               0.1 m    j = 7
          1.29125 2.58250 1.29125  ;; 21-PWR AP Hot    5.165 m  j = 8-10
                            0.1  ;; gap               0.1 m    j = 11
          1.29125 2.58250 1.29125  ;; 44-BWR AP        5.165 m  j = 12-14
                            0.1  ;; gap               0.1 m    j = 15
          1.29125 2.58250 1.29125  ;; 44-BWR AP        5.165 m  j = 16-18
                            0.1  ;; gap               0.1 m    j = 19
          0.89750 1.79500 0.89750  ;; 5-DHLW Short      3.59 m   j = 20-22
                            0.1  ;; gap               0.1 m    j = 23
          1.29125 2.58250 1.29125  ;; 21-PWR AP        5.165 m  j = 24-26
                            0.1  ;; gap               0.1 m    j = 27
          1.29125 1.29125          ;; 1/2 44-BWR AP    2.5825 m j = 28-29
          ) ;; total length of drift = 35.3320 m
      (dz
        1.0e-30    20.244     4.014     7.207     5.596  ;;  1-  5:      atm     tcw12
tcw13     ptn21     ptn22
          2.021    12.510     6.504    30.000    11.279  ;;  6- 10:    ptn23     ptn24
ptn25     ptn25     ptn26
          1.992    15.586    30.000    18.252    20.000  ;; 11- 15:    tsw31     tsw32
tsw32     tsw33     tsw33
         15.000    10.000    10.000     6.000     6.000  ;; 16- 20:    tsw33     tsw33
tsw33     tsw33     tsw33
          4.477     4.477     6.000     6.000     6.000  ;; 21- 25:    tsw34     tsw34
tsw34     tsw34     tsw34
          6.000     3.328     6.000     6.000     6.000  ;; 26- 30:    tsw34     tsw35
tsw35     tsw35     tsw35
          3.000     3.000     3.000     3.000     1.500  ;; 31- 35:    tsw35     tsw35
tsw35     tsw35     tsw35
          2.000     1.000     1.000     0.500     0.300  ;; 36- 40:    tsw35     tsw35
tsw35     tsw35     tsw35
          0.200     0.200     0.200     0.200     0.200  ;; 41- 45:    tsw35     tsw35
tsw35     tsw35     tsw35
          0.200     0.200     0.200     0.200     0.200  ;; 46- 50:    tsw35     tsw35
tsw35     tsw35     tsw35
          0.200     0.335     0.015     0.5975    0.7285 ;; 51- 55:    tsw35     tsw35
tsw35     tsw35     tsw35
          0.7285    0.2895    0.403     0.403     0.800  ;; 56- 60:    tsw35     tsw35
tsw35     tsw35     tsw35
          1.200     1.500     2.500     3.000     3.000  ;; 61- 65:    tsw35     tsw35
tsw35     tsw35     tsw35
          6.000     6.000     6.000     6.000     6.000  ;; 66- 70:    tsw35     tsw35
tsw35     tsw35     tsw35
          6.000     6.000     5.391     6.000     6.000  ;; 71- 75:    tsw35     tsw35
tsw35     tsw36     tsw36
```

```
          6.000     3.914     3.914     6.000     6.914  ;; 76- 80:    tsw36     tsw36
tsw36     tsw37     tsw37
         10.000    10.000     1.904     6.592    15.039  ;; 81- 85:    tsw38     tsw38
tsw38     tsw9z      ch1z
         20.000     0.293    20.303    20.273    20.303  ;; 86- 90:     ch2z      ch2z
ch3z      ch4z      ch5z
         17.578    19.688    14.326     4.102   1.0e-30  ;; 91- 95:     ch6z       pp4
pp3       pp2        wt
      )
      (mat
         (atm       atm     1  nx  1  ny   1   1)
         (tcw12     tcw12   1  nx  1  ny   2   2)
         (tcw13     tcw13   1  nx  1  ny   3   3)
         (ptn21     ptn21   1  nx  1  ny   4   4)
         (ptn22     ptn22   1  nx  1  ny   5   5)
         (ptn23     ptn23   1  nx  1  ny   6   6)
         (ptn24     ptn24   1  nx  1  ny   7   7)
         (ptn25     ptn25   1  nx  1  ny   8   9)
         (ptn26     ptn26   1  nx  1  ny  10  10)
         (tsw31     tsw31   1  nx  1  ny  11  11)
         (tsw32     tsw32   1  nx  1  ny  12  13)
         (tsw33     tsw33   1  nx  1  ny  14  20)
         (tsw34     tsw34   1  nx  1  ny  21  26)
         (tsw35     tsw35   1  nx  1  ny  27  73)
         (tsw36     tsw36   1  nx  1  ny  74  78)
         (tsw37     tsw37   1  nx  1  ny  79  80)
         (tsw38     tsw38   1  nx  1  ny  81  83)
         (tsw9z     tsw9z   1  nx  1  ny  84  84)
         ( ch1z         ch1z        1  nx  1  ny  85  85)
         ( ch2z         ch2z        1  nx  1  ny  86  87)
         ( ch3z         ch3z        1  nx  1  ny  88  88)
         ( ch4z         ch4z        1  nx  1  ny  89  89)
         ( ch5z         ch5z        1  nx  1  ny  90  90)
         ( ch6z         ch6z        1  nx  1  ny  91  91)
         (  pp4         pp4         1  nx  1  ny  92  92)
         (  pp3         pp3     1  nx  1  ny  93  93)
         (  pp2         pp2     1  nx  1  ny  94  94)
         (wt            pp2     1  nx  1  ny  95  95)
     (hstrk     tsw35       1  nx  1  ny  35  62)
     (dr        drift       1   1   1   ny  42  42)
     (dr        drift       1   3   1   ny  43  43)
     (dr        drift       1   4   1   ny  44  45)
     (dr        drift       1   5   1   ny  46  47)
     (dr        drift       1   6   1   ny  48  50)
     (dr        drift       1   7   1   ny  51  55)
     (dr        drift       1   6   1   ny  56  56)
     (dr        drift       1   5   1   ny  57  57)
;; WP1 half 21-PWR PWR AP WP
     (dro_wp1   dro_wp1     1   1   1   3   42  42)
     (dro_wp1   dro_wp1     1   3   1   3   43  43)
     (dro_wp1   dro_wp1     1   4   1   3   44  45)
     (dro_wp1   dro_wp1     1   5   1   3   46  47)
     (dro_wp1   dro_wp1     1   6   1   3   48  50)
     (dro_wp1   dro_wp1     1   7   1   3   51  55)
     (dro_wp1   dro_wp1     1   6   1   3   56  56)
     (dro_wp1   dro_wp1     1   5   1   3   57  57)
     (dri_wp1   dri_wp1     1   2   1   3   54  57)
     (ds_pwr1-1 drpshld 1   3   1   2   53  53)
     (ds_pwr1-1 drpshld 3   3   1   2   54  57)
     (pwr1-1    pwr     1   1   1   2   55  56)
     (dr    drift       1   1   3   3   55  56)
;; Gap1
     (dr    drift       1   1   3   3   55  56)
     (ds_gap1   drpshld 1   3   3   3   53  53)
     (ds_gap1   drpshld 3   3   3   3   54  57)
;; WP2 full 5-DHLW Long WP
     (dro_wp2   dro_wp2     1   1   4   7   42  42)
     (dro_wp2   dro_wp2     1   3   4   7   43  43)
     (dro_wp2   dro_wp2     1   4   4   7   44  45)
     (dro_wp2   dro_wp2     1   5   4   7   46  47)
     (dro_wp2   dro_wp2     1   6   4   7   48  50)
     (dro_wp2   dro_wp2     1   7   4   7   51  55)
     (dro_wp2   dro_wp2     1   6   4   7   56  56)
```

```
     (dro_wp2   dro_wp2     1   5   4   7   57  57)
     (dri_wp2   dri_wp2     1   2   4   7   54  57)
     (ds_dhlw-l1    drpshld 1   3   4   6   53  53)
     (ds_dhlw-l1    drpshld 3   3   4   6   54  57)
     (dhlw-l1   dhlw-l      1   1   4   6   55  56)
;; Gap2
     (dr    drift       1   1   7   7   55  56)
     (ds_gap2   drpshld 1   3   7   7   53  53)
     (ds_gap2   drpshld 3   3   7   7   54  57)
;; WP3 full 21-PWR AP Hot WP
     (dro_wp3   dro_wp3     1   1   8   11  42  42)
     (dro_wp3   dro_wp3     1   3   8   11  43  43)
     (dro_wp3   dro_wp3     1   4   8   11  44  45)
     (dro_wp3   dro_wp3     1   5   8   11  46  47)
     (dro_wp3   dro_wp3     1   6   8   11  48  50)
     (dro_wp3   dro_wp3     1   7   8   11  51  55)
     (dro_wp3   dro_wp3     1   6   8   11  56  56)
     (dro_wp3   dro_wp3     1   5   8   11  57  57)
     (dri_wp3   dri_wp3     1   2   8   11  54  57)
     (ds_pwr2-1 drpshld 1   3   8   10  53  53)
     (ds_pwr2-1 drpshld 3   3   8   10  54  57)
     (pwr2-1    pwr     1   1   8   10  55  56)
;; Gap3
     (dr    drift       1   1   11  11  55  56)
     (ds_gap3   drpshld 1   3   11  11  53  53)
     (ds_gap3   drpshld 3   3   11  11  54  57)
;; WP4 full 44-BWR AP WP
     (dro_wp4   dro_wp4     1   1   12  15  42  42)
     (dro_wp4   dro_wp4     1   3   12  15  43  43)
     (dro_wp4   dro_wp4     1   4   12  15  44  45)
     (dro_wp4   dro_wp4     1   5   12  15  46  47)
     (dro_wp4   dro_wp4     1   6   12  15  48  50)
     (dro_wp4   dro_wp4     1   7   12  15  51  55)
     (dro_wp4   dro_wp4     1   6   12  15  56  56)
     (dro_wp4   dro_wp4     1   5   12  15  57  57)
     (dri_wp4   dri_wp4     1   2   12  15  54  57)
     (ds_bwr1-1 drpshld 1   3   12  14  53  53)
     (ds_bwr1-1 drpshld 3   3   12  14  54  57)
     (bwr1-1    bwr     1   1   12  14  55  56)
;; Gap4
     (dr    drift       1   1   15  15  55  56)
     (ds_gap4   drpshld 1   3   15  15  53  53)
     (ds_gap4   drpshld 3   3   15  15  54  57)
;; WP5 full 44-BWR AP Adjusted WP
     (dro_wp5   dro_wp5     1   1   16  19  42  42)
     (dro_wp5   dro_wp5     1   3   16  19  43  43)
     (dro_wp5   dro_wp5     1   4   16  19  44  45)
     (dro_wp5   dro_wp5     1   5   16  19  46  47)
     (dro_wp5   dro_wp5     1   6   16  19  48  50)
     (dro_wp5   dro_wp5     1   7   16  19  51  55)
     (dro_wp5   dro_wp5     1   6   16  19  56  56)
     (dro_wp5   dro_wp5     1   5   16  19  57  57)
     (dri_wp5   dri_wp5     1   2   16  19  54  57)
     (ds_bwr2-1 drpshld 1   3   16  18  53  53)
     (ds_bwr2-1 drpshld 3   3   16  18  54  57)
     (bwr2-1    bwr     1   1   16  18  55  56)
;; Gap5
     (dr    drift       1   1   19  19  55  56)
     (ds_gap5   drpshld 1   3   19  19  53  53)
     (ds_gap5   drpshld 3   3   19  19  54  57)
;; WP6 full 5-DHLW Short WP
     (dro_wp6   dro_wp6     1   1   20  23  42  42)
     (dro_wp6   dro_wp6     1   3   20  23  43  43)
     (dro_wp6   dro_wp6     1   4   20  23  44  45)
     (dro_wp6   dro_wp6     1   5   20  23  46  47)
     (dro_wp6   dro_wp6     1   6   20  23  48  50)
     (dro_wp6   dro_wp6     1   7   20  23  51  55)
     (dro_wp6   dro_wp6     1   6   20  23  56  56)
     (dro_wp6   dro_wp6     1   5   20  23  57  57)
     (dri_wp6   dri_wp6     1   2   20  23  54  57)
     (ds_dhlw-s1    drpshld 1   3   20  22  53  53)
     (ds_dhlw-s1    drpshld 3   3   20  22  54  57)
     (dhlw-s1   dhlw-s      1   1   20  22  55  56)
```

```
;; Gap6
     (dr    drift       1   1   23  23  55  56)
     (ds_gap6   drpshld 1   3   23  23  53  53)
     (ds_gap6   drpshld 3   3   23  23  54  57)
;; WP7 full 21-PWR AP WP
     (dro_wp7   dro_wp7     1   1   24  27  42  42)
     (dro_wp7   dro_wp7     1   3   24  27  43  43)
     (dro_wp7   dro_wp7     1   4   24  27  44  45)
     (dro_wp7   dro_wp7     1   5   24  27  46  47)
     (dro_wp7   dro_wp7     1   6   24  27  48  50)
     (dro_wp7   dro_wp7     1   7   24  27  51  55)
     (dro_wp7   dro_wp7     1   6   24  27  56  56)
     (dro_wp7   dro_wp7     1   5   24  27  57  57)
     (dri_wp7   dri_wp7     1   2   24  27  54  57)
     (ds_pwr1-2 drpshld 1   3   24  26  53  53)
     (ds_pwr1-2 drpshld 3   3   24  26  54  57)
     (pwr1-2    pwr     1   1   24  26  55  56)
;; Gap7
     (dr    drift       1   1   27  27  55  56)
     (ds_gap7   drpshld 1   3   27  27  53  53)
     (ds_gap7   drpshld 3   3   27  27  54  57)
;; WP8 half 44-BWR AP WP
     (dro_wp8   dro_wp8     1   1   28  29  42  42)
     (dro_wp8   dro_wp8     1   3   28  29  43  43)
     (dro_wp8   dro_wp8     1   4   28  29  44  45)
     (dro_wp8   dro_wp8     1   5   28  29  46  47)
     (dro_wp8   dro_wp8     1   6   28  29  48  50)
     (dro_wp8   dro_wp8     1   7   28  29  51  55)
     (dro_wp8   dro_wp8     1   6   28  29  56  56)
     (dro_wp8   dro_wp8     1   5   28  29  57  57)
     (dri_wp8   dri_wp8     1   2   28  29  54  57)
     (ds_bwr1-2 drpshld 1   3   28  29  53  53)
     (ds_bwr1-2 drpshld 3   3   28  29  54  57)
     (bwr1-2    bwr     1   1   28  29  55  56)
     (in        invert      1   4   1   ny  58  58)
     (in        invert      1   2   1   ny  59  59)
      ) ;; end of material assignment

(radcon
      (surface-offset 0 0  0)
      (include "/data34/TSPA03/radcon/DDT/preliminary_DTN/P2WR5C10-DDT55-01_1e-
11.radcon")
) ;; close radcon
  ) ;; end genmsh

;; ********************** Solver options
************************************************************
(include "/data30/TSPA01/run_control_param/run_control_param_SMT-v02")

);; end of model input

;; ******************** Done
!****************************************************************
```

ATTACHMENT VI
LDTH- AND DDT-SUBMODEL THERMAL-RADIATION CONNECTION CALCULATION

INTENTIONALLY LEFT BLANK

ATTACHMENT VI
LDTH- AND DDT-SUBMODEL THERMAL-RADIATION CONNECTION CALCULATION

The LDTH and DDT submodels include heat transfer by thermal radiation inside the drift. The LDTH and DDT submodels represent thermal-radiative heat transfer between the drip shield, drift wall, and invert surfaces. The DDT submodels also represent thermal-radiative heat transfer between the waste package, drip shield, and invert surfaces beneath the drip shield. The determination of the thermal-radiation coefficients requires one direct input, which is the emissivity of the surfaces. The emissivity of the drift wall and invert surfaces is taken to be 0.9, which is in the middle of the range given for rocks (0.88 to 0.95) in Table A.11 of *Fundamentals of Heat and Mass Transfer* (Incropera and DeWitt 1996). The process of determining thermal-radiation connections for the LDTH and the DDT submodels is done by hand following these steps:

1. Compile a list of model gridblocks that have at least 1 face contacting air within the drift

2. For each pair of gridblocks in this list

   a. Determine if there is a clear path (line of sight between face centers) between the air contacting face of each block

   b. If a clear path exists, calculate the thermal-radiation coefficient for that connection and write a "radcon" entry in NUFT format (see *Reference Manual for the NUFT Flow and Transport Code, Version 2.0* (Nitao 1998))

      $$\text{coeff} = (\sigma\, e\, (N1 \times R)(-N2 \times R)\, A1\, A2) / \pi\, |R|^4$$

where:

σ = Stefans Constant
π = pi
e = emissivity
A1 = area of grid block face 1 (radiating)
A2 = area of grid block face 2 (connecting)
N1 = unit vector normal to face 1
N2 = unit vector normal to face 2
R = distance from center of face 1 to center of face 2

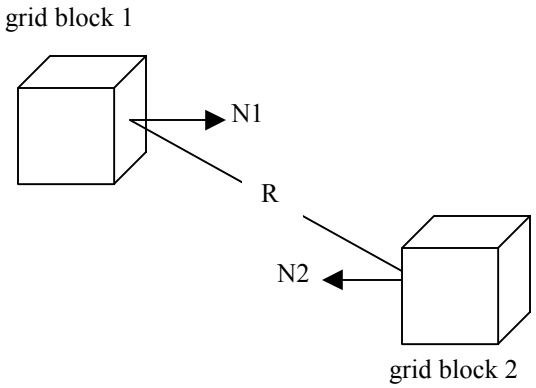

Radcon files are located in DTN: LL030808623122.036. The file names are:

```
P2WR5C10-DDT55-01_full.radcon
ldth0_300m.radcon
P2WR5C10-DDT55-01v.radcon
```

ATTACHMENT VII
EXTRACTION/MICROABSTRACTION PROCESS FOR MSTHAC (BUILDING VIRTUAL LDTH AND SDT "CHIMNEY" SUBMODELS)

INTENTIONALLY LEFT BLANK

ATTACHMENT VII
EXTRACTION/MICROABSTRACTION PROCESS FOR MSTHAC (BUILDING VIRTUAL LDTH AND SDT "CHIMNEY" SUBMODELS)

Extract MSTHAC v7.0 information from real LDTH and SDT "chimney" submodel output

For the first stage of the multiscale thermohydrologic model abstraction process, MSTHAC v7.0 reads the NUFT output files for the SMT, SDT, LDTH, and DDT submodels, extracts the requested time histories, and saves them to a MSTHAC v7.0 "extraction" file. In order to perform the extraction, a MSTHAC v7.0 input file is created using the format defined in the MSTHAC 7.0 user's manual. A set of input files is created for each LDTH-/SDT-submodel "chimney" location, with input files corresponding to each of the AMLs for which the LDTH and SDT submodels are run (e.g., AMLs of 66, 55, 27, and 14 MTU/acre). The resulting input files are run using MSTHAC 7.0.

Interpolate extracted real LDTH and SDT "chimney" submodel output to the SMT-submodel locations (virtual LDTH and SDT "chimney" submodel extraction files)

Note that 108 out of 2874 of the SMT-submodel repository-gridblock locations correspond to actual LDTH/SDT-submodel locations. As discussed in Attachement I, these 108 locations generally occur for every fourth emplacement drift (see Figure 6.2-3). LDTH/SDT submodels are always placed at the ends of drifts and are usually placed at one or two locations along the central portion of those drifts. For the other locations that lie in between the 108 LDTH/SDT-submodel locations, it is necessary to interpolate LDTH- and SDT-submodel results. These interpolated LDTH and SDT submodels are called "virtual" LDTH and SDT submodels.

The process of creating virtual LDTH and SDT "chimney" submodel extraction files is carried out with the use of chimney_interpolate v1.0. The software code chimney_interpolate v1.0 reads a control file that defines the following information: (1) name of a "real" chimney-submodel extraction file, (2) fractional weighting for this real chimney-submodel file (note that these weighting factors are the same as those used to interpolate percolation flux, as described in substep 6 of step 8 in Attachment I), (3) name of a second real chimney-submodel extraction file, (4) fractional weighting for this file and (5) the name of the virtual chimney-submodel extraction that will be created. Note that the two "real" chimney submodels straddle the target location where the interpolation occurs. The software code chimney_interpolate v1.0 does a simple linear interpolation between the two input files using the specified weights for each of the real chimney submodels.

The interpolation process is the same as that carried out for percolation flux (see substep 6 of step 8 of attachment I). The interpolation process is two step: (1) "row-wise" interpolation along the drifts containing real chimney submodels and (2) "column-wise" interpolation to obtain virtual chimney submodels for the drifts lying between the drifts containing the real chimney submodels. First, "virtual" LDTH and SDT submodels are interpolated for all intermediate locations along the emplacement drifts that contain "real" LDTH and SDT submodels. Once these drifts have all of the virtual LDTH and SDT submodels created for the entire row of SMT-submodel repository gridblocks, the "column-wise" interpolation process is conducted to create the virtual chimney submodels for the repository drifts lying between those with the real chimney submodels. The specified weighting factors for this linear interpolation process are the

same as those used in interpolating the percolation flux for the SMT-submodel repository gridblocks, as is described in Attachment I (see Substep 6 of Step 8). The output is a virtual chimney-submodel extraction file at each SMT-submodel location and for each AML (e.g., 66, 55, 27, and 14 MTU/acre). This process is only conducted for the SDT and LDTH submodels. There are approximately 69,000 such files created. These files can be found in DTN: LL030808523122.035. File names follow the conventions:

LDTH submodels: (panel #)#(i index):(j index)-LDTH(AML)-1Dds_mc-(percolation case)I-0(parameter case).m-f.EBS.ext.extract_LDTH_rev_14
SDT submodels: (panel #)#(i index):(j index)-SDT(AML)-00-01.ext.extract_SDT_rev_0

Create *.in files for each virtual NUFT LDTH "chimney" submodel

For the purposes of micro-abstraction, MSTHAC v7.0 requires the following: (1) the coordinates of the LDTH "chimney" submodels, (2) the real number for the AML (e.g., the real number for an AML of 66 MTU/acre is 65.784 MTU/acre), and (3) the present-day-, monsoonal-, and glacial-transition-climate percolation fluxes for that LDTH-submodel location. Note that 108 out of 2874 of the SMT-submodel repository-gridblock locations correspond to actual LDTH-submodel locations. For the other locations, interpolated LDTH- and SDT-submodel results are obtained; these interpolated LDTH and SDT submodels are called "virtual" LDTH and SDT submodels. To obtain this information, MSTHAC v7.0 reads a *.in file associated with each LDTH submodel. The format of the *.in file is specified by the NUFT user's manual (Nitao 1998) (see Attachment V), and the MSTHAC 7.0 user's manual specifies the required information for this file. A "virtual" LDTH-submodel *.in file is created for each SMT-submodel repository-gridblock location. Note that the only purpose for the virtual LDTH-submodel *.in files is to supply MSTHAC v7.0 with the percolation flux for the glacial-transition climate for each of the SMT-submodel repository gridblock locations. Although it is not required, the virtual LDTH-submodel *.in files also contain the percolation-flux values for the present-day and monsoonal climates as well. The percolation-flux values that were interpolated for each of the SMT-submodel repository gridblock locations (see substep 6 of step 8 in Attachment I), along with the coordinates of that location, are edited into each of the virtual LDTH-submodel *.in files with the use of scripts containing standard UNIX commands. There is a script for each of the three infiltration-flux cases: (1) create_virtual_in_SCRIPT_ma for the mean-infiltration-flux case, (2) create_virtual_in_SCRIPT_la for the lower-infiltration-flux case, and (3) create_virtual_in_SCRIPT_ua for the upper-infiltration-flux case. These three scripts, along with the instructions and control files for running these scripts, are found in DTN: LL030808523122.035. The names of these virtual LDTH-submodel *.in files use the following convention:

(panel #)#(i index):(j index)-LDTH(AML)-1Dds_mc-(infiltration-flux case)i-0(parameter case).in

Note that the infiltration-flux-case labels are:

1. mi, which stands for mean infiltration flux
2. ui, which stands for upper infiltration flux
3. li, which stands for lower infiltration flux

Note also that the i and j indices are those from the SMT submodel and that the Panel numbers are P1, P2E, P2W, P3, and P5 (see Figure 6.2-3). The parameter case is 2, which is for the modified-mean-infiltration-flux property set.

Run MSTHAC v7.0 at all SMT-submodel locations using virtual SDT and LDTH "chimney" submodel extraction files, in conjunction with DDT and SMT submodel extraction files

Once the virtual SDT- and LDTH-submodel extraction files have been created and the virtual LDTH-submodel *.in files have been created, MSTHAC v7.0 can be run to generate the micro-abstraction output file at each SMT-submodel location. This process also requires DDT-submodel extraction files, as well as the SMT-submodel extraction file. This process is carried out by first creating an abstraction MSTHAC v7.0 input file, as defined in the MSTHAC 7.0 user's manual. Once the input files are created, MSTHAC 7.0 is run with these files as input and the micro-abstraction output files are generated at each SMT-submodel location.

INTENTIONALLY LEFT BLANK

ATTACHMENT VIII
BINNING CALCULATIONS

INTENTIONALLY LEFT BLANK

ATTACHMENT VIII
BINNING CALCULATIONS

Bin Indexes

Bin indexes were calculated for each SMT-submodel location based on the rank of the percolation flux associated with the location. The general calculation procedure is as follows:

1. Sort SMT-submodel locations by ascending values of percolation flux
2. Calculate quantile values for each sorted point according to the rank of the point in the sorted data set
3. Assign bin indexes according to quantile intervals.

Binning was performed according to specifications provided by the Performance Assessment Department. Glacial-transition climate state (median case) was specified as the percolation flux source. Binning quantiles were as follows:

Bin Index	Quantile Range
Bin 1	less than 5 percent
Bin 2	greater than or equal to 5 percent less than 30 percent
Bin 3	greater than or equal to 30 percent less than 70 percent
Bin 4	greater than or equal to 70 percent less than 95 percent
Bin 5	greater than or equal to 95 percent

Bin indexes were calculated for each of the 2,874 SMT-submodel locations.

Bin the MSTHAC v7.0 output and reformat it for TSPA

After all 2,874 MSTHAC v7.0 microabstractions have been created for a particular percolation case, the output is processed to produce the set of information required by TSPA. To facilitate their work, TSPA requires the micro-abstraction to be processed two different ways: "WAPDEG" binning and "TSPA" binning. Note that WAPDEG is a process model that uses MSTHM output. Because the WAPDEG model is downstream of the MSTHM (with respect to model-to-model parameter flow, WAPDEG does not produce any output required by the MSTHM. The total binned files are:

22,992 (from WAPDEG) + 5,748 (from TSPA) = 28,740

WAPDEG Binning

The first processing (WAPDEG binning) involves reporting the T_wp, RH_wp, T_ds and RH_ds for each SMT-submodel location and each waste package type. There are 8 waste package types which form two waste package groups:

Group1 : DHLW : dhlw-l1, dhlw-s1

Group2 : CSNF : pwr1-1, pwr2-1, bwr1-1, bwr2-1, pwr1-2, bwr1-2

For WAPDEG purposes, we are interested in each repository location and each waste package type, therefore, there are 2,874 locations × 8 waste package type = 22,992 typical waste packages reported.

Since the WAPDEG binning produces a large number of output files, the files are concatenated using a UNIX shell script so that all locations falling within a bin and all waste packages of a given type (CSNF or DHLW) are include in a single file. This process creates 5 (# of bins) × 2 (number of waste package groups) = 10 output files for delivery. A second set of 10 files is provided in the WAPDEG format that only uses the "typical waste package" as explained below. Hence a total of 20 WAPDEG files are provided for each infiltration flux case.

TSPA Binning

The second process (TSPA binning) involves determining the most typical location given a set of locations that define a "bin". For TSPA purposes, we are interested in the most typical waste package (see below) in a group / bin, therefore, there are 5 bins × 2 groups = 10 typical waste packages reported. A bin is a set of SMT-submodel locations that have similar percolation values and is defined by the TSPA organization. For the purposes of this processing, the waste packages are grouped into two waste package type groups (CSNF and DHLW). For each bin, two output files are created, one for the most typical CSNF package and one for the most typical DHLW package. There are 5 (# of bins) × 2 (waste package groups) files created for this type of processing. This results in an additional 2,874 locations × 2 waste package groups = 5,748 files.

The TSPA binning results of typical waste packages are concatenated using a UNIX shell so that all locations falling within a bin and all waste packages of a given type (CSNF or DHLW) are included in a single file. This process creates 5 (# of bins) × 2 (number of waste package groups) = 10 output files for delivery.

Typical Waste Package Determination

The most typical package is selected by compiling for each waste package type and bin member, peak waste package temperature, and duration of boiling at the drift wall. These datum are sorted from low to high, and a percentile assigned to each. For each waste package type and location in the list, the typical package is the one who is most median on the two parameter spaces.

To do this processing, reformat_EXT_to_TSPA v1.0 is used. The software code reformat_EXT_to_TSPA v1.0 takes the name of an input file as its only input. The format of this file is defined in the software code reformat_EXT_to_TSPA v1.0 user's manual.

Binning files are delivered as output from reformat_EXT_to_TSPA v1.0.

Binning Algorithm

For each location in a bin and waste package in a waste package group:

1. Calculate peak waste package temperature
2. Calculate boiling duration at the waste package
3. Sort peak waste package temperature from high to low
4. Sort boiling duration from low to high
5. Assign percentile rank to each waste package temperature
6. Assign percentile rank to each boiling duration

For each included waste package type / location in the bin:

1. Calculate deviation of percentile rank from median (50 percent) for peak waste package temperature
   a. if current loc/waste package type is ranked 47 percent, deviation = 0.50 – 0.47 = 0.03
2. Calculate deviation of percentile rank from median (50 percent) for boiling duration
   b. if current loc/waste package type is ranked 54 percent, deviation = 0.50 – 0.54 = –0.04
3. Calculate sum of squared deviations from Step 1 and 2
   c. $0.03^2 + 0.04^2 = 0.0025$

For the current bin / waste package group, select the waste package/location with the smallest squared deviation (this is the most typical package).

INTENTIONALLY LEFT BLANK

ATTACHMENT IX
MULTISCALE MODEL APPROACH TO THERMOHYDROLOGY AT YUCCA MOUNTAIN

INTENTIONALLY LEFT BLANK

ATTACHMENT IX
MULTISCALE MODEL APPROACH TO THERMOHYDROLOGY AT YUCCA MOUNTAIN

MSTHM Concept

The MSTHM approach breaks the solution of thermohydrologic modeling at Yucca Mountain into smaller pieces by varying dimensionality requirements (one-, two-, or three-dimensional) as needed for detail. The MSTHM approach subdivides the problem into thermal and thermohydrologic submodels. By subdividing the problem into more tractable pieces, more efficient thermal-conduction and thermal-radiation submodels are used to address the three-dimensional nature of the heated repository footprint and mountain-scale heat flow and the three-dimensional geometric details of the engineered components in the emplacement drifts, waste-package-to-waste-package heat-generation variability, and drift-scale heat flow. Two-dimensional thermohydrologic models, which are much more efficient than three-dimensional thermohydrologic models, are used to model all thermohydrologic variables in detail, within the emplacement drifts and in the adjoining host rock.

MSTHM Spatial Scales

Two spatial scales are considered for the MSTHM: (1) a mountain scale (on the order of hundreds to thousands of meters) and (2) a drift-scale (on the order of fraction of meters). Drift-scale modeling includes the coupling of drift-scale processes both within the engineered barrier system and within the near field environment. Mountain-scale processes are needed to account for the influence of the ground surface, the water table, and most importantly, the influence of repository edge cooling effects. In addition to coupling the drift scale and mountain scale, the MSTHM also allows for consideration of the effect of different waste package types (e.g., different CSNF waste packages, co-disposal of DHLW) on the various performance measures.

MSTHM Submodels

The MSTHM simulates processes under a range of heat loading conditions to capture the edge effects within the repository and the discrete nature of waste packages. MSTHM simulates at various locations within the domain to account for variations in stratigraphy and infiltration. This is accomplished by simultaneously solving four “submodels” at different spatial scales. These four submodels comprising the MSTHM are categorized into four NUFT submodel types (SMT, SDT, DDT, and LDTH) The MSTHM also results in two MSTHAC v7.0 models (LMDH and DMTH). A consistent naming convention is used for these submodels. The first letter applies to the thermal loading where S is the “smeared” area averaged heat loading, L is the “line” heat loading, and D is the “discrete” point heat loading. The second letter applies to the spatial scaling where M is the “mountain” scale and D is the “drift” scale. The last letters refer to the variables considered where T indicates that only “thermal conduction” variables are considered and where thermohydrologic indicates that all “thermohydrologic” variables are considered.

The four different NUFT submodels (listed below) are solved simultaneously at different spatial scales:

- **SMT Submodel** – The 3D smeared-source mountain-scale thermal-only submodel.
- **LDTH Submodel** – The line-source drift-scale thermal-hydrology submodel.
- **SDT Submodel** – The one-dimensional smeared-source drift-scale thermal-only submodel.
- **DDT Submodel** – The three-dimensional discrete-source drift-scale thermal-only submodel.

The MSTHM processes the four NUFT submodels using MSTHAC v7.0 to produce the two following models:

- **LMTH Model** – The intermediary three-dimensional line-source mountain-scale thermohydrologic model.
- **DMTH Model** – The final three-dimensional discrete-source mountain-scale thermohydrology model.

Figure IX-1 illustrates the general conceptual relation between the four NUFT submodels (identified by red text) and the two MSTHAC v7.0 submodels (identified by blue text). The successive nature of the NUFT submodel execution followed by the MSTHAC v7.0 calculation for final output is illustrated in the flowchart of Figure IX-2.

The fundamental concept behind MSTHM is that two-dimensional representations of drift-scale thermal-hydrology (the LDTH submodels) can account for mountain-scale edge cooling processes by changing horizontal distance of the adiabatic boundary in the drift-scale model. For locations within an infinite (x and y) expansive repository, the drift-scale model adiabatic boundary distance would be the half-way point between drifts. Edge effects within the model are accommodated by allowing the adiabatic boundaries to extend in time to mimic the cooling process. The distance to the adiabatic boundary is measured using the areal mass loading (AML) factor, which reports the heat input per unit area (reported in metric tonnes of uranium/acre, MTU/acre). As the distance to the adiabatic boundary increases, the AML decreases.

The relation between the time-varying AML at any given point in the repository is determined by interpolating the necessary width to the adiabatic boundary needed for an SDT submodel at the point to match the SMT-submodel-predicted temperature. This is merely a superposition process justified by the linear nature of the conduction-only energy equation. Once this AML history is established, it is applied to the LDTH submodel which introduces the dimensionality of the heat source (a waste package) and the hydrology of the system. The final component of MSTHM is the inclusion of thermal-radiative heat transfer with the DDT submodel. Here the temperature redistribution due to the variation between hotter waste packages, colder waste packages, and gaps between waste packages for one location in the repository is determined. This temperature difference is then applied to the two-dimensional thermohydrologic results to give complete thermohydrologic histories for all locations and all waste packages within the repository.

MSTHM Model Process

The MSTHM can be subdivided into the two specific "steps" illustrated in Figure IX-2. Step 1 is the simultaneous execution of the four NUFT submodels. Step 2 is the assembly of the NUFT submodel results into final MSTHM results through the use of MSTHAC v7.0. These processes are discussed in detail below.

STEP 1: NUFT Submodel Execution

A three-dimensional SMT-submodel simulation determines the temperature history for specific simulated repository life-cycle event. This three-dimensional conduction-only submodel has the total energy of the repository delivered over a smeared heat-source. Taking advantage of the fact that the transient conduction equation is linear and super-positional, the temperature generated at any given location of the 3D SMT submodel at any given point in time can be simulated by a one-dimensional SDT conduction-only submodel of a certain heat input. This heat input can be characterized as the "emplaced heat input" divided by the lateral "width" of drift that the SDT heating occurs resulting in an areal heat loading, referred to here as an AML. By superposing SDT submodels to create an SMT-submodel temperature, an AML-varying history referred to as an $AML_{hstr,eff}$ can be used to describe the heat-up and cool-down of that particular location of the repository. MSTHM accomplishes at each *chimney location* in the repository area, a two-dimensional LDTH submodel solves for thermohydrologic processes (e.g., percolation rates, hydrologic properties). At each location, an AML curve is generated which describes the temperature history due to a specified heat input to the LDTH submodel.

The three-dimensional SMT and the one-dimensional SDT submodels solve for thermal conduction only and both share the same smeared-heat-source approximation and thermal-conduction representation of heat flow. The one-dimensional SDT submodels are executed at the same 108 locations and for the same AMLs as are the LDTH submodels providing a linkage between the SMT and the LDTH submodels. The common repository location of the SDT submodel and LDTH submodel drift wall temperatures allows for the SMT submodel temperature to be corrected for both the influence of thermohydrologic processes on temperature and for the influence of two-dimensional drift-scale dimensionality (orthogonal to the axis of the drift). This is accomplished by interpolating between AML histories. The SMT, SDT, and LDTH submodels share a blended heat-generation history of the entire waste package repository; hence, the heat-generation history is effectively that of an average waste package.

The three-dimensional DDT submodel is a drift-scale submodel, which includes individual waste packages with distinct heat-generation history. The DDT submodel solves for thermal conduction and accounts for thermal radiation in addition to thermal conduction between the waste package and drift surfaces. The drift wall temperatures for an average waste package, calculated with the combined use of the LDTH, SMT, and SDT submodels, are then further modified to account for waste-package-specific deviations using the DDT submodel.

One complete MSTHM simulation requires multiple NUFT submodel executions to simulate the entire repository. Each MSTHM simulation includes the following NUFT submodel executions:

- 1 SMT-submodel execution for the mountain
- 1 DDT-submodel × 4 AMLs execution at one location in the repository
- N SDT-submodel locations × 4 AMLs
- N LDTH-submodel locations × 4 AMLs.

STEP 2: MSTHM assembly process

The use of MSTHAC v7.0 to assemble the execution results of the NUFT submodels into final output is the second part of MSTHM process (see Figure IX-2). MSTHAC v7.0 assembles the execution results from the submodels at the N locations within the repository creating time-varying AML curves.

The MSTHM assembly process can be broken into six calculation stages which center on the construction of two time-varying AMLs: an effective AML for the host rock ($AML_{hstrk,eff}$) and a specific AML ($AML_{specific}$) for specific waste package locations along the drift. The $AML_{hstrk,eff}$ varies spatially and temporally and is the interpolated AML that would be prescribed for an insulated heat submodel (SDT) to predict the temperature produced by a mountain-scale submodel (SMT). The $AML_{specific}$ incorporates the discrete nature of the waste packages using the DDT submodel. Both AMLs are used to interpret LDTH-submodel results to the LMTH and DMTH models. The six-stage process of MSTHM assembly is illustrated as an overview in Figure IX-2. Each stage is explained in detail below in conjunction with Figures IX-3 through IX-7.

Assembly Stage 1: Assemble $AML_{hstrk,eff}$ (Figure IX-3)

The SDT-submodel temperature histories are plotted for each of the N spatial locations for a "family" of four AMLs (66, 55, 27, and 14 MTU/acre for this model report). For each spatial location, the plotted family of SDT-submodel temperature histories is plotted against the time history of the temperature from the SMT submodel. The $AML_{hstrk,eff}$ is interpolated by determining the AML needed for the SDT submodel to generate the SMT temperature at any given time.

Assembly Stage 2: Interpolate LMTH (Figure IX-4)

The LMTH results are determined by taking the thermohydrologic output from the LDTH submodels and plotting the time-history of the variables for each of the family of AMLs. First for each of the N locations, the thermohydrologic output history from the LDTH submodel is plotted for each of the four AMLs. Second, the thermohydrologic history for the LMTH at any given time t* is determined by interpolating the thermohydrologic value at $AML_{hstrk,eff}(t^*)$ from the LDTH histories (note that the LDTH and DDT submodels include radiative heat transfer between the waste package, drip shield, and drift wall surfaces). As radiative heat transfer is proportional to the temperature difference between two surfaces raised to the fourth power, i.e., ΔT^4, linear interpolation between two bounding AML curves is not sufficient to accurately calculate a result. To address this issue, MSTHM submodels are run at a variety of AMLs.

Hence, interpolations are performed over a small enough range that piecewise linear interpolation adequately characterizes the underlying nonlinear process of radiative heat transfer.

Assembly Stage 3: Calculate DMTH (Figure IX-5)

The discrete thermohydrologic values are calculated from the LMTH submodel by incorporating the DDT submodel temperature results. Here, the temperature variation along the average temperature of the LMTH submodel accounts for differences in waste package loading. The temperature difference is calculated using the $AML_{hstrk,eff}$ and the temperature from the DDT submodel. This difference is then superimposed on the LMTH submodel to yield DMTH submodel results.

Assembly Stage 4: Assembling AMLspecific (Figure IX-6)

The procedure for assembling $AML_{specific}$ is very similar to that of assembling $AML_{hstrk,eff}$. The temperature history from the LDTH submodel is plotted for each of the N spatial locations for a "family" of four AMLs (66, 55, 27, and 14 MTU/acre). Along with the family of LDTH submodel temperature histories at each spatial location is plotted the time history of the temperature from the DMTH model. The $AML_{specific}$ is interpolated by determining the AML needed for the LDTH submodel to generate the DMTH- model temperature at any given time.

Assembly Stage 5: Interpolate Thermohydrologic Variables for DMTH (Figure IX-7)

The DMTH results are determined by taking the thermohydrologic output from the LDTH submodels and plotting the time-history of the variables for each of the family of AMLs. First for each of the N locations, the thermohydrologic output history from the LDTH submodel is plotted for each of the four AMLs. The thermohydrologic history for the DMTH at any given time t* is determined by interpolating the thermohydrologic value at $AML_{specific}(t^*)$ from the LDTH histories.

Assembly Stage 6: Determine Relative Humidity for the Waste Package and Drip Shield

The relative humidity on top of the drip shield and on the waste package is calculated as a function of the saturated pressures in the drift.

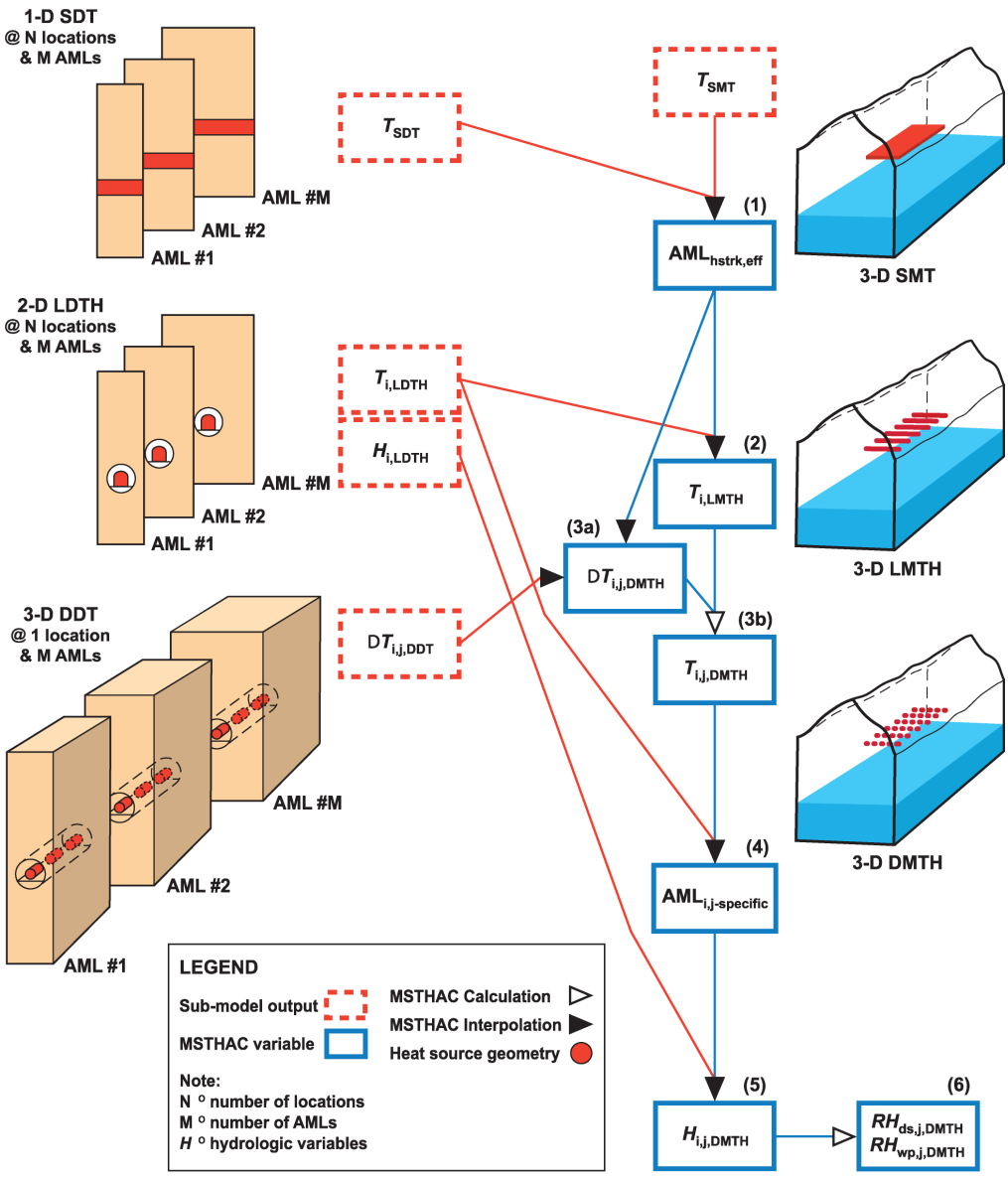

Figure IX-1. Six-stage flow chart diagram of the Multiscale thermohydrologic Model (MSTHM). SDT, LDTH, and DDT submodels are run a different AMLs (left side). SMT, LMTH, and DMTH models are the series of three-dimensional mountain-scale models of increasing complexity (right side). The six stages illustrate the process of constructing intermediate variables.

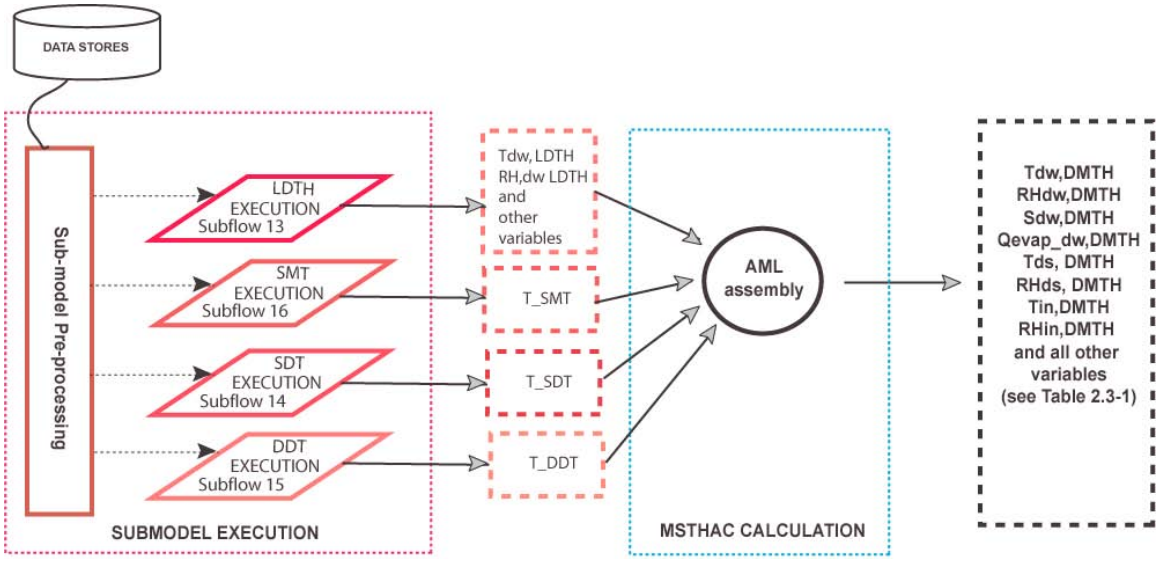

Figure IX-2. MSTHM flowchart is shown in two steps: (1) NUFT submodel execution in red, and (2) MSTHM processing of final output using MSTHAC v7.0 (blue).

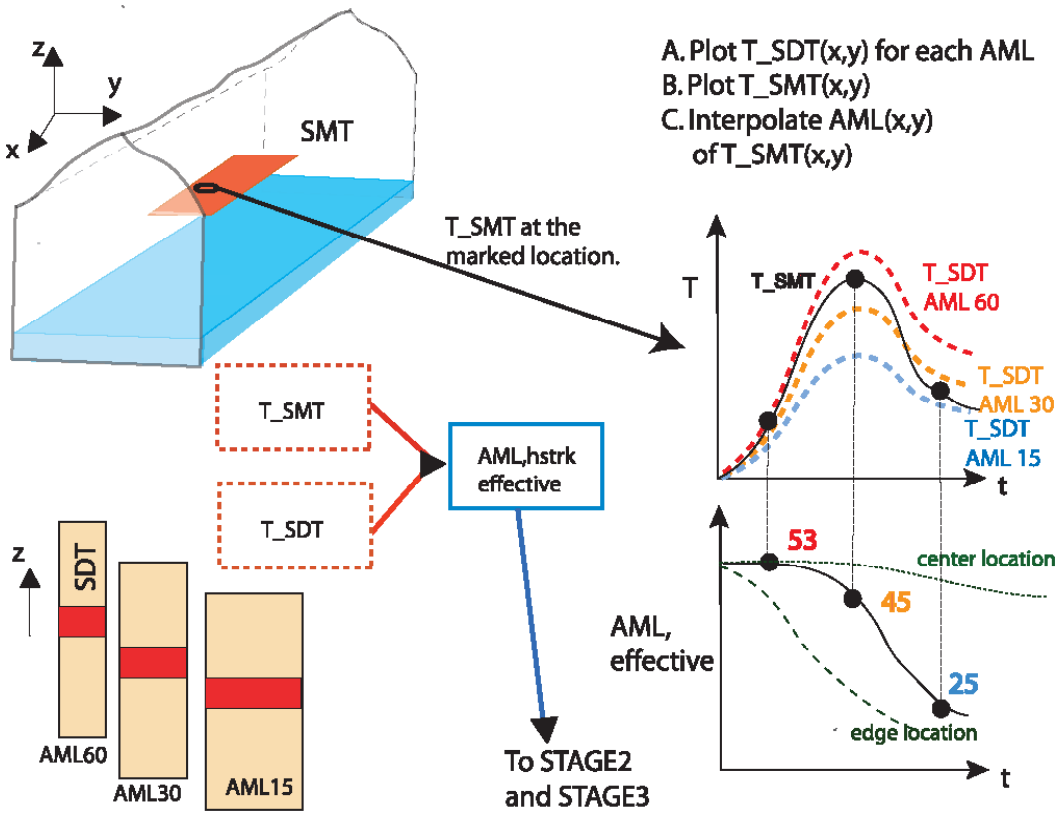

Figure IX-3. MSTHM Stage 1 involves the interpolation of the variable AMLeffective from the SMT-submodel temperature T_SMT and the family of SDT-submodel temperatures T_SDT at three different AMLs.

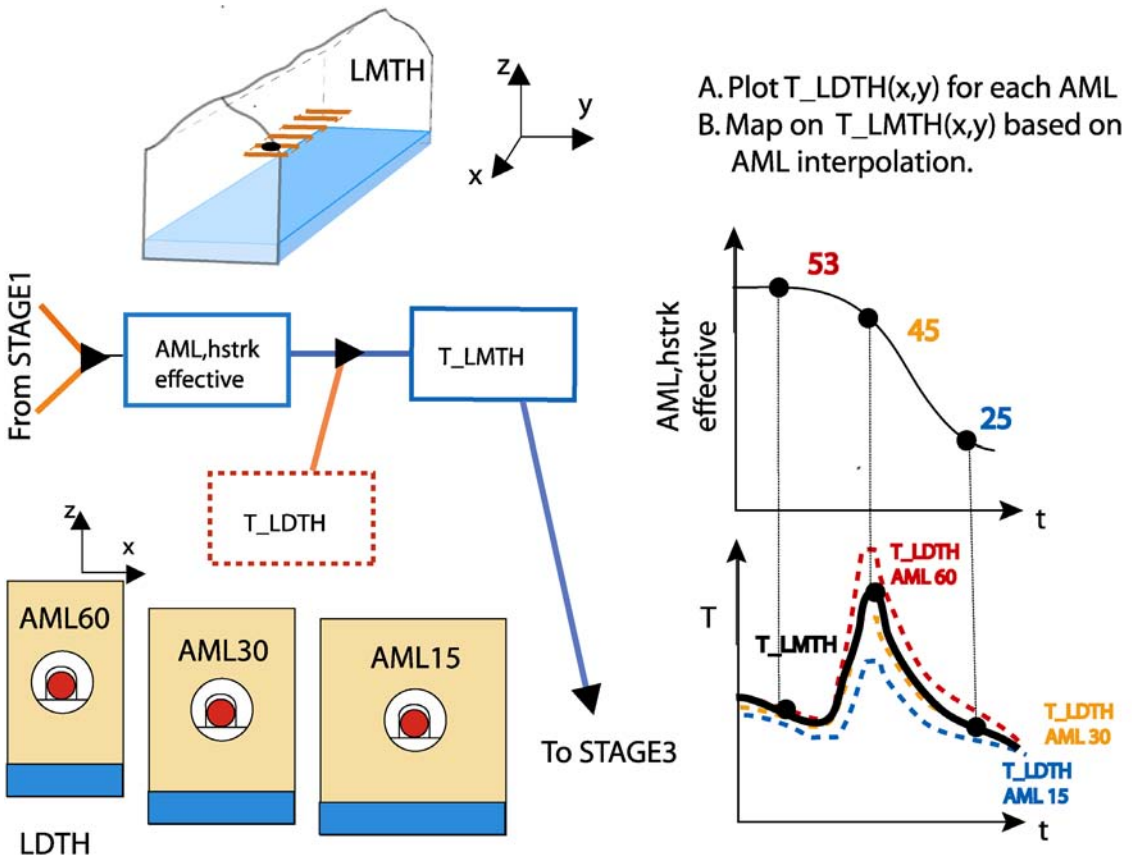

Figure IX-4. MSTHM Stage 2 involves the interpolation of the LMTH-model temperature T_LMTH from the variable AMLhstrk,eff and the family of LDTH-submodel temperatures T_LDTH.

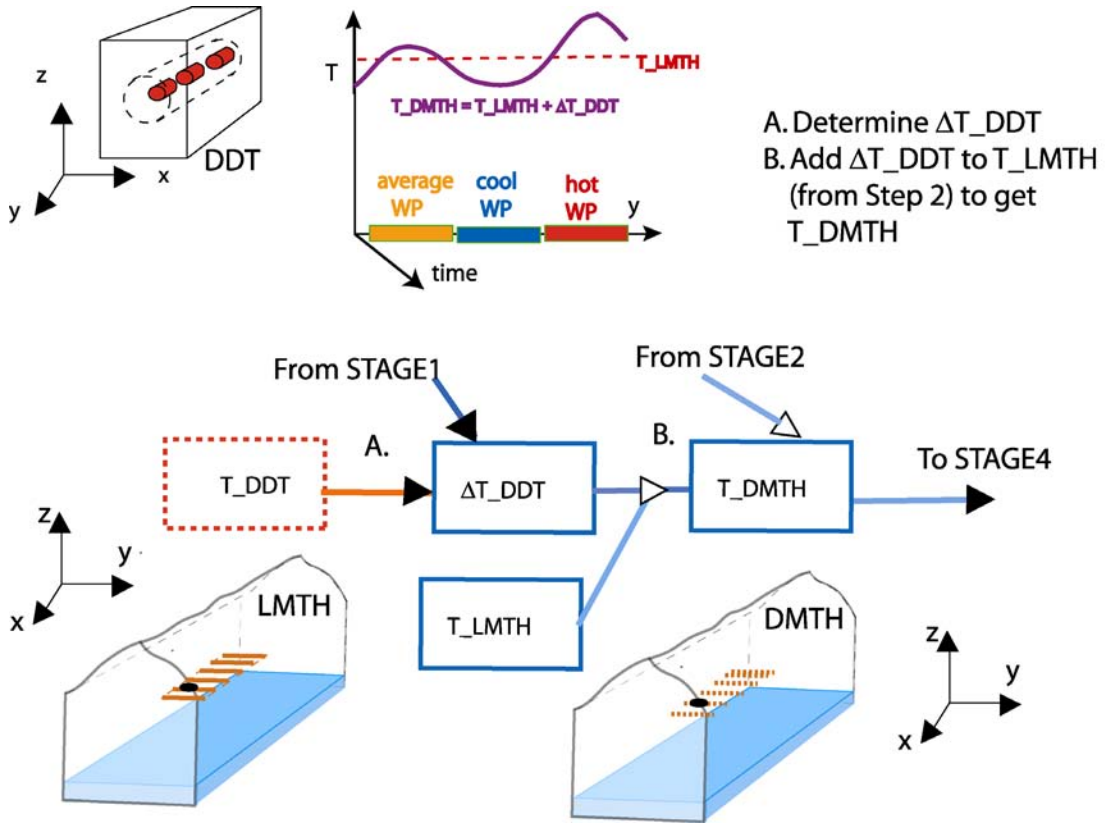

Figure IX-5. MSTHM Stage 3 involves the calculation of the DMTH-model temperature T_DMTH from the LMTH-model temperature T_LMTH and DDT-submodel temperature T_DDT.

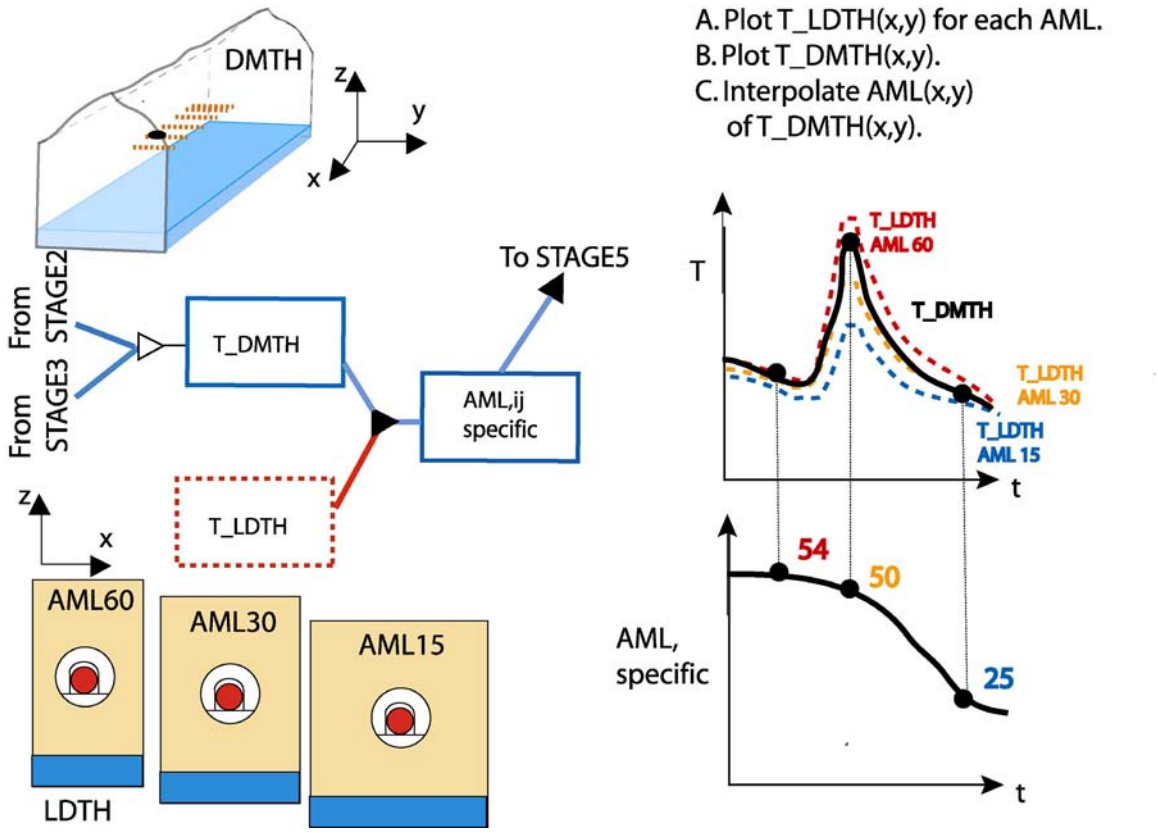

Figure IX-6. MSTHM Stage 4 involves the interpolation of the variable AMLspecific from the DMTH-model temperature T_DMTH and the family of LDTH-submodel temperatures T_LDTH.

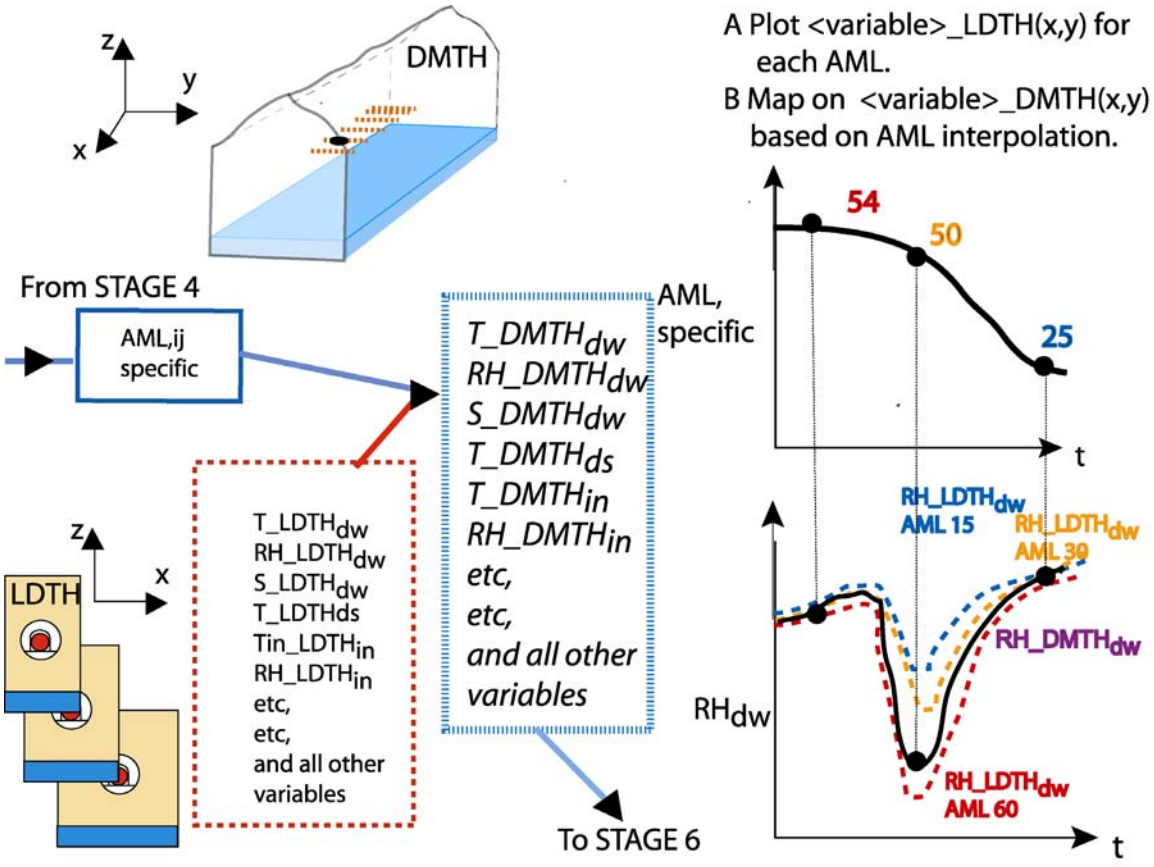

Figure IX-7. MSTHM Stage 5 involves the determination of each hydrologic variable (e.g., *RH*) using the variable AML, specific and the corresponding family of LDTH-submodel hydrologic variable values.

INTENTIONALLY LEFT BLANK